



# Measurement of the muon neutrino cross section through charged-current interactions and search for Lorentz invariance violation at the T2K experiment

Benjamin Quilain

## ► To cite this version:

Benjamin Quilain. Measurement of the muon neutrino cross section through charged-current interactions and search for Lorentz invariance violation at the T2K experiment. High Energy Physics - Experiment [hep-ex]. Ecole polytechnique X, 2014. English. NNT : . tel-01413989

**HAL Id: tel-01413989**

**<https://polytechnique.hal.science/tel-01413989>**

Submitted on 12 Dec 2016

**HAL** is a multi-disciplinary open access archive for the deposit and dissemination of scientific research documents, whether they are published or not. The documents may come from teaching and research institutions in France or abroad, or from public or private research centers.

L'archive ouverte pluridisciplinaire **HAL**, est destinée au dépôt et à la diffusion de documents scientifiques de niveau recherche, publiés ou non, émanant des établissements d'enseignement et de recherche français ou étrangers, des laboratoires publics ou privés.

# Measurement of the muon neutrino cross section through charged-current interactions and search for Lorentz invariance violation at the T2K experiment

Neutrino oscillation

PHD THESIS

dissertation submitted and defended in public the 18<sup>th</sup> December 2014 for the degree of

Doctorat de l'École polytechnique  
Spécialité physique des particules

by


Benjamin QUILAIN

## Dissertation committee :

Jury president	: Tsuyoshi NAKAYA
Thesis referee	: Jose BUSTO
Thesis referee	: Marcos DRACOS
Examiner	: Michel GONIN
Examiner	: Michel GUIDAL
Examiner	: Antonin VACHERET
Thesis director	: Olivier DRAPIER

---

# Acknowledgments

 E travail de thèse présenté dans ce manuscrit a été la partie émergée de l’iceberg qu’ont constitué ces trois années de thèse. Celles-ci ont été l’occasion de nombreuses découvertes, dont les facettes multiples ont été évidemment d’ordre scientifique, mais également l’occasion d’une introspection propre à tout travail solitaire. Le travail quotidien qu’implique toute recherche amène son lot d’aventures qui, s’il est toujours intrigant et passionnant, jette également souvent l’explorateur dans des difficultés qu’il n’est pas toujours aisé de surmonter. Dans nombre de cas, il m’a été donné la possibilité de découvrir seul les façons de maintenir le cap malgré les vents contraires, qui est un apprentissage naturel allant de pair avec le travail de recherche. Cependant, bon nombre de situations m’ont également enseigné l’impossibilité de surmonter seul la totalité des obstacles et m’ont amené à prendre conscience de la chance que j’ai pu avoir de pouvoir compter sur d’inestimables compagnons de route. Leur soutien et leur aide ont parfois pris la forme d’actions explicites qui m’ont sauvé des flots, mais parfois aussi, d’un travail de l’ombre accompli sur la durée qui, s’il est plus difficilement perceptible pendant la traversée, a été l’élément essentiel qui a permis à cette aventure d’atteindre les rives opposés. Ainsi, j’aimerais rendre justice à ces personnes au travers de ces maigres remerciements, qui seront de toute façon, trop courts.

En premier lieu, j’aimerais adresser mes remerciements à mon directeur de thèse, Olivier DRAPIER. D’abord, pour la confiance qu’il m’a accordée en me donnant une grande liberté dans la conduite de mes recherches. Cela a été essentiel à la maturation des idées qui sont ici présentées, mais également dans la découverte des différentes facettes qui constituent le quotidien de la recherche. Je le remercie d’avoir patiemment veillé sur mon travail, avec distance mais aussi une grande attention, dont les formes les plus explicites ont été les soirées prolongées lors de la rédaction de ce manuscrit, ou la construction du banc test qui y est présenté. L’occasion m’est aussi donné de le remercier d’avoir partagé avec moi sa vision intuitive de la physique, qui m’a tantôt permis de saisir davantage l’essence d’un problème, tantôt jeté des ponts entre des solutions similaires que nous avons pu développer pour un problème commun (l’unfolding par exemple). Sa capacité à instantanément saisir les contraintes clefs d’un problème, en particulier expérimentales, ont été l’occasion d’un apprentissage constant pour un étudiant au savoir très théorique. Enfin, je remercie Olivier pour son soutien permanent, sa gentillesse et son amitié.

J’aimerais également remercier Michel GONIN pour m’avoir m’a accueilli dans son groupe de recherche. Après avoir principalement étudié la physique théorique, je souhaitais faire de la physique expérimentale pour apercevoir ce qu’il se passait de l’autre côté du voile. Je remercie Michel de m’avoir donné l’opportunité de soulever un coin de ce dernier, et de m’avoir convaincu de le faire au travers de la physique des neutrinos en particulier avec le détecteur INGRID. Le nombre de personnes restreint travaillant sur ce détecteur m’a donné une grande autonomie, me permettant de découvrir un large spectre de la physique expérimentale, alternant les tâches “hardwares” ou “softwares”. Je tiens à le remercier également pour son enthousiasme et sa motivation sans faille, qui permettent d’insuffler un perpétuel élan aux projets qu’il dirige ainsi qu’aux personnes qui l’entourent. Enfin, il m’est ici donné l’occasion de remercier Michel, mais aussi Olivier, pour avoir constamment anticipé et retiré bon nombres d’épines sur ma route en s’occupant sans rechigner des tâches moins gratifiantes qu’implique la recherche, et cela a été essentiel dans l’aboutissement de cette thèse.

Durant ces trois années, j’ai eu enfin le plaisir de partager mon bureau avec Thomas MUELLER. J’aimerais d’abord le remercier pour les nombreux enseignements qu’il m’a dispensés, que ce soit en

---

physique des neutrinos ou dans l'utilisation avancée du C++ ou du FORTRAN. Cela a été une grande chance que de pouvoir discuter avec lui, tant nos approches de la physique étaient différentes, l'une théorique, l'autre expérimentale. Finalement, je pense que nous sommes parvenus à la fois à une bien meilleure compréhension, ainsi qu'à attirer l'autre chacun de l'autre côté. Par ailleurs, je le remercie de son aide et son soutien en toutes circonstances, et du temps passé ensemble que ce soit sur les plateaux de région parisienne, sur les sommets alpins ou dans les diverses contrées du Japon.

Au sein du LLR, j'ai également pu compter sur plusieurs chercheurs en dehors du groupe neutrino avec lesquels j'ai pu naturellement avoir de nombreuses interactions, qui ont été essentielles durant ces trois années. Parmi ceux-ci, j'aimerais particulièrement remercier Frédéric FLEURET et Pascal PAGANINI. S'il est nécessaire de faire un court résumé qui ne rendra pas justice à l'aide qu'ils m'ont apportée, je remercie Frédéric pour m'avoir fait découvrir la physique des ions lourds dans ses multiples aspects, pour nos discussions à son sujet, mais également pour ses conseils toujours avisés ayant résolu, clarifié ou enrichi bon nombre de mes travaux. S'il fallait choisir un exemple parmi d'autres, l'étude d'asymétrie de lumière détaillée dans le Chapitre 3 est née des nombreuses discussions que nous avons pu avoir. J'aimerais sincèrement remercier Pascal pour m'avoir constamment permis d'approfondir ma compréhension de la physique, et plus particulièrement, en théorie des champs. Son enthousiasme, son questionnement perpétuel et son intuition pour y trouver des réponses ont rendu cet exercice fascinant, et je regretterai ces discussions à présent que cette page se tourne. J'aimerais également lui faire part de ma gratitude pour son soutien, ainsi que sa capacité à trouver la solution aux nombreux problèmes que je suis venu lui soumettre, d'ordre scientifique ou non.

Je ne peux pas non plus oublier de remercier tous les anciens et les modernes du groupe neutrino, Christophe BRONNER, Joao Pedro Athayde Marcondes DE ANDRE, James IMBER et Margherita BUIZZA-AVANZINI pour avoir donné vie à ce groupe. En particulier, je remercie Christophe et JP d'avoir partagé leurs expériences et conseils précieux respectivement à propos des détecteurs INGRID et Super-Kamiokande. J'aimerais aussi remercier Daniel SUCHET pour son enthousiasme et sa curiosité que je partage, qui ont suscité de nombreuses discussions allant de la physique des neutrinos à celle des atomes froids, en passant par le boson de Higgs. Pour des raisons similaires, je remercie Matthieu LICCIARDI d'être venu réaliser son stage sur INGRID qui a abouti à de nombreuses interactions enrichissantes autant au sujet de la physique théorique qu'expérimentale.

Enfin, si ces trois années au LLR ont été si profitables, c'est également en grande partie grâce à l'environnement de travail exceptionnellement stimulant dont j'ai pu bénéficier. Ainsi, j'aimerais remercier chaleureusement Jean-Claude BRIENT pour m'avoir permis de réaliser cette thèse dans son laboratoire. En outre, j'adresse mes remerciements à l'intégralité du service administratif, et en particulier, à Thu BIZAT, Elodie DUBOIS et Brigitte MAROSQUESNE pour leur aide dans l'accomplissement de ces tâches quotidiennes qui ont rendu mon travail bien plus aisé, tâches administratives auxquelles je rechange le plus. Je remercie le service mécanique et en particulier, Alain BONNEMAISON et Oscar FERREIRA, dont l'expérience dans la conception des détecteurs INGRID et WAGASCI a été des plus enrichissantes tant ce domaine m'était inconnu. J'aimerais remercier également le service électronique, et en particulier Rémi CORNAT, Franck GASTALDI et Sébastien RATEAU autant pour leur pédagogie dans l'explication de concepts électroniques qui m'étaient étrangers, que pour leur aide dans la réalisation du banc test de la diaphonie entre scintillateurs (Chapitre 4). Enfin, je tiens à remercier le service informatique, et en particulier Eric BEYER, pour toute l'aide dont j'ai pu bénéficier.

Malgré la brièveté de ces lignes, j'aimerais remercier chaleureusement tous les physiciens du laboratoire avec qui j'ai pu échanger, et en particulier Louis KLUBERG, Denis BERNARD, Christophe OCHANDO, Yves SIROIS et Philippe BUSSON. Enfin, je remercie tout particulièrement les étudiants en thèse et en post-doc au LLR, avec qui j'ai pu partager les joies et aléas du travail de thèse, et en particulier Alice, Nadir, Yacine, Ivo, Thomas(-nino), Nicolas, Luca, Hélène, David, Jonathan, Emilien et Olivier.

During this thesis, I had the opportunity to participate in two large collaborations, the T2K and SK collaborations. I would like to thank first the SK collaboration, and in particular, SUZUKI Yoichiro

---

and SHIOZAWA Masato for allowing me to use the cone generator data and stay at Mozumi to work on the corresponding analysis. Though I was not a SK collaborator, many researchers brought me a tremendous help by sharing their experiences as if I were, and I would like to express my sincere gratitude to all of them for such a warm welcome. In particular, I'm thankful to HAYATO Yoshinari for having supervised my stay at Mozumi. I would like to express my thanks to MINE Shunichi for allowing me to participate in the cone generator project, and the constant help he provided me thanks to his knowledge of the SK detector. I would like to thank him also for having allowed me to visit and discover the SK detector. Finally, I would like to express special thanks to MORIYAMA Shigetaka for his very precious help throughout the whole cone generator project, for having shared his vast experience on SK calibration, and provided many comments that drastically improved the cone generator analysis.

Second, I would like to thank the T2K collaboration, and especially, the INGRID group. The INGRID and PM detectors are projects held in collaboration between the LLR and the Kyoto University. During these three years, I had the chance to benefit from the help and experience of many Kyoto University members. I first would like to thank NAKAYA Tsuyoshi for having allowed me to stay three months in Tokai to work together with his group. This on-site experience was one of the most fruitful and stimulating experience in my thesis, and led me to decide to continue my research in the Kyoto University group. I would like to express my sincere thanks to Professor NAKAYA for having offered me this possibility through a post-doctoral position. I would like to thank MINAMINO Akihiro for his leadership in the INGRID project and his constant help during my stay in Tokai. And, I would like to thank KIKAWA Tatsuya for his help on the analyses we were performing on INGRID and the PM, and for his tremendous work on the reconstruction tools.

As for the entire T2K collaboration, I would like to thank everyone I worked with and had the chance to benefit from their experience, help and comments. I would like to express my thanks to Francesca DI LODOVICO, Roberto SACCO, Alex CLIFTON for their constant and precious help on the Lorentz violation analysis performed with INGRID. I would like also to thank Marco ZITO and Claudio GIGANTI for having shared their experience, and the very fruitful discussions we had. I would like to thank especially Claudio for his help on the Lorentz violation search during our stay in Tokai. My gratitude is also expressed to Jacques DUMARCHEZ for having kindly allowed me to find a free home in Japan during my long term stays. And in this small village of Tokai, I would like to thank everyone with which shared some bonds that were crucial to make it a nice experience: Claudio, Javi, Stefania, Laura, Megan, Andy, Linda...

I would like to express my sincere gratitude to my dissertation committee, NAKAYA Tsuyoshi, Jose BUSTO, Marcos DRACOS, Michel GONIN, Michel GUIDAL and Antonin VACHERET for having read this long manuscript. I would like to thank them a lot for having shared their comments, and addressed some questions that helped to improve this document quality. In particular, I thank them for coming from different shores and having shared their experiences on different aspects of high energy physics with me.

Pour finir, j'aimerais remercier infiniment mes parents, mes deux soeurs, mon frère cadet ainsi que Laure qui m'ont apporté leur soutien inconditionnel, m'accompagnant dans les nombreux tumultes qu'occasionne un travail de thèse, sans pour autant pouvoir profiter des accalmies et des bonheurs que peut procurer ce dernier. Je les remercie de cet espace de liberté qu'ils m'ont toujours donné, pour cette absence de projection forcée m'ayant permis d'osciller à ma guise bien qu'ils ne puissent jamais en observer le résultat. Et, j'aimerais y associer ma famille et mes amis proches que l'espace m'empêche ici de citer explicitement.

---

# Contents

<b>1</b>	<b>Neutrinos in the Standard Model and beyond</b>	<b>5</b>
1.1	The Standard Model . . . . .	5
1.1.1	Generation of bosons and fermions masses . . . . .	10
1.1.2	Neutrino masses in the extension of the Standard Model . . . . .	14
1.1.3	Limits of the Standard Model . . . . .	18
1.2	Neutrino oscillations in vacuum . . . . .	18
1.2.1	The general theory of oscillations . . . . .	18
1.2.2	Three flavour neutrino oscillation in vacuum . . . . .	22
1.2.3	Two-flavour approximation in the three neutrino case . . . . .	24
1.3	Three-flavour neutrino oscillation in matter . . . . .	27
1.3.1	General oscillation in matter . . . . .	27
1.3.2	The neutrino mass hierarchy . . . . .	32
1.3.3	The matter effects in T2K . . . . .	33
1.4	Determination of the PMNS matrix . . . . .	33
1.4.1	The solar neutrino sector . . . . .	34
1.4.2	The atmospheric neutrino sector . . . . .	39
1.4.3	The reactor neutrino sector before T2K starts . . . . .	42
1.4.4	Current knowledge on $\theta_{13}$ out of T2K . . . . .	45
<b>2</b>	<b>The Tokai to Kamioka experiment</b>	<b>47</b>
2.1	Physics motivations . . . . .	47
2.2	The T2K experiment . . . . .	48
2.2.1	The off-axis technique . . . . .	48
2.2.2	The Neutrino Beam . . . . .	51
2.2.3	Near detectors . . . . .	57
2.2.4	The Super-Kamiokande far detector . . . . .	64
2.3	Neutrino appearance search at T2K . . . . .	67
2.3.1	The neutrino flux prediction . . . . .	67
2.3.2	The near detector constraints . . . . .	69
2.3.3	Oscillations at far detector . . . . .	70
<b>3</b>	<b>Experimental study of light scattering in Super Kamiokande using single cone generator data</b>	<b>75</b>
3.1	Introduction . . . . .	75
3.2	The CG vessel . . . . .	76
3.3	The CG MC . . . . .	78
3.3.1	Principle . . . . .	78
3.3.2	Photon flux measurement . . . . .	78
3.3.3	Using photon flux data to generate the photon distribution input for SKDETSIM . . . . .	87
3.4	Data Taking in SK . . . . .	88
3.4.1	Description of the setup inserted in SK and the data taking . . . . .	88
3.4.2	Measurement of the CG vessel position and direction in SK . . . . .	89
3.5	Single cone data analysis . . . . .	93

3.5.1	Basic analysis method . . . . .	93
3.5.2	Vertical vertex and horizontal directional dependence of charge profile comparison between data and MC . . . . .	94
3.5.3	Study of the disagreement between data and MC in the charge profile comparison	97
3.5.4	Summary of the single cone analysis . . . . .	104
3.6	Charge asymmetry of the CG setup . . . . .	105
3.6.1	Charge asymmetry of CG in the SK detector . . . . .	105
3.6.2	Charge asymmetry hypothesis test in photon flux data . . . . .	110
3.7	Conclusion of the single cone analysis in SK . . . . .	118
<b>4</b>	<b>Charge calibrations of the INGRID and PM detectors</b>	<b>119</b>
4.1	Introduction to INGRID and PM detectors detection process . . . . .	120
4.1.1	Scintillator . . . . .	120
4.1.2	Wavelength shifting fiber (WLS) . . . . .	121
4.1.3	Multi-pixel photon counter (MPPC) . . . . .	121
4.1.4	Electronics and analog-to-digital converters (ADC) . . . . .	122
4.2	Charge response calibration . . . . .	123
4.3	Calibration results using INGRID data . . . . .	126
4.3.1	Neutrino event and sand muon selections . . . . .	126
4.3.2	Low and high gain channel charge ranges . . . . .	128
4.3.3	ADC non linearity calibration validation . . . . .	131
4.3.4	Birks saturation correction . . . . .	134
4.3.5	Optical cross-talk between the SciBar type scintillators . . . . .	134
4.4	Scintillator cross-talk measurements . . . . .	140
4.4.1	Scintillator cross-talk measurements . . . . .	140
4.5	T2K charge stability with time . . . . .	147
<b>5</b>	<b>Measurement of the muon neutrino <math>CC0\pi</math> double differential cross section</b>	<b>149</b>
5.1	Cross-sections and interaction models . . . . .	149
5.1.1	Introduction . . . . .	149
5.1.2	Interactions with a quark . . . . .	151
5.1.3	Free nucleon . . . . .	152
5.1.4	Interaction with a nucleus . . . . .	154
5.1.5	Meson exchange currents . . . . .	160
5.2	$CC0\pi$ signal definition for a model independent study . . . . .	162
5.3	The $CC0\pi$ selection . . . . .	163
5.3.1	Muon particle identification . . . . .	166
5.3.2	$CC0\pi$ selection . . . . .	174
5.4	Cross section analysis method . . . . .	180
5.4.1	Number of $CC0\pi$ selected events . . . . .	183
5.4.2	Efficiency . . . . .	184
5.4.3	Neutrino flux prediction . . . . .	184
5.4.4	Number of target nucleons . . . . .	184
5.4.5	$p_\mu$ and $\theta_\mu$ binning . . . . .	186
5.5	The Bayesian unfolding method . . . . .	186
5.5.1	Introduction to unfolding and motivations . . . . .	186
5.5.2	Unfolding method construction . . . . .	187
5.6	Systematic and statistical errors . . . . .	193
5.6.1	Statistical error estimation . . . . .	194
5.6.2	Flux related systematics . . . . .	194
5.6.3	Detector systematics . . . . .	197
5.6.4	Cross section model systematics . . . . .	207
5.6.5	Summary . . . . .	210
5.7	Cross section measurement results . . . . .	213

5.7.1	The double differential cross section result . . . . .	213
5.7.2	The spectral function model . . . . .	214
5.7.3	The axial mass fit . . . . .	219
5.7.4	Effect of meson exchange currents . . . . .	219
5.8	Conclusions . . . . .	221
<b>6</b>	<b>Search for Lorentz invariance violation at the T2K near detector</b>	<b>223</b>
6.1	Introduction . . . . .	223
6.1.1	The Standard Model Extension and Lorentz invariance spontaneous symmetry breaking . . . . .	224
6.1.2	Lorentz violation in neutrino oscillations . . . . .	225
6.1.3	Application to short baseline compared to standard oscillation . . . . .	227
6.1.4	The Lorentz violation search in INGRID . . . . .	229
6.2	The INGRID selection . . . . .	230
6.2.1	The neutrino baseline . . . . .	232
6.2.2	The muon neutrino selection . . . . .	232
6.2.3	Signal sample . . . . .	241
6.3	Corrections and systematic uncertainties . . . . .	241
6.3.1	INGRID detector effects . . . . .	242
6.3.2	Neutrino beam effects . . . . .	247
6.3.3	Residual rate correction . . . . .	250
6.3.4	Summary . . . . .	252
6.4	The discrete Fourier transform . . . . .	252
6.4.1	Sidereal time variation thresholds . . . . .	254
6.4.2	Sensitivity on the SME parameters . . . . .	256
6.4.3	Day and night LSP distributions . . . . .	258
6.4.4	Results . . . . .	259
6.5	The likelihood method . . . . .	261
6.5.1	Motivations . . . . .	261
6.5.2	Results . . . . .	263
6.6	Energy dependent study . . . . .	263
6.6.1	INGRID module energy . . . . .	263
6.6.2	LV energy dependent study . . . . .	264
6.7	Future sensitivity at T2K near detectors . . . . .	264
<b>A</b>	<b>Cone generator systematic errors and tables</b>	<b>I</b>
A.1	Systematic error estimation . . . . .	I
A.1.1	Evaluation of systematic errors for SK data set . . . . .	I
A.1.2	Evaluation of systematic errors coming from photon flux measurement . . . . .	III
<b>B</b>	<b>Timing calibration of the INGRID detector</b>	<b>XI</b>
B.1	TFB mean time difference: . . . . .	XI
B.2	Time walk: . . . . .	XI
<b>C</b>	<b>Calculation of the neutrino cross section on a free quark</b>	<b>XIII</b>
C.1	Basics of the cross section . . . . .	XIII
C.2	Calculation of the amplitude . . . . .	XV
C.3	$ M ^2$ energy dependency . . . . .	XVIII
C.4	Cross section dependency on $q^2$ . . . . .	XIX
<b>D</b>	<b>Calculation of the neutrino cross section on a nucleon</b>	<b>XXIII</b>
<b>E</b>	<b>Charge corrections and hit matching</b>	<b>XXVII</b>
E.1	dx correction . . . . .	XXVII
E.2	Correction of the attenuation in the optical fiber . . . . .	XXVII

<b>F</b>	<b>PM unfolding method validation</b>	<b>XXXI</b>
<b>G</b>	<b>Likelihood tests for the search of Lorentz invariance violation</b>	<b>XXXIX</b>
G.1	The tests of the one parameter fit . . . . .	XXXIX
G.2	The five parameter fit . . . . .	XL
G.2.1	Flat toy experiments . . . . .	XL
G.2.2	Signal toy experiments . . . . .	XLI

## Glossary

**T2K:** The Tokai to Kamioka experiment, a long-baseline experiment studying neutrino oscillation through the production of muon neutrinos or anti-neutrinos.

**INGRID:** Interactive Neutrino GRID which is the on-axis near detector of T2K.

**PM:** The Proton Module, an INGRID-like module where the iron layers are removed.

**SK:** The Super-Kamiokande detector, which is the far detector from the T2K experiment.

**POT:** The number of Protons On Target. Number of protons that hit the T2K target.

**CG:** The Cone Generator setup, a device that generates a ring-shaped light pattern.

**MPPC:** Multi-Pixel Photon Counter which are the photo-detectors used in the T2K near detectors to measure the charge deposition of a particle going through a scintillator.

**TFB:** Trip-T front end boards which are the electronics card used in the T2K near detector.

**ADC:** Analog-to-digital converters that are used to convert the MPPC output into a digital number that can be stored in a PC.

**p.e:** The number of photo-electrons, a unit to measure the charge deposit collected and converted in electrons by the MPPC.

**CC:** Interaction occurring through the exchange of a charged current (a charged  $W$  boson).

**NC:** Interaction occurring through the exchange of a neutral current (a  $Z^0$  boson).


**CC0 $\pi$ :** A CC interaction without any pion emission out of the interacting nucleus.

**SME:** The Standard Model Extension, which extend the Standard Model of particle physics by adding possibility of spontaneous symmetry breaking of the Lorentz invariance.

**LV:** The Lorentz invariance violation, which is predicted by the SME.



# Introduction

HE neutrino is a very singular particle among the known elemental constituents. It is the only matter constituent that interacts through the sole weak interaction. Its story started in 1896, when Becquerel accidentally discovered the radioactive decays during his researches on phosphorescence phenomena [1]. In 1914, Chadwick measured a continuous spectrum of the electrons produced in a radioactive  $\beta^-$  decay, which seemed to violate both energy, momentum and spin conservations [2]. Different solutions were investigated, among which possible violations of the energy, momentum and spin conservations. In 1930, Pauli postulated the existence of an unseen particle to “save” these symmetries, the neutrino [3]. This particle should have a spin 1/2, a negligible mass compared to the proton and weakly interact with matter since it had not been observed so far. In particular, this particle should carry no electric charge to be invisible by all the existing experiments. In 1934, Fermi invented the weak interaction theory to describe the  $\beta$  decay and incorporated the neutrino [4].

This “ghost particle” has been only observed in 1956, by Reines and Cowan observing the antineutrino flux produced by the Savannah River reactor [5]. In 1962, a second neutrino type was observed at Brookhaven [6], which highlighted the existence of electron and muon neutrinos associated to the charged electron and muon weak interactions. The existence of a third neutrino flavour, the tau neutrino associated to the tau particle, has been observed later at the DONUT experiment in 2000 [7]. The LEP experiments have shown that only three neutrino flavours were produced in the  $Z^0$  boson decay [8], which implies that the three  $\nu_e$ ,  $\nu_\mu$  and  $\nu_\tau$  are the only active and light neutrinos.

In the late 1960s, Davis observed the solar neutrino flux in the Homestake mine [9]. A neutrino deficit was observed as compared to the predictions of the Sun Standard Model. This discrepancy is known as the “Solar neutrino anomaly”. Among other solutions, a possible explanation was the disappearance of the observed  $\nu_e$  due to an oscillation into other neutrino flavours. This implies that the neutrino should have a mass, which was not necessary in the original particle Standard Model. Twenty years later, the Kamiokande and IMB experiments observed also a discrepancy between the observed and expected flux of neutrino produced in the Earth’s atmosphere. It was in 1998 that the Super-Kamiokande experiment proved that this atmospheric neutrino anomaly was due to their oscillations [10]. In 2001, the SNO collaboration has definitely shown that the neutrino oscillation solves the Solar neutrino anomaly, through the observation of the entire flavour content of the Sun neutrino flux [11]. The neutrino oscillation is parameterised by six quantities: three mixing angles  $\theta_{12}$ ,  $\theta_{23}$  and  $\theta_{13}$ , two independent squared mass differences ( $\Delta m_{21}^2$ ,  $\Delta m_{32}^2$ ) and one CP violation phase  $\delta_{CP}$ . The measurements through solar, atmospheric, reactor and accelerator experiments have measured the four parameters  $\theta_{12}$ ,  $\theta_{23}$ ,  $\Delta m_{21}^2$ ,  $|\Delta m_{32}^2|$  (which sign is still unknown) but only set an upper limit on the  $\theta_{13}$  mixing angle at the beginning of this thesis work. This measurement was crucial since a non zero  $\theta_{13}$  value is necessary for any CP violation to happen in neutrino oscillation. The Tokai to Kamioka (T2K) experiment has been designed primarily in order to measure this last remaining unknown mixing angle  $\theta_{13}$ , and possibly constrain the  $\delta_{CP}$  parameter. We will discuss in this thesis how the constraints on this mixing angle, but also on the CP violation search, are affected by the cross section model uncertainties.

We will introduce the Standard Model of particle physics in order to present the neutrino specificities in chapter 1. In this chapter, we will especially describe the neutrino oscillation framework, along with the status of the oscillation measurements before T2K started. In the second chapter, we will describe the whole T2K experiment. In particular, we will focus on the on-axis near detector

INGRID, that we have mainly used in this thesis work. We will also provide a description of the T2K far detector, Super-Kamiokande, a calibration of which has been also performed in this work. We will finally introduce T2K oscillation measurements and highlight that the current main systematic error comes from cross section models.

In the third chapter, we will present the calibration study we have done with the Super-Kamiokande detector. This study is conducted using a device called “the cone generator”, which we have first studied before proceeding to a Super-Kamiokande detector calibration. This setup was constructed prior to this thesis, with the goal to mimic the  $\pi^0$  induced Cherenkov rings to study them in the Super-Kamiokande detector.

In the fourth chapter, we have conducted a charge calibration of the on-axis T2K detector INGRID in order to identify the secondary particles that are produced in the interaction of the neutrino in the detector. In particular, the charge deposition was not calibrated before, and is compulsory to perform the analyses we will present in chapters 5 and 6.

We have used this calibration in chapter 5 in order to conduct the first double differential cross section measurement at the on-axis T2K detector. We have especially studied the neutrino interaction through quasi-elastic charged current, which is the dominant interaction at the T2K energy and provides the largest systematic error in the oscillation analyses. In this chapter, we will first introduce the cross section model basics, in order to highlight the importance of cross section measurements based on final states of interactions. Secondly, we will present the particle identification we performed to identify the final state particles, together with the determination of the lepton momentum in this non-magnetised detector. We will then present the cross section measurement and discuss the result in the light of the current neutrino interaction models.

In the sixth chapter, we will present the Lorentz invariance violation search we performed at the T2K on-axis detector. The Lorentz invariance violation is predicted in the theories beyond the current particle Standard Model. We will introduce in this chapter the very basics of the impact of such a violation on the neutrino flux detected at the on-axis INGRID detector, and in particular, a time neutrino oscillation. We will then present the development we have done to separate the neutrino flavours at the near detector, and finally present the first Lorentz violation search at the T2K experiment.


# Chapter 1

## Neutrinos in the Standard Model and beyond

*What I see in Nature is a magnificent structure that we can comprehend only very imperfectly,  
and that must fill a thinking person with a feeling of humility.*

Albert Einstein

### 1.1 The Standard Model

 THE Standard Model of particle physics is the current theory that describes both the elementary matter constituents, the fermions, and their interactions through a unified field theory. In the current situation, four fundamental interactions are known: the strong, the electromagnetic, the weak and the gravitational interactions listed by decreasing intensities at low energy scales ( $E \ll 100$  GeV). The Standard Model is incomplete, since it only focuses on the first three interactions, but cannot describe gravitation with the same formalism. The Standard Model is essentially based on a surrounding Minkowsky spacetime ruled by the Lorentz symmetries. On top of the spacetime structure, the Standard Model assumes the existence of local symmetries, called “gauge symmetries”, whose generators are the vectors of the associated interactions. These mediator particles are called bosons. We will present an overview of the three interactions the Standard Model:

- The “strong” interaction (quantum chromodynamics, “QCD”) is described by the  $SU(3)_c$  gauge group. This group has eight generators, that are called gluons. By definition, these generators are the vectors of the strong interaction. Because of the  $SU(3)$  non abelian structure, its generators do couple to each other. The gluons are massless particles in the Standard Model. Associated to the three symmetries of this group, three quantities are conserved: the blue, red and green colours. The denomination of “strong” interaction comes from the high value of the coupling constant  $\alpha_S$ , compared to other interactions (see Table 1.1). Since  $\alpha_S \sim 1$ , the cross section estimation through perturbation theory is not as relevant as for other interactions. This is especially true in the confinement region limit ( $L \sim 10^{-15}$  m) where large  $\alpha_S$  values are involved. A treatment of the non perturbative regime can be undertaken using the lattice QCD theory [12].
- The quantum electromagnetic interaction (QED) is described by the  $U(1)_{QED}$  gauge group. It has only one generator, which correspond to the observed photon. Since  $U(1)$  has an abelian structure, the photon does not couple with other photons. Following Noether’s theorem, a conserved quantity is associated: the electric charge. Since all gauge theories are local by definition, the electric charge is imposed to be locally conserved by Noether’s theorem. The intensity of the electromagnetic interaction is ruled by the fine structure constant  $\alpha = \frac{e^2}{4\pi\epsilon_0\hbar c}$  (at the tree level) for a particle of electric charge  $e$  as the electron (see Table 1.1). As we will see, the  $U(1)$  description of the electromagnetic interaction is a part of a unified electroweak interaction, which is equivalent to electromagnetism at  $E \ll 100$  GeV, due to the mass of the weak vector bosons.

Interaction	Coupling constant	value
strong	$\alpha_S(m_Z)$	$\sim 0.1185$
electromagnetic	$\alpha = e^2/4\pi\epsilon_0\hbar c$	$\sim 1/137.04$
weak	$G_F/(\hbar c)^3$	$\sim 1.1664 \times 10^{-5} \text{ GeV}^{-2}$
gravitation	$G_N/(\hbar c)$	$\sim 6.7084 \times 10^{-39} (\text{GeV}/c^2)^{-2}$

Table 1.1: Values of the coupling constants for the four known fundamental interactions. One notices that the weak and gravitational coupling constants have dimensions. Values extracted from [13].

1 <sup>st</sup> generation	Fermions			bosons	
	2 <sup>nd</sup> generation	3 <sup>rd</sup> generation		gauge	Higgs
$\begin{pmatrix} u \\ d \end{pmatrix}$	$\begin{pmatrix} c \\ s \end{pmatrix}$	$\begin{pmatrix} t \\ b \end{pmatrix}$		8 $g$	
				$\gamma$	$h^0, h^+$
$\begin{pmatrix} \nu_e \\ e \end{pmatrix}$	$\begin{pmatrix} \nu_\mu \\ \mu \end{pmatrix}$	$\begin{pmatrix} \nu_\tau \\ \tau \end{pmatrix}$		$Z^0, W^+, W^-$	

Table 1.2: The particle scheme in the Standard Model.

- The electroweak interaction (EW) is described by the  $SU(2)_L \times U(1)_Y$  gauge group. It has four generators: the  $W^1, W^2, W^3$  bosons for  $SU(2)_L$  and the  $B$  boson for  $U(1)_Y$ . As in the case of gluons, the  $W$  bosons can couple to each others because of  $SU(2)$  non abelian structure. We will see that the effective vector bosons are not strictly the four mentioned, but stem from a rotation of them in the four boson space. The effective vector bosons are massive, which limits their self-coupling at low energy ( $E \ll M_W$ ) unlike the strong interaction. The three associated conserved quantum numbers are the weak isospin norm  $I$ , its third components  $I_3$  and the hypercharge  $Y$ . We will see that the electromagnetic charge can be deduced and constructed from  $Y$  and  $I_3$ , since the electroweak interaction gathers the description of both electromagnetic and weak interactions.

Therefore, each particle has a set of quantum numbers that describes how it transforms under the Lagrangian gauge symmetries, *i.e* how it couples to the different interactions. On top of that, the particles and their interactions take place in a flat Minkowsky spacetime. It implies that each particle also possesses a spin and momentum that describe how the particle transform under spacetime transformations (respectively rotations and boosts). The vector bosons are integer spin particles, and follow to the Bose-Einstein statistics that allows them to occupy the same quantum states. A contrario, the fermions are half-integer spin particles and obey the Fermi-Dirac statistics which is ruled by the Pauli exclusion principle. At the present time, twelve fermions have been discovered. The fermions are themselves arranged in two categories: the quarks which are subject to the strong interaction, and the leptons which are not. Finally, the particles in the sub families are gathered in weak isospin doublet, to form what is called “generation” or “flavour”. Three generations are known both in the lepton and quark sectors (see Table 1.2).

A last piece is necessary in the Standard Model puzzle in order to generate the observed  $W, Z$  bosons and fermions masses, without breaking the  $SU(2)_L \times U(1)_Y$  Lagrangian symmetry. This is the Higgs boson. We will give further detail on particle mass generation in Section 1.1.1.

In the Standard Model, the neutrinos are the only particles that are only sensitive to the weak interactions. We will propose in this thesis a measurement of their cross sections in Chapter 5. Prior to this, we will first introduce in detail the underlying electroweak interaction, and introduce the neutrino oscillation phenomenon.

### Fermi’s theory of weak interactions

In 1934, Fermi introduced the weak interaction in order to explain the neutron decay ( $\beta^-$ ) [4]:

$$n \rightarrow p + e^- + \bar{\nu}_e \quad (1.1.1)$$

At this time, the neutrino had not been observed but introduced by Pauli to explain the continuous electron spectrum in this decay [14]. The interaction Lagrangian density was assumed to be “electromagnetic like”:

$$L = G_F(\bar{u}_p\gamma^\mu u_n)(\bar{u}_e\gamma_\mu u_{\nu_e}) \quad (1.1.2)$$

where the different  $u$  are the particle spinors and  $G_F$  is the Fermi coupling constant that replaces the electromagnetic charge in these new “weak interactions”. The term “weak” comes from this interaction cross section is smaller than for electromagnetic interactions at low energy ( $E \ll m_W = 80.385 \pm 0.015$  GeV) which is theoretically due to the lower value of  $G_F$  compared to electromagnetic constant  $e$  (see Table 1.1). In Fermi theory, interactions were assumed to be point-like. In reality, they can be described through the propagation of  $W^{+/-}$  bosons, which can be well approximated by a point-like interaction at low energy ( $E \ll m_W$ ) considering their large mass. This explains why the Fermi coupling constant has a dimension, since it contains both the actual dimensionless weak coupling constant ( $g_w$ ) and the W boson propagator which is approximated by a point-like interaction.

### Weak interactions (maximal) parity violation

In 1956, Lee and Yang [15] suggested that this weak interaction does not behave as the others under spatial parity transformation in order to solve the  $\theta - \tau$  puzzle. This puzzle corresponded to the observation of two particles having very similar properties (same mass and lifetime) but which decayed differently through the weak interaction. These particles are now known to be the very same charged kaons, that can decay through (positive kaon):

$$\theta^+ \rightarrow \pi^+ + \pi^0 \text{ and } \tau^+ \rightarrow \pi^+ + \pi^+ + \pi^-. \quad (1.1.3)$$

The two final states have opposite parities. The hypothesis of a similar particle that decays through an interaction that violates parity conservation was not obvious at that time. As all the other interactions were conserving parity, parity conservation was assumed to be an universal symmetry. Parity violation would indicate that the weak interaction distinguishes left from right, *i.e* different conclusions would emerge from an experiment and its image in a mirror.

In the very same year, the experimental evidence was shown by Wu’s experiment who observed the weak decay of a polarised  $^{60}\text{Co}$  nucleus [16]. Not only Wu confirmed the Lee and Yang hypothesis, but also tend to observe a maximal violation of the parity symmetry in weak interactions. Namely, if an interaction occurs, its mirror image is totally suppressed. More precisely, Wu has shown that the electrons emitted in  $^{60}\text{Co}$  decay populate the angular region corresponding to a negative helicity state (defined in following section). This has lead to re-formulate Fermi’s theory.

### The chirality of fermions

The weak interaction ability to discriminate between left and right now imposes to know the particle left or right nature (“handedness”). A new quantum number, the “chirality”, is therefore introduced for each particle. Two chirality states are possible: the left- (L) and right- (R) handed chiralities. The chirality is defined using two projectors  $P_L, P_R$  based on the  $\gamma^5$  Dirac matrix:

$$P_L = \frac{1}{2}(I - \gamma^5) \text{ and } P_R = \frac{1}{2}(I + \gamma^5). \quad (1.1.4)$$

The Dirac matrices commutation directly implies that  $P_L P_R \psi = 0$  (a left particle has no right component). It follows that a fermion field can be written with a left-only and right-only component:

$$\psi = \psi_L + \psi_R = P_L \psi + P_R \psi \quad (1.1.5)$$

Note that this number is not an “intrinsic” quantum number of the particle, *i.e* a Lorentz- and time-invariant quantity of the particle, as can be the charges that derive from gauge symmetry (electric

charge, isospin, colour...) applying Noether's theorem. The chirality transformation operates separately on the left and right fermions representation changing the fermion field:  $\psi_L \rightarrow e^{-i\gamma^5} \psi_L$  and  $\psi_R \rightarrow e^{i\gamma^5} \psi_R$ . The fermion mass term from the Dirac Lagrangian is:

$$L_D^{mass} = -\frac{m}{2} \bar{\psi} \psi = \frac{m}{2} (\bar{\psi}_L \psi_R + \bar{\psi}_R \psi_L) \quad (1.1.6)$$

since  $P_L P_R = 0$ . The mass term chirality transformation leads to a residual phase, showing that any massive fermionic particle has not a definite chirality: the mass mixes the right and left chirality states. Since the Lagrangian is not conserved, it implies that the chirality evolves with time for a free particle. However, one shows that the chirality operator commutes with the rotation and boost generators, which guarantee that the chirality is Lorentz-invariant.

It was tempting at that time to identify the particle handedness with its helicity. A particle helicity is given by its intrinsic angular momentum projection  $h = \frac{\vec{p} \cdot \vec{s}}{|\vec{p}|}$  with  $\vec{p}$  and  $\vec{s}$  the fermion momentum and spin. Applying the parity transformation, the helicity becomes:  $h_{\text{Mirror}} = \frac{-\vec{p} \cdot \vec{s}}{|\vec{p}|} = -h$  which makes the helicity an ideal candidate for the quantum number that would define handedness. However, the helicity is not Lorentz invariant in general: for a massive particle, one may always find a reference frame more boosted than the particle to observe a different momentum direction and a similar spin. This cannot be done with a massless particle, and one demonstrates that the chirality and helicity are the very same quantity in this case. As the weak interaction concerns not only massless particles, one absolutely wants it not to vary with the referential. Therefore, the weak interaction theory must be constructed with the chirality instead. However, the helicity is a useful quantum number since chirality cannot be directly observed. For the electrons of the Wu experiment ( $\sim 1$  MeV), their high energy compared to their mass tends to make them quasi ultra-relativistic and one can therefore identify the negative helicity states observed as left-handed chirality. For a massive particle, helicity and chirality are very distinct numbers: the first is time conserved for a free particle but is not Lorentz invariant while the latter is but is not conserved with time or through weak interaction.

### V-A structure of weak interactions

The Fermi interaction can be modified to take into account the experimental observation that weak interactions maximally violates parity. The observations having shown that only the left-handed particles (and right-handed antiparticles) couple with the weak interaction, the structure is simply changed to:

$$L = G_F (\bar{u}_p \gamma^\mu u_n) (\bar{u}_e \gamma_\mu u_{\nu_e}) \quad (1.1.7)$$

$$= G_F (\bar{u}_p \gamma^\mu \frac{1}{2} (I - \gamma^5) u_n) (\bar{u}_e \gamma_\mu \frac{1}{2} (I - \gamma^5) u_{\nu_e}) \quad (1.1.8)$$

This structure is called vector-axial ("V-A") due to the additional axial  $\gamma^\mu \gamma^5$  current to the vector  $\gamma^\mu$  current, the latter being the only one observed in the strong and electromagnetic interactions.

### Electroweak unification

In the 60s, Glashow, Salam and Weinberg have shown that the weak and the electromagnetic interactions can be described as effective low energy theories of a unified electroweak interaction. This interaction is based on the group symmetry  $SU(2)_L \times U(1)_Y$ . The original Standard Model electroweak Lagrangian is therefore composed of interactions transported by the three  $W$  bosons from  $SU(2)_L$  gauge group and the  $B$  boson from  $U(1)_Y$  gauge group. The  $W$  bosons couple the left-handed particles (and separately, right-handed antiparticles) with the  $g_w$  coupling constants, while the  $B$  boson does not discriminate between chirality and couple the particles with the coupling constant  $g_B$ .

We'd like then to deduce the electromagnetic coupling constant  $\alpha$ , the electric charge and the photon  $A_\mu$  from the electroweak coupling constants, conserved quantum numbers and vector bosons respectively. We'd also like to retrieve the  $W_\mu^+$  and  $W_\mu^-$  vector bosons of the weak interactions. One shows that these two can be deduced by a linear combination of the  $W_\mu^1$  and  $W_\mu^2$  electroweak fields:

$$W_\mu^\pm = \frac{1}{\sqrt{2}} [W_\mu^1 \mp i W_\mu^2] \quad (1.1.9)$$

These fields represent the vector bosons of the weak charged current interaction (CC) that had been presented before. The point-like interaction through  $G_F$  is replaced by a vertex whose coupling constant is  $g_w$  and a  $W_\mu^\pm$  propagator:

$$\frac{G_F}{\sqrt{2}} \rightarrow \frac{g_w^2}{2} \times i \frac{-g^{\mu\nu} + q^\mu q^\nu / M_W^2}{q^2 - M_W^2} \quad (1.1.10)$$

which is equivalent when the boson momentum ( $q$ ) is negligible with respect to  $M_W$ , to:

$$\frac{G_F}{\sqrt{2}} = \frac{g_w^2}{8M_W^2} \quad (1.1.11)$$

As for the photon, it cannot be the  $B$  field since the latter couples with electromagnetic neutral particles (neutrino). However, it can neither be the charged  $W$  bosons, nor the  $W^3$  since the latter also couples to neutrino (since it is a doublet of the whole  $SU(2)_L$ ). In fact, the photon is a linear combination of the neutral fields  $W^3$  and  $B$ . A rotation of the two fields within a “Weinberg base” defines the photon, and inevitably another vector boson. A striking confirmation of the electroweak unification was observed at the Gargamelle experiment in 1973, who observed the neutrino neutral current interactions [17]. The associated boson  $Z^0$  has been only observed in 1983 at the UA1 experiment [18]. The Weinberg rotation is defined by the Weinberg angle  $\theta_w$ :

$$\begin{pmatrix} A_\mu \\ Z_\mu \end{pmatrix} = \begin{pmatrix} \cos \theta_w & \sin \theta_w \\ -\sin \theta_w & \cos \theta_w \end{pmatrix} \begin{pmatrix} B_\mu \\ W_\mu^3 \end{pmatrix} \quad (1.1.12)$$

The vector currents of the electroweak interaction Lagrangian can also be re-written in order to retrieve the electromagnetic one. Starting from the electromagnetic current, one shows that the difference with the charged current creates a residual current that is exactly the contribution of the hypercharge current (can be deduced only if the isospin, charge and hypercharge of each particle is known):

$$j_{QED}^\mu - j_3^\mu = \frac{1}{2} j_Y^\mu \quad (1.1.13)$$

Using Noether’s theorem, it directly follows the Gell-Mann-Nishijima [19] relation between the conserved quantities:

$$Q = I_3 + \frac{Y}{2} \quad (1.1.14)$$

The basic idea of the Lagrangian re-writing that allows to express the electromagnetic interaction from the electroweak interaction is to maintain electromagnetic equal coupling for the left- and right-handed fields of the fermions. No parity violation has been observed in the electromagnetic interactions, and therefore, the left- and right-handed fields of the same fermion have the same charge and coupling constant. From this constraint, one deduces the fundamental relation in the re-writing of the Lagrangian:

$$g_w \sin \theta_w = g_B \cos \theta_w = \alpha \quad (1.1.15)$$

Considering  $\cos^2 \theta_w + \sin^2 \theta_w = 1$ , we obtain the electromagnetic constant from the electroweak coupling constants only (no role of the Weinberg angle anymore):

$$\alpha = \frac{g_w g_B}{\sqrt{g_w^2 + g_B^2}} \quad (1.1.16)$$

and deduce the Weinberg angle from the coupling constant only:

$$\cos \theta_w = \frac{g_w}{\sqrt{g_w^2 + g_B^2}}, \quad \sin \theta_w = \frac{g_B}{\sqrt{g_w^2 + g_B^2}} \quad (1.1.17)$$

On top of retrieving the electromagnetic constant, we observe that the Weinberg angle is not an additional parameter in the Standard Model but is fixed by the coupling constants. As we have explained, this directly comes from the fact that the Weinberg angle is fixed by the observation of

$\alpha$	$C_V$	$C_A$
$\nu_e, \nu_\mu, \nu_\tau$	$\frac{1}{2}$	$\frac{1}{2}$
$e, \mu, \tau$	$-\frac{1}{2} + 2 \sin^2 \theta_w$	$-\frac{1}{2}$
$u, c, t$	$-\frac{1}{2} - \frac{4}{3} \sin^2 \theta_w$	$\frac{1}{2}$
$d, s, b$	$-\frac{1}{2} + \frac{2}{3} \sin^2 \theta_w$	$-\frac{1}{2}$

 Table 1.3: Vector and axial coupling coefficients that rules the fermions coupling with the  $Z^0$  boson.

parity conservation in the electromagnetic interactions. The remaining Lagrangian part that does not belong to the electromagnetic or the weak charged current interactions corresponds to the neutral coupling constant to the  $Z^0$  boson:

$$g_{NC} = \frac{g_w}{\cos \theta_w} = \sqrt{g_w^2 + g_B^2} \quad (1.1.18)$$

### Charged and neutral current interactions

The CC interactions only occurs for left-handed states. On the contrary, the neutral current interactions both affect the right and left-handed components due to their mixing with  $U(1)_Y$ . However, on the contrary to the electromagnetic interaction, the neutral current coupling constant differs for the left and right-handed states of a particle. Parity is neither a symmetry of neutral current interactions, nor maximally violated by them. For this reason, we define the coupling coefficients  $C_V$  and  $C_A$  (see Table 1.3) to adapt the maximal violation terms of the charged current interactions  $(I - \gamma^5)$  into the general form  $(C_V - \gamma^5 C_A)$  for the neutral current interactions. The two Lagrangian densities can be written as:

$$L_{int}^W = - \sum_{\alpha=e,\mu,\tau} \frac{g_w}{\sqrt{2}} ([\bar{\nu}'_\alpha \gamma^\mu \frac{1}{2} (I - \gamma^5) \alpha'] W_\mu^- + [\bar{\alpha}' \gamma^\mu \frac{1}{2} (I - \gamma^5) \nu'_\alpha] W_\mu^+) \quad (1.1.19)$$

$$L_{int}^{Z^0} = - \sum_{\alpha=e,\mu,\tau} \frac{g_w}{\cos \theta_w} [\bar{\nu}'_\alpha \gamma^\mu \frac{1}{2} (C_V^\alpha - C_A^\alpha \gamma^5) \nu'_\alpha + \bar{\alpha}' \gamma^\mu \frac{1}{2} (C_V^\alpha - C_A^\alpha \gamma^5) \alpha'] Z_\mu^0 \quad (1.1.20)$$

We will bring more details about these interactions in the Chapter 5 of this thesis where we will study the charged current interactions of a muon neutrino. From this point, we will distinguish the fermion mass and flavour states. The electroweak interactions occurring through the flavour states, we will denote the flavour basis with a “ ’ ”. This notation has been omitted from the start but will now always be used.

### 1.1.1 Generation of bosons and fermions masses

#### Boson masses in the standard model

The Standard Model Lagrangian is based on exact gauge theories. In fact, the introduction of a mass term for any vector boson explicitly breaks the gauge invariance. The weak interaction therefore introduces a problem since the W and Z boson masses have been observed respectively at  $80.385 \pm 0.015$  GeV and  $91.1876 \pm 0.0021$  GeV [13]. In order to maintain the Lagrangian gauge symmetries, a spontaneous symmetry breaking was proposed to explain the weak gauge boson mass. “Spontaneous symmetry breaking” does not mean that the Lagrangian loses its symmetry properties, but that only its solutions break them (here at low energy). This mechanism was proposed in 1964 by Brout, Englert [20] and Higgs [21]. The Standard Model original Lagrangian is completed through the introduction of a  $SU(2)_L$  complex doublet Higgs field:

$$\Phi(x^\mu) = \begin{pmatrix} \phi^+(x^\mu) \\ \phi^0(x^\mu) \end{pmatrix} \quad (1.1.21)$$

where  $\phi^+$  ( $I_3 = +\frac{1}{2}$ ) and  $\phi^0$  ( $I_3 = -\frac{1}{2}$ ) are respectively a positively charged and a neutral scalar field. This form is imposed due to the fact that a doublet immediately requires two states with one

$e$  charge difference ( $W^\pm$  transition) and we need these fields to have a neutral electric charge. The broken solution will be along this neutral component in order not to affect the photon and give it a mass. Following the Gell-Mann-Nishijima formula, the whole Higgs doublet has an hypercharge  $Y = 1$ . The Higgs doublet is added to the Lagrangian Standard Model through:

$$L_{Higgs} = (D_\mu \Phi)^\dagger (D^\mu \Phi) - V(\Phi^\dagger \Phi) \quad (1.1.22)$$

where  $D_\mu$  is the covariant derivative that takes into account weak gauge boson transformation to maintain  $SU(2)_L \times U(1)_Y$  invariance. The coupling of the Higgs boson with the electroweak boson will come through this term.  $V$  is the potential defined by:

$$V(\Phi^\dagger \Phi) = \mu^2 (\Phi^\dagger \Phi) + \lambda (\Phi^\dagger \Phi)^2 \quad (1.1.23)$$

where  $\lambda$  is the autocoupling constant of the Higgs field and  $\mu$  is a function of the Higgs field mass which is ordinary defined in the Lagrangian by  $\frac{m_h^2}{2} \Phi^\dagger \Phi$  which implies  $m_h = \sqrt{-2\mu^2}$  with  $\mu^2 < 0$  and  $m_h$  the mass of the Higgs boson. The potential is shown for a  $U(1)$  field  $\phi$  instead of the  $SU(2)_L$  field  $\Phi$  in Figure 1.1. The symmetry is broken due to the Higgs field falling in the potential minimum to minimise its energy.

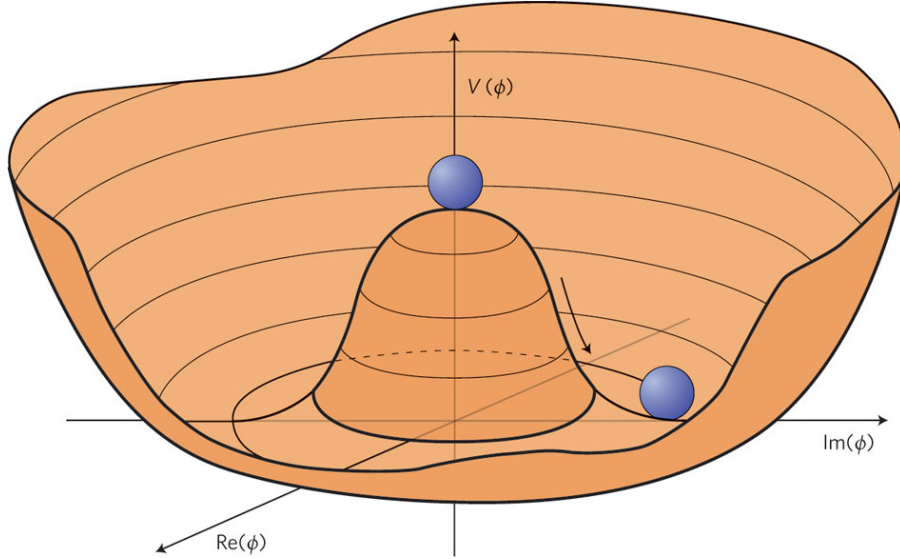


Figure 1.1: A Higgs-like potential in the case of a  $U(1)$  spontaneous symmetry breaking.

The minimum can be obtained deriving Eq 1.1.23 in  $SU(2)_L$  and corresponds to the radius defined by the potential of  $v^2 \equiv 2 \cdot \Phi^\dagger \Phi = \frac{-\mu^2}{\lambda}$  (the factor 2 comes from normalisation). The value  $v$  is the so-called vacuum expectation value (VEV) and corresponds to the ground state (vacuum) energy. The Higgs field ground state is no more  $\Phi_0 = 0$  but:

$$\Phi_0 = \frac{1}{\sqrt{2}} \begin{pmatrix} 0 \\ v \end{pmatrix} \quad (1.1.24)$$

where the VEV only affects the second component  $\phi^0$  and not  $\phi^+$  since the universe vacuum is experimentally electrically neutral as far as we know. Moreover, if the component along  $\phi^+$  is broken, the electromagnetic interaction symmetry  $U(1)_{QED}$  should be somehow broken and the photon would have a mass, which contradicts the observations. Note that the three other components ( $Im(\phi^0), Re(\phi^+)$  and  $Im(\phi^+)$ ) where symmetry is unbroken are the Goldstone bosons. They are essential in the Higgs mechanism since they will be elegantly re-absorbed by the three massive bosons ( $W^+, W^-$  and  $Z^0$ ) as their third spin component, since the original massless particles have only two spin components. The impact of the Higgs mechanism on the whole Lagrangian is done by changing the Higgs field  $\Phi$  into:

$$\Phi(x^\mu) = \frac{1}{\sqrt{2}} \begin{pmatrix} 0 \\ v + h(x^\mu) \end{pmatrix} \quad (1.1.25)$$

where  $h$  is the physical Higgs boson. In this thesis, we will not go through the whole re-writing of the Standard Model Lagrangian implementing the spontaneous symmetry breaking (it can be found in [22]), but we will directly give the W and Z bosons masses that naturally emerge from the covariant derivative coupling of the Higgs to the vector bosons:

$$m_W = \frac{g_w v}{2} \quad \text{and} \quad m_Z = \frac{g_w v}{2 \cos \theta_w} = \frac{m_w}{\cos \theta_w} \quad (1.1.26)$$

### Fermion masses in the Standard Model

In the minimal Higgs mechanism we have introduced, the Higgs only couples with gauge bosons to restore the Lagrangian gauge invariance. But the fermion masses only occur in the Lagrangian through the mass term that couples the right and left-handed components of the fermion field (Eq 1.1.6). As we have seen, the right-handed  $\psi_R$  components are singlets while  $\psi_L$  are doublets of the electroweak interaction. It follows that the mass term is not invariant under  $SU(2)_L$  transformations, *i.e.* is not gauge invariant. On top of generating the boson masses, the Higgs field we introduced allows to generate fermion masses while maintaining the Lagrangian gauge invariance. We will only focus on the lepton masses though the same process could be similarly applied to quarks. In order to simplify the notations, we denote the left-handed doublet as:

$$L_L'^\alpha \equiv \begin{pmatrix} \nu_{\alpha L}' \\ \alpha_L' \end{pmatrix} \text{ where } \alpha = e, \mu, \tau \quad (1.1.27)$$

where  $\nu_{\alpha L}'$  is the  $\alpha$  flavour neutrino left-handed field ( $I_3 = +1/2$ ,  $Y = -1$ ) and  $\alpha_L'$  the  $\alpha$ -flavour fermion left-handed field ( $I_3 = -1/2$ ,  $Y = -1$ ). Note that these fields are the flavour fermion fields, described using a ' to distinguish them from the mass states. The singlet right-handed fields can be denoted as:

$$(\nu_{\alpha R}') , (\alpha_R') \text{ with } \alpha = e, \mu, \tau \quad (1.1.28)$$

Since they are singlets, the right-handed fields are isospin state  $I = 0 \implies I_3 = 0$ . However, the right-handed lepton has a negative electric charge, while the neutrino is neutral. From Gell-Mann-Nishijima relations, it follows  $Y_{\alpha_R'} = -2$ , while  $Y_{\nu_{\alpha R}'} = 0$ . The right-handed neutrino is therefore sterile: it does not couple with the W, Z and  $\gamma$  explicitly, nor with the gluons since it is a lepton. In the strict definition of the Standard Model, as no neutrino mass has been observed, there is no need to add a sterile right-handed neutrino field. In a first place, we consider that the neutrino is massless, and no right-handed neutrino fields.

The lepton mass term is generated through an additional coupling with the Higgs boson (replacing the mass term) through a Yukawa coupling [23]:

$$L_{Yukawa} = - \sum_{\alpha, \beta = e, \mu, \tau} (g'_{\alpha\beta} \overline{L_L'^\alpha} \Phi \beta_R' + g'_{\alpha\beta} {}^* \overline{\alpha_R'} \Phi^\dagger L_L'^\beta) \quad (1.1.29)$$

where  $g'_{\alpha\beta}$  is the coupling matrix between the right and left-handed field. This matrix is a complex  $3 \times 3$  matrix which is not diagonal in general due to possible differences between flavour (interaction) and mass states of a lepton field. The Yukawa coupling term is invariant under  $SU(2)_L \times U(1)_Y$  transformations: the Higgs field is also a doublet of the electroweak interaction that can form a  $SU(2)_L$  singlet with the fermion field and has the hypercharge  $Y = +1$  that cancels with the  $Y_{\overline{L_L'}} = 1$  and  $Y_{\beta_R} = -2$  to guarantee the  $U(1)_Y$  invariance. One observes that the Higgs boson hypercharge that has been set to guarantee no mass to the photon fits elegantly with the need to preserve gauge invariance in fermion couplings. The lepton masses are then generated from the Higgs potential symmetry breaking we explained, and their Yukawa couplings become:

$$L_{Yukawa} = - \left( \frac{v + h}{\sqrt{2}} \right) \sum_{\alpha, \beta = e, \mu, \tau} (g'_{\alpha\beta} \overline{\alpha_L'} \beta_R' + h.c) \quad (1.1.30)$$

where we can clearly observe the contribution of the VEV that will generate the lepton mass, and the trilinear Higgs coupling with leptons. In order to exhibit the lepton masses, we will rotate the

Lagrangian from the flavour to the mass state basis where the  $g'_{\alpha\beta}$  matrix is diagonal by definition. To simplify the rotation, we will re-write the lepton fields as a vector in the flavour and mass basis:

$$L_{Yukawa} = -\left(\frac{v+h}{\sqrt{2}}\right)\mathbf{g}_L^T \mathbf{l}'_R + h.c \quad \text{with} \quad \mathbf{l}'_{L/R} \equiv \begin{pmatrix} e'_{L/R} \\ \mu'_{L/R} \\ \tau'_{L/R} \end{pmatrix} \quad (1.1.31)$$

We will denote  $l_{L/R}$  the left- and right-handed lepton vectors in the mass states. As we discussed, this basis is defined by the diagonality of the Yukawa coupling matrix. Its diagonalisation leads to the mass eigenvalues that define the left and right transfer matrices  $V_{L/R}^l$ :

$$g = \begin{pmatrix} g_e & 0 & 0 \\ 0 & g_\mu & 0 \\ 0 & 0 & g_\tau \end{pmatrix} \quad \text{and} \quad g = V_L^{l\dagger} g' V_R^l \quad (1.1.32)$$

Though left and right components are mixed in the mass state, the rotation to flavour state is different because they are not affected by the same interactions. Therefore, the left and right transfer matrices are not the same. In the mass-states basis, the Yukawa coupling becomes:

$$L_{Yukawa} = -\left(\frac{v+h}{\sqrt{2}}\right)\mathbf{g}_L^T \mathbf{l}_R + h.c \quad (1.1.33)$$

where:

$$\mathbf{l}_L = V_L^{l\dagger} \mathbf{l}'_L \quad \text{and} \quad \mathbf{l}_R = V_R^{l\dagger} \mathbf{l}'_R. \quad (1.1.34)$$

The Lagrangian can be expanded for each flavour due to  $g$  matrix diagonality and finally provides the lepton mass terms:

$$L_{Yukawa} = - \sum_{\alpha=e,\mu,\tau} \frac{v g_\alpha}{\sqrt{2}} (\bar{l}_L^\alpha l_R^\alpha + \bar{l}_R^\alpha l_L^\alpha) - \sum_{\alpha=e,\mu,\tau} \frac{g_\alpha}{\sqrt{2}} (h \bar{l}_L^\alpha l_R^\alpha + h \bar{l}_R^\alpha l_L^\alpha). \quad (1.1.35)$$

The electron, muon and tau are rather defined by their kinematics and their masses, than through their electroweak interactions. For this reason, we will prefer to define the mass states as the actual lepton fields:

$$l^e \equiv e, \quad l^\mu \equiv \mu, \quad l^\tau \equiv \tau. \quad (1.1.36)$$

The mass term definition of Eq 1.1.6 is therefore retrieved through a gauge invariant term. The lepton masses are therefore given through their Higgs coupling constants and the vev:

$$m_\alpha = \frac{g_\alpha v}{\sqrt{2}} \quad \text{with} \quad \alpha = e, \mu, \tau \quad (1.1.37)$$

We only went through this whole process for the charged leptons. The neutrinos are neglected since they are massless, which implies that the Yukawa coupling matrix is null. We re-write Eq 1.1.20 in the mass state basis of the charged leptons:

$$L_{int}^W = - \sum_{\alpha=e,\mu,\tau} \frac{g_w}{\sqrt{2}} ([\bar{\nu}'_\alpha \gamma^\mu \frac{1}{2} (I - \gamma^5) V_L^l l^\alpha] W_\mu^+ + [\bar{l}^\alpha V_L^{l\dagger} \gamma^\mu \frac{1}{2} (I - \gamma^5) \nu'_\alpha] W_\mu^-) \quad (1.1.38)$$

$$L_{int}^{Z^0} = - \sum_{\alpha=e,\mu,\tau} \frac{g_w}{\cos \theta_w} [\bar{\nu}'_\alpha \gamma^\mu \frac{1}{2} (C_V^\alpha - C_A^\alpha \gamma^5) \nu'_\alpha + \bar{l}^\alpha \gamma^\mu \frac{1}{2} (C_V^\alpha - C_A^\alpha \gamma^5) l^\alpha] Z_\mu^0. \quad (1.1.39)$$

We remark the neutral current interaction is the same in the flavour and mass states. This is expected since this interaction is not sensitive to the lepton flavour.

### 1.1.2 Neutrino masses in the extension of the Standard Model

As we will describe in Section 1.2, it has been experimentally confirmed in 1998 in Super-Kamiokande that neutrinos oscillate. As discussed in the same Section, this is only possible if the neutrinos are massive. In this case, right-handed neutrino fields can be added to the Lagrangian as for charged leptons. These right-handed neutrino fields have no electric charge, are singlets of the weak interaction (since right-handed) which leads to a null hypercharge using Gell-Mann-Nishijima relation. Since they are leptons, it means these neutrino right-handed fields are not sensitive to any interaction, except the gravitation. They are therefore called “sterile”. As was done for the charged leptons, we will now discuss how massive neutrino fields can be added without explicitly breaking the gauge invariance. We will see that the neutrino may acquire mass not only through the classic Higgs generation of a Dirac mass we have already seen, but also through Majorana mass generation. This feature is only possible for neutrinos which are the only known electrically neutral fundamental fermions.

#### Neutrino Dirac mass

This case is exactly symmetric with respect to what has been done for other fermions. The very same deduction can be applied, defining an original right-handed neutrino flavour state on top of the existing left-handed one:

$$\nu'_{\mathbf{R}} \equiv \begin{pmatrix} \nu'_{eR} \\ \nu'_{\mu R} \\ \nu'_{\tau R} \end{pmatrix} \text{ and the pre-existing } \nu'_{\mathbf{L}} \equiv \begin{pmatrix} \nu'_{eL} \\ \nu'_{\mu L} \\ \nu'_{\tau L} \end{pmatrix} \quad (1.1.40)$$

The exact same procedure leads to the neutrino mass states  $|\nu_1\rangle, |\nu_2\rangle, |\nu_3\rangle$  defined by the neutrino Yukawa coupling matrix that differs from charged lepton one (different masses):

$$g^\nu = \begin{pmatrix} g_1^\nu & 0 & 0 \\ 0 & g_2^\nu & 0 \\ 0 & 0 & g_3^\nu \end{pmatrix} \text{ and } g^\nu = V_L^{\nu\dagger} g'^\nu V_R^\nu \quad (1.1.41)$$

were the transfer matrices  $V_{L/R}^\nu$  are given by the mass eigenstates components in the flavour basis:

$$\nu_{\mathbf{R}} = V_R^{\nu\dagger} \nu'_{\mathbf{R}} \equiv \begin{pmatrix} \nu_{1R} \\ \nu_{2R} \\ \nu_{3R} \end{pmatrix} \text{ and the pre-existing } \nu_{\mathbf{L}} = V_L^{\nu\dagger} \nu'_{\mathbf{L}} \equiv \begin{pmatrix} \nu_{1L} \\ \nu_{2L} \\ \nu_{3L} \end{pmatrix} \quad (1.1.42)$$

The diagonalisation provides the neutrino mass state values according to the Higgs VEV and their Yukawa coupling:

$$m_i = \frac{g_i^\nu v}{\sqrt{2}} \text{ with } i=1,2,3 \quad (1.1.43)$$

which leads to modify the interaction Lagrangian Eq 1.1.39 into:

$$\begin{aligned} L_{int}^W &= - \sum_{\alpha=e,\mu,\tau} \sum_{i=1,2,3} \frac{g_w}{\sqrt{2}} ([\bar{\nu}^i V_L^{\nu\dagger} \gamma^\mu \frac{1}{2} (I - \gamma^5) V_L^i] W_\mu^+ + h.c) \\ &= - \sum_{\alpha=e,\mu,\tau} \sum_{i=1,2,3} \frac{g_w}{\sqrt{2}} ([\bar{\nu}^i U_{PMNS}^\dagger \gamma^\mu \frac{1}{2} (I - \gamma^5) U_{PMNS}^i] W_\mu^+ + h.c) \\ L_{int}^{Z^0} &= - \sum_{\alpha=e,\mu,\tau} \frac{g_w}{\cos \theta_w} [\bar{\nu}^\alpha \gamma^\mu \frac{1}{2} (C_V^\alpha - C_A^\alpha \gamma^5) \nu^\alpha + \bar{\nu}^\alpha \gamma^\mu \frac{1}{2} (C_V^\alpha - C_A^\alpha \gamma^5) \nu^\alpha] Z_\mu^0 \end{aligned} \quad (1.1.44)$$

defining the Pontecorvo-Maki-Nakagawa-Sakata matrix as:

$$U_{PMNS} = V_L^\nu V_L^{\nu\dagger} \quad (1.1.45)$$

which is in fact the  $3 \times 3$  transfer matrix from the lepton flavour basis to the neutrino flavour one. Therefore, a charged lepton does not interact with a neutrino massive state, but with a linear combination of the massive states that define a flavour state. The very same effect occurs in the quark

sector, through the CKM matrix (Cabbibo-Kobayashi-Maskawa) but within the  $d, s, b$  components *i.e* the isospin  $I_3 = -1/2$ . This is equivalent in the quark sector to describe this mixing with the  $I_3 = +1/2$  components, but unfortunately, the convention is the opposite and has been chosen before the lepton sector. In the lepton sector, the convention was chosen differently given the very large masses of the charged lepton component compared to the neutrino one, that prevent the first to reasonably oscillate at observable large distances (on top of the difficulty to identify a charged lepton weak interaction to project on flavour state).

### Neutrino Majorana mass

The neutrino Dirac mass generation requires an additional right-handed neutrino field, that cannot be observed except in gravitational effects. On top of this, the mass ratio between two states of a isospin doublet is  $10^5$  at least (for the  $\nu_e$  and  $e$ ) in the lepton sector. This is very particular to leptons since the mass of the two components of the first generation quark doublet are within the same order of magnitude, in the case of the up and down quarks. This will require the Yukawa coupling to be several orders of magnitude lower for the neutrinos than for any other existing particle. This gap is not seen for the charged leptons and for the quarks, which tends to outline that the neutrino mass generation process could be different than for the other particles. In fact, Majorana has shown [24] that the propagation of a spin 1/2 fermion is not necessarily described by the Dirac equation. In fact, in the latter, the particle is a four components (which are scalar and complex) spinor:

$$\psi = \begin{pmatrix} \psi_L \\ \psi_R \end{pmatrix} = \begin{pmatrix} \psi_L(+1/2) \\ \psi_L(-1/2) \\ \psi_R(+1/2) \\ \psi_R(-1/2) \end{pmatrix} \quad (1.1.46)$$

The description of a particle with only a two-component spinor (Weyl spinor),  $\psi_L$  for example, only holds for a massless particle since the Dirac mass term couples  $\psi_L$  and  $\psi_R$  (Eq 1.1.6). Majorana has shown that the right- and left-handed components are not necessarily independent, but that one can be obtained from the other through particle-antiparticle conjugation:

$$\psi_R = \eta \psi_L^c = \eta' C \overline{\psi_L}^T \quad (1.1.47)$$

where  $C$  is the charge conjugation matrix,  $\psi_L^c$  is the  $\psi_L$  field antiparticle conjugate, and  $\eta$  is a Majorana phase whose choice has no impact on observations, and will be then chosen as  $\eta = 1$ . This leads to the antiparticle conjugation:

$$\psi_R = \psi_L^c = C \overline{\psi_L}^T \quad (1.1.48)$$

Assuming the observed conservation of electric charge, the Majorana description can therefore only hold for a neutral elementary particle, since the electric charge of  $\psi_R$  and  $\psi_L$  are opposite. The only elementary fermionic particle that matches this neutrality requirement is the neutrino. For a neutrino field  $\nu$ , its four degrees of freedom in the Dirac description now become:

$$\nu = \nu_L + \nu_R = \nu_L + \nu_L^c \quad (1.1.49)$$

which implies that only the two components of the  $\nu_L$  spinor describe the neutrino. The Eq 1.1.49 implies therefore that:

$$\nu = \nu^c \quad (1.1.50)$$

which means the neutrino is its own antiparticle. This unique feature among the leptons is only seen in the boson sector for the neutral photon and the  $Z^0$  bosons. The two unobserved  $\nu_R$  degrees of freedom are removed, which simplifies the neutrino description and follows elegantly the Occam's razor assumption, at least in the present state of observations since we cannot experimentally probe the gravitational interactions of neutrinos. The Majorana description contains both the left-handed neutrino and right-handed neutrino behaviours. The Dirac mass term of Eq 1.1.6 can therefore be changed in the Lagrangian to the Majorana description:

$$L_M^L = -\frac{1}{2} M_L (\overline{\nu_L^c} \nu_L + \overline{\nu_L} \nu_L^c). \quad (1.1.51)$$

This Lagrangian obviously breaks the  $SU(2)_L$  gauge invariance *i.e* the isospin conservation by a factor of two. This was also the case for the Dirac description, but we have shown that the Higgs isospin scalar doublet allows to maintain the Lagrangian isospin symmetry. In the case of the Majorana description, one shows that the same scalar doublet cannot be used. Taking for example the hypercharge quantum number, we have seen that the Higgs field hypercharge is  $Y_\Psi = 1$ , while  $Y_{\nu_L} = -1$ . If we re-write the mass term in Eq 1.1.51 with a similar Yukawa coupling to the Higgs field as for the Dirac description, we obtain:

$$L_M^L \sim g^{Majorana} \bar{\nu}_L^c \Psi \nu_L + h.c \quad (1.1.52)$$

which has a total hypercharge  $Y_{L_M} = +1$  which also violates the  $U_Y$  invariance. One shows [25] that the addition of a new Higgs isotriplet (that can be generated from two Higgs doublets for example) on top of the existing Higgs can solve this issue, at the cost of changing the VEV due to the new Higgs potential broken symmetry. This would modify the W and Z boson masses which are measured with high accuracy, and therefore, is only possible if the VEV of the new Higgs field ( $u$ ) is smaller than the existing uncertainties on the  $Z^0$  and  $W^\pm$  masses ( $\sim 1 - 10$  MeV).

Independently from any Higgs mechanism, we observe also that the lepton number conservation is violated in the Majorana Lagrangian (Eq 1.1.51). Applying the lepton global symmetry  $\nu_L \rightarrow e^{i\theta} \nu_L$ , one deduces this conservation is violated by a factor two. This violation should be very small due to the neutrino mass, and is actively searched for especially in neutrinoless double beta decay searches. It is interesting to mention that this scenario occurs in the Grand Unified Theories that try to unify QCD with electroweak interactions at higher energy. In particular, the number of leptons and baryons are not separately conserved, but their difference is  $(L - B)$  which can be interpreted as a global “matter (fermion) conservation”.

### The see-saw mechanism

Given the Majorana and Dirac descriptions of the neutrino we discussed, the neutrino mass can be generated by three mechanisms:

- If only the left-handed neutrino field  $\nu_L$  exists, the neutrino is a Majorana particle. This conclusion is difficult to draw considering the issue on gravitation we described.
- If no violation of lepton number conservation is observed, the neutrino should be a Dirac particle. The  $\nu_R$  is theoretically observable.
- In the most general case, the neutrino may have both Dirac and Majorana mass terms, and in this case, a Majorana particle.

In fact, the Lagrangian construction in Quantum Field Theory is based on the assumption that any possible term that does not violate the acceptable symmetry should be incorporated. This is opposite to the Occam’s razor and simplicity, but has been historically also widely used. If we accept the idea of a very small violation of the lepton number conservation, the neutrino mass can emerge both from the Dirac and Majorana terms. The Dirac term explicitly requires a  $\nu_R$  field, and the Majorana description can be extended to the right-handed sector in addition to Eq 1.1.51 without particular effort:

$$L_M^R - \frac{1}{2} M_R (\bar{\nu}_R^c \nu_R + \bar{\nu}_R \nu_R^c) \quad (1.1.53)$$

Since there is no coupling between the right and left-handed neutrino fields in the Majorana description, there is no requirement that the left and right masses are equal. Summing the contributions from Majorana (Eqs 1.1.51 and 1.1.53) and from the Dirac mass term in Eq 1.1.6, we obtain the Dirac and Majorana Lagrangian mass term for N lepton mass states:

$$L_{mass}^{D+M} = -\frac{1}{2} (n_L^T C M n_L + h.c) \quad (1.1.54)$$

where  $n_L$  is the neutrino state doublet:

$$n_L = \begin{pmatrix} \nu_L \\ (\nu_R)^c \end{pmatrix} = \begin{pmatrix} \nu_L \\ (\nu^c)_R \end{pmatrix} \quad (1.1.55)$$

and  $M$  the mass matrix:

$$M = \begin{pmatrix} M_L & m_D \\ m_D^T & M_R \end{pmatrix}. \quad (1.1.56)$$

We will describe the case of only one mass term (one generation) to gain in clarity. In this case, the  $M$  matrix is a  $2 \times 2$  matrix and  $m_D^T = m_D$  is the neutrino Dirac mass,  $M_L$  and  $M_R$  are respectively its left and right Majorana mass terms. The fields  $\nu_L$  and  $\nu_R$  are two Weyl spinors (two degrees of freedom), which in total correspond to four degrees of freedom, as in the pure Dirac case. To obtain the real mass states, we diagonalise the mass matrix. The eigenvalues are:

$$m_{1,2} = \frac{M_R + M_L}{2} \mp \sqrt{\left(\frac{M_R - M_L}{2}\right)^2 + m_D^2} \quad (1.1.57)$$

These masses are real but can be of either sign depending on CP parity of the eigenvector. Their positiveness will be restored in what follows. The eigenvectors  $\chi_{1,2L}$  are generally obtained through the 2D rotation in the mass states plane:

$$n_L = \begin{pmatrix} \nu_L \\ (\nu_R)^c \end{pmatrix} = \begin{pmatrix} \cos \theta_{SS} & \sin \theta_{SS} \\ -\sin \theta_{SS} & \cos \theta_{SS} \end{pmatrix} \begin{pmatrix} \chi_{1L} \\ \chi_{2L} \end{pmatrix} \quad (1.1.58)$$

and the diagonalisation fixes the eigenvector values by setting the “see-saw”  $\theta_{SS}$  angle:

$$\tan 2\theta_{SS} = \frac{2m_D}{M_R - M_L} \quad (1.1.59)$$

which leads to re-write the Lagrangian density in the diagonal mass sector:

$$L_{mass}^{D+M} = -\frac{1}{2}(m_1 \chi_{1L}^T C \chi_{1L} + m_2 \chi_{2L}^T C \chi_{2L}) + h.c. = \frac{1}{2}(|m_1| \bar{\chi}_1 \chi_1 + |m_2| \bar{\chi}_2 \chi_2) \quad (1.1.60)$$

Having defined  $\chi_{1,2}$  as:

$$\chi_1 \equiv \chi_{1L} + \eta_1 (\chi_{1L})^c, \quad \chi_2 \equiv \chi_{2L} + \eta_2 (\chi_{2L})^c \quad (1.1.61)$$

where  $\eta_{1,2} = 1$  for  $m_{1,2} > 0$  and  $\eta_{1,2} = -1$  for  $m_{1,2} < 0$ . One observes in the latter definition that  $\chi_1$  and  $\chi_2$  have two degrees of freedom each, and are two Majorana neutrinos. For this reason, in the most general case of a Dirac and Majorana neutrino, the effective mass states are Majorana neutrinos. This was expected since we started with  $\nu_L$  and  $\nu_R$  fields which have two degrees of freedom each, and since the mass matrix has two different eigenvalues, it has two distinct eigenvectors that should have two degrees of freedom each. We will now analyse the latter result in different limit cases:

- The Dirac description is retrieved if  $M_L = M_R = 0$  which implies a mixing angle  $\theta_{SS} = 45^\circ$  and  $|m_1| = |m_2| = m_D$  with opposite CP parities. The eigenvectors (Majorana mass states) are therefore degenerated. Only one mass state having four degrees of freedom implies necessarily that the equivalent neutrino is a Dirac neutrino having a mass  $m_D$ . It is a linear combination of the degenerated Majorana states  $\chi_{1,2}$ .
- The Majorana case is instead retrieved for  $m_D = 0$ . The mass matrix is diagonal in the original Majorana basis and the “Majorana only” description is retrieved. There is no mixing ( $\theta_{SS} = 0$ ).
- The pseudo-Dirac limit corresponds to  $m_D \gg M_L, M_R$ . This is very similar to the pure Dirac case, and we find  $\theta \sim 45^\circ$  with two masses  $|m_1| \simeq |m_2|$ . In this limit, the two Majorana masses states are almost degenerated and behave mostly as a unique Dirac field. Due to Majorana very small masses, the pseudo-Dirac neutrinos only contribute to the double beta decay in proportion of  $\frac{M_R + M_L}{2}$ . In this case, the current no-observation of such a process may be explained if the neutrino mixing is in this limit.
- The so called “see-saw” state where  $M_L \ll m_D \ll M_R$ . This is called the see-saw mechanism since it explains the very small masses of the observed neutrino states through a Dirac mass which has similar order of magnitudes than the charged lepton one, and a very heavy right Majorana mass. The latter has not any constraint as for the Dirac mass, since the right-handed Majorana

term does not violate the isospin invariance (it is not coupled to any electroweak interaction) and therefore, no Higgs mechanism is needed to explain it. On the contrary, we have seen it is quite complicated to preserve the gauge invariance along with the introduction of a left-handed Majorana term, though not impossible. In the type I see-saw mechanism, it is therefore assumed  $M_L = 0$ . We will keep  $M_L \neq 0$  here since the gauge invariance can be preserved in some Standard Model extensions we discussed. We therefore obtain the mass eigenvalues:

$$m_1 \simeq M_L - \frac{m_D^2}{M_R}, \quad m_2 \simeq M_R \quad (1.1.62)$$

and the eigenvectors:

$$\chi_1 \simeq \nu_L + \eta_1 (\nu_L)^c, \quad \chi_2 \simeq (\nu_R)^c + \eta_2 \nu_R \quad (1.1.63)$$

The mixing angle in this case is very small  $\theta_{SS} \simeq \frac{m_D}{m_R} \ll 1$  since the admixture of the  $\nu_R$  singlet in  $\chi_2$  is almost maximal. On the other hand, though this singlet admixture is small in  $\chi_1$  ( $\sim \frac{m_D}{m_R}$ ), it is not negligible compared to the very small  $M_L$ , though the latter has a large admixture. The  $\chi_1$  small mass is therefore guaranteed by the Majorana left term small mass, but also, by the high  $\nu_R$  Majorana mass that suppresses the Dirac mass contribution: this is the heavy right-handed neutrino that makes the left one light. This is an elegant explanation of the small masses of left-handed neutrinos: their small masses is not due to an abnormally small Yukawa coupling with the Higgs, but to their right-handed term that have a very large mass (which is allowed since not related to the Higgs mechanism). Assuming for example a Dirac mass similar to the electron  $\sim 0.5$  MeV, a neutrino mass compatible with the current limits  $m_\nu \sim 0.1$  eV [26] would imply  $M_R \sim 10^4$  GeV. For a neutrino having a Dirac mass equal to the heaviest known particle (the top quark),  $m_D \sim 200$  GeV would require  $M_R \sim 10^{15}$  GeV which corresponds to the typical energy of Grand Unified Theories. We note here that the number of sterile right-handed neutrinos has no necessity to be equal to the number of active neutrinos for the see-saw mechanism to happen, as the squared matrix can be replaced by a rectangular one.

### 1.1.3 Limits of the Standard Model

As we have seen, the Standard Model is built on gauge interactions occurring in a flat Minkowsky spacetime. But gravitation is understood through general relativity as a local spacetime deformation by a massive (in fact, energetic) object. Therefore, gravitation cannot be treated as the other interactions through gauge theories on a flat spacetime, but is related to the spacetime structure itself. A dimensional analysis [27] shows that a naive treatment of gravitation leads to a non-renormalisable theory, which is due to the non vanishing dimension of the gravitation constant. It indicates that the gravitation theory should be replaced for high energy, explicitly for energies around the Planck scale  $E_p \sim 10^{19}$  GeV where running coupling constants should lead to a non-negligible gravitational contribution. Considering the energy at which physics will be studied in this thesis, we will assume that gravitational effects can be neglected.

## 1.2 Neutrino oscillations in vacuum

### 1.2.1 The general theory of oscillations

In the most general case, particle propagation states (massive states) may not correspond to the particle detection states (or flavour states). In this case, we have seen a mixing occurs between the flavour and the mass neutrino states through the PMNS matrix we defined in Eq 1.1.45. This mixing lead to the phenomenon named neutrino oscillation.

A flavour state  $|\nu_\alpha\rangle$  produced in a charged current interaction as  $\mu^- \rightarrow e^- + \bar{\nu}_e + \nu_\mu$  can be written as a mixing of massive states:

$$|\nu_\alpha\rangle = \sum_{i=1}^N U_{\alpha i}^* |\nu_i\rangle \quad (1.2.1)$$

with  $N$  and  $|v_i\rangle$  the number and corresponding massive neutrino states.  $U_{\alpha i}^*$  is the matrix that transforms the flavour neutrino state basis into the massive neutrino state one, the so-called PMNS matrix. At the present time, three neutrino flavour states have been observed:  $|\nu_e\rangle$ ,  $|\nu_\mu\rangle$  and  $|\nu_\tau\rangle$  that implies  $F \geq 3$  with  $F$  the number of flavour neutrino states. In fact, the number of neutrino state is constrained by the LEP  $Z^0$  boson decay width as shown in Figure 1.2. For this reason, the constraints on the number of neutrino only apply to light and active neutrinos. The behaviour of  $F$  flavour independent

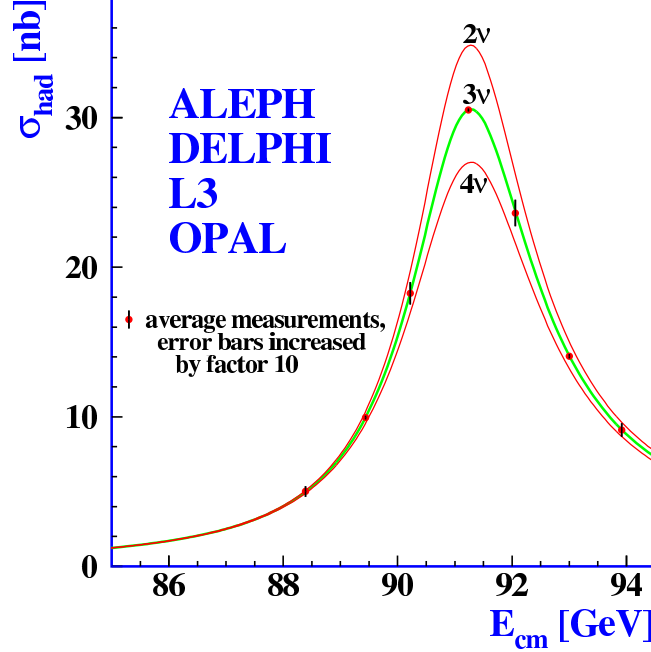


Figure 1.2: Measurement of the hadron cross sections around the  $Z$  resonance at the LEP. Different neutrino scenario are fitted assuming Standard Model coupling and negligible mass. Extracted from [8].

neutrino states can be described in terms of  $N$  independent massive neutrino states only if  $F=N$ , *i.e.* the PMNS matrix is square. In this section, we will describe the neutrino oscillation scheme for any number of flavour neutrino states (keeping  $F=N$ ).

By definition, the neutrino massive states are the eigenvectors of the free Hamiltonian (we will describe the neutrino propagation through matter in Section 1.3):

$$H |v_i\rangle = E_i |v_i\rangle. \quad (1.2.2)$$

Using the Schrödinger equation, we can deduce the massive neutrino states time evolution from  $t = 0$  to  $t$ :

$$i \frac{d}{dt} |v_i(t)\rangle = H |v_i(t)\rangle \stackrel{\text{invacuum}}{=} E_i |v_i(t)\rangle. \quad (1.2.3)$$

The time evolution of a single massive neutrino state can therefore be described as a plane wave:

$$|v_i(t)\rangle = e^{-iE_i t} |v_i\rangle \quad (1.2.4)$$

where we have denoted  $v_i(t=0) \equiv v_i$ . We can deduce the time evolution of a flavour neutrino state by using Eq 1.2.4 to re-write the Eq 1.2.1:

$$|v_\alpha(t)\rangle = \sum_{i=1}^N U_{\alpha i}^* |v_i(t)\rangle = \sum_{i=1}^N U_{\alpha i}^* e^{-iE_i t} |v_i\rangle. \quad (1.2.5)$$

The time evolution of a flavour neutrino state can be written only in terms of initial flavour neutrino state using the unitarity of PMNS matrix to invert Eq 1.2.1 which becomes:

$$|v_i\rangle = \sum_{\beta=1}^F U_{i\beta} |v_\beta\rangle \quad (1.2.6)$$

and finally leads to:

$$|\nu_\alpha(t)\rangle = \sum_{i=1}^N \sum_{\beta=1}^F U_{\alpha i}^* U_{i\beta} e^{-iE_i t} |\nu_\beta\rangle. \quad (1.2.7)$$

This shows that a neutrino produced in the initial flavour state  $|\nu_\beta\rangle$  will evolve into a superposition of  $N=F=3$  flavour states if the PMNS matrix is not diagonal (*i.e.*, flavour are not mass states). The probability of an initial flavour state  $|\nu_\alpha\rangle$  to evolve into a flavour state  $|\nu_\beta\rangle(t)$  is then:

$$P_{\nu_\alpha \rightarrow \nu_\beta}(t) \equiv |\langle \nu_\beta(t) | \nu_\alpha \rangle|^2 = \sum_{i=1}^N \sum_{j=1}^N U_{\alpha i}^* U_{i\beta} U_{\alpha j} U_{j\beta}^* e^{-i(E_i - E_j)t}. \quad (1.2.8)$$

One observes that we retrieve the expected  $P_{\nu_\alpha \rightarrow \nu_\beta}(0) = \delta_{\alpha\beta}$  using the PMNS matrix unitarity. In this whole thesis, we will assume that neutrinos are ultrarelativistic particles considering their negligible mass regarding their velocity. In this case, the energy of a neutrino mass state can be approximated by:

$$E_i = \sqrt{p_i^2 + m_i^2} \simeq p_i + \frac{1}{2} \frac{m_i^2}{p_i}. \quad (1.2.9)$$

We will assume here that all neutrino mass states have the same momentum but a different mass ( $p_i = p$ ,  $\forall i$ ). This leads to:

$$E_i - E_j = \frac{m_i^2 - m_j^2}{2p} = \frac{\Delta m_{ij}^2}{2p} \quad (1.2.10)$$

with  $\Delta m_{ij}^2 \equiv m_i^2 - m_j^2$  the neutrino squared mass difference between the mass states  $j$  and  $i$ . In the case of ultrarelativistic neutrinos that we describe, the neutrino momentum  $p = E$  and the distance of the neutrino from its source are directly related to the time elapsed  $L=t$ . The propagation phase in Eq 1.2.8 is then written under this hypothesis:

$$P_{\nu_\alpha \rightarrow \nu_\beta}(t) \simeq \sum_{i=1}^N \sum_{j=1}^N U_{\alpha i}^* U_{i\beta} U_{\alpha j} U_{j\beta}^* e^{i(\frac{\Delta m_{ij}^2}{2E})L}. \quad (1.2.11)$$

We observe an oscillating term between the different flavour neutrino states. The oscillating phase  $\phi$  is:

$$\phi = \frac{\Delta m_{ij}^2}{2E} L. \quad (1.2.12)$$

The oscillation phase suggests we can measure the neutrino squared mass differences through neutrino oscillation phase measurement at a given neutrino energy  $E$  and for a given distance from the neutrino source  $L$  (baseline). The PMNS matrix can be also determined through neutrino oscillations since their amplitude only depend on it. We finally separate the  $i$  and  $j$  mass states in Eq 1.2.11 depending if  $i = j$  or not and obtain:

$$P_{\nu_\alpha \rightarrow \nu_\beta}(t) \simeq \sum_i |U_{\alpha i}|^2 |U_{\beta i}|^2 + 2 \operatorname{Re} \sum_{i>j} U_{\alpha i}^* U_{i\beta} U_{\alpha j} U_{j\beta}^* e^{-2\pi i \frac{L}{L_{ij}^{osc}}} \quad (1.2.13)$$

which separates the contribution of a constant and oscillating term which depends on the “oscillation length” parameter:

$$L_{ij}^{osc} = \frac{4\pi E}{\Delta m_{ij}^2}. \quad (1.2.14)$$

This oscillation length can be defined as the wavelength of the oscillation. The role of the constant term is not clear in the plane wave approximation we have shown. In fact, assuming a neutrino detector having a spatial extension  $L^{det} > L^{osc}$ , the oscillating term does not disappear unless  $L^{det}$  is a multiple of the oscillation wavelength, *i.e.*  $L^{det} = \lambda L^{osc}$ . This is just to say the obvious fact that the integral of a plane wave is zero only in the case of an integration interval equal to a multiple of the wavelength. In reality, we will see it is not the case and the oscillation term effect may be lost for

$L^{det} > L^{osc}$  (which is rather impossible except for the case of high  $\Delta m^2$ ).

In fact, the plane wave is only an approximation. In reality, the neutrinos are emitted by a non permanent source and are spatially localised as a particle should be. The plane wave approximation should therefore be changed into the wave packet formalism. The calculation in Quantum Field Theory is rather complicated and detailed in [22]. It leads to replace Eq 1.2.13 by:

$$P_{\nu_\alpha \rightarrow \nu_\beta(t)} \simeq \sum_i |U_{\alpha i}|^2 |U_{\beta i}|^2 + 2Re \sum_{i>j} U_{\alpha i}^* U_{i\beta} U_{\alpha j} U_{j\beta}^* e^{-2\pi i \frac{L}{L_{ij}^{osc}} - (\frac{L}{L_{ij}^{coh}})^2 - 2\pi^2 \eta (\frac{\sigma_x}{L_{ij}^{osc}})} \quad (1.2.15)$$

where  $\eta \propto 1$  and depends on the production/detection and  $L_{ij}^{coh}$  is the coherent distance of the interferences defined by:

$$L_{ij}^{coh} = \frac{4\sqrt{2}E^2}{|\Delta m_{ij}^2|} \sigma_x \quad (1.2.16)$$

where  $\sigma_x$  is the uncertainty (resolution) on the particle localisation, whose square is the quadratic sum of the spatial uncertainties on the production and detection processes of the particle:  $\sigma_x^2 \simeq (\sigma_x^P)^2 + (\sigma_x^D)^2$ . It is more intuitive to think about the production and detector resolution in momentum, which is related to the spatial uncertainty through the Heisenberg relation  $\sigma_x \sigma_p = \frac{1}{2}$ . Let's describe the different phases that rule neutrino oscillations in the case of a wave packet in Eq 1.2.15:

- $2\pi i \frac{L}{L_{ij}^{osc}}$  which is the standard oscillation term we observed in the plane wave approximation. It describes an oscillation between neutrino flavours with the distance according to the wavelength  $L_{ij}^{osc} \propto \frac{E}{\Delta m_{ij}^2}$  which depends on the mass states.
- A term describing the loss of coherence between the different mass states (*i.e* wavelength) that tends to suppress the oscillation at long distance for  $L \gg L_{ij}^{coh}$ . Since the different mass states have the same energy with different masses, their momenta are slightly different and they do not propagate exactly at the same speed. When the distance is too large compared to their energy and mass differences that rule their relative speed, the oscillation effect is lost and only the constant term will remain. We show here that the coherence length can be retrieved through simple hypothesis. In the two-flavour case, we will describe the wave packet by the weighted sum of the plane wave associated to  $|\nu_1\rangle$  and to  $|\nu_2\rangle$ . In fact, these two packets are not exactly plane waves since the neutrino flavour energy has an uncertainty that will impact  $\sigma_x$ , the spatial uncertainty. The mean position of a massive state  $i$  at the time  $t$  can be given by:  $x_i(t) = vt = \frac{p_i}{E}$ , assuming that the neutrino energy is the same as the flavour initial state, and the momentum difference comes from the mass difference. We can then express the difference between the two plane wave positions at a time  $t$ :

$$\Delta x \equiv x_2(t) - x_1(t) = \frac{p_2 - p_1}{E} t \quad (1.2.17)$$

We can re-write the momentum difference in terms of the squared mass difference. A mass term momentum is given by  $p_i = \sqrt{E^2 - m_i^2}$ . Assuming the neutrino is ultrarelativistic, we obtain  $p_i \simeq E - \frac{m_i^2}{2E}$  which leads to change Eq 1.2.17 in terms of squared mass differences:

$$\Delta x \simeq \frac{m_1^2 - m_2^2}{4E^2} t = \frac{\Delta m_{12}^2}{4E^2} L \text{ since } L=t \quad (1.2.18)$$

Intuitively, the coherence is lost if the average packet position difference between the two mass states is large compared to one packet spatial extension. Assuming the two mass state packets have the same spatial extension which is close to  $\sigma_x$ , we deduce that the coherence is lost if:

$$\frac{\Delta x}{\sigma_x} \gg 1 \iff \frac{\Delta m_{12}^2}{4E^2 \sigma_x} L \gg 1 \iff L \gg \frac{4E^2 \sigma_x}{\Delta m_{12}^2} \quad (1.2.19)$$

We have retrieved the coherence length definition given in Eq 1.2.16 with the difference of a factor  $\sqrt{2}$  through our very naive calculation. This clearly illustrates that two neutrinos with

a large squared mass difference will quickly loose their coherence, as for neutrinos of relatively small energy since their mass difference will have a larger impact on their velocity difference. We also observe that this term disappears when we have absolutely no spatial resolution on the neutrino ( $\sigma_x = \infty$ ) at the production or the detection. This is expected since we retrieve the plane wave description in this case (perfect energy resolution, infinite spatial extension). However, the coherence is lost if the neutrino is detected and produced with a perfect resolution on the particle position ( $\sigma_x = 0$ ). In this limit, neutrinos do not have any spatial extension, and cannot oscillate since they do not have a wave behavior.

- Finally, a localisation term  $2\pi^2\eta(\frac{\sigma_x}{L_{ij}^{osc}})^2$  describes the wave packet localisation itself compared to oscillation wavelength. One observes that the coherence is lost (and the oscillation term disappears) if  $\sigma_{x_{ij}}^{osc}$  i.e if the detector or the production is large enough to contain several oscillations. We observe that the plane wave description is therefore wrong in such a case, since the wave packet description implies the oscillation to disappear for large sources or detector vertex resolution lower than the oscillation wavelength. This can be understood since the oscillation is directly averaged in this case, and we expect to only observe an effect on the rate as shown in Eq 1.2.15.

We observe that the plane wave approximation is right only in the case of  $L_{ij}^{coh}$  and  $\sigma_{x_{ij}}^{osc}$ , which is almost always verified practically. Given the present three-flavour neutrino scenario, the measurements lead to  $\Delta m_{12}^2 \sim 10^{-5} \text{eV}^2$  and  $\Delta m_{13}^2 \sim 10^{-3} \text{eV}^2$ . As for the  $L_{ij}^{coh}$  hypothesis, we can imagine that the most probable case in which the coherence is lost is for the solar neutrino which have a low energy ( $\propto 1 \text{ MeV}$ ) and very long baseline  $1 \text{ a.u} \sim 1.5 \times 10^{11} \text{ m}$ . The worst case occurs for a short coherent distance, which also means small space uncertainty. Let's assume that the creation process is localised in the Sun (with a point-like spatial resolution) and a detector vertex resolution of  $\sim 1 \text{ cm}$ , which implies  $\sigma_x \sim 1 \text{ cm}$ . Under these unrealistic hypotheses, we obtain  $L_{ij}^{coh} \sim 10^7 \text{ m} \ll L_{Sun \rightarrow Earth}$ . This indicates we expect the coherence to be lost for the solar neutrinos detected on Earth. We will see in Section 1.4 that this is experimentally the case. We observe that in the case of atmospheric, reactor or accelerator neutrinos, the baselines are too short (and the speed/energy are too high in the case of atmospheric/accelerator) to observe the wave packet decoherence. As for the localisation term, it disappears in the case of low detector vertex resolution and for small oscillation wavelengths  $L_{ij}^{osc} = \frac{4\pi E}{\Delta m_{ij}^2}$ . As an example, let's imagine a detector with a poor  $1 \text{ m}$  vertex resolution which aims to observe reactor neutrino oscillation. It corresponds to a less favourable case to observe oscillation since it implies small oscillation length due to low energy  $E \sim 1 \text{ MeV}$  and a relatively high frequency  $\Delta m_{13}^2 \sim 10^{-3} \text{eV}^2$ . We find  $L^{osc} \sim 1 \text{ m}$ , which means that the coherence may be lost if the vertex resolution is several times larger than  $1 \text{ m}$ . For example, the Double Chooz vertex resolution is  $\sim 10 \text{ cm}$  [28], which guarantees that the coherence is kept and that the oscillation effect can be seen. Note the decoherence may also concern the possible sterile neutrino, since an oscillation at very short distance (high frequency  $\Delta m_{41}^2 \sim 1 \text{ eV}^2$ ) is predicted. In all cases where coherence is lost, the oscillation is reduced to the constant term with baseline and neutrino energy:

$$P_{\nu_\alpha \rightarrow \nu_\beta(t)} \simeq \sum_i |U_{\alpha i}|^2 |U_{\beta i}|^2 \quad (1.2.20)$$

In general, an oscillation experiment tries to avoid the decoherence since the constant rate is only an averaged effect, whose variations are less important than at the oscillation maximum. Moreover, decoherence prevents from any relative shape study (with different energy  $E$ ) that often helps to cancel most of the systematic errors. In this thesis, we will apply the plane wave formalism in all cases, except for solar neutrino observation.

### 1.2.2 Three flavour neutrino oscillation in vacuum

As we have explained in Section 1.1, the current knowledge in the neutrino field leads to the three active flavour neutrinos as the most likely scenario. Unless the opposite is specified, we will not consider any sterile neutrino in this Section. In the standard neutrino scenario, six flavour mixings

are possible:

$$\nu_e \rightleftharpoons \nu_\mu \rightleftharpoons \nu_\tau \rightleftharpoons \nu_e \quad (1.2.21)$$

Through the very same way we proceed in the two flavours case, we can show that a  $N \times N$  unitary complex matrix does have  $2N^2 - N^2 = N^2$  complex degrees of freedom. It can be shown [22] in general that the mixing matrix  $U$  can be parametrised through the choice of independent degrees of freedom:

$$\frac{N(N-1)}{2} \text{ mixing angles} \quad (1.2.22)$$

$$\frac{N(N+1)}{2} \text{ phases} \quad (1.2.23)$$

In the three neutrino case, it leads to three mixing angles and six independent phases. Using the conservations of the number of leptons fields (global  $U(1)$  invariance), it can be shown as in the two neutrino case [22] that only one of these six phases is a physical observable independent degree of freedom, considering Dirac neutrino. The three-flavour oscillation probability can therefore be described by:

- 3 mixing angles in the PMNS matrix,  $\theta_{12}$ ,  $\theta_{23}$  and  $\theta_{13}$ .
- 2 independent squared mass differences  $\Delta m_{21}^2$  and  $\Delta m_{32}^2$ , since  $\Delta m_{31}^2 = \Delta m_{32}^2 + \Delta m_{21}^2$
- 1 CP violating phase  $\delta_{CP}$ . Unless the opposite is specified, we will assume  $\delta_{CP} = 0$  in most of the figures that will be shown in this thesis.

The 3D mixing matrix  $U$  can be written as the product of three 2 dimensional rotations:

$$U = \begin{pmatrix} 1 & 0 & 0 \\ 0 & c_{23} & s_{23} \\ 0 & -s_{23} & c_{23} \end{pmatrix} \times \begin{pmatrix} c_{13} & 0 & s_{13}e^{-i\delta_{CP}} \\ 0 & 1 & 0 \\ -s_{13}e^{i\delta_{CP}} & 0 & c_{13} \end{pmatrix} \times \begin{pmatrix} c_{12} & s_{12} & 0 \\ -s_{12} & c_{12} & 0 \\ 0 & 0 & 1 \end{pmatrix} \quad (1.2.24)$$

$$U = \begin{pmatrix} c_{12}c_{13} & s_{12}c_{13} & s_{13}e^{-i\delta_{CP}} \\ -s_{12}c_{23} - c_{12}s_{23}s_{13}e^{i\delta_{CP}} & c_{12}c_{23} - s_{12}s_{23}s_{13}e^{i\delta_{CP}} & s_{23}c_{13} \\ s_{12}s_{23} - c_{12}c_{23}s_{13}e^{i\delta_{CP}} & -c_{12}s_{23} - s_{12}c_{23}s_{13}e^{i\delta_{CP}} & c_{23}c_{13} \end{pmatrix} \quad (1.2.25)$$

where we defined:

$$c_{ij} = \cos \theta_{ij} \text{ and } s_{ij} = \sin \theta_{ij} \quad (1.2.26)$$

The complete expression of the oscillation probability can be derived from Eq 1.2.13. Figure 1.4 shows the main behaviour of the oscillation probability  $P_{\nu_\mu \rightarrow \nu_e}$  with  $L/E$ , given the oscillation parameters current values (see Table 1.4). We will go through the essential points of the three flavour oscillation:

- As we have seen, the neutrino oscillation varies with the baseline/Energy ratio ( $L/E$ ). Neutrinos with higher energies have therefore larger oscillation wavelengths.
- We remind that neutrino oscillation is due to the phase difference between the mass states since these states do not propagate with the same velocity due to their mass differences. This naturally implies that neutrinos of larger energy oscillate at longer distances since their propagation speed (their energy) is less affected by their mass difference than for lower energy neutrinos. For a given neutrino energy, the phase shift between the mass term with distance is ruled by the inverse of the squared mass difference. The measured squared mass differences are such that  $|\Delta m_{12}^2| \ll |\Delta m_{23}^2|$ . This implies that the oscillations are mainly ruled by  $|\Delta m_{23}^2|$  for small  $L/E \sim \frac{1 \text{ km}}{\text{MeV}}$  as it is the case for T2K. On the other hand, the  $|\Delta m_{12}^2|$  low frequency rules the oscillation for large  $L/E \sim \frac{100 \text{ km}}{\text{MeV}}$ . For the reasons explained in previous Section, the effect of the phase change between the first/second and third mass states will be averaged out and contribute as a rate term. These two effects can be clearly seen comparing Figure 1.3 and 1.4 which respectively show the flavour oscillation coming from the phase shift between the first/second mass state and the third, and between the first and second mass terms. We notice that only the absolute value of the squared mass difference impacts on the oscillations in vacuum.

- The flavour oscillation amplitudes are ruled by the mixing angles. The  $\theta_{13}$  mixing angle is far smaller than the other mixing angles (see Table 1.4). The impact is the very small amount of  $\nu_\mu$  oscillation to  $\nu_e$  from Tokai to Super-Kamiokande ( $L/E \simeq 500$  km/GeV), as can be seen in Figure 1.3. On the other hand, the  $\theta_{23}$  angle is compatible with a maximal mixing case ( $\theta_{23} \simeq 45^\circ$ ) given the current knowledge we have on this angle. This can be observed in Figure 1.3 since this angle is the main contributor to the  $\nu_\mu$  disappearance observed at Super-Kamiokande.
- The CP violation phase effects come in factor of the other mixing angle amplitude product. It follows that CP violation in the lepton sector affects neutrino oscillations only if none of the mixing angles is null, which has been lately verified for  $\theta_{13}$  [29], [30], [31]. This implies the CP violation phase can only be measured after the other parameters are very well known. The measurement of the CP violation phase can only be performed through appearance measurements, since  $P_{\nu_\alpha \rightarrow \nu_\alpha}$  is obviously CP invariant (from CPT invariance). Thus,  $\delta_{CP}$  can be measured in a single appearance experiment comparing neutrino and anti-neutrino oscillation probability, but can also be deduced from the appearance experiment given the knowledge on other mixing parameters from  $\delta_{CP}$  insensitive experiments (disappearance). The impact of  $\delta_{CP}$  on the  $\nu_\mu \rightarrow \nu_e$  oscillation in T2K is shown in Figure 1.5. The maximal deviation from the non CP violation is obviously obtained for maximal CP violation  $\delta_{CP} = 90^\circ$  or  $270^\circ$  which respectively correspond to the lowest and highest oscillation probability in neutrino mode (the contrary will occur in antineutrino mode). Due to accelerator and cross section issues, it is easier to obtain a high statistics in neutrino than in antineutrino mode in accelerator based experiments. Several reasons cumulate to explain this effet. In the case of T2K, the beam is produced with a proton collision on a target. The charge conservation, but also the quark content of the target (valence u-d quarks, no  $\bar{u}$ ) will favour the  $K^+$  and  $\pi^+$  production, which mainly decay in  $\nu_\mu$  (see Chapter 2). On top of this, the antineutrino cross section is suppressed by a factor two to three compared to neutrino, due to different vertex contributions in the Feynman diagrams. For this reason, the most favourable scenario for T2K to measure CP violation effect would be for  $\delta_{CP} = 270^\circ$ . We notice the difference between  $\delta_{CP} = 0^\circ$  and  $\delta_{CP} = 180^\circ$  only impacts the oscillation wavelength, which would require a very accurate measurement of  $|\Delta m_{32}^2|$ .
- We have summarised the whole T2K oscillation probability in Eq 1.2.27 in which the contribution of each term is identified by a different colour. The leading order term (magenta) is differently affected by the CP odd term (red) when changing from neutrino to antineutrino beam. The matter effects (dark blue) are also changed due to an opposite potential that is seen for antineutrino than neutrino ( $a \rightarrow -a$ ). The matter effect contribution will be further detailed in Section 1.3. Finally, additional CP even term (green) and small contribution of far solar term (light blue) oscillations are taken into account.

$$\begin{aligned}
 P(\nu_\mu \rightarrow \nu_e) = & 4c_{13}^2 s_{13}^2 s_{23}^2 \sin^2 \Delta_{31} \\
 & + 8c_{13}^2 s_{12} s_{13} s_{23} (c_{12} c_{23} \cos \delta - s_{12} s_{13} s_{23}) \cos \Delta_{32} \sin \Delta_{31} \sin \Delta_{21} \\
 & - 8c_{13}^2 c_{12} c_{23} s_{12} s_{13} s_{23} \sin \delta \sin \Delta_{32} \sin \Delta_{31} \sin \Delta_{21} \\
 & + 4s_{12}^2 c_{13}^2 (c_{12}^2 c_{23}^2 + s_{12}^2 s_{23}^2 s_{13}^2 - 2c_{12} c_{23} s_{12} s_{23} s_{13} \cos \delta) \sin^2 \Delta_{21} \\
 & - 8c_{13}^2 s_{12}^2 s_{23}^2 \frac{aL}{4E} (1 - 2s_{13}^2) \cos \Delta_{32} \sin \Delta_{31} \\
 & + 8c_{13}^2 s_{13}^2 s_{23}^2 \frac{a}{\Delta m_{31}^2} (1 - 2s_{13}^2) \sin^2 \Delta_{31}
 \end{aligned} \tag{1.2.27}$$

### 1.2.3 Two-flavour approximation in the three neutrino case

Nowadays, any fits of the oscillation probability is done in the three-flavour framework (if no sterile neutrino). However, the two-flavour approximation has been highly used in the past as the  $\theta_{13}$  value was known to be small. It allows to draw simpler conclusions, and we will see it may be applied as a good approximation of the three neutrino description. In this case, the mixing matrix is a  $2 \times 2$

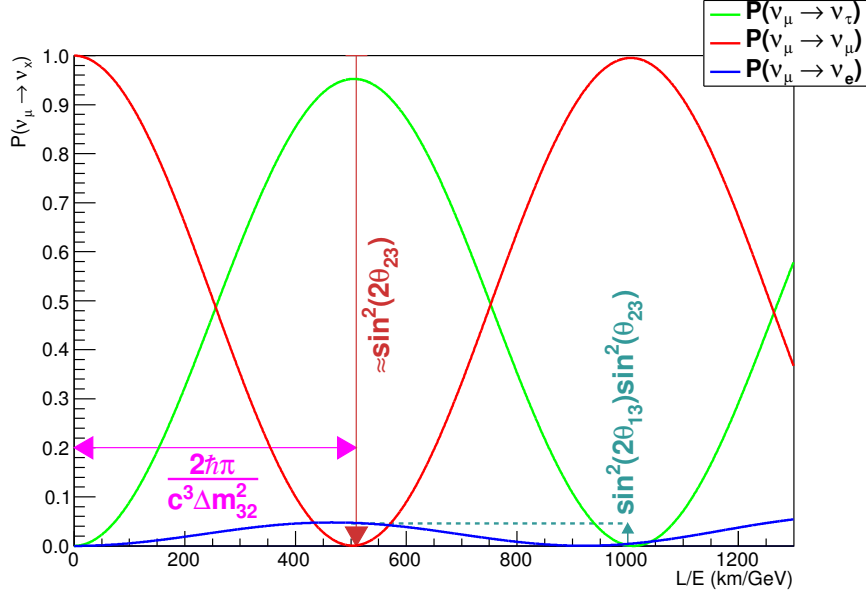


Figure 1.3: Three flavour oscillation considering the parameters summarised in Table 1.4 and assuming a pure  $\nu_\mu$  beam production. This is a reasonable approximation of T2K running in neutrino mode. The Super-Kamiokande detector is located at the first oscillation maximum  $L/E \approx 500$  km/GeV.

parameter	best fit (2008)	best fit (2014)
$\sin^2 2\theta_{12}$	$0.846^{+0.033}_{-0.026}$ ( $0.304^{+0.022}_{-0.016}$ )	$0.846^{+0.021}_{-0.021}$
$\sin^2 2\theta_{23}$	$1.00^{+0.00}_{-0.02}$ ( $0.50^{+0.07}_{-0.06}$ )	$0.999^{+0.001}_{-0.018}$
$\sin^2 2\theta_{13}$	$0.040^{+0.062}_{-0.036}$ ( $0.01^{+0.016}_{-0.011}$ )	$0.093^{+0.008}_{-0.008}$
$\Delta m_{21}^2 (\text{eV}^2)$	$7.65^{+0.23}_{-0.20} \times 10^{-5}$	$7.53^{+0.18}_{-0.18} \times 10^{-5}$
$\Delta m_{32}^2 (\text{eV}^2)$	$2.40^{+0.12}_{-0.11} \times 10^{-3}$	$2.44^{+0.06}_{-0.06} \times 10^{-3}$

Table 1.4: Summary of the knowledge on mixing parameters in 2008 (Ref [32]) compared to 2014 (Ref [13]). In parenthesis is shown the  $\sin^2 \theta$  value of each angle to simplify the link with Figure 1.22 for the reader. The errors shown correspond to the  $1\sigma$  errors. The whole measurements are done assuming  $\delta_{CP} = 0$ .

unitary complex matrix which has four independent real degrees of freedom. One shows [22] that the four degrees of freedom correspond to one real amplitude (mixing angle  $\theta$ ) and three phases through the re-parametrisation:

$$U = \begin{pmatrix} \cos \theta e^{i\omega_1} & \sin \theta e^{i(\omega_2+\eta)} \\ -\sin \theta e^{i(\omega_1-\eta)} & \cos \theta e^{i\omega_2} \end{pmatrix} = \begin{pmatrix} \omega_1 & 0 \\ 0 & \omega_2 \end{pmatrix} \begin{pmatrix} e^{i\eta} & 0 \\ 0 & 1 \end{pmatrix} \begin{pmatrix} \cos \theta & \sin \theta \\ -\sin \theta & \cos \theta \end{pmatrix} \begin{pmatrix} e^{-i\eta} & 0 \\ 0 & 1 \end{pmatrix} \quad (1.2.28)$$

It can be shown that some of these phases are not observable since they correspond to a global rotation of the lepton fields. Since the number of leptons is conserved in the Standard Model, these phases will be re-absorbed in the field definitions to finally give the mixing matrix:

$$U = \begin{pmatrix} \cos \theta & \sin \theta \\ -\sin \theta & \cos \theta \end{pmatrix} \quad (1.2.29)$$

The oscillation probability in the two flavour case is deduced from Eq 1.2.13 and gives:

$$P_{\nu_\alpha \rightarrow \nu_\beta(t)} = \frac{1}{2} \sin^2 2\theta (1 - \cos \Delta m^2 \frac{L}{2E}) = \sin^2 2\theta \sin^2(\frac{\Delta m^2 L}{4E}) \quad (1.2.30)$$

$$P_{\nu_\alpha \rightarrow \nu_\alpha(t)} = 1 - \sin^2 2\theta \sin^2(\frac{\Delta m^2 L}{4E}) \quad (1.2.31)$$

where  $\Delta m^2$  is the squared mass difference between the two mass states. The oscillation probability can be drawn only after retrieving the SI units from the natural unit we have used. A dimension estimation

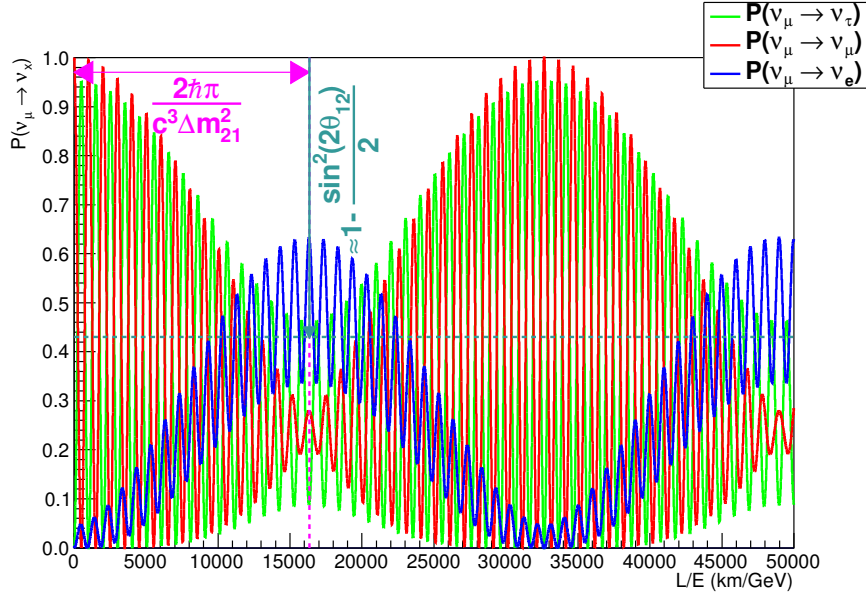


Figure 1.4: Long distance three-flavour oscillation considering the parameters summarised in Table 1.4 and assuming a pure  $\nu_\mu$  beam production. One observes the long distance effect of the “solar oscillation”.

shows that:  $[\frac{\Delta m^2 L}{4E} \equiv \frac{\hbar}{c^3}]$  which implies that the correct factor to have a dimensionless oscillation phase is:  $\Delta m^2 L c^3 / 4 \hbar E$ . This phase can be approximated for convenience to:

$$1.27 \frac{\Delta m^2 [\text{eV}^2] L [\text{km}]}{E [\text{GeV}]} \quad (1.2.32)$$

Figure 1.7 illustrates the  $\nu_\mu$  disappearance that occurs in T2K in the case we neglect matter effect (Section 1.3) and assuming two-flavour approximation. Super-Kamiokande position is located at the first oscillation maximum (295 km at 0.7 GeV) and one observes the coherence loss at long distance that we introduced in the previous Section. As has been illustrated in Figure 1.3, the  $\nu_\mu$  disappearance can be relatively well approximated by a two-flavour oscillation between  $\nu_\mu$  and  $\nu_\tau$ . It is a combination of both  $\theta_{13} \ll \theta_{23}$  and  $\Delta m_{32}^2 \gg \Delta m_{12}^2$  that allows this approximation. Since  $\Delta m_{32}^2 \gg \Delta m_{12}^2$ , we can separate oscillations at small  $L/E \sim \frac{\text{km}}{\text{MeV}}$  where the  $\nu_\mu$  oscillates through  $\nu_e$  with  $\sin^2 2\theta_{13} \sin^2 \theta_{23}$  amplitude to large  $L/E \sim \frac{100 \text{ km}}{\text{MeV}}$  where the oscillation amplitude is  $1/2 \times \sin^2 2\theta_{12}$ . Since T2K experiment focuses on  $L/E \sim \frac{\text{km}}{\text{MeV}}$ , the second oscillation has not still developed and  $\nu_e$  appearance is only affected by the factor  $\sin^2 2\theta_{13} \sin^2 \theta_{23}$ . Since  $\theta_{13} \ll \theta_{23}$ , the contribution of this appearance to the whole  $\nu_\mu$  disappearance ( $\sim \sin^2 2\theta_{23}$ ) is negligible. Therefore, we can approximate the  $\nu_\mu$  disappearance as a  $\nu_\mu \rightarrow \nu_\tau$  oscillation. In these 2 conditions, the oscillation probability may be re-written (defining  $\Delta m^2 \equiv \Delta m_{32}^2$ ) as:

$$P_{\nu_\alpha \rightarrow \nu_\alpha} = 1 - 4|U_{\alpha 3}|^2(1 - |U_{\alpha 3}|^2) \sin^2(\Delta m^2 \frac{L}{4E}) \quad (\text{disappearance}) \quad (1.2.33)$$

$$P_{\nu_\alpha \rightarrow \nu_\beta} = 4|U_{\alpha 3} U_{\beta 3}|^2 \sin^2(\Delta m^2 \frac{L}{4E}) \quad (\text{appearance}) \quad (1.2.34)$$

Note this approximation also holds to study  $\nu_e$  disappearance at large  $L/E \gg \frac{100 \text{ km}}{\text{MeV}}$ , as for the solar neutrinos. The oscillation due to  $\Delta m_{23}^2$  is averaged out by the finite detector resolution. Only the oscillation between the first and second mass states will remain (no more degenerated at this  $L/E$ ) with a limited amplitude coming from the averaged mixing of the third mass state with the observed flavour states. In the case we observe solar neutrinos, the oscillation amplitude will be only slightly shrunk by a factor  $\cos^4 \theta_{13}$  (see Eq 1.4.4, similar to solar neutrino oscillations) which allows to study  $\theta_{12}$  and  $\Delta m_{12}^2$  values independently from the other parameters.

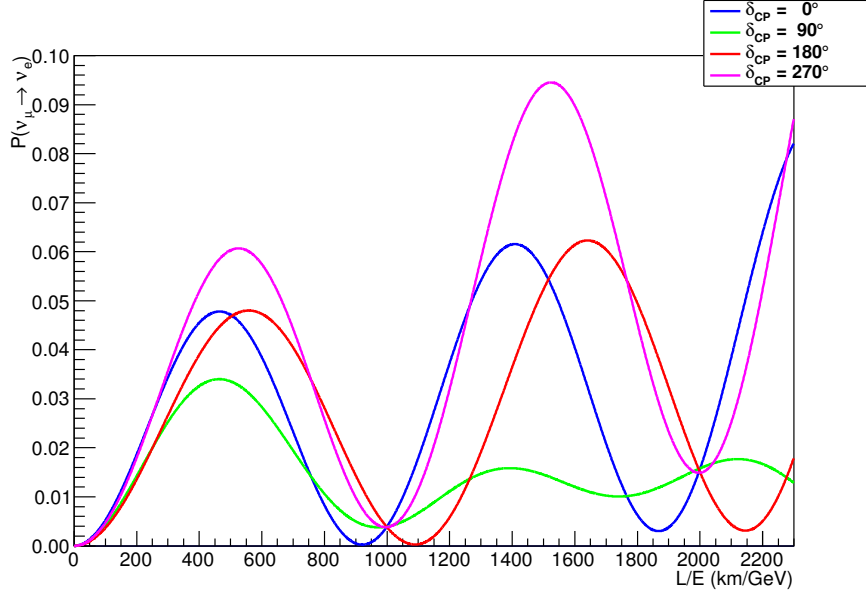


Figure 1.5: Impact of different CP violation phases on the  $\nu_e$  appearance at T2K assuming a pure  $\nu_\mu$  beam production. One observes a maximal effect for  $\delta_{CP} = 270^\circ$ , but also the effect increases at larger L/E for the following oscillation maxima.

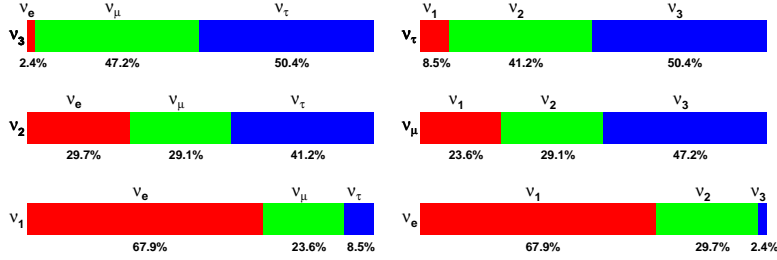


Figure 1.6: The flavour and mass state mixing given the mixing angle in Table 1.4.

## 1.3 Three-flavour neutrino oscillation in matter

### 1.3.1 General oscillation in matter

We described in Eq 1.2.4 the time evolution of the neutrino mass states. If the propagation does not occur in vacuum, the Hamiltonian will not only be a free Hamiltonian anymore but should take into account the “interaction of neutrino mass states” through matter. However, the neutrino interaction with matter naturally occurs through weak interaction of the flavour states. We therefore write this interaction Hamiltonian  $H_M$  as diagonal in the flavour states, while the free Hamiltonian  $H_V$  is diagonal along the neutrino mass states. The complete Hamiltonian:

$$H = H_V + H_M \quad (1.3.1)$$

will therefore be not diagonal in any of the mass or flavour basis. We will first detail the form of  $H_M$  in order to bring further conclusions on the interplay between propagation ( $H_V$ ) and matter effects ( $H_M$ ), *i.e* between neutrino flavour and mass states. We will assume the standard three active flavour scenario. When the neutrino interacts in matter, two outcomes are possible: either the flavour neutrino is changed in the associated charged lepton through W boson exchange with a nucleon (protons or neutron), or it is coherently scattered through the exchange of a  $Z^0$  boson with a proton, neutron or matter electron or W boson with an electron. Figure 1.9 shows the possible Feynman diagrams. As for charged current (CC) or neutral current (NC) interaction of a neutrino with a nucleon, each flavour will be equally scattered or suppressed. The same goes for NC interactions of a neutrino on a matter electron. Note that this equal suppression is not entirely true for CC interaction with a

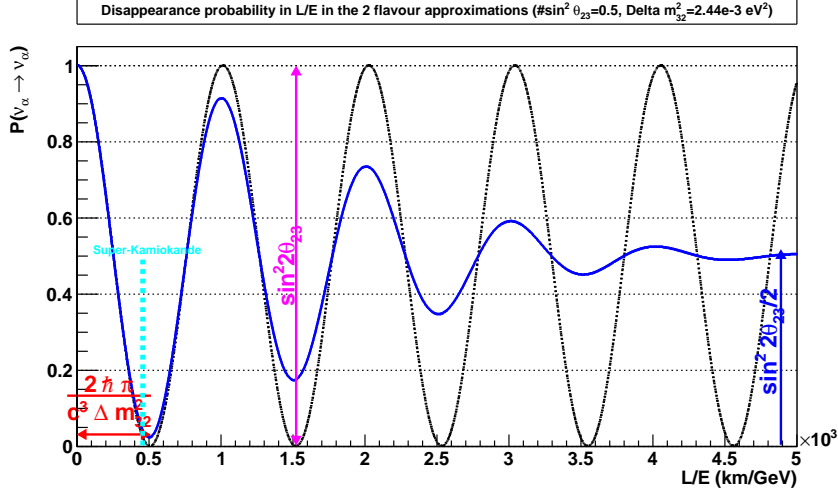


Figure 1.7: The coherence loss in the two-flavour scenario and assuming a mass squared difference  $\Delta m_{32}^2$ . This is a reasonable approximation of the  $\nu_\mu$  disappearance at T2K, where the Super-Kamiokande far detector is located at  $L/E \simeq 500$  km/GeV. One observes the mixing angle has been chosen maximal ( $\theta = 45^\circ$ ) to reproduce the effect of  $\theta_{23}$  according the constraints shown in Table 1.4.

nucleon due to the different masses of the outgoing leptons, but we can neglect this cross section effect for high ( $E \gg 1$  GeV) energy neutrinos. This leads the matrix  $H_M$  to be diagonal and have the same eigenvalues for each flavour, meaning the matter effect will not change the flavour composition (*i.e.*  $H_M \propto I$ ). However the matter (in the Earth or the Sun) naturally contains only nucleons and electrons but no  $\mu^-$  or  $\tau^-$ . For this reason, the  $\nu_e$  neutrinos will have a singular behaviour in comparison with the other species due to the very last diagram: a CC interaction with an  $e^-$  that can only occur for the  $\nu_e$  neutrinos. The  $\nu_e$  interacting more with matter than the other flavour, we expect this species to have a higher “equivalent interacting mass” in matter than the other flavour species. In conclusion, all neutrino flavours do have an interacting mass that depends on the amount of nucleons/electrons in the matter (*i.e.* density) while the  $\nu_e$  has an additional term that depends only on the electron density.

Considering only the neutrino interactions where the neutrino is scattered, it leads [22] to a matter Hamiltonian (in the flavour basis):

$$H_M = \begin{pmatrix} \sqrt{2}G_F(N_e - \frac{1}{2}N_n) & 0 & 0 \\ 0 & -\sqrt{2}G_F\frac{1}{2}N_n & 0 \\ 0 & 0 & -\sqrt{2}G_F\frac{1}{2}N_n \end{pmatrix} \quad (1.3.2)$$

where  $G_F$  is the Fermi constant (weak interaction coupling),  $N_e$  and  $N_n$  are respectively the electron and neutron densities in the material. Note this form is valid under the three hypothesis of matter:

- neutral ( $N_e = N_p$ )
- unpolarised
- non-relativistic

With a proper Lagrangian derivation, one shows [22] that the proton and electron NC contributions are cancelling due to opposite vector coupling ( $g_V$ ) and same content of matter in electrons and protons (valid in the case of neutral matter). The opposite sign in the CC contribution of the electron and NC of the neutrons comes from the different vector coupling constants due to neutrons and electrons different hypercharge. While the CC interaction with electrons adds a supplementary energy to the existing neutrino free energy, the interaction with neutrons contributes negatively. Reverting the oscillation point of view in the flavour basis instead, it follows that the equivalent  $\nu_e$  energy is higher than the other flavour states, which means a time evolution of the wave amplitude at higher frequencies (Eq 1.2.4). We will come back on this issue in the two-flavour approximation. We note that in the

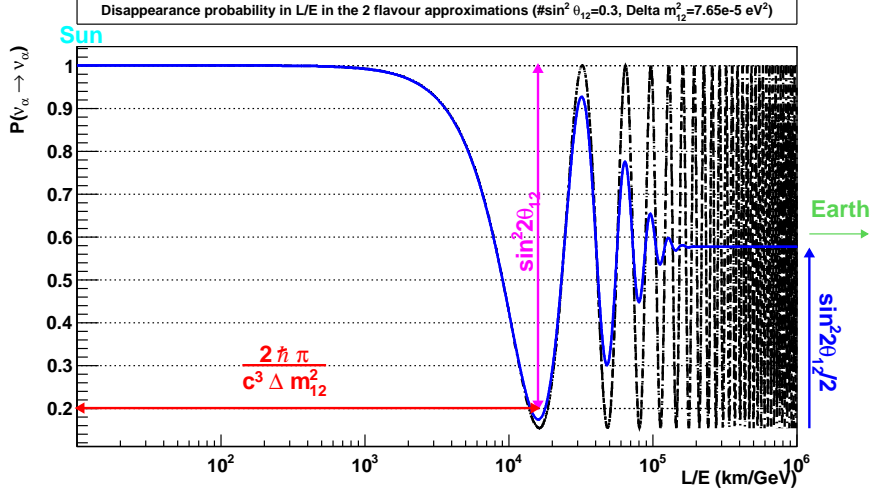


Figure 1.8: The coherence loss in the two flavour scenario and assuming a mass squared difference  $\Delta m_{21}^2$  and a mixing angle  $\theta_{12}$ . This is a reasonable approximation of the  $\nu_e$  disappearance of solar neutrino. One observes the averaging of the oscillation prior reaching the Earth.

case of sterile neutrinos, they will not be affected anyhow by the passage through matter. We will now deduce the impact of the matter term on the neutrino flavour oscillation. For this, we must describe directly the time evolution of the flavour states this time. As the free variation is given in the mass state basis, we have applied the inverse PMNS matrix to obtain its form in the flavour basis, where matter effects are decoupled. It follows that:

$$H^F |\nu_\alpha\rangle = H_V^F |\nu_\alpha\rangle + H_M^F |\nu_\alpha\rangle \quad (1.3.3)$$

where F denotes the flavour basis (and upper M will denote the mass state basis).  $H_M^F = H_M$  we previously defined, and  $H_V^F = U_{PMNS} H_V^M U_{PMNS}^*$  where  $H_V^M$  is the diagonal vacuum oscillation matrix in the mass state we defined in Eq 1.2.4. The different oscillations of the neutrino in matter as compared to in vacuum due to this Hamiltonian additional term, and the possible resonance that we will describe, is referred to as the Mikheyev-Smirnov-Wolfenstein (MSW) effect [33]. In order to simplify<sup>1</sup> the illustration of this effect, we will here consider a two-neutrino case ( $\nu_e$  and  $\nu_\mu$ ). We will illustrate the MSW effect that happens in the Sun. The matter effects will be denoted as:

$$A \equiv 2\sqrt{2}EG_F N_e. \quad (1.3.4)$$

The calculation of  $H^F$  from Eq 1.3.3 gives:

$$H^F = \frac{1}{4E} \begin{pmatrix} -\Delta m^2 \cos 2\theta + A & \Delta m^2 \sin 2\theta \\ \Delta m^2 \sin 2\theta & \Delta m^2 \cos 2\theta - A \end{pmatrix} \quad (1.3.5)$$

in the case of a neutrino produced with the energy E. The Hamiltonian is then diagonalised which defines a natural basis diagonal to the free and matter effects, that we will denote with N. The diagonalisation finally leads to [22]:

$$H^N = \frac{1}{4E} \begin{pmatrix} -\Delta m_N^2 & 0 \\ 0 & \Delta m_N^2 \end{pmatrix} \quad (1.3.6)$$

where  $\Delta m_N^2$  is the effective mass splitting in matter (oscillation frequency in L/E) defined by:

$$\Delta m_N^2 = \sqrt{(\Delta m^2 \cos 2\theta - A)^2 + (\Delta m^2 \sin 2\theta)^2}. \quad (1.3.7)$$

<sup>1</sup>in the three flavour case, the calculation and length of the formula makes them impractical to show in this thesis

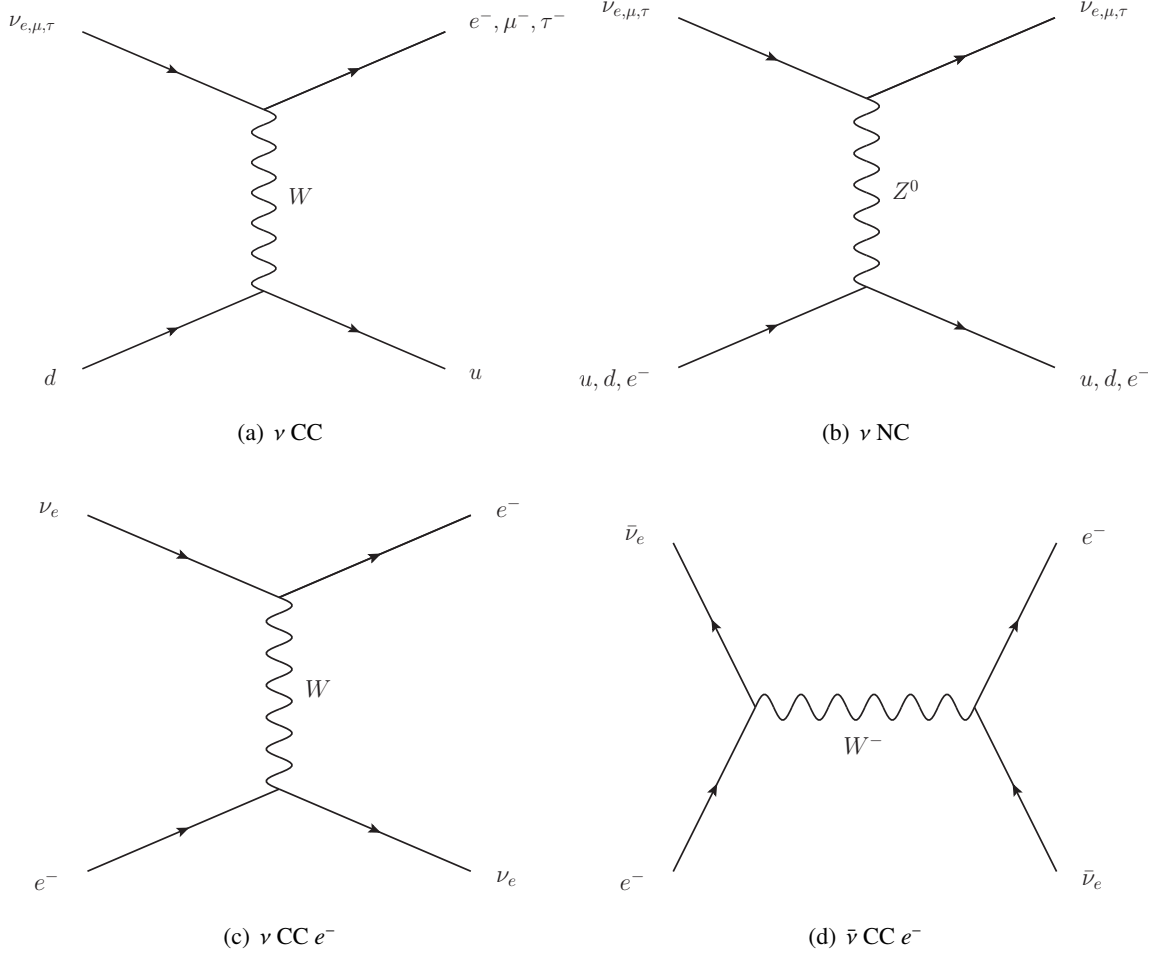


Figure 1.9: The Feynman diagrams of the flavour neutrino and antineutrino interactions in the “normal” matter (no  $\mu^-$ , no  $\tau^-$ , no anti-matter). We have drawn the quark state rather than the nucleon state. One observes the singular treatment of  $\nu_e$  and  $\bar{\nu}_e$  in comparison with the other flavour states due to the lack of  $\mu^-$  and  $\tau^-$  in matter.

Here we defined  $\Delta m_N^2$  as positive, assuming the neutrino mass state defined as 2 is the more massive one by definition. The eigenvalues found in the diagonalisation give the transfer matrix  $U_N$  from the flavour to the diagonal basis  $H^N = U_N^* H^F U_N$ :

$$U_N = \begin{pmatrix} \cos \theta_N & \sin \theta_N \\ -\sin \theta_N & \cos \theta_N \end{pmatrix} \quad (1.3.8)$$

where  $\theta_N$  is the effective mixing angle of neutrinos in matter given by:

$$\tan 2\theta_N = \frac{\tan 2\theta}{1 - \frac{A}{\Delta m^2 \cos 2\theta}}. \quad (1.3.9)$$

The eigenstates are no more the neutrino free mass states  $|\nu_{1,2}\rangle$  but some equivalent mass states that are the independent states when the neutrino passes through matter with a given density. Note that these eigenstates do change with the density, and that we retrieve the neutrino free mass states in the case of zero density ( $\tan 2\theta_N = \tan 2\theta$ ). The same goes for the oscillation frequency (mass splitting).

We'd like to present this result in a slightly different form to simplify the conclusions:

$$\Delta m_N^2 = \Delta m^2 \sqrt{(\cos 2\theta - \frac{A}{\Delta m^2})^2 + (\sin 2\theta)^2} \quad (1.3.10)$$

$$= \Delta m^2 \sqrt{(\cos 2\theta - \frac{2\sqrt{2}L^{osc}G_F N_e}{4\pi^2})^2 + (\sin 2\theta)^2} \quad (1.3.11)$$

$$= \Delta m^2 \sqrt{(\cos 2\theta - \frac{L^{osc}}{L^{int}})^2 + (\sin 2\theta)^2} \quad (1.3.12)$$

where we define the oscillation length in vacuum  $L^{osc}$  as in Eq 1.2.14 and the mean interaction length of a flavour  $\nu_e$  in matter as:

$$L^{int} = \frac{4\pi}{A}. \quad (1.3.13)$$

Note the difference with the interaction Lagrangian,  $L_{int}$ . We have allowed us to use this definition since  $G_F N_e$  indicates the average interaction probability in matter (interaction probability on an electron times the number of electrons). In the same way, we have re-defined the mixing angle:

$$\tan 2\theta_N = \frac{\tan 2\theta}{1 - \frac{L^{osc}}{L^{int} \cos 2\theta}} \quad (1.3.14)$$

- For  $L^{osc} \ll L^{int}$  which corresponds to negligible matter effects, the matter does not impact on neutrino oscillation and the mixing angle and mass squared differences in matter are equal to their value in vacuum  $\tan^2 2\theta_N = \tan^2 2\theta$  and  $\Delta m_N^2 = \Delta m^2$  respectively. Assuming  $\theta_{12} = 33.4^\circ$  (Table 1.4), the  $\nu_e$  is mainly constituted of  $\nu_1$ . If  $\Delta m_{21}^2 > 0$ , it implies that the equivalent “mass”, or energy of the  $\nu_e$  flavour state is lower than for  $\nu_\mu$  state.
- For  $L^{osc} \gg L^{int}$  which corresponds to large matter effect, lots of neutrino interactions with matter happen within one oscillation wavelength. If the mass effect is high enough ( $A \gg |\Delta m_{21}^2|$ ), it follows that the equivalent energy for a  $\nu_e$  is higher than for a  $\nu_\mu$ . If we define  $\nu_2$  the higher mass state also in matter, it follows this mass state oscillations also occurs for shorter distances than for  $\nu_1$ . The  $\nu_e$  energy (probability amplitude frequency) will be therefore far closer to the  $\nu_2$  than to the  $\nu_1$ , which implies that the  $\nu_e$  will be exclusively  $\nu_2$ . This maximal mixing is expressed through  $\tan^2 2\theta_N \rightarrow 0$  but with  $\tan^2 2\theta_N \leq 0$  which indicates  $\theta_N = 90^\circ$ . Because  $\nu_2$  is the higher mass state, and corresponds to  $\nu_e$ , it scales with the mass effects that enhance the  $\nu_e$  energy without any bound, and so does the subsequent mass splitting  $\Delta m_N^2$ .
- For  $L^{osc} = L^{int} \cos 2\theta$ , the mass splitting original difference in  $\nu_1$  and  $\nu_2$  is almost cancelled out by the energy gain of  $\nu_e$  compared to  $\nu_\mu$ . Since the two flavour and mass states will exhibit a similar “effective” energy, their phase changes with the same frequency, which leads to a maximum mixing between the different flavour states:  $\theta_N = 45^\circ$  *i.e.*:

$$|\nu_e\rangle = 0.71 |\nu_1\rangle + 0.71 |\nu_2\rangle \quad , \quad |\nu_\mu\rangle = -0.71 |\nu_1\rangle + 0.71 |\nu_2\rangle \quad (1.3.15)$$

This leads to a minimum in the mass splitting between  $\nu_1$  and  $\nu_2$ ,  $\Delta m_N^2 = \Delta m_{21}^2 |\sin \theta|$  since almost similar energies. Note that this is only possible since  $\nu_e$  mostly contains  $\nu_1$  in vacuum which is the lighter mass state. In the opposite case (if  $\nu_e$  were mainly composed of  $\nu_2$  in vacuum), the energy gain from interaction would have only increased the mass state energy difference. We will then retrieve the large matter effects without going through a resonance. For this reason, the resonance can only occur if  $\theta_{12} < 45^\circ$ . For a given mixing angle, the sign of the mass hierarchy between  $\nu_1$  and  $\nu_2$  will therefore impact differently the oscillation due to matter effects. We will see that this resonance is crucial to explain the observation on Earth of solar  $\nu_e$  disappearance, leading to the measurement of the sign of  $\Delta m_{12}^2$ .

Figure 1.10 shows the behaviour of the mixing angle with the matter density, along with the mass state components of each flavour state. The evolution of the effective mass of each state is shown

in Figure 1.11 and clearly indicates what has been explained. For very high electron densities, the  $\nu_e$  is produced with a much larger energy (“equivalent mass”) than the other flavour states. The  $\nu_2$  being the most massive state by definition, it will then only be mixed with the  $\nu_e$  flavour. The lower the density, the lower the effective  $\nu_e$  “effective mass” difference with  $\nu_\mu$ . The  $\nu_2$  most massive states will no longer be constituted of only  $\nu_e$  but also of  $\nu_\mu$  whose proportion increases with the decreasing density. It therefore exists a resonance if vacuum  $\nu_e$  equivalent mass is lower than  $\nu_\mu$ , *i.e.* if  $\nu_e$  is more mixed with the smaller mass state  $\nu_1$ . The resonance is reached when  $\nu_e$  and  $\nu_\mu$  have an equivalent effective mass, which therefore implies  $\nu_2$  is constituted of the same  $\nu_e$  and  $\nu_\mu$  proportions, as  $\nu_1$ . For densities smaller than the resonance, the most massive state “equivalent mass” is therefore not mainly ruled by  $\nu_e$  but by the higher  $\nu_\mu$  proportions that have a fixed mass in the medium. On the contrary, the mass of the lighter state  $\nu_1$  is now ruled by the  $\nu_e$  equivalent mass that continues to decrease until it reaches the no density state (vacuum) at which  $\nu_1 = m_1^{Vacuum}$ . Note this description is possible only in the adiabatic approximation, meaning no oscillation  $\nu_{1N} \rightleftharpoons \nu_{2N}$  occurs in matter, but only flavour mixing changes. This is realised if the spatial density variations are small as compared to the oscillation length in matter.

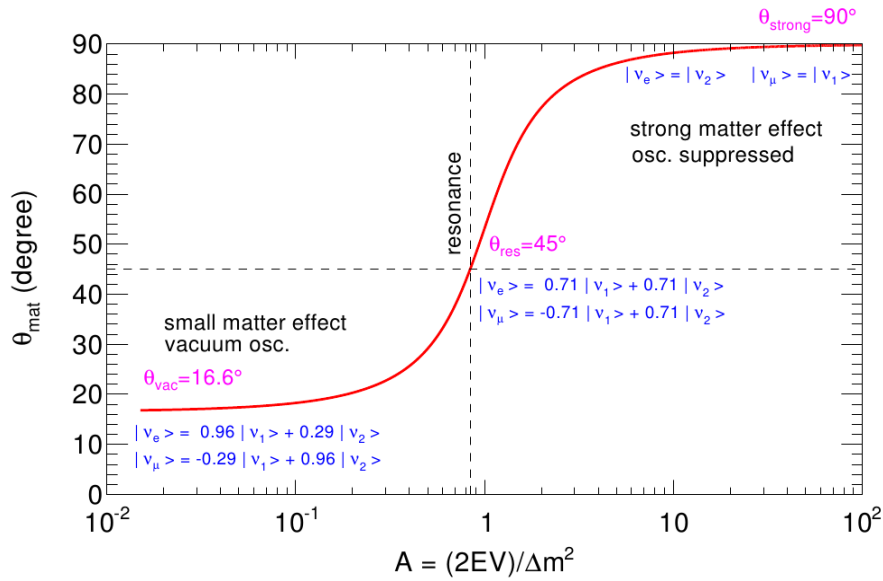


Figure 1.10: Mixing angle variations with the electron potential in matter, for a mixing angle in vacuum  $\theta_{\text{vac}} = 16^\circ$ . The maximal mixing occurs for a potential  $A = 1$ , at which the minimal mass splitting is observed (Figure 1.11). Reproduced from the original [22].

### 1.3.2 The neutrino mass hierarchy

We have seen that in vacuum, the oscillation probability frequency (in  $L/E$ ) is only sensitive to the absolute value of the squared mass differences. But this is not the case in matter. In the previous section, we observed that the resonant mixing only appears in matter if  $\nu_e$  is more mixed with the smaller mass state (in vacuum). Since the mixing angles between flavour and mass states in vacuum are known, the oscillation measurements of neutrino propagating through matter should lead to a possible determination of the mass hierarchy between the  $\nu_1$ ,  $\nu_2$  and  $\nu_3$ . We will see in Section 1.4 that the matter effects are important in the Sun, and have been observed in the solar neutrino experiment. We will show these experiments are sensitive to the  $\nu_1 \rightleftharpoons \nu_2$  oscillations due to their very long baseline. For this reason, the mass hierarchy between the  $\nu_1$  and  $\nu_2$  neutrino has been measured through the solar neutrino experiment, and it was found that  $m_1 < m_2$ . As for the  $\nu_3$ , the determination of its mass hierarchy with the two other states is still unknown. In fact, we will see that the  $\nu_2 \rightleftharpoons \nu_3$  oscillation occurs for shorter baselines (for the same energy), which implies that this oscillations should be observed with higher sensitivity (no averaging) using neutrino sources on Earth. The atmospheric neutrino are in principle good candidates, but the Earth small density imposes a very

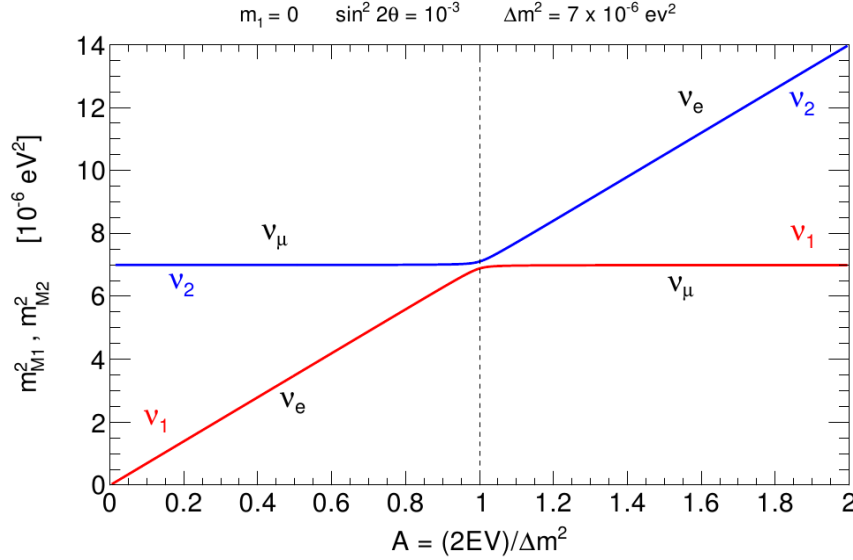


Figure 1.11: Mass squared variations with the electron potential in matter. Reproduced from the original [22].

sensitive experiment to determine the remaining unknown mass hierarchy. The remaining unknown hierarchy of  $m_3$  compared to  $m_1 < m_2$  is known as the mass hierarchy problem. The normal hierarchy corresponds to the case where  $m_3 \gg m_2 > m_1$ , and the inverted to  $m_2 > m_1 \gg m_3$ . Unless the opposite is specified, we will assume the normal hierarchy in most of the figures.

### 1.3.3 The matter effects in T2K

In the case of T2K, matter effects happen due to neutrino oscillation through the Earth. For T2K relatively small baseline (295 km), we will assume the neutrino only propagate through the crust, which has an average density of  $2.6\text{g/cm}^3$ . Figure 1.12 compares the variation of the  $\nu_e$  appearance due to matter density effects. We observe that the matter effects only barely impact the appearance probability ( $\leq 10\%$ ) compared to vacuum oscillations. The normal hierarchy enhances the oscillation  $\nu_\mu \rightarrow \nu_e$  through passage through the Earth. In fact, if  $\nu_3$  has a higher mass, we expect the effective mass squared difference in matter  $\Delta m_{31}^2_N$  to be reduced:  $\nu_1$  has a larger mixing with  $\nu_e$  than  $\nu_3$  (Figure 1.6) and  $\nu_e$  acquires a higher equivalent mass in matter than other flavours. Comparing Figures 1.10 and 1.11, we have seen that this equivalent smaller mass squared difference will imply mixing angle closer from  $45^\circ$  than in vacuum, which will enhance the mixing. On the contrary, if the neutrino masses are ordered in the inverted hierarchy, the equivalent mass splitting will be higher than in vacuum and one expects the mixing to be even more reduced due to matter effects, as observed in Figure 1.12.

Through the neutrino matter effect in Earth, the accelerator based experiments as T2K are able to determine the mass hierarchy between the  $\nu_{1,2}$  and  $\nu_3$  mass states. The  $\nu_e$  being mostly contained in  $\nu_1$  and  $\nu_2$  in vacuum, one expects an MSW resonance only if  $\nu_1$  corresponds to a lighter mass state compared to  $\nu_3$ , although very low matter effect prevents T2K from having a high sensitivity in the next years.

## 1.4 Determination of the PMNS matrix

We have seen that the PMNS matrix can be factorised in three 2D rotation matrices. Each of these matrix parameters (mixing angles and CP phase) along with the associated mass squared differences can be measured observing neutrinos from different sources. This is mostly due to the differences between the mass square splitting, but also relative amplitude, that allows to be sensitive to different oscillations when observing neutrinos from different sources (*i.e* baseline and energy). The

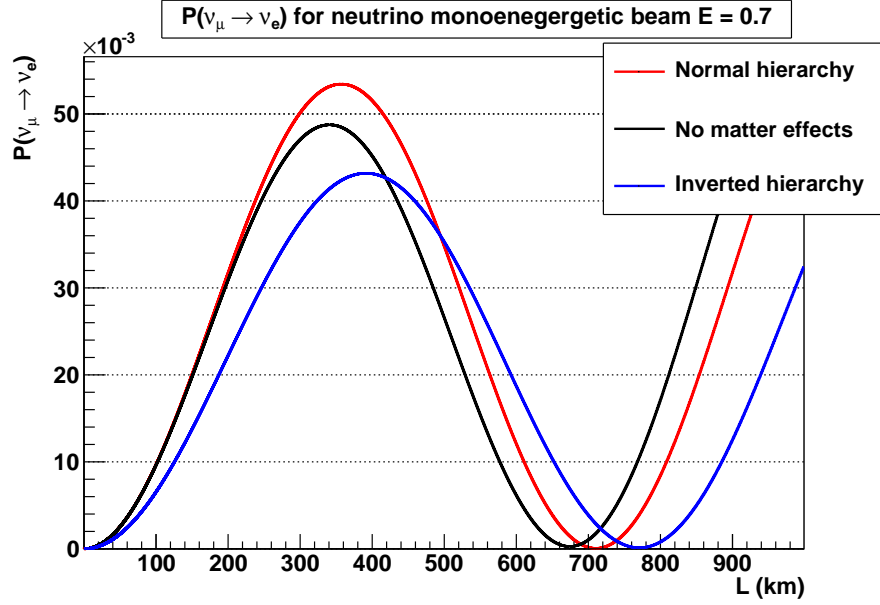


Figure 1.12: Impact of matter effects on the  $\nu_e$  appearance at T2K assuming a pure  $\nu_\mu$  beam production. One observes the enhanced oscillation in the case of normal hierarchy.

factorisation exhibits the different sector in the PMNS matrix:

$$U = \begin{matrix} \text{Atmospheric (\& LBL Accelerator)} \\ \begin{pmatrix} 1 & 0 & 0 \\ 0 & c_{23} & s_{23} \\ 0 & -s_{23} & c_{23} \end{pmatrix} \end{matrix} \times \begin{matrix} \text{Reactor (\& LBL Accelerator)} \\ \begin{pmatrix} c_{13} & 0 & s_{13}e^{-i\delta} \\ 0 & 1 & 0 \\ -s_{13}e^{i\delta} & 0 & c_{13} \end{pmatrix} \end{matrix} \times \begin{matrix} \text{Solar (\& VLB Reactor)} \\ \begin{pmatrix} c_{12} & s_{12} & 0 \\ -s_{12} & c_{12} & 0 \\ 0 & 0 & 1 \end{pmatrix} \end{matrix}. \quad (1.4.1)$$

We have summarised in the Table 1.5 the baseline and neutrino energies of several experiments, along with their sensitivities to different mass squared differences. The sensitivity shown here corresponds to the first oscillation maxima. Observation of these maxima occurs when:

$$\frac{\Delta m^2 L}{2E} \sim 1. \quad (1.4.2)$$

The oscillation experiment located at large  $L/E$  compared to the oscillation length are only sensitive to the averaged transition probability. The measurement of the mass splitting can only be given through a lower limit, and the mixing angle can be measured but with reduced sensitivity compared to experiment located at the oscillation maximum. On the other hand, the neutrino sources have a spatial extension as well as the detector. On top of that, the neutrino sources are not generally mono-energetic and the detector has a finite energy resolution. The oscillation should therefore be averaged over the uncertainty on the baseline and neutrino energy. Finally, two analysis can be generally performed: a rate only analysis by counting a given neutrino flavour, and a shape analysis that takes into account the neutrino energy spectrum. The rate analysis is then averaged over the neutrino energy spectrum, which reduces the sensitivity to the oscillation maximum and poorly disentangles the effect of  $\Delta m^2$  and  $\theta$ . On the contrary, the shape analysis allows to obtain a  $L/E$  coverage. If the resolution and the neutrino spectrum are large enough, one covers several oscillation maxima, which allows to clearly distinguish the impact of the mixing angle on the amplitude from the impact of  $\Delta m^2$  on the oscillation wavelength.

### 1.4.1 The solar neutrino sector

The stars, and in particular the Sun, are the source of an intense neutrino flux. The neutrino production mainly occurs through the thermonuclear fusion of hydrogen atoms in the Sun core. This reaction is also the original source of the photon production in the Sun, that counterbalances the gravitation

Experiment type	$L$	$E$	Sensitivity $\Delta m^2$	Examples
SBL reactor	$\sim 10$ m	$\sim 1$ MeV	$\sim 0.1 \text{ eV}^2$	Bugey, Rovno
SBL accelerator	0.01-1 km	0.01-10 <sup>2</sup> GeV	1-10 <sup>2</sup> eV <sup>2</sup>	LSND, MiniBooNE
LBL reactor	$\sim 1$ km	$\sim 1$ MeV	$\sim 10^{-3} \text{ eV}^2$	CHOOZ, Palo Verde
LBL accelerator	$\sim 10^3$ km	$\gtrsim 1$ GeV	$\gtrsim 10^{-3} \text{ eV}^2$	K2K, MINOS
Atmospheric	20-10 <sup>4</sup> km	0.5-10 <sup>2</sup> GeV	$\sim 10^{-4} \text{ eV}^2$	Super-Kamiokande
VLB reactor	$\sim 10^2$ km	$\sim 1$ MeV	$\sim 10^{-5} \text{ eV}^2$	KamLAND
Solar	$\sim 10^{11}$ km	0.2-15 MeV	$\sim 10^{-12} \text{ eV}^2$	GALLEX/GNO, SNO

Table 1.5: The different types of neutrino oscillation experiments given their distance with the neutrino source (SBL = Short Baseline, LBL = Long BaseLine et VLB = Very Long Baseline) along with the neutrino energy and the experiment sensitivity to  $\Delta m^2$ . The list presented here is not exhaustive. We remind that an oscillation experiment is sensitive to  $\Delta m^2$  higher than the numbers shown in this Table, but the corresponding effects are averaged due to detector finite resolution. The numbers shown here correspond to the first oscillation maximum. [22]

effects and produces the Sun light that we can see from the Earth. The fusion operates through the effective conversion of four protons and two electrons into one helium nucleus, two electron neutrinos and energy production:

$$4p + 2e^- \rightarrow {}^4\text{He} + 2\nu_e + 26,73 \text{ MeV}. \quad (1.4.3)$$

While the Sun core is opaque to photons, the  $\nu_e$  propagation will only be smally affected by the high density (MSW effect only) because they are only sensitive to weak interactions. For this reason, the solar neutrino observation provides a barely affected image of the Sun core, which the photons cannot do. Figure 1.13 shows the neutrino image of the Sun as seen by Super-Kamiokande. The produced

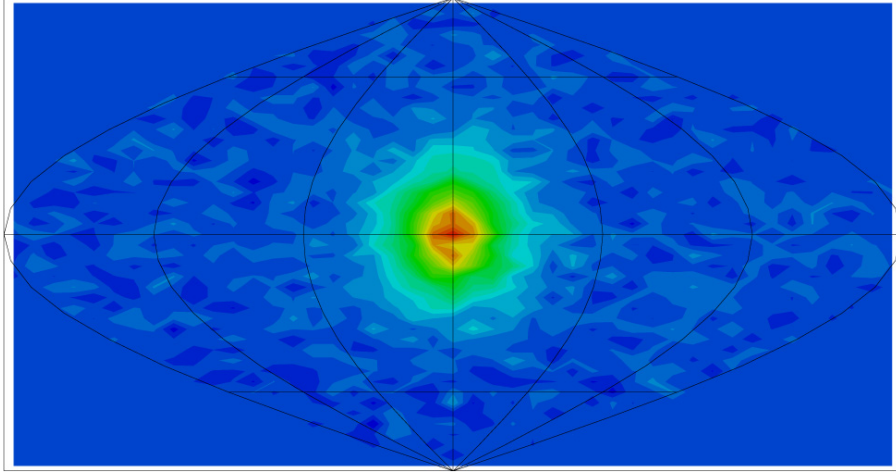


Figure 1.13: The Sun observed through its neutrino flux in Super-Kamiokande. Taken from [34].

neutrino flux has a very high intensity of about  $6.5 \times 10^{10} \text{ cm}^{-2} \cdot \text{s}^{-1}$ . Neutrinos are measured on Earth with an energy spectrum that spreads from 1 to 14 MeV. Figure 1.14 shows the produced neutrino flux in the Sun. The  $\nu_e$  flux has been historically first measured in the Homestake experiment and disagrees with the predictions prior to oscillation scenario. The later observations in Homestake [9], gallium experiments SAGE [35] and GALLEX/GNO [36][37] and in the Kamiokande [38], Super-Kamiokande [39] and SNO [11] experiments are also in disagreement with the expected solar neutrino flux, based on the Sun Standard Model. Moreover, these disagreements vary with the experiments as shown in Figure 1.15 between 50% and 70%. The solar neutrino deficit has been first raised in 1968 with the Homestake experiment measurements and solved in 2001 by the SNO experiment. The observed deficit of  $\nu_e$  flavour could not discriminate between possible problem in the Sun Standard Model, or from  $\nu_e$  oscillation into other flavours that have not been measured. The SNO experiment was conceived to discriminate between these two hypotheses through the measurement of the sum of the different flavour contributions. In this experiment, the heavy water spheric detector allows to observe both the  $\nu_e$  through CC interactions, but also the whole neutrino content through NC

interactions (neutron detection capability) or electron scattering. The results for the different channels are displayed in Figure 1.15 and clearly shows the  $\nu_e$  only represents one third of the total neutrino flux. This total neutrino flux is in agreement with the Sun Standard Model prediction, which validate the Sun Standard Model and explains the solar neutrino deficit by a  $\nu_e$  flavour oscillation into other flavours between the Sun and the Earth.

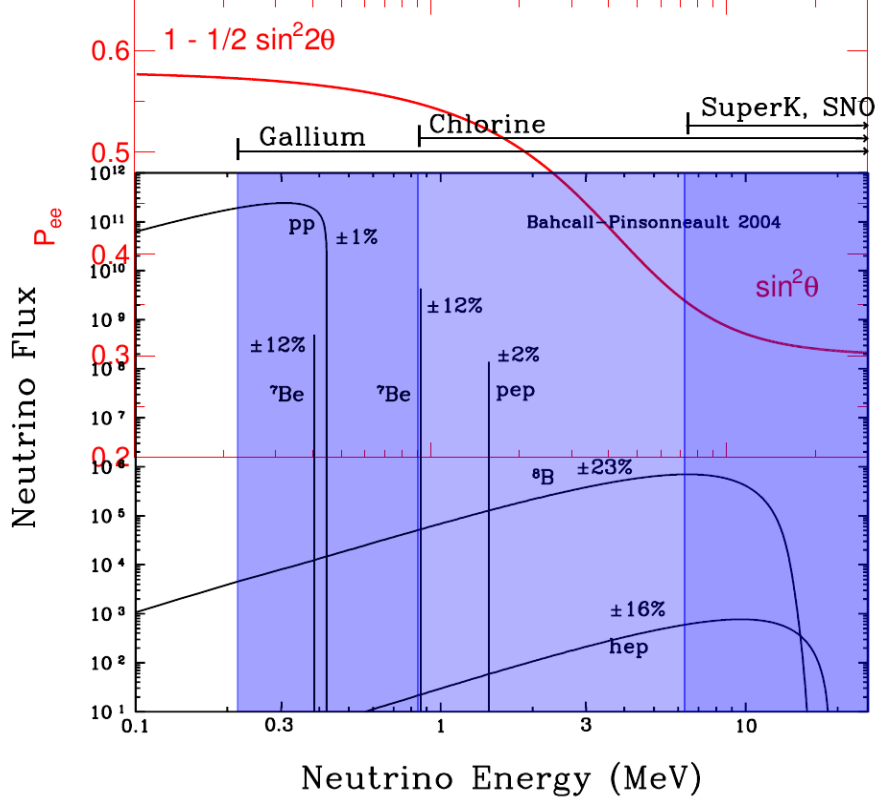


Figure 1.14: The solar neutrino energy spectrum coming from the different reaction cycles in the Sun [40]. The energy threshold of Super-Kamiokande and SNO is typically a few MeVs, while it is 0.233 MeV and 0.814 MeV respectively for the Gallium and Chlorine experiments. The survival probability  $P_{ee} = P_{\nu_e \rightarrow \nu_e}$  shows both the average rate decrease due to  $\theta_{12}$  effect (similar to Eq 1.4.4). One observes the larger disappearance with neutrino energy which is due to the decrease of the interaction length  $L^{int}$  in the Sun with the neutrino energy and so, the increase of the MSW effect.

The accurate measurement of the associated mixing angle and mass splitting was only possible using the KamLAND experiment results [41] (A posteriori, since the solar neutrino oscillation are averaged on Earth). KamLAND is a reactor based experiment that observes electron antineutrinos produced by surrounding Japan nuclear powerplants. The average distance of KamLAND from the different reactors weighted by their respective fluxes is  $L_0 = 175$  km. At this distance, the oscillation probability can be written as:

$$P_{\bar{\nu}_e \rightarrow \bar{\nu}_e} \simeq 1 - \frac{1}{2} \sin^2 2\theta_{13} - \cos^4 \theta_{13} \sin^2 2\theta_{12} \sin^2 \left( \frac{\Delta m_{21}^2 L}{4E} \right) \quad (1.4.4)$$

The averaged term allows to measure the mixing angle  $\theta_{13}$ . We will come back on this issue in the dedicated reactor section. The oscillation amplitude depends on the  $\theta_{13}$  and  $\theta_{12}$  mixing angles. Due to the uncertainty both on  $\theta_{13}$  (not measured) value, the KamLAND experiment is not mainly dedicated to measure the mixing angle  $\theta_{12}$ . On the opposite, the main success of the KamLAND experiment is its world leading accurate measurement of the mass splitting since the oscillation frequency in Eq 1.4.4 provides a direct measurement of the mass splitting  $\Delta m_{21}^2$  that governs  $\nu_1 \rightleftharpoons \nu_2$  oscillations. Mainly using the shape analysis in  $L/E$  shown in Figure 1.16, KamLAND measured the squared mass splitting  $\Delta m_{21}^2 = (7.59 \pm 0.21) \times 10^{-5} \text{ eV}^2$  [41].

**Total Rates: Standard Model vs. Experiment**  
Bahcall–Serenelli 2005 [BS05(OP)]

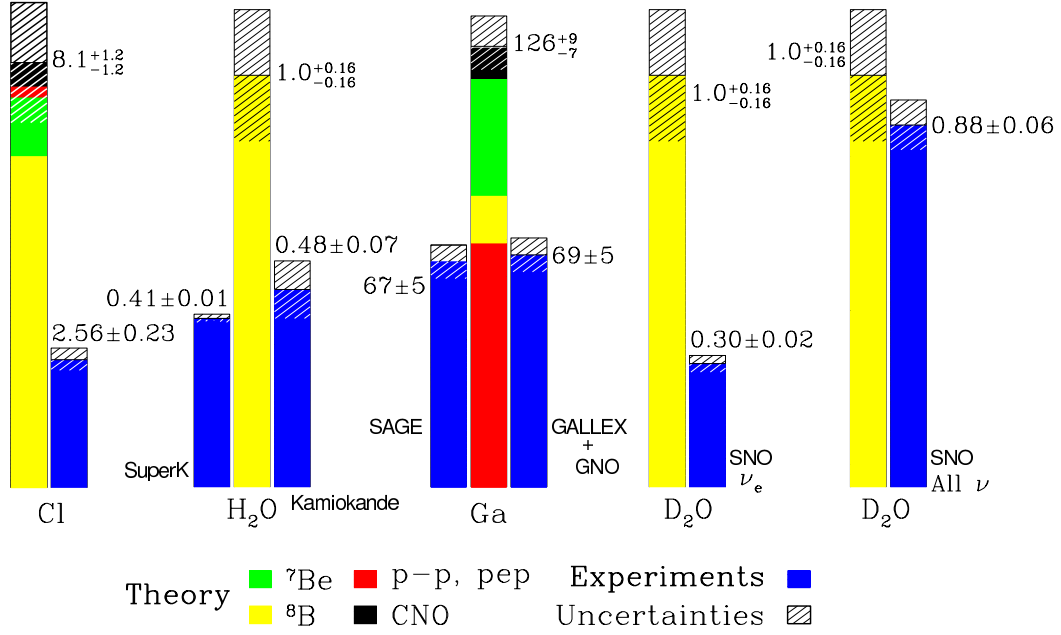


Figure 1.15: Results overview of the measured solar neutrino fluxes compared to predictions of the Sun Standard Model [[40]].

The hatched region shown in Figure 1.17 corresponds to this “effective” baseline scan using the antineutrino energy determination (achieved measuring the  $e^+$  energy). We assumed here that the reactor antineutrinos that may be detected have an energy  $E_\nu \in [1.8, 8.0]$  MeV by combining the reactor production and antineutrino cross section effects (this range was deduced from [42]). We may have been slightly optimistic, since KamLAND has been only sensitive to one oscillation maximum because of statistics (Figure 1.16), whereas 4 maxima are indicated in the hatched region of Figure 1.17. We can observe that the oscillation due to the solar terms is significantly larger and less frequent than for the reactor terms, which illustrates the parameters different values shown in Table 1.4.

This measurement has been crucial to deduce the associated mixing angle  $\theta_{12}$ . As we have seen, the KamLAND experiment amplitude also depends on the other mixing angles, that lead to an important uncertainty. But the accurate measurement of  $\Delta m_{21}^2$  implies that solar neutrino oscillations are averaged on Earth, due to loss of coherence of the wave packet. The oscillation probability of solar neutrino can be written in the two-flavour approximation averaged out:

$$\langle P_{\nu_e \rightarrow \nu_e} \rangle = 1 - \frac{1}{2} \sin^2 \theta = \frac{1}{2} (1 + \cos^2 2\theta) \quad (1.4.5)$$

where the effect is shown in Figure 1.8. The maximal averaged mixing cannot be higher than  $\frac{1}{2}$  in the case of maximal mixing angle  $\theta = 45^\circ$ . The observation of  $> 50\%$   $\nu_e$  disappearance in the Chlorine or SNO experiments (Figure 1.15) is therefore incompatible with a large mixing angle scenario. The explanation lies in the matter effects that happen during neutrino propagation from the Sun core to external regions, that change some of the originally produced  $\nu_e$  in the core into  $\nu_\mu$  after leaving the most central parts of the Sun. We have seen that the neutrino produced in the Sun core will have mass states proportions ruled by  $\theta_N$ . Assuming a very high density in the Sun core, we have seen that it corresponds to a quasi total flavour conversion  $\theta_N \simeq 90^\circ$ , which implies  $|\nu_e\rangle \simeq |\nu_2\rangle$ . Under adiabatic

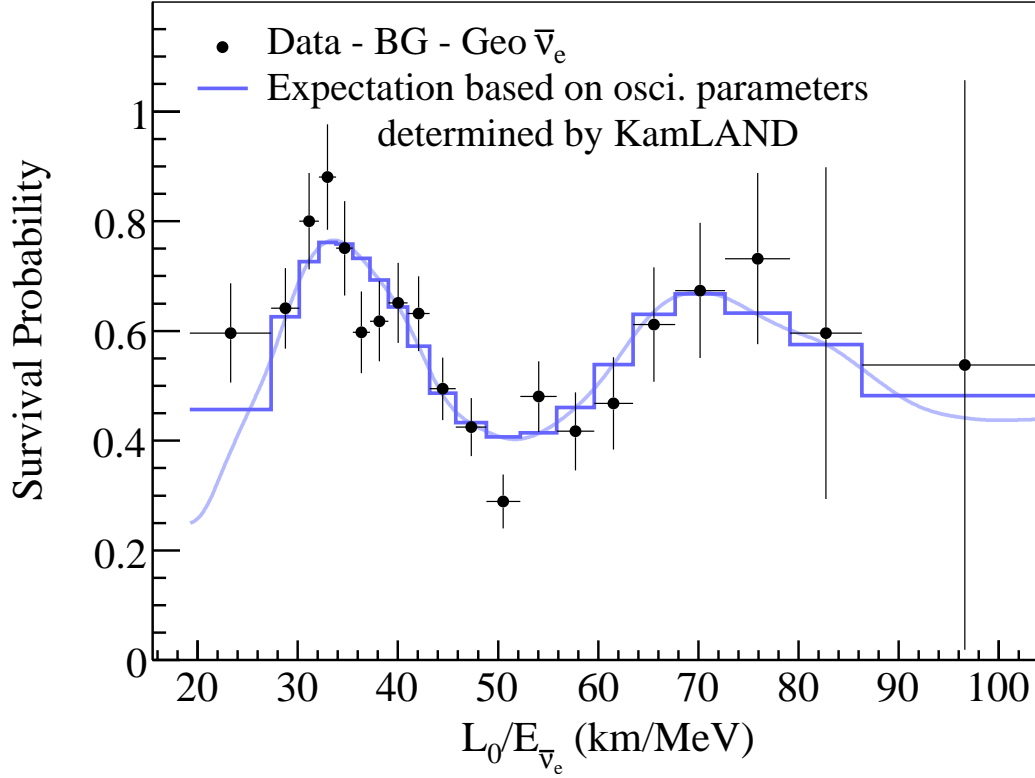


Figure 1.16: Flux ratio of observed  $\bar{\nu}_e$  at KamLAND with the expected flux in the non oscillation scenario. The best fit values for the oscillation parameters are shown in blue. The baseline  $L_0$  is averaged for the different reactors baseline and weighted given their relative fluxes. The average distance is  $L_0 = 175 \text{ km}$ . Taken from [41].

hypothesis, the  $|\nu_2\rangle$  proportions remain the same until they leave the Sun, but their content changes from only  $|\nu_e\rangle$ :

$$|\nu_2\rangle = -\sin\theta_N |\nu_e\rangle + \cos\theta_N |\nu_\mu\rangle \simeq -|\nu_e\rangle \quad (1.4.6)$$

$$|\nu_1\rangle = \cos\theta_N |\nu_e\rangle + \sin\theta_N |\nu_\mu\rangle \simeq |\nu_\mu\rangle \quad (1.4.7)$$

to a content which is majoritary  $\nu_\mu$  due to  $\theta_{12}$  value:

$$|\nu_2\rangle = -\sin\theta |\nu_e\rangle + \cos\theta |\nu_\mu\rangle \quad (1.4.8)$$

$$|\nu_1\rangle = \cos\theta |\nu_e\rangle + \sin\theta |\nu_\mu\rangle \quad (1.4.9)$$

Therefore, the  $\nu_e$  are not only affected by the vacuum oscillation, but also by the MSW effects that change a part of the original  $\nu_e$  to  $\nu_\mu$  in the Sun. The oscillation formula on Earth is changed to:

$$\langle P_{\nu_e \rightarrow \nu_e} \rangle_{MSW} = \frac{1}{2}(1 + \cos 2\theta_N \cos 2\theta). \quad (1.4.10)$$

In the case of resonance,  $\cos 2\theta_N$  and  $\cos 2\theta$  has an opposite sign that explains that the observed solar neutrino deficit on Earth may be higher than 50%. On top of this, the interaction length  $L^{int}$  decreases with the neutrino energy, which implies that the MSW effect consequently increases. It follows we expect a higher  $\nu_e$  disappearance for high energy neutrinos, that has been observed in the different experiments due to their different threshold (Figure 1.15 and Figure 1.14). The density profile in the Sun has been predicted [40] which fixed the different  $\theta_M$  values in the Sun. Therefore, the mixing angle  $\theta_{12}$  can be immediately measured. We summarise the final result combining KamLAND that mainly fixes the mass splitting and the solar experiments that mainly measure the mixing angle in Figure 1.18:

$$\Delta m_{21}^2 = 7.65_{-0.20}^{+0.23} \times 10^{-5} \text{ eV}^2 \quad \sin^2 \theta_{12} = 0.304_{-0.016}^{+0.022}. \quad (1.4.11)$$

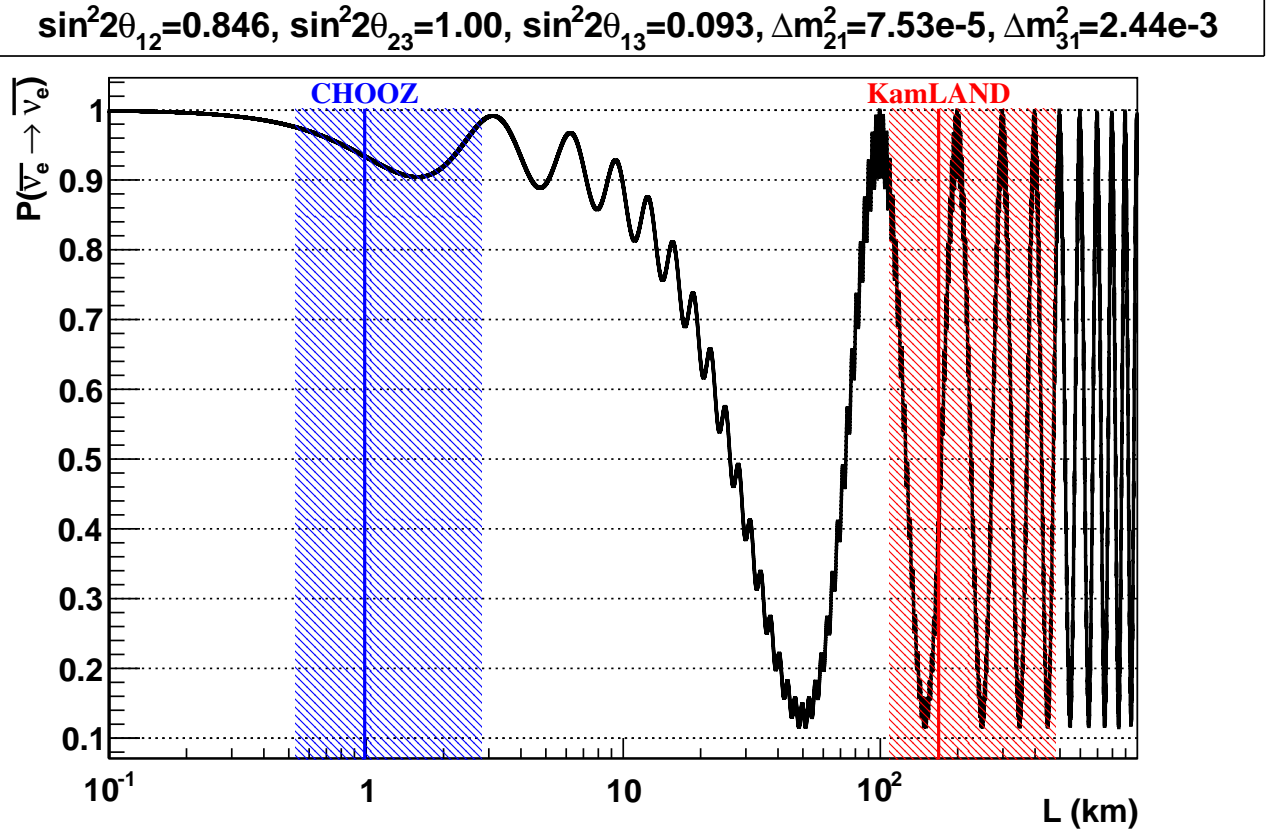


Figure 1.17: Antineutrino survival probability with the baseline assuming 3 MeV neutrinos. The straight lines are the baseline of CHOOZ (blue) and KamLAND (red) experiments, and the hatched region corresponds to their potential sensitivity in  $L/E$  using different baseline (KamLAND) or different neutrino energy (CHOOZ, KamLAND).

### 1.4.2 The atmospheric neutrino sector

The cosmic rays are mainly constituted of protons and a small proportion of heavier nuclei produced in outer space. These particles that reach the upper atmosphere interact with the surrounding matter, leading mostly to pion and kaon production. The pion decay occurs before reaching the Earth ground, producing muon neutrinos or antineutrinos:

$$\pi^+ \rightarrow \mu^+ + \nu_\mu, \quad \pi^- \rightarrow \mu^- + \bar{\nu}_\mu \quad (1.4.12)$$

In first approximation, we assume that the number of positive and negative produced mesons is similar. The kaon decays also have a role in the neutrino production, but at higher energy, as will be explained in Chapter 2 for the T2K neutrino beam production which is similar (with a narrower energy spectrum) to the meson production in the atmosphere. The produced muons also participate both to the muon and electron neutrino/antineutrino production, through their decay:

$$\mu^+ \rightarrow e^+ + \nu_e + \bar{\nu}_\mu, \quad \mu^- \rightarrow e^- + \bar{\nu}_e + \nu_\mu \quad (1.4.13)$$

Since the SK detector is not sensitive to the lepton charge, the oscillations of atmospheric neutrinos will be studied using the ratio of muon and electron flavour neutrinos detected:

$$R_{\mu/e} = \frac{\phi_{\nu_\mu} + \phi_{\bar{\nu}_\mu}}{\phi_{\nu_e} + \phi_{\bar{\nu}_e}} \quad (1.4.14)$$

The lifetime of a muon is two order of magnitudes longer than for a pion (respectively  $2.2 \times 10^{-6}$  s and  $2.6 \times 10^{-8}$  s). Therefore, whereas most of the pions decay before reaching the Earth (unless

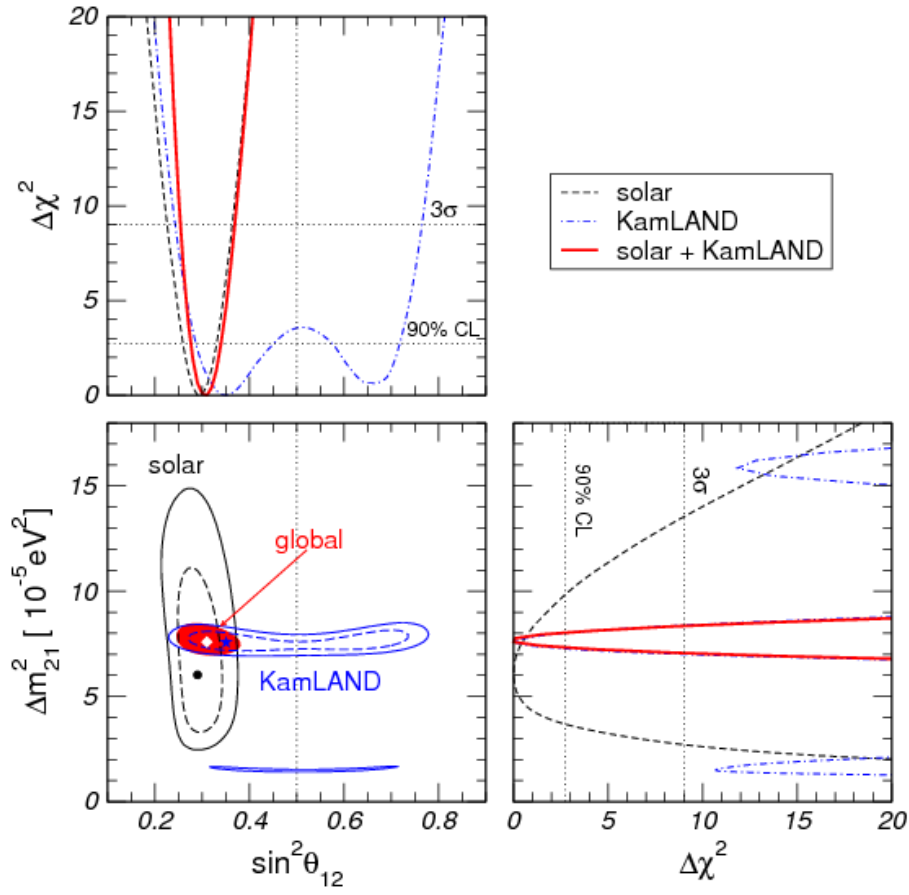


Figure 1.18: Combined fit of the solar sector parameters with the solar and KamLAND constraints. Extracted from [32]. One clearly identifies that the solar neutrino observation provides an accurate measurement on the  $\theta_{12}$  mixing angle while KamLAND constrains mainly the mass squared difference.

Experiment	Kamiokande	IMB	Soudan2	Super-Kamiokande
$R_{\mu/e}^{\text{sub-GeV}}$	$0.60 \pm 0.09$	-	$0.69 \pm 0.12$	$0.658 \pm 0.038$
$R_{\mu/e}^{\text{multi-GeV}}$	$0.57 \pm 0.11$	$0.54 \pm 0.12$	-	$0.702 \pm 0.106$

Table 1.6: The ratio between the observed flavour ratio  $R_{\mu/e}$  and the Monte-Carlo expected one if no flavour oscillation occurs for the main atmospheric neutrino experiments. The sub-GeV and multi-GeV events have been separated.

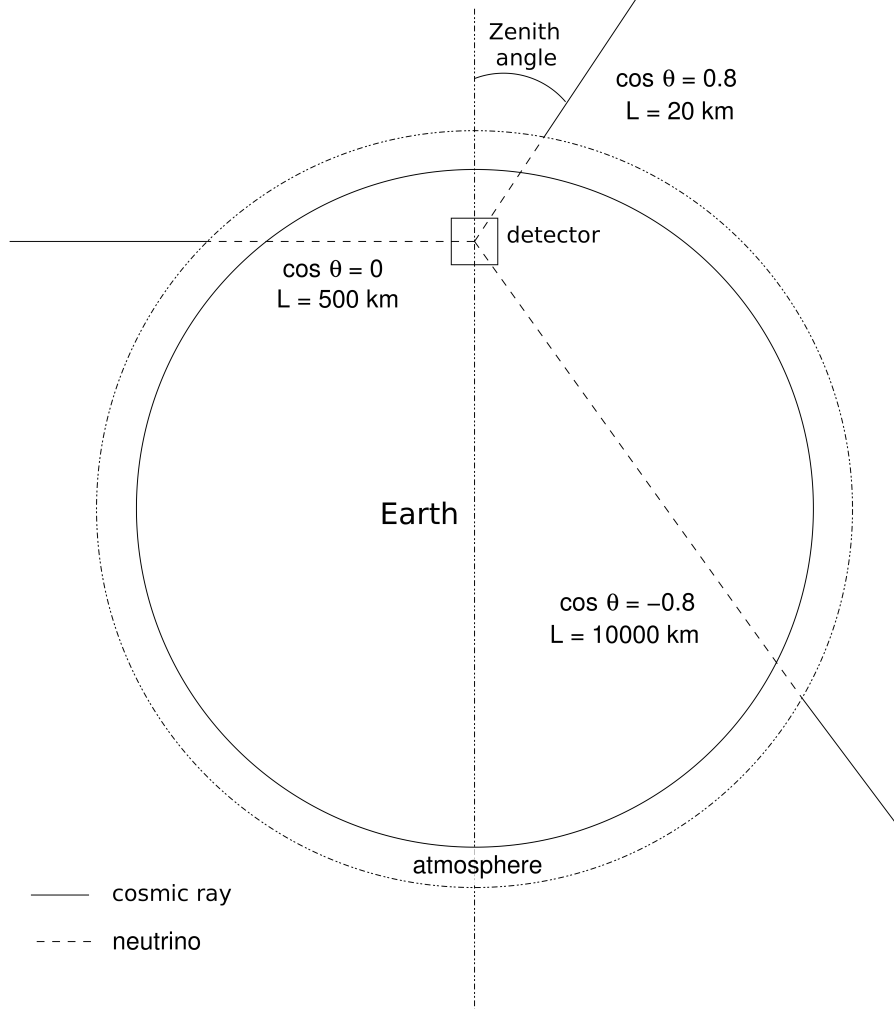


Figure 1.19: Schematc view of the atmospheric neutrino detection principle.

$E \sim 100 \text{ GeV} - 1 \text{ TeV}$  which is a negligible contribution in the spectrum), the muons having  $E > 1 \text{ GeV}$  mostly reach the Earth without decaying. This affects the flavour rate differently, and therefore, the study is divided between sub-GeV and multi-GeV events. For the sub-GeV events, the muon decay occurs and we therefore expect:

$$\frac{\phi_{\nu_\mu} + \phi_{\bar{\nu}_\mu}}{\phi_{\nu_e} + \phi_{\bar{\nu}_e}} \simeq 2 \quad (1.4.15)$$

while we expect an even higher ratio for the multi-GeV events neglecting the kaon contributions. The observed flavour ratio has been compared to the expected one in Table 1.6 for different neutrino experiments Kamiokande [38], IMB [43], Soudan2 [44] and Super-Kamiokande [10].

This observed ratio is significantly lower than expected in the simulation up to more than  $8\sigma$  for the most accurate experiment, Super-Kamiokande. One hypothesis to explain this  $\nu_\mu$  deficit is a flavour neutrino oscillation, that may whether change  $\nu_\mu \rightleftharpoons \nu_e$  or  $\nu_\mu \rightleftharpoons \nu_\tau$ . The latter is not observed since atmospheric neutrino are mainly detected through CC interactions, and the short  $\tau$  lifetime leads to its immediate decay into  $\mu$  in the detector for the typical atmospheric neutrino energies. The typical distances between atmospheric neutrino production and detection points vary between  $L \sim 15 \text{ km}$  to

$L \sim 13000 \text{ km}$ , depending if the production occurs in the atmosphere at the detector zenith or nadir, while their broad energy spectrum is studied from several MeV to several GeV. If an oscillation has occurred, it could not come from the solar like  $\nu_1 \rightleftharpoons \nu_2$  conversion since at atmospheric energy of 1 GeV:

$$L_{12}^{osc}[\text{km}] = \frac{1.27E[\text{GeV}]}{\Delta m_{21}^2} \gtrsim 16000 \text{ km} \quad (1.4.16)$$

which means that the oscillation would barely and only occur for the neutrino produced in the antipode atmosphere. A lower oscillation length is therefore favoured (so a higher mass splitting), which possibly means an oscillation  $\nu_1 \rightleftharpoons \nu_3$  or  $\nu_2 \rightleftharpoons \nu_3$ . This hypothesis was tested through a shape analysis by varying the  $L/E$  for the observed neutrino. Depending on the neutrino direction, the zenith angle is reconstructed and the distance with the detector is therefore extrapolated (Figure 1.19). Assuming that the atmospheric neutrino production is isotropic, the number of detected electrons or muons should verify the following symmetry in both sub and multi-GeV samples:

$$N_\ell(\cos \theta) = N_\ell(-\cos \theta) \quad (\ell = e, \mu) \quad (1.4.17)$$

One observes the importance to detect the neutrino through CC interactions, since the associated lepton direction is very similar to its parent one. The neutrino energy is reconstructed in the detector. Figure 1.20 shows the result for the Super-Kamiokande experiment and clearly indicates the  $\nu_\mu$  disappearance. Though some discrepancies with the expected rate are observed in the electron sub-GeV sample, no  $L/E$  dependency is seen, which rules out the possibility that it is due to  $\nu_\mu \rightleftharpoons \nu_e$  oscillation at the same  $\Delta m^2$ . An hypothesis of a different and shorter baseline oscillation  $\nu_\mu \rightleftharpoons \nu_e$  is ruled out by the agreement between data and no-oscillation scenario for higher energy samples. One therefore deduces that the main cause of the  $\nu_\mu$  disappearance occurs through  $\nu_\tau$  oscillation:

$$P_{\nu_\mu \rightarrow \nu_\tau} \simeq \sin^2 2\theta_{23} \sin^2\left(\frac{\Delta m_{32}^2 L}{4E}\right). \quad (1.4.18)$$

Historically, the CHOOZ and Palo Verde experiments have not observed any  $\bar{\nu}_e \rightarrow \bar{\nu}_\mu$  oscillation (CPT equivalent  $\nu_\mu \rightarrow \nu_e$ ) for similar  $L/E$  which validates the  $\nu_\mu \rightarrow \nu_\tau$  oscillation scenario. Note that a posteriori, this null observation was obviously due to the very low  $\theta_{13}$  value. The Super-Kamiokande experiment 90% confidence levels are:

$$\sin^2 2\theta_{23} > 0.92, \quad 1.6 \times 10^{-3} \leq \Delta m_{32}^2 \leq 3.9 \times 10^{-3} \quad (1.4.19)$$

The atmospheric sector is also precisely probed through long baseline neutrino experiments also studying  $\nu_\mu$  disappearance. The MINOS experiment uses the NuMI beamline to produce a 1–10 GeV almost pure  $\nu_\mu$  beam (or  $\bar{\nu}_\mu$ ). The experiment far detector is installed  $L = 735 \text{ km}$  away to be sensitive to the  $\nu_2 \rightleftharpoons \nu_3$  oscillation. The latest MINOS shape study allows a thinner mass splitting determination than in existing atmospheric experiments, the latter mainly constraining the mixing angle value. The global fit is shown in Figure 1.21 and combines the Super-Kamiokande and MINOS results to give the parameters constraints (reminding  $\Delta m_{31}^2 = \Delta m_{32}^2 + \Delta m_{21}^2$  thus  $\Delta m_{31}^2 \simeq \Delta m_{32}^2$ ):

$$|\Delta m_{31}^2| = 2.40_{-0.11}^{+0.12} \times 10^{-3} \text{ eV}^2, \quad \sin^2 \theta_{23} = 0.50_{-0.06}^{+0.07} \quad (1.4.20)$$

### 1.4.3 The reactor neutrino sector before T2K starts

Prior to T2K installation, the main remaining unknown parameters in the three-neutrino model were  $\theta_{13}$  and the CP violation phase  $\delta_{CP}$  as summarised in Table 1.4. We have shown the existing constraints both on  $\Delta m_{31}^2$  and  $\theta_{13}$  in Figure 1.22. At that time, the main constraint came from the reactor CHOOZ experiment associated to the Super-Kamiokande and accelerator experiments that indirectly constrain  $\theta_{13}$  by fixing the  $\Delta m_{31}^2$  frequency. The reactor based experiments observe the disappearance of

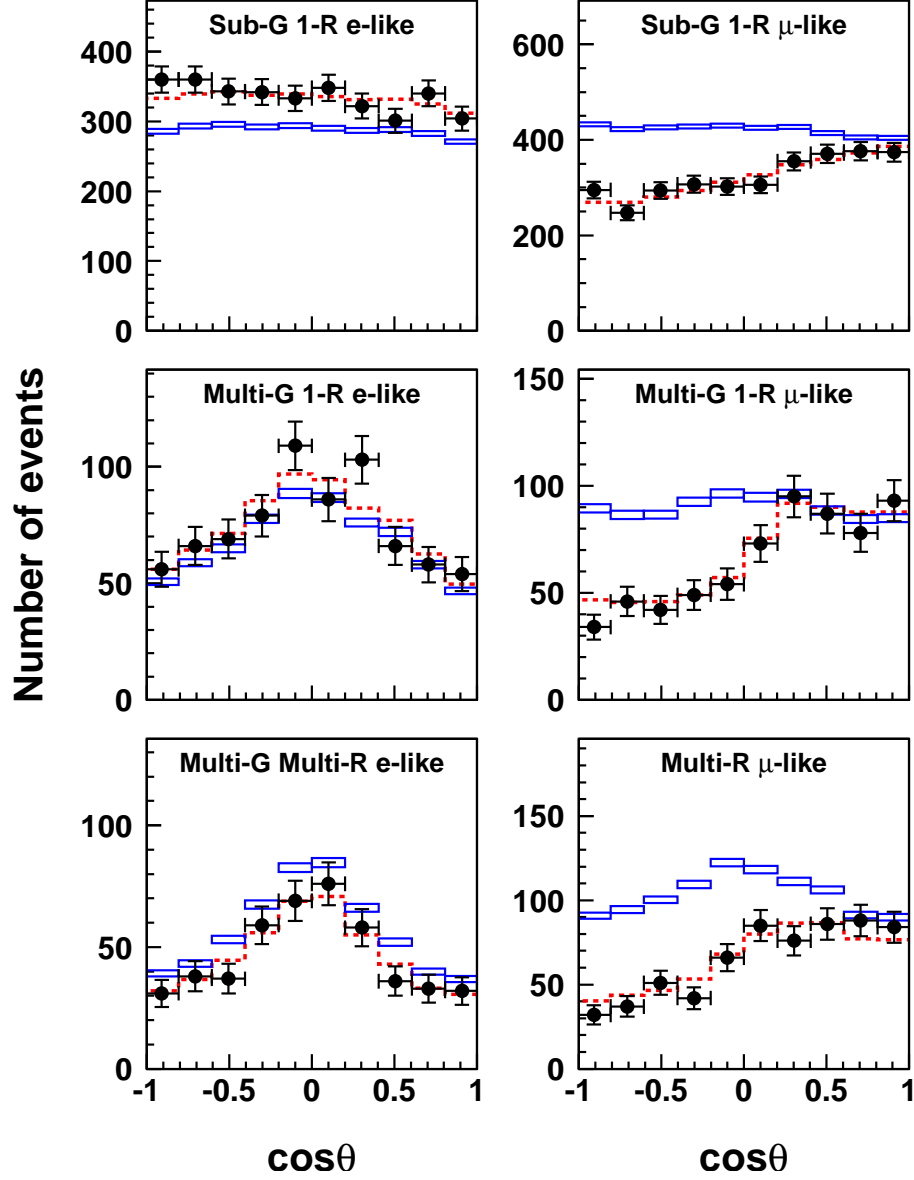


Figure 1.20: Number of detected neutrinos at Super-Kamiokande with the zenith angle for e-like events (left) and  $\mu$ -like events (right). The sub and multi-GeV events are separated. Multi-GeV events are categorised into one or multi Cherenkov rings events. The blue box represents the flux without any oscillation and the data are in black with their statistical errors. The oscillation parameters best fit values are obtained by the fit (red dotted) of the data distributions and provide the parameters central values:  $\sin^2 \theta_{23} = 1$ ,  $\Delta m^2 = 2.5 \times 10^{-3} \text{ eV}^2$  [45].

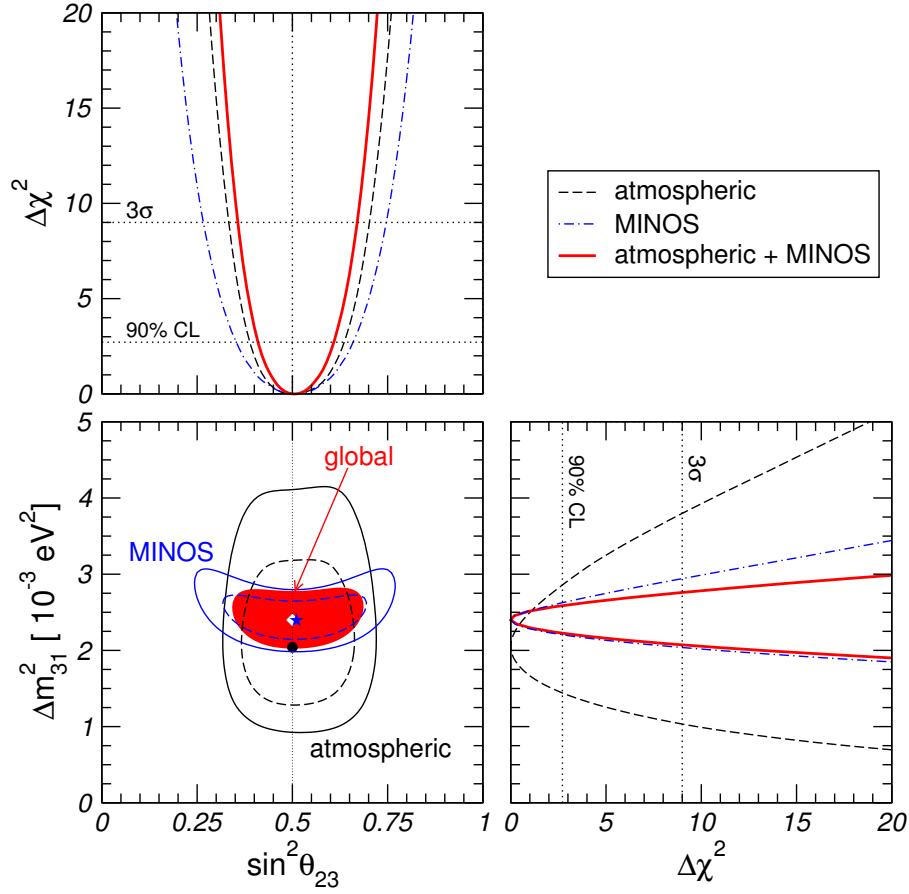


Figure 1.21: Constraints on the  $\theta_{23}$  and  $\Delta m^2_{32}$  parameters in 2008 from existing atmospheric and MINOS experiments [32]. The global fit value lead to the constraint  $\sin^2\theta_{13} = 0.010^{+0.016}_{-0.011}$ .

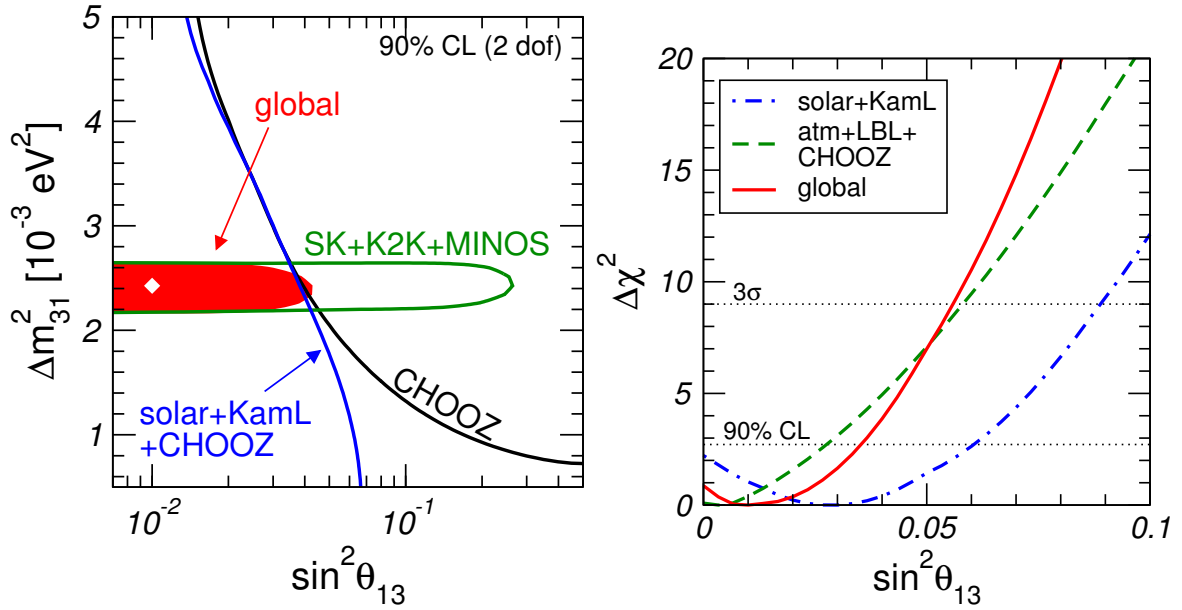


Figure 1.22: Constraints on the  $\theta_{13}$  parameter in 2008 from existing experiments [32]. The global fit value lead to the constraint  $\sin^2\theta_{13} = 0.010^{+0.016}_{-0.011}$ .

electron antineutrinos produced in nuclear power plants. The oscillation formula gives the  $\bar{\nu}_e$  survival probability:

$$P_{\bar{\nu}_e \rightarrow \bar{\nu}_e} \simeq 1 - \sin^2 2\theta_{13} \sin^2\left(\frac{\Delta m_{31}^2 L}{4E}\right) \quad (1.4.21)$$

The antineutrinos from reactors have a lower energy ( $\sim 3$  MeV) as compared to accelerator based experiment ( $\sim 1$  GeV). Since neutrino oscillation occurs for constant  $L/E$ , the baseline to observe similar oscillations is broadly reduced by 3 orders of magnitude. As an example, the CHOOZ experiment was located at  $L \sim 1$  km from the nuclear power plant. The CHOOZ experiment found no evidence of  $\bar{\nu}_e$  disappearance at 90% confidence level [46] which set a higher limit on  $\theta_{13}$  value. We'd like to emphasise that the CHOOZ experiment only constrains  $\theta_{13}$  for large  $\Delta m_{31}^2 > 1.10^{-3} \text{ eV}^2$  values. For lower frequencies (*i.e.*  $\Delta m_{31}^2 \ll 1.10^{-3} \text{ eV}^2$ ), it immediately follows that the oscillation occurs for larger  $L/E$  and could not be observed at the CHOOZ detector. Since CHOOZ only observes no  $\bar{\nu}_e$  disappearance, it cannot conclude if this is due to an inappropriate baseline or to a low  $\theta_{13}$ . It follows that the knowledge of  $\theta_{13}$  is highly correlated to the existing limits on  $\Delta m_{31}^2$  in the CHOOZ experiment (reactor in general), which experiments combining disappearance and appearance as T2K, OPERA, MINOS or NOvA can disentangle.

This limit is refined using the combination of KamLAND and solar neutrino results. As KamLAND is nearly 100 times further away from the reactor cores than the CHOOZ experiment for the same energy (Figure 1.17), the impact of  $\theta_{13}$  on the oscillation is averaged out due to detector resolution. Unfortunately, the uncertainties on the  $\bar{\nu}_e$  flux prevents from a direct  $\frac{1}{2} \sin^2 2\theta_{13}$  measurement through normalisation. As for the amplitude, the measurement of the amplitude  $\theta_{12}$  is unfortunately affected by the averaged  $\theta_{13}$  effect, which explains the  $\cos^4 \theta_{13} \sin^2 2\theta_{12}$  term in Equation 1.4.4 on top of the normalisation  $\frac{1}{2} \sin^2 2\theta_{13}$  term. The poor knowledge on  $\theta_{13}$  prevented KamLAND from competing with solar experiment for the  $\sin^2 2\theta_{12}$  determination. This measurement is done using both the shape and rate of the oscillated spectrum. However, the main constraints come rather from the rate than from the shape [47]. The oscillation probability when averaged over the whole energy range becomes:

$$P_{\bar{\nu}_e \rightarrow \bar{\nu}_e} \simeq 1 - \frac{1}{2} \sin^2 2\theta_{13} - \frac{1}{2} \cos^4 \theta_{13} \sin^2 2\theta_{12}. \quad (1.4.22)$$

Since  $\theta_{13} \simeq 0$ , the  $\cos^4 \theta_{13}$  is close from a maximum and does not vary much with the  $\theta_{13}$  value. The interplay of  $\theta_{13}$  then essentially comes from the  $\frac{1}{2} \sin^2 2\theta_{13}$  terms. Therefore, for a given measured rate in KamLAND:  $1 - \frac{1}{2}(\sin^2 2\theta_{13} - \cos^4 \theta_{13} \sin^2 2\theta_{12}) \simeq 1 - \frac{1}{2}(\sin^2 2\theta_{13} + \sin^2 2\theta_{12}) = \text{Constant}$ , there is a natural anti-correlation between  $\theta_{13}$  and  $\theta_{12}$  which is shown in Figure 1.23. However, the constraint on the  $\theta_{12}$  coming from the solar experiment only slightly depends on  $\theta_{13}$ . This explains the constraints KamLAND and solar experiments bring on  $\theta_{13}$  value. Firstly, the upper limit is roughly independent from the  $\Delta m_{31}^2$  value (while  $\Delta m_{21}^2 \ll L/E_{\text{KamLAND}}$ ) since the effect will be averaged out anyway for smaller frequency. Secondly, it brings a non-significant constraint on  $\theta_{13} \neq 0$  due to solar constraints on  $\theta_{12}$  (Figure 1.23) that impacts the KamLAND measurement. It explains the effects shown in Figure 1.22.

#### 1.4.4 Current knowledge on $\theta_{13}$ out of T2K

The current generation experiments has been essentially designed to measure the remaining unknown mixing angle, the  $\theta_{13}$  value. They can be divided in two categories:

- The reactor-based experiments Double-CHOOZ, Daya-Bay and RENO that observes  $\bar{\nu}_e$  disappearance and allow a direct measurement of  $\theta_{13}$ .
- The accelerator based experiments T2K and NOvA that measure the combined effect of  $\theta_{13}$  (and other mixing angles) and  $\delta_{CP}$  through  $\nu_\mu \rightarrow \nu_e/\bar{\nu}_\mu \rightarrow \bar{\nu}_e$  oscillations. The parameters  $\theta_{23}$  and  $\Delta m_{32}^2$  can be also constrained mainly through  $\nu_\mu$  disappearance. Though small, the matter effects can be also probed and provide constraints on the  $\Delta m_{32}^2$  sign.

In July 2001, the T2K collaboration published the first indication of a non-zero  $\theta_{13}$  value with a  $2.5\sigma$  confidence level. This result was confirmed in December when the Double-CHOOZ collaboration

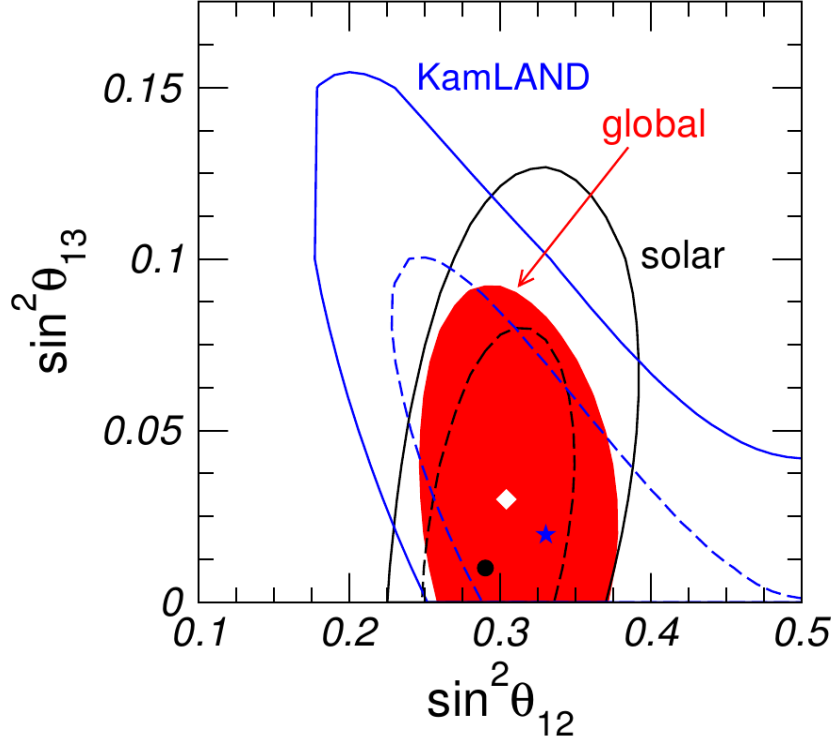


Figure 1.23: Constraint on the  $\theta_{13}$  and  $\theta_{12}$  parameters in 2008 [32] coming from the KamLAND and solar experiment interplay.

published its results that increased to  $3\sigma$  the confidence in a non-zero  $\theta_{13}$  value when combined with MINOS and T2K. The observation ( $> 5\sigma$ ) of a non-zero  $\theta_{13}$  value was operated by the Daya-Bay collaboration in April 2012 [29]. The measured value at that time was:  $\sin^2 2\theta_{13} = 0.092 \pm 0.016(stat) \pm 0.005(syst)$ . Since that time, both RENO [30] and additional constraints from Daya-Bay have confirmed this result and increased the constraints on  $\theta_{13}$  to the present value:

$$\sin^2 2\theta_{13} = 0.093 \pm 0.008. \quad (1.4.23)$$

We will see in Chapter 2 that the T2K experiment has also observed a non-zero  $\theta_{13}$  value observing neutrino appearance [31], but these results indicate tensions with the current  $\theta_{13}$  reactor value.

## Chapter 2

# The Tokai to Kamioka experiment

*We are trying to prove ourselves wrong as quickly as possible, because only in that way can we find progress.*

Richard P. Feynman

### 2.1 Physics motivations

THE T2K experiment has been designed to study neutrino oscillations, particularly in the  $\nu_\mu$  to  $\nu_e$  appearance and  $\nu_\mu$  disappearance channels. It is a long baseline experiment with a high intensity  $\nu_\mu$  flux produced at J-PARC (Japan Proton Accelerator Research Complex) and detected 295 km away in the Water Cherenkov detector Super-Kamiokande (SK). A complex of near detectors is installed at 280 m from the target, in order to monitor the neutrino beam flux. In this complex, the INGRID detector is located on the neutrino beam axis, while the ND280 detector is located on the alignment of the target and SK,  $2.5^\circ$  away from the neutrino beam axis. A schematic view is shown in Figure 2.1. The main goals of the T2K experiment are:

1. Observe the first  $\nu_\mu$  to  $\nu_e$  oscillation. This would directly imply the oscillation amplitude term  $\theta_{13} \neq 0$ .
2. Measure with world leading precision the amplitude and frequency terms  $\theta_{23}$  and  $\Delta m_{32}^2$ . The most straightforward channel is the  $\nu_\mu$  disappearance channel.
3. If  $\theta_{13} \neq 0$ , T2K can probe the CP symmetry violation in the leptonic sector for the first time. This may be achieved by comparing  $\nu_\mu$  to  $\nu_e$  and  $\bar{\nu}_\mu$  to  $\bar{\nu}_e$  appearances.

In this Section, we will describe in details the 3 main T2K goals in the light of the changes on mixing parameters shown in Table 1.4.

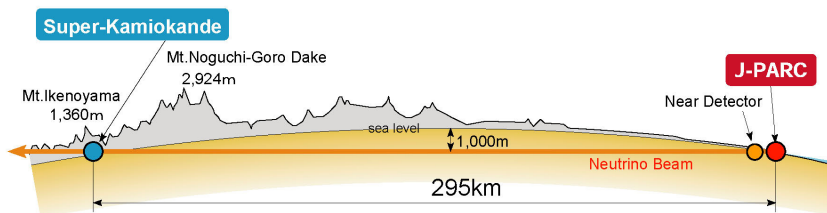


Figure 2.1: The T2K experiment layout.

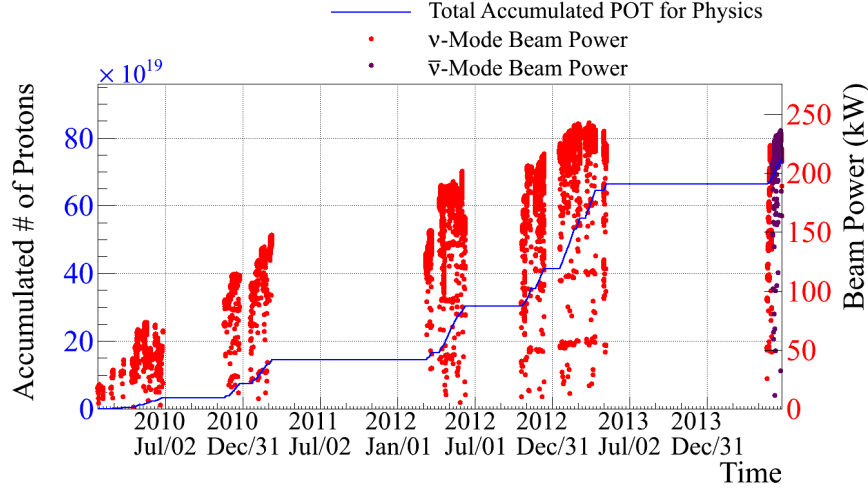


Figure 2.2: The T2K experiment data taking history for the data sample used in this thesis. One identifies the contributions of run one to four data, along with the increasing beam intensity.

## 2.2 The T2K experiment

### 2.2.1 The off-axis technique

T2K is the first off-axis neutrino experiment: the neutrino beam is not directly aimed at the SK far detector but  $2.5^\circ$  away. For comparison, though the MINOS and OPERA experiments are on-axis, the NOvA experiment is also off-axis. Though aiming a neutrino beam off-axis highly reduces its intensity at the detectors, the current generation of long baseline neutrino experiments uses this technique due to its very interesting benefits.

#### Oscillated neutrino maximisation

We introduced that the neutrino oscillation depends on the ratio between the neutrino baseline and energy. Assuming a fixed baseline for an experiment, only a narrow band in the neutrino spectrum has a non-negligible probability to oscillate before reaching the far detector. This is shown in Figure 2.3 for the on-axis beam. On top of this, an on-axis experiment induces a large contamination from non-oscillated neutrinos that may directly impact the measurement if muons are misidentified as electrons. Finally, it implies an important constraint on the choice of the baseline in relation with the energy of the accelerator that produces neutrinos. In the case of T2K, important constraints were given on the baseline since the SK detector was already installed and the geography of Japan implied to install the accelerator complex near the sea shore. Therefore, the neutrino energy (and so, the proton one) should have been chosen very carefully according to the T2K experiment needs, and the knowledge on the  $\Delta m_{32}$  frequency at that time. First, the J-PARC accelerator complex is not only dedicated to T2K. Second, an unfortunate baseline and energy choice could have highly impacted the T2K discovery potential in case of a slight mis-estimation of  $\Delta m_{32}$ . The off-axis technique solves these issues since it allows to select the neutrino beam energy by varying its angle with the target-SK direction.

In the case of a neutrino beam (we will see that T2K can also produce antineutrino beam), most of the  $\nu_\mu$  production occurs through the pion decay process:  $\pi^+ \rightarrow \mu^+ + \nu_\mu$ . Assuming a massless neutrino, its energy may be written as a function of its angle  $\theta$  with the pion direction and the pion momentum as:

$$E_\nu = \frac{m_\pi^2 - m_\mu^2}{2(E_\pi - p_\pi \cos(\theta))} \quad (2.2.1)$$

For a given  $E_\pi$ , one observes that  $E_\nu$  is decreasing with  $\theta$  due to a lower effect of the pion boost. The behaviour of  $E_\nu$  is less straightforward and is shown in the right part of Figure 2.3. First, one observes that the neutrino energy is reduced with the off-axis angle. Second, one sees that the neutrino energy is relatively independent from the pion momentum value for off-axis angles above  $2^\circ$ . Therefore, one can

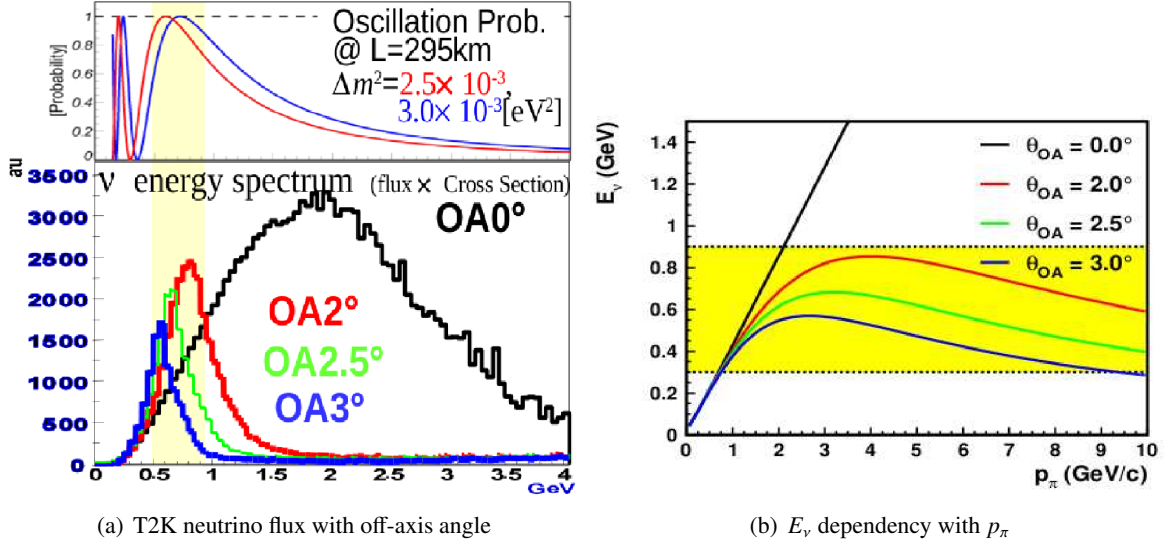


Figure 2.3: The neutrino spectrum with the T2K beam off-axis angle (left). On the right is shown the behaviour of the neutrino energy with their parent pion momentum for different off-axis angles. The neutrino energy is reduced with the off-axis angle, and so is its dependency on pion momentum. This allows to tune the neutrino energy while narrowing its energy spectrum. Taken from [48].

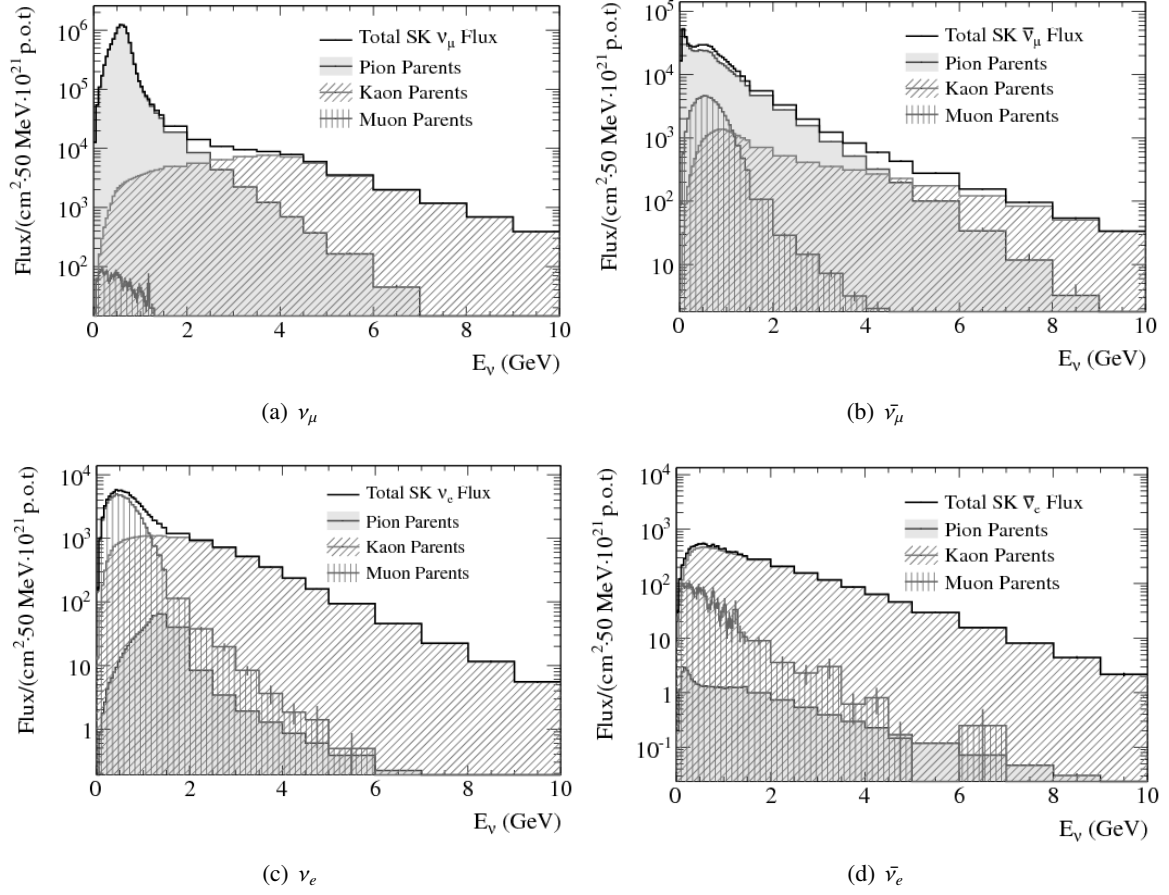
align the neutrino flux mean energy around the maximum oscillating region and minimise the number of non-oscillated neutrinos (background) by reducing the spectral width. This technique is particularly adapted to neutrino beams since they have a broad energy spectrum due to the impossibility to focus neutral particles and to the short average distance crossed by their pion parent that prevents from accurately focusing them. The counter-part of this technique is a decrease in the total neutrino rate, despite a gain in the absolute number of oscillated neutrinos (Figure 2.3). In the future, this may be solved by focusing the muons that have a longer lifetime than pions and using their decay neutrinos. The T2K  $2.5^\circ$  off-axis angle shifts the average energy of the neutrino beam from 2.7 GeV on-axis to 700 MeV at the off-axis detectors. One understands that it is crucial to measure the off-axis angle with a high accuracy since it highly impacts the neutrino spectrum rate and shape. The INGRID on-axis detector has been explicitly installed for this purpose.

### Reduction of background contamination

The off-axis technique considerably reduces the background due to beam intrinsic  $\nu_e$  (non-oscillated at SK) which is the dominant background at SK in the  $\nu_e$  appearance analysis. We have summarised in Table 2.1 the different meson and muon decay modes contributing to the  $\nu_\mu$  flux (may be applied to  $\bar{\nu}_\mu$  by using the corresponding antiparticles). One observes that the  $\nu_\mu$  are mainly produced by  $\pi^+$ , and by charged and neutral  $K$ . However, a non-negligible fraction of  $K$  also produce  $\nu_e$  contamination, and so do  $\pi^-$  which decay in  $\bar{\nu}_\mu$ . On top of this, the  $\mu^+$  decay also increases the  $\nu_e$  and  $\bar{\nu}_\mu$  production. One observes that their impact is limited by an appropriated choice of the decay volume (95 m) compared to the muon average flight distance.

In a nutshell, most of the  $\nu_\mu$  come from  $\pi^+$ , while the main fraction of  $\nu_e$  and  $\bar{\nu}_\mu$  contamination is due to  $\mu^+$  for low energy neutrinos ( $E_\nu < 1.5 \text{ GeV}$ ) and by  $K$  decay for higher energy ( $E_\nu > 1.5 \text{ GeV}$ ). This scheme is summarised in Figure 2.4.

The choice of the off-axis angle reduces  $E_\nu$  and implies that most of the  $\nu_e$  contamination is due to the  $\mu^+$  decay. One shows [49] that the angular dispersion of  $\nu_e$  produced by  $\mu^+$  decay is smaller than the one resulting from  $K$  decay. This explains why the  $\nu_e$  intrinsic contamination decreases with the off-axis angle. Quantitatively, the  $\nu_e$  intrinsic contamination is reduced from 1% to 0.5%.


 Figure 2.4: Neutrino spectra at SK shown according to their parent particle and a  $2.5^\circ$  off-axis angle.

Meson	Average travel distance	Decay mode	Branching ratio
$\pi^+$	8 m	$\pi^+ \rightarrow \mu^+ + \nu_\mu$ $\pi^+ \rightarrow e^+ + \nu_e$	99.988% 0.012%
$K^+$	4 m	$K^+ \rightarrow \mu^+ + \nu_\mu$ $K^+ \rightarrow \pi^+ + N \cdot \pi^0$ with N=1 or 2 $K^+ \rightarrow 2\pi^+ + \pi^-$ $K^+ \rightarrow \pi^0 + e^+ + \nu_e$ $K^+ \rightarrow \pi^0 + \mu^+ + \nu_\mu$	63.55% 22.42% 5.59% 5.07% 3.35%
$K_L^0$	16 m	$K_L^0 \rightarrow \pi^- + e^+ + \nu_e$ $K_L^0 \rightarrow \pi^- + \mu^+ + \nu_\mu$	40.55% 27.04%
$\mu^+$	660 m	$\mu^+ \rightarrow e^+ + \nu_e + \bar{\nu}_\mu$	100%

 Table 2.1: Summary of the decay modes of the produced mesons in the T2K experiment that will lead to neutrino production. We assumed a neutrino mode, though this can also be applied to the anti-neutrino case by changing the particle signs. Only the decay modes for branching ratios  $> 0.01\%$  are shown here. The  $\mu^+$  are produced through meson decays and have been shown here since they interfere in the neutrino production. Mostly taken from [49].

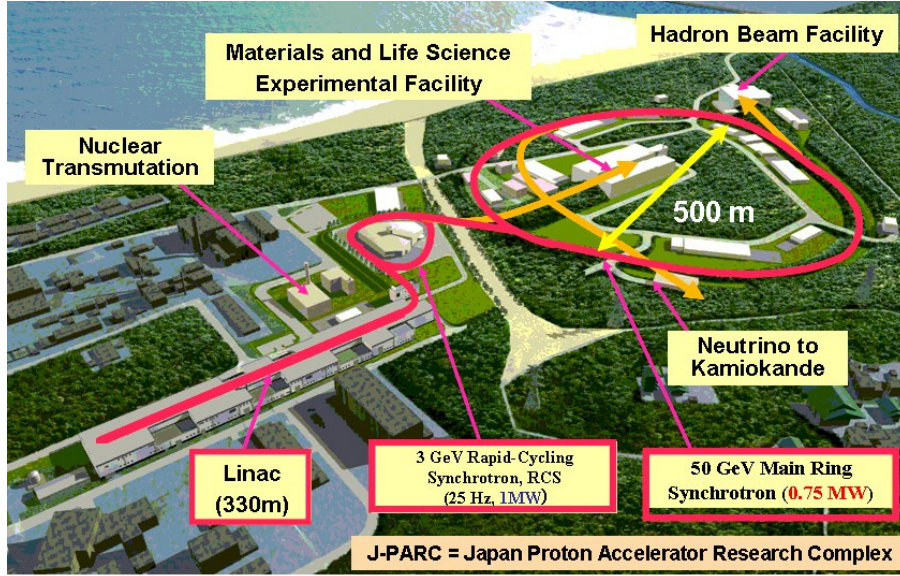


Figure 2.5: The J-PARC accelerator complex. The acceleration sequence is shown from the LINAC to the main ring. Extracted from <http://www.teilchen.at/news/334>.

### 2.2.2 The Neutrino Beam

Unlike experiments at the LHC where the largest possible energy is required to favor the discovery of new particles, neutrino accelerator experiments mainly focus on very high intensity beams to compensate neutrino very small cross sections. As we have seen, the neutrino energy mainly imposes the baseline of the accelerator experiment to study oscillation. It impacts the neutrino rate due to cross section variation in the GeV region, as will be seen in Chapter 5. This variation ( $\propto E_\nu$  for  $E_\nu > 1$  GeV) is not of first importance relatively to the beam intensity, and is mainly due to the cross section increase of deep inelastic processes which are poorly known currently (Chapter 5).

The T2K beam is produced at the J-PARC facility, located in Tokai, Japan. The whole accelerator complex is a collaboration between KEK (The High Energy Accelerator Research Organization) and the Japan Atomic Energy Agency (JAEA), and its construction started in 2001. The J-PARC complex is composed of several accelerators to produce an intense proton beam used for various experiments. Particularly, the intense T2K neutrino beam is generated by the decay of mesons and muons resulting from the 30 GeV proton beam hitting a carbon target. The neutrino beam production can be separated in a primary and secondary beam line that we will describe.

#### Proton acceleration

The high intensity proton beam is obtained by a serie of 3 accelerators illustrated in Figure 2.5.

**The linear accelerator (LINAC)** The first acceleration step is performed by a standard 249 m linear accelerator.  $H^-$  ions are produced with a 50 keV energy and accelerated up to 181 MeV through a sequence of radio-frequency quadrupole (up to 3 MeV), drift-tube LINAC (up to 50 MeV) and two synchrotrons. The maximum beam power is 30 kW. The ion spread in momentum is limited to  $\Delta p/p < 0.1\%$  to be injected in the following RCS.

**The Rapid Cycling Synchrotron (RCS)** The  $H^-$  ions are converted to protons by hitting charge-stripping foils at the RCS injection. The 348 m RCS accelerates the 181 MeV beam up to 3 GeV using radio-frequency cavities with a 25 Hz cycle. Magnetic alloy core radio-frequency cavities are used to obtain an important electric field gradient (20 kV/m) which was not possible with classical ones. The proton beam trajectory is curved using 24 dipole magnets and is focused using 60 quadrupole magnets. The protons are then injected either in the “Material and Life Science Experimental Facility” (MLF) or in the final accelerator prior to neutrino production, the main ring.

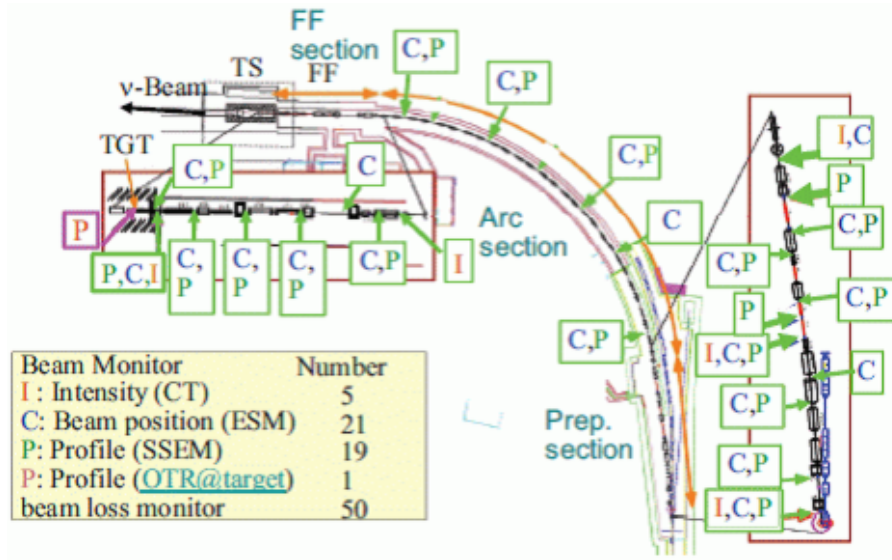


Figure 2.6: The T2K neutrino primary beam line. It is divided in three main sections: the preparation (Prep.), the arc (Arc) and the final focusing (FF) sections prior to hit the target (TS).

**The Main Ring (MR)** The main ring is a 50 GeV synchrotron. It is composed of three linear sections of 116.1 m and three circular 406.4 m long sections for a total length of 1567.5 m. The proton beam trajectory is curved by a 96 dipole magnets and focused by 216 quadrupole and 72 sextupole non-superconducting magnets. The proton acceleration is performed using the same radio-frequency cavities as used in the RCS. Though the MR has been designed to accelerate protons up to 50 GeV, it is now limited to 30 GeV with an average beam power of 150 kW. It will reach the nominal 750 kW value in the next years. The accelerated proton beam is then extracted in two different ways: a “slow extraction” to supply the “Hadron Experimental Facility” or a “fast extraction” for the neutrino beam line.

### The neutrino primary beam line: from proton extraction to target

The protons are extracted from the main ring to the neutrino primary beam line within a single turn (“fast extraction”). This fast extraction is performed by five kicker magnets and a set of eight septum magnets. The fast extraction is compulsory to keep the proton beam time structure which is the main discriminator between signal and background in the downstream detectors. The extraction may be repeated every two seconds. We will detail the beam structure at the end of this section.

The primary beam line main purposes are both to steer the neutrino beam towards the near and far detector complex and to focus the beam on the carbon target. The first 54 m of the primary beam line is a linear part that prepares the beam to be accepted by the following arc section (see Figure 2.6). The latter is a 147 m arc section that curves the beam direction by  $80.7^\circ$  to guide it towards the ND280 complex and SK. At this stage, superconducting magnets are used both to focus and guide the proton beam. Finally, the proton beam enters the last focusing section where ten normal conducting magnets guide the beam  $3.64^\circ$  downward, toward the far SK detector. It takes into account the curvature of the Earth and the off-axis angle. In addition, this section focuses the proton beam for the last time before it reaches the target.

In the primary beam line, both beam position and intensity are monitored using four devices (see [50]):

- The ElectroStatic Monitors (ESM) that monitor the beam position.
- The Secondary Segmented Emission Monitors (SSEM) that monitor the beam profile.
- The Beam Loss Monitors (BLM).
- The current transformers (CT) that measure the proton beam intensity.

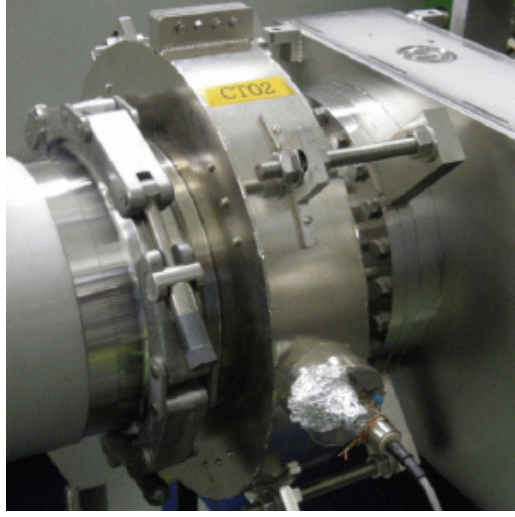


Figure 2.7: A current transformer (CT02) photo. This device is crucial to monitor the number of protons on target.

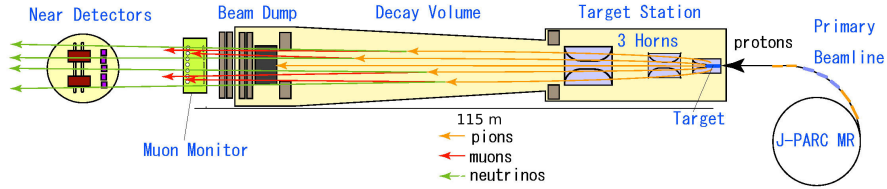


Figure 2.8: The T2K neutrino secondary beamline.

We'd like to draw the reader's attention especially on the five CTs located along the primary beam line to monitor the proton beam intensity. Their positions are shown in Figure 2.6 and a CT picture is displayed in Figure 2.7. These devices have a crucial importance in the T2K analysis since they directly impact the neutrino rate. We will use them in Chapters 5 and 6 to determine the number of protons on target (POT). We will only use the information of the very last CT on the beamline (CT05) which measures the most downstream beam condition before protons hit the target.

### The neutrino secondary beam line: from target to neutrinos

The secondary beam line allows to obtain a neutrino beam from the incoming protons. It is made of a carbon target, three high current toroidal field magnets known as "horns", a decay volume and a muon monitor detector. The horns are located into a target station filled with helium gas, which is connected to the downstream decay volume. There is a distance of 115 m separating the target from the muon monitor (see Figure 2.8). The role of each of these constituents is detailed hereafter.

**Meson production in the carbon target** The incoming protons hit a graphite target to produce mesons, which are mainly  $\pi^{+/-}$  and  $K^{+/-}$ . More positive mesons ( $\pi^+$  and  $K^+$ ) are produced due to charge conservation reasons. The target is a cylinder of 26 mm diameter for a 90 cm length shown in Figure 2.9. The choice of the material and shape of the target is essentially based on two different constraints:

- The target durability. When exposed to the intense proton beam, the target undergoes a high temperature elevation and damages from radioactivity. The material must have a relatively low atomic number (temperature rising is approximately linear with the number of nucleons) and high fusion and sublimation points to prevent from melting. The graphite matches these two criteria.
- The target volume. The target diameter must be large enough to encompass the entire proton beam. The target must be long enough to maximise the number of interacting protons but thin

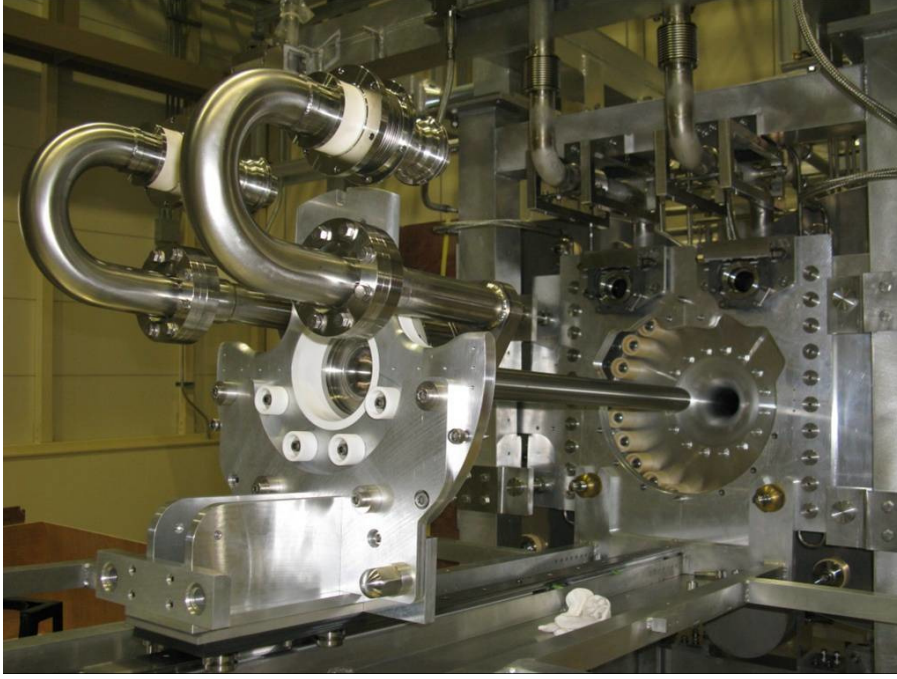


Figure 2.9: The T2K target inserted in the first horn.

enough to prevent secondary particles from re-interacting in the target.

The target is located inside a cooling helium gas vessel, along with the three horns. As shown in Figure 2.9, the target is placed inside the first magnetic horn to prevent from an important depletion of the beam intensity due to the angular dispersion of the parent mesons. This will be described in the next paragraph.

**The meson focusing horns** Three magnetic horns are used to select positive or negative charge mesons and focus the meson beam. The horns produce a toroidal field that allows to select either the  $\pi^+$ ,  $K^+$  to generate a main neutrino beam, the  $\pi^-$ ,  $K^-$  to generate a main anti-neutrino beam, and to defocus the particles with the opposite charge. This operation is only done by reverting the horn current. The horn current is pulsed with the beam spills, and designed to operate up to 320 kA. As for now, T2K is operating with a 250 kA current in the horns. The horns are necessary to produce an intense neutrino beam in the direction of the near and far detectors. Typically, a horn reduces the meson angular dispersion by a factor of two. In the case of T2K, the first and second horns being relatively close, the three-horns system is equivalent to a two-horns complex (see Figure 2.10). The focused mesons with appropriate charge then cross the decay volume.

**Neutrino production in the decay vessel** The decay vessel is a 96 m long volume which is “almost” paved-shape and is filled with helium gas (to reduce the pion absorption). Its transverse dimensions are 1.4 m (width)  $\times$  1.7 m (height) upstream, and 3.0 m (width)  $\times$  5.0 m (height) at the end of the tunnel. As was discussed in Section 2.2.1, the decay volume is long enough to maximise the amount of decaying pions ( $< L_{Decay} \simeq 8$  m) though preventing a large amount of  $\mu^+$  from decaying ( $< L_{Decay} \simeq 260$  m). The helium gas reduces the possible pion re-absorption that may occur in the air. A picture of the decay vessel is shown in Figure 2.11.

The decay vessel ends with a large beam dump to stop the remaining hadrons and low energy muons  $E_\mu < 5$  GeV. The beam dump material (graphite, iron and copper) and shape has been designed to minimise the possibility of melting. The high energy muons are detected in the downstream muon monitor.

**The Muon Monitor (MuMon)** The MuMon is located just downstream the beam dump, 118 m away from the T2K target (Figure 2.8). It has been designed to detect the high energy muons escaping from

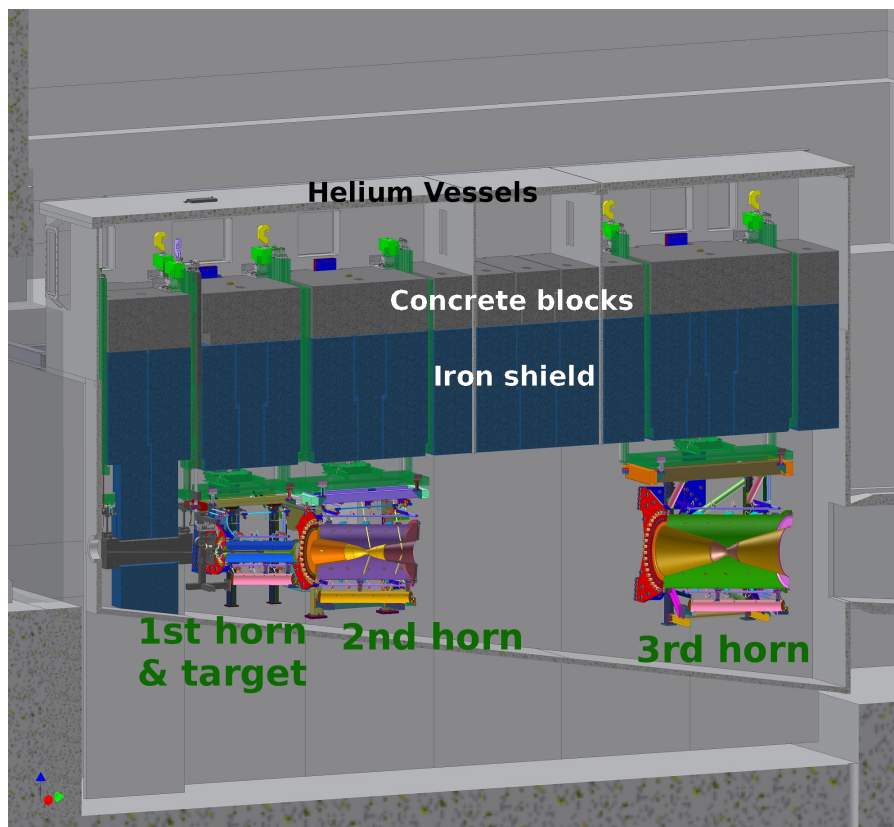


Figure 2.10: Schematic view of the T2K target and 3 horns just upstream the decay volume. The latter can be partially seen on the right.



Figure 2.11: Transverse picture of the T2K decay vessel.



Figure 2.12: The muon monitor (MuMon). The ionisation chamber is shown on the left and the PIN photodiodes-based detector on the right. The muon and neutrino beams go from the left to the right.

the T2K beam dump. It has been installed to monitor both neutrino beam direction and intensity through the measurement of the muon beam characteristics. The MuMon has a 3% resolution on the neutrino beam intensity and 0.25 mrad resolution on the beam angle. We will describe in more details this detector since we have used it in the Lorentz violation search that will be presented in Chapter 6. In particular, it is important to highlight that the MuMon has intrinsic resolutions of 0.1% and 0.3 cm respectively on the “muon beam” intensity and center position.

The MuMon is constituted of two independent detectors, shown in Figure 2.12. Both detectors cover a transverse  $1.50 \times 1.50 \text{ m}^2$  area. The upstream detector is constituted of seven ionisation chambers, each containing seven sensors in a  $150 \times 50 \times 1956 \text{ mm}^3$  aluminium gas tube. The sensors are parallel alumina-ceramic electrodes between which a 200 V voltage is applied (sensor active volume =  $75 \times 75 \times 3 \text{ mm}^3$ ). The ionisation chamber gas is either Ar with 2%  $\text{N}_2$  for low beam intensity or He with 1%  $\text{N}_2$  for high intensity. The gas temperature, pressure and oxygen conditions are respectively kept at  $34^\circ\text{C}$  with a  $1.5^\circ\text{C}$  gradient with a  $\pm 0.2^\circ\text{C}$  uncertainty,  $130 \pm 0.2 \text{ kPa}$  and below 2 ppm.

The downstream detector is based on  $7 \times 7$  PIN Hamamatsu photodiodes. Each photodiode has a  $10 \times 10 \text{ mm}^2$  active area with a depletion layer of  $300 \mu\text{m}$  thickness.

**The neutrino beam structure** We will describe the neutrino beam structure that will reach the near (ND280 and INGRID) and the far (SK) detectors. We have seen that the beam is composed mainly of  $\nu_\mu$  with a 0.5% intrinsic  $\nu_e$  contamination in the neutrino mode. The off-axis technique involves a neutrino energy peaked around 700 MeV for the off-axis detectors.

**Interest of a pulsed beam** We have seen that the fast extraction technique allows T2K to keep the MR proton beam structure. The main interest of this structure is to use pulsed current horns which are necessary given the very high intensity of the current. As we observe, it allows to reduce the background contamination (cosmic muons, atmospheric neutrinos...) using the time coincidence of the detected event with the expected beam time arrival.

**Beam structure** The current T2K beam has a spill structure. One spill occurs every 3.5 s (kicker magnet extraction) and beam bunches are spread over a  $4.2 \mu\text{s}$  time window. Each spill is made of eight neutrino bunches of 60 ns that occur every 581 ns in the spill. At the nominal 750 kW MR



Figure 2.13: The T2K near detector complex. The INGRID vertical and horizontal modules can be seen on the bottom part. The ND280 off-axis detector is visible on the top part with its magnet open.

intensity, each spill corresponds to  $3.3 \times 10^{14}$  protons. During the T2K Run I (March to June 2010), only six bunches per spill were delivered.

### 2.2.3 Near detectors

The near detector complex is located 280 m downstream the T2K target. It is constituted of an on-axis detector, INGRID, and an off-axis detector complex named ND280. The whole near detector complex is presented in Figure 2.13. Each detector has a specific use that is detailed in this section. Since most of the work shown in this thesis has been accomplished using the on-axis detector, we will only briefly introduce the off-axis detector before giving more details on the on-axis one.

#### The ND280 detector complex

The important uncertainties ( $\sim 10\%$ ) on the neutrino flux require a near detector to control the neutrino flux prior to any oscillation. Ideally, this detector would be a replica of the far detector and should intercept the very same flux in order to cancel the relative systematic error. In practice, this is obviously complicated with one neutrino beam: the cylindrical 33 m diameter SK located at 295 km would require a water Cherenkov near detector having a 30 cm diameter at 280 m. Without considering any statistical issue and detector capability of such a small detector, the different size in

the detector would fatally imply edge effects (the Cherenkov shower length for a given muon energy is fixed). In addition, the interacting target would be too small to observe the neutrinos, without considering the impossibility to reconstruct the Cherenkov ring in this case. We have taken this small example to summarise both the crucial importance of ND280, but also some of its limitations:

- The near detector reduces the  $> 10\%$  uncertainty on the neutrino fluxes by measuring both the flavour composition and spectra of the off-axis beam. In fact, the ND280 measurement is a convolution of both the flux and the interaction neutrino cross sections. The spectra are measured according to their production mode in ND280 to maximise the constraints on the extrapolated SK flux. The production modes are classified upon their final states as charged current interactions CC- $0\pi$  ( $\nu_\mu + n \rightarrow \mu^- + p$ ), CC- $1\pi$  ( $\nu_\mu + n \rightarrow \mu^- + p + \pi^{+/-}$ ), CC-Others or neutral current interactions NC. The detailed classification of each interaction will be given in Chapter 5. We highlight here that neutrinos are mainly detected through CC- $0\pi$  processes at T2K neutrino energies ( $E_\nu < 1$  GeV). Each type of charged current interaction is fitted independently. The difference between SK and ND280 intercepted flux implies a non trivial extrapolation of the ND280 measurements to the SK detector. The difference between ND280 (mainly downstream-going particles) and SK detector ( $\sim 4\pi$ ) acceptance for secondary particles naturally amplifies this difference. This implies that the extrapolation can only be done using the T2K simulation, and that the result will be affected by a non-vanishing difference coming from neutrino flux uncertainties. On top of this, the two detectors have a different target material (Hydrocarbon in ND280, water in SK) which naturally generates an uncertainty coming from the neutrino cross section ratio between hydrocarbon and water.
- The main background in the SK observation of oscillated  $\nu_e$  (roughly one half of the total background) is the intrinsic  $\nu_e$  beam contamination. ND280 is crucial since it measures this contamination to reduce the associated systematics in the neutrino oscillation measurements.
- The second main background at SK for the  $\nu_e$  appearance search is due to  $\nu_\mu$  or oscillated  $\nu_\tau$  NC $\pi^0$  interactions (roughly one third of the total background), where the  $\pi^0$  decays in two photons which in turn create Cherenkov rings by converting into  $e^+/e^-$ . For this reason, a ring associated to a photon is 99% similar to a pure electron ring. If one of the two photons is missed (superimposed rings or faint ring), this event may be mistaken with a one ring electron event which is the signal of a  $\nu_e$  interacting through a CC- $0\pi$  interaction. The ND280 detector should measure the NC $\pi^0$  cross section with the highest possible accuracy to reduce the uncertainty associated to this reaction. In the same way, the NC- $1\pi^+$  and CC- $1\pi^+$  are important backgrounds in the  $\nu_\mu$  disappearance analysis. Their accurate measurement by ND280 is also one important goal of this detector.

To perform these measurements, the detector is composed of several sub-detectors shown in Figure 2.14. All the ND280 sub-detectors are installed within the former UA1 and NOMAD experiment magnet except the side muon range detector. The magnetisation is essential to discriminate the particle charges. The magnet generates a transverse horizontal magnetic field relatively to the neutrino beam direction. The magnet inner space is a rectangular parallelepiped of  $88 \text{ m}^3$  volume. The T2K experiment operates the magnet with a 3 kA current which corresponds to a 0.2 T magnetic field inside the magnet.

The T2K neutrino beam will first go through the  $\pi^0$  detector (P0D) before reaching the Tracker composed of three Time Projection Chambers (TPC) and two Fine Grain Detectors (FGD) and going through the downstream electromagnetic calorimeter (Downstream ECAL) as shown in Figure 2.14. A typical neutrino event interacting in the upstream FGD is shown in Figure 2.15

**The  $\pi^0$  detector (P0D)** The P0D has been designed especially to measure the NC $\pi^0$  cross section in water. This detector is composed of three successive modules. The external modules are used as electromagnetic calorimeters and are made of seven vertical and horizontal scintillator planes interleaved with 4 mm lead planes. The central module contains both the water target and a tracker. In this central part, twenty-five vertical and horizontal scintillator planes are interleaved with twenty-five

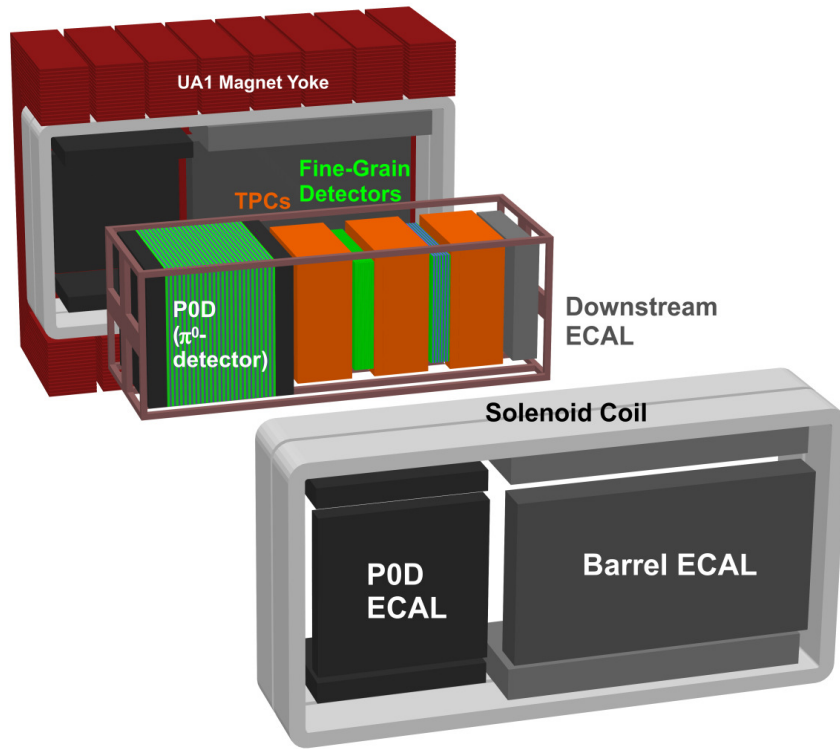


Figure 2.14: The off-axis ND280 near detector complex. The external former UA1 magnet surrounds the POD (green), TPCs (orange), FGDs (light green) and calorimeters (black and grey). The external SMRDs are shown in red.

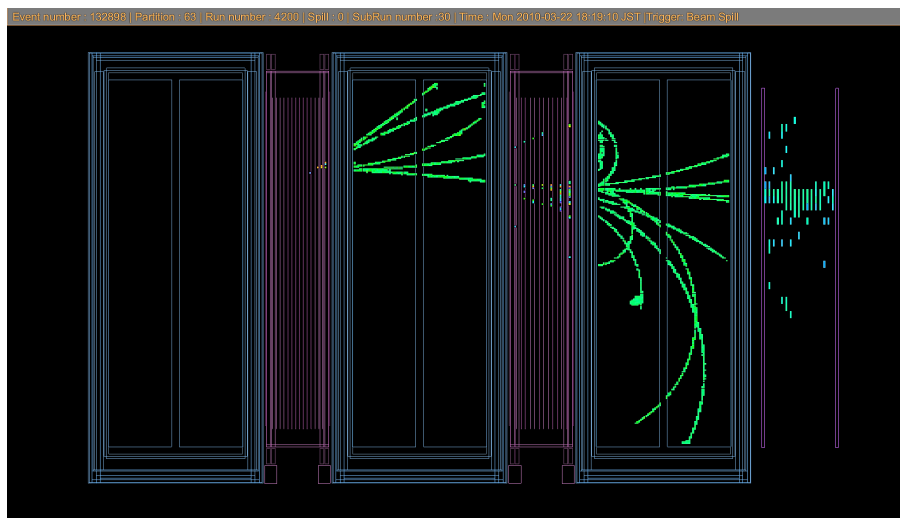


Figure 2.15: A typical events occurring in the first (upstream) FGD and propagation to the downstream TPCs, FGD and calorimeters. One observes the shower produced by the passage of the bottom particle in the second FGD.

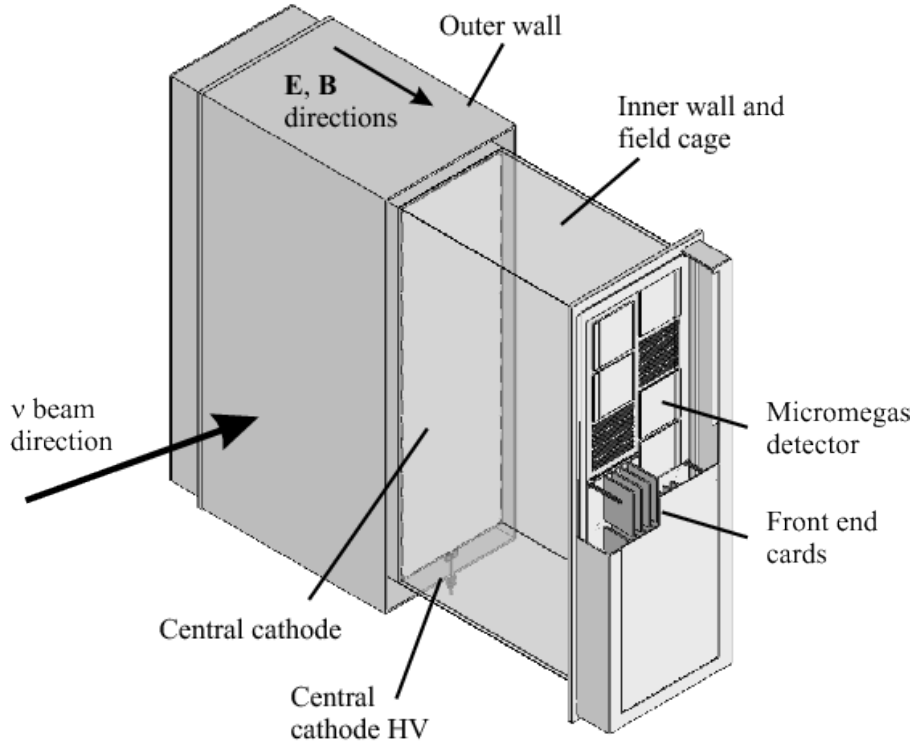


Figure 2.16: Simplified cut-away drawing showing the main aspects of the TPC design.

(3 cm long) water target planes and twenty-five (1.6 mm long) brass planes to increase particle energy loss. The total target mass is 2850 kg. The strategy to determine the  $\text{NC}\pi^0$  cross section only on water (mainly oxygen) is to remove the contribution of brass and carbon scintillator targets by comparing the cross sections measured in the POD water filled and water out.

**The Tracker** The neutrino spectra, intrinsic  $\nu_e$  contamination and various cross sections are measured in this detector. As such, this detector possesses a powerful particle identification to determine the secondary particle of the different cross section types. The two FGD constitute the main neutrino target of the tracker. The upstream FGD is only made of thirty horizontal and thirty vertical polystyrene scintillator planes, that constitute both the hydrocarbon target and a fine grain tracker. Each scintillator has dimensions of  $0.96 \times 0.96 \times 184.3 \text{ cm}^3$ . The downstream FGD is made of seven horizontal and seven vertical similar scintillator planes with six (3 cm) long water planes. The water and hydrocarbon target of this FGD allows to measure their relative cross section in order to reduce the uncertainty arising from the target difference between ND280 and SK. The mass of each of the FGD is  $\sim 1$  ton.

The TPC allows to reconstruct charged particle tracks with a very high resolution. It is mainly necessary to determine the particle track curvature in the magnetic field to measure the particle momentum and charge. The TPC are  $2.5 \times 2.5 \times 0.90 \text{ m}^3$  volumes filled with an inner Ar based gas and an outer  $\text{CO}_2$  insulating gas (see Figure 2.16). A high voltage is applied between the surrounding dynodes to drift the particles ionised along the track. The particle position transverse to the electric field (longitudinal and one transverse direction from neutrino beam direction) can be therefore directly measured, while the longitudinal coordinates along the electric field should be extrapolated from the ion drift time.

**The Calorimeter** The tracker is surrounded by a barrel and a downstream electromagnetic calorimeters that are used to identify and measure the energy of the particles that leave the tracker. For example, they are used to measure the decay electron energy from the  $\nu_e$  interactions or the photon energy from the  $\pi^0$  decay. Each side and downstream module is made of thirty-two scintillator planes

separated by thirty-one 1.75 mm lead planes. The downstream module has three more scintillators and lead planes.

**The side muon range detector (SMRD)** Finally, side muon range detectors are installed out of the magnet (red external detectors in Figure 2.14). Their primary goal is both to veto the incoming cosmic muons, but also to measure the high angle muons that are difficult to reconstruct with the TPC. They are made of four to five scintillator planes.

We will give some more details on the use of ND280 in the neutrino oscillation measurements in Section 2.3.

## INGRID

INGRID (Interactive Neutrino GRID) is the on-axis detector of the T2K experiment. It has been designed for two main purposes:

- Monitor the neutrino flux intensity.
- Monitor the neutrino beam off-axis angle

Ideally, this detector would give real time informations. It is not possible due to the very low neutrino cross section. Therefore, a day by day information is provided instead. The measurement along the proton beamline and the muon flux detected in the MuMon are then used on top of INGRID to give a real time information.

The INGRID detector basically needs a high interaction rate to monitor the beam in a short period, coupled with a device to detect the decay products of the neutrino interaction. The most straightforward way is to detect the associated lepton ( $\mu^-$  in the neutrino beam) produced during neutrino charged current interaction in the detector ( $\sim 75\%$ ). The neutral current interactions are much more difficult to reconstruct, and only represent 25% of the total.

Moreover, INGRID should have an important space coverage in order to monitor the beam shape and center since the beam average width is  $\sim 10$  m at 280 m from the target. For this purpose, the INGRID detector is a complex of modules assembled in a cross-shape structure, made of seven horizontally aligned and seven vertically aligned “standard INGRID” modules. A picture of INGRID is shown in Figure 2.17. The modules are placed every 1.5 m for a total 10.3 m horizontal and vertical transverse width. The neutrino beam first reaches the vertical modules and 4 m downstream, the horizontal ones. In addition, two “shoulder” or “off-cross” standard modules have been installed to monitor the beam shape asymmetry. Finally, a different module, the “Proton Module” (PM) has been installed in 2010 in between the central horizontal and vertical INGRID modules to study neutrino cross sections.

**INGRID standard module** A standard INGRID module is a longitudinal sandwich of eleven scintillator tracking planes and nine iron target planes in between (Figure 2.18). A tracking plane is composed of one vertical plane and one horizontal plane pressed against one another (with isolation in between), each made of twenty-four scintillator bars. Each tracking plane has therefore forty-eight channels, and a proper electronic board. The INGRID scintillator are bars which are 120.3 cm long, 5 cm wide and 1 cm thick. A scintillator plane has therefore a  $120.3 \times 120 \times 1$  cm<sup>3</sup> dimension. The INGRID iron layers have the same transverse dimensions as the tracking planes, but a longitudinal thickness of 6.5 cm, to increase the interacting rate of incoming neutrinos. Note that the most downstream iron plane has not been installed as shown on the event display in Figure 2.19. We will see that it has no incidence on the neutrino rate, since the reconstruction requires several consecutive and “active” tracking tracking planes to remove the background. Each of the scintillator planes is isolated from the incoming direct light using black plastic foils. The INGRID tracking and iron layers are supported by a mechanical structure and are not pressed against one another. The distance between two INGRID tracking planes is 10.7 cm. The dimension of an INGRID module (without its veto planes) is therefore

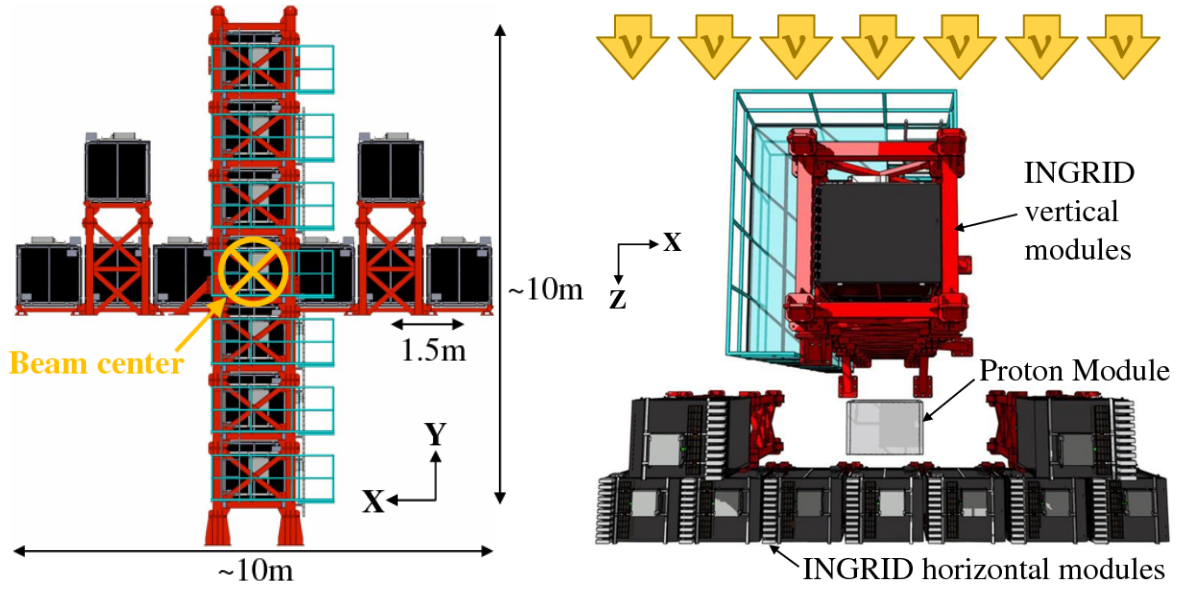


Figure 2.17: The INGRID front (left) and upper (right) view from the on-going neutrino beam.

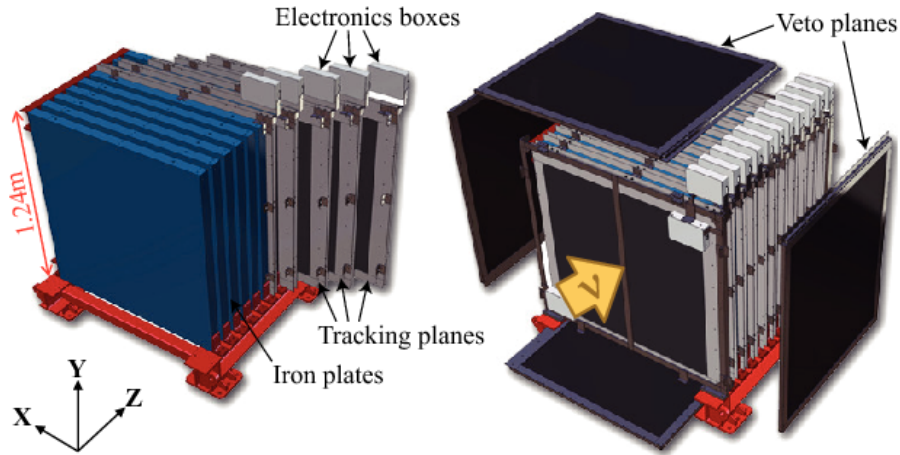


Figure 2.18: A standard INGRID module. On the left, we have shown the module inner part with the blue iron layers and the black scintillator planes. We have shown the same module on the right with the bottom, top and side “veto planes” (black) added.

$120.3 \times 120 \times 109 \text{ cm}^3$ . The main neutrino target in a module is constituted in average by 785 kg of iron.

Each INGRID module is embedded in a larger structure composed of four additional scintillator layers that are used as veto. No additional layer is added on the front since the first tracking plane can be directly used as a veto. A veto plane is composed of only one layer of twenty-two scintillators. The scintillator shapes are similar to the INGRID standard tracking plane, at the minor difference of being slightly longer for the top and side veto planes (129.9 cm) and slightly shorter for the bottom one (111.9 cm) in order to maximise the active area and take into account the mechanical structure geometry. The INGRID module with its veto planes has a volume of  $124 \times 124 \times 109 \text{ cm}^3$ . Note that the inner horizontal INGRID modules have not any veto on their right but use the left veto planes of their right neighbour module instead. The same goes for the bottom plane of vertical modules. Modules in the cross are separated by 26 cm, which justifies this common use of veto planes.

Since the beginning of T2K, more than  $6 \cdot 10^6 \nu_\mu$  have been detected in the INGRID cross modules.

**The Proton Module (PM)** The PM detector has been installed to study the neutrino cross sections. In most of the cases, only the charged lepton can be seen when a neutrino interacts in a standard INGRID

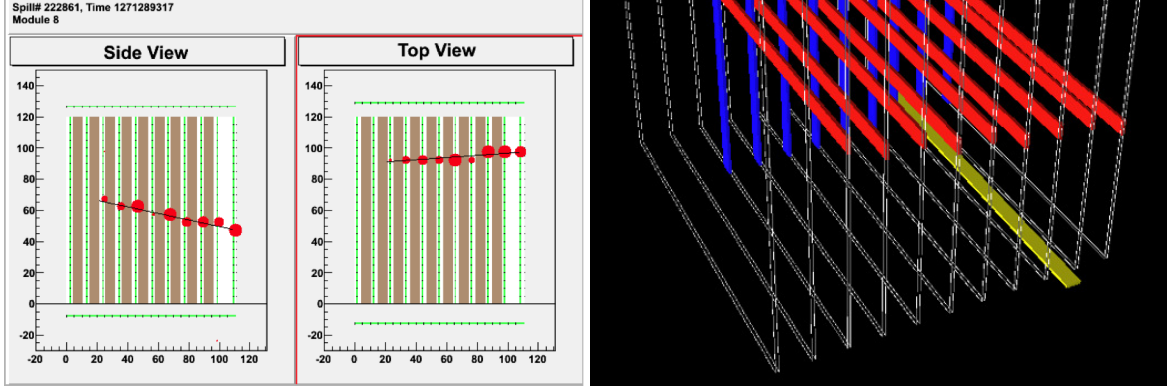


Figure 2.19: Typical event display occurring in INGRID modules. On the left, we have shown the separated side and top 2D views, where the red dots represents the particle energy deposition. The brown and green rectangles represents respectively the iron and the scintillator layers. One observes the lack of iron layer between the two last scintillator planes. The same event is shown on the right (in yellow), with the vertical and horizontal scintillator hit as shown in blue and red respectively.

module. Though it allows to measure the charged current interaction rate on iron (“CC-inclusive”), it has absolutely no capability to discriminate between the different charged current interaction types, nor to reconstruct most of the neutral current interactions. For this reason, the PM was installed in between the INGRID vertical and downstream horizontal modules. Considering its goal, the iron layers have been removed as compared to an INGRID standard module, in order to possibly reconstruct the tracks of pions and protons, giving the eponymous name to this module. The counter-part is the reduction of the neutrino statistics as compared to a standard INGRID module. To maximise the detector capabilities, the vertical and horizontal scintillator planes in a module are not pressed against one another anymore, except for the most upstream vertical and horizontal planes. Each scintillator plane is now longitudinally spaced from its neighbour by 2.3 cm. Moreover, the number of scintillator planes has been increased from  $11 \times 2$  to  $18 \times 2$ , mainly to increase detector acceptance, reconstruction and particle identification since the stopping matter has been clearly reduced from a standard INGRID module [48]. The PM dimensions (with the veto) are  $124 \times 124 \times 81.8 \text{ cm}^3$  from the front of the first scintillator plane to the end of the last one. The PM has also four veto planes (bottom, top and two side planes) which are the same as for INGRID standard module. We describe hereafter the structure of the inner planes.

The two most upstream planes are gathered in a tracking plane as in INGRID, where the vertical and horizontal planes are each composed of twenty-four scintillators. On the other hand, the thirty-four other planes are different from in INGRID standard modules (Figure 2.20). For these, each scintillator plane is composed of thirty-two scintillators:

- eight INGRID type scintillators (dimensions  $120.3 \text{ cm} \times 5 \text{ cm} \times 1 \text{ cm}$ ) on each external parts of the plane, so sixteen scintillators in total. This represents a transverse active area of  $2 \times 120.3 \times 40 \text{ cm}^2$ .
- sixteen SciBar type scintillators (dimensions  $120.3 \text{ cm} \times 2.5 \text{ cm} \times 1.3 \text{ cm}$ ) in the central part of the plane. This represents a transverse active area of  $120.3 \times 40 \text{ cm}^2$ .

The SciBar type scintillators (2.5 cm) are one half narrower than the INGRID type scintillators (5 cm). They have been installed in order to increase the detector granularity in the central part

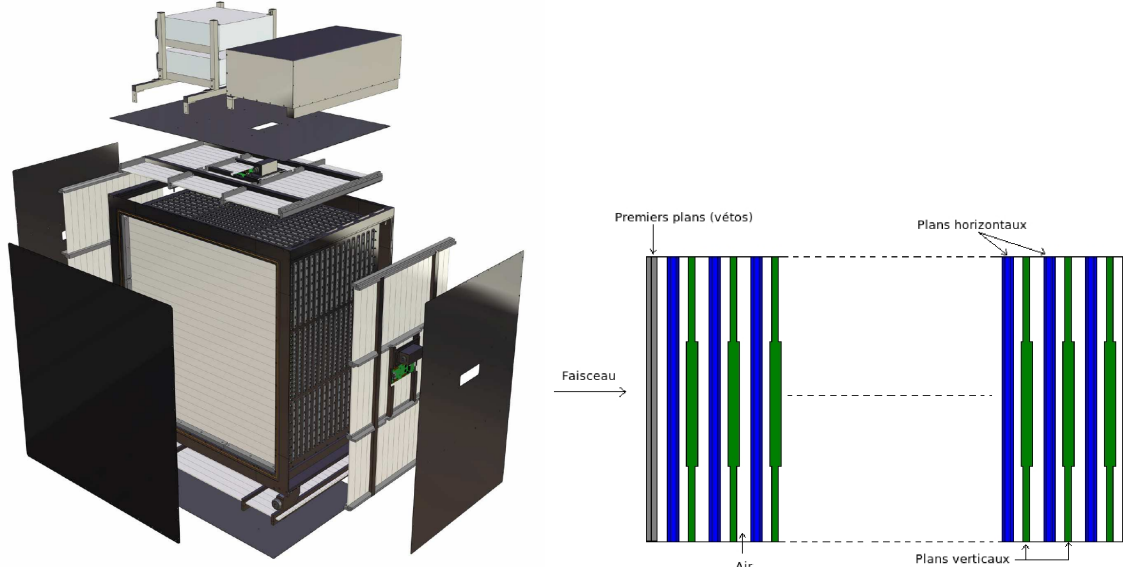


Figure 2.20: On the left, the PM is shown. On the right, a PM side view is shown to illustrate the scintillator plane positioning.

where most of the reconstructed events have tracks. As an example, the detector angular resolution for a track produced in the center of the module is  $3.5^\circ$  using SciBar type scintillators instead of  $6.8^\circ$  for the INGRID type scintillators. This detector resolution is mainly used to discriminate between the different tracks produced near the neutrino vertex. In most of the case where several tracks are produced, the tracks being produced in the neutrino beam direction due to momentum conservation. Therefore, a higher granularity is required especially for the short tracks, to discriminate between the tracks. As an example, the detector angular resolution for a track crossing  $3 \times 2$  scintillator layers is  $30^\circ$  in the case of INGRID type scintillators. This would imply that no short tracks (mainly protons) could be reconstructed if none of the track angle in the XZ or the YZ plane with the lepton direction is  $> 30^\circ$ . This would importantly limit the detector acceptance, which justifies the use of narrower scintillators to reach a  $15^\circ$  resolution for these short tracks and identify protons. Note that these scintillators are slightly thicker, which will positively impact the energy deposition as will be seen in Chapter 4. This scintillator structure can be seen on the event display of Figure 2.21.

We highlight here that the PM is really close ( $< 30$  cm) from the downstream INGRID horizontal central module. For this reason, the horizontal module information will be added to the PM for neutrino events interacting in the latter, as shown in Figure 2.21. This will be the crucial point to determine the muon momentum in the measurement shown in Chapter 5.

### 2.2.4 The Super-Kamiokande far detector

The Super-Kamiokande (Super-Kamioka-Nucleon-Decay-Experiment, SK) is the far detector of the T2K experiment. It is a 22.5 ktons (Fiducial volume) cylindrical water Cherenkov detector. SK has been operating since 1996, and is currently in its fourth phase. It has been used for solar and atmospheric neutrino observations, some of which still bringing the best constraints on oscillation parameters (Chapter 1). The detector is also used to search for the proton decay predicted by unified theories, or to observe neutrinos emitted by supernovae occurring in the Milky-Way. Its ancestor, the Kamiokande detector, became famous when observing the 1987A supernova in 1987 [51]. SK has been installed under the Mount Ikenoyama in a former mine near the Kamioka town, Gifu prefecture, Japan. It is located 1 km below the peak in order to shield the experiment against most of the incoming cosmic background. This represents an equivalent 2.7 km water thickness, which stops cosmic muons having an energy lower than 1.3 TeV.

A schematic view of the whole detector is shown in Figure 2.22. The detector is composed of two different parts: an outer (OD) and an inner detector (ID), separated by a structure where photo-

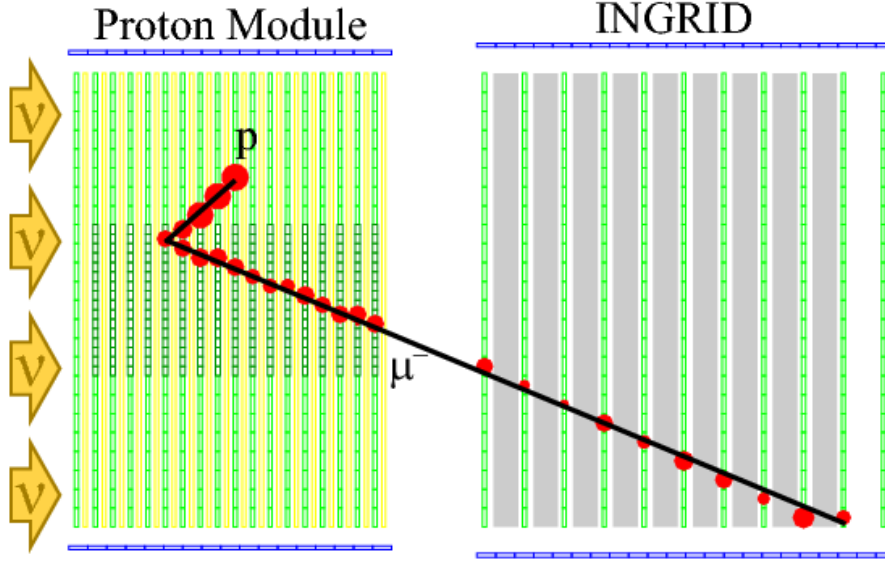


Figure 2.21: An event display of a  $\nu_\mu$  interacting through a charged current quasi-elastic interaction in the PM. The produced  $\mu^-$  also crosses the downstream central INGRID horizontal (Module 3).

multiplier tubes (PMT) are mounted. The whole cylinder is filled with ultra-pure water surrounded by photo-multiplier tubes. It has a 39.3 m diameter and a 41.4 m height. The ID corresponds to the inner concentric cylinder volume which is 33.8 m in diameter for a 36.2 m height. The part between the ID and whole cylinder is the OD.

**The outer detector (OD)** The 1885 8-inches PMTs of the outer detector are facing the pit wall: they are only mounted on the top, the bottom and the barrel of the common structure with the inner detector. The walls of the OD are covered with “Tyvek”, a highly reflective material that compensates the poor PMT coverage in the OD. In fact, this coverage only slightly affects SK analysis since the OD is mainly used as a veto. It then accomodates with a poor vertex resolution but should mandatorily collect as much light as possible. The distance from the pit wall to the OD PMT is  $\sim 2.6$  m.

**The inner detector (ID)** On the other hand, the ID is composed of 11129 twenty-inch PMTS facing towards the interior of the detector. They are mounted on the top, bottom and barrel of the inner detector wall. The PMTs are mounted at a  $\sim 70$  cm distance from their neighbours. Unlike the OD, the vertex resolution is essential in the ID and is decreased by the reflected light. Therefore, the PMT uncovered areas on the wall are covered by acrylic “black-sheet” to reduce the reflection on the wall as much as possible. The total PMT coverage is about 40% of the total inner detector wall surface. The inner detector pure water represents a 32.5 kton target area. For the physics analysis, a smaller fiducial volume is used to remove edge effects (near the walls) where the detector performances are really low. The fiducial volume is composed of the water volume contained in an inner equivalent cylinder located 2 m away from the ID walls. The fiducial volume of the SK detector is therefore reduced to 22.5 kton of water.

### The Cherenkov effect

The detection in SK is based on the Cherenkov effect. The charged particle moving faster than light in water produces an intense light emission, called the Cherenkov light, which is observed in the PMTs. In the case of neutrino interactions, the decay charged particles as charged leptons, pions or protons produce Cherenkov light while their speed is higher than the speed of light in the medium. Indeed, any charged particle interacts with the water medium henceforth producing light. However, for a particle speed  $v < c_{\text{medium}}$ , this light is not emitted coherently and is too faint to significantly activate the SK PMTs. For particles which have a speed  $v \geq c_{\text{medium}}$ , this light is emitted coherently, and may

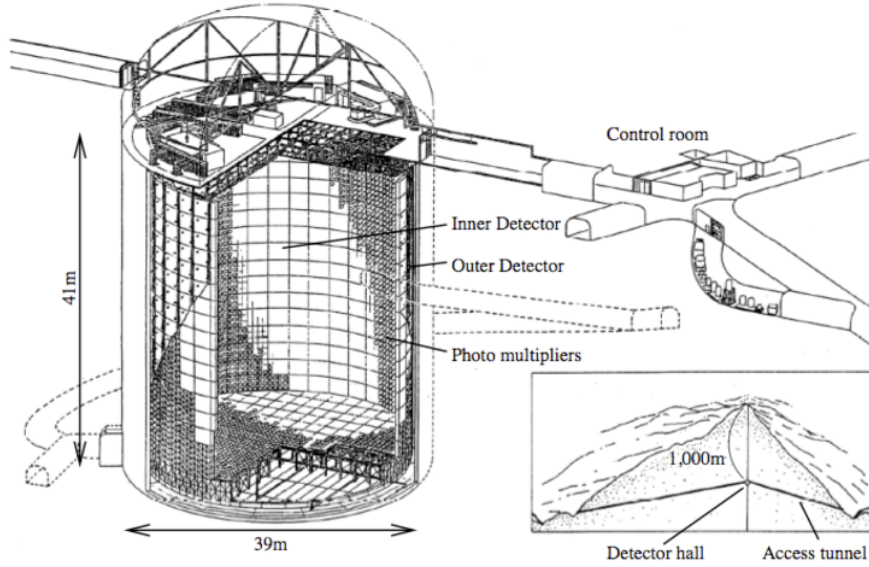


Figure 2.22: The SK tank schematic view. The structure separating the inner and outer detector parts is shown, along with the reflective Tyvek surface in the latter.

therefore be detected. In this case, the spherical phase front combines coherently in a conic shape coherent phase front (see Figure 2.23). The cone angle with the particle direction can be estimated from simple geometrical considerations as:

$$\cos \theta = \frac{c_{\text{medium}}}{v} = \frac{1}{\beta n} \quad (2.2.2)$$

where  $\beta = \frac{v}{c}$  and  $n$  is the refractive index of the medium. An ultra-relativistic particle in the detector mainly has a speed close to the speed of light in vacuum when produced. It loses energy (and so, slows down) interacting with water during its propagation. Particles with relatively low velocities or crossing an important fraction of the detector will stop their Cherenkov emission when reaching  $v < c_{\text{medium}}$ . The lower the particle velocity is at a given position on its trajectory, the more it interacts with water and so loses energy. For this reason, we will consider here that the particle travels at the speed of light in vacuum and suddenly loses all its energy, slowing down under  $c_{\text{medium}}$ . Assuming this hypothesis, the light cone should have a constant angle along the track of the particle in water ( $n = 1.34$ )  $\theta \sim 42^\circ$ . The slower the particle is, the smaller this angle will be.

When projected on SK wall, the light cone forms an annular light shape that is used for particle identification.

The muons and electrons interact with the same intensity with the surrounding medium. However, due to their smaller mass, this similar interaction affects more the electron trajectory than the muon one. For this reason, the electrons produce a superposition of slightly different light cones, while muons produce a cleaner light cone. The projected ring on the SK wall is then fuzzier for an electron and sharper for a muon. This difference is used for the particle identification at SK to discriminate between their respective parent neutrino  $\nu_e$  and  $\nu_\mu$ . We have illustrated this difference in Figure 2.24. This separation is a key point to discriminate between the neutrino flavour to study their oscillations.

### SK detector use in T2K

The SK detector discriminates the T2K events from the other neutrinos using the spill structure of the neutrino beam. A specific trigger at SK is based on a signal sent from J-PARC containing the GPS time of the spill. The GPS time is then corrected by the neutrino time of flight from J-PARC to SK assuming they travel at the speed of light, which represents a  $\sim 984 \mu\text{s}$  correction. The data recorded in a  $\pm 500 \mu\text{s}$  time window around the expected neutrino arrival time are then saved. Finally, the timing of the SK PMT hits is checked with a different clock system using a rubidium atomic clock

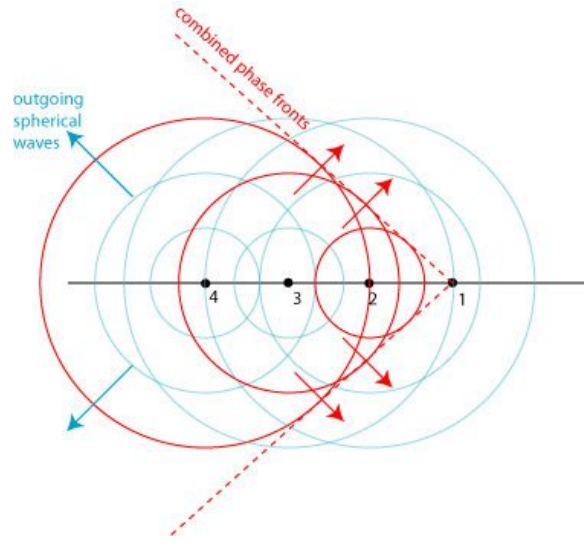


Figure 2.23: The Cherenkov effect for a ultra-relativistic particle in the medium. In red is shown the coherent phase front that will be detected by SK PMTs. Taken from <http://skullsinthestars.com/2009/11/20/reversing-optical-shockwaves-using-metamaterials/>

and two independent GPS modules. Only the events that occur in a  $[-2 \mu\text{s}, 10 \mu\text{s}]$  time window around the expected neutrino beam time will be kept for the T2K analysis. Further details will be given in Section 2.3.

## 2.3 Neutrino appearance search at T2K

The T2K experiment oscillation analyses are based either on  $\nu_\mu$  disappearance or  $\nu_e$  appearance. The neutrino flux expected at SK is estimated both using neutrino flux simulation and the constraints provided by near detector measurements. In this section, we will detail the different steps that lead to the current T2K oscillation result. We will finally briefly mention the T2K discovery and measurement potential for the next years.

### 2.3.1 The neutrino flux prediction

The neutrino flux predictions are estimated for each detector using a Monte-Carlo simulation driven by the data. The neutrino secondary beamline simulation is produced. The proton interactions in the graphite target are simulated using the FLUKA software. The meson propagation until the neutrino beam production is simulated using JNUBEAM, a GEANT3-based Monte-Carlo. This simulation parameters are tuned according to the primary or secondary beam line measurements (intensity, horn current...).

The original uncertainties on the neutrino flux prediction are high, due to the poor knowledge on the hadron production. In order to reduce these uncertainties, the FLUKA simulation is tuned using external data from the NA61/SHINE (SPS Heavy Ion and Neutrino Experiment) [52][53] collaboration. This experiment is based at CERN using the SPS to produce a proton beam with the same energy as in T2K. Two different targets are used: a T2K replica target and a thin target, with a downstream detector in order to accurately measure and constrain the hadron production in similar conditions as in T2K. This allows to reduce the T2K simulated beam uncertainty to 10 – 15%. We have shown the fractional error for the neutrino flux predictions at SK in Figure 2.25. In the phase space region (in hadron momentum and angle) uncovered by NA61/SHINE, other external data sets [54], [55], [56] are used to constraint the FLUKA flux prediction.

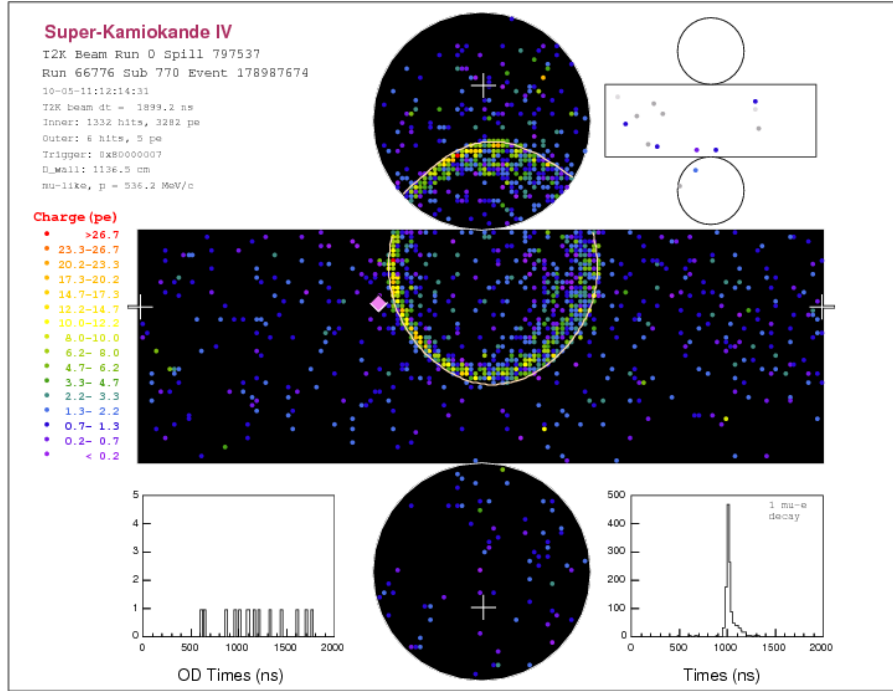
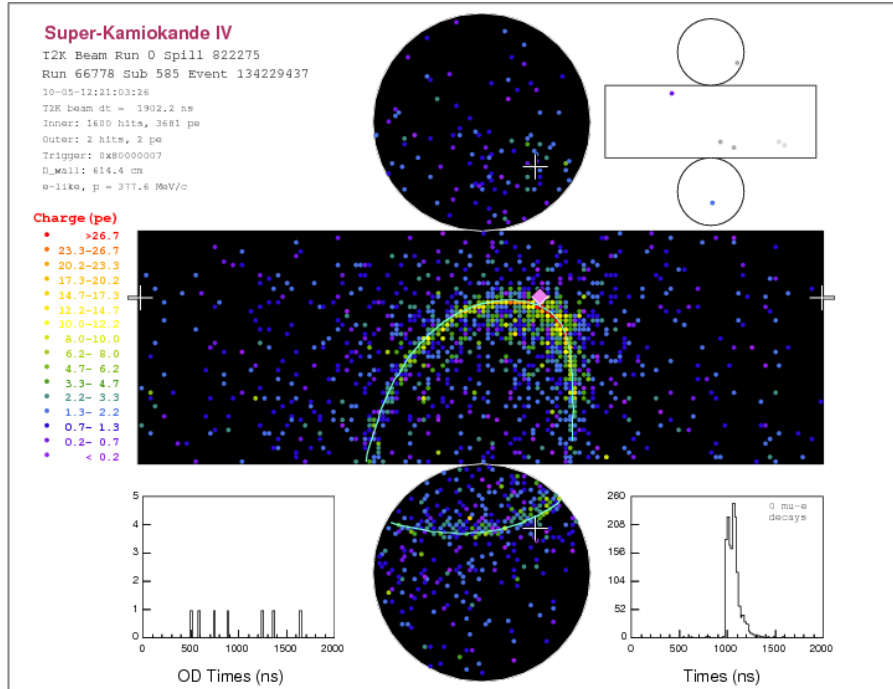

 (a)  $\mu^-$  ring from a parent  $\nu_\mu$ 

 (b)  $e^-$  ring from a parent  $\nu_e$ 

Figure 2.24: Event displays of a candidate muon (top) and electron (bottom) events in SK. The T2K cylinder is “un-rolled”. Each PMT is represented by a pixel whose color depends on the charge measured by the PMT. On the top view, the large and sharp Cherenkov ring is typical of muons, while the fuzzy and thin Cherenkov ring in the bottom is an “electron-like” signature. The event timing is also shown.

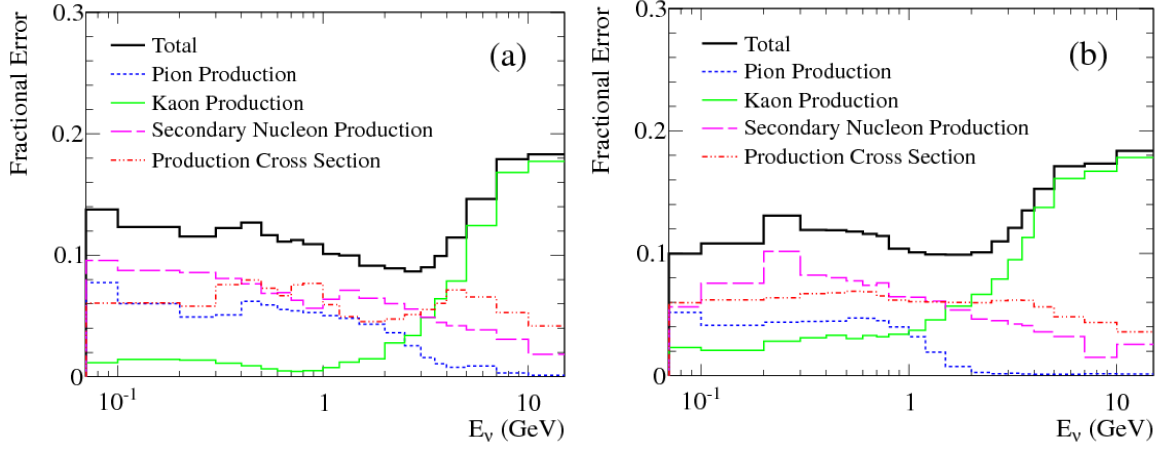


Figure 2.25: The T2K flux errors at SK after NA61/SHINE experiment constraints shown for  $\nu_\mu$  (left) and  $\nu_e$  (right) for a neutrino mode beam. This error only shows contributions from the hadron production errors. Additional errors as horn current or off-axis angle for example, are finally required. They are significantly smaller than the hadron production errors.

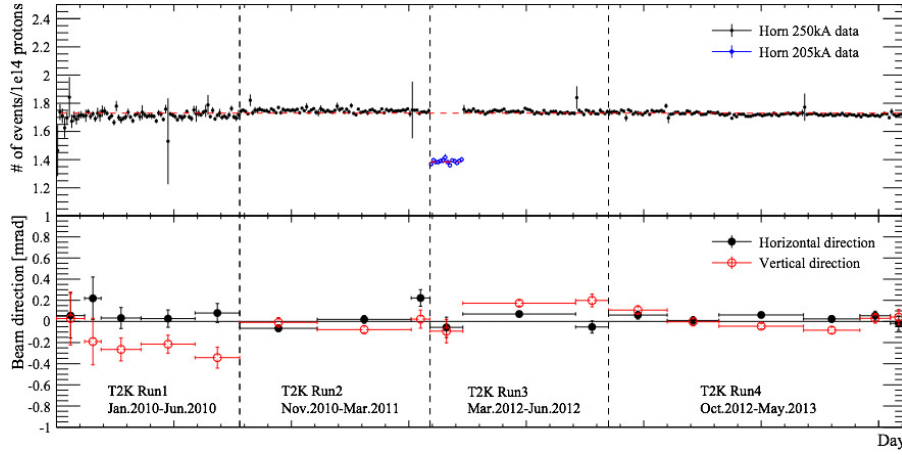


Figure 2.26: Neutrino beam intensity and direction measured with the INGRID detector for Run I to IV.

### 2.3.2 The near detector constraints

#### The beam off-axis angle

The off-axis measurement is crucial to determine the neutrino spectrum in T2K. The INGRID detector has been especially designed to perform this measurement. Figure 2.26 shows both the neutrino beam intensity and direction for the T2K run I to IV data. One remarks that the horn current decrease (from 250 to 205 kA) during the T2K run III-a produces a visible depletion of the neutrino beam intensity. The beam direction is kept within 1 mrad which corresponds to a 2% systematic effect in the neutrino flux prediction at SK.

#### The ND280 constraints

The ND280 detector measures the CC- $0\pi$ , CC- $1\pi$  and CC-Others rates and allows to compare them to the expected number of events. These data constraints are added to the simulation in order to refine the flux extrapolation at the far detector and decrease the associated systematic error. For comparison purpose, we have shown in Figure 2.27 the difference between the number of expected and measured events for these samples, and the impact of ND280 to better constrain them. The constraints are given according to the lepton (muon most of the time) angle and momentum instead of the neutrino energy in order to reduce the cross section model dependency (we will detail this for INGRID in Chapter 5).

The systematic error reductions of the  $\nu_\mu$  and  $\nu_e$  extrapolated fluxes at SK are shown in Figure 2.28.

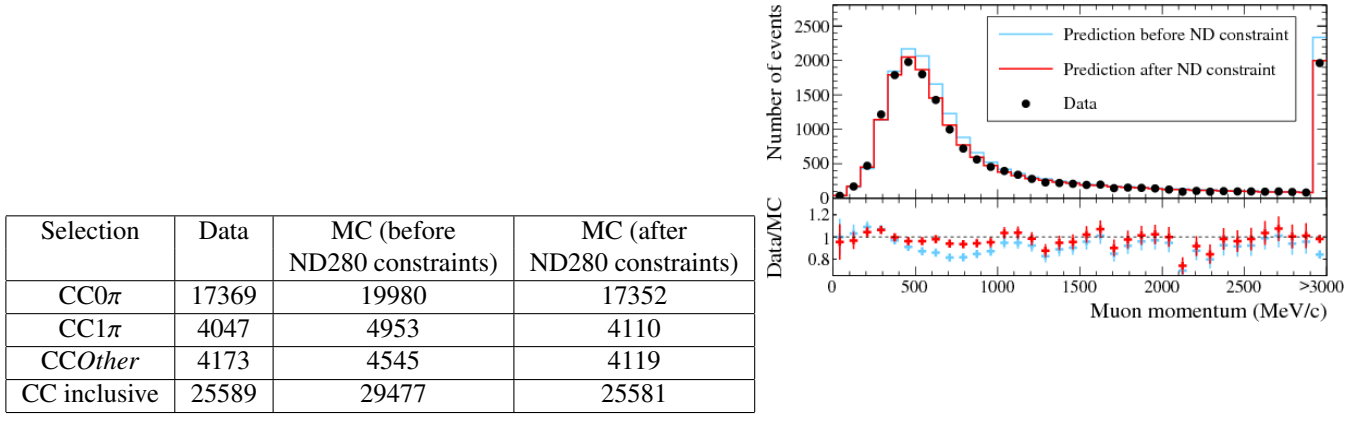


Figure 2.27: Impact of ND280 data constraints on MC prediction at ND280. On the left is shown the impact of ND280 data on the MC prediction for each charged current interactions. On the right is shown the impact of ND280 on the muon momentum distribution predictions.

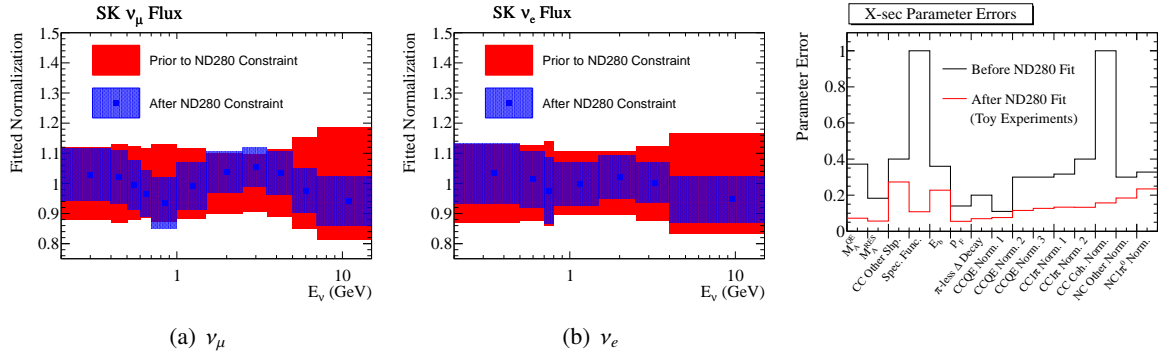


Figure 2.28: Impact of the ND280 constraints on the flux prediction and the associated systematics at SK for the  $\nu_\mu$  (left) and  $\nu_e$  (center) fluxes. The reduction of the cross section parameters brought by ND280 fit is shown on the right part. These parameters will be studied in Chapter 5.

The most striking effect is the decrease of the neutrino flux and cross sections uncertainties from  $> 20\%$  to  $\sim 3\%$  in both the  $\nu_\mu$  and  $\nu_e$  sample. We have also shown the impact of the ND280 constraints on the cross section errors only, in Figure 2.28.

### 2.3.3 Oscillations at far detector

The ND280 constrained flux simulation is extrapolated at the SK far detector in order to accurately predict the neutrino spectra for each flavour. Two different selections are applied on this MC and data for the  $\nu_e$  appearance and  $\nu_\mu$  disappearance measurements. We will describe here the  $\nu_e$  appearance measurement, but details on the disappearance study can be found in [57].

#### The $\nu_e$ appearance

The  $\nu_e$  event selection is mainly based on the rejection of  $\nu_\mu$  events, and the reduction of the two main backgrounds: the intrinsic  $\nu_e$  contamination and the NC $\pi^0$  interactions. The selection that is applied is (shown in Figure 2.29):

1. Event fully contained in the fiducial volume (distance to the inner detector wall  $> 2$  m).
2. Only one reconstructed Cherenkov ring to select only the CC0 $\pi$  events (the proton has rarely enough transferred momentum to produce a detected Cherenkov radiation).
3. The reconstructed ring is “e-like” to remove most of the  $\nu_\mu$  contamination (rejection efficiency is  $\sim 96\%$  for  $\sin^2 \theta_{13} = 0.1$ ). The ring charge profile sharpness is used as the main criterion.

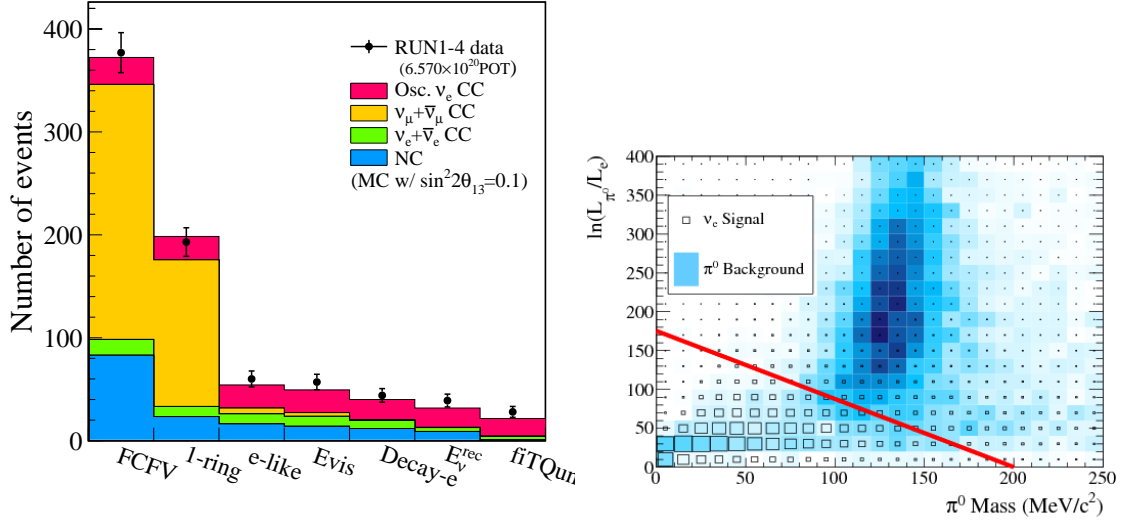


Figure 2.29: On the left: the event breakdown of the  $\nu_e$  event selection. The MC predictions assumes  $\sin^2 2\theta_{13} = 0.1$ . On the right: The logarithm value of the ratio of the  $\pi^0$  likelihood by the  $e^-$  likelihood in comparison with the reconstructed  $\pi^0$  mass. One observes the MC predicted  $\pi^0$  background (in blue).

4. The reconstructed electron momentum  $p_e$  is required to be above 100 MeV/c<sup>2</sup> to remove the low energy background as decay electrons produced by muons (from CC  $\nu_{\mu}$ ) or pions (from NC) below the Cherenkov threshold or from surrounding radioactive decays.
5. No decay electron found, to further decrease the rate of misidentified  $\nu_{\mu}$ .
6. The reconstructed neutrino energy is positive and smaller than 1250 MeV. As observed in Figure 2.29, this selection is applied mainly to reduce the beam intrinsic  $\nu_e$  contamination. The beam intrinsic  $\nu_e$  have relatively larger energies (broader spectrum) due to their kaon parent at high energy than the  $\nu_{\mu}$  as shown in Figure 2.4. Assuming the  $\nu_{\mu}$  spectrum is almost a Dirac distribution, the oscillated  $\nu_e$  has the very same energy than the  $\nu_{\mu}$  which is smaller than the intrinsic  $\nu_e$ .
7. The fitQun algorithm  $\pi^0$  rejection criterion is applied. We have shown this criterion on the left of Figure 2.29. The reconstructed  $\pi^0$  mass criteria is improved (as compared to former studies) comparing the likelihood of the reconstructed ring to come from a one ring  $\pi^0$  or from an electron event. Events that satisfy  $\ln(L_{\pi^0}/L_e) < 175 - 0.875m_{\pi^0}$  (MeV/c<sup>2</sup>) only are selected. The NC rejection efficiency of this cut is  $\sim 90\%$ .

We have summarised the selection both on data and MC sample in Figure 2.30 assuming  $\sin^2 2\theta_{13} = 0.1$ .

**The  $\theta_{13} \neq 0$  observation** In 2013, T2K announced the first discovery of  $\nu_e$  appearance in a  $\nu_{\mu}$  beam with a  $7.3\sigma$  significance. The non-zero value of  $\theta_{13}$  is obtained by estimating the background assuming  $\sin^2 2\theta_{13} = 0$  instead of  $\sin^2 2\theta_{13} = 0.1$  and is presented in Figure 2.29. This result is therefore totally independent from any assumption on the  $\delta_{CP}$  value since this term only comes if  $\theta_{13} \neq 0$ . The T2K experiment has observed 28  $\nu_e$  events, for an expected background of  $4.92 \pm 0.55$  in the case of a no-oscillation scenario. Two shape studies have been performed, with lepton kinematic variables (momentum/angle) or with neutrino energy that gave similar confirmation of the reactor result. We have shown the first one in Figure 2.31.

**The  $\theta_{13}$  and  $\delta_{CP}$  best fit values** On top of providing the discrepancy with a non-oscillated background, the T2K experiment has extracted the constraints on the  $\sin^2 2\theta_{13}$  value assuming  $\delta_{CP} = 0$ . The

Selection	Data	$\nu_\mu \rightarrow \nu_e$	$\nu_\mu + \bar{\nu}_\mu$	$\nu_e + \bar{\nu}_e$	NC	Total MC
		CC	CC	CC		
Interactions in FV		27.1	325.7	16.0	288.1	656.8
FCFV	377	26.2	247.8	15.4	83.0	372.4
+Single ring	193	22.7	142.4	9.8	23.5	198.4
+ $e$ -like ring	60	22.4	5.6	9.7	16.3	54.2
+ $p_e > 100 \text{ MeV}/c$	57	22.0	3.7	9.7	14.0	49.4
+No decay $e$	44	19.6	0.7	7.9	11.8	40.0
+ $E_\nu^{\text{rec}} < 1250 \text{ MeV}$	39	18.8	0.2	3.7	9.0	31.7
+Non- $\pi^0$ -like	28	17.3	0.1	3.2	1.0	21.6

Figure 2.30: Data and the expected signal and background events assuming  $\sin^2 2\theta_{13} = 0.1$ ,  $\sin^2 \theta_{23} = 0.5$ ,  $\Delta m_{32}^2 = 2.4 \times 10^{-3} \text{ eV}^2$  and  $\delta_{CP} = 0$ . From [31].

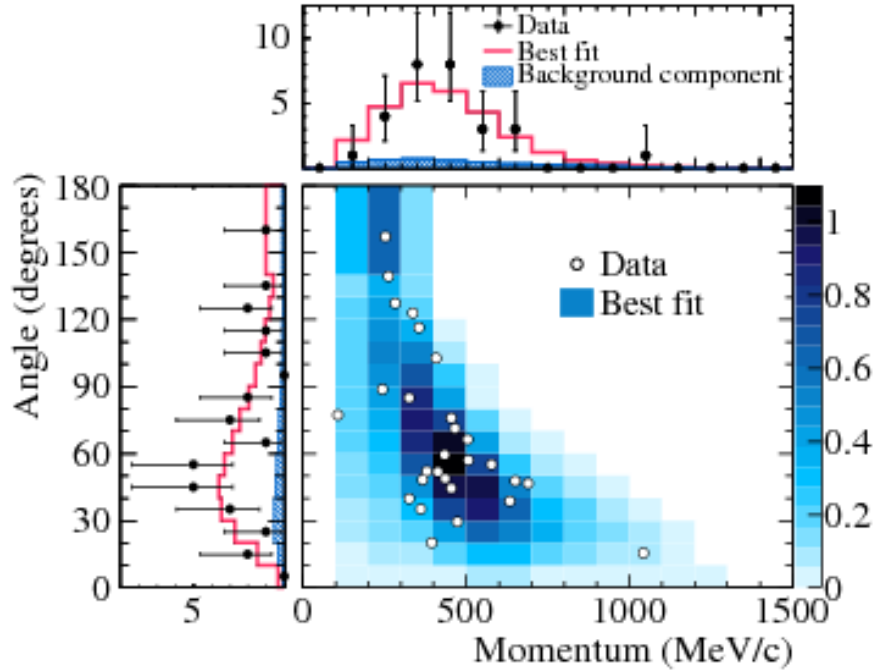


Figure 2.31: The  $(p_e, \theta_e)$  distribution for  $\nu_e$  candidate events with the MC prediction (magenta) for the best fit value  $\sin^2 2\theta_{13} = 0.140$  (normal hierarchy). The background is shown in blue. [31]

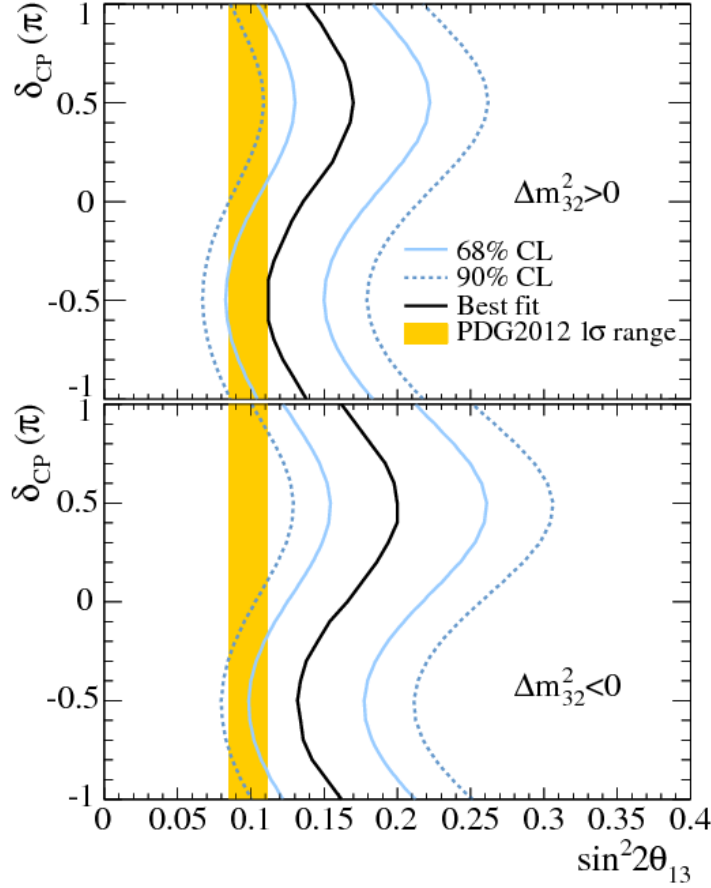


Figure 2.32: The 68% and 90% confidence levels allowed region in the  $\sin^2 2\theta_{13}$ - $\delta_{CP}$  phase space, assuming a normal (top) and inverted (bottom) hierarchies, taken from [31]. The yellow shaded region shows the average  $\theta_{13}$  values in [13]. The atmospheric parameters  $\sin^2 2\theta_{23}$  and  $\Delta m_{32}^2$  are varied in the fit with the disappearance constraints [57].

associated best fit values and their  $1\sigma$  errors in the two mass hierarchies was found as:

$$\sin^2 2\theta_{13} = 0.136^{+0.044}_{-0.033} \text{ (NH)}, \quad \sin^2 2\theta_{13} = 0.166^{+0.051}_{-0.042} \text{ (IH)} \quad (2.3.1)$$

One observes the tension between these values and the reactor best fit that we have shown in Chapter 1. This tension is especially true in the inverted hierarchy since we have seen (Chapter 1) that the oscillations effect are decreased in this case. A very large  $\theta_{13}$  should be therefore introduced to explain the higher neutrino rate than predicted with the reactor neutrino constraint.

Assuming the large neutrino rate observed at T2K is not only due to statistical fluctuations, this discrepancy with the reactor measurement can be interpreted as a CP violation effect. The reactors are not sensitive to any CP violation effect since their observation is based on neutrino disappearance (the fact that it is antineutrino therefore plays no role). On the opposite, T2K is sensitive to the impact of  $\delta_{CP}$  in the appearance study as shown in Chapter 1. The difference between the two measurements can therefore be interpreted as a large effect of CP violation. The  $\theta_{13}$  and  $\delta_{CP}$  are therefore fitted together with T2K data and the result is shown in Figure 2.32 along with the reactor constraint shaded region. As shown in Chapter 1, the largest CP violation enhancement in T2K appearance (in neutrino mode) occurs for  $\delta_{CP} = -\frac{\pi}{2}$ . One observes that the T2K data favour such a large and negative CP violation parameters to retrieve a mixing angle close to the reactor constraints, given the unexpected larger appearance effect that was observed. Assuming the reactor constraints for  $\theta_{13}$ , the  $\delta_{CP}$  is fitted with the T2K data and the sole  $\delta_{CP}$  parameter constraints are shown in Figure 2.33. The fit results exclude regions where  $\delta_{CP} \in [0.19\pi, 0.80\pi]$  and  $\delta_{CP} \in [-\pi, -0.97\pi] \cap [-0.04\pi, \pi]$  respectively for the normal and inverted hierarchies.

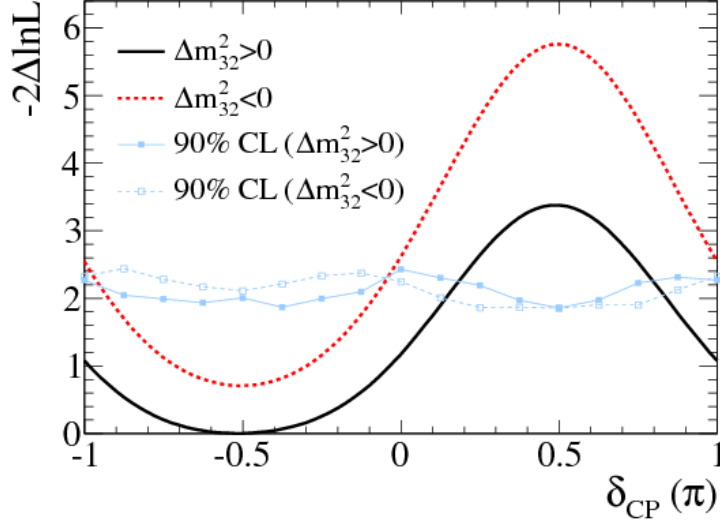


Figure 2.33: The log likelihood value as a function of  $\delta_{CP}$  for normal (black solid) and inverted (red dotted), inserting the reactor constraint on  $\sin^2 2\theta_{13}$  [13]. The likelihood is marginalised over  $\sin^2 2\theta_{13}$ ,  $\sin^2 2\theta_{13}$  and  $\Delta m^2_{32}$ . Taken from [31]

Error source [%]	$\sin^2 2\theta_{13} = 0.1$	$\sin^2 2\theta_{13} = 0$
Beam flux and near detector	2.9	4.8
(without ND280 constraint)	(25.9)	(21.7)
Uncorrelated $\nu$ interaction	7.5	6.8
Far detector and FSI + SI + PN	3.5	7.3
Total	8.8	11.1

Figure 2.34: The uncertainty on the predicted number of signal  $\nu_e$  for each systematic uncertainties for two different assumptions of  $\sin^2 2\theta_{13}$ . The uncorrelated interactions come from the part of the neutrino cross section model uncertainties that cannot be constrained by ND280. Taken from [31].

**Cross section model uncertainties** Figure 2.34 shows the systematic error on the neutrino appearance result. The largest systematic error on neutrino flux is sub-dominant using the near detector constraints. As for now, the higher systematic on the T2K appearance results comes from the uncertainties on cross section models. Since the CP violation search is provided through the appearance channel, the cross section uncertainty is the dominant error that reduces the T2K sensitivity to CP violation. Moreover, this systematic error will not be reduced by comparing neutrino and antineutrino, given the difference between the cross sections in these two modes. This conclusion motivates the measurement of the neutrino charged current quasi-elastic interaction that we will present in Chapter 5.


## Chapter 3

# Experimental study of light scattering in Super Kamiokande using single cone generator data

*La pensée n'est qu'un éclair au milieu d'une longue nuit, mais c'est cet éclair qui est tout.*

Henri Poincaré

### 3.1 Introduction

 IN the search of the  $\nu_e$  appearance in the T2K experiment, the particle identification in SK plays a major role in the  $\nu_\mu$  and  $\nu_e$  separation. This particle identification is based on the shape of the Cherenkov ring produced by ultra-relativistic particles in the SK water. More precisely, the identification is done using a likelihood of the “charge profile” created by particle Cherenkov light in the detector. The “charge profile” represents the charge deposition in the SK PMTs with the angle to the particle direction. The ring charge is therefore integrated through rotation over the particle direction. It has been observed in various samples, a charge deficit in the backward region of the detector for a simulated particle producing a Cherenkov radiation as compared to data. It corresponds to a region of the detector where most of the light is composed of reflected and scattered light. In this region, a 10% to 20% discrepancy can be observed in various samples, as the muons going through the detector (multi-GeV events), the muons stopped inside the tank (Sub-GeV events) and the decay electrons from  $\mu$  or charged  $\pi$  [58]. This charge deficit in the MC simulation can occur not only for very large angles with the particle direction, but also in angular regions close to the expected Cherenkov peak ( $\sim 42^\circ$ ). This difference will be taken into account in the T2K systematic error evaluation using different samples to evaluate the different background sources and comparing data and MC. For example, in the case of  $\nu_e$  intrinsic contamination, this difference between data and MC charges will be taken into account since atmospheric  $\nu_e$  data and MC will be compared to evaluate the systematic error. The same goes for the hybrid- $\pi^0$  sample, a data and MC based sample, that will be compared to an MC-MC based one to estimate the systematic errors related to the  $\pi^0$  background. In the present work, we will investigate the source of this discrepancy between MC and data in order to reduce the T2K systematic errors coming from this part of the SK simulation.

The SK detector is calibrated using a vast amount of calibration sources, which can be either light sources (*e.g.* Xe lamp, Autolaser and so on.) or physical events (*e.g.* through going  $\mu$ ...). Among them, the light sources have a photon flux extremely different from the physical events. In order to address the issues previously mentioned, we have developed and used a new multi-ring calibration source, the Cone Generator (CG). Compared to other calibration sources, the CG has the advantage to generate a ring shaped event anywhere and in any direction in the tank, as the Cherenkov light emitting particles do. We have to say here that this is not the original goal of this device, to help the reader to understand its shape. The CG has been originally designed to evaluate the  $\pi^0$  background systematic error. Since no pure  $\pi^0$  data sample exists, the CG was conceived to generate a  $\pi^0$ -like

event superimposing two light ring emitters that mimic the two photons from a  $\pi^0$  decay. However, the complicated simulation of this device and its imperfect reproduction of the time and charge deposition of a Cherenkov ring has prevented the CG from being used this way, much earlier than the beginning of this thesis work. We will show in this Chapter that this device can be used for another calibration goal: the study of the backward charge deficit in SK simulation.

In this Chapter, we will first describe the CG itself, and how the MC simulation for photons flux has been developed. We will then present a detailed data analysis based on single cone data taken in SK tank in September 2011. We will investigate the source of the charge discrepancy in the CG device and show it comes from combined improper simulation of the dark noise and light reflection on the tank walls in the SK simulation. We will finally study the CG ring charge characteristics in order to allow possible future improvements and applications.

As we have described the study presented here in a Super-Kamiokande internal note that is not available outside the collaboration, we have summarized the essential of this note in this chapter. In particular, this note contains a part of the work of Joao Pedro Athayde Marcondes de Andre. In particular, Joao Pedro Athayde Marcondes De Andre and Mine Shunichi have taken the data analyzed here both for the photon flux and in Super-Kamiokande. We would like to emphasize that the data taking procedures and MC development have been already detailed in [49] and are described here so the reader can understand the motivations of this work. The whole MC refinement and data analysis performed in Sections 3.3, 3.4, 3.5 and 3.6 are exclusive to this thesis work.

### 3.2 The CG vessel

The CG vessel is composed by a “delrin vessel”, which is built using delrin plastic, inside of which is placed a 5 cm diameter “diffuser ball” connected to an optical fiber. At the edge of the optical fiber inside the “diffuser ball” is placed a 10000 ppm MgO tip to increase light diffusion in the ball. The diffuser ball itself is doped with 1500 ppm of MgO. The other end of the optical fiber is connected to a laser diode. The data set we used in this thesis has been taken with a laser diode source with a wavelength of 405 nm (Scientex Co.)<sup>1</sup>. The schematic view of CG vessel is shown in Figure 3.1. A picture of the CG vessel is also shown in Figure 3.2.

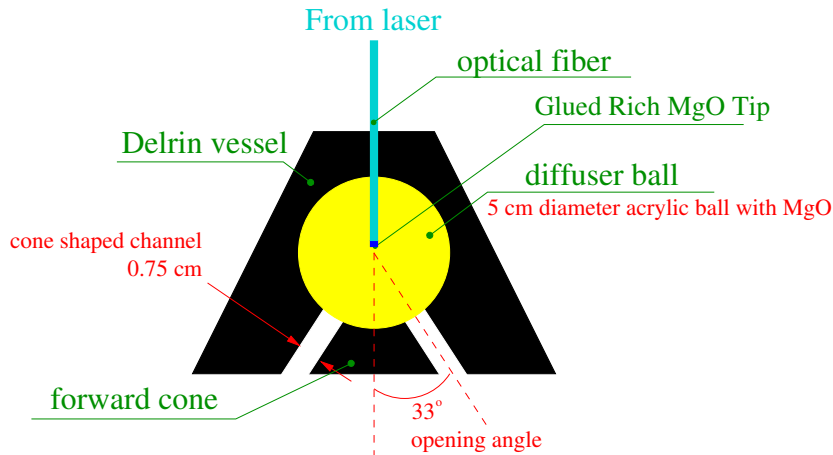


Figure 3.1: Schematic view of the CG vessel (sliced along the optical fiber direction).

Due to propagation in the optical fiber, and diffusion/reflection in the diffuser ball or cone shaped channel, the light loses the polarization it could have after leaving the laser diode. Thus, in our studies the light emitted by the CG is considered unpolarized, on the contrary to light composing true Cherenkov rings.

In an independent pre-measurement, the diffuser ball light intensity was verified to be symmetric by rotation around the fiber axis to a precision of the percent level.

<sup>1</sup>same as used for auto-laser data taking to monitor water quality in SK-IV.

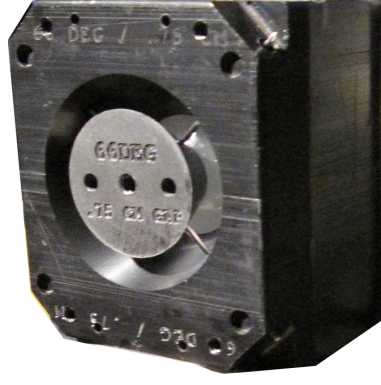


Figure 3.2: Front view of the CG vessel. The delrin vessel, the diffuser ball and the forward cone fixed to the delrin vessel with the metallic pins that are shown.

The delrin vessel is shaped to allow a cone of light to be emitted from the diffuser ball. By adding another part to the delrin vessel, called “forward cone”, the light from the CG vessel produces a ring on the surface to which it is projected, as can be seen in Figure 3.3.

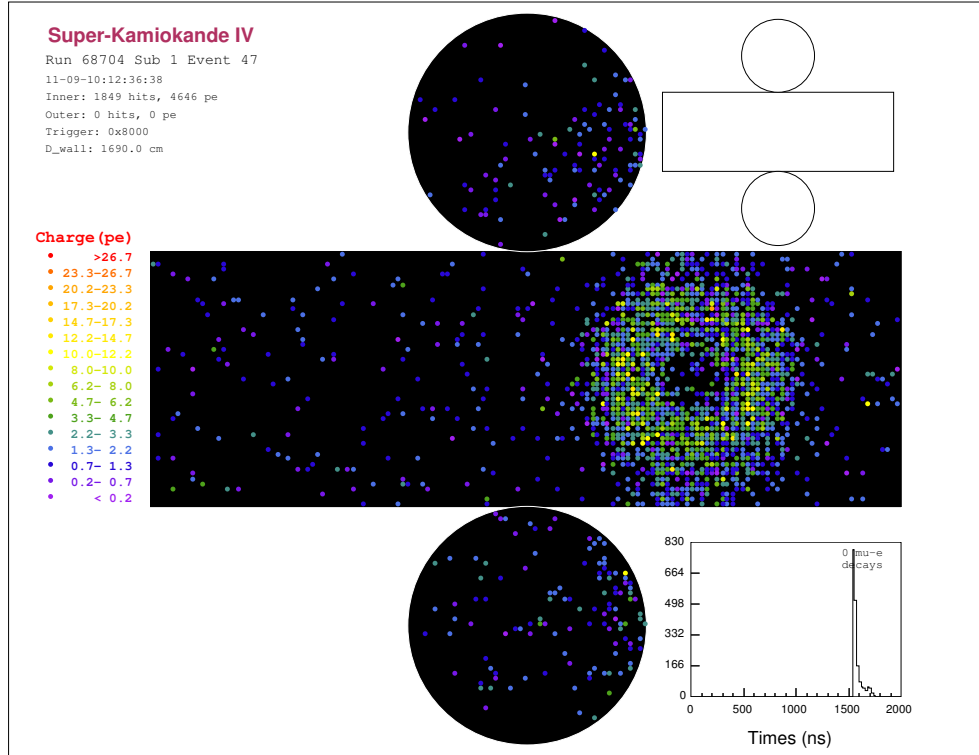


Figure 3.3: Event Display of the run 68704 (0m, -Y) in SK detector. Further details and descriptions of this event are given in section 3.4 .

The opening angle of the cone and width of the cone shaped channel, which are shown in red in Figure 3.1, are both determined by the dimensions of the delrin vessel and the forward cone. Even though several delrin vessels and forward cones with different dimensions were made, we chose to study one combination of delrin vessel and forward cone in more detail. The combination used has an opening angle of  $33^\circ$  and a width of the cone shaped channel of 0.75 cm as shown in Figure 3.1. This combination was imposed in this thesis to compare with the previous single cone data taken in July 2010. This leads to have a different opening angle than the e-like events, which produce a Cherenkov ring of about  $42^\circ$ .

### 3.3 The CG MC

#### 3.3.1 Principle

The CG is a rather complicated device. The photon flux highly depends on the characteristics of each of its components: laser light emission, propagation through optical fiber, scattering and reflection in the diffuser ball and so on. For this reason, we have constructed and developed an experimental setup to measure this photon flux. The CG MC was developed on the following basis:

- CG is treated as a spherical light source.
- We have measured the 3D photon flux on a sphere around the CG. This sphere is called virtual sphere and appears in Figure 3.4 as a  $(R) = 13$  cm radius sphere. This measurement has been performed using an independent experimental setup, called the “Photon flux measurement” setup that will be described in subsection 3.3.2.
- The measured photon flux is then inserted in the SK detector simulator (SKDETSIM tuned with water parameters from 2009/04) to propagate photons in the SK detector.

Given these principles and the “photon flux measurement” setup design, it means:

- No backward charge input to SKDETSIM.
- Un-polarized photon flux is assumed as input to SKDETSIM.
- Measurement error of photon flux is taken into account as shape error of charge profile of single cone MC events as described in Appendix A.

#### 3.3.2 Photon flux measurement

##### Setup description

The goal of this setup is to measure the photon flux emitted by the CG, that is, to measure the distribution of direction and position of the photons emitted by the CG vessel on the virtual sphere defined in Figure 3.4. We will first describe the overall setup before going into details on the mechanical part of the setup shown in Figure 3.5 and in Figure 3.6. From upstream to downstream, the setup is constituted of a 20 Hz NIM clock module connected to a 405 nm laser diode (Scientex Co.). For this study, we chose a 5 ns time width for laser signal, with an intensity of 100 mA. This time window was chosen maximal to increase the statistics during the photon flux measurement. In this study, we assumed the width of the time window does not impact anything but the intensity of the ring light pattern. This laser diode is connected with an optical fiber to the CG immersed in water as shown in Figure 3.5. Finally, a 1 inch PMT (Hamamatsu Co.) detects light emitted from the CG in a given angular configuration controlled by 3 motors linked to a CAMAC ADC module (Lecroy Co.) and controlled by a computer.

The photon flux measurement setup was designed to measure the intensity of the photon flux on a 13 cm virtual sphere surrounding the CG. Therefore, for this technical part, the PMT is mounted on a moving structure on top of the CG vessel inserted in a water tank filled with SK water. On the top of the water tank, we have mounted a 0.5 mm thick acrylic plate, the “collimator plate”, as shown in Figure 3.5. In the middle of this collimator plate, a 3 mm diameter hole, the collimator hole, is located at 13 cm of the CG vessel and used to define at which point of the virtual sphere we measure the distribution of the photon direction. The collimator hole was designed so that light from CG vessel escapes without reflection on its contour. Finally, on top of the acrylic plate, the PMT is mounted on a half arc structure located at 30 cm from the collimator hole to detect light emitted from CG vessel. For the measurement purpose, while the position of the photon flux on the virtual sphere is changed by rotating the CG vessel, the direction in which the photon flux is measured is changed by rotating the PMT. The position on the virtual sphere for which data is taken is given by the angle “CGV” (controlled by motor 2 in Figure 3.5), which corresponds to the  $\theta$  angle in Figure 3.4. In this study,

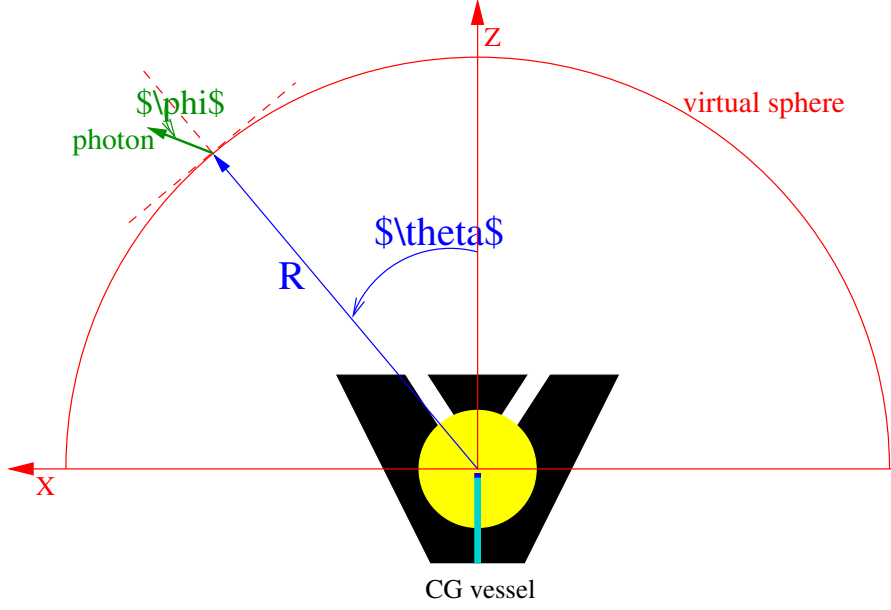


Figure 3.4: Scheme of the virtual sphere of radius  $R$  defined around the CG vessel (red). At each point of the virtual sphere (with position vector in blue) described by the angle  $\theta$  we measure the photon flux intensity at each photon direction (green) described by the angle  $\phi$ . In the current “photon flux measurement setup”  $R = 13$  cm,  $\theta$  corresponds to the CGV angle (defined in Figure 3.5) and we assume the virtual sphere is symmetric by rotation around the  $Z$  axis, and  $\phi$  corresponds to the (PMTV, PMTH) angles defined in the text. We also define the CGH angle, which defines the angle of the rotation around the  $Z$  axis for a point on the virtual sphere.

we assumed that the CG vessel and diffuser ball are symmetric by rotation around the  $Z$  axis and therefore, only one “CGV” angle is required to define a position on the virtual sphere. An additional study has been performed to check this symmetry and is presented in Section 3.6. The direction at which data is taken is given by the angles “PMTV” and “PMTH” (controlled respectively by motor 1 and 3 in Figure 3.5), which correspond to the decomposition of the  $\phi$  angle shown in Figure 3.4 as the projection of the direction on the  $R$  vector (“PMTV”) and the angle with respect to the plane perpendicular to the  $R$  vector direction (“PMTH”).

### Data taking

Each photon flux data taking consists of 2 different data sets that are measured at the same time. The so called “sequential data” is taken automatically by the DAQ for each PMTV and PMTH changing the CGV angle within the given range using a fixed step size, and then by changing automatically the PMTV angle within the given range and fixed step size. Each “sequential data” is taken at a fixed PMTH angle. Before and after each “sequential data” we measured the photon intensity at a given angle (CGV, PMTV, PMTH)=(34°, 0°, 0°) to control the time variation of the measured laser intensity. This data set is called “stability data”. The data set directly used to simulate the photon flux of the CG is the collection of the “sequential data” for all PMTH in the given range and step.

The photon flux intensity is measured for each given angle (CGV, PMTV, PMTH) during “sequential data” integrating over 100 laser flashes. The ADC distribution obtained is used to estimate the mean ADC value at the given angle which is proportional to the light intensity at the given angle once the ADC pedestal is subtracted. For example, the ADC distribution for (CGV, PMTV, PMTH)=(34°, 0°, 0°) taken during “sequential data” taking is shown in Figure 3.7. The ADC value is then converted to photo-electrons (p.e) using the difference between pedestal and first photo-electron peak values as shown in Figure 3.8. The same procedure is applied to measure the photon intensity of “stability data” however the ADC distribution is measured using 1000 pulses from the laser instead of 100 pulses as is the case for “sequential data”.

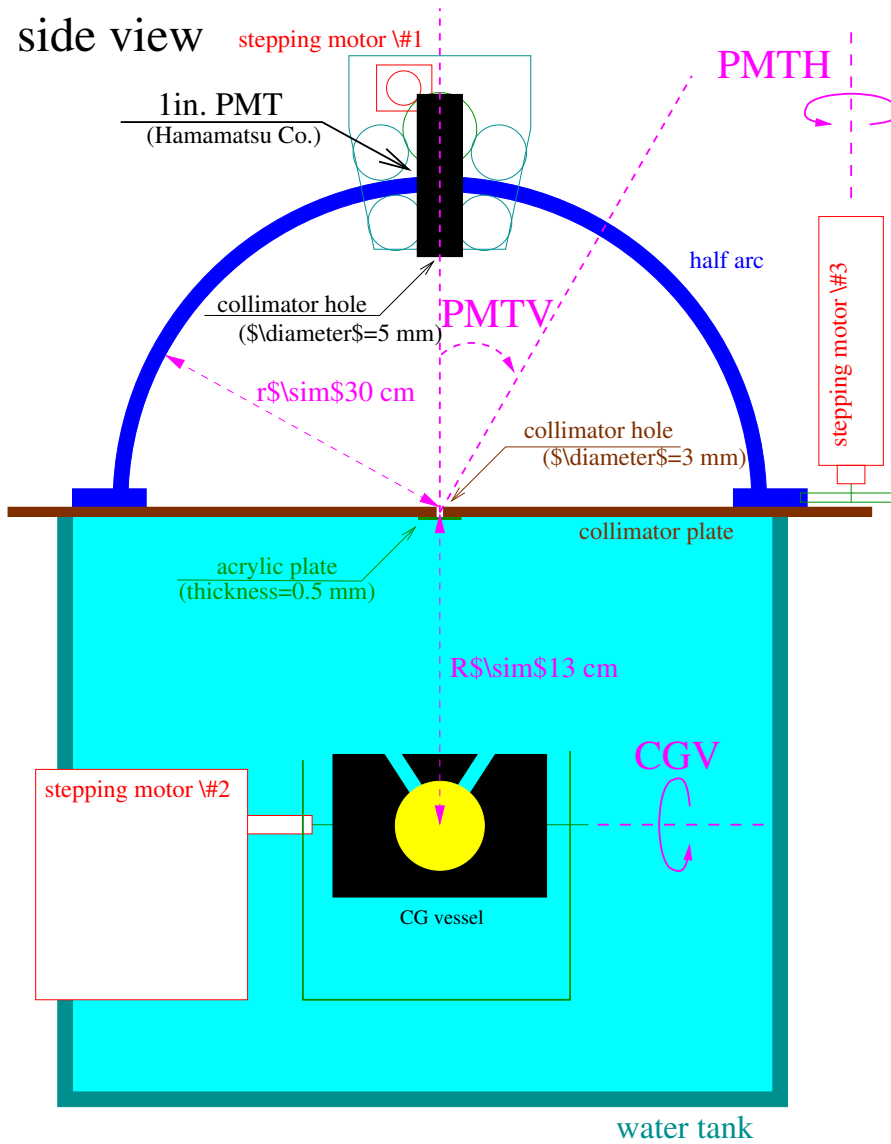


Figure 3.5: Side view of the “photon flux measurement setup”. The CG vessel is inserted in a water tank, here shown filled with water. The CG vessel is connected to the stepping motor #2. The rotation of the CG vessel using this motor defines the “CGV” angle as shown. Above the CG vessel is a collimator plate with a collimator hole aligned between the CG vessel and the PMT at the top of the half arc, as shown. Via the rotation of the stepping motor #1, the PMT is moved along the half arc as shown by the “PMTV” angle. Finally, the half arc itself is rotated using the stepping motor #3 around the vertical axis passing through the collimator hole in the collimator plane, as defined by the “PMTH” angle, here shown at the stepping motor axis.

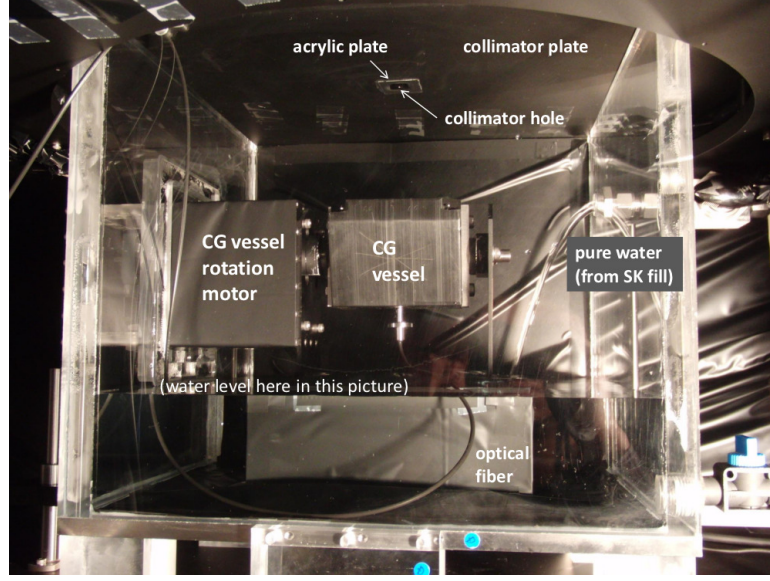


Figure 3.6: Picture of the Photon Flux setup measurement from under the acrylic plate. Therefore, the CG motor and the CGV vessel are clearly visible, as well as the connection to the optical fiber.

In this thesis, we have only used the data set taken in May 2011, and summarized in Table 3.1 with the corresponding configuration used for the “sequential data” taking. The difference of the photon flux data taken in May 2011 with respect to previous data is the addition of the water tank, to measure the photon flux of the CG under water (as it is the case when we insert the CG vessel in the SK tank). The water used to fill the water tank is the same as the water used to fill the SK tank.

For the May 2011 photon flux data taking, in addition to the usual “stability data” taken before and after each “sequential data” we also measured “stability data” in the day preceding our photon flux measurement and during the third day after we had finished taking “sequential data”. These measurements were performed to evaluate the stability of the observed intensity of the laser in a longer period of time in order to be more sensitive to the degradation of the quality of the water stored in the “water tank” of the setup. Finally, we highlight that we measured only  $CGV > 0^\circ$  in the data sets already mentioned, and will assume symmetries that will be described in subsection 3.3.3.

## Results

The charge distributions measured from data taken at different PMTH are shown in Figure 3.9. These charge pattern trends can be explained by geometrical considerations. As an example, we will focus on  $PMTH = 90^\circ$  and  $PMTH = 0^\circ$  profiles:

- For  $PMTH = 90^\circ$ , the CG and PMT move in the same plane, therefore a change in the PMT position is compensated by a change in the CG direction for the PMT to continue observing the same cone shaped channel from a different angle. It is expected a rather linear correlation between CGV and PMTV angles due to the difference in reflected and direct light flux intensities.

Table 3.1: Summary of date and configuration at which we have taken “photon flux data” in May 2011. In the table are shown the ranges and steps of the “CGV”, “PMTV” and “PMTH” angles at which the data were taken following the format : minimum value  $\rightarrow$  maximum value (step).

date	“sequential data” range (step) of			CG vessel in
	CGV	PMTV	PMTH	
05/2011	$0^\circ \rightarrow 66^\circ (2^\circ)$	$-24.3^\circ \rightarrow 24.3^\circ (1.35^\circ)$	$0^\circ \rightarrow 90^\circ (10^\circ)$	water

\* For these data sets, stability data was taken at  $CGV = 30^\circ$  and not  $CGV = 34^\circ$ .

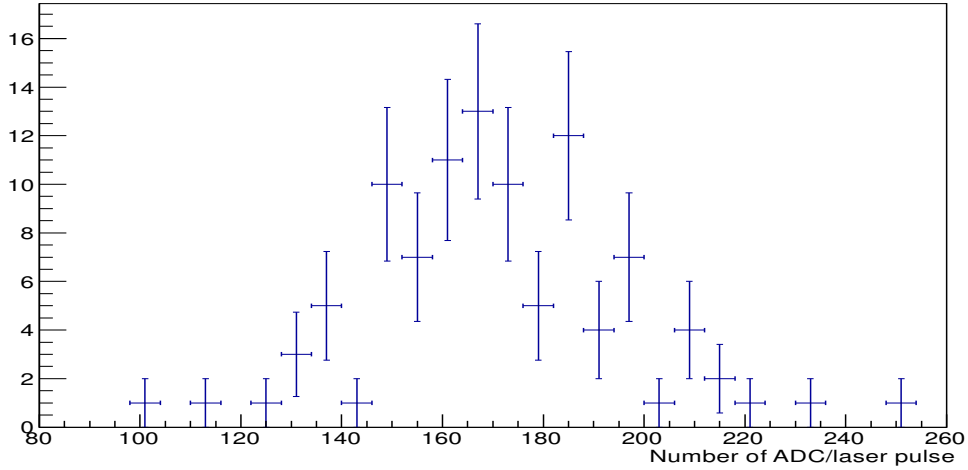


Figure 3.7: ADC distribution for angles  $(\text{CGV}, \text{PMTV}, \text{PMTH}) = (34^\circ, 0^\circ, 0^\circ)$  taken during “sequential data” taking. This configuration measures the light in the peak region of the CG ring. For several laser pulses, a Gaussian shape is expected.

- Since the PMT rotates in the plane perpendicular to the CG movement when  $\text{PMTH} = 0^\circ$  and the CG vessel is symmetric with respect to CG direction, we expect a PMTV symmetry in relation to  $\text{PMTV} = 0^\circ$ .
- Successive measurements of PMTV slices for  $\text{PMTH} = 0^\circ$  and increasing CGV are expected to measure different cuts of the charge distribution relative to the CG direction, with the maximum light flux intensity for direct light from the CG arriving at the PMT, creating a single spot centered around  $\text{PMTV} = 0^\circ$ . Above this region we do not expect any light to be observed given that the PMT would never be pointed towards the cone shaped channel of the CG vessel.

**Pedestal measurement** In addition to sequential and stability data, we have also taken pedestal data before the start of the data taking. The PMT is set at its initial position  $(\text{CGV}, \text{PMTV}, \text{PMTH}) = (0^\circ, 0^\circ, 0^\circ)$  and data are taken without any light emission from the laser diode, providing an independent sample to estimate the pedestal value. The results shown in Figure 3.10 gives a pedestal value about 45.0 ADC counts.

However, sequential data can also be used to perform such an estimate. In fact, from geometrical considerations we do not expect to have any direct light from the cone generator vessel arriving at several  $(\text{CGV}, \text{PMTV}, \text{PMTH})$  measured with the “sequential data”. This is the case for example for  $\text{CGV} = 66^\circ$  and  $\text{PMTV} < 0^\circ$  for any  $\text{PMTH}$ , or for  $\text{CGV} = 66^\circ$  and  $\text{PMTH} \leq 60^\circ$  for any  $\text{PMTV}$ . We have decided to use measurements at these angles to evaluate the time fluctuation of the pedestal measurement during sequential data taking. The result from this measurement shown in Figure 3.11 is that the pedestal value was constant during data taking with mean value of about 45.0 ADC counts. These data are within  $1\sigma$  agreement with data from the pedestal run, which confirms their reliability. We have also shown the time variation for different periods fitted by an order one polynomial on the left plot of Figure 3.12. We observe that the reduced  $\chi^2$  are nearly the same as for the constant fitting, and moreover, that the time variation is in  $1.25\sigma$  agreement with no time variation. Since this fitting is highly dependent on the the fitting start and end, we showed another period fitted by an order one polynomial on the right plot. We observed that the gradient of the curve is opposite, and in  $1\sigma$  agreement with the time independent pedestal assumption. Henceforth, we concluded that the previous  $1.25\sigma$  was only due to statistical fluctuations and the PMT pedestal has no significant time variations.

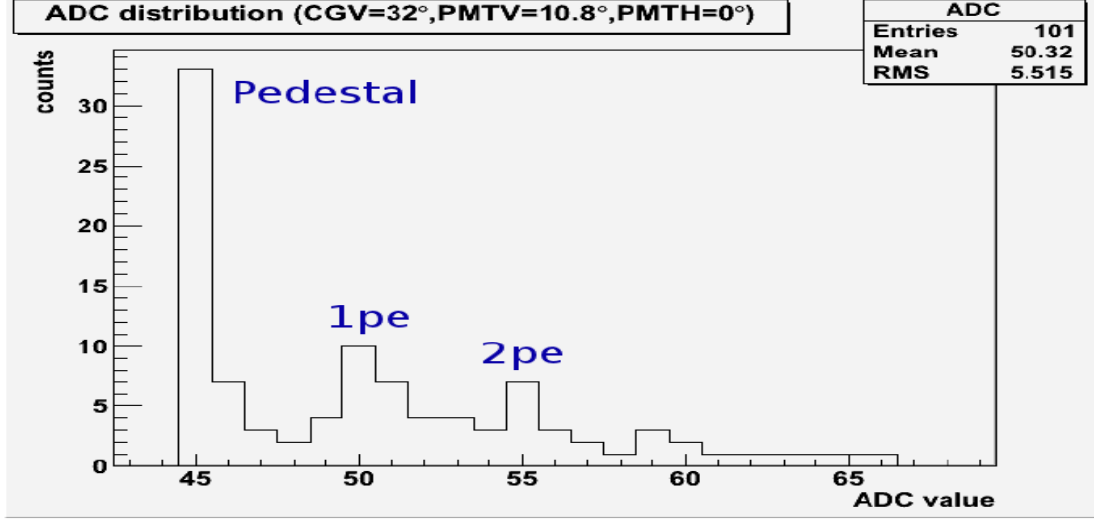


Figure 3.8: ADC distribution for a given angle (CGV, PMTV, PMTH)= (32°, 10.8°, 0°). We can clearly distinguish the pedestal value around 45 ADC counts, and the positions of the first and second photo-electron peaks.

**Laser intensity stability** Using the “stability data” the time dependence of the light intensity measured by the PMT is evaluated. In this measurement both the time variation of the intensity emitted by the laser diode and the time variation of the water quality in the water tank are taken into account. The result (in Figure 3.13) shows that the laser intensity was stable during all data taking and thus no time dependent laser intensity correction is needed.

**PMTV motor offset** Though the photon flux shape shown in Figure 3.9 correspond to our expectations, we observed no symmetry around PMTV=0°. This problem is due to a constant offset in the placement of the photomultiplier on the half-arc given by the position sensor. It is thus necessary to correct the value of the PMTV angle by a constant offset by assuming that the charge distribution at PMTH=0° is symmetric and measuring its offset from data taken by changing PMTV while CGV and PMTH are constant. For this measurement we have used data where we expect the 2 reflection peaks to be symmetric. Namely, we used the data taken with CGV=22° and PMTH=0° shown in Figure 3.14 where the measured PMTV offset is given by  $-0.9^\circ \pm 0.1^\circ(\text{syst})$  that is calculated by fitting a two Gaussian function given by (3.3.1) that is also shown in Figure 3.14. The fitted parameters in eq. (3.3.1) are a scaling constant ( $K$ ), the width of the peaks ( $\sigma_{\text{peak}}$ ) that is considered to be the same in both peaks, the position of the peak if they were symmetrical with respect to PMTV=0° ( $\mu_{\text{peak}}$ ) and the offset of this mean position with respect to the PMTV=0° position ( $\lambda_{\text{offset}}$ ).

$$\left\{ \exp \left[ -\frac{1}{2} \left( \frac{\text{PMTV} - \mu_{\text{peak}} - \lambda_{\text{offset}}}{\sigma_{\text{peak}}} \right)^2 \right] + \exp \left[ -\frac{1}{2} \left( \frac{\text{PMTV} + \mu_{\text{peak}} - \lambda_{\text{offset}}}{\sigma_{\text{peak}}} \right)^2 \right] \right\} \quad (3.3.1)$$

**CG vessel shift** During a last data taking, we fixed (PMTV, PMTH)=(0°, 0°) and changed CGV from -45° to +45°. On the contrary to all other samples, this “CGV offset sample” allows to measure the 2 light peaks, and therefore, a possible “CGV offset” if the profile is not symmetric around  $\text{CGV} = 0^\circ$ . To measure this, we use the same procedure as for the PMTV offset, and fit the distribution by a two Gaussian functions.

The results of this data taking which are presented in Figure 3.15 show that there is clearly an offset in the CGV angle measurement, of about  $-1.35^\circ$ . Moreover, the 2 peaks are not symmetric in shape. We will consider 2 possible origins of this offset:

1. A pure CGV motor offset (motor 2), as in the case of the PMTV motor (motor 1). In this case, the effect would lead to a constant shift in photon positions. This would lead to an increase of

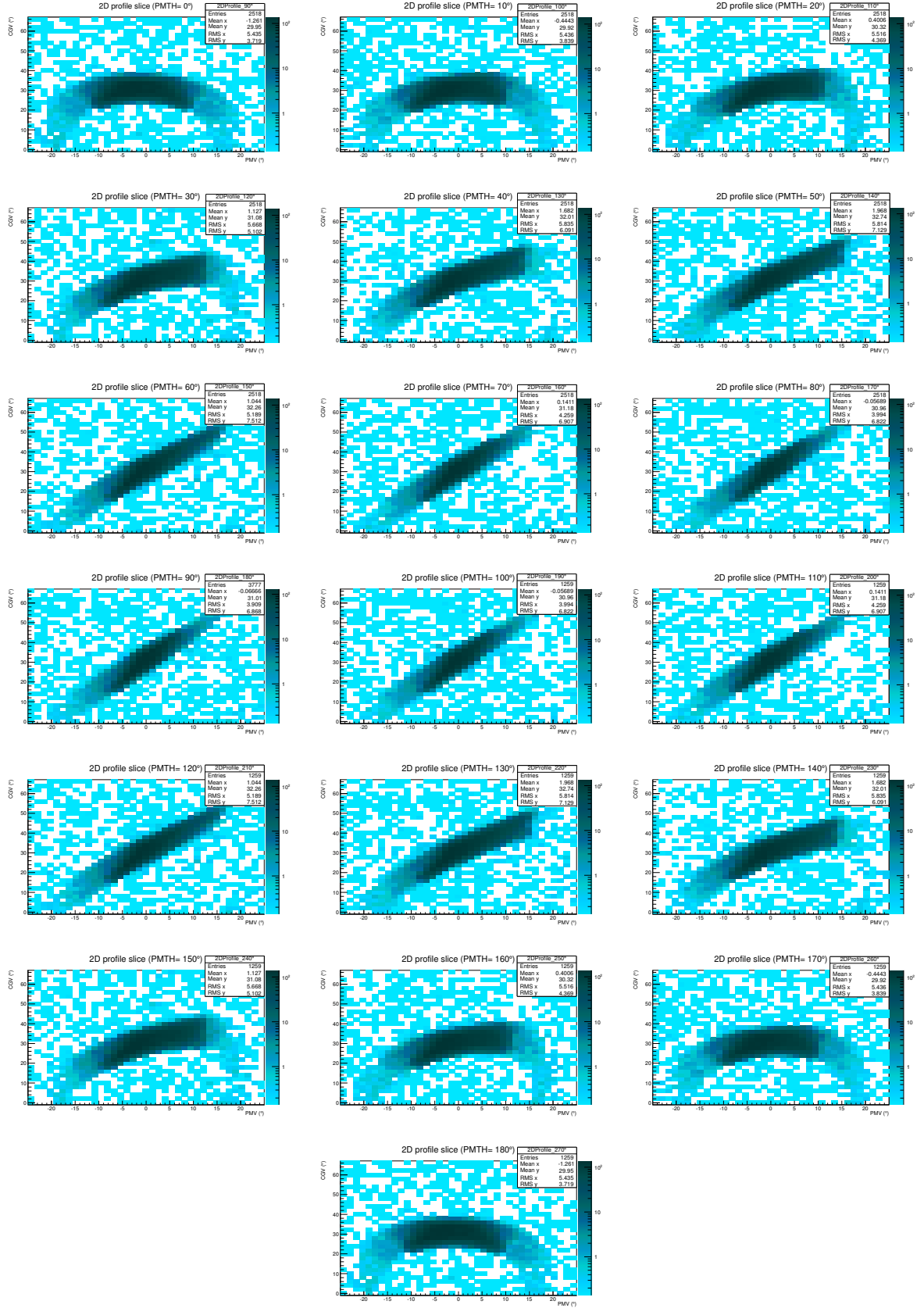


Figure 3.9: ADC measurements (pedestal subtracted) as function of CGV and PMTV for different PMTH.

the MC opening angle.

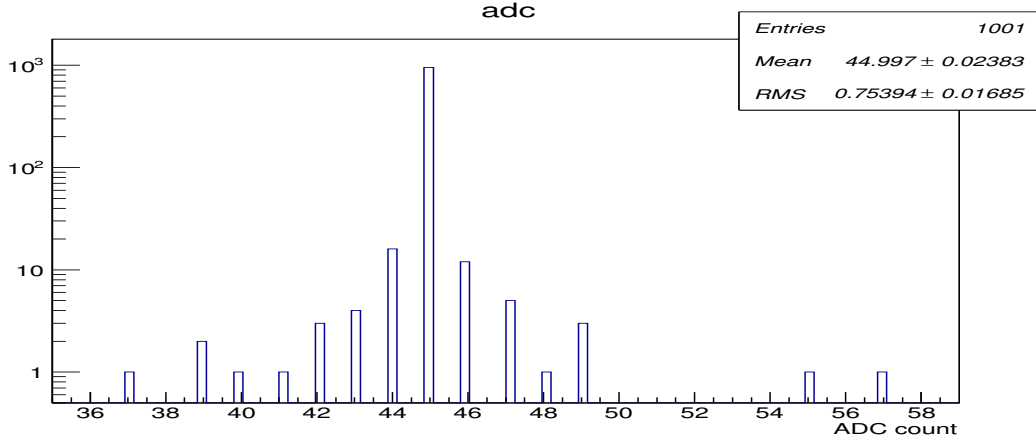


Figure 3.10:

Pedestal value in ADC count for the “pedestal run data” in logarithmic scale. The average pedestal value is about 45.0 ADC counts.

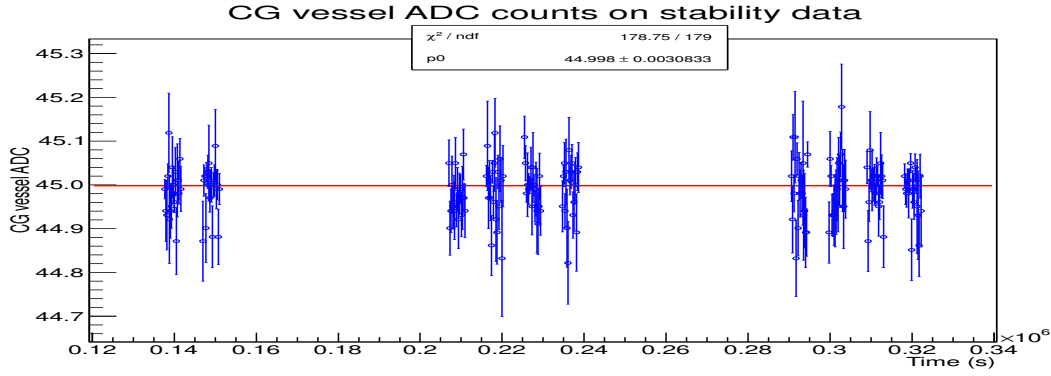


Figure 3.11: Time stability of the measurement of the PMT pedestal using “sequential data” for a (CGV, PMTV, PMTH) region where no direct light from the CG vessel is expected.

2. The CG is misaligned with the collimator hole/PMT setup (see Figure 3.5). In fact, the CG has been removed and replaced before the different data taking, which increases the probability of a misalignment. The offset measured would correspond to a 3.1 mm shift of the CG with the collimator hole/PMT. Though it also creates a constant shift in the photon position, it also impacts directly on direction. In fact, such a shift would favor the higher angle and in that sense, would contribute to artificially widen the photon distribution.

On the contrary to the PMTV motor offset, no CGV motor offset was observed during the data taking. From this, we conclude that the most likely source for this CGV offset was a shift of the CG parallel to the CGV moving plane.

**Corrections** The photon flux data is taken with water filled up to the collimator hole, where a thin acrylic layer is put to ensure the water surface is flat. It is therefore necessary to correct the measured photon intensity for each angle set to take into account the refraction of light between the water-acrylic and the acrylic-air surfaces.

The first effect to be corrected is the difference between the angle at which the photon was emitted and measured, which changes due to the refraction in the interface between the air, the acrylic and the water, and which is described by the Snell-Descartes law. This law links the incident angle of the photon ( $\text{PMTV}_{\text{inc}}$ ) to the refraction index of the mediums and to the refracted angle ( $\text{PMTV}_{\text{ref}}$ ) measured by the setup. The Snell-Descartes law used for this correction is given by the equation (3.3.2), where we note that the passage of the photons through the acrylic layer does not affect the relation between the angle of the photon in water in relation to the angle of the photon in the air.

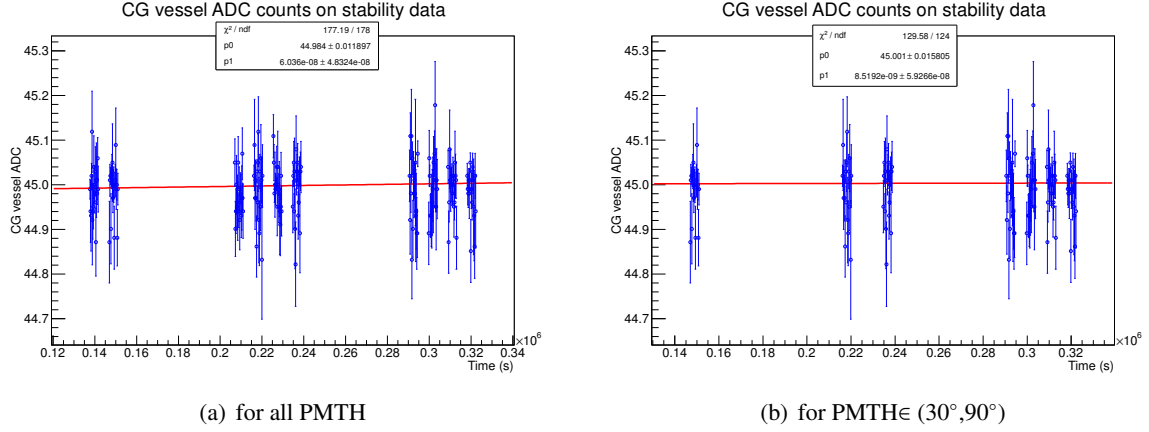


Figure 3.12: Linear fit of the PMT pedestal variation in time using “sequential data” for a (CGV, PMTV, PMTH) region where no direct light from the CG vessel is expected.

$$PMTV_{\text{inc}} = \arcsin\left(\frac{n_{\text{water}}}{n_{\text{air}}} \sin PMTV_{\text{ref}}\right) \quad (3.3.2)$$

The second effect to be corrected is the difference in the refraction probability as a function of the angle at each surface. The refraction probability is described by the Fresnel equations, where the probability is described as a function of the photon polarization, incident angle and refraction coefficient of the mediums. For each angle we need to correct the observed photon flux intensity by how much light passed through the water-acrylic and acrylic-air interfaces. At each interface, for unpolarized light, the correction of the light intensity given by Fresnel equation is shown in equation (3.3.3), where  $I_b$  is the light intensity before the light reaches the surface,  $I_a$  is the light intensity after light goes through the surface,  $\theta_i$  is the incident angle at the interface and  $\theta_r$  is the refracted angle.

$$I_b = I_a \left( 1 - \frac{1}{2} \left[ \left( \frac{\sin(\theta_r - \theta_i)}{\sin(\theta_r + \theta_i)} \right)^2 + \left( \frac{\tan(\theta_r - \theta_i)}{\tan(\theta_r + \theta_i)} \right)^2 \right] \right)^{-1} \quad (3.3.3)$$

At the acrylic-air interface,  $I_a$  is the light intensity measured by the PMT<sup>2</sup> and the  $\theta_r$  angle is given by the measured PMTV (after PMTV offset correction). The  $\theta_i$  is calculated from the  $\theta_r$  and the refraction index of air and the acrylic via Snell-Descartes law. The intensity of light inside the acrylic, given by  $I_b$ , will be called  $I^{acr}$  and the incident angle  $\theta_i$  will be called  $\theta^{acr}$  for the next step of the corrections.

At the acrylic-water interface,  $I_a$  is the light intensity inside the acrylic layer given by  $I^{acr}$  previously calculated and the refracted angle  $\theta_r$  is given by  $\theta^{acr}$ . The incident angle  $\theta_i$  is again calculated by the Snell-Descartes law. The light intensity inside the water  $I_b$  is what is considered to be the light intensity measured by the photon flux at a given angle after the all corrections.

Finally, we added a correction due to the collimator hole apparent surface, which depends on the PMTV incident angle. Assuming  $I_c$  and  $I_i$  are respectively the corrected and PMT collected intensities, this correction is purely geometric and calculated as:

$$I_c = \frac{I_i}{|\cos(PMTV)|} \quad (3.3.4)$$

After all the corrections described in this subsection are applied, the photon flux data is used to generate a photon distribution used as input for the SKDETSM simulation that is described in the next subsection.

<sup>2</sup>The light intensity is given by the (ADC - pedestal) mean value.

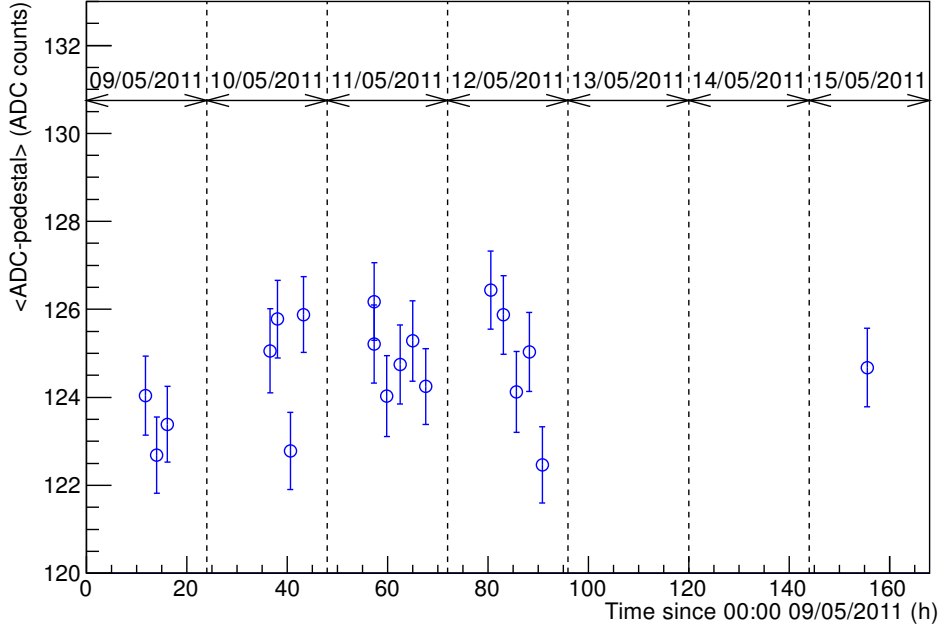


Figure 3.13: ADC counts value with constant pedestal subtracted for “stability data” as a function of time. We only consider “sequential data” on the 10<sup>th</sup>, 11<sup>th</sup> and 12<sup>th</sup> of May 2011, however we have left the laser diode turned on with water in the water tank for a longer time (one day before and three days after the “sequential measurements” were completed) in order to better estimate the time stability of the system. The average laser intensity for stability data is about 124.6 ADC counts.

### 3.3.3 Using photon flux data to generate the photon distribution input for SKDETSIM

As explained previously, the photon flux data consists of the measurement of light intensity from the CG vessel at several different positions and directions given by (CGV, PMTV, PMTH). We should note that the photon flux data provides a relative measurement of the light intensity from the CG vessel. Therefore the normalization of the number of photons emitted by the CG per event needs to be done by tuning the total charge observed in the simulation with respect to the mean total charge of data taken at SK. This adjustment is performed to have better than 1% agreement between data and MC.

The light intensity distribution as a function of the position and direction of the photon from the CG vessel is obtained by interpolating the photon flux data measured at several different positions and directions. The interpolated function is then normalized and transformed into a probability density function used as input for SKDETSIM. This is done assuming different symmetries: the photon position has been measured only for one region of the CG ring, i.e, only one CGH (see legend of Figure 3.4). We assume the ring to be symmetric under CGH variations. Moreover, we only took the photons direction for  $\text{PMTH} \in [0^\circ, 90^\circ]$ , and so, we assume a symmetry to deduce the photons direction in the remaining region  $\text{PMTH} \in [90^\circ, 180^\circ]$ .

We could not directly perform an interpolation in all photon flux data since three-dimensional interpolations are not available in C++ libraries. We have therefore decided to separately obtain a distribution of position of the photons and the distribution of the direction of the photons for each position. The distribution of the position of the photons was obtained by interpolating the photon flux data taken for different CGV, integrated for all PMTV and PMTH taking into account the solid angle each (PMTV, PMTH) set represents. The distribution of the direction of the photons for each position was obtained by interpolating the two-dimensional (PMTV, PMTH) distribution for the given position. We have also taken into account the difference in the solid angle represented by each (CGV, PMTV, PMTH) bin to correctly estimate the photon flux distribution.

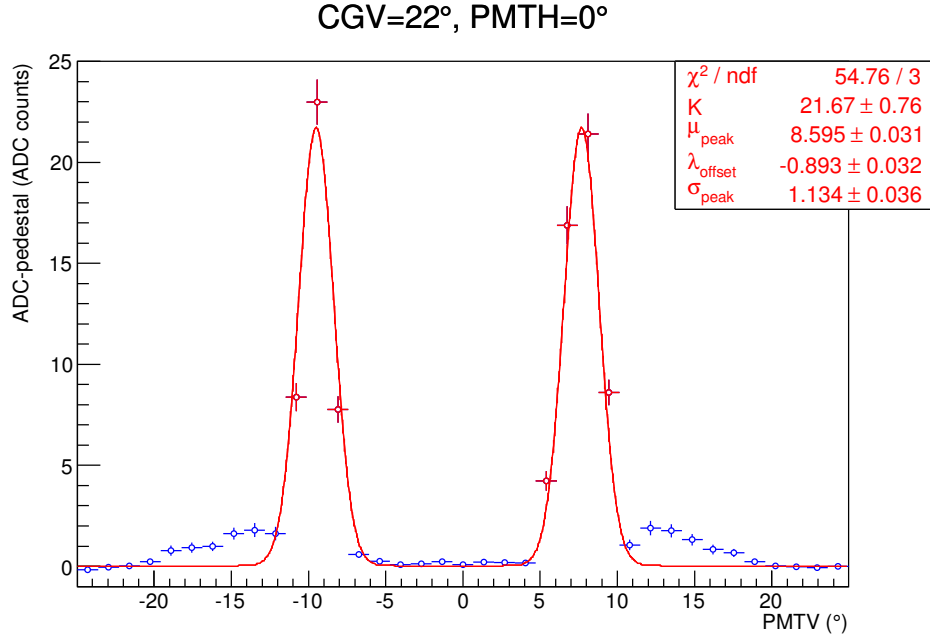


Figure 3.14: Number of ADC counts with pedestal subtracted, measured as a function of PMTV for PMTH=0° and CGV=22° (red and blue points). In red are shown the PMTV values for which we expect to measure mainly direct light from the CG vessel, while in blue are shown the remaining measured points. This distribution is used to calculate the PMTV offset by fitting equation (3.3.1) (red curve) using the points shown in red. The fitted parameters are shown on the top right of the Figure with fit errors.

## 3.4 Data Taking in SK

### 3.4.1 Description of the setup inserted in SK and the data taking

In order to take data in SK using the single CG vessel, a pole system is used to place the vessel at the desired position and direction inside the SK detector. The pole system is composed by 10 separate poles of 2 meters each which allow the placement of the CG vessel at 10 different Z positions along the vertical axis inside the detector, separated by 2 meters from one another. The lowest position we can place the CG vessel is near the center of the detector in the vertical direction ( $Z=0$  m in SK coordinates). At the end of the pole system, the CG vessel is screwed to a horizontal plate. It is also possible to attach a second CG vessel at the back of this horizontal plate even though no data was taken using this configuration. Below this plate, a “Locator vessel” is placed under a U-shaped structure. Figure 3.16 shows the end of the pole system with the CG vessel and the “Locator vessel” installed.

In table 3.3 is shown a summary of the single cone data taking from June 2011, and used here. The data presented here consists of a set of 4 different directions (+y, +x, -y, -x) at 3 different heights in the SK tank: +8m, 0m, +16m. For a given height, we rotate the CG around the pole system center anti-clockwise in the successive 4 different directions, and then rotate it clockwise back to its initial position to avoid twisting the optical fiber. This last position is used to check data reproducibility after having rotated the pole system. Then, the laser is shut down, and the CG altitude is changed. After having checked direction alignment, the same procedure is applied at +8m, +0m and +16m in the tank. Finally, a last data set was taken at +8m in the +y direction, to check data reproducibility after the change in heights and the shutdown of the laser diode. For each run, we choose the laser power supply intensity to be 100 mA and the signal time window as 5 ns to be closer to the time width of an electron electromagnetic shower.

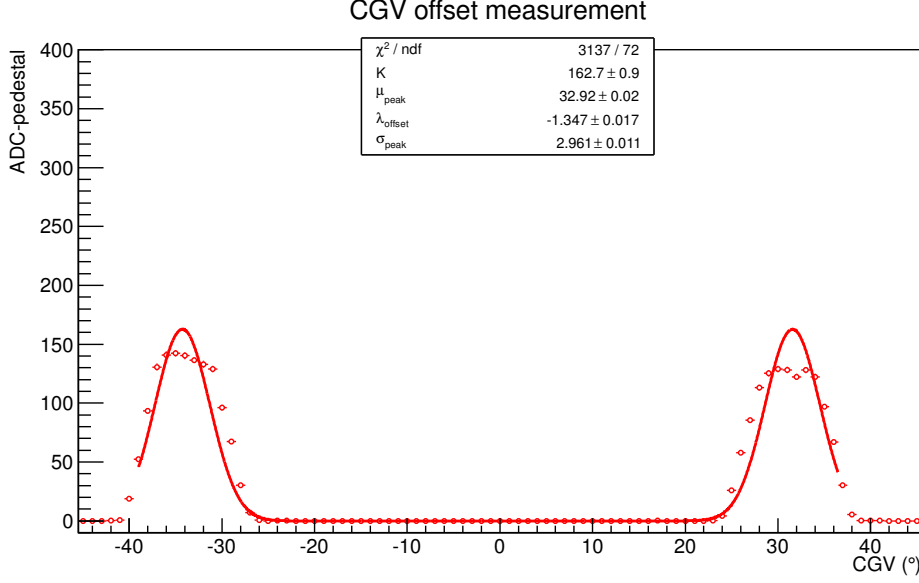


Figure 3.15: Charge distribution for “CGV Offset Data” taken with PMTV=0°

### 3.4.2 Measurement of the CG vessel position and direction in SK

The pole system was designed to place precisely the vessel inside the SK detector. However, it is necessary to measure the position and direction of the CG in the SK tank. In fact, due to mechanical design, the position and direction evaluated only with the pole system would lead to bias and errors too large to use the cone generator as it was originally thought ( $\pi^0$  systematic error evaluation). Therefore, we have performed position and direction measurements using the “Locator vessel”.

The “Locator vessel” used for the “Locator data taking” is a delrin vessel similar to the CG vessel. However, instead of having a cone shaped opening for the light, it has five cylindrical holes at the four vertical surfaces and at the bottom of the vessel. Data taken using this vessel is used to measure the position and direction of the CG vessel inside the SK detector. The optical fiber is inserted on the top of the “Locator vessel” by the hole situated in the top face of the cube. The Locator generates 4 laser spots in the barrel and one spot at the bottom of the tank shown in Figure 3.17. By measuring the center of each spot in the barrel and assuming that the two lines drawn from the center of opposite spots cross at the position of the “Locator vessel” (as shown on Figure 3.18), we can determine the position of the Locator and then of the CG given that the relative position between the CG vessel and the Locator vessel is known.

Up to now, we did not have to use the information of the timing distribution to measure the position and direction of the “Locator vessel” because we consider the current method gives a sufficient precision.

Furthermore the Z coordinate of the “Locator vessel” position is determined by the pole system itself as even a large shift ( $\sim 1$  m) of the “Locator vessel” in the XY plane would correspond to a  $\sim 3$  cm shift in the Z position<sup>3</sup>, whereas the maximum XY shift measured amounts to only 15 cm.

We have calculated the center of each spot for the “Locator data” taken in run 68676. The distribution of each Locator spot is shown in Figure 3.19 where we have fitted a Gaussian function to the peak of each distribution to obtain the parameters shown in table 3.2.

Using the measured mean position for each spot we have calculated the position of the Locator as the crossing point of the lines  $\overline{L_{+x}L_{-x}}$ ,  $\overline{L_{+y}L_{-y}}$  and  $\overline{L_{+z}L_{-z}}$ . Note that the  $L_{+z}$  point is the “calibration hole” that corresponds to the upper end of the pole system. Therefore, we have used 3 combinations of 2 spot lines. For each combination, a vertex is reconstructed, which leads to 3 different vertices. In this way, this setup is used to give an estimation of the systematic error on the Locator position. Indeed,

<sup>3</sup>This shift was calculated assuming the connection between poles of the pole system is rigid: the pole system is equivalent to a single pole which is not deformable. Even though this is not exactly true, it is a reasonable approximation of the pole system used.

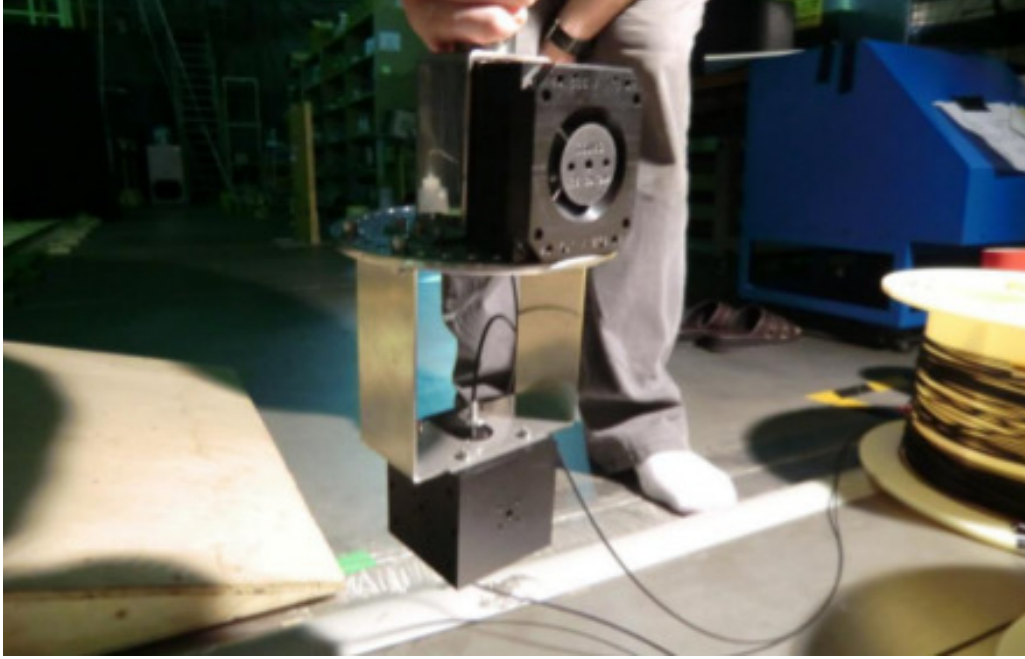


Figure 3.16: Picture of the equipment used to lower the CG vessel and Locator vessel into SK. The poles from the pole system are connected to the disk plate supporting the CG vessel. A “U” shaped metal plate to which the locator is screwed is attached below the disk. This picture was taken before inserting the CG for the 2011 data taking at SK.

Table 3.2: Fit results used to obtain the center of each Locator spot (see Figure 3.19). The uncertainties quoted here are given by the fitting procedure and therefore could be underestimated given the quality of the fits shown in Figure 3.19.

Name	Constant (pe)	Mean (°)	Sigma (°)
$L_{+x}$	$38.052 \pm 0.031$	$-1.865 \pm 0.009$	$8.638 \pm 0.015$
$L_{+y}$	$30.838 \pm 0.028$	$89.667 \pm 0.010$	$9.023 \pm 0.018$
$L_{-x}$	$35.729 \pm 0.029$	$183.247 \pm 0.008$	$8.933 \pm 0.013$
$L_{-y}$	$35.849 \pm 0.031$	$-88.305 \pm 0.008$	$8.011 \pm 0.013$

it contains an estimation of the error due to a twist or a non vertical pole system, or non-centered holes in the locator setup, or asymmetric light directions. In fact, we’ll keep the mean position of these 3 vertices as the position, and the difference between the vertex and this position is taken as the systematic error.

In table 3.4, we can verify if there is any particular shift in the pole system direction, due to the pole bars floatability or natural bending. Therefore, we compared the calibration hole position with the A5 spot position and finally, with the reconstructed vertex estimated by Locator. It reveals a shift of the A5 spot towards  $+90^\circ$  from the CG direction, particularly at  $+8$  m and  $+0$  m. Given the shift appears suddenly at  $+8$  m, we can deduce that it is likely to be a bent pole bar that creates such an effect rather than floatability, because of the constant direction shift and very good reproducibility. A misalignment of locator holes is unlikely, because it would imply the  $+16$  m data to be the most shifted. In this way, the only remaining hypothesis is a bending of some pole bars between  $+16$  m and  $+8$  m. However, this bending effect on the reconstructed vertex is taken into account in our systematic error estimation.

As for the CG direction estimation, we decided to use the direction between the reconstructed vertex and the Locator spot emitted in the direction of CG ring. We used the uncertainty on the vertex position to estimate the uncertainty on the reconstructed direction. By construction, there is a full correlation of these two errors. Finally, we deduce the CG vertex by measuring explicitly its

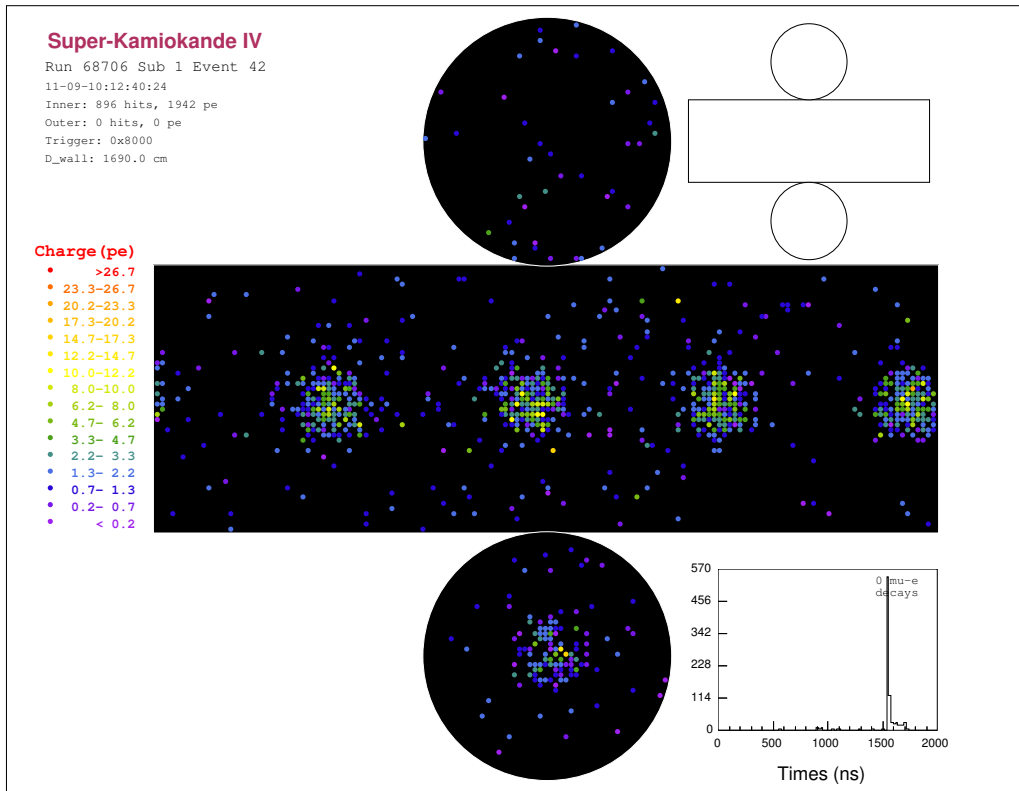


Figure 3.17: Event display of a locator event in SK.

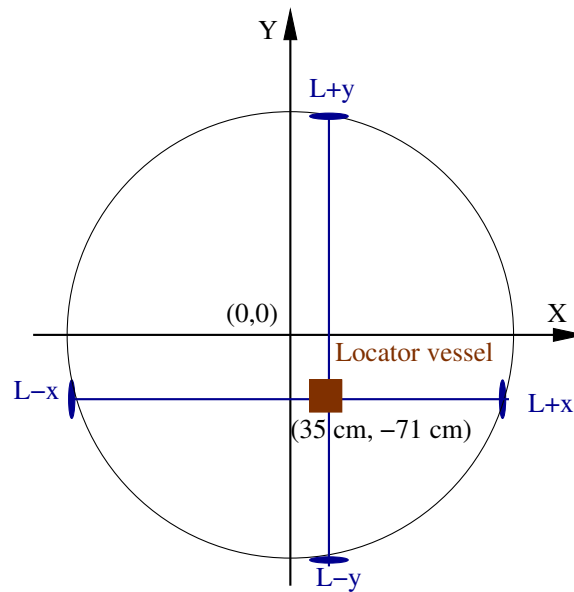


Figure 3.18: Schema of the Locator vessel data taking with the four spots produced on the wall of the SK tank. Note that this schema is not to scale.

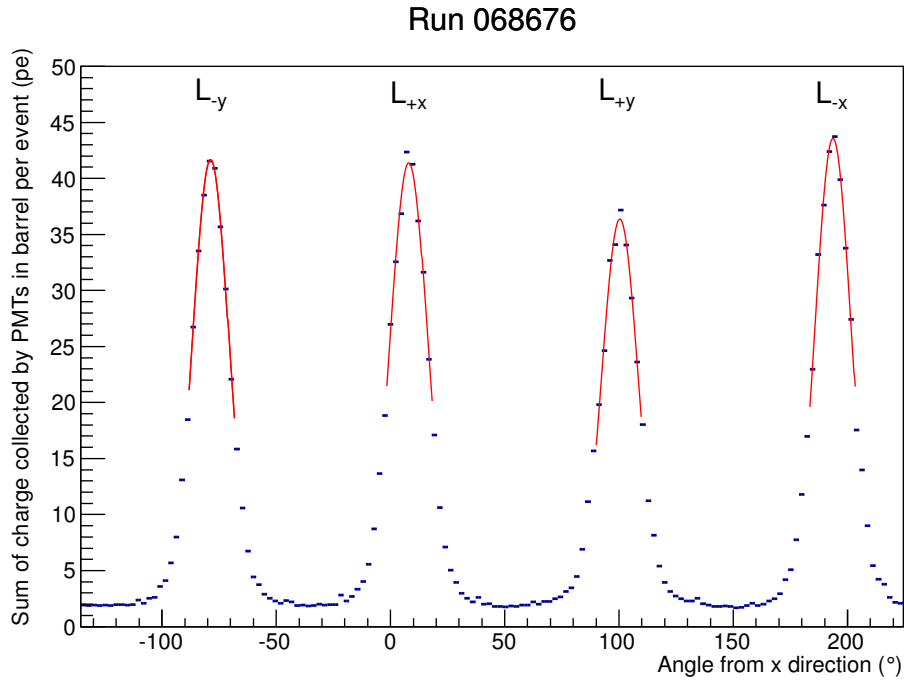


Figure 3.19: Distribution of the integrated charge on a column of PMTs on the SK barrel as a function of the angle of the PMTs from the  $x$  direction measured from the center of the SK tank for run 68676. Each spot shown in the Figure 3.18 is identified here. In red are shown the fits performed to the peak of each spot to measure its center. We fitted a Gaussian function to each spot peak to avoid having to take into account the effects of scattering in the water of the SK tank, reflection at the SK tank wall and dark noise of SK PMTs. This Locator run corresponds to a CG run towards  $+y$  direction. Because setup position in the tank is shifted toward  $-y$  value, and because of absorption, we expect the  $+y$  spot to have the minimum and the  $-y$  to have the maximum intensities.

Table 3.3: Measured position and direction of the Locator vessel using the Locator data for the studied single cone data runs. The position and direction of the CG are obtained from the position and direction of the Locator through measurements of the experimental apparatus geometry made before inserting it inside the SK tank.

Single cone data Run	Nominal Altitude and Direction	Run of Locator data	(X,Y) vertex measured with Locator data (cm)	Angle between the Locator spots expected and measured position (°)
68674	(8 m, +Y)	68676	(25.6±5.1, -68.8±1.1)	0.51±0.17
68678	(8 m, +X)	68680	(38.5±2.6, -70.4±7.1)	0.88±0.25
68684	(8 m, -Y)	68684	(36.9±4.7, -84.6±5.0)	1.17±0.17
68686	(8 m, -X)	68688	(24.6±5.1, -82.9±0.2)	1.29±0.12
68690	(8 m, +Y)	68692	(24.3±4.0, -69.7±1.8)	1.27±0.13
68696	(0 m, +Y)	68698	(22.9±2.3, -66.7±1.8)	10.65±0.08
68700	(0 m, +X)	68702	(36.5±1.2, -66.7±4.3)	10.65±0.14
68704	(0 m, -Y)	68706	(36.7±6.7, -80.9±2.3)	10.60±0.25
68708	(0 m, -X)	68710	(22.3±5.2, -79.1±5.3)	11.62±0.21
68712	(0 m, +Y)	68714	(22.0±0.8, -65.4±3.1)	11.71±0.16
68718	(16 m, +Y)	68720	(29.5±3.3, -64.9±2.3)	-3.95±0.11
68722	(16 m, +X)	68724	(37.9±4.2, -68.8±2.9)	-3.23±0.11
68726	(16 m, -Y)	68728	(34.9±1.6, -78.4±3.3)	-3.42±0.06
68730	(16 m, -X)	68732	(24.7±1.5, -74.4±1.8)	-3.11±0.06
68734	(16 m, +Y)	68736	(28.3±3.3, -64.7±2.3)	-3.30±0.11
68739	(8 m, +Y)	68741	(25.6±5.3, -69.0±0.8)	0.60±0.17

distance between locator and CG diffuser ball. Given the accuracy of such a measurement (1 mm), we decided not to add any systematic error and to use the locator vertex error as the only error on the CG vertex. For the CG direction, we simply keep the locator one and use its systematic error as the CG direction systematic error. The result from the measurement of the position and direction of the Locator taking into account the estimated systematic errors due to vertex position and direction reconstructions are presented in table 3.3.

From “Locator data” analysis, we can conclude that positions measured are consistent for different data sets that are taken with the same conditions. Besides, for runs that have been taken at the same nominal direction and altitudes, the angle from the nominal direction is within 1° from each other, which corresponds to the precision of the tool used to set the direction of the pole system.

### 3.5 Single cone data analysis

In this Section, we first present the analysis method we apply to investigate some of the Super-Kamiokande detector properties. In particular, we test the Super-Kamiokande detector circular and height uniformity. We finally investigate the backward charge anomaly.

#### 3.5.1 Basic analysis method

In previous sections, we presented CG MC and data samples. In this section, we used the charge profile comparison between CG data and CG MC to understand the SK detector. Charge profile represents the charge of events, that is proportional to the amount of light detected by the PMTs, as a function of the angle from the CG direction. Therefore, for a given angle around the CG direction, all light emitted at this angle is integrated around the CG direction and represents only one bin value in the charge profile. For this study, the value shown is not the light measured event by event, but the averaged light measurements over all events taken in data samples or generated in the MC.

For this comparison, charge profile systematic errors from data and MC are evaluated in Appendix A. Significant differences between data and MC beyond shape errors are used to study SK detector.

In Section 3.5.2, we will first present a comparison between MC and a typical CG data run to estimate  $\frac{MC}{Data}$  differences. This result has been used to study SK detector dependence on vertical

Table 3.4: Position of the Bottom Locator Spot (A5). To check alignment, it has to be compared with the calibration hole (35.3 cm, -70.7 cm)

Run Number	Altitude	Nominal Direction	A5 spot (X, Y) in cm
68696	0 m	+Y	(11.0, -75.9)
68700	0 m	+X	(30.1, -57.0)
68704	0 m	-Y	(47.8, -74.7)
68708	0 m	-X	(31.1, -92.7)
68712	0 m	+Y	(12.3, -75.8)
68674	8 m	+Y	(-6.6, -76.2)
68678	8 m	+X	(22.6, -50.3)
68682	8 m	-Y	(52.3, -81.5)
68686	8 m	-X	(25.6, -104.4)
68690	8 m	+Y	(-6.8, -77)
68718	16 m	+Y	(-27.2, -80.2)
68739	8 m	+Y	(-6.8, -77.8)

vertex or horizontal directions of the CG. Finally, the differences between CG data and MC observed in Section 3.5.2 have been studied in Section 3.5.3.

In all this section, CG MC events are generated using vertex and directions measured by the locator setup described in Section 3.4. As explained in section 3.3.3, normalization of MC is adjusted on data by changing the number of photons in MC so that the charge profile integral agrees with data better than 1%.

### 3.5.2 Vertical vertex and horizontal directional dependence of charge profile comparison between data and MC

#### Typical Charge Profile Comparison

The results for a typical run are shown in Figure 3.20. In the main peak region (from  $15^\circ$  to  $55^\circ$ ), the agreement between data and MC is within the 4% shape error in most of the bins. However, the data peak shape tends to be larger than the MC one, but within the systematic error. The most propable source is a mechanical shift between the CG and the locator directions which is described in Section 3.6 and associated systematic error is evaluated in Appendix A. In fact, integrating light of the charge profile around a direction which is not the center tends naturally to increase the charge profile width.

Moreover, out of the peak region, and mainly in the backward region (*i.e* from  $100^\circ$  to  $180^\circ$ ), our MC reflection tuning is affected by the modification of Rayleigh scattering. In one word, the Rayleigh scattering represents the scattering of light on punctual and dipolar molecules. This happens mainly on the water molecules. The scattered light is emitted in similar proportions forward and back of the incident photon direction. This can be seen since the electric field of the incident photon is exactly the same whether it is “observed” from the front or the back. One understands that it is not the case in the transverse plane due to polarization. On the contrary, the Mie scattering occurs on larger molecules compared to the wavelength, and produces an asymmetric scattering which is mainly in the incident light direction. It mainly occurs on the large molecules of impurities in the Super-Kamiokande tank. The two different types of scattering are summarized in Figure 3.21. One understands that the Rayleigh scattering will mostly affect the backward region, while the Mie scattering will mainly affect this region for reflected light on the black-sheet.

Consequently, we expected MC to be lower than data in the backward and front regions, which contain relatively more reflected light. In fact, we defined the backward region as angles  $> 90.3^\circ$ , based on the study from the photon flux measurement, where we observed no light at maximal angles ( $CGV = 66^\circ$  and  $PMTV = 24.3^\circ$ ). Note that, considering the distance from CG to SK wall ( $\sim 15$  m)

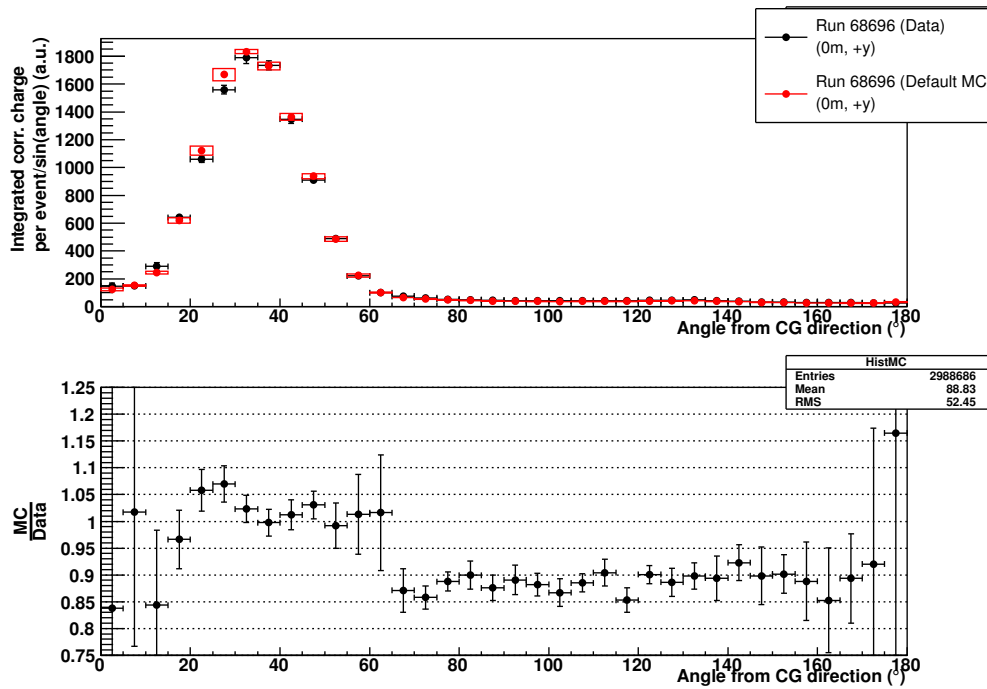


Figure 3.20: Comparison of the data and MC for a typical run at  $z = 0$  m

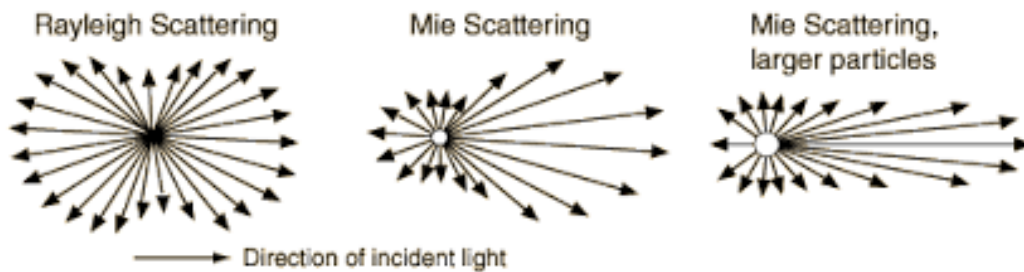


Figure 3.21: The Rayleigh and Mie scattering of light in a material depending on the incident light direction. Taken from <http://hyperphysics.phy-astr.gsu.edu/hbase/atmos/blusky.html>

Table 3.5: Summary of MC deficit compared to Data in backward region ( $100^\circ - 180^\circ$ ). This correspond to  $1 - \frac{MC}{Data}$  for different runs.

	68674	68696	686700	68704	68708	68718
MC deficit in backward region	11.0%	11.5%	9.6%	8.8%	10.7%	10.7%

relatively to the virtual sphere radius ( $R = 13$  cm), we can consider the virtual sphere as pointlike. In this backward region, using all bins, we measure a difference between Data and MC equal 11.5% for this run. Results for other runs are summarized in Table 3.5. These results are compatible with observations that have been made in other data samples, such as stopping or through going muons. Though differences with CG are expected, these samples show a deficit between 20% and 10 % in the backward region, confirming results obtained with the CG in Figure 3.20. This indicates a common source of discrepancy between the different channels. We used the CG for a dedicated study on this issue, as presented in section 3.5.3.

### Vertical vertex dependence

The September 2011 CG data sample contains different Z vertex positions, as described in Table 3.3. Therefore, we used these relative differences between data samples to study the SK detector vertical vertex dependence. Because the SK detector is not invariant with Z translations, we used the  $\frac{MC}{Data}$  ratio for this study, rather than a pure data to data comparison. The data and MC ratio for different Z vertex is shown in Figure 3.22. We observe that the peak shape for a vertex at 16 m is different from the two other Z vertices, which should be caused mainly by the high impact of position and direction uncertainty due to the closeness of the cylinder top. Moreover, the MC peak position seems to be shifted to the right of the data. This is a hint that the error on the mechanical shift is not perfectly estimated (or may not be constant between runs) and that a data sample to evaluate this effect should be taken separately in the future (we developed this point in Section 3.7). The front region does not present such a discrepancy, as the different runs are in agreement within the error bars. In the out-of-peak region, the difference between 16 m and other heights it is not statistically significant ( $< 2\sigma$  but very localized), and probably due to geometrical causes (closeness of the top of the tank) since it seems that there is no particular pattern emerging gradually from +8 m to +16 m.

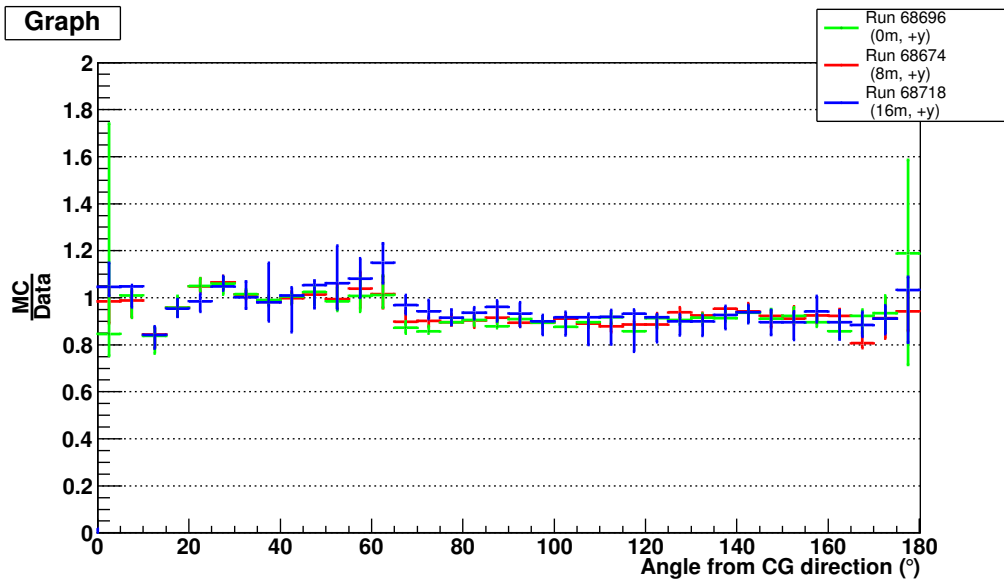


Figure 3.22: Charge Profile ratios  $\frac{MC}{Data}$  for Data sets at different z vertex positions

To quantitatively evaluate the detector uniformity, we focus on the backward region. In fact, this region is most sensitive to detector aspects (light absorption in water, scattering, reflection on the

black sheet or PMTs, etc.) since light in this region is scattered or/and reflected on SK walls. To set a coherent estimator, we consider all bins in the backward region and use their correlation to determine the detector uniformity. To have a safe estimation, we use run 68696 (0 m) as a default run and compare it with runs 68674 (8 m) and 68718 (16 m) which cover all studied altitudes. Applying this criterion, we estimate the p-value and found an agreement between these runs in the backward region to be 42% and 83% p-values, which clearly confirms the qualitative results.

### Horizontal direction dependence

As shown in Table 3.3, September 2011 data samples also contain runs for several horizontal directions. We used these samples to check the SK detector uniformity with direction, with an identical approach as explained in Section 3.5.2. On Figure 3.23, we show the direct  $\frac{MC}{Data}$  ratio. The charge profile agreement between MC and data seems to be uniform between the 4 directions at 0 m within the systematic errors which confirms the SK detector uniformity with direction.

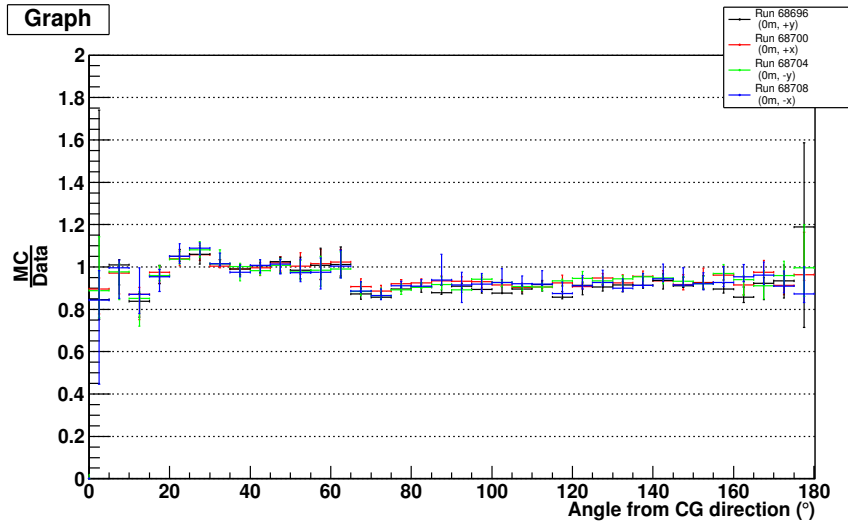


Figure 3.23: Charge Profile ratios  $\frac{MC}{Data}$  for Data sets in different horizontal directions

### 3.5.3 Study of the disagreement between data and MC in the charge profile comparison

In Section 3.5.1, we observed a nearly constant disagreement of 10% between data and MC in the backward regions for different heights and different directions. In this section, we try to study possible sources such as dark noise tuning or reflection on SK PMTs and black sheet. At first, default MC SKDETSIM is known to have a bias because of some errors in the simulation of Rayleigh scattering. These errors affect the tuning of various parameters, including PMT and black sheet reflection parameters, which have precisely been tuned in a new MC production. Therefore, as a first step, we proposed to study the impact of this new MC production on charge profiles differences between Data and MC. In a second step, we used timing distribution of charge in the SK detector to separate effects from reflection, scattering or dark noise. An example of such a timing distribution is displayed in Figure 3.24 for run 68696 (0m, +y direction). It shows that, though MC and data charges are in agreement during CG light detection (1000-1300 ns time window), a charge discrepancy tends to appear in the time region where no CG light is emitted. More explicitly, before and after CG light emission, MC seems constantly lower than data. Since the charge profiles are drawn by integrating light on the whole time period, such a difference between data and MC may lead to important discrepancies in these profiles.

### New version of SKDETSIM implementation

As compared to default MC, only PMT and black sheet reflection coefficients have been tuned in this version after Rayleigh scattering correction. A comparison between data and this new MC version

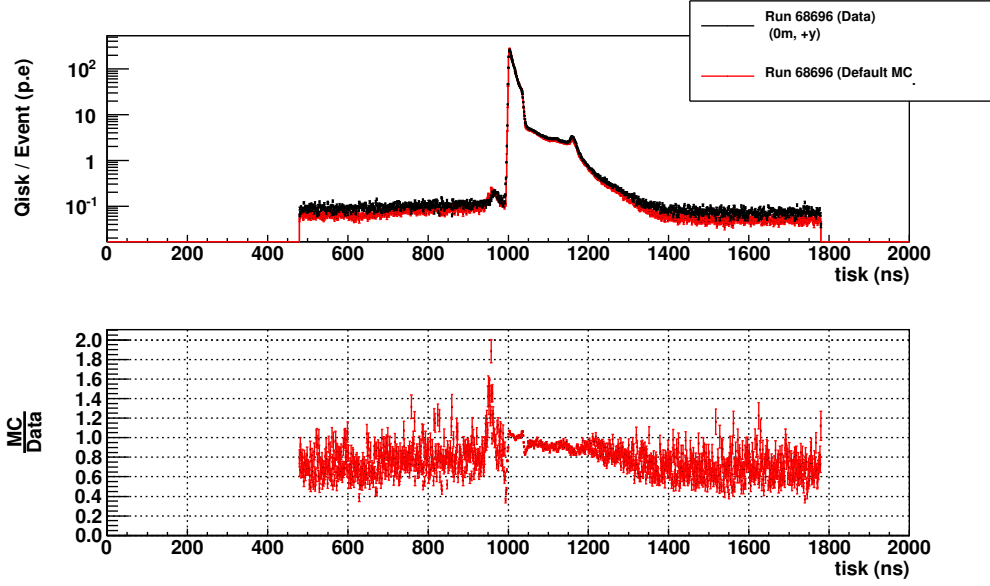


Figure 3.24: Data and MC charge Distributions with time for run 68696. The time “Tisk” represented on the horizontal axis is set as a 1300 ns time window around the event trigger

is displayed in Figure 3.25. Though small changes appear out of the peak region, particularly from  $70^\circ$  to  $180^\circ$  from CG direction, they never exceed 2 % in each bin (removing first and last bins which are widely affects by detector geometry and statistics). More precisely, in the backward region of run 68696 (0m, +y direction), the  $\frac{MC}{Data}$  disagreement is reduced from 11.5% to 11.1%. Therefore, PMT and black sheet reflection tuning of the new version of SKDETSIM cannot explain the observed MC/Data discrepancy.

### Dark noise study

**Dark noise rate and charge distribution** Considering Figure 3.24, MC seems constantly lower than data when no CG light is emitted. If this discrepancy is due to dark noise tuning, we expect to have less light in this region for the MC simulation than for data. However, since the overall CG MC charge is tuned on data (see Section 3.3.3), this absolute effect is removed and only relative effects remain. Therefore, isotropic charge from dark noise has more impact on backward region than peak region, because of the small amount of CG light in the first compared to the last one. This effect can be observed in Figure 3.20. In this way, dark noise charge distribution seems a likely hypothesis to explain such a disagreement. However, such a difference could be either due to dark noise rate, or to the dark noise charge distribution itself. To study this in more details, we zoomed in time window from 500ns to 800ns in Figure 3.24. The result is visible in Figure 3.26 and clearly confirms a relative disagreement of 31.1% between Data and MC. For obvious reasons, this region will be called “off-time” region, while the time region where the CG event occurs (here 1000-1300 ns time window) will be named “on-time” region from now on.

**Dark noise rate** To decorrelate the two contributions from dark noise rate and charge, we use as a variable the number of PMTs hit. In fact, the total number of hits during the PMT charge integration time (300 ns) is negligible as compared to the total number of PMTs. Hence, we can assume that the situation where several dark noise hits occur in the same PMT during charge accumulation is highly unlikely. Therefore, the dark noise rate can be considered as directly proportional to the number of PMTs hit in the “off-time” region. We can observe in Figure 3.27 that the timing distribution of the number of PMTs hit seems in better agreement between data and MC than the charge distribution with time. A zoom in on the “off-time” region (see Figure 3.28) clearly shows that the disagreement between MC and Data only amounts to 5.4%. Therefore, we can conclude that the dark noise rate

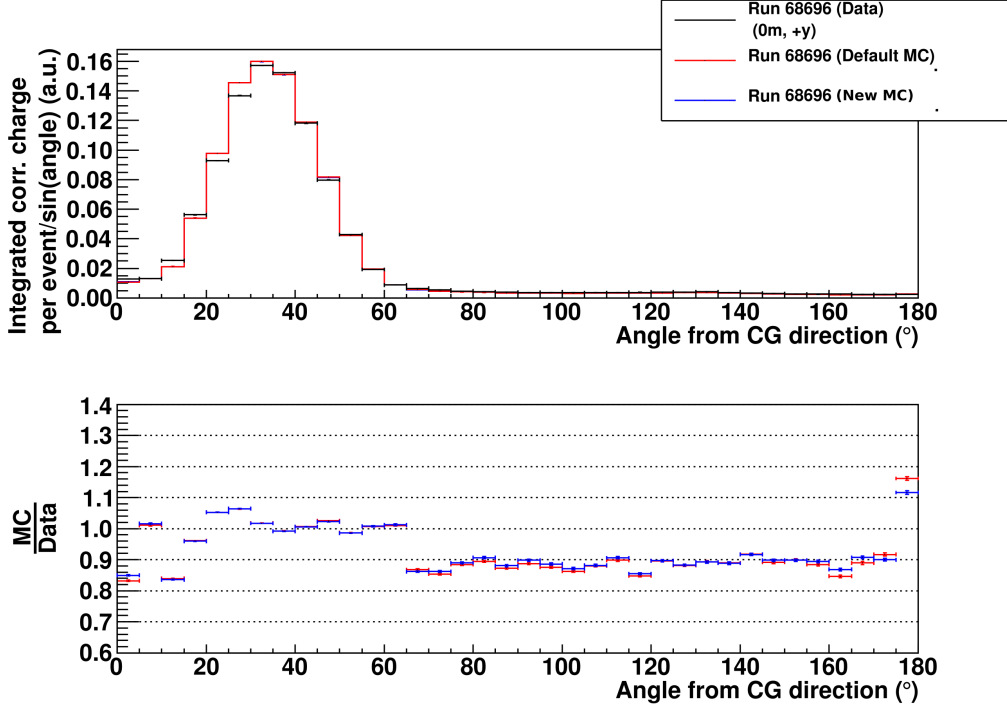


Figure 3.25: Charge Profile comparison between data, default MC and new MC version where PMT and black sheet reflection coefficients has been tuned after Rayleigh scattering correction.

is reasonably well tuned and cannot explain the 31.1% magnitude of the charge discrepancy between CG data and MC.

**Dark noise charge distribution** The second possible source of discrepancy comes from the charge distribution of dark noise in SK. In SKDETSIM, the 1 photo-electron distribution has been tuned using “Nickel” data. The Nickel source consists of a Californium source ( $^{252}\text{Cf}$ ) surrounded by Nickel  $^{58}\text{Ni}$  powder mixed into plastic. Spontaneous fission of  $^{252}\text{Cf}$  emits neutrons from 2-14.2 MeV which thermalize before being absorbed by  $^{58}\text{Ni}$  and forming an excited state of  $^{59}\text{Ni}$ . Gammas emitted by deexcitation of this nucleus have a 9.0 MeV energy and are used to calibrate the 1 p.e peak because of their very low energy. More details on this setup are given in [59]. In this section, we use the CG to study whether using its “on-time” data set to generate the photo-electron peak distribution still holds for the dark noise.

Because of different time and charge distribution, “on-time” distribution of Nickel data is different from the one for CG. We will use the CG for a similar study to evaluate quantitatively the charge distribution in “on-time” and “off-time” regions. However, CG direct light certainly does not follow a 1 p.e distribution because of its high intensity. Nevertheless, most of the PMTs out of the cone region only receive scattered and reflected light, which should present a rough 1 p.e profile. In addition, we will study the “off-time” regions which should not be affected by differences between Nickel and CG data.

Considering definition of “off/on-time” regions for CG we introduced before, we have generated charge distribution corresponding to these two regions. On the left part of Figure 3.29, we can observe a shift of the 1 p.e value for data compared to MC in “on-time” region. This effect is expected because an increase of the SK PMT gain has been measured on a large time period in [59], with an average increasing of 1% per year. This affects the MC tuning which has not been done simultaneously with data taking, but with April 2009 data). Considering the gain increase between April 2009 (data used in MC tuning) and September 2011 (CG data taking), we expect roughly a 2.5% increase in data for the 1 p.e position as compared to MC.

As a very raw check of consistency, we can measure the 1 p.e position for this sample of CG data. As displayed in Figure 3.30, we have fitted the distribution by a Gaussian function around the peak

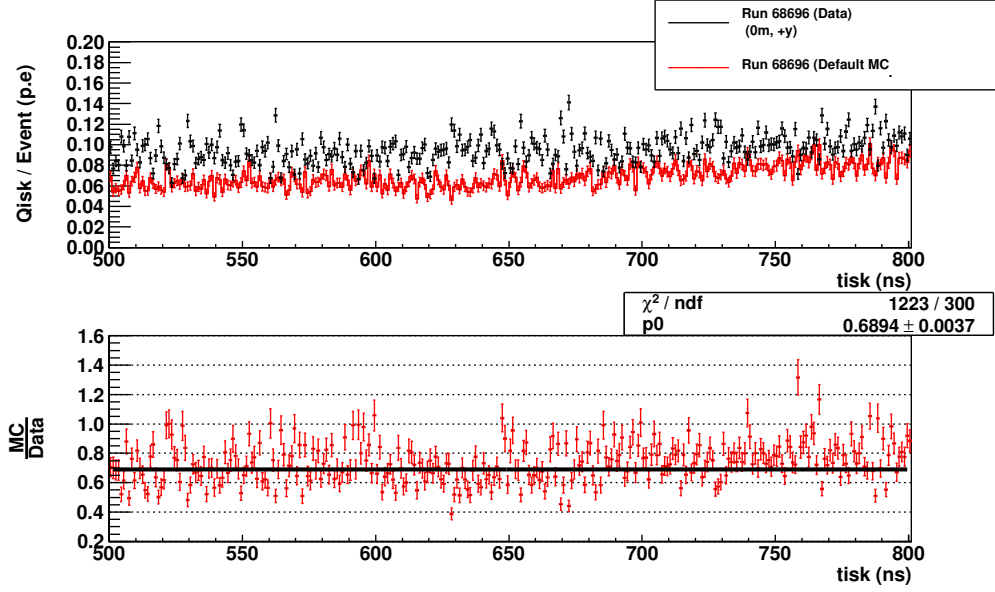


Figure 3.26: Data and MC charge Distributions with time for run 68696 in the 500-800 ns region. The ratio  $\frac{MC}{Data}$  is fitted with a constant to estimate the differences in charge between MC and Data.

Table 3.6: Results of expected discrepancy between data and MC dark noise rate and charge.

	Number of Hits	Charge Distribution Mean	Total Charge	$\frac{TotalChargeData - TotalChargeMC}{TotalChargeData}$
Data	$45841 \pm 214$ Hits	$1.79 \pm 0.01$ p.e	$82055 \pm 384$ p.e	$27.0 \pm 0.7\%$
MC	$44363 \pm 211$ Hits	$1.35 \pm 0.01$ p.e	$59890 \pm 527$ p.e	

and measured the difference between MC and Data as  $= 3.1 \pm 0.4(stat.)\%$ . We have not considered here systematic errors arising from the choice of time window or other systematic error as scattering, reflection on PMT or black sheet. Moreover, the 2.5% variation in gain we expect arises from a rough analysis of the average PMT gain increase per year. However, the 1 p.e higher peak value for data than MC measured by this fit is compatible with the rough 2.5% expectations, confirming CG sensitivity to the PMT gain increasing and consistency of the CG sample with other data sets.

As for the “off-time” region, MC and data charge distribution shapes are clearly different. It confirms that “on-time” Nickel data distribution upon which CG MC dark noise is tuned does not represent exact dark noise charge distribution. Let us remark that a global scaling of the charge by 31% does not reproduce the data at all. Moreover in Figure 3.29-right, the mean value of data “off-time” distribution seems considerably higher than MC, because of numerous hits with a high charge. We checked that these hits could not be direct light hits arising at such a time because of charge accumulation during 300 ns. In fact, we can use the 1500-1700 ns region to get rid of any possible direct light component, and observe in Figure 3.31 a similar discrepancy.

In order to compare quantitatively this difference between MC and data, we calculate the expected total charge difference in the detector. While the number of entries of each of these distributions shows the number of hits in SK, the mean value of these distributions corresponds to the mean charge of a data and MC dark noise hit. To take into account all the charge differences, we multiply the charge of a dark noise hit by the number of hits. Having already observed that the rate is well tuned enough, we expect most of the discrepancies coming from the mean charge of a hit (*i.e* distribution mean).

Considering Table 3.6 results, we conclude that the  $\frac{MC}{Data}$  difference due to total dark noise charge is 27.0%. Considering that the number of dark noise hits is underestimated by 5.4%, and assuming a 4 – 4.5% change in PMT gain over time, we see that the dark noise charge distribution explains quite well the 31.1% differences between MC and Data charge in the “off-time” region.

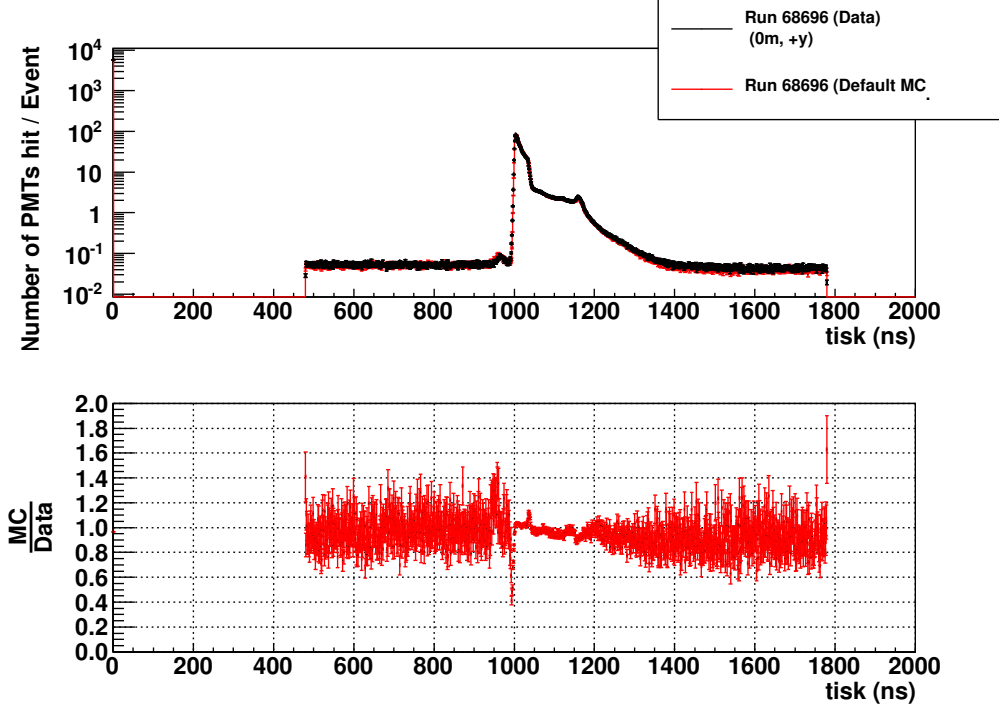


Figure 3.27: Number of PMTs hit with time in Data and MC for run 68696

**Impact on MC** In order to check this result, and to measure impacts on the charge profile study, we have generated a MC changing only dark noise charge by 31.1%. At first, we have checked the timing distribution (Figure 3.32), which is now in a better agreement in the overall region than before this tuning (Figure 3.24). On the bottom plot of Figure 3.32, the  $\frac{MC}{Data}$  ratio in the “off-time region” is shown, and has changed from 68.9% in Figure 3.24 to 98.8%.

We have also checked impacts of such a discrepancy on the charge profile comparison. Figure 3.33 clearly shows an improvement in the agreement between MC and Data in most of the individual bins backward region of 3 – 6%. We have also estimated the impact on the overall backward region, taking into account the correlations between bins. In this region,  $\frac{MC}{Data}$  ratio disagreement for run 68696 is reduced from 11% to 6% with the new MC production. Therefore, the main origin in CG MC and data discrepancy in the backward region turns out to be the dark noise charge tuning in the MC simulation. Moreover, we can clearly see that it only affects direct light region in very small proportion, which was expected given the small relative amount of hits coming from dark noise hits in this region. Finally, it is important to specify that the impact on CG backward region is important (around 5%) because charge is integrated on the full time window (1300 ns width) to generate charge profiles for CG. Therefore, for other samples which use a shorter time window, the relative effect of dark noise would be lower than for CG.

### Timing distributions

For timing distributions, we show a difference between the time at which the light reaches the PMT and the time of flight of the corresponding photon from CG. This time of flight was estimated taking only into account the distance from CG to PMT ( $\frac{(Distance_{CG-PMT}) \cdot n_{water}}{c}$ ), and therefore, is really consistent only for direct light. However, this time of flight correction erases most of geometrical discrepancies in the detector, and shows only differences arising from CG light or detector water/reflection parameters. As before, we have used run 68696 as our test run and displayed associated timing distribution in Figure 3.34. We can clearly identify 3 regions:

- The main peak region ( 910-940 ns) that coincides with direct light reaching PMTs
- A region where charge is slowly decreasing with time (950-1050 ns): constituted of scattered

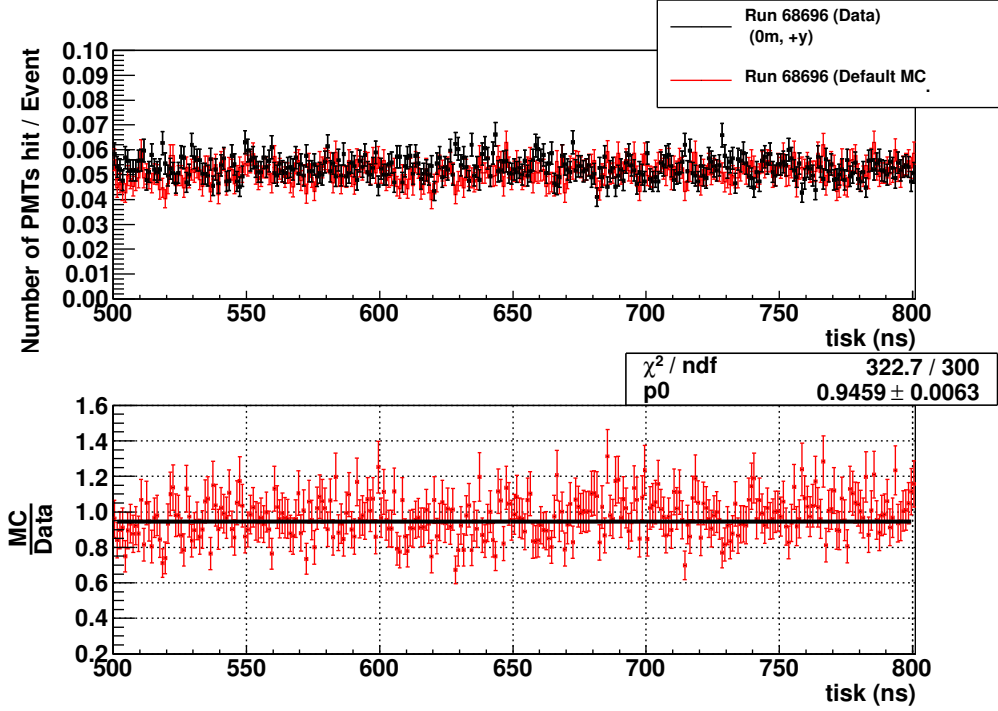


Figure 3.28: Number of PMTs hit with time in Data and MC for run 68696. The ratio  $\frac{MC}{Data}$  is fitted with a constant and shows a 94.6% agreement between Data and MC (average  $\frac{MC}{Data}$  ratio).

light with small amount of reflected light. Therefore, although the amount of scattered light is decreasing with time, it is almost compensated by increasing reflection light.

- Another peak region (1040 ns/1080 ns) with quick charge decrease corresponding to reflected light peak in the backward region, which then decreases with time.

We will respectively name these 3 regions “direct”, “scattered” and “reflected” light regions. On Figure 3.34, differences are observed in direct light timing. However, they can be due to MC trigger time tuning and laser intensity shape, which negligibly affects the charge profile. In this section, we will focus on discrepancies observed in the reflected light region, where MC seems lower than data. To study this effect in more details, we have selected light in the backward region and plotted the corresponding timing distributions.

On Figure 3.35, a comparison between data and MC is drawn for different angles from CG main direction. We have chosen 3 angular regions out of the main peak region to isolate scattered and reflected light:  $60^\circ - 90^\circ$ ,  $90^\circ - 120^\circ$  and  $120^\circ - 180^\circ$  from CG direction. We expect reflection light proportion compared to scattered light to increase with angle, and scattered light proportion to be important close to the peak region. Comparing the 3 regions in Figure 3.35 confirms this trend, with a reflection peak that tends to become higher and to be shifted towards later times at higher angle. We observe that the main source of discrepancy is located in the reflection peak at backward angles, where MC has a strong deficit of light. Thus; it seems that MC/data differences are due to the reflection of light on PMTs and black sheet, even when using the reflection tuning of the new MC production.

The CG setup is not adapted to measure independently the several parameters required for reflection tuning. Hence, we cannot proceed to a re-tuning of the MC reflection parameters to check whether the MC/Data disagreement is due or not to the way reflected light is taken into account in the MC. Instead, we have removed the reflection peak in the backward region in both data and MC charge profiles. Though there is still a component of reflection in the other regions, most of reflected light is gathered in this peak. This method gives some estimation of the effect of data and MC reflection disagreement. To remove the “reflected light region”, a timing cut has been performed on different time windows for the different angles to take into account differences in timing distribution. Time windows used for different angular regions are described in Table 3.7. Finally, we have displayed charge profile

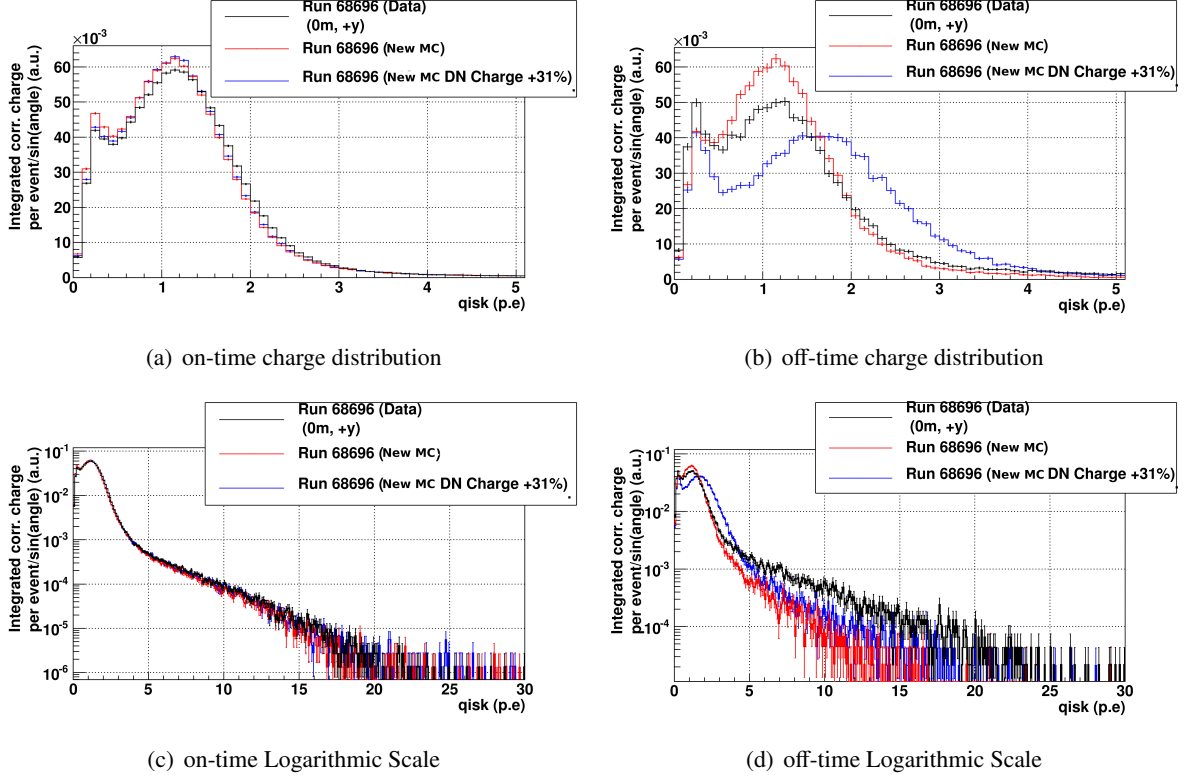


Figure 3.29: Charge distribution for on-time and off-time data and MC

Table 3.7: Timing Cut Summary

	60° – 90°	90° – 120°	120° – 180°
Timing Cut (Removed Region)	950-1050 ns	1000-1100 ns	1050-1100 ns

comparison with and without timing cut of reflection peak in Figure 3.36. Qualitatively, we observe that the agreement between MC and Data has significantly improved. Quantitatively, in the backward region, the overall disagreement decreased from 6.3% (with SKDETSIM, and dark noise charge tuning) to 2.5% for typical run 68696 (0 m, +y dir.). This is the second source of errors between data and MC (3.8%) after dark noise charge tuning.

However, MC and Data are still in a 2.5% disagreement in the backward region. So, we explored another possible source: light scattering in water. In fact, as PMT and black sheet reflection, the tuning of scattering of light in water is affected by Rayleigh scattering correction.

### Tuning of light scattering in water

A new MC production where scattering in water has been tuned after Rayleigh new corrections, has been developed by the SK calibration group. We have implemented these new scattering functions in CG MC to check possible contribution of this source to MC/Data discrepancy. We have displayed the results in Figure 3.37. As can be seen from this figure, for new PMT and black sheet reflection coefficient tuning, changes are too small to explain our MC/Data discrepancy in the backward region. Nevertheless, the agreement between data and MC increases by 1 – 3% in most of the bins of the backward region. In all the backward region, the  $\frac{MC}{Data}$  disagreement decreased from 2.5% after having tuned the dark noise charge and removed reflection peak, to 1.4%. Henceforth, though this effect is not negligible, there remain some sources that constantly shift light in the MC backward region to lower values. To finally discriminate between possible remaining sources, we will use timing charge distributions.

It still remains a discrepancy around the peak region (0 – 20° and 60 – 90°) with two identified possible sources (Figures 3.37 and 3.36):

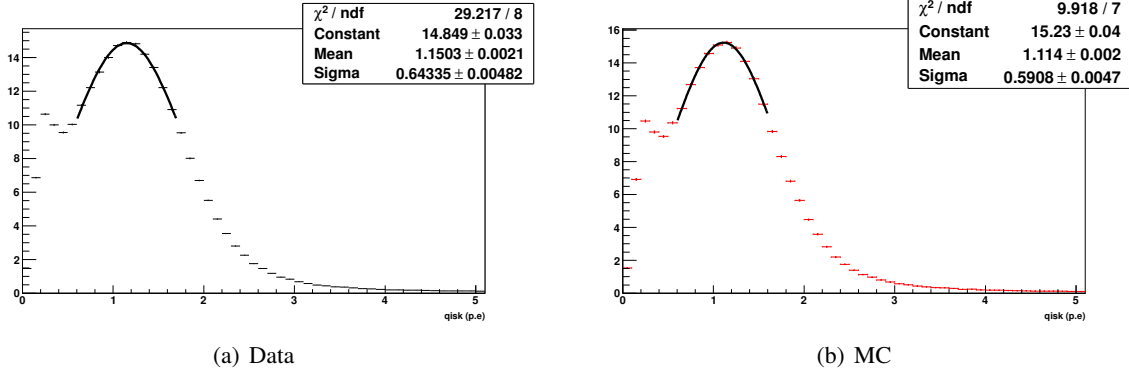


Figure 3.30: Fit of 1 p.e peak by a gaussian function. The relative difference  $\frac{Data-MC}{Data} = 3.1\%$ . Given the relatively high  $\chi^2$  value for data, Data error will be re-weighted by  $\sqrt{\chi^2/NDF}$  i.e  $\delta(DataMean) = 0.004 \text{ p.e.}$ . Propagating the error we find relative difference =  $3.1 \pm 0.4(stat.)\%$ .

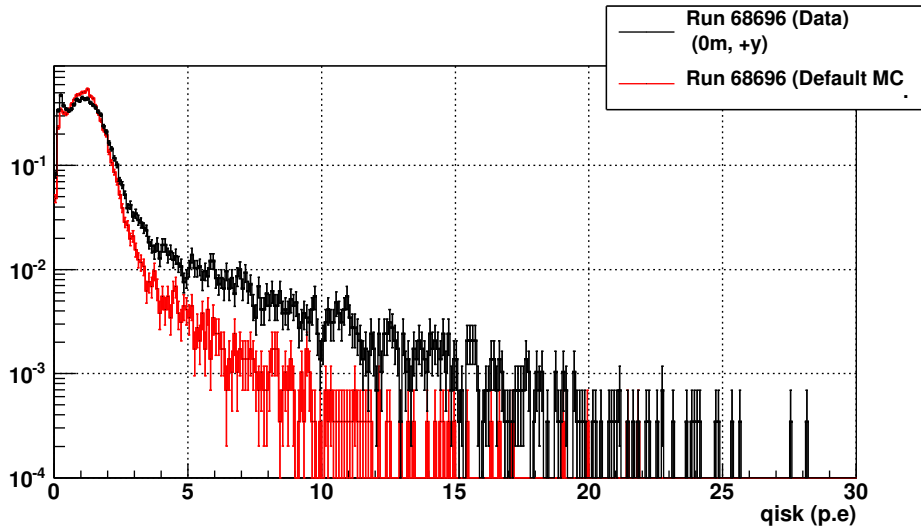


Figure 3.31: Charge Distribution for data and MC in the 1500-1700 ns region (off-time)

- The reflection peak tends not to be separated from other light sources (as it is at higher angles) around the peak region, and so, our cut is not as efficient as in the far backward region
- As described previously, we observed a shift between the CG direction and the locator direction. Integrating around the CG direction makes the data charge profile peak to be wider than the MC one, since the integration point is no longer the ring center. Such an effect could be easily estimated since our systematic error evaluation takes this effect into account.

### 3.5.4 Summary of the single cone analysis

The single cone analysis is based on a simulation using the photon flux data taking, which is compared to data taken in SK. We have first evaluated the MC and data systematic errors, which are summarised in Table 3.8. It shows an average  $\leq 5\%$  error in the cone forward region, and a slightly higher error in the backward region. We used this estimation to investigate two effects:

- The detector vertical uniformity and rotational isotropy. We observed the detector is isotropic within the systematic errors, which is summarised in Figures 3.22 and 3.23.

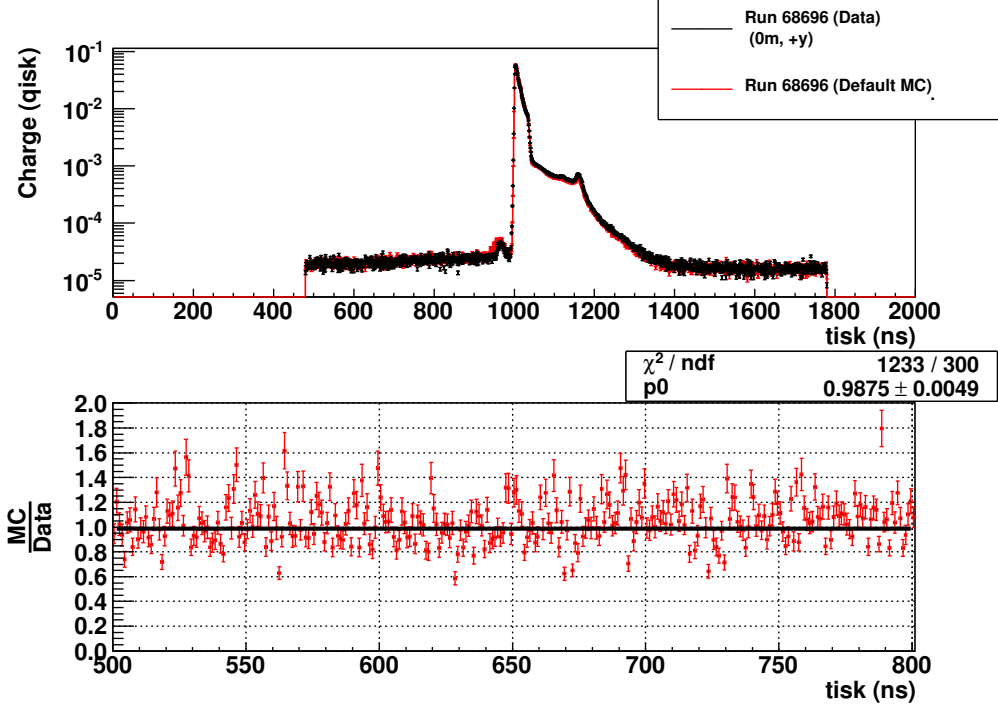


Figure 3.32: Timing charge distribution comparison between MC and Data. On the bottom plot, a zoom in is done in the “off-time” region.

- The 10% discrepancy between data and MC in the cone backward region. We investigated several aspects of the simulation. We concluded the MC lack of light was due to the unperfect simulation of the dark noise, the light reflection on the SK wall and PMTs, and in minority, the scattering of light in water. The quantitative impact of these different sources is summarised in Table 3.9. One observes the data and MC comparison before and after correcting these effects and removing most of the reflected light respectively in Figures 3.20 and 3.36.

## 3.6 Charge asymmetry of the CG setup

### 3.6.1 Charge asymmetry of CG in the SK detector

So far, we only studied charge profiles in one dimension (angle from CG direction). In addition, we decided to perform some studies using the 2D charge distribution in the SK detector. Such 2D distributions can be seen in Figure 3.38 at  $z$  vertex = 0 m, which presents different patterns of light for data and MC. This leads us to study the ring charge asymmetry from the photon flux setup. However, given uncertainties on reconstructed position and direction, we decided not to study asymmetry as a function of angle in the ring shape, but to perform a “coarse-grain analysis” dividing the ring into 2 regions Left and Right, and then 2 others, Top and Bottom.

Our MC will be our comparison reference, since it was generated symmetrically. Indeed, the MC contains the local geometrical effects (discrete PMT distributions, efficiency of each PMTs and so on) of SK detector, erasing differences due to vertex position or CG direction.

We studied several hypotheses to explain this charge asymmetry observed in Figure 3.38. The most upstream one is the tilt of the optical fiber in the diffuser ball. The second one is a global asymmetry of the diffuser ball itself, due to inhomogeneity in the MgO distribution. The third one is a shift of the forward cone with respect to the CG vessel. Finally, an inhomogeneity of the CG channel (forward cone or delrin vessel) could lead to such diffusion inhomogeneity. Before going into details, we decided to subtract the charge from MC to Data, to suppress geometrical effects. Runs in different directions can be visualized in Figure 3.39, which clearly indicates a top-right asymmetry in

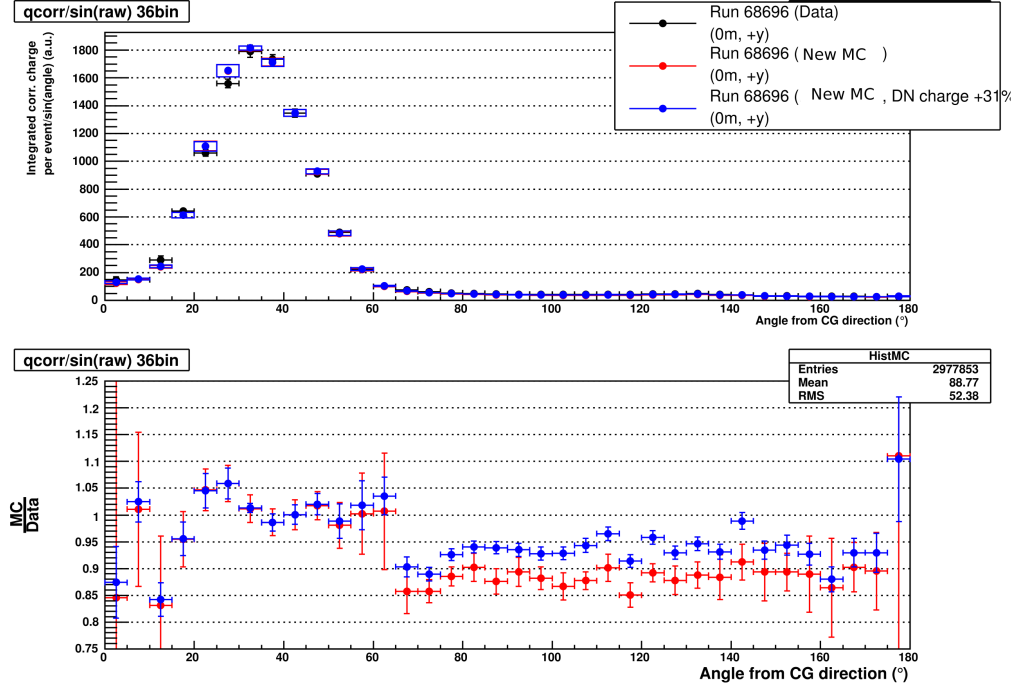


Figure 3.33: Charge Profile comparison between new MC production and data with and without dark noise charge modification.

comparison with the left-bottom region. Moreover, the data ring seems to be shifted on the left of the MC ring. Note that the dead PMTs are not taken into account in our MC, though the efficiency of each PMT is corrected.

To distinguish between these different asymmetry sources, and consequently change our default MC or correctly evaluate systematic errors, we need a quantitative study of the effects mentioned previously. For this purpose, we slice the 2D charge profiles to study a 1D distribution containing 2 peaks (Ex: Left and Right Peaks).

### The top-bottom asymmetry

We need to define a region with a high charge in order not to be affected by dead PMTs, and error on the CG vertex position and direction. Therefore, we integrate the charge in the horizontal plane between the “horizontal angles (see Figure 3.40)  $\phi \in [-10^\circ, 10^\circ]$ ”. Note that a larger integration range would have smeared out the 2 peaks in the 1D charge distribution shown in Figure 3.41. The comparison between MC and Data shown on this figure clearly shows:

- in the data, there is more charge in the bottom region than in top one.
- in the inner top peak region, there is a large disagreement between data and MC ( $z \in [600 \text{ cm}, 1100 \text{ cm}]$ ), which illustrates what has been seen in Figures 3.39.

In order to determine the source of this charge asymmetry, we have to quantify more carefully the observations. In this way, we fit the two peak regions with a Gaussian function. Though this method gives a first estimation, we expect that a Gaussian fit will overestimate the position of the top peak, because of its shape.

The light asymmetry should be quantified and not depend on detector parameters (water absorption, scattering, reflection on walls and so on) if the MC is correctly tuned. The light emitted by the CG that fills the bottom region of the charge profile (Figure 3.41) is noted  $E_{Data_B}$  (“E” stands for expectation) and  $O_{Data_B}$  is the corresponding light that SK PMTs receive in the same bottom region (“O” stands for observation). Our goal is to compare the light emitted by the CG in the bottom and

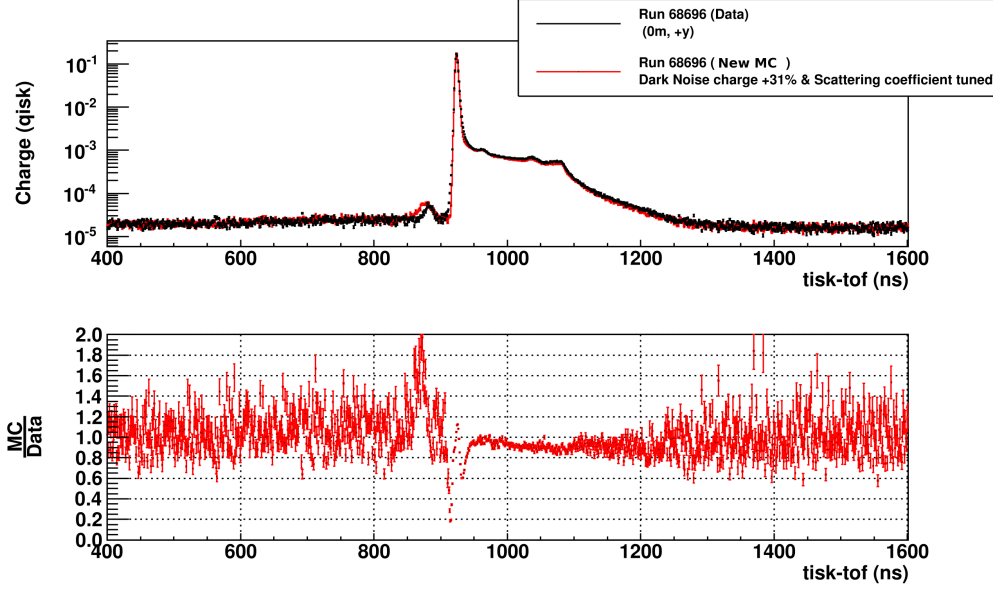


Figure 3.34: Timing charge distribution between Data and MC with dark noise charge and scattering coefficient modifications.

top regions, i.e  $\frac{E_{Data_B}}{E_{Data_T}}$ . Having the information only on the observed light, we use the MC to obtain the emitted light:

- We assume that the PMT coverage is correctly simulated in the MC
- If  $A_{Data_B}$  is the light absorption coefficient in the data bottom region, and is correctly tuned in the MC (i.e  $A_{Data_B} = A_{MC_B} = A_B$ ), we have the relations:  $O_{Data_B} = E_{Data_B} * A_B$  (we remove the PMT coverage, similar in MC and data)

Given these two assumptions, we observe:

$$Q_{asym_{BT}} = \frac{E_{Data_B}}{E_{MC_B}} / \frac{E_{Data_T}}{E_{MC_T}} = \frac{O_{Data_B}}{O_{MC_B}} / \frac{O_{Data_T}}{O_{MC_T}} \quad (3.6.1)$$

Our expectations are quite simple to discriminate between our different hypothesis:

1. Assuming some bending of the optical fiber, the light should have a particular direction in the diffuser ball, different from the ring center. The region where the light is directed should receive more photons, and should have a peak shifted towards large Z values, because of the shift of the light average direction. In the region with less light, the peak should be shifted towards Z=0 m (inner part of the cone). Moreover, we do not expect any particular differences in the peak widths at first order, though the peaks could be widened by reflections in the cone channel.
2. Assuming some diffuser ball asymmetry, we would expect only differences in absolute charge of the two peaks. The data and MC should have the same global shape. Moreover, in this case, we do not expect any shift of the two Gaussian peak positions, nor a modification of their width.
3. In case of a vertical shift of the forward cone, we expect to observe a low intensity peak shifted towards the high Z values (outer part of the cone), and an intense peak shifted towards Z=0 m. A schematic view to explain this is presented in Figure 3.43. Moreover, we expect the most intense peak to be larger than the other one, because of a larger cone channel. Finally, we expect the low intensity peak to be asymmetric because of reflections inside the CG channel (see Figure 3.43).

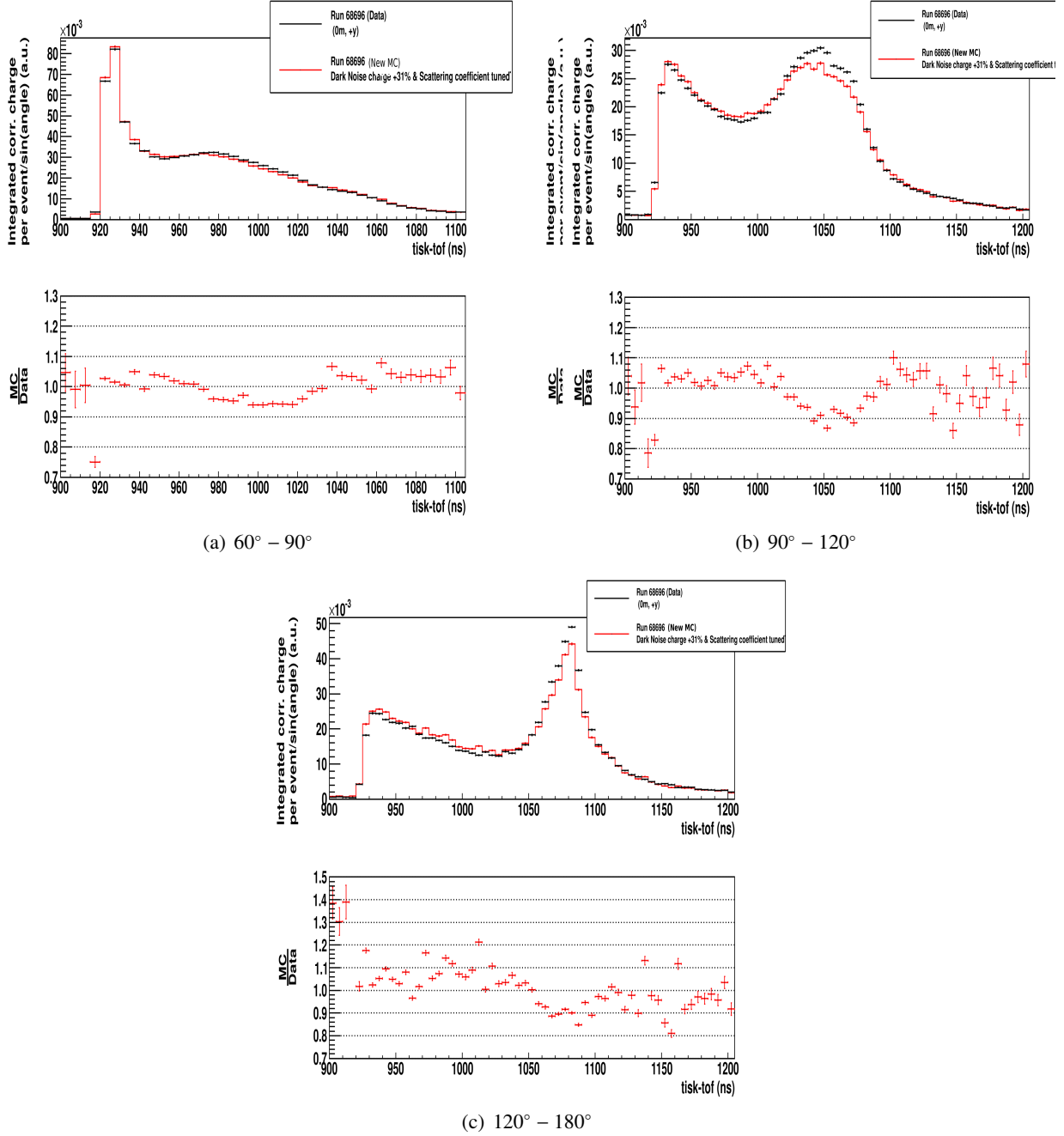


Figure 3.35: Timing charge distributions in different angular regions from CG main direction.

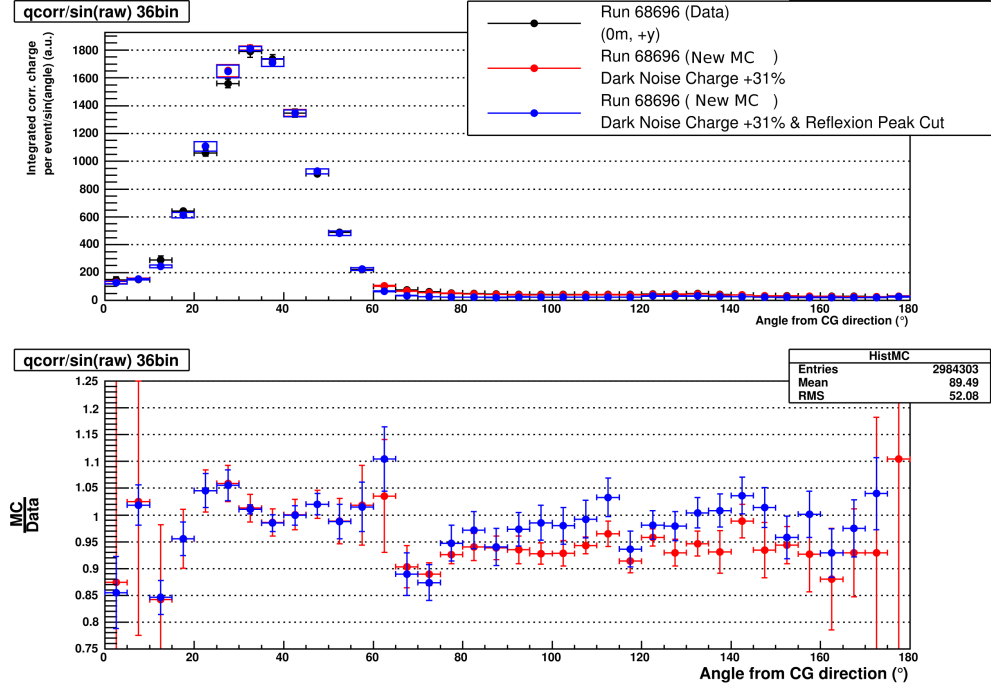


Figure 3.36: Charge profile distribution ratio with and without reflection peak cut in Data and MC.

4. A global asymmetry in reflections or shape of the forward cone or the delrin vessel should have only local effects. This could not generate a charge asymmetry, but it can shift peaks and change their widths.

Considering the table 3.10, the errors on the width are too high to be discriminant. However, the peak positions clearly indicate a constant shift of the top peak towards higher  $z$  values. This peak is the one that has the less charge. Referring to our expectations, this indicates that the source of this light asymmetry is a shift of the forward cone. Particularly, due to this peak position shift, the second and forth hypothesis are refuted. Since the peak with the lower charge is shifted towards higher  $z$  values, the first hypothesis is also refuted. Moreover, in Figure 3.39, the missing charge in the top left region (positive high  $z$ , negative  $\theta$ ) seems to appear in the bottom left region. This shows a correlation between the charge of these 2 peaks, which is well explained by a shift of the forward cone.

### The Left-Right asymmetry

Here, we integrate the charge between 2 different “vertical” angles, namely for  $\theta \in [-10^\circ, 10^\circ]$  (see Figure 3.40), in order not to be affected by dead PMTs or errors on the CG vertex position and CG direction. This range has been chosen also to keep the 2 peaks visible in the 1D distribution. The height of this integration region corresponds to  $z = \sim \pm 3$  m.

The comparison between data and MC can be seen in Figure 3.42. Concerning the shape, the left peak seems more or less gaussian and similar in shape in MC and Data. The reason is this peak is the one measured in the photon flux data taking used to generate the MC.

Similarly to the top-bottom asymmetry, there is a large disagreement in shape between the MC and data for the right peaks, namely in the region corresponding to the inner of the cone ( $\phi \in [20^\circ, 40^\circ]$ ). In fact, the photon flux is considerably lower for data than for MC in this region, though it agrees very well in the peak region corresponding to the outer part of the ring. This first observation is a hint that the diffuser ball asymmetry hypothesis (hypothesis 2) cannot explain the charge pattern. To quantify this assumption and discriminate between other hypotheses, we compare the left and right peaks fitting them with a Gaussian function, keeping in mind the right peak position is over-estimated (due to its shape).

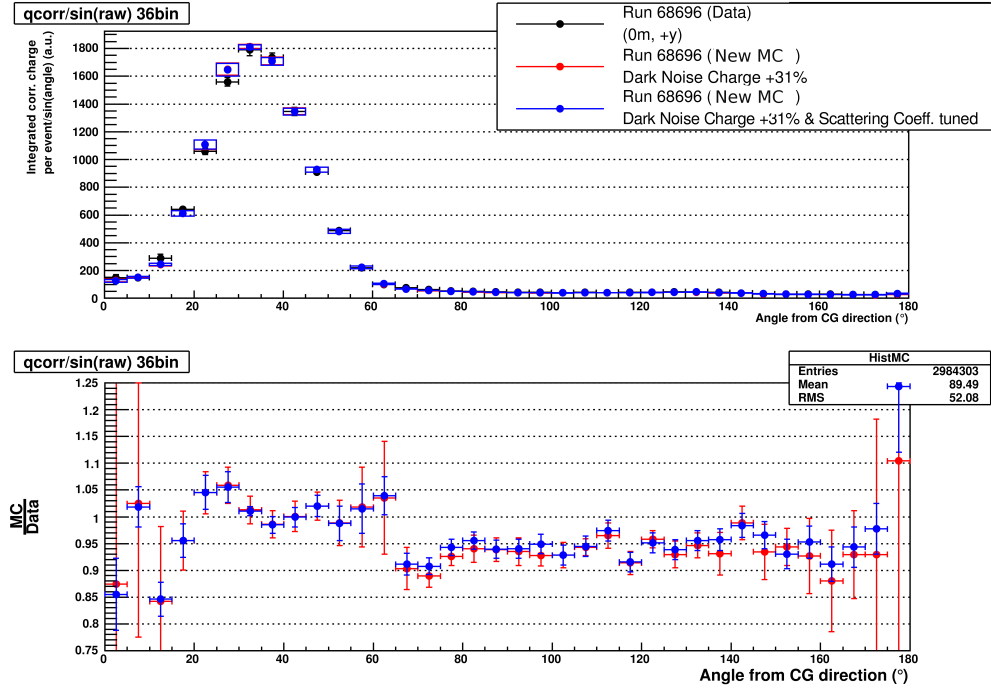


Figure 3.37: Charge Profile comparison between new MC production with dark noise charge modification with and without scattering coefficients modifications.

Results of this procedure are shown in Table 3.11. We can notice that the charge asymmetry is more dependent on the run than the top-bottom one. Nevertheless, the results constantly indicate that the left region contains more charge than the right one. Moreover, the right peak seems constantly shifted the most toward high angle regions, which confirms the forward cone shift hypothesis. The uncertainty on width is still too high to be conclusive. However, the right peak seems considerably shifted and the left peak seems also shifted in the data. The left peak should not be shifted, as it corresponds to the part of the cone which was measured in the Photon Flux data taking, and used to generate the MC. In this way, we conclude that there is a constant shift of about  $0.7^\circ$  between the reconstructed direction and the ring center given by the mean positions of the two peaks. This shift was not observed in the top-bottom plot, and therefore, it probably comes from a misalignment between the CG and the locator directions due to the mounting plate device that is too imprecise.

### 3.6.2 Charge asymmetry hypothesis test in photon flux data

To further confirm the forward cone shift hypothesis, we check data involving less dependence on other physics phenomena: the photon flux data. This data set depends mainly on CG only, given scattering and reflection in the small water tank are small. For this study, we use the only data set where the two peaks (left and right) have been taken, keeping in mind that only photons with a PMTV direction of  $0^\circ$  are measured. First, we have to find out which peak of photon flux data corresponds to which peak in the data taken at SK, since this detail of the configuration had not been recorded at the time of the data taking. In Figure 3.42, the left peak of the data is the one which agrees most with the MC. As it is the right peak in Figure 3.15 that has been taken to generate the MC, we deduce that the right peak in the Photon Flux data taking corresponds to the left peak in the SK data. Therefore, we deduce some constraints on these two peaks: The left peak should be larger and closer to the center, while having more charge. Moreover, the peak shift, the width and the charge asymmetry should vary altogether. To quantify such a change, we will suppose a forward cone shift around the diffuser ball, as described in Figure 3.43.

To evaluate the change in each quantities, we need to characterize the light emitted by the diffuser ball. Our first assumption is that it emits a uniform photon distributions in both position and

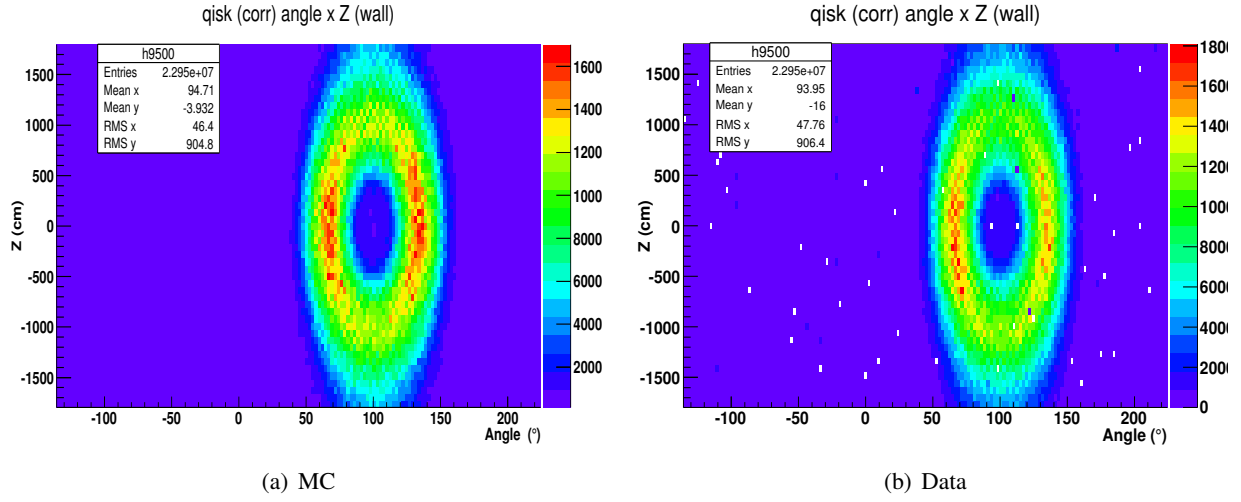


Figure 3.38: 2D Charge Profiles as a function of the azimuthal angle with a position corresponding to the SK center, and the +Y direction

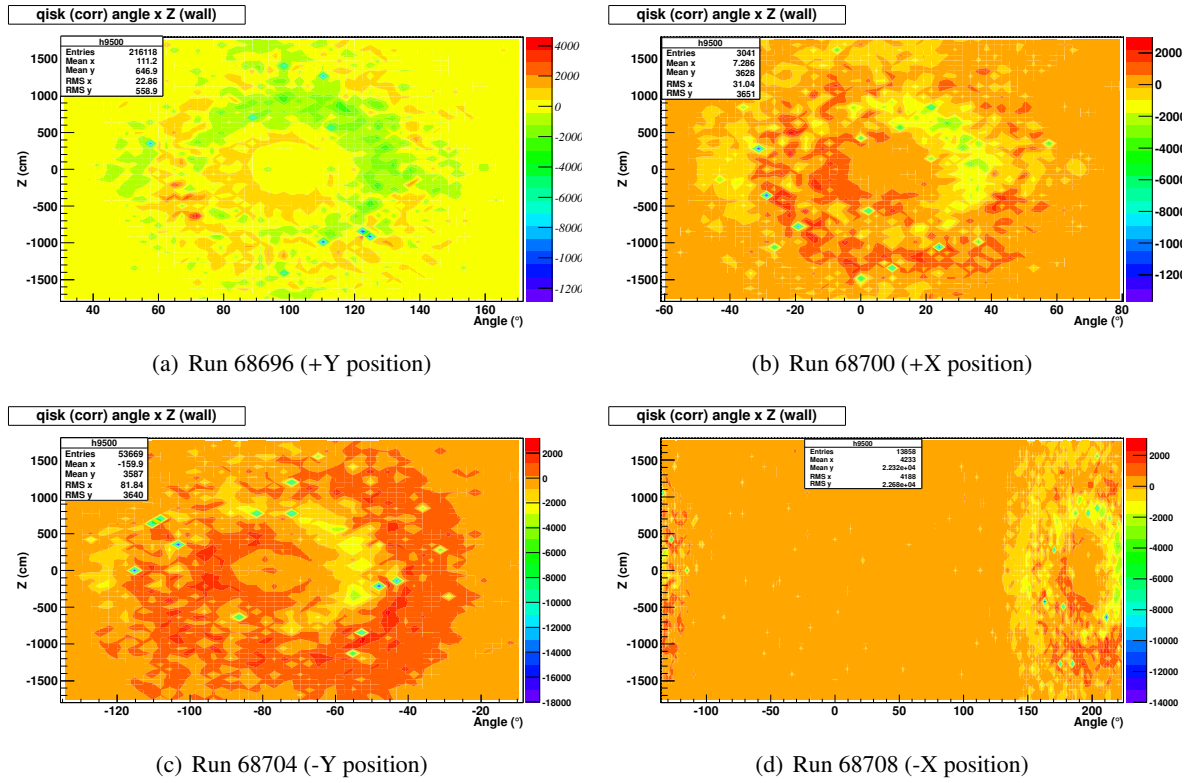


Figure 3.39: Data-MC 2D Charge Profiles as a function of azimuthal angle. It shows the discrepancy of charge distributions in the data

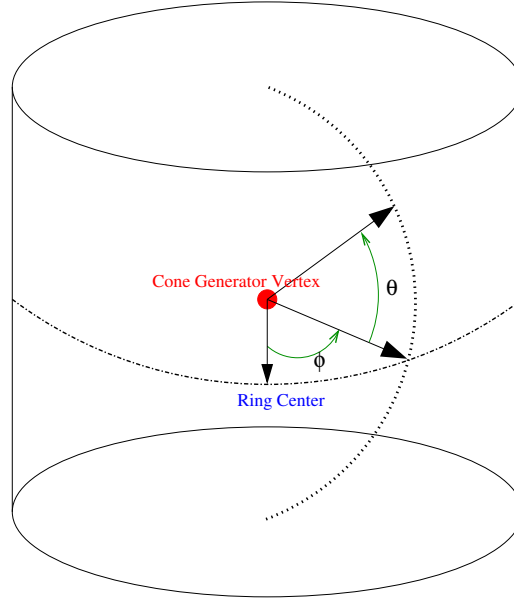


Figure 3.40: Coordinates used to determine slices of 2D charge Profiles

direction. We assume that the photons emitted by a radial point on the sphere is  $\lambda_{\alpha,p}$  with  $\alpha$  the emission direction with respect to the channel direction, and  $p$  the position on the sphere. Considering Figure 3.44, we can deduce the distribution of direct light as shown in Figure 3.45.

This width ( $\sim 40^\circ$ ) at the peak basis is much wider than what we observed in Figure 3.15 (peak basis width  $\sim 15^\circ$ ). Thus, instead of considering a uniform photon distribution, we will suppose that the light source is more or less localized at the diffuser ball center, which seems reasonable given the optical fiber position. Such an assumption leads to a peak width of direct light which is limited by the edge of the CG channels, around  $9.7^\circ$ , which is compatible with the  $15^\circ$  observed (where reflections on the channels increase the width). For this reason, we approximate the direct light to have a trapezoid shape, as shown in the right plot of Figure 3.45. Moreover, to take into account the PMT spatial extension, a convolution is done using the same Gaussian function for the left and right peaks. In this way, we consider the photons to be emitted from the ball center. Given this hypothesis, we consider the change in peak directions, width and charge with a forward cone shift of  $0.7^\circ$  around the diffuser ball, which corresponds to a 8% light asymmetry. Let us remark that it corresponds only to a 350 micrometers mechanical shift in the metallic pins. We consider that changes in width are determined by dWL and dWR in Figure 3.43, because the higher edges of the channel determine the width of the direct light beam. Concerning the asymmetry observed in SK, we consider the shift dL since the total amount of light emitted is directly proportional to this quantity (assuming absorption in the channel walls are similar). Moreover, for SK data, we integrated in a given region small enough to consider the light emitted in a peak as a rectangle, which width is proportional to dL and height  $H$  is equal to the region we chose to integrate ( $H = \theta \pm 10^\circ$  i.e around  $H = \pm 3 m$ ). Since  $H$  is independent from the forward cone shift, the effect on light asymmetry of such a shift would be directly proportional to dL.

The results are summarized in table 3.13. If the hypothesis that there exists a shift of the forward cone is correct, we are supposed to find relative left/right peak positions, widths and light asymmetry in agreement with the estimates obtained in the previous paragraph. We cannot check this quantities in Super-Kamiokande, because the peak position and width highly depend on absorption, scattering, and discrete PMT distribution of SK. Moreover, fitting also the reflected light, we expect to find the outer reflection peak to be far from the direct light peak compared to inner peak, in the left region, while they are supposed to be more or less at same distance from the direct light peak in the right region. To quantify this, we consider for each peak the difference between inner an outer peak with the direct light center. Namely, we consider  $R_{Left/Right} = \frac{2(D_{out}-D_{in})}{(D_{out}+D_{in})}$  with  $D_{in/out} = \text{Mean}_{in/out} - \text{Direct Light Mean}$ .

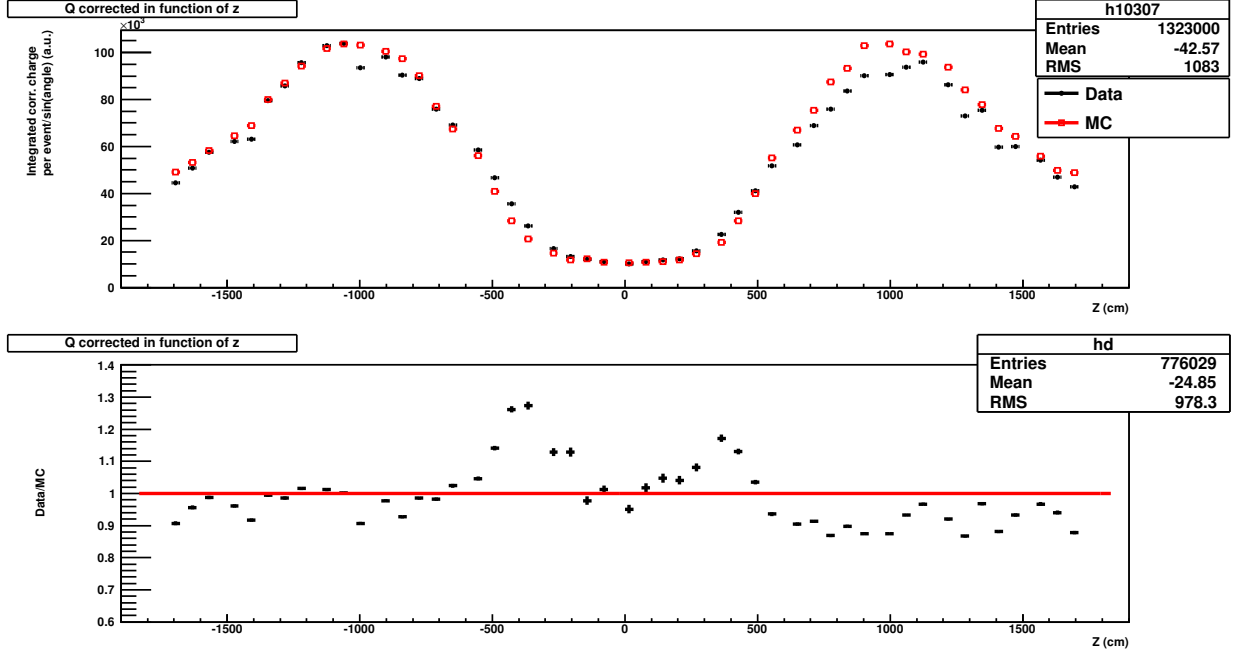


Figure 3.41: Charge distributions with  $z$  position in SK detector for data and MC. We show results for the typical run 68696 ( $z=0\text{m}$ ,  $+y$  di.).

Considering the  $\chi^2$  value in Figure 3.46, the fit seems reasonable, mostly for the right peak, which validates our model. Moreover, the width difference between the left and right peaks is coherent with our expectation estimated in Table 3.13, though slightly smaller. Concerning the peak shift, the comparison between the fit and our expectations confirms that a shift of the forward cone only cannot explain such a huge peak shift, that a shift of the CG vessel is necessary to account for the data. However, assuming that all the peak shift is due to the shift of the CG vessel is surely abusive, given the fact that according to our model, about  $0.3^\circ$  of the shift correspond to a possible shift of the forward cone. Finally, the charge asymmetry is opposite to our expectations. This quantity is difficult to use here, since we only take into account a very small part of the total light (the only available data set is for  $PMTV = 0^\circ$ ). In this way, we can imagine one peak to have more photons in a particular direction different from this one, which can obviously introduce a bias. Quantities as peak position and width are less subject to this bias. On the other hand, the shift of the reflected light peak is exactly as expected: the reflected peaks are less symmetric around the right peak, and its outer reflection peak is shifted towards higher CGV.

In a nutshell, we first concluded that there exists a mechanical shift of the CG with respect to the locator. In the future, this alignment should be checked before any data taking.

In addition, there are strong hints for a forward cone shift in different data sets: the correlation between top-right and bottom-left charge, the direction in the peak shifts and the peak shape in SK data. To test this hypothesis, we proposed a model in the photon flux data, which brings some evidence of this forward cone shift. Finally, such a shift could also explain the differences between left peak positions in table 3.11. They are due to a relatively bad tuning of the MC since we replaced the CGV shift by a total CG vessel shift, and did not take into account the forward cone shift contribution. These differences should not impact much on the study presented in Section 3.5, because we analyzed the charge profile (integration of total charge around the ring center). Due to this integration, a difference in ring width between data and MC is observed constantly in Section 3.5. As for the future, this forward cone shift should be tested with a particular photon flux data set, and reduced for further studies using the CG, such as  $\pi^0$  background or ring counting algorithm studies.

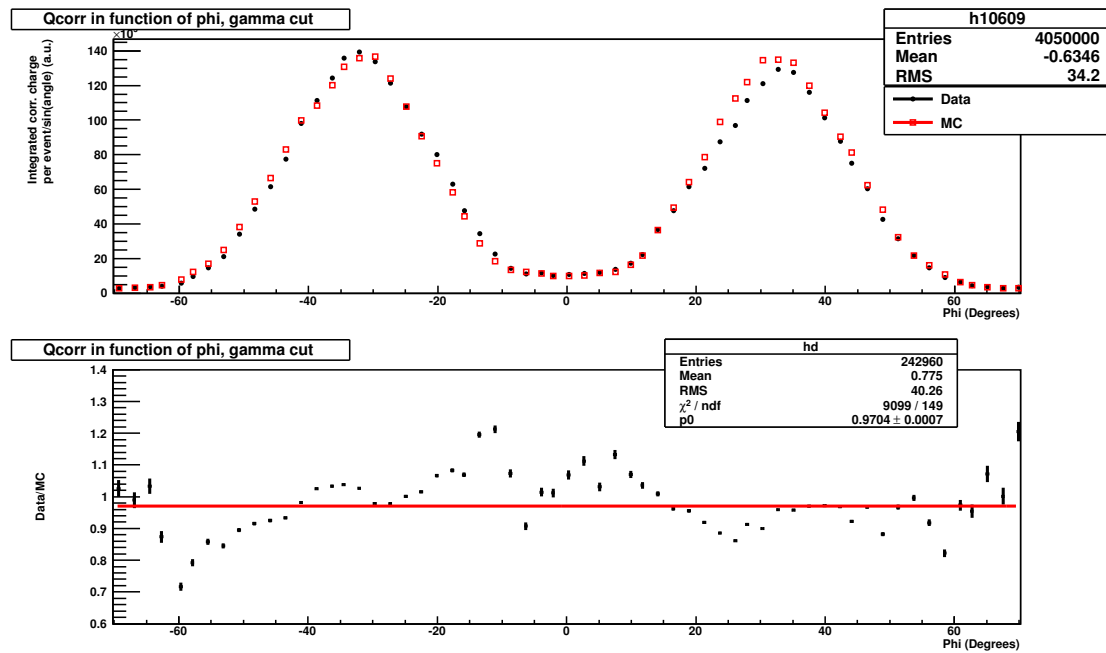


Figure 3.42: Charge Distribution for the horizontal slice of the 2D charge profile with CG in the configuration (0m, +Y direction)

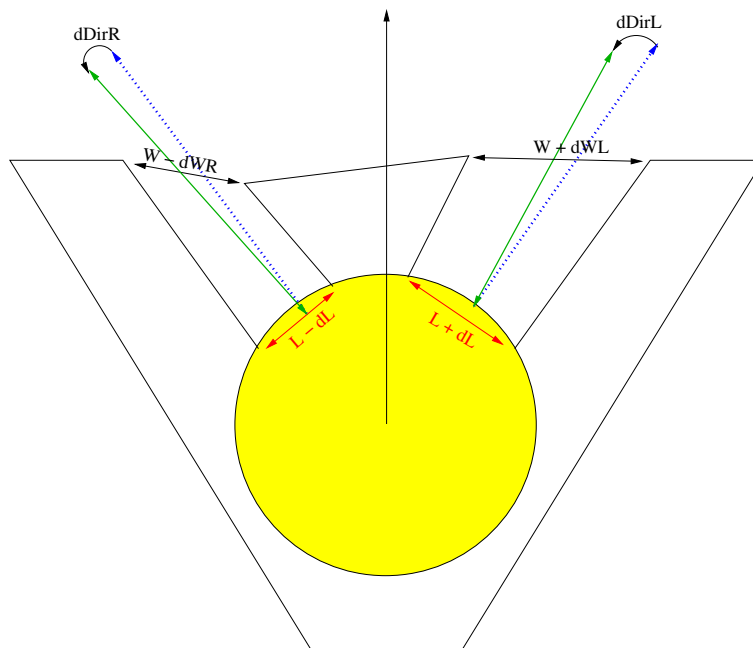


Figure 3.43: Schematic View of a shifted forward Cone

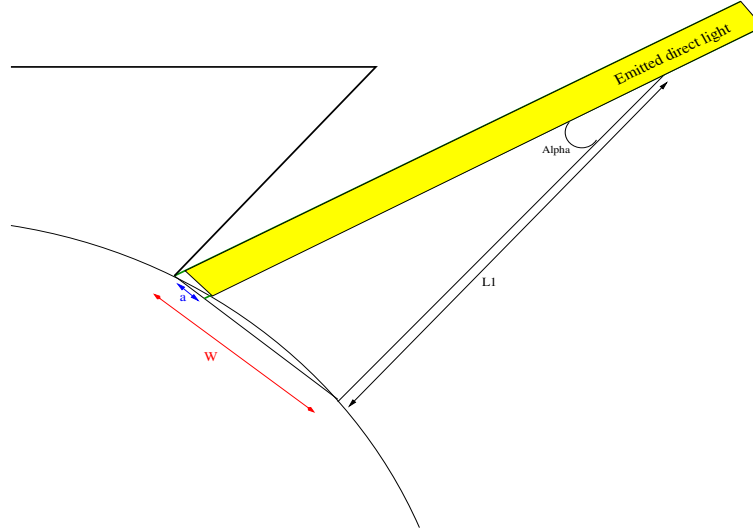


Figure 3.44: Diffuser ball surface that emits light emitted in a given direction  $\alpha$  which is not reflected on the channel walls

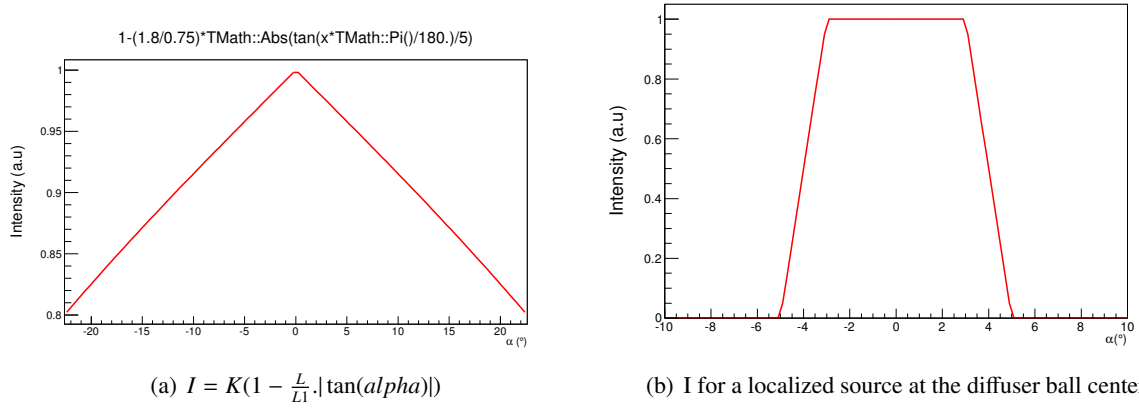


Figure 3.45: Direct light intensity distribution  $I$  (see Figure 3.44 and Figure 3.43 for variable definitions)

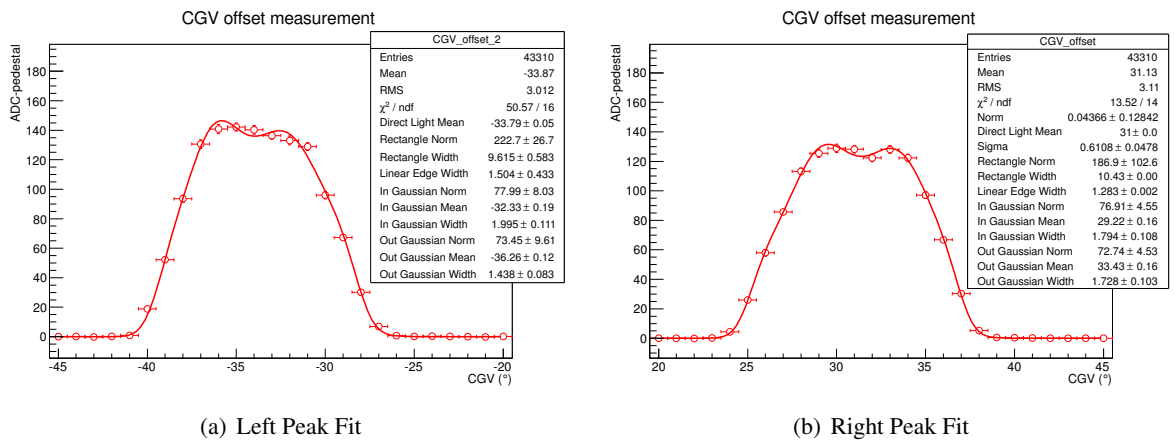


Figure 3.46: Fitting of our model on “CGV offset data”

Table 3.8: Systematic Error estimated for each bin for the Run 68696 (0 m, +Y direction). We represented the lower and upper values of  $1\sigma$  error (lower error bound, upper error bound) in percent. See Appendix A for more details.

Angle (°)	Pedestal	Laser Inten- sity	CG Vessel shift	PMTV offset	PMT light col.	Total MC	Shift of di- rection	Rec. CG ver- tex/direction	Total Data Error
2.5	(0, 8)	(0, 8)	(0, 8)	(0, 3)	(13, 52)	(13, 54)	(0, 81)	(0, 0)	(0, 81)
7.5	(2, 0)	(2, 0)	(3, 0)	(4, 0)	(7, 1)	(9, 1)	(0, 1)	(0, 2)	(0, 2)
12.5	(0, 0)	(2, 0)	(1, 0)	(4, 1)	(9, 5)	(10, 5)	(0, 1)	(2, 0)	(2, 1)
17.5	(0, 1)	(1, 0)	(1, 0)	(2, 2)	(3, 4)	(4, 5)	(0, 2)	(1, 1)	(1, 2)
22.5	(0, 0)	(0, 0)	(0, 1)	(2, 3)	(1, 1)	(2, 3)	(1, 0)	(1, 1)	(1, 1)
27.5	(0, 0)	(0, 0)	(1, 0)	(2, 2)	(2, 1)	(3, 3)	(3, 0)	(0, 1)	(3, 1)
32.5	(0, 0)	(0, 1)	(0, 0)	(0, 0)	(0, 1)	(0, 2)	(0, 1)	(0, 1)	(0, 1)
37.5	(1, 0)	(0, 0)	(0, 0)	(2, 1)	(1, 1)	(2, 2)	(2, 0)	(1, 0)	(2, 0)
42.5	(1, 0)	(0, 0)	(2, 0)	(2, 1)	(1, 0)	(3, 1)	(1, 0)	(0, 1)	(1, 1)
47.5	(1, 0)	(0, 0)	(2, 0)	(2, 2)	(3, 1)	(4, 2)	(3, 0)	(1, 0)	(3, 0)
52.5	(0, 0)	(0, 0)	(0, 4)	(3, 2)	(3, 4)	(4, 6)	(1, 0)	(0, 2)	(1, 2)
57.5	(0, 1)	(0, 1)	(5, 7)	(1, 2)	(4, 4)	(6, 8)	(2, 0)	(1, 0)	(3, 0)
62.5	(0, 2)	(0, 1)	(3, 2)	(1, 2)	(4, 7)	(5, 8)	(0, 2)	(0, 2)	(0, 3)
67.5	(1, 1)	(0, 0)	(0, 1)	(1, 1)	(1, 3)	(2, 4)	(2, 0)	(1, 0)	(2, 0)
72.5	(1, 1)	(1, 0)	(0, 0)	(0, 1)	(0, 2)	(1, 3)	(0, 0)	(0, 1)	(0, 1)
77.5	(0, 0)	(0, 0)	(0, 1)	(0, 1)	(1, 1)	(1, 2)	(1, 0)	(0, 1)	(1, 1)
82.5	(0, 0)	(0, 1)	(0, 1)	(1, 1)	(1, 1)	(2, 2)	(2, 0)	(1, 1)	(2, 1)
87.5	(0, 2)	(0, 1)	(0, 2)	(0, 2)	(0, 2)	(0, 4)	(0, 0)	(1, 1)	(1, 1)
92.5	(0, 1)	(0, 0)	(1, 0)	(0, 0)	(1, 1)	(1, 1)	(0, 0)	(0, 1)	(0, 1)
97.5	(0, 1)	(0, 0)	(0, 2)	(0, 1)	(0, 2)	(0, 3)	(2, 0)	(1, 0)	(2, 0)
102.5	(0, 2)	(0, 1)	(0, 2)	(0, 1)	(0, 3)	(0, 4)	(0, 0)	(0, 1)	(0, 1)
107.5	(0, 0)	(0, 0)	(1, 0)	(0, 0)	(2, 1)	(2, 1)	(1, 0)	(1, 0)	(1, 0)
112.5	(1, 1)	(0, 0)	(0, 0)	(0, 1)	(2, 2)	(2, 2)	(3, 0)	(1, 1)	(3, 1)
117.5	(0, 1)	(0, 0)	(0, 2)	(0, 1)	(0, 2)	(0, 3)	(0, 0)	(1, 1)	(1, 1)
122.5	(1, 0)	(1, 0)	(1, 0)	(1, 0)	(3, 1)	(4, 1)	(3, 0)	(1, 1)	(3, 1)
127.5	(0, 0)	(0, 1)	(1, 0)	(1, 0)	(2, 1)	(2, 1)	(1, 0)	(1, 1)	(1, 1)
132.5	(0, 0)	(0, 1)	(0, 0)	(1, 1)	(1, 2)	(2, 2)	(2, 0)	(2, 0)	(3, 0)
137.5	(0, 1)	(0, 0)	(0, 2)	(1, 1)	(0, 1)	(1, 2)	(1, 0)	(0, 3)	(1, 3)
142.5	(0, 1)	(0, 0)	(0, 1)	(0, 2)	(2, 2)	(2, 4)	(2, 0)	(3, 1)	(3, 1)
147.5	(0, 2)	(0, 1)	(0, 1)	(0, 2)	(0, 3)	(0, 4)	(0, 0)	(1, 2)	(1, 2)
152.5	(0, 0)	(1, 0)	(1, 0)	(0, 1)	(2, 1)	(3, 2)	(0, 0)	(2, 3)	(2, 3)
157.5	(0, 1)	(0, 0)	(1, 1)	(0, 2)	(2, 3)	(2, 3)	(0, 0)	(1, 1)	(1, 1)
162.5	(0, 3)	(0, 1)	(0, 3)	(0, 2)	(0, 4)	(0, 6)	(0, 0)	(3, 1)	(3, 1)
167.5	(0, 0)	(3, 0)	(0, 1)	(0, 0)	(6, 2)	(7, 2)	(5, 0)	(1, 2)	(6, 2)
172.5	(0, 4)	(0, 0)	(2, 1)	(1, 0)	(6, 4)	(6, 5)	(6, 0)	(2, 6)	(6, 6)
177.5	(10, 0)	(10, 0)	(5, 0)	(8, 0)	(25, 0)	(30, 0)	(15, 0)	(15, 40)	(21, 40)

Table 3.9: List of error sources impact on  $\frac{MC}{Data}$  agreement in the backward region for a typical run (run 68696)

	Dark noise charge tuning	Reflection peak removal	Scat. coefficients new tuning	Others
Change in $\frac{MC}{Data}$ agreement	4.2%	3.8%	1.1%	2.2%

Table 3.10: Fitting Results of slices in different directions for Top-Bottom asymmetry

Run number	Data-MC Left Peak (in cm)	Data-MC Right Peak (in cm)	$1 - Q_{asym_{BT}}(\%)$
68696 (0m, +y)	Position: $2 \pm 11$ Width: $1 \pm 20$	Position: $8 \pm 11$ Width: $-1 \pm 21$	7.6
68700 (0m, +x)	Position: $-10 \pm 7$ Width: $-15 \pm 11$	Position: $21 \pm 10$ Width: $-3 \pm 17$	5.5
68704 (0m, -y)	Position: $-27 \pm 12$ Width: $8 \pm 19$	Position: $12 \pm 19$ Width: $6 \pm 34$	7.0
68708 (0m, -x)	Position: $-6 \pm 12$ Width: $2 \pm 22$	Position: $48 \pm 13$ Width: $0 \pm 22$	9.3
68712 (0m, +y)	Position: $-4 \pm 11$ Width: $0 \pm 20$	Position: $9 \pm 11$ Width: $-4 \pm 21$	7.0

Table 3.11: Fitting Results for Left-Right asymmetry (for different slices).

Run number	Data-MC Left Peak (in $^\circ$ )	Data-MC Right Peak (in $^\circ$ )	$1 - Q_{asym_{LR}}(\%)$
68696 (0m, +y)	Position: $0.4 \pm 0.2$ Width: $-0.1 \pm 0.3$ RMS: -0.1	Position: $0.4 \pm 0.2$ Width: $0.1 \pm 0.3$ RMS: 0.2	5.7
68700 (0m, +x)	Position: $0.7 \pm 0.2$ Width: $0.0 \pm 0.3$ RMS: -0.1	Position: $0.7 \pm 0.2$ Width: $0.0 \pm 0.3$ RMS: 0.1	6.8
68704 (0m, -y)	Position: $0.9 \pm 0.3$ Width: $0.0 \pm 0.4$ RMS: 0.0	Position: $1.0 \pm 0.3$ Width: $0.8 \pm 0.5$ RMS: 0.1	3.4
68708 (0m, -x)	Position: $0.4 \pm 0.3$ Width: $-0.2 \pm 0.5$ RMS: 0	Position: $0.8 \pm 0.2$ Width: $0.0 \pm 0.3$ RMS: 0.2	0.6
68712 (0m, +y)	Position: $0.3 \pm 0.2$ Width: $-0.3 \pm 0.3$ RMS: 0	Position: $0.5 \pm 0.2$ Width: $-0.2 \pm 0.3$ RMS: 0.2	6.0
68674 (0m, +y)	Position: $0.9 \pm 0.3$ Width: $0.1 \pm 0.4$ RMS: -0.2	Position: $1.2 \pm 0.2$ Width: $-0.2 \pm 0.2$ RMS: 0.1	4.7
68678 (0m, +x)	Position: $1.1 \pm 0.3$ Width: $0.1 \pm 0.5$ RMS: 0.2	Position: $1.7 \pm 0.2$ Width: $-0.1 \pm 0.3$ RMS: 0.1	5.7
68682 (0m, -y)	Position: $0.2 \pm 0.3$ Width: $-0.7 \pm 0.4$ RMS: 0.2	Position: $1.7 \pm 0.2$ Width: $-0.2 \pm 0.4$ RMS: 0.2	0.6
68686 (0m, -x)	Position: $0.3 \pm 0.2$ Width: $0.0 \pm 0.3$ RMS : 0.0	Position: $0.3 \pm 0.3$ Width: $-0.2 \pm 0.5$ RMS: 0.1	1.5

Table 3.12: Expected impact on our “CGV offset data” and SK data of a  $0.7^\circ$  forward cone shift

	Left peak	Right peak position	Asymmetry
Peak Position	$0.3^\circ$	$0.3^\circ$	8%
Peak Width	6.2%	6.1%	

Table 3.13: Fitting results of our model on “CGV offset data”

	Peak shift	Peak Width Difference	Charge Asymmetry		$R_L$	$R_R$
Direct Light	$1.39 \pm 0.05^\circ$	$8.5 \pm \%$	-5.6%	Reflected Light	51%	32%

### 3.7 Conclusion of the single cone analysis in SK

We have presented here the complete single cone analysis using 2011/09 data and summarized the obtained results.

For a typical run with vertex at (0 m, +y direction), the charge profile from MC is in agreement with data in the 4% shape error in the main ring region. In the backward region, MC is constantly lower than Data by 11% which is beyond the 5% shape error. As for different  $z$  positions, and for different directions, the disagreements between MC and data are also similar to this. This result confirms trends observed in other control samples as stopping muons, through going muons and decay electrons. Finally, we have not observed any vertex and direction dependence with a probability of 42% and 12% respectively. This CG study indicates no inhomogeneity in the SK detector, except for the absorption, to which the current CG setup is not sensitive.

Moreover, we have studied possible sources of this disagreement between MC and Data. In fact, we observed that the dark noise charge tuning was the main source, and the tuning proposed decreased the disagreement by 5% in the run 68696 (vertex at  $z=0$  m, +y direction) we studied. As secondary sources, implementation of new MC production and of new scattering functions introduced in Section 3.5.3 also reduced this disagreement in the backward region. However, we measured that the  $\frac{MC}{Data}$  ratios still have a 5% discrepancy in this region. Finally, time distribution comparisons indicated that the main source of the remaining disagreement may come from the reflection tuning in SKDETSIM.

In Appendix A.1, we have listed systematic errors that affects CG profile in Table A.1 and A.2, and we emphasize that dominant systematic errors come from statistical fluctuation due to PMT light collection, CG vessel shift, reconstructed vertex position and direction shift depending on altitude of the vertex. On one hand, the error due to PMT light collection in some bins would be reduced taking more data at these angle during the photon flux measurement process. Another possibility would be to change laser diode to increase intensity during the photon flux measurement. Concerning CG vessel shift, main source of error comes from the high  $\chi^2$  value of the fitting function. One way to improve fit quality is to understand expected light pattern, using for example results developed in Section 3.6. Using basically such a fitting function decreases  $\frac{\chi^2}{NDF}$  value roughly from 44 to 3, and therefore, decreases the error on CG vessel shift by a factor 4. Finally, the error on reconstructed vertex position and shift direction are dominant in some regions. Concerning the mechanical shift, alignment can be checked with an optical table on which the CG center is aligned. Then using the locator laser spot, alignment with the CG center may be estimated.

Though this study indicated the source of discrepancy, the CG has not been designed to properly measure the black-sheet and PMT reflection. This study can be cross checked and improved in the future using laser data taken in the Super-Kamiokande tank. The second calibration that can be performed would be the use of the off-time dark noise data to tune the dark noise charge distribution. The various checks and simulation tuning we have performed in this analysis will be used in the future for all physics analyses, but also for the two CG setup to estimate  $\pi^0$  background and evaluate reconstruction algorithm performances.


However, as we observed, this CG setup is quite a complicated device and its imperfections, such as the mobile forward cone, can make precise measurements difficult. Due to these limitations, this setup developed in 2009, could not be used as previously planned. To improve the reproducibility of this device (in context of two CG analysis), a completely new design could be easily studied to further investigate the important SK characteristics, using for example simple and cheap 3D printed cone channels, the geometry of which would be under much better control than the one of the CG we have studied here.

## Chapter 4

# Charge calibrations of the INGRID and PM detectors

*A theory is something nobody believes, except the person who made it.  
An experiment is something everybody believes, except the person who made it.*

Albert Einstein

 THE INGRID detector has been used mainly to monitor the beam intensity and shape through the detection of  $\nu_\mu$ . The event selection is based on the muon detection with the INGRID tracker, which doesn't require an accurate calorimetry. Only a 2.5 photo-electron cut for each hit is applied to remove most of the electronic dark noise hits.

In this thesis, we will use the PM and INGRID respectively for cross section measurements (Chapter 5) and Lorentz invariance violation study (Chapter 6). Both require a better calibration of the charge response of the detectors. This will be also true for future uses of these detectors, and we have listed several examples below:

1. For  $\nu_\mu$  cross section measurements in iron (INGRID) or carbon (PM): we have shown that  $\nu_\mu$  cross section measurements should be based on particle identification which relies on  $\frac{dE}{dx}$  (see Chapter 5). In this particular example, one needs an accurate charge response calibration to clearly distinguish muons from protons.
2. For Lorentz invariance violation study: we need a  $\nu_\mu/\nu_e$  separation to be able to see a potential  $\nu_\mu$  disappearance in  $\nu_e$  (see Chapter 6). We have shown that charge response calibration helps to improve electrons and muons track separation. Note that this study could be used also for a possible  $\nu_e$  cross section measurement.
3. For future identification of  $\nu/\bar{\nu}$  in the anti-neutrino run: we can imagine using vertex energy to distinguish a  $\nu$  charged current interactions producing a proton from an  $\bar{\nu}$  that produces a neutron in the final state.

We will perform the charge calibration in the INGRID and PM detectors to carry out these different measurements. The main issue we tackled was the correction of the INGRID analog-to-digital converter (ADC) non linearities which has been extensively studied in this chapter.

We will first measure and correct the ADC non linear response to a given charge. We will show the improvement in the charge deposition agreement between MC and data in Section 4.2. Thanks to this calibration, we discovered an anomaly in charge deposition in the PM. The study of this anomaly will be presented in Section 4.3, and clearly indicates a possible optical cross-talk between the scintillators. This cross-talk is not taken into account in the simulation. We will confirm this hypothesis by a set of measurement (Section 4.4), and will correct it.

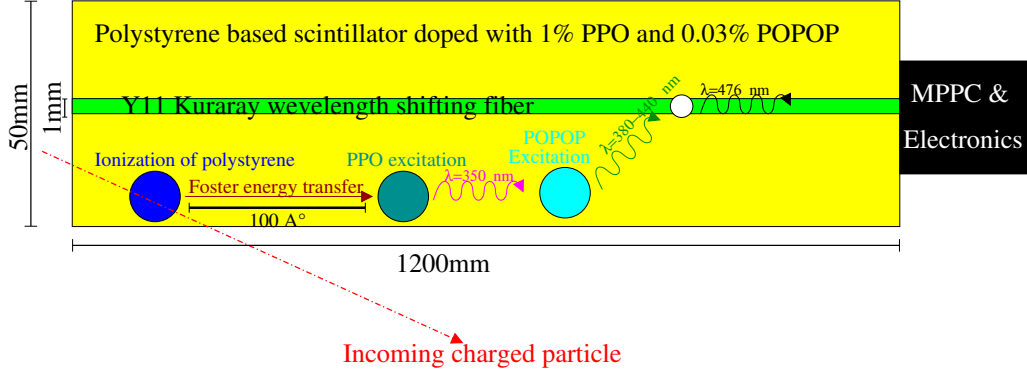


Figure 4.1: Schematic view of the processes from the passage of particle in a scintillator to the emission of a light signal that can be measured by the MPPC.

## 4.1 Introduction to INGRID and PM detectors detection process

The basic features of the INGRID and PM detectors have already been introduced in Chapter 2. We now describe these detection processes in details: from the particle propagation to the read-out. The detection principle of a charged particle by the INGRID and PM is based on:

1. An active polystyrene scintillator slab producing photons after excitation due to the passage of a charged particle, described in Section 4.1.1.
2. A wavelength shifting fiber to collect the photons, described in Section 4.1.2.
3. A multi-pixel photon counter (MPPC) to convert the photons in a measurable current, described in Section 4.1.3.
4. An analog-to-digital converter to digitise the analog current, described in Section 4.1.4.

These various steps of the detection are illustrated in Figure 4.1.

### 4.1.1 Scintillator

When a charged particle penetrates a scintillator slab, it excites the scintillator molecules. The scintillator is constituted of polystyrene doped with 1% PPO (2,5-Diphenyloxazole) and 0.03% POPOP by weight. Most of the excited molecules are polystyrene. It is interesting to note that most of the scintillating light that reaches the optical fiber does not come directly from these excited molecules. In fact, the deexcitation light emitted would be soon re-absorbed by the polystyrene, which would highly limits its propagation to the fiber. Moreover, the pure polystyrene molecules have a relatively long decay time ( $\sim 16$  ns [13]) which could highly limit the detector time resolution. For these two reasons, a primary wavelength shifter (the PPO) is used. The polystyrene molecules transfer a part of their energy through “Forster energy transfer” [13] [60] to the PPO molecules. This transfer corresponds to a dipole-dipole interaction which implies a  $1/(r/R_0)^6$  efficiency variation with  $r$  the distance between the acceptor and donor and  $R_0$  the Forster distance of this pair. This constant for our scintillator type allows energy transfers from  $10 \text{ \AA}$  to  $100 \text{ \AA}$ , which corresponds to the average distance  $\langle D \rangle$  between a given polystyrene molecule and its closest PPO molecule. Assuming a mean separation of  $\sim 30 \text{ \AA}$  between two polystyrene molecules, the 1% PPO concentration is needed to keep a  $\langle D \rangle \sim 30 \times \sqrt{3}100 \text{ \AA} = 140 \text{ \AA}$  and therefore allows a sufficient amount of Forster energy transfer to the PPO molecules.

The PPO molecules are consequently in an excited state. They deexcite through light emission at a wavelength peaked at  $\lambda \sim 350$  nm as shown in the right part of Figure 4.2. Comparing the two Figures 4.2, one remarks the absorption and emission spectrum overlap is small, though not negligible around  $300 - 340$  nm. This naturally limits the mean free path of the emitted photons because of re-absorption. A second wavelength shifter, the POPOP, is then used to increase the mean free path

of the photons and shift the light wavelength to convenient optical wavelength (370 – 450 nm) to be propagated after shifting through the fiber. The absorption and emission spectra of the POPOP shown in Figure 4.3 clearly demonstrates ability of the 0.03% POPOP to shift the  $\langle 350 \text{ nm} \rangle$  emitted light from the PPO. The negligible overlap between POPOP emission and PPO absorption spectra and the small POPOP concentration allows a relatively large attenuation length in INGRID scintillators, which has been measured using 3 GeV test electron beam as 10.5 cm. This attenuation length also takes into account the light reflected on the scintillator coating ( $\text{TiO}_2$ ) and the scintillator geometry (light collection by the fiber) and is naturally higher than in case of no-boundary (no coating) scintillators.

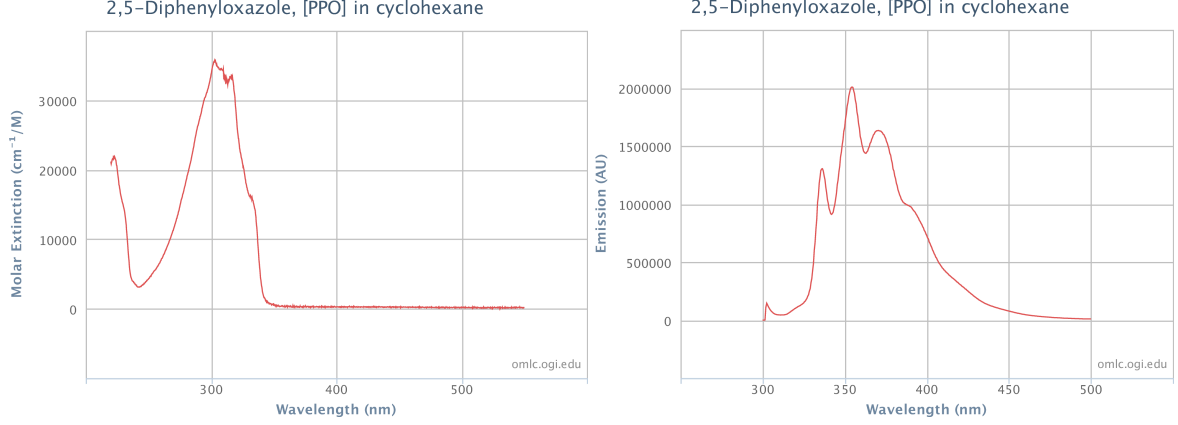


Figure 4.2: Absorption (left) and emission (right) spectra of the PPO molecule.

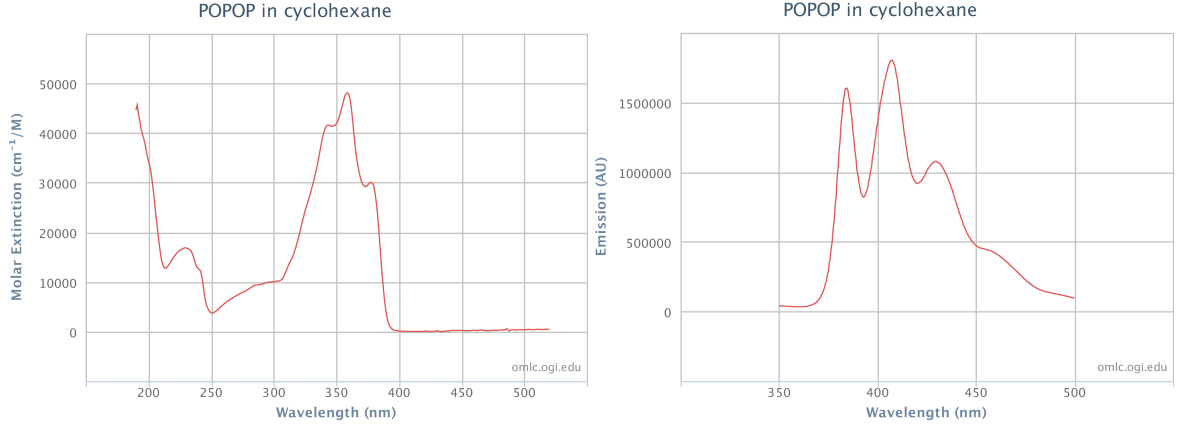


Figure 4.3: Absorption (left) and emission (right) spectra of the POPOP molecule.

After being shifted by the POPOP, the light emission peak is 420 nm.

#### 4.1.2 Wavelength shifting fiber (WLS)

The emitted photons may hit and propagate through the 120 cm WLS. These fibers are 1 mm diameter Kuraray double-clad Y-11, and are inserted in a 3 mm hole in the center of the scintillator bars. The maximum of their absorption spectrum is located around 430 nm (blue) while they deexcite emitting a photon spectrum centered around 476 nm (green) to minimize the self-absorption [50]. One edge of the fiber is connected to a multi-pixel photon counter (MPPC), while the other one is polished and painted using  $\text{TiO}_2$  reflective painting. The attenuation length in the WLS has been measured using the 3 GeV electron beam as  $L = 241.7 \text{ cm}$ .

#### 4.1.3 Multi-pixel photon counter (MPPC)

The photons then hit the MPPC. The T2K Hamamatsu MPPC are  $1.3 \times 1.3 \text{ mm}^2$  arrays of 667 independent light-sensitive pixels (photodiodes) operating in Geiger (avalanche) mode shown in Figure 4.4.

The overvoltage of  $\Delta V = V - V_b$  is the difference between the voltage applied to each photodiode and their breakdown voltage. The operational voltage of the photodiode is about 70 V which corresponds to  $\Delta V \sim 1$  V. The Geiger mode implies that each photodiode operates in binary mode and the response of each photodiode is non linear with the amount of hitting photons. Since several photons may hit the same photodiode for high charge deposition, possible MPPC non linearities should be corrected. The T2K MPPC produces electrons (“photo-electrons”, “p.e”) with a  $\sim 10^6$  gain. It is important to notice that the MPPC gain is highly sensitive to external conditions as temperature or humidity (changing the MPPC dielectric properties).

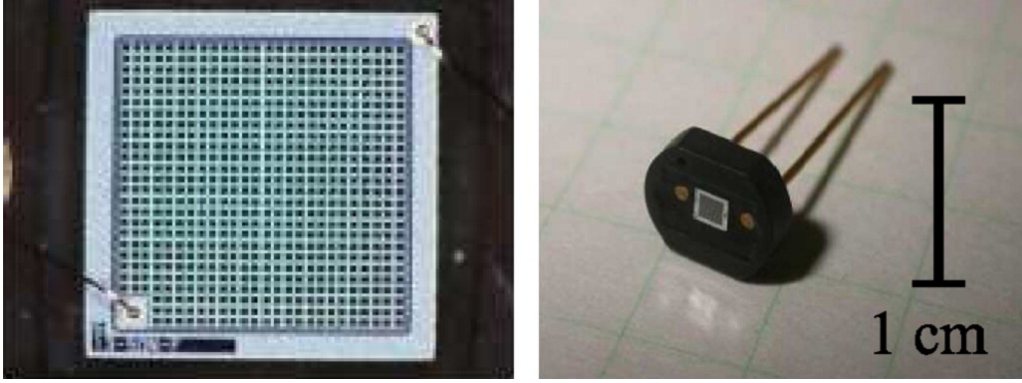


Figure 4.4: The T2K multi-pixel photon counter (MPPC), an array of 667 independent photodiodes.

#### 4.1.4 Electronics and analog-to-digital converters (ADC)

The MPPC readout is operated by Trip-T front end boards (TFBs) shown in Figure 4.5. In particular, the Trip-T are constituted of one low gain and one high gain channels, which are constructed respectively using a  $C_{Hi} = 100$  pF and a  $C_{Lo} = 10$  pF capacitance. Each capacitance is charged ( $Q_{Hi/Lo} = C_{Hi/Lo} \times U$ ) during the 480 ns INGRID integration cycle and then discharged. This naturally generates a gain difference of a factor of ten between the two channels in order to operate accurately on a broader dynamical range. Each channel is connected to a 10 bits ADC, which naturally allows  $2^{10} = 1024$  values to discretize the analog charge that can then be sent to computers.

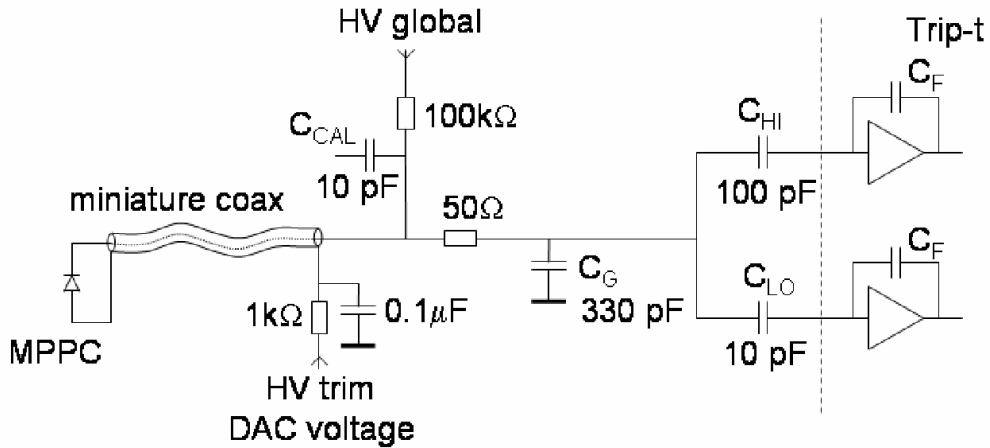


Figure 4.5: The electronic architecture from the MPPC output to the low and high gain channel separation.

The input voltage (*i.e* charge) has to fall within the range where the ADC operates. This range is selected by the choice of a reference voltage  $V_{ref}$ . The range from 0 to  $V_{ref}$  is discretized within the 1024 values, using series of resistances in the case of flash ADCs (Figure 4.6). A comparator is used between the input charge and various discrete charges to find the input charge corresponding digitised value as illustrated in Figure 4.6. The high gain channel allows to digitise accurately low

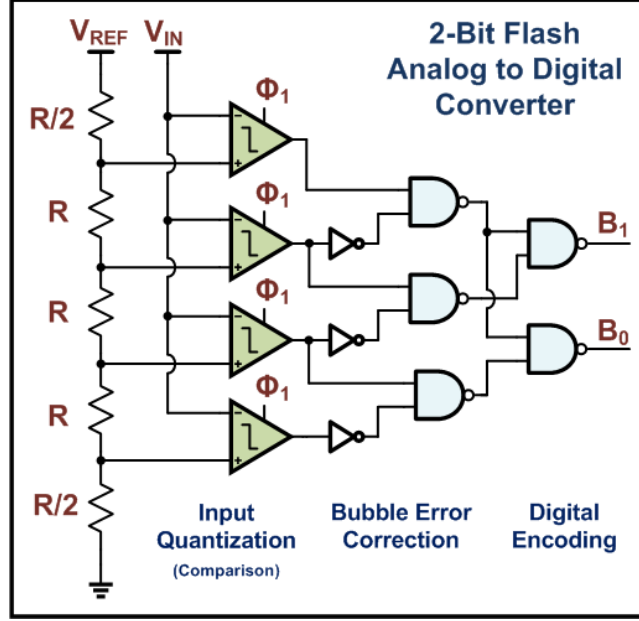


Figure 4.6: The example of a 2 bit flash ADC. Extracted from [61].

input charges. The other side of the coin is that the ADC saturates for relatively low input charges ( $\sim 40$  p.e (see Section 4.2) which correspond to the input voltage  $V$  reaching the reference voltage  $V_{ref}$ . On the contrary, the low gain channel has a smaller accuracy for low charge measurements, but a broader range that allows to even measure the high energy deposition in the scintillator. However, the ADC performances are not uniform over the dynamical range. In particular, ADC are known to have a non linear response with the input voltage over the possible digital range. These non linearities may highly impact the digitised charge value and should be corrected before using the charge as a variable in the analyses. In this thesis, we have performed this non linearity calibration which is presented in Section 4.2.

## 4.2 Charge response calibration

### Gain monitoring

In Section 4.1, , we noticed that the MPPC gain may vary during data taking due to changing external conditions. For this reason, it is crucial to monitor the gain for all MPPC channels in order to correct these variations. For each MPPC and each low/high gain channels, the noise spectra are registered to measure the pedestal and the gain. Figure 4.7 shows both the low and high gain distributions for one of the MPPC channels. The pedestal and one photo-electron peak positions are estimated using a gaussian fit. For each input charge  $Q$ , the pedestal  $P$  is first subtracted which gives the number of ADC counts separately for the low and high gain channels. Second, the remaining charge is divided by the gain  $G$  to deduce the number of photo-electrons: Charge in p.e =  $\frac{Q-P}{G}$ . For the high gain channel, the gain is measured as the difference between the one photo-electron peak and the pedestal value and is generally  $G \sim 10$ . For the low gain channel, one remarks in Figure 4.7 that the gain is too small to discriminate between these two peaks. The low gain value is therefore deduced from the high gain value divided by a factor of ten. It assumes no gain variations downstream the low and high gain separation in Figure 4.5. This assumption seems reasonable at the first order since the MPPC is the main cause gain variation, but neglects any possible differences in the separate electronics of these two channels. For each data set, we apply corrections using such distributions to remove possible variations coming from the MPPCs. One remarks that electronics variations are also taken into account in this measurement.

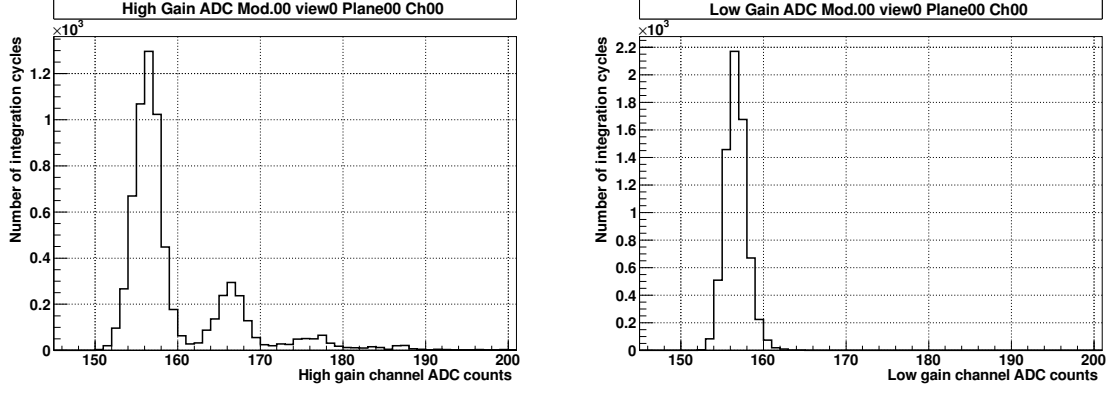


Figure 4.7: Gain and Pedestal measurement. How these curves are generated. In this case, gaussian fit gives pedestal =  $156.31 \pm 0.02$ , and 1 p.e =  $166.37 \pm 0.07$  for HG distribution, which implies a gain =  $10.06 \pm 0.07$ . For LG, pedestal value =  $156.66 \pm 0.02$ .

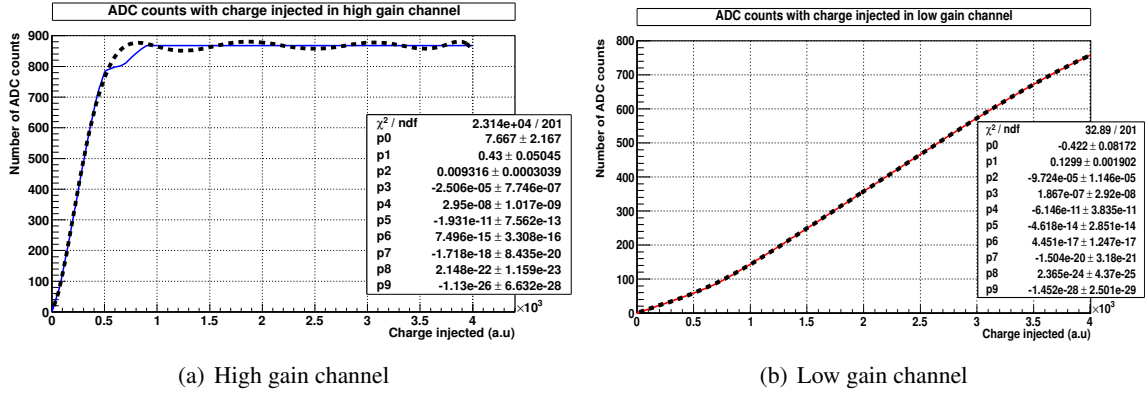


Figure 4.8: Data showing number of ADC counts for a given input charge in the high gain channel (left) and low gain channel (right). The pedestal values has already been subtracted. Data are fitted by a degree 9 polynomial (dashed) to remove possible discontinuous variations between data points.

### ADC non-linearity measurements

We introduced in Section 4.1.4 the ADC non linearities over their whole operating range. To evaluate and correct these effects, each Trip-T has a charge injection circuit. It generates a chosen charge in the circuit. This allows to inject an increasing charge to measure the ADC response for a large set of input charges. The charge injection runs we are using in this thesis have been taken in January 2011 together with Thomas Dealtry. Figure 4.8 shows an example of the outputs of these charge injection runs for chosen high and low gain channels. One remarks the saturation of the ADC response in the high gain channel for an input charge around 500 a.u. Figure 4.9 clearly shows the non linearities over the range for different channels.

For each channel, the ADC distribution is fitted by a degree nine polynomial to remove possible discontinuities between data points. These fitting functions will be used to correct ADC non linearities. Figure 4.8 shows some examples of these fits. Finally, Figure 4.9 shows the different behaviour of various Trip-T channels. This clearly indicates that a different non linearity correction should be used for different Trip-T to minimise the difference between channels.

### ADC non-linearity corrections

We explained in Section 4.2 that the channel gain was measured from time to time to correct potential variations coming from the MPPC or electronics. It is independent from the charge deposition in the scintillator. We will now modulate these corrections with the input charge in order to correct for the ADC non linearities.

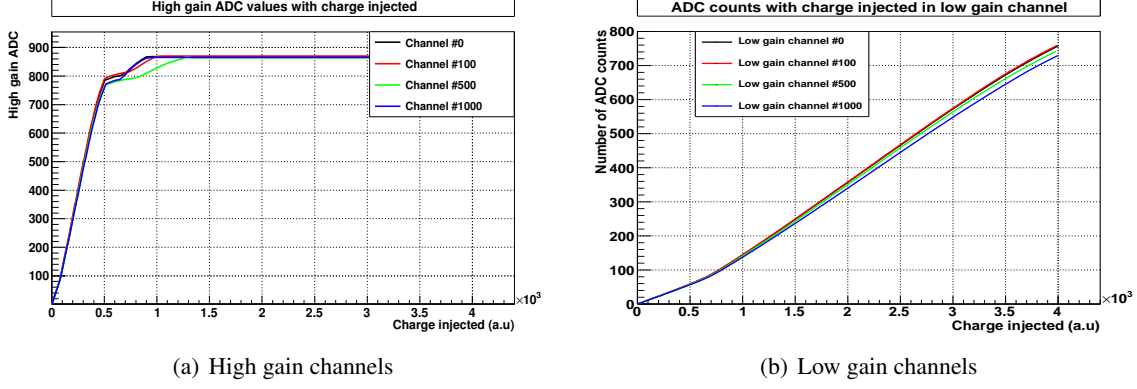


Figure 4.9: Data showing number of ADC counts for a given input charge in the high gain channel (left) and low gain channel (right) for different channels (Trip-T). The pedestal values has already been subtracted. One notices the ADC non linear response which is illustrated more clearly for charges around 100 a.u for high gain channels or charges around 800 a.u for low gain channels.

This procedure is described in the following steps, and replaces the former gain correction described in Section 4.2. For a given charge deposition in the scintillator:

1. The high and low gain ADC counts are subtracted by their respective pedestals measured as in Section 4.2 to deduce the number of relative ADC counts, that we will note “# ADC counts”.
2. The number of relative ADC counts is corrected by a gain  $G_{\text{corr}} = G \cdot C_{\text{ADC counts}}$  which is obtained after correction of the gain measured in the channel  $G$ . The correction factor  $C_{\text{ADC counts}}$  depends on the charge (in ADC counts) and is described below.

The latest point we raised provides the real charge input in a channel:

$$Q_{\text{signal}} = \frac{\text{\#ADC counts}}{G \cdot C_{\text{ADC}}} \quad (4.2.1)$$

and we would like naturally to extract the correction from the known gain measurement point in the high gain channel (used as a pivot):

$$Q_{\text{\#ADC}_G} = \frac{\text{\#ADC}_G}{G} \quad (4.2.2)$$

with  $\text{\#ADC}_G$  the relative ADC counts separating 1 photo-electron from pedestal. It provides the correction factor:

$$C_{\text{ADC}} = \frac{Q_{\text{\#ADC}_G} \cdot \text{\#ADC counts}}{Q_{\text{signal}} \cdot \text{\#ADC}_G}. \quad (4.2.3)$$

The ratio  $\frac{Q_{\text{\#ADC}_G}}{Q_{\text{signal}}}$  is estimated using the charge injection runs. For the given signal  $Q_{\text{signal}}$  in photo-electrons (hit in data), the number of ADC count is measured and the associated charge in arbitrary units can be retrieved using polynomial fit of distributions shown in Figure 4.9. Let's note  $Q'_{\text{signal}} = \frac{\text{\# ADC counts}}{\text{Gradient}(\text{\#ADC counts})}$  this associated charge (in arbitrary units) to distinguish it from  $Q_{\text{signal}}$  in photo-electrons. The gradient( $\text{\#ADC counts}$ ) is simply the conversion factor evaluated using polynomial fits and depends on the number of ADC counts because of the non linearities. Since  $Q$  and  $Q'$  are simply expressed in different units (so differ by a constant factor), we obtain:

$$\frac{Q_{\text{\#ADC}_G}}{Q_{\text{signal}}} = \frac{Q'_{\text{\#ADC}_G}}{Q'_{\text{signal}}} = \frac{\text{Gradient}(\text{\#ADC counts}) \cdot \text{\#ADC}_G}{\text{Gradient}(\text{\#ADC}_G) \cdot \text{\# ADC counts}} \quad (4.2.4)$$

which finally gives the correction factor:

$$C_{\text{ADC}} = \frac{\text{Gradient}(\text{\#ADC counts})}{\text{Gradient}(\text{\#ADC}_G)} \quad (4.2.5)$$

and thus we obtain the input charge corrected by ADC non linearities from Eq 4.2.1:

$$Q_{\text{signal}} = \frac{\# \text{ ADC counts}}{G \frac{\text{Gradient}(\# \text{ADC counts})}{\text{Gradient}(\# \text{ADC}_G)}} \quad (4.2.6)$$

This correction is only possible for the high gain channel since the gain measurement is not directly possible for the low gain channel. But the charge injection runs provides a pivot that allows to deduce the low gain value from the high gain. Using the polyomial fits, we can estimate the input charge  $Q'_{\# \text{ADC}_G}$  (in arbitrary units) associated to the 1 p.e peak in high gain channel. Using the polyomial fit for the low gain channel, one retrieves the corresponding number of ADC in low gain channel  $\# \text{ADC}_G^{\text{Low}}$ . We deduce directly the gain in the later channel:  $G^{\text{Low}} = \frac{\text{ADC}_G^{\text{Low}}}{1 \text{ p.e}}$ . This procedure allows to check the low gain values instead of relying on the capacitance theoretical values. Moreover, it allows to apply now the same procedure as described above (for high gain channels) to correct the ADC non linearities in the low gain channel. We applied this procedure for all the channels in the sixteen INGRID modules and in the PM.

### 4.3 Calibration results using INGRID data

In this section, we apply the calibration of Section 4.2 to the INGRID and PM data. We use the INGRID data that were taken shortly after the charge injection runs we are using, namely T2K run 3c data (April-May 2012). We use the “sand muon” data sample in order to allow accurate comparison with the MC. The so called “sand muons” are muons produced by the T2K beam neutrinos interacting in the rock surrounding the detector. These sand muons represent a very pure sample of muons that are reaching the INGRID detector and are used for various purposes in this thesis.

#### 4.3.1 Neutrino event and sand muon selections

We present here the two data samples that will be used in this analysis: the neutrino event and the sand muon samples.

##### Neutrino event sample

The neutrino event sample is based on the original identification of a the decay muon emitted through charged current interaction of a neutrino in the detector. In both INGRID and the PM, this selection is based on the same nine cuts:

1. Timing clustering: the reconstruction is started if there are more than 6 hits (charge deposition  $> 2.5$  p.e) in a 100 ns window in an INGRID or PM module. All the hits within a  $\pm 50$  ns of the average time of the cluster are considered to be a part of it. This allows to reduce the random MPPC noise hits contamination. For SciBar type scintillators in the PM, a hit is not defined by a charge deposition higher than 2.5 p.e but higher than 10 p.e. We added this cut to the original reconstruction to remove the optical cross-talk effect that has been observed in Section 4.3.5 and measured in Section 4.4. The motivations to choose the 10 p.e value are explained in Section 4.3.5. Therefore, prior to Section 4.5, the 10 p.e cut will not be applied unless the opposite is specified.
2. Number of active planes selection: one active plane is defined as a coincidence of a hit of more than 6.5 p.e both on the x and y view of a same tracking plane. 2 active planes at least are required in this selection to further reduce the MPPC noise contamination.
3. Two-dimensional track reconstruction: the algorithm is based on the cellular automaton method used in the K2K SciBar detector. This consists in an iterative procedure that gathers hits of the same plane in “clusters” and matches them with different plane clusters in “cells”. This algorithm starts from the downstream planes to the upstream ones and adds different clusters in a “neighbour” by performing a linear fit for 2 cells and checking that the reduced  $\chi^2 < 1.5$ .

Each time a cell has an upstream neighbour, the cell state value is increased by one. This allows to identify the end points of a candidate track as the higher cell values which does not have any neighbour with higher state value. This procedure has a tolerance of one non-hit plane in order to deal with possible hit inefficiency. When this procedure is finished, a final iterative procedure is used to check if the whole track is linear and not only constituted of neighbours which are aligned two by two. Starting from the most downstream points of each possible candidate tracks, each cell is added layer by layer and a linear fit is done for each new layer added. The tracking is stopped during this iterative process if the most upstream cell is reached or if the  $\chi^2 > 2$  after having added a cell. This algorithm is summarised in [62].

4. Three-dimensional track reconstruction: the 2-dimensional tracks are matched between the XZ and YZ views. The matching requires that the distance between the most upstream points of each track is  $\leq 3$  planes. If several tracks of YZ view can be matched with one of the XZ view, the track with the closest upstream plane from the one in the XZ view is matched. If several tracks match this criterion, the tracks with the closest downstream points are matched. Note that in the case of the PM, the two latter criteria are not used. It allows several tracks of one 2-dimensional view to be matched with the same 2-dimensional track in the other view. In the case the proton and the muon are superimposed in one of the two view, this condition is necessary to reconstruct the proton (which has a lower penetration depth in most of the cases).
5. Vertexing: several three-dimensional tracks are searched and gathered in a vertex. A pair of three-dimensional tracks are gathered in the same vertex if they satisfy the following condition on their most upstream points:

$$|\Delta Z_X| + |\Delta Z_Y| \leq 1 \text{ plane} \quad (4.3.1)$$

where  $\Delta Z_{X(Y)}$  are the plane difference between the most upstream point in the XZ (respectively YZ) planes. On top of this “longitudinal condition”, a “transverse condition” is also used:

$$\sqrt{|\Delta X| + |\Delta Y|} < 15.0 \text{ cm} \quad (4.3.2)$$

where  $\Delta X$  ( $\Delta Y$ ) is the distance between the X (respectively Y) position of the 2 track vertices. When two tracks are identified to belong to the same vertex, the most upstream point of the longest track is defined as the vertex. If the two tracks have the same length, the upstream point of the track with larger charge per unit length is used as the vertex. More than 2 tracks can belong to the same vertex, and in this case, the same vertex definition is used as in the case of 2 tracks.

6. Beam timing cut: requires that the event timing is within  $\pm 100 \text{ ns}$  around the expected neutrino bunch timing. The event timing is defined as the time of the channel with the largest number of photo-electrons in the cluster. This cut mainly removes contamination from external background as cosmic ray muons.
7. Upstream VETO cut: the event is rejected if it has a hit in the first tracking plane (in the first two planes for PM). Moreover, the event is also rejected if it has a hit in the side veto planes that is closer than  $8.0 \text{ cm}$  from the extrapolation of the track. These two cuts allow to remove mostly the high contamination from the sand muons coming from the wall.
8. Fiducial volume cut: the event is rejected if its vertex is located out of the fiducial volume (FV). The INGRID fiducial volume is defined as a square transverse area of  $\pm 50 \times \pm 50 \text{ cm}^2$  that spreads from the first iron layer to the ninth tracking plane. The last iron plane and 2 last tracking planes are removed since the tracking requires at least 2 neighbours which means 3 tracking planes. The PM fiducial volume has the same transverse area that spreads from the second to the sixteenth tracking plane. This cut allows to remove the sand muons that may pass the veto cut.

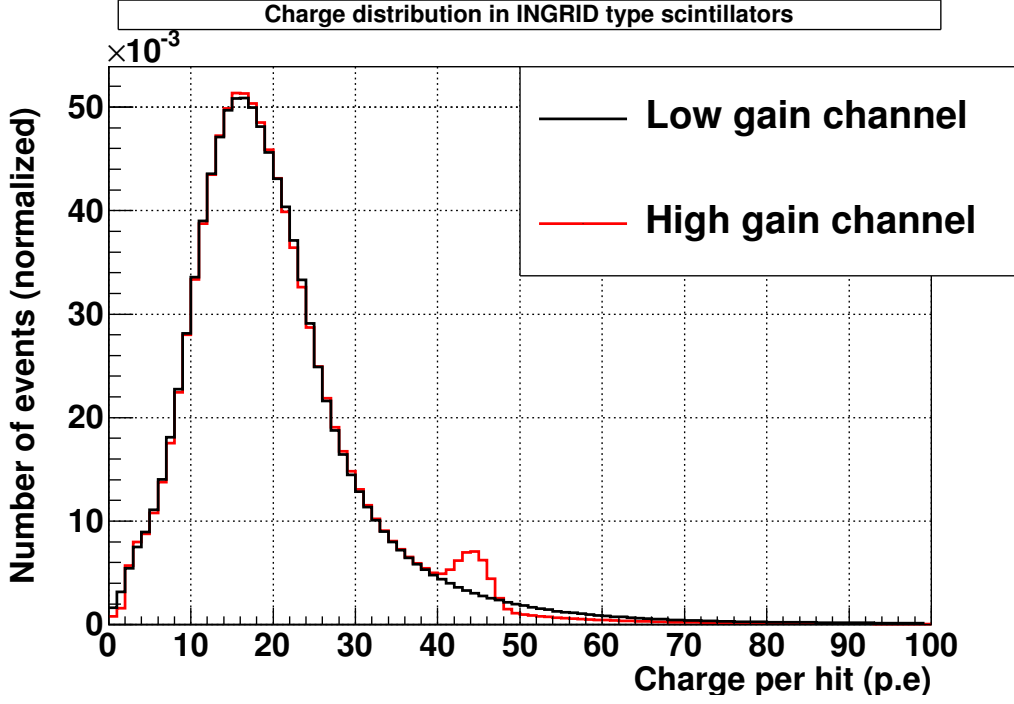


Figure 4.10: Charge distribution of the sand muons data for the low and high gain channels.

#### Sand muon sample

As described earlier, the sand muon sample is used for various calibrations and studies. The selection is exactly similar to the event neutrino selection, removing the upstream veto and the fiducial volume cuts.

#### 4.3.2 Low and high gain channel charge ranges

The low and high gain channels have been installed to allow an accurate charge measurement in different charge ranges. In this section, we determine the interplay between these 2 channels in order to reach the best performances in charge measurements. Figure 4.10 shows the charge distribution of the sand muon sample data for both the low and high gain channels. One observes the ADC saturation around 50 p.e in the high gain channel which imposes the use of the low gain channel for such input charges and higher. On the other side, one observes the shift in the peak corresponding to the minimum ionizing particles between low and high gain channels. On top of this, Figure 4.11 shows a difference in charge distributions for low charges ( $< 10$  p.e) between the two channels. This indicates the low gain channel should not be used over the whole range and we will prefer to use high gain channel for low charge values. For symmetry reasons, it seems reasonable to use the mean charge deposition  $\frac{\text{Charge in low gain channel} + \text{Charge in high gain channel}}{2}$  to determine the regions where low or high gain channels should be used. This also prevents from possible fluctuations in one of the 2 channel responses that may happen if we were only using the charge of one of the two channels. In order to optimize charge calibration, we'd like to separate the charge range in two regions where one should use either the low gain channel information or the high gain channel channel one. This limit must be defined so that the changes between the two regions is done continuously, *e.g* without sudden variations in the charge distribution. To match this criterion, we have studied the distribution of the charge ratio between high and low gain channel for a given hit  $\frac{\text{Charge in high gain channel}}{\text{Charge in low gain channel}}$ . Ideally, the limit should be set for a ratio distribution which:

1. has a mean value close to 1, which guarantees no shift in the average charge response of the channels between low and high charge regions.
2. has the lowest root mean square as possible, which guarantees that this limit would give a correct charge response for each individual channels.

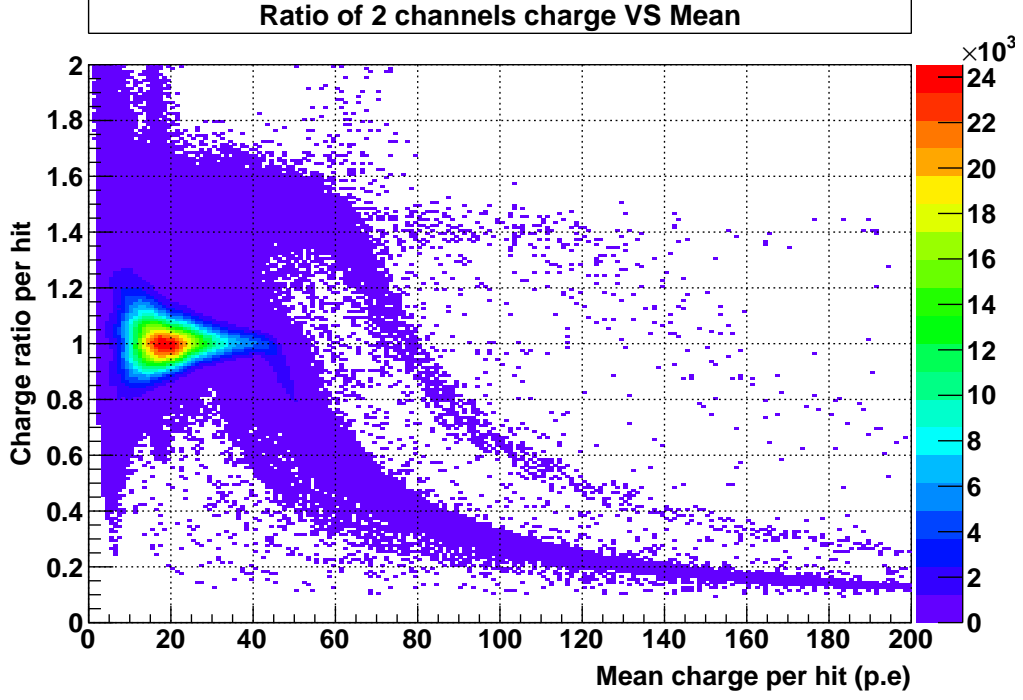


Figure 4.11: Ratio of the charge in the high gain channel by charge in the low gain channel  $\frac{\text{Charge in high gain channel}}{\text{Charge in low gain channel}}$  with the mean charge value  $\frac{\text{Charge in low gain channel} + \text{Charge in high gain channel}}{2}$ .

Figure 4.11 shows the variation of the charge ratio with the mean charge deposition. One observes that the ratio value seems centered around one for charges before high gain channels saturation, which confirms that there is no global shift between low and high gain channels. On top of this, one notices that the width of the ratio distribution decreases when the mean charge increases until the high gain saturation is reached. This was expected since one expects the resolution of the low gain channel to increase gradually with charge and match the high gain channel resolution at some point. This point should be reached before the high gain channel saturation provided that a correct choice of ADC (10 bits) and gain differences between low and high channel was done.

In order to determine quantitatively the limits between the 2 regions, we projected the ratio values for different mean charges and fitted the ratio distributions by a gaussian. Figures 4.12 shows the results for mean charge going from 35 to 44 p.e. Table 4.1 summarises the mean and root mean square values of the fitting gaussians.

One observes in Figure 4.12 that the high gain channel saturation appears on the distribution at 42 p.e. The distribution is clearly shifted towards lower charge ratio which indicates a smaller charge in the high than in the low gain channel. This shows that the limit value should be chosen at a lower value, preferentially at 41 p.e according to results in Table 4.1 and following the arguments we developed above. However, this table also shows that root mean squared and mean gaussian values are similar for 39 p.e to 41 p.e. In order to minimise the shift between the low and high gain charge regions, but also to remain safely far from the saturation region, we decided to set our cut value at  $\frac{\text{Charge in low gain channel} + \text{Charge in high gain channel}}{2} = 39$  p.e. This later criterion minimises the risk of saturation in the case of gain variations between the T2K data sets. These potential variations will be studied in Section 4.5.

Both results for the INGRID type scintillators of the INGRID detector are shown. Note that the same calibration has been applied to the PM because the MPPCs and electronics are the same.

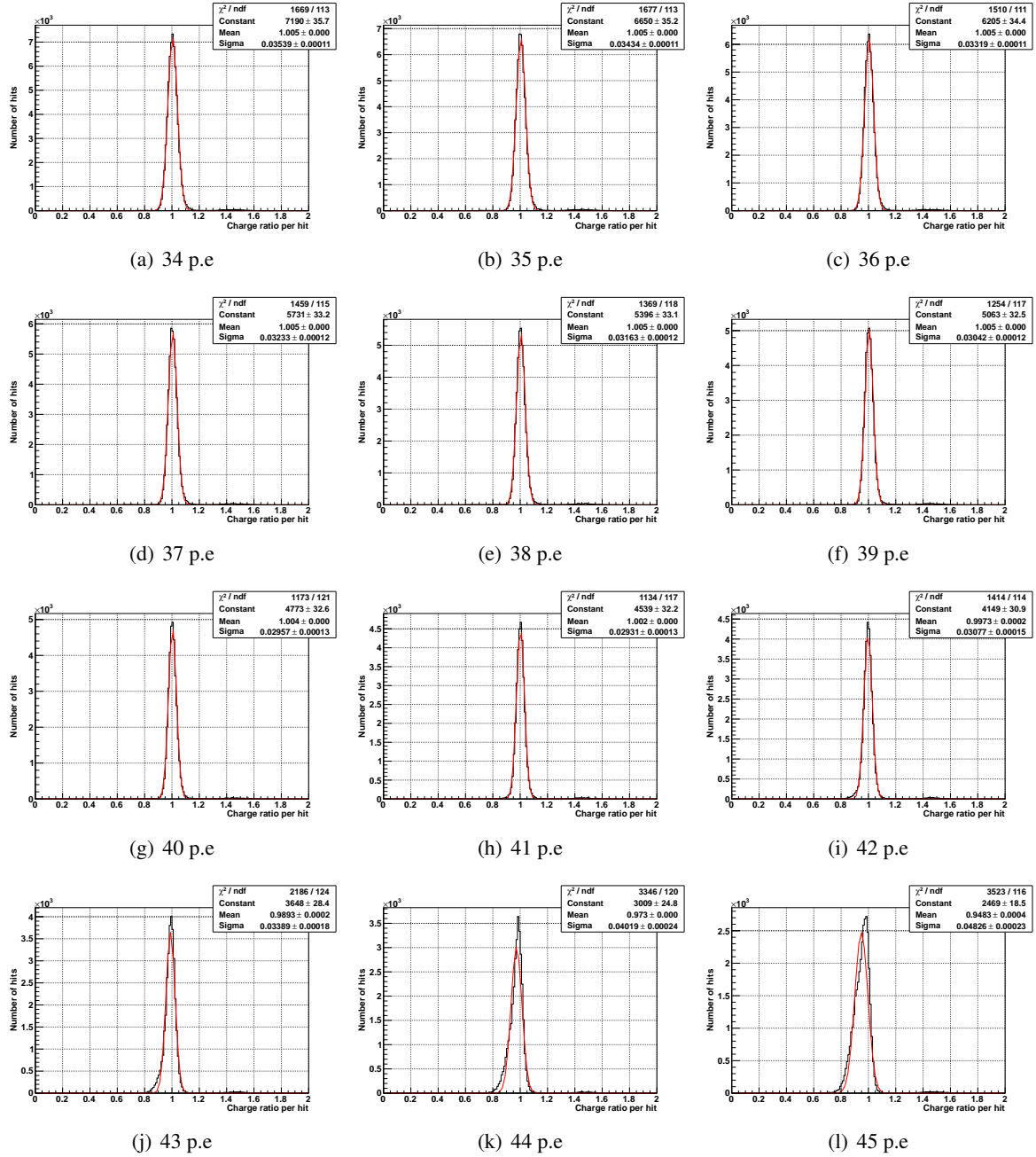


Figure 4.12:  $\frac{\text{Charge in high gain channel}}{\text{Charge in low gain channel}}$  distributions for mean charges ( $\frac{\text{Charge in low gain channel} + \text{Charge in high gain channel}}{2}$ ) varying from 34 to 45 p.e. The distributions are fitted by a gaussian to extract their mean and root mean square.

	34 p.e	35 p.e	36 p.e	37 p.e	38 p.e	39 p.e	40 p.e	41 p.e	42 p.e	43 p.e	44 p.e	45 p.e
Mean $\mu$	1.005	1.005	1.005	1.005	1.005	1.005	1.004	1.002	0.997	0.989	0.973	0.948
RMS $\sigma$	0.035	0.034	0.033	0.032	0.032	0.030	0.030	0.029	0.031	0.034	0.040	0.048

Table 4.1: Values of the mean  $\mu$  and root mean square  $\sigma$  of the gaussian fits for different mean charge values (34 to 45 p.e).

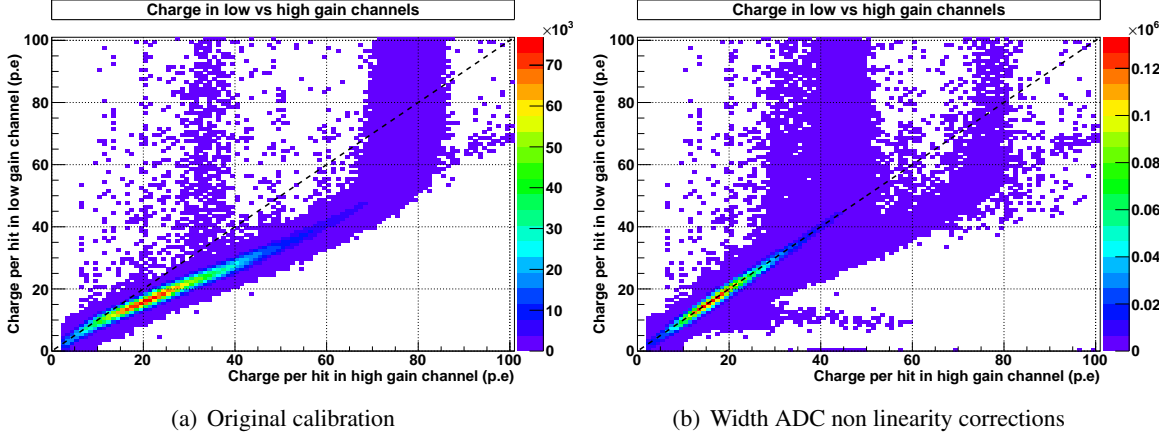


Figure 4.13: Low and high gain channel response comparison for various input signals in the case of correction (or not) of the ADC non linearity effect.

### 4.3.3 ADC non linearity calibration validation

#### Differences with previous data set

Figure 4.8 shows that the low gain ADC channel seems to behave linearly from 0 to nearly 100 ADC counts. This range corresponds approximatively to 0 to 100 p.e given the gain of the low channel. Since the gain is deduced from the high channel measurement, one expects that the charge deposition should be correctly deduced in the low gain channel. On the contrary, the high gain channel should have a higher resolution in the same range, but with a high probability of non-linearities (Figure 4.8). At first order, the low gain channel should be used to check if ADC non linearity has been efficiently corrected in the high gain channel and if it seems reasonable to use the high gain channel high resolution in this range. Figure 4.13 shows the comparison between high and low gain channel measurements for the same charge deposition in the case of ADC non linearities corrected (right) or not (left). One observes the original shift between low and high gain channel responses in the case of lack of correction. For example, a 40 p.e signal in the low gain channel is measured to be 60 p.e in the high gain channel. As primarily shown in Figure 4.11, this effect is clearly corrected when the correction method is applied (right of Figure 4.13). This clearly confirms the validity of the correction, while emphasizing the difference with the lack of correction in the former calibration.

#### Comparison with simulation

In this section, we show how the ADC non linearity calibration improves the agreement between data and simulation. For the INGRID detector only, Figure 4.14 shows the charge deposition distribution for the sand muon sample in the case of the INGRID scintillators. One observes the improvement of data and MC agreement obtained by correcting the ADC non linearities. However, we observe a residual discrepancy between data and MC in the low charge region around 5 p.e. This effect is further described in Section 4.3.4 and related to the simulation of the low energy hadrons, probably coming from neutrons slowed down in the INGRID iron. On top of this, the minimum ionization peak (MIP) is broader in data than in MC. This effect is probably due to the under estimation of the electronic noise in the simulation. One concludes the agreement between MC and data is better than 10% in the MIP region and the average agreement between data and MC in the high charge region ( $> 60$  p.e)

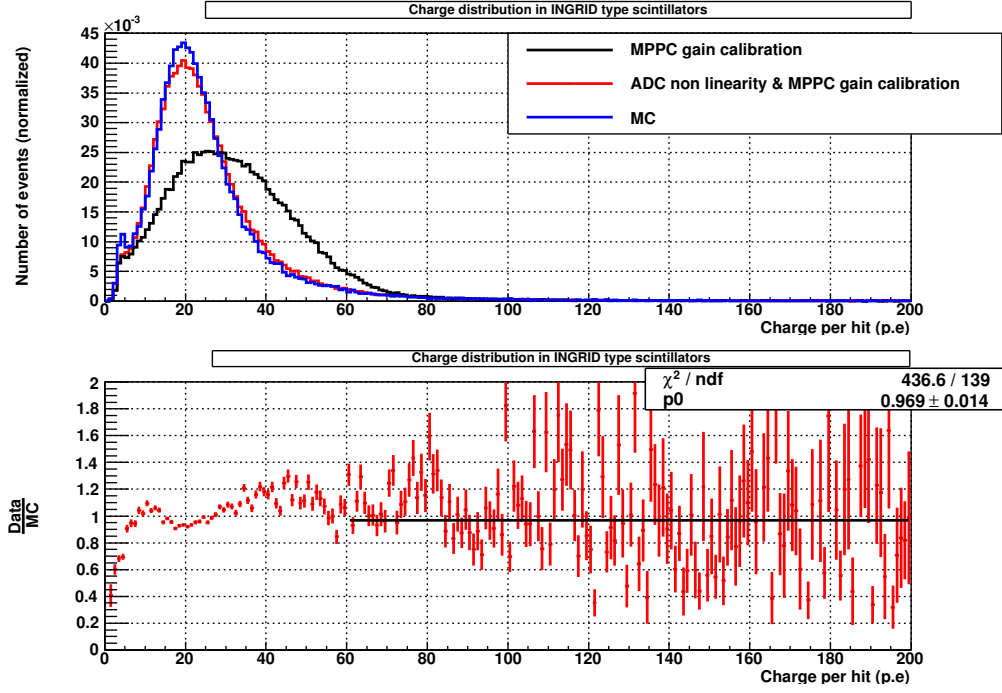


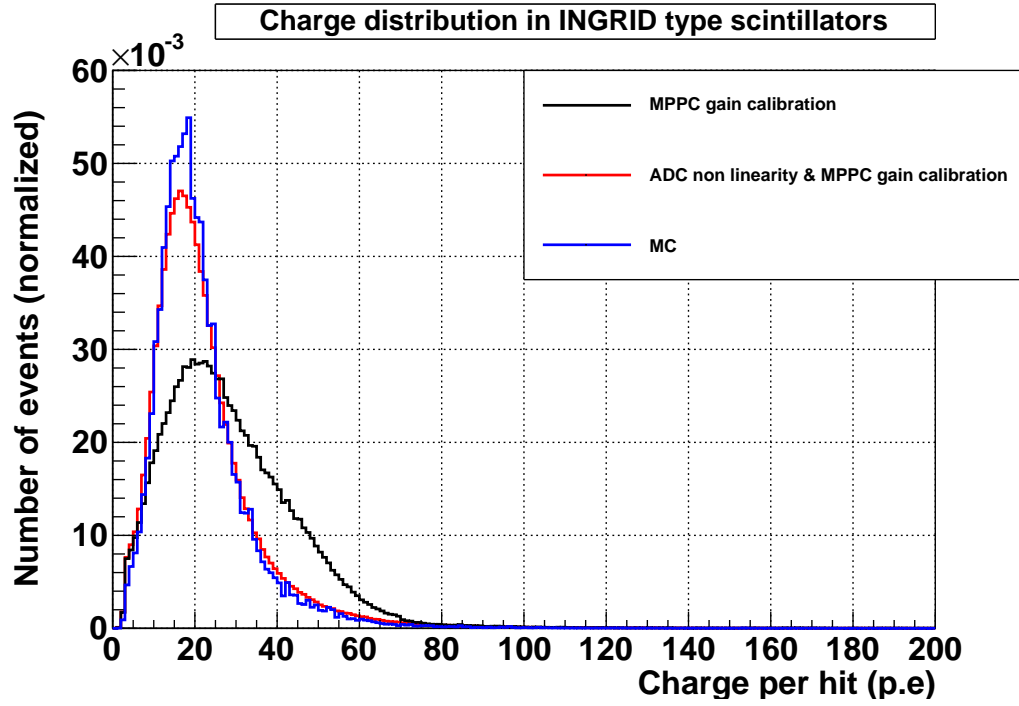
Figure 4.14: Charge distribution of the hits of sand muon sample in INGRID comparing new and former calibration to the simulation. As for the former calibration, we have applied the same cut to discriminate between regions to use either low or high channel regions (namely 39 p.e)

is around 3%.

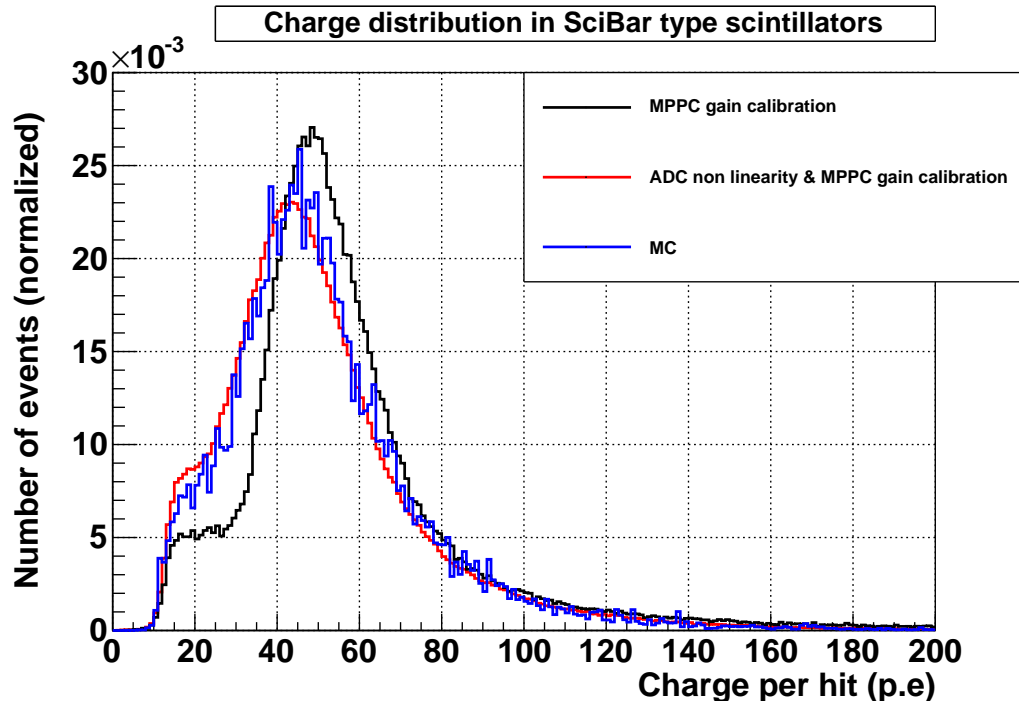
We performed the same comparison for the INGRID and SciBar type scintillators of the PM. We described in Section 2 that each PM tracking plane possesses 32 scintillators of two different types: INGRID or SciBar types. These SciBar type scintillators have smaller width and larger thickness ( $120 \times 2.5 \times 1.3 \text{ cm}^3$ ) in order to increase resolution in the detector central part while keeping a high light collection efficiency. Figure 4.15 shows the charge deposition distributions for INGRID type scintillators of the PM. It clearly indicates the same trend as INGRID type scintillators of INGRID. The improvement of the agreement using ADC non-linearity calibration is clearly visible. As for the SciBar type scintillators located near the detector center, one observes a slightly better agreement between data and MC than in the INGRID, except at low charge value. This discrepancy is due to remaining optical cross-talk that is not perfectly removed by the cross-talk cut we introduced. This effect is presented and measured in Sections 4.3.5-4.4. This comparison validates the use of calibration study to take into account ADC non linearities, and we will use this new calibration for all the analyses detailed in this thesis.

One notices the higher value of the MIP ( $\sim 42 \text{ p.e}$ ) for SciBar type scintillators than for INGRID type ones ( $\sim 17 \text{ p.e}$ ). This is mainly due to the higher light collection efficiency by the fiber due to the smaller width of the SciBar scintillators: 2.5 cm instead of 5.0 cm. Such a geometry allows a higher light collection for the same charge deposition and a lower attenuation in the scintillator. Moreover, the higher SciBar type scintillator thickness (1.3 cm) as compared to the INGRID ones (1.0 cm) allows a 30% larger energy deposition in the scintillator.

Chronologically, after the development of this new calibration, its higher resolution on charge revealed some formerly hidden discrepancies between data and MC. We have mainly corrected them in the simulation and the reconstruction used in this thesis (Figures 4.14 and 4.15). In the following sections, we will present these discrepancies, and how we determined their physical origins and corrected them.



(a) INGRID type scintillators



(b) SciBar type scintillators

Figure 4.15: Charge distributions of the hits of sand muon sample in PM comparing new and former calibration to the simulation. The results has been shown both for INGRID type (top) and SciBar type scintillators (bottom) of the PM.

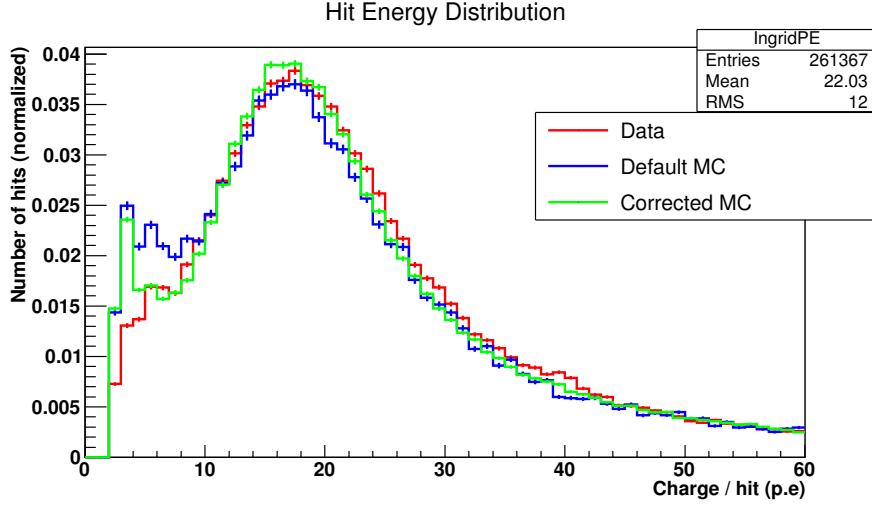


Figure 4.16: Charge distribution for neutrino events sample comparing data and mc simulation with (Corrected) and without (Default) Birks attenuation corrected. The MC simulation used in this thesis has Birks attenuation saturation corrected.

#### 4.3.4 Birks saturation correction

Using the original INGRID MC, we had compared the data and simulation just after performing the new calibration. At that time, an important discrepancy between data and MC was still observed in the charge distribution of the neutrino event sample. Figure 4.16 shows this disagreement between the data (red) and the original INGRID MC (blue).

This investigation leads us to improve the Birks saturation effect in the simulation, which was not correctly taken into account before. This effect corresponds to a non linear behaviour of the scintillator with the photon density produced by the passage of a charged particle. In particular, the higher the density (the  $\frac{dE}{dx}$  of the particle in the material) is, the higher the non linearity. This effect can be modeled using the Birks attenuation formula [13]:

$$\frac{dL}{dx} = L_0 \frac{dE/dx}{1 + c_B dE/dx} \quad (4.3.3)$$

where  $L$  is the the luminescence,  $L_0$  the luminescence for low photon density and  $c_B$  the Birks attenuation constant of the material. As for INGRID and PM polystyrene scintillators, this constant has been determined using measurements in the SciBooNE experiment that uses the same Fermilab scintillators:  $c_B = 0.0208$  MeV/cm. We have investigated this effect and have found it corresponds to a problem in low energy hadrons simulation, by stopping the hadrons having  $E < 5$  MeV (see Figure 4.17).

We have then implemented a new function to correct this effect in the MC used in this thesis and have shown the effect in the transformation on charge distributions in Figure 4.16. Though most of the difference with data has been washed out, we can still observe a discrepancy for very low charge ( $\sim 4$  p.e) which remains unexplained in the present work. First, we have decided data and MC similarity is enough for the analyses we performed in this thesis (Chapter 5 and 6). Second, we have paved the way for possible future corrections by showing that this residual effect should come from remaining imperfections in the low energy hadrons simulation (Figure 4.17) or their daughter particles.

#### 4.3.5 Optical cross-talk between the SciBar type scintillators

In the selection defined in Section 4.3.1, we defined a cut to remove optical cross-talk in the scintillator. In the original selection (*i.e* prior to this thesis), this cut did not exist since the cross-talk effect had not been investigated. In fact, the ADC non linearity calibration we have performed has increased the resolution on charge distribution. During the validation of the calibration, we have discovered and

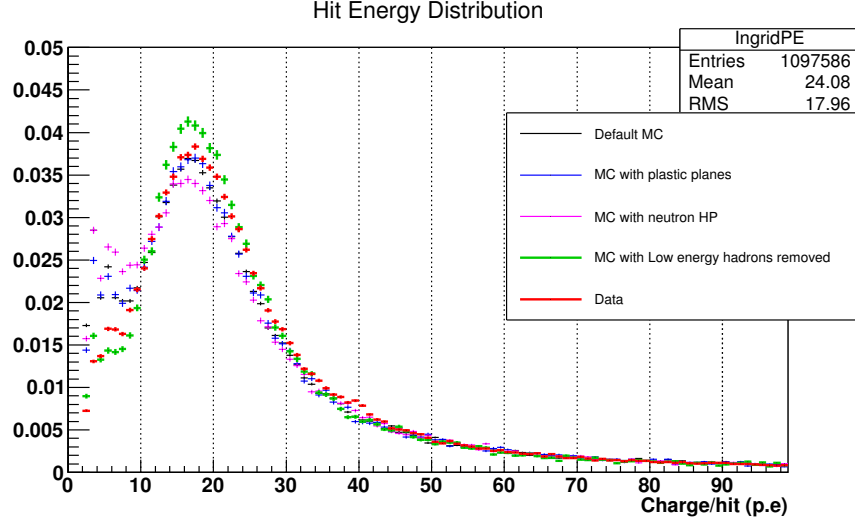


Figure 4.17: Charge distribution for neutrino events sample data and various MC simulation. The original (Default MC) simulation exhibits a large discrepancy with data. Different hypotheses have been investigated to understand this effect, some of which are shown on this figure. In particular, we have simulated the plastic planes that surround INGRID planes to check possible effects on delta electron stopping (Blue). Having found the effect comes from low energy hadrons, we have changed the simulation GEANT4 physics lists [63], namely from the default QGSP/BERTINI (black) to NEUTRONHP, that has higher performances in the low energy neutron simulation (Magenta). Finally, we produced a MC sample for which hadrons are removed when they slow down to a momentum lower than 5 MeV/c (green). This sample indicates better agreement with data.

measured an anomaly in the low charge region that we investigated. In this section, we show that this discrepancy comes from an optical cross-talk between the scintillators. We will then present the setup we built to measure and confirm this effect (Section 4.4).

#### Discrepancy in low charge region for SciBar type scintillators

Figure 4.18 shows (Figure 4.19) the charge distribution for MC and data for sand muons (respectively neutrino event) selection without the cross-talk cut applied. These distributions have been normalised to the number of tracks reconstructed in the PM. For the INGRID type scintillators of the PM we observe a 2.2% hit excess in data in the low charge region (2.5 – 10 p.e) for the neutrino event sample. We will see later that this disagreement is not clearly understood but is small enough to be taken as a systematic error.

The main difference between data and MC can be observed in the SciBar type scintillators. We notice a hit excess in the data in the low charge region (2.5 – 10 p.e) both in the sand muon and the neutrino event samples. This excess has been evaluated in Table 4.2 as the difference between data and MC in this region. A 2.9% excess is observed in the sand muon sample, and a 6.4% excess for the same charge region is measured in the neutrino event sample. This excess is only measured in the SciBar type scintillators in these proportions, and seems to represent a higher percentage of the total number of hits in the case of neutrino event sample than in the case of sand muon one.

	MC	Data	Data-MC		MC	Data	Data-MC
Sand muons	3.0%	5.9%	2.9%	Sand muons	8.7%	10.4%	1.8%
Neutrino events	5.4%	11.8%	6.4%	Neutrino events	8.4%	10.6%	2.2%

Table 4.2: Proportion of the low charge hits  $\in [2.5, 10]$  p.e for data and MC is the sand muon and neutrino event samples.

Possible hypotheses were investigated and we have performed the analyses to discriminate between

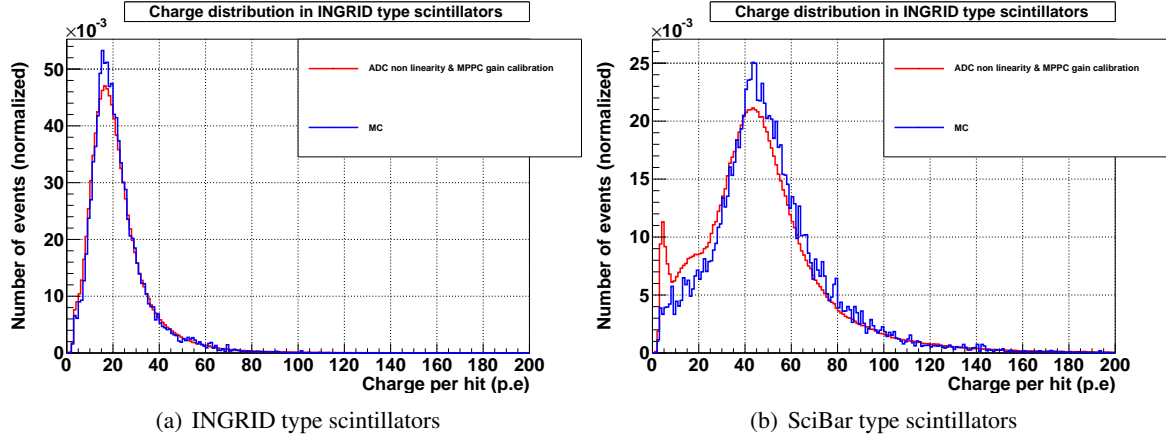


Figure 4.18: Data (red) and MC (blue) charge comparison for the sand muon sample.

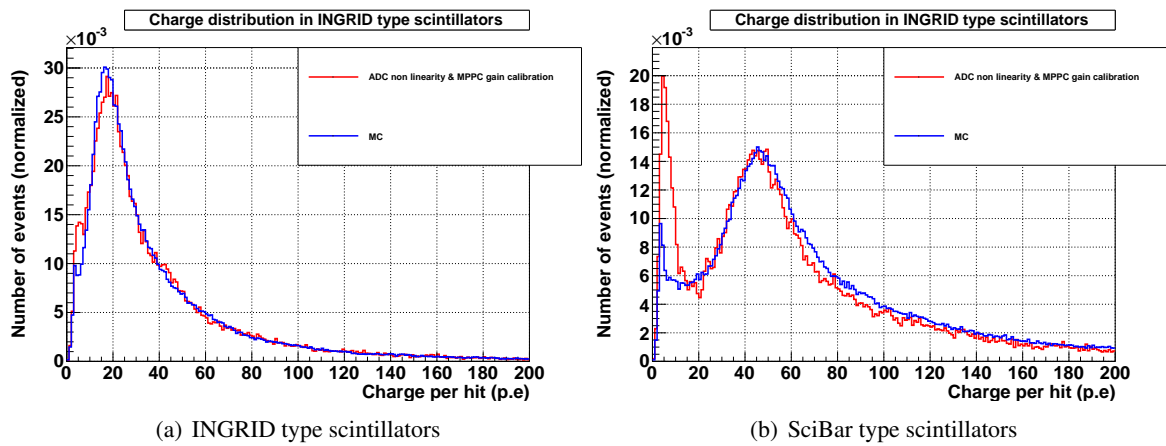


Figure 4.19: Data (red) and MC (blue) charge comparison for the neutrino event sample.

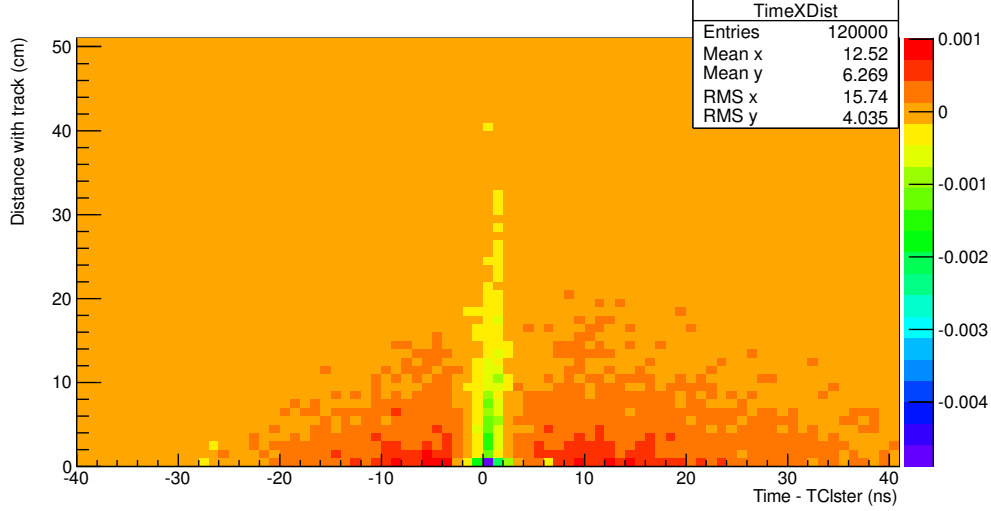


Figure 4.20: Data-MC subtraction of the relative timing and distance distributions for the low charge hits ( $< 8$  p.e) registered in the PM. An original discrepancy exists due to thinner MC time distribution. However, one observes the data excess occurs for hit which are in time and spatially closed to the track.

these possible following sources:

1. Additional damaged channels during the data period used for comparison, that are not taken into account in the simulation.
2. Estimation of the MPPC dark noise that differently affects the center (where SciBar type scintillators are located) and the edge of the detectors since the reconstruction is not homogeneous inside the detector.
3. Neutron background that may affect differently the center and the edge for similar reasons of inhomogeneity in the detector reconstruction.
4. Some particular events/particles which leave a lower charge deposition than neutrino simulated events. These particles may come from the near INGRID modules, the wall or from interactions in the PM.
5. An effect which is observed in all neutrino events but not simulated in the MC as various forms of cross-talk (optical, electronic...) but also decayed particles that may be not simulated (low energy particles for example).

### Characterisation of the anomaly

This anomaly is first investigated by combining the proximity in timing and distance of these low charge hits with the reconstructed track. The low charge hits are defined here as having a charge deposition  $\leq 8$  p.e. Figure 4.20 shows this 2-dimensional distribution. Note that we developed and applied a timing calibration to increase the accuracy of the timing. This calibration is presented in Appendix B. The MC distribution has been subtracted from the data one to show the discrepancy between these two and emphasize the charge excess in data. We observe the low charge excess is in time with the signal which shows it cannot be due to the dark noise simulation. Furthermore, it is mainly located closer than 5 cm from the track, which confirms it cannot be due to a possible neutron or other particle external background. The low charge excess is clearly correlated with the signal. Second, we will show these “abnormal hits” are not isolated, but occurs in a cluster of hit in the same tracking plane. To do so, we have shown in Figure 4.21 the charge deposition in SciBar scintillators only for “single hits” in a 2D PM plane. Here, the term “single” means that we added the charge information of a hit when this is the only hit of the track occurring in the 2D plane. Figure 4.21 shows the corresponding charge distribution. We observe that most of the event excess in the low charge

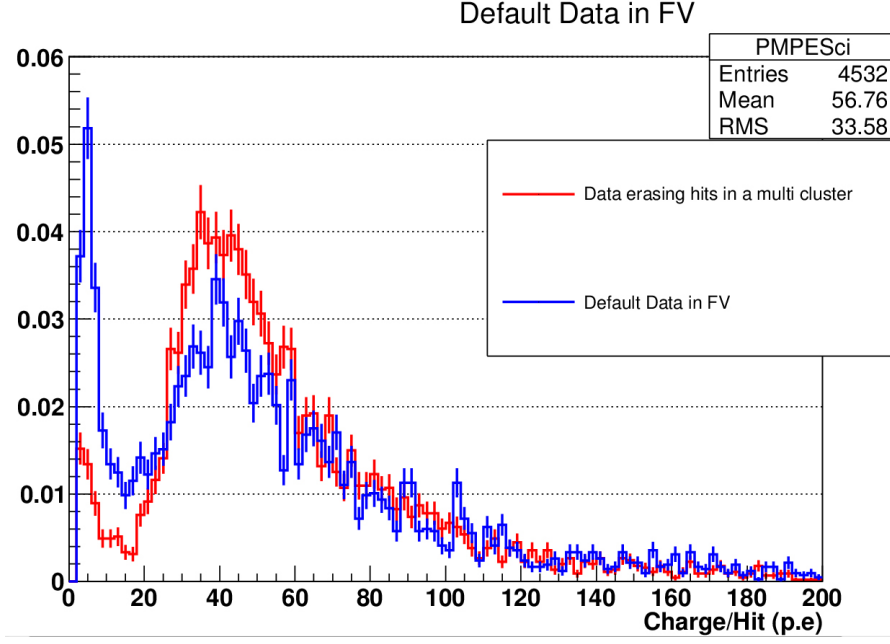


Figure 4.21: Charge deposition comparison between hits of neutrino events tracks with only hits which are isolated in a tracking plane.

region disappear when the non-single hits are removed. We conclude that the low charge excess is not due to specific particles, but is present in most of neutrino and sand muon events due to several hits in the same plane. It leads us to consider three remaining sources for the low charge excess:

1. An unperfect simulation of the scintillators (dead zone and coating of the scintillator, spacing... are not well tuned) that will affect the particles that cross several scintillators in the same plane .
2. Optical cross-talk between the scintillators. The difference between INGRID and SciBar type scintillators would be due to the smaller thickness of the coating for SciBar type scintillators that fails to stop a non-negligible amount of photons (see Figure 4.22).
3. Electronic cross-talk between two MPPCs or two wires. This last argument is very unlikely givent that MPPCs are located in separate black boxes and shielded wires has been used.
4. Signal due to “delta” electrons knocked-out by the particle, that can travel to the neighbour scintillator. Simulations of these delta electrons can be innacurate in the INGRID MC, since the scintillator coating is not simulated as an active region. These electrons are often emitted in the transverse plane and can therefore generate neighbour hits near the main track.

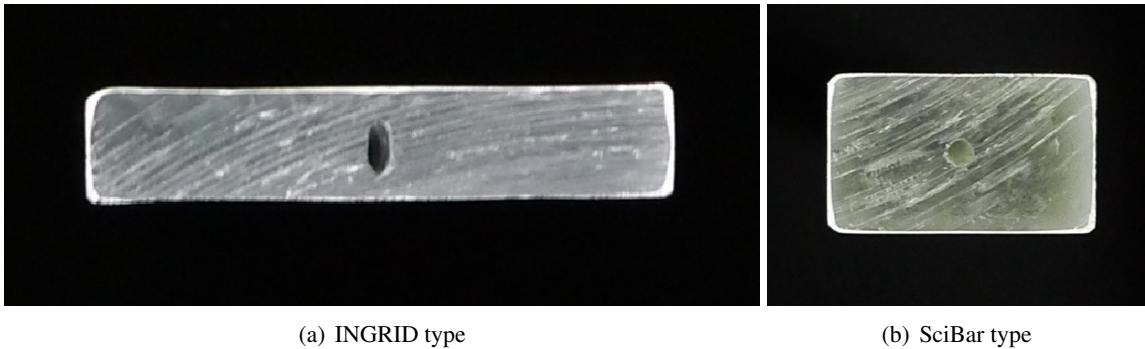


Figure 4.22: Transverse cut of INGRID and SciBar type scintillators. The INGRID and SciBar type scintillator have respectively transverse dimensions 5.0 cm×1.0 cm and 2.5 cm×1.3 cm.

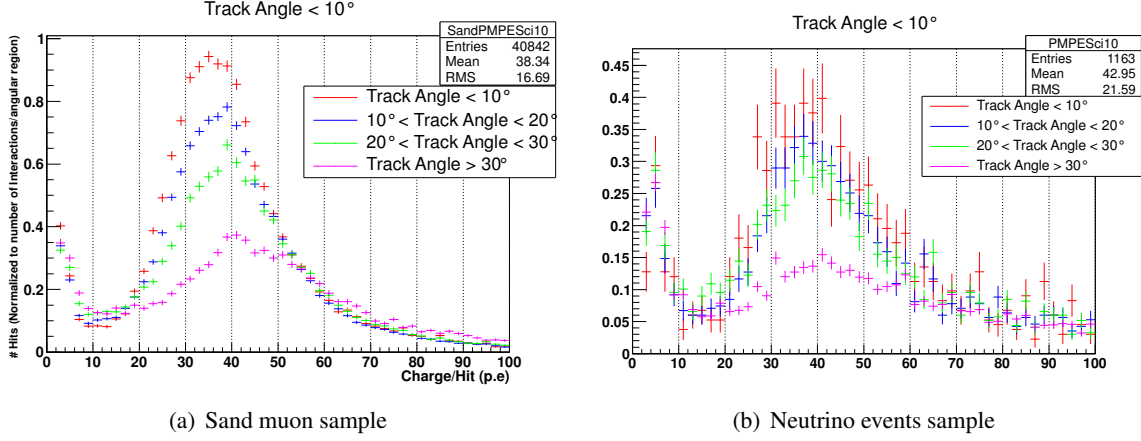


Figure 4.23: Charge deposition distribution of the hits belonging to a sand muon track (left) and neutrino event candidate (right) separating the tracks with their angles.

The first hypothesis is removed by considering sand muon tracks at various angles. One expects the probability of a particle to cross several scintillators in the same plane to increase with the particle angle. We have shown in Figure 4.23 that the charge excess at low energy does not depend on the particle angle.

### Hints of optical cross-talk

We have studied the hits neighbouring the track in order to discriminate between the remaining hypotheses. In particular, we have studied the probability of a low energy neighbour hit (“secondary hit” < 6 p.e) to appear near a higher energy hit in a 2D tracking plane. We have shown that this probability increases with the charge of the hit that has the highest charge in the tracking plane (“main hit”). We used the sand muon through-going (non-stopping in the detector) sub-sample to perform this study, in order to study only minimum ionizing particles. One expects, for the different hypotheses:

1. For particles crossing 2 scintillators in the same plane, the higher the charge deposition of a main hit (long path in the scintillator), the lower should be the energy in the secondary hit due to a smaller path across it. This implies an anti-correlation between the charge of the main hit and the probability to create secondary hits.
2. For the optical cross-talk, the higher the charge of the main hit is, the higher should be the signal in the secondary hit due to the increasing number of propagating photons to its neighbours. One expects a positive correlation between charge deposition in the main hit and probability to have a secondary hit. Moreover, one expects a close to linear relation between these 2 quantities due to the linear variation of number of photons propagating from the main to the secondary scintillators with the charge deposition in the main hit. This cross-talk is not simulated in the MC.
3. In case of electronic cross-talk, one expects a similar prediction as for optical cross-talk.
4. In case of delta electrons, their distribution  $N$  can be written as [13]:

$$\frac{dN}{dTdx} \sim \frac{F(T)}{T^2\beta^2} \quad (4.3.4)$$

with  $\beta$  the velocity of the particle that knocked-out the delta electron and  $T$  the kinetic energy of the emitted electron. Given the Bethe-Block  $\frac{dE}{dx}$  formula, this implies correlation between the charge deposition in the main scintillators and the probability to create secondary hits on each side of the scintillator. Since the charge deposition is also correlated non-linearly with the particle velocity (Bethe-Block formula), it is not trivial to predict the linearity of the probability of secondary hit with the charge of the main hit.

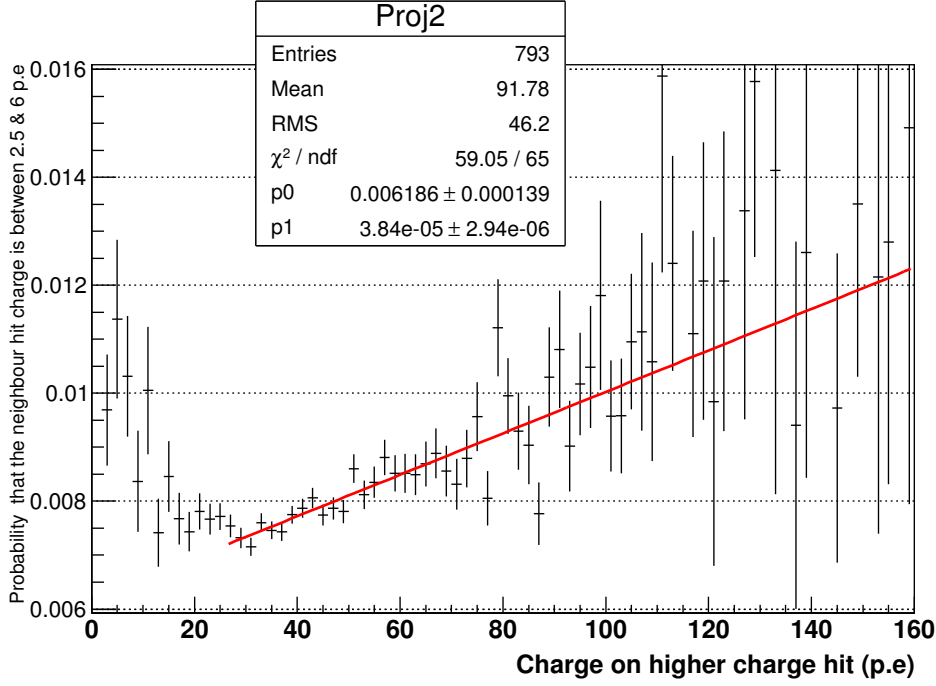


Figure 4.24: Probability for a neutrino event track to have a low energy transverse neighbour hit with the charge of the main hit.

Figure 4.24 shows the probability of secondary hits with the charge of the main hit. One clearly sees two different trends. For low charge in the main hit ( $< 30\text{p.e.}$ ), one observes an anti-correlation with the probability to observe a secondary hit. This region corresponds to hits under the MIP value (around  $40\text{p.e.}$  in SciBar type scintillator), which indicates that this behaviour is due to particles crossing several scintillators in the same plane. The anti-correlation behaviour is in agreement with the expectations. For higher energy, one clearly observes a linear correlation between the probability of a secondary hit and charge in the main hit. This indicates a cross-talk effect or possibly the increasing amount of delta electrons produced with the increasing main hit charge. As discussed earlier, given the linear behaviour, an optical cross-talk hypothesis is clearly favoured. Quantitatively, this observation would correspond to a 8% cross-talk effect at minimum ionising peak value ( $\sim 40\text{p.e.}$  in SciBar type scintillators). In order to ultimately verify this effect, we installed a dedicated setup to measure a possible optical cross-talk effect, which will be described in Section 4.4.

## 4.4 Scintillator cross-talk measurements

### 4.4.1 Scintillator cross-talk measurements

The aim of this study is to determine the probability for some light emitted in a scintillator to give a signal higher than  $2.5\text{p.e.}$  in an adjacent slab, both for SciBar type and for INGRID type scintillators.

#### Experimental setup

The experimental setup is displayed in Figure 4.25. It consists of three scintillator slabs equipped with the same wavelength shifting fibers and MPPCs as used in the INGRID and PM detectors. The length of the slabs has been chosen as  $60\text{cm}$ , which corresponds to the half of the real ones, in order to facilitate their installation in the dark room. The reflective layer of the central slab (numbered as slab #0) has been machined in order to allow for direct light injection from the top of the slab, at any  $y$  position perpendicular to the longest dimension. This  $y$  transverse position is adjustable by means of a screw (see Figure 4.26-left). The  $x$  position of the injection slit has been chosen at the middle of the slab. The three slabs are mechanically constrained to ensure a tight contact between them, as in the real detectors. The white paint at the ends of the slabs is covered by black adhesive tape to avoid

direct light passage between slabs. The scintillator slabs can be changed to SciBar or INGRID type without changing anything else in the setup. The sets of one fiber and one MPPC can be swapped between slabs to check for possible differences in gain of the sets for the conversion of light to electrical signal.

An ultraviolet (UV) light emitting diode (LED) sends light via an optical fiber. Two different wavelengths have been tested for the LED, namely  $400 \pm 3$  nm (model “BIVAR-UV5TZ-400-15”) and  $355 \pm 15$  nm (model “OSA OPTO LIGHT-EOLD-355-525”) and give very similar results. The light coming out of the optical fiber (CAEN model BF1KFCFC-040M) can be seen in Figure 4.26-right, where it is converted to visible light by means of a wavelength shifting polystyrene bar. The light beam is parallel, 0.5 mm in diameter, and its propagation is clearly visible within the 1.5 cm thickness of the bar, despite some absorption. The UV wavelength of 355 nm corresponds to the maximum of emission of the PPO molecule (which is also the maximum of absorption of the POPOP, see Figure 4.27-left). Although the geometry of this UV beam does not exactly reproduce the light emitted by a minimum ionizing particle in the scintillator, we assume that this arrangement allows to correctly mimic the effect of a particle going through the slab. Furthermore, the 355 nm wavelength is absorbed by the titanium dioxide contained in the reflective layer (see Figure 4.27-right), which ensures that we do not introduce any UV light that could directly go from one slab to the adjacent one. From this point of view, the other wavelength (400 nm) seem less adequate, and has been used as a cross-check. As shown later, the similar results obtained with both wavelengths indicate that the direct UV light traversing the reflective layer is negligible with respect to the light emitted by the scintillator itself. The temperature and humidity are monitored during the entire test. Their stability ( $T = 22.2 \pm 0.3^\circ\text{C}$  and  $H = 39.5 \pm 1\%$ ) ensures that there is no large variation of the MPPC gain during the procedure.

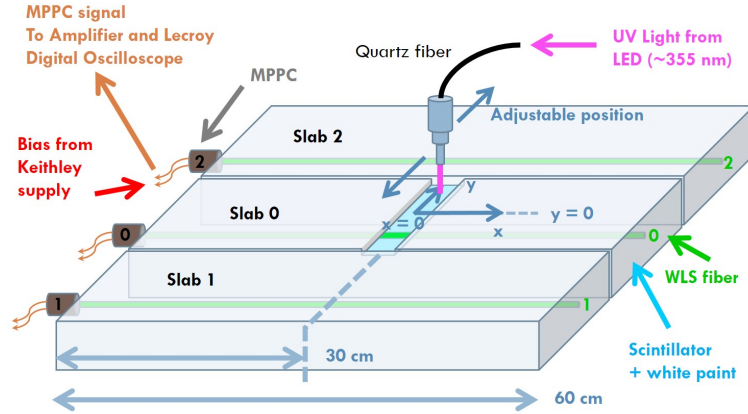


Figure 4.25: Schematic view of the experimental setup used to measure the optical cross-talk between adjacent scintillators.

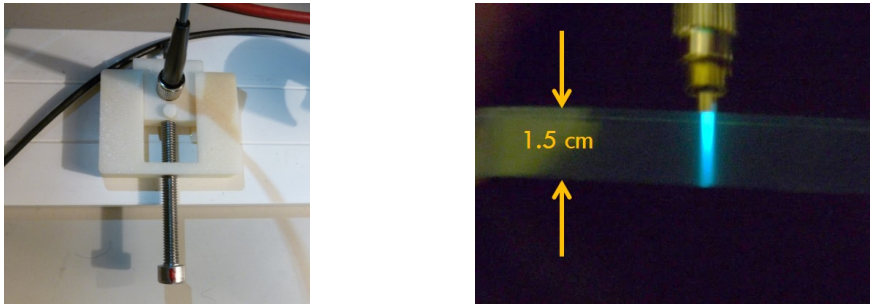


Figure 4.26: Left: picture of the position adjustment device used for light injection. Right: view of the UV light beam injected in the scintillator slab. A wavelength shifting polystyrene bar is used to make the UV light visible on the picture.

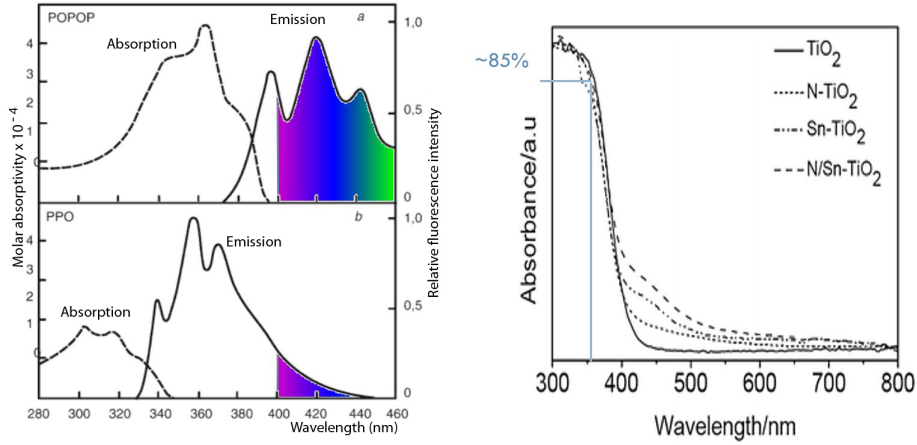


Figure 4.27: Left: absorption and emission curves for the POPOP (top) and PPO (bottom) molecules. Right: absorption factor of titanium dioxide as a function of the wavelength. A wavelength of 355 nm corresponds to  $\sim 85\%$  of the maximum absorbance.

The UV LED is powered via a dedicated capacitor that is charged by an Agilent U8001A power supply providing a voltage between 2V and 5V, depending on the required amount of light we want to inject. The discharge of the capacitor is triggered by an Agilent 33210A pulser, which signal is sent to a transistor according to the setup shown in Figure 4.28-left. The pulser also triggers the digital oscilloscope, and its frequency is chosen to be 1 kHz.

The high voltage is provided by a Keithley 2612 power supply, and brought to the MPPC photon counter by shielded cables, through a  $10\text{k}\Omega$  resistor and a 10 nF capacitor is used for decoupling. The signal from the MPPC is then sent to a small amplifier. This setup, shown in Figure 4.28-right, allows to minimize the electronics noise.

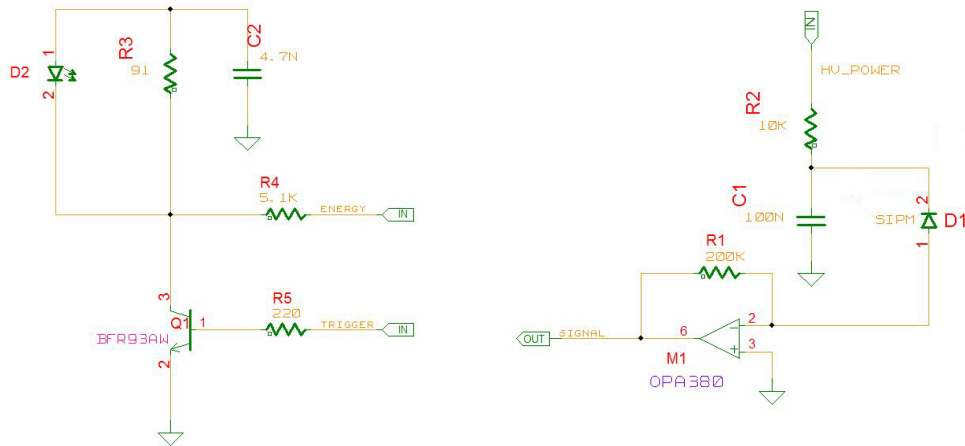


Figure 4.28: Left: schematic view of the setup used to power the UV LED (“D2” on the left). Right: schematic view of the setup used for the MPPC (represented by the diode noted “SIPM D1” on the right). The signal is sent to an “OPA657” amplifier which gain is chosen  $\approx 2 \times 10^5$ , and all connections are made using shielded cables.

A digital oscilloscope Lecroy HRO 66Z is used to visualize the signals received from the MPPCs. It is also used as a data acquisition system to directly count the number of events where the cross-talk signal is seen above the 2.5 p.e. threshold. A picture of the setup is shown in Figure 4.29. Figure 4.30 shows a typical signal as received from the MPPC attached to the central slab and displayed by the digital oscilloscope when a light pulse is sent by the LED. One clearly sees a small pedestal and the peaks corresponding to 1, 2, 3, ... up to 12 p.e.

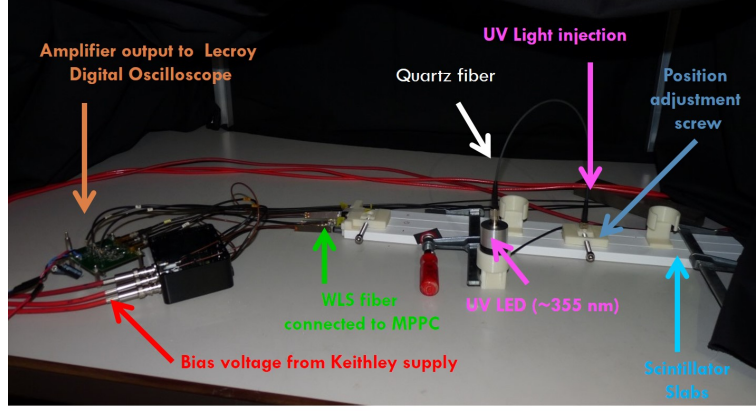


Figure 4.29: Picture of the cross-talk measurement setup installed in the dark room. The power supplies, the pulser and the digital oscilloscope have been installed outside the dark room and are not shown here.

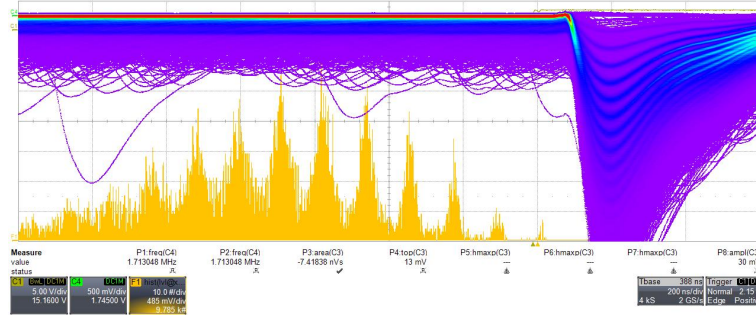


Figure 4.30: On this screen view of the digital oscilloscope, one clearly sees the signal from the central MPPC when light is injected in the corresponding slab (purple and blue curves) as well as the yellow peaks corresponding to signal maxima. The pedestal is the small yellow rightmost peak, and the peaks corresponding to 1, 2, 3, ... up to 12 p.e are clearly distinguished from right to left.

## Measurement

The principle of the measurement itself is the following:

- We begin with the SciBar type scintillators. The light is injected in the central slab (hereafter called “slab 0”), at a fixed position  $y = +6\text{mm}$ . This position is arbitrary chosen at the beginning, as it corresponds to the middle of the distance between the wavelength shifting fiber and the edge of the SciBar slab.
- The first procedure consists in sending in the slab 0 a quantity of light that is tuned in order to give an MPPC signal similar to what is observed for a minimum ionizing particle (i.e.  $\approx 40$  p.e.).
  - We choose the high voltage value for the central MPPC in order to have a low gain. This is achieved using a voltage of  $68.3\text{V}$ , slightly over the “breakdown” voltage for this particular MPPC called MPPC0 ( $68.0\text{V}$ ).
  - We inject small light pulses in slab 0 and observe the signal peaks corresponding to 1, 2, 3, etc ... p.e. This allows to determine the conversion factor between electrical signal and the number of p.e (see Figure 4.31-left).
  - Then, we increase the amount of light per pulse (by increasing the voltage of the LED power supply), in order to measure a voltage for the MPPC0 signal that corresponds to

40 p.e. (see Figure 4.31-right). The individual peaks for 38, 39, 40, ... p.e. cannot be separated, which justifies the preceding step of the procedure.

- By swapping the sets of MPPC+fiber between the slabs, we check for possible discrepancies between the detection efficiency of the different sets. The maximum discrepancy observed amounts to  $\pm 6\%$ , the effect of which on the cross-talk measurement is discussed later in this section.
- The amount of light injected in slab 0 now remains fixed throughout the entire procedure of cross-talk measurement.
- We now want to measure the signal detected on one of the adjacent slabs, namely “slab 2”. For this:
  - We turn off the light injection in slab 0
  - We adjust the high voltage of slab 2 MPPC in order to observe a dark noise rate similar to what is measured in the INGRID and PM detectors, that is 1% of events above 2.5 p.e. The result is obtained for 68.67V, whereas the breakdown voltage of this particular “MPPC2” is 68.19V. An example of the corresponding peaks are shown in Figure 4.32-left.
- The high voltage of MPPC2 now remains the same, and we turn the light injection back on in slab 0.
- For different positions of the light injection device in slab 0, we now measure the percentage of events with a signal above 2.5 p.e. in MPPC2. An example of the corresponding peaks is shown in Figure 4.32-right.

On Figure 4.32-right, it is clearly seen that when light is injected in slab 0, one or two photoelectrons are often detected by MPPC2. In this example, 3 or more p.e. are seen in 9% of the cases. As can be seen from these curves, 4 or even 5 p.e. are sometimes detected, and all these signals are in time with the light that is injected in slab 0. The discrepancy we have observed between the efficiencies of the different fiber+MPPC sets ( $\pm 6\%$ ) corresponds to a discrepancy in the number of p.e. detected, and leads to a systematic error on this measurement of  $6\% \times 9\% = 0.54\%$ .

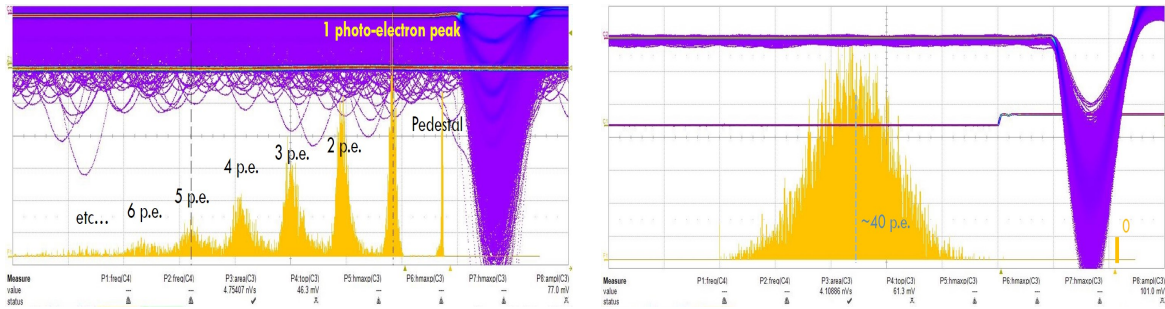


Figure 4.31: Left: on this screen view of the digital oscilloscope, the signal from the MPPC0 corresponds to the purple and blue curves, and the yellow peaks correspond to the same signal integrated over 500ns, as in the INGRID and PM detectors. These peaks allow to determine the gain of the detection chain, in nVs/p.e. Right: here, the yellow peak position corresponds to a signal of 40 p.e. detected by the MPPC0.

### Results for SciBar type scintillators

We first check that the amount of light detected in slab 0 does not depend on the y position of the light injection. This is true within 5%, except for position  $y=0$ , due to light injection in the wavelength shifting fiber itself. The amount of cross-talk is then measured following the procedure

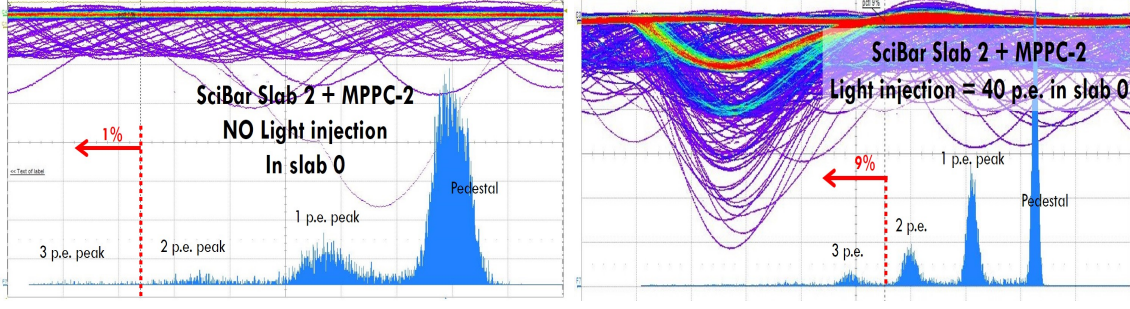


Figure 4.32: Left: dark noise detected in SciBar Slab 2: on this screen view of the digital oscilloscope, the blue peaks correspond to the signal of MPPC2 integrated over 500ns, in the absence of light injection in slab 0. The high voltage of MPPC2 is tuned in order to measure 1% of the events above 2.5 p.e., as in the real detectors. Left: Cross-talk signal detected in SciBar Slab 2 with the nominal 40 p.e. light injection in slab 0. One sees that for this particular test, 9% of the events give a signal above 2.5 p.e. The corresponding signal is in time with the trigger of the LED, and clearly visible on the purple curves (the oscilloscope time scale has been arbitrarily changed with respect to Figure 4.31, to make all curves more visible).

described above, for different  $y$  positions of light injection. Figure 4.33 shows the results for SciBar type scintillators. The more precise measurements have been performed for 355 nm and for slab 2. For these measurements, an additional systematic error has been taken as 0.5%, to take into account the different results obtained when measuring several times the same point. The cross-check results obtained for slab 1 and 2 (mainly for positive  $y$  positions) and for 400 nm are also shown. These last points have been measured with a 1% precision only due to some options of the oscilloscope functions we used to analyse the peaks, hence the larger error bars. Several trends can be seen in these results:

- results obtained for slab 1 are very similar to those obtained for slab 2, and are almost independent on the value of  $y$ , which means that the cross-talk does not depend on the distance between the light injection point and the adjacent slab considered,
- 8 to 10% of the events show signal above 2.5 p.e. in both slabs 1 and 2. This is in agreement with the charge excess observed in neutrino data (Table 4.2),
- the amount of cross-talk seems to be very similar for both wavelengths used for injection, namely 355 and 400 nm, which indicates that this cross-talk is due to the light emitted by the scintillator itself rather than to the light we inject,
- The amount of cross-talk decreases when the position of light injection reaches the center of the slab, probably because the central hole in the scintillator leads to a lower light emission,
- The amount of cross-talk decreases when the position of light injection reaches the edge of the slab, at least for positive  $y$  values. This is due to light injection reaching the reflective layer. This reflective layer is not reachable for negative  $y$  values, due to mechanical restrictions of the adjustable screw.

A black adhesive tape inserted in between the two slabs is sufficient to make this cross-talk disappear. The same disappearance is obtained by inserting a third slab, which shows that this cross-talk effect has no influence on the next to adjacent channels.

### Results for INGRID type scintillators

We now study the INGRID type scintillators using exactly the same procedure as for SciBar ones. The amount of light injection is first tuned to give 20 p.e. in slab 0, which corresponds to a minimum ionizing particle in INGRID type scintillators. This lower signal as compared to SciBar type scintillators is due to their lower thickness and larger width. Then, we check that the amount of light detected in slab 0 does not depend on the  $y$  position of the light injection. As previously, this is true within

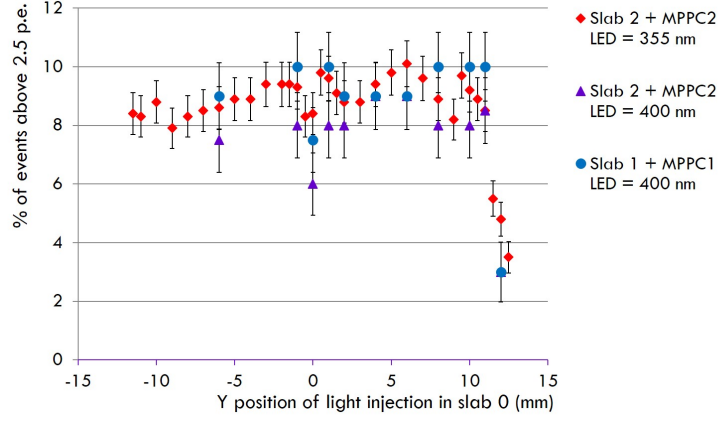


Figure 4.33: Results obtained for cross-talk in the SciBar type scintillators. When the light corresponding to a minimum ionizing particle is injected in slab 0, it is observed that 8 to 10% of the events show signal above 2.5 p.e. in both adjacent slabs (1 and 2)

5%, except for  $y = 0$ , where we observe a 20% increase due to direct UV light injection in the fiber. As previously, the high voltage of the adjacent slab's MPPC2 is tuned in order to observe 1% dark noise above 2.5 p.e., and the injecting LED is then turned on. This time, no difference is observed with or without injecting light in slab 0. Indeed, only 1% dark noise can be seen, for any position of the light injection system between  $y = -21$  mm and  $y = +21$  mm, which correspond to the extreme values before reaching the reflective layer. In order to check for any possible mistake in our test, we then increase the amount of light injected in slab 0 up to 80 p.e., which corresponds to four times the light emitted by a minimum ionizing particle in the INGRID type slabs. With such an amount of injected light, and with the 400 nm LED only, some signal starts to be visible for extreme positions. An example of this phenomenon for  $y = +20$  mm is shown in Figure 4.34, where a clear 1 p.e. signal can be seen in time with the pulser. On the same screen view, another curve is barely seen for 2 p.e., but it is important to notice that no 3 p.e. curve is observed, and the amount of signal above 2.5 p.e. is still 1%. With the LED emitting at 355 nm, no such signal is seen, which seems to indicate that it is due to direct UV light traversing the  $\text{TiO}_2$  reflective layer, and not to scintillator-emitted light.

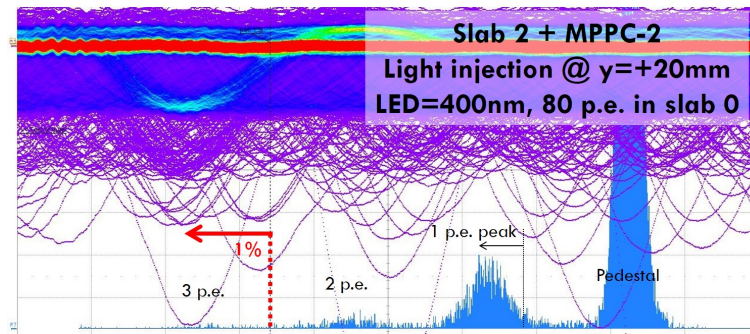


Figure 4.34: Results obtained for cross-talk in the INGRID type scintillators. When the light corresponding to 4 times more than a minimum ionizing particle is injected in slab 0, we observe some cross-talk effect at the 1 p.e. level, but still no signal above 2.5 p.e. This small cross-talk effect is seen with the 400 nm emitting LED only, and for extreme positions towards the adjacent slab.

## Conclusion

We studied the cross-talk between scintillators in conditions that have been chosen as close as possible to the real conditions in the PM. For SciBar type scintillators, we observe that in 8 to 10% of the cases,

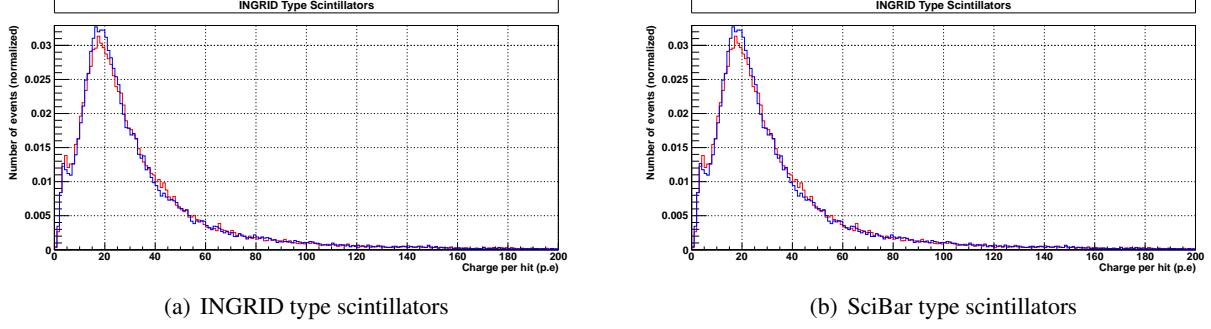


Figure 4.35: Charge distributions of the hits of neutrino event sample in PM comparing the new calibration (data in red) with the simulation (blue). The results has been shown both for INGRID type (top) and SciBar type scintillators (bottom) of the PM.

a signal above the 2.5 p.e. threshold is seen in the adjacent channel on both sides, that is due to optical cross-talk between slabs. No such effect is seen on INGRID type scintillators, probably because of their much thicker  $\text{TiO}_2$  reflective layer. This justifies the higher value of the cut used in the analysis of the PM data, as these signals do not correspond to any particle. No additional correction are applied on the MC attenuation length in the scintillator. Since the latter has been measured in the same scintillators, it means the light escaping effect is already taken into account. Figure 4.35 shows the comparison between data and MC of the neutrino event sample after the calibration and removing the optical cross-talk. It confirms the general improvement of the agreement between data and MC that we have shown for sand muon (see Figure 4.15). The comparison with Figures 4.14 and 4.19 shows that the calibration is crucial to perform any particle identification based on the charge deposition.

## 4.5 T2K charge stability with time

To finish the T2K charge calibration study, we will proceed to a time stability check. We have used so far a given data set corresponding to a part of T2K run 3 (June 2012) and we should check if the calibration holds for different time period. For this purpose, we have used the T2K beam data after PM installation, namely from run 2 to run 4, which has been taken between November 2010 and July 2013. The study is performed using the “sand muon” sample that guarantees an almost pure minimum ionization peak position (MIP), and a very high statistics. The T2K data taking period has been separated in 200 constant time intervals. For each time interval, the charge distribution is fitted by a gaussian whose mean is reported in Figure 4.36. We have shown the relative variations of the mean MIP around the nominal MIP value that corresponds to the data set we used so far in this chapter. One observes variations within  $\pm 10\%$ , with a distinct higher average for run 2 as compared to the other runs. We have shown the variations for the distinct scintillator types to show that the variations are similar between the scintillator types, but also between the INGRID modules and the PM. This confirms the charge calibration consistency between the different modules and scintillator types. As for the global time variation, we interpret it as a possible effect of afterpulse rate or cross-talk (between pixels) within the MPPC. In fact, we have calibrated the MPPC gain in Section 4.2 to take into account possible effects from external condition variations (bias voltage, temperature, humidity...). However, the crosstalk and the afterpulse rates are not calibrated with time. The crosstalk in an MPPC corresponds to the situation when a photon hit one pixel, but where the neighbour pixel avalanche is also triggered. The crosstalk varies with bias voltage, temperature or humidity conditions. On the other hand, the afterpulse corresponds to the case when charge carriers in the pixel Silicon are trapped temporarily due to imperfect Silicon semiconductor. These carriers are released with a time delay and can produce another avalanche. The afterpulse rate is then expected to vary with the bias voltage. For this reason, it is possible to observe a time variation in the mean charge value due to these effects. We therefore interpreted the calibration we performed as stable with time, but that can be improved in the future, by measuring the temperature (sensors already exist) and applied bias voltage to correct the crosstalk and afterpulse rate of the MPPC. In the analyses

presented in this thesis, we will take this remaining time variation as a systematic error.

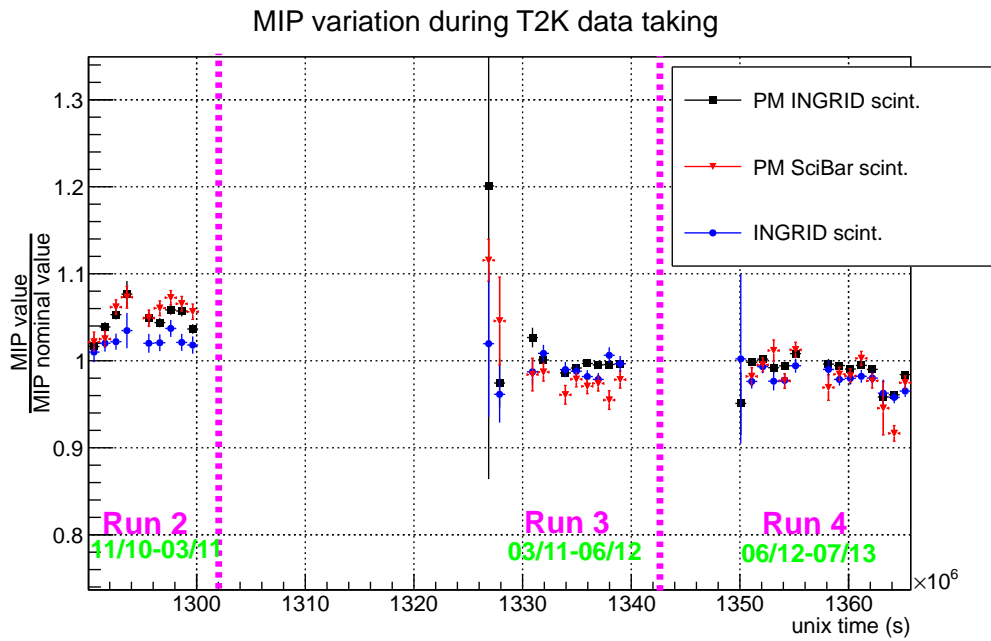


Figure 4.36: Time variation of the minimum ionisation peak position relatively to the data default. The default data corresponds to the middle of run 3 data that have been used in the charge calibration we have shown.

## Chapter 5

# Measurement of the muon neutrino $\text{CC}0\pi$ double differential cross section

*Just because things get a little dingy at the subatomic level doesn't mean all bets are off.*

Murray Gell-Mann

**S**YSTEMATIC ERRORS on neutrino cross-sections are the dominant cause of systematic errors in neutrino oscillation measurements. To reduce these systematics, a better knowledge of various neutrino cross-sections is required. Historically, the neutrino cross section has been measured as a function of the neutrino energy, which is not directly measurable and depends on nuclear models. Since there is an important uncertainty on these models, it leads to distinguish the interactions using some model independent quantities, that are measurable: the interaction final states. Namely, we decided to classify the interactions by the observation of a charged lepton, and number of pions in the final state, since the main model uncertainty comes from the pion production, absorption and exchange models.

In T2K, neutrinos dominantly interact through charged current interactions with no pion in the final state ( $\text{CC}0\pi$ ) which represents 68% of the selected charged current interactions in ND280 in the appearance measurements (Chapter 2). The  $\text{CC}1\pi$  and other charged current interactions represents both 16% of the charged current total interactions selected. For this reason, we decided to focus on the measurement of  $\text{CC}0\pi$  cross-sections. More accurately, we studied the double differential cross-section of  $\text{CC}0\pi$  interactions in the PM, with muon momentum ( $p_\mu$ ) and angle ( $\theta_\mu$ ). This differential cross-section measurement provides more constraints on neutrino interaction models, and in the direct comparison with T2K neutrino spectrum expected at Super-Kamiokande.

In this chapter, we will first introduce the neutrino cross section basics. Then, we will describe the selection we developed to enhance  $\text{CC}0\pi$  purity. We will particularly highlight the particle and muon identification which is crucial to both select the interaction and identify the muon. This identification is based on the charge deposition in the PM, which has been calibrated in Chapter 4. Afterwards, we will present the Bayesian unfolding method we developed based on [64], in order to unsmear the detector effects in our result. Finally, we will present the  $\text{CC}0\pi$  double differential cross section measurement in the PM and discuss its impact.

## 5.1 Cross-sections and interaction models

### 5.1.1 Introduction

The neutrino interacts only through weak interactions. For this reason, the cross sections of different neutrino flavour are small at  $E_\nu \sim \text{GeV}$ . We show the cross section of neutrino (divided by energy) through charged current processes in Figure 5.1 from  $E_\nu \in [100 \text{ MeV}, 500 \text{ GeV}]$ . One observes that the

neutrino charged current interaction cross section increases almost linearly with the neutrino energy and is measured as  $\sim 10^{-38} \text{ cm}^2/\text{GeV}$  for high energy ( $E_\nu \gg m_\mu$ ).

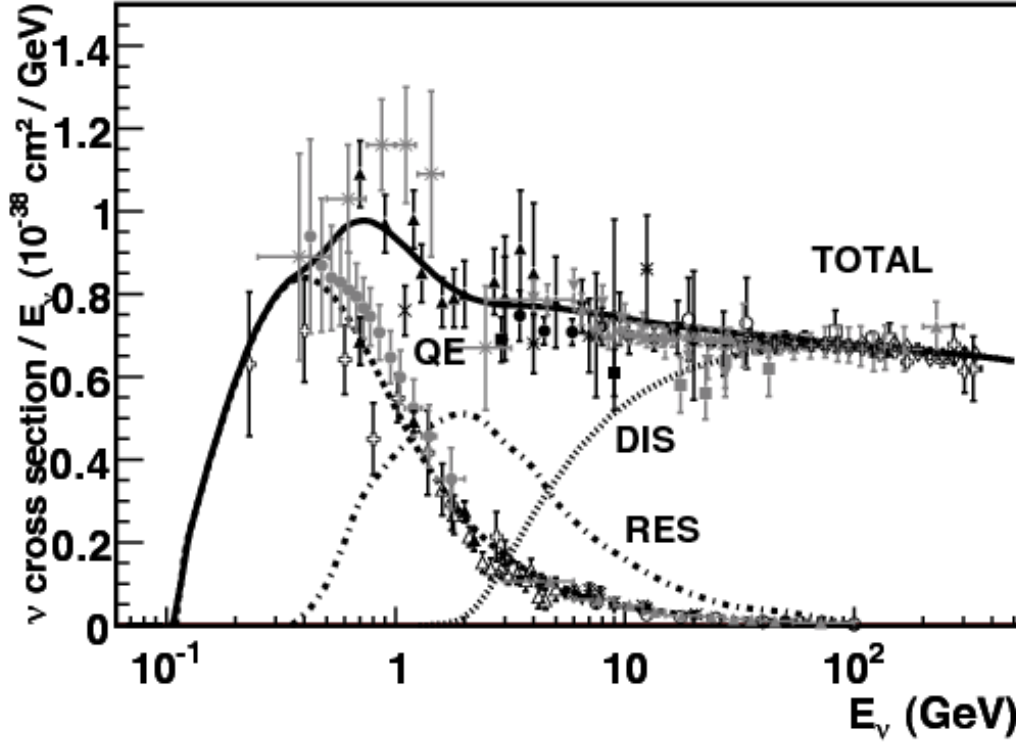


Figure 5.1: Total neutrino CC cross sections per nucleon **divided by neutrino energy** and plotted as a function of energy. The important increase from  $E_\nu \sim 100 \text{ MeV}$  to  $1 \text{ GeV}$  is due to the kinematics of the process which should produce a muon. Taken from [65]. See Figure 5.3 for the legends of the different data sets.

One observes that the charged current quasi-elastic interaction (CCQE) dominates at low energy, and especially in the T2K off-axis energy range:

$$\nu_\mu + n \rightarrow \mu^- + p \text{ (CCQE)} \quad (5.1.1)$$

As was shown in Chapter 2, INGRID intercepts a neutrino flux of higher energy which implies that a significative amount of neutrino interacts through resonant  $\pi$  production. This production occurs through the production of a baryonic resonance (a  $\Delta^{++}$  for example) that decays to generate a pion:

$$\nu_\mu + p \rightarrow \mu^- + \Delta^{++} \rightarrow \mu^- + p + \pi^+ \text{ (resonant CC}\pi\text{)} \quad (5.1.2)$$

$$\nu_\mu + n \rightarrow \mu^- + \Delta^+ \rightarrow \mu^- + n + \pi^+ \text{ (resonant CC}\pi\text{)} \quad (5.1.3)$$

This production is therefore limited by the production threshold of the baryon and occurs at higher energy. One observes the peak (per GeV cross section) in Figure 5.1 that corresponds to the mass resonance for  $E_\nu \sim q^2 \sim m_\Delta = 1.232 \text{ GeV}$  with:

$$q^2 = (p_\nu - k_\mu)^2 \quad (5.1.4)$$

the four-momentum transfer from the neutrino to the nucleus. At even higher energies ( $E_\nu \sim 5 \text{ GeV}$ ), the neutrino is more likely to exchange a virtual  $W$  boson with a  $q^2$  large enough to resolve the quarks in the nucleus and therefore introduce a deep inelastic scattering (DIS). The signature of the DIS is the production of several mesons (mostly  $\pi$ ) or baryons. We have shown the three neutrino-nucleus interactions in Figure 5.2.

In this section, we will focus on the CCQE cross sections which are dominant in the CC0 $\pi$  interactions. Figure 5.3 shows the neutrino cross section of the specific CCQE process. Most of the

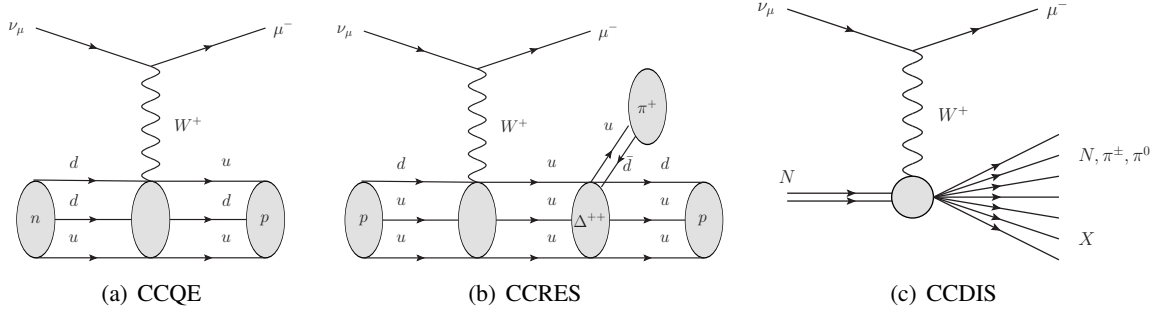


Figure 5.2: Neutrino charged current interaction with a nucleus through quasi-elastic (left), resonant (center) and DIS processes.

constraints are provided by bubble and drifting chamber experiments along with NOMAD [66] and MiniBooNE [67] constraints. Apart from the latter, one observes that the CCQE cross sections are in general agreement with the model which uses an axial mass  $M_A = 1.0$  GeV. The meaning of this parameter will be further discussed in Section 5.1.3. In Section 5.1, we will first describe the neutrino interaction with a quark, and then, with a free nucleon model which is used for the prediction in Figure 5.3. We will finally consider more complicated models and discuss the neutrino cross section model used in T2K. We will show that the cross section result interpretations of Figure 5.3 highly depend on the model, and especially, the MiniBooNE apparent disagreement with other measurements. It is therefore necessary to correctly understand these models in order to interpret the PM cross section results that we will show in Section 5.7.

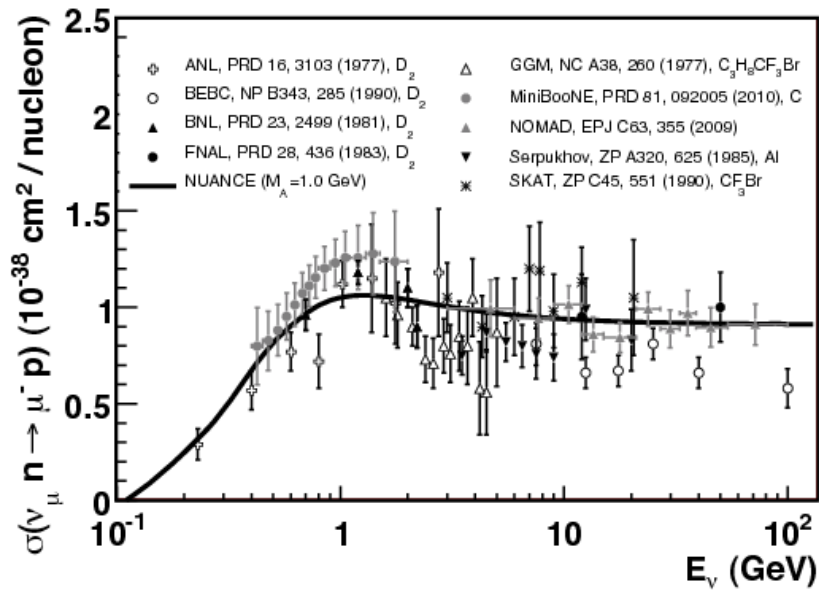


Figure 5.3: Existing measurements of the  $\nu_\mu$  elastic scattering cross section on a neutron ( $\bar{\nu}_\mu + n \rightarrow p + \mu^-$ ). The free nucleon is assumed, along with an axial mass  $M_A = 1.0$  GeV. Taken from [65].

### 5.1.2 Interactions with a quark

The distinction between the different neutrino interactions occurs only for a nucleon or nucleus. The charged current interaction of a neutrino with a single quark is only  $\nu_\mu + d \rightarrow \mu^- + u$ , as shown in Figure 5.4. The cross section may be derived directly using the electroweak theory. We calculated this cross section from the basis in Appendix C.

In the approximation of the small masses, we found the neutrino cross section in the center of mass

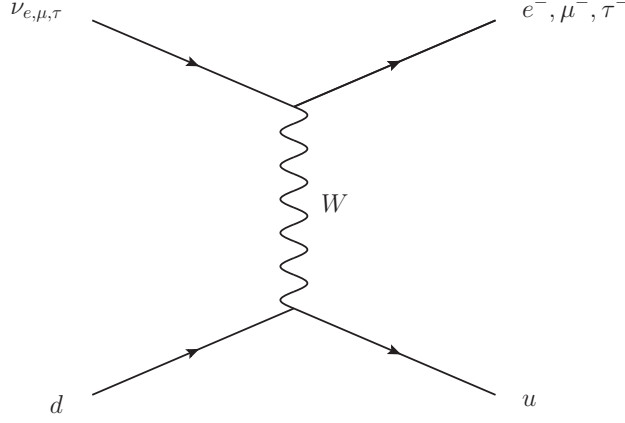


Figure 5.4: The charged current interaction of a neutrino with a down quark.

frame:

$$\overline{|M|^2} = \frac{1}{8} G_F^2 s^2 \text{ the squared module of the amplitude.} \quad (5.1.5)$$

$$\frac{d\sigma}{d\Omega^*} = \frac{1}{512\pi^2} G_F^2 s \quad (5.1.6)$$

$$\sigma = \frac{G_F^2 s}{\pi} \quad (5.1.7)$$

where  $G_F$  is the Fermi constant,  $\Omega^*$  the solid angle of the outgoing lepton and  $s$  the squared energy available in the center of mass frame ( $s = (E_d^{*2} + E_{\nu}^{*2})$  where “\*” indicates that quantities are given in the center of mass frame).

**$\sigma$  linear energy dependency:** We observe that the cross section depends linearly on  $s$ . The Lorentz invariant quantity  $s$  becomes  $s = (p_1 + p_2)^2 = (E_1 + E_2)^2 - (\vec{p}_1 + \vec{p}_2)^2$ . Assuming that the neutrino mass is negligible compared to the  $d$  quark mass, we obtain:  $|\vec{p}_1| = E_1$ ,  $E_2 = m_2$  and  $|\vec{p}_2| = 0$ , which implies that  $s = 2E_1 m_2$ . We have shown in Appendix C that the cross section is Lorentz invariant in the case of colinear incoming particles. Therefore, in the lab frame, the neutrino charged current cross section on a free quark varies linearly with the neutrino energy. In Appendix C, we assumed that  $q^2 \ll M_W$  and considered small lepton and quark masses, which implies that this approximation holds only in the neutrino energy range  $E_\nu \in [\sim 1 \text{ GeV}, \lesssim m_W^2]$ . One observes that this linear dependency agrees with the experimental data shown in Figure 5.1 for the charged current inclusive (CC inclusive) measurements.

We will now introduce how this behaviour is extrapolated to the case of a neutrino interaction with a whole nucleus, as it really happens.

### 5.1.3 Free nucleon

Since quarks are bound in nucleons, we have to estimate the cross section of neutrinos with a target nucleon  $N$ . Figure 5.2 shows the CCQE interaction of a neutrino with a nucleus. Its cross section can be estimated similarly than in the case of a free quark. The difference will be in the hadronic sector current, where we should replace the quark current by a nucleon current taking into account quark interactions, valence and sea quarks. One therefore obtains (see Appendix D):

$$\frac{d\sigma}{dQ^2} = \frac{G_F^2 |V_{ud}|^2 M_N^2}{8\pi(p_\nu \cdot p_{N_i}^2)} [A(Q^2) \pm \frac{s-u}{M_N^2} B(Q^2) + \frac{(s-u)^2}{M_N^4} C(Q^2)] \quad (5.1.8)$$

with

$$A = \frac{(m^2 + Q^2)}{M_N^2} [(1 + \eta)G_A^2 - (1 - \eta)F_1^2 + \eta(1 - \eta)F_2^2 + 4\eta F_1 F_2 - \frac{m^2}{4M_N^2} ((F_1 + F_2)^2 + (G_A + 2G_P)^2 - (\frac{Q^2}{M_N^2} + 4)G_P^2)] \quad (5.1.9)$$

$$B = \frac{Q^2}{M_N^2} G_A (F_1 + F_2) \quad (5.1.10)$$

$$C = \frac{1}{4} (G_A^2 + F_1^2 + \eta F_2^2) \quad (5.1.11)$$

$\eta = \frac{Q^2}{4M_N^2}$  The form factors  $F_1(Q^2)$ ,  $F_2(Q^2)$ ,  $G_A(Q^2)$  and  $G_P(Q^2)$  are respectively called Dirac, Pauli, axial and pseudo-scalar weak charged current form factors of the nucleon [22].

The axial form factor is often assumed [22] as a dipole for low  $Q^2$  value, *e.g.*  $\lesssim 1 \text{ GeV}^2$ .

$$G_A(Q^2) = \frac{g_A}{(1 + \frac{Q^2}{M_A^2})^2} \quad (5.1.12)$$

This dipolar axial structure has been validated experimentally by numerous experiments in the  $\lesssim 1 \text{ GeV}$  region, which are summarised in Figure 5.5 (electron scattering:  $\pi$  electroproduction) extracted from [68].

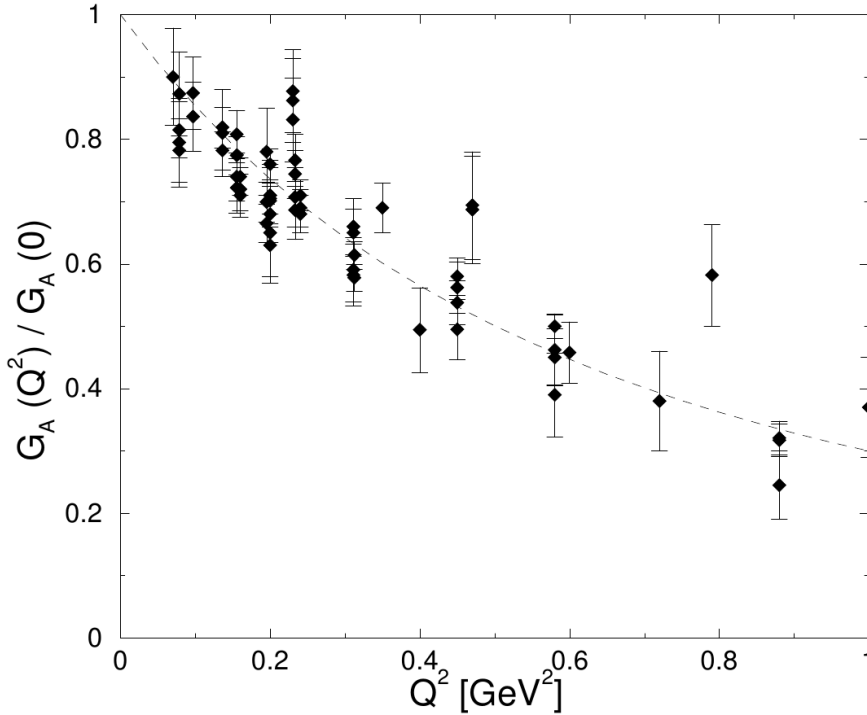


Figure 5.5: Experimental data for the normalised axial form factor from pion electroproduction experiments in the threshold region. The dashed line shows a dipole fit with an axial mass  $M_A = 1.1 \text{ GeV}$ . Taken from [68].

In Appendix D, we introduced that the vector part can be deduced in electron scattering experiments by charged current conservation. These measurements are more accurate, since the electron beam energy can be easily selected (on the contrary to neutrino beam that are created after decays of produced hadrons). Moreover, we introduced (see Appendix D) that the pseudo-scalar weak charged current  $G_P$  is directly deduced through  $G_A$  measurements under partially conserved axial charged current hypothesis. Therefore, we can deconvolute the problem by fixing the vector form factors and measure only the axial one in neutrino experiments. Since the axial coupling  $g_A$  can be deduced from  $g_V$  measuring neutron lifetime, the neutrino scattering experiments have focused on fitting the axial

mass  $M_A$  value through cross section measurements. These measurements have been done mostly in bubble chamber experiments in Argonne or BNL laboratories, and are summarised in Figure 5.6. The resulting  $M_A$  value that has been fitted separately for neutrino scattering and electroproduction experiments:

$$M_A = 1.026 \pm 0.021 \text{ GeV neutrino scattering} \quad (5.1.13)$$

$$M_A = 1.069 \pm 0.016 \text{ GeV charged } \pi \text{ electroproduction} \quad (5.1.14)$$

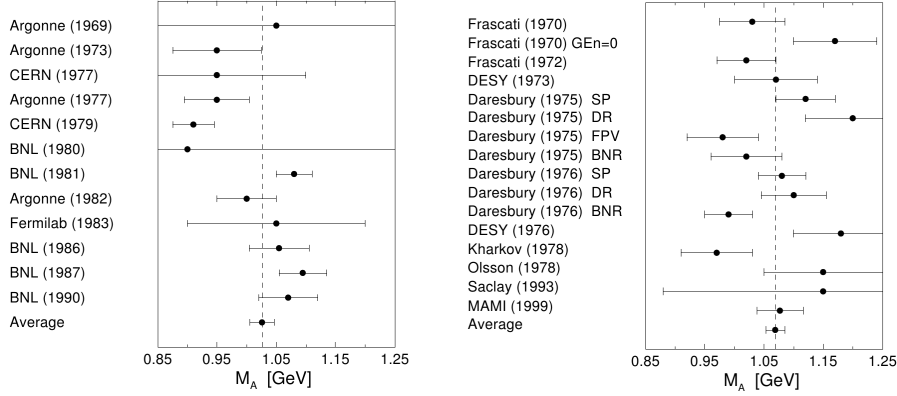


Figure 5.6: Axial mass  $M_A$  extraction for neutrino scattering (left) and  $\pi$  electroproduction experiments (right). The targets (protons or deuterons, but also aluminium, iron, freon and propane) are made of small atomic nuclei in average. Taken from [68].

One observes in Equation 5.1.12 that the larger  $M_A$ , the higher is the axial coupling and then the higher the neutrino cross section will be for a given momentum exchanged. Moreover, one observes that the effect of  $M_A$  only significantly occurs at low energies  $q^2 \lesssim M_A^2$ . Therefore, one interprets  $M_A$  as an effective mass of the nucleon representing the axial current contribution to the interaction with a neutrino.

#### 5.1.4 Interaction with a nucleus

In the previous section, we described the interaction of a neutrino with a single nucleon (in the strong isospin symmetry approximation, see Appendix D). The interaction of a neutrino with the nucleus ( $Z$  protons,  $A-Z$  neutrons) is more complicated due to the inter-nucleon interactions. To estimate the charged current quasi-elastic cross section with a nucleus composed of  $Z$  protons and  $A-Z$  neutrons, one should assume a descriptive model for the nucleon interactions. In the case of CCQE interaction of a neutrino with independent fermions (so-called “impulse approximation”), the  $|M|^2$  probabilities are summed in the cross section for the  $A-Z$  different input neutrons, which have different momenta. Given that the momentum of a single nucleon may be different from the whole nucleus, the total cross section is given by [69]:

$$\frac{d\sigma}{dE_l d\Omega_l} = \frac{p_l}{8(2\pi)^4 M_T^2 E_\nu} \int d^3 \vec{p}_i F(\vec{p}_i, \vec{q}, \omega) |M_{\nu Nucleon}|^2 \quad (5.1.15)$$

with  $E_l$ ,  $\Omega_l$  the lepton energy and solid angle,  $p_i$  the initial 3-momentum of a nucleon,  $\vec{q}$  the 3-momentum transfer,  $M_T$  the target nuclear mass and  $M_{\nu Nucleon}$  the scattering amplitude of a neutrino on a free nucleon described in Eq D.0.18.

The function  $F(\vec{p}_i, \vec{q}, \omega)$  represents the distribution of nucleon momenta in the nucleus. It is often assumed [69] that  $F(\vec{p}_i, \vec{q}, \omega)$  simply corresponds to the convolution of a single particle by a single hole Green functions (propagators). It represents the creation of a hole of energy  $\omega'$  and creation of a particle of energy  $(q^0 = \omega) - \omega'$ . This Green function approximation assumes that we can decompose

neutrino interaction with the nucleus in a sum of neutrino interaction with single nucleons and re-interaction of the leaving particles with the nucleus. In this approximation,  $F(\vec{p}_i, \vec{q}, \omega)$  becomes:

$$F(\vec{p}_i, \vec{q}, \omega) = \frac{M_T}{(2\pi)^2 V} \int \frac{d\omega'}{p_i^0(p_i^0 + \omega)} P_h(\vec{p}_i, \omega') P_p(\vec{p}_i + \vec{q}, \omega - \omega') \quad (5.1.16)$$

with  $V$  the spatial normalisation volume. As hole and particle Green function,  $P_{h/p}(p, E)$  can be defined as:

$$P_h(p, \omega) = \langle N | a_p^\dagger \delta(H - E_N - \omega) a_p | N \rangle \quad (5.1.17)$$

$$P_p(p, \omega) = \langle N | a_p \delta(H - E_N - \omega) a_p^\dagger | N \rangle \quad (5.1.18)$$

$P_h(p, \omega)$  represents the probability to create a hole of momentum  $\vec{p}$  and energy  $\omega$ , which corresponds in fact to the probability to find an existing nucleon in this energy state. The initial nucleon repartition in the nucleus is then contained in  $P_h$ . There exists several models to describe these initial contents, some of them are:

1. relativistic Fermi gas of nucleons that we will discuss in Section 5.1.4. In particular, this model depends on a Fermi momentum which is the maximum momentum for initial nucleons in the nucleus.
2. Spectral function model which is described in Section 5.1.4.

On the opposite,  $P_p(p, \omega)$  represents the probability to create a particle of momentum  $\vec{p}$  and energy  $\omega$  above the nucleus ground state  $|N\rangle$  of energy  $E_N$ . Therefore, it contains the informations on final state interactions. As for nucleus initial state, different models exist to describe the nucleus final state:

1. Impulse approximation, which assumes neutrino-nucleus interaction is only a sum of neutrino interactions with single nucleons, with no final state interactions.
2. The relativistic Fermi gas. It imposes that final state nucleons should have an energy above the Fermi momentum.
3. Optical potential models that allow interactions of a neutrino where several outgoing nucleons are emitted. These final state interaction effects are described in Section 5.1.4.

The different models used in the neutrino generators as NEUT (we will use in this thesis) correspond to choices of  $F(\vec{p}_i, q, \omega)$ . We have studied some of these models in the following sections

### Relativistic Fermi gas model

The relativistic Fermi gas model (RFG) is based on the Fermi description of energy states in a solid. The Fermi description occurs for same species fermions, so there is a neutron Fermi sea and a proton Fermi sea. If no interaction occurs, the nucleons occupy the level of their respective Fermi sea and pile-up in energy because of the Pauli principle. For the neutron and proton seas, there is a Fermi energy (Fermi momentum  $|p_F\rangle$ ) which is the energy of the most energetic fermion in case of gas temperature equal to 0. A QE interaction of a neutrino creates a hole in the neutron Fermi sea and a particle in the proton Fermi sea. As the proton Fermi sea already occupies all states up to the Fermi energy, the new proton has to populate higher energy levels. Being above the Fermi energy, this proton is normally ejected (free particle). Note that re-interactions may occur in the nucleus after the primary interaction and are known as final state interactions and described in Section 5.1.4. On the contrary, in the neutron Fermi sea, a hole appears under the Fermi energy and may introduce a neutron rearrangement to fill this hole and minimise the nucleus energy. The most important part in this picture is that the proton should be created above the Fermi level. Therefore, too low kinetic energy protons with momentum  $|\vec{p}| < p_F$  cannot be created, which is known as “Pauli blocking”. The Pauli blocking naturally introduces a difference with what may be called “free nucleons” with no Pauli exclusion principle and simple sum of interaction probabilities over the A-Z neutrons. As a consequence, we

expect the cross section of neutrinos on a RFG to be slightly lower than for free nucleons. Moreover, one expects a threshold in neutrino energy so that the transferred energy to proton ( $\Delta m + Q^2 + E_F^n$ ) is large enough to go above the proton Fermi energy. This should happen mostly in the nucleus with a low number of neutrons ( $A-Z \gtrsim Z$ ), in which  $E_F^n$  is not significantly higher than  $E_F^p$ . On the contrary, in a nucleus with dominant amount of neutrons, one expects that the initial neutron has often enough kinetic energy so that the final proton is created above the Fermi energy. In these nuclei, the difference between free nucleons and RFG should be lower. In the following, we will not consider difference between neutron and proton seas anymore and will refer to a “nucleon sea” to simplify the scheme.

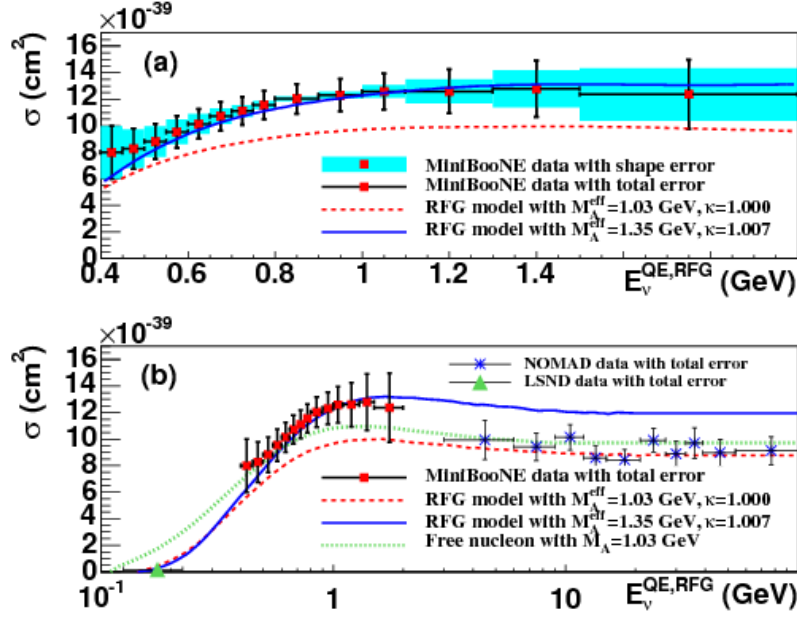


Figure 5.7: Flux unfolded MiniBooNE  $\nu_\mu$  CCQE cross section per nucleon as a function of neutrino energy [67].

The mathematical application of the RFG to nucleon description has been described by Smith and Moniz in Ref [70]. It corresponds to replace the hole and particle propagator in Eq 5.1.18 by:

$$P_h^{RFG}(\vec{p}, \omega) = \delta(p^0 + \omega - E_B) V \theta(p_F - |\vec{p}|) \quad (5.1.19)$$

$$P_p^{RFG}(\vec{p}, \omega) = \delta(p^0 - \omega) V \theta(|\vec{p}| - p_F) \quad (5.1.20)$$

where  $p_F$  is the Fermi momentum and  $p^0 = \sqrt{|\vec{p}|^2 + M^2}$  with  $\vec{p}$  the momentum of the created particle. The Heaviside function  $\theta(|\vec{p}| - p_F)$  imposes that  $|\vec{p}| \geq p_F$  while  $\delta(E_p - \omega)$  imposes that the outgoing particle has an energy  $E_p = \omega$ , the energy transferred from the W boson. As we discussed, this indirectly imposes that this reaction only occurs if the energy transferred  $\omega$  is high enough so that  $|\vec{p}| \geq p_F$ , *i.e* to create the particle state above the Fermi sea. In this model, we have  $V = 3\pi^2 N / p_F^3$  that represents the volume of the Fermi sphere (N is the number of target nucleons A-Z in the nucleus). Eq 5.1.16 then becomes for RFG:

$$F(\vec{p}_i, \vec{q}, \omega) = \frac{M_T V}{(2\pi)^2 p_i^0 p_f^0} \delta(p_f^0 - p_i^0 + E_B - \omega) \theta(|\vec{p}_f| - p_F) \theta(p_F - |\vec{p}_i|) \quad (5.1.21)$$

with  $p_f$  and  $p_i$  the final and initial nucleon four-momenta. The RFG model can be improved adding a binding energy of the nucleon to the whole nucleus,  $E_B$ . The only difference will be that the energy of the outgoing particle will be slightly reduced ( $p_f^0 = p_i^0 - E_B + \omega$  due to the binding energy). This model has been widely used for several decades and particularly as a basis to fit the axial mass parameter in the bubble chamber experiments as described in Figure 5.6. This model only depends on Fermi momentum  $p_F$  and binding energy  $E_B$  for each nucleus type. For example, in the present case of the cross section on carbon, the parameters have been set in the analysis we will present to:

$$p_F = 250 \text{ MeV} \cdot \text{c}^{-2}, \quad E_B = 25 \text{ MeV} \cdot \text{c}^{-2}. \quad (5.1.22)$$

One observes that the condition  $\delta(p_f^0 - p_i^0 + E_B - \omega)$  reduces the phase space possibility for the exchanged boson energy ( $(q^0 = \omega) - \omega'$ ) as compared to the case  $E_B = 0$ . The exchanged boson energy should be higher to maintain  $p_f^0 \geq 0$ . The consequence of the phase space reduction is that the binding energy reduces the cross section. One observes that this effect is mainly relevant at low energy, ( $E_\nu \sim E_B$ ) where the phase space of  $\omega$  is smaller so reduced in larger proportions.

We will now describe the limit of the RFG model, in order to finally introduce the modern treatment of the neutrino cross sections with a nucleus.

**Initial nucleon repartition failure** A first limit of the RFG model is that it fails to reproduce simple nuclei behaviours, as observation of a continuous Pauli blocking with outgoing nucleon momentum (obviously discrete in the basic RFG), or local differences in nucleon distributions in the nucleus. It has been attempted to solve these issues by:

- Turning the Fermi momentum  $p_F$  in a local variable  $p_F(\vec{r})$  in the nucleus to take into account the local density variations. Note that it has nothing to do with the interaction itself but only with the nucleon density.
- Assuming a non-constant potential, *i.e* binding energy ( $E_B(\vec{r}) \sim E_B(\vec{p})$ ) in the nucleus. This allows to take into account non-uniform nuclear effects.

We will describe the spectral function model that encompasses these effects in a more adequate model.

**Nucleus final state and impulse approximation failure** Recently, the MiniBooNE experiment provided a measurement of the axial mass [67]:

$$M_A = 1.35 \pm 0.17 \text{ GeV} \cdot c^2 \quad (5.1.23)$$

which represents a variation of nearly  $2\sigma$  from the axial mass fitted in Equation 5.1.14. Some hints of a large  $M_A$  was also found in K2K [71] and MINOS [72] measurements, but not in NOMAD [73] (which has a smaller uncertainty):

$$M_A = 1.20 \pm 0.12 \text{ GeV} \cdot c^2 \text{ K2K } ^{16}\text{O} \quad (5.1.24)$$

$$M_A = 1.14 \pm 0.11 \text{ GeV} \cdot c^2 \text{ K2K } ^{12}\text{C} \quad (5.1.25)$$

$$M_A = 1.19 \pm 0.17 \text{ GeV} \cdot c^2 \text{ MINOS } ^{56}\text{Fe} \quad (5.1.26)$$

$$M_A = 1.07 \pm 0.07 \text{ GeV} \cdot c^2 \text{ NOMAD } ^{12}\text{C} \quad (5.1.27)$$

In particular, the MiniBooNE measurement shows a higher neutrino cross section than the one predicted by the existing constraints on data. Considering a RFG model, it led MiniBooNE to fit a higher axial mass value,  $M_A = 1.35 \text{ GeV}$ . A proposed explanation was that the assumption of RFG was wrong and some interactions occur between the neutrino and the entire nucleus (not only nucleon per nucleon), which implies that the impulse approximation is wrong. These measurements, along with the former measurement from bubble chamber experiments are shown in Figure 5.3 and 5.7. An alternative model was then proposed in [74] to take into account the whole nuclear effects, interacting through meson exchange currents (MEC). These effects are expected to be small in proton or deuterium targets of the bubble chamber experiments, but not on  $^{12}\text{C}$  which is MiniBooNE target. These effects will be further described later in this section.

### Spectral functions

Instead of a RFG model, the nucleon repartition in the nucleus is described with a probability  $P_h(\vec{p}, E)$  (this is the hole Green function of Eq 5.1.18) to find a nucleon with a momentum  $\vec{p}$  which will leave the nucleus with an energy  $E$ . This allows to take into account the local density effects, but also local nuclear effects. This spectral function may be estimated for each nuclei using a density and nuclear effect models along with a many body calculation [75]. In particular, the short range nucleon correlations (2 points correlations and more) can be taken into account using higher order terms in

the Taylor development of the correlation function. However, a mean field approximation (nucleons feel a mean effect from other nucleons) and only short range correlations are often only considered.

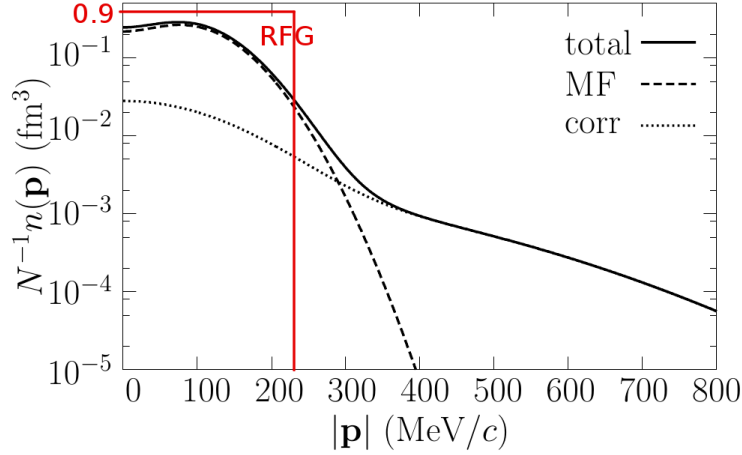


Figure 5.8: Momentum distribution of nucleons in  $^{16}\text{O}$ . The Mean field approximation (MF) and short range correlations (corr) are respectively represented by the dashed and dotted lines. Modified from [76].

As one expects, this model reproduces way better the complex distribution of nucleons in a nucleus and the nuclear interactions. Figure 5.8 shows the expected difference with a RFG model for a  $^{16}\text{O}$  nucleus. In particular, one observes that the mean field approximation alone leads to a smaller initial momentum, as in the case of a RFG approximation. This is expected since the mean field approximation is similar to a RFG with an additional local binding energy  $E_B$ . On the other hand, the short range correlations affect not only the smallest momentum region, but also allow nucleons to have large momenta. These short range correlations occur on top of the mean field approximation and have generally a higher intensity than the latter. One of the reason is a probable screening effect between nucleons in the mean field approximation. This higher intensity allows some nucleons to have large momenta ( $\geq 2 \times p_F$ ) while remaining bounded to the nucleus. As in the case of an RFG having a binding energy, the cross section predictions are lower than in the RFG non-binded case, especially at low energies ( $E_\nu \sim p_F$ ) where the binding effect has more impact. We have generated the CC0 $\pi$  cross section as a function of the energy in the PM in Figure 5.9, and compared the RFG and the spectral function models. One observes a cross section depletion in the low energy region ( $E_\nu < 1 \text{ GeV}$ ) for the spectral function model. The impact at higher energy is visibly negligible.

### Final state interactions

We describe the final state interactions (FSI) before the mesons exchange current. The reason is the FSI can be directly implemented in the model of the impulse approximation shown in Equation 5.1.18, through the outgoing particle propagator  $P_p$ . The FSI induce re-interactions of the outgoing hadronic particle in the nuclear medium, through strong interactions, except for elastic scattering that also occurs through electromagnetic interactions. The common re-interactions are shown in Figure 5.10, and are:

1. Meson elastic scattering
2. Meson absorption
3. Pion or meson production
4. Charge exchange

These interactions modify the final state of the interaction in two different ways: they change the outgoing hadrons kinematics (due to elastic scattering) but also the particle content of the final state

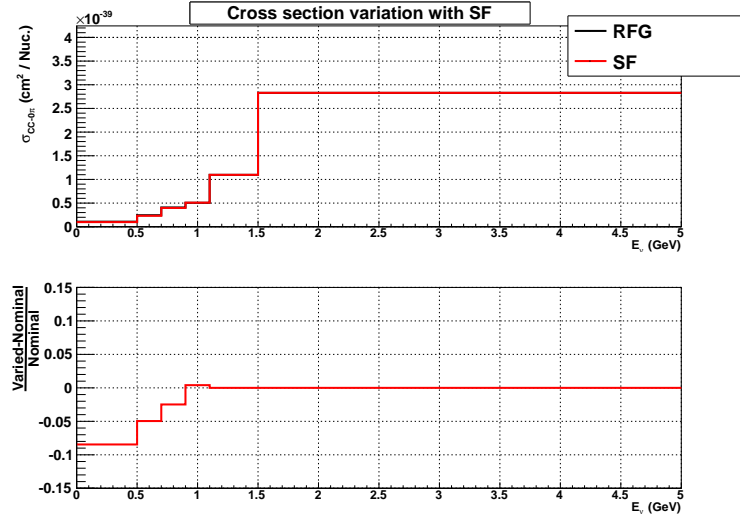


Figure 5.9:  $CC0\pi$  cross section (top) as a function of the energy comparing the RFG (black) and spectral function (red), and their relative difference (bottom). This has been generated using NEUTv5.1.4.2.

in case of absorption, pion production or charge exchange. A true  $CC1\pi$  interaction subjected to a  $\pi$  absorption can therefore be mistaken and reconstructed as a “CCQE-like” interaction. Therefore, in the case true interactions (at the vertex) are studied, one needs to assume a final state interaction model in order to retrieve the true interaction from the reconstructed one. We decided to measure the  $CC0\pi$  cross section since it is based on direct observable, and in principle removes these model dependencies. This allows to study different models a posteriori with the same data sample. Practically, this model independency is not total since the detector is unable to reconstruct all the particle outgoing from the nucleus.

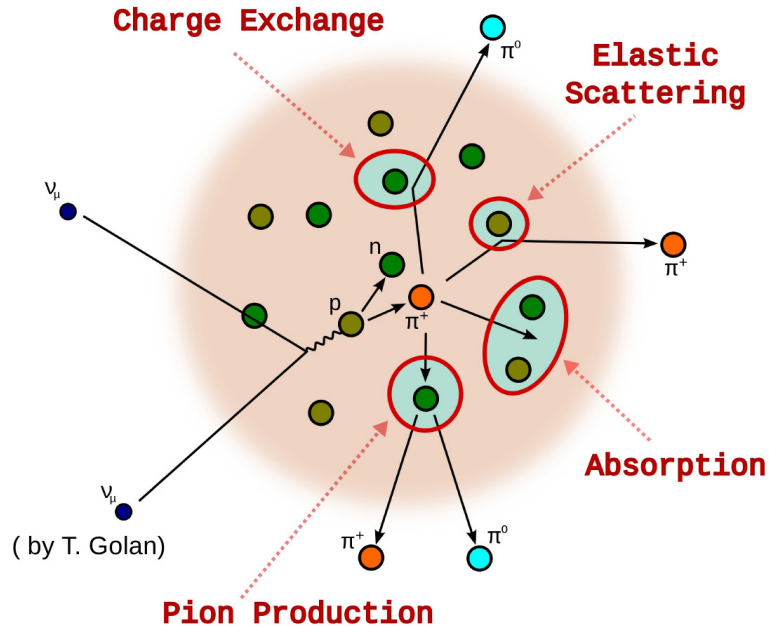


Figure 5.10: Different final states interaction in a nucleus. Taken from [77].

The  $CC0\pi$  interactions should be affected by the pion production and absorption. We have studied an example of a  $\pm 50\%$  change of the  $\pi$  absorption in the carbon nucleus. We expect an increasing  $\pi$  absorption should result in an increased  $CC0\pi$  cross section, by increasing the contamination from  $CC - N\pi$  ( $N \geq 1$ ) where the  $\pi$  is absorbed. This result is shown in Figure 5.11. We also observe an increasing effect with the neutrino energy. We interpret this as an increasing contribution from  $CC - N\pi$  ( $N \geq 1$ , with  $\pi$  absorbed) with neutrino energy. Indeed, we observed (Figure 5.1) the  $CC - N\pi$

cross sections increase relatively to CCQE cross section with neutrino energy and starts to bring a noticeable contribution for  $E_\nu > 500 \text{ MeV}$ , which is confirmed in Figure 5.11.

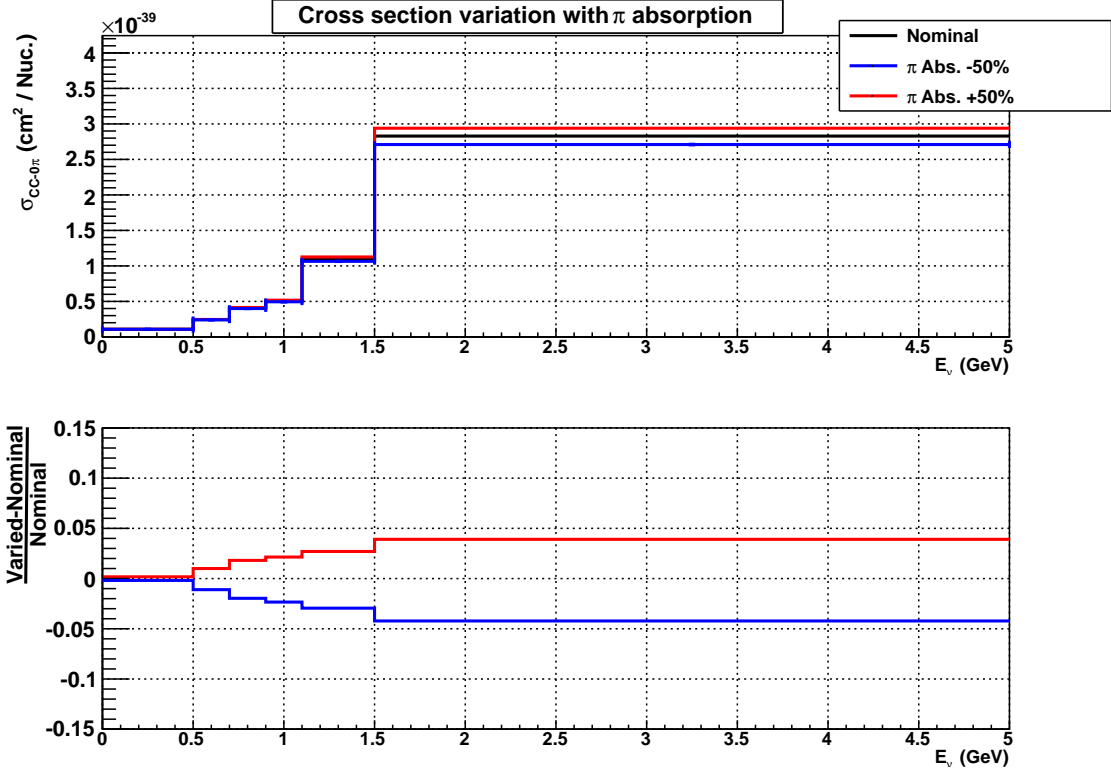


Figure 5.11:  $\text{CC}0\pi$  cross section as a function of the energy comparing the nominal RFG (see Table 5.8) with the same model where  $\pi$  absorption is decreased of 50% (blue) and increased by the same amount (red). This has been generated using NEUTv5.1.4.2

### 5.1.5 Meson exchange currents

The impulse approximation assumes that the neutrino interacts individually with the nucleons. This approximation does not take into account the possible nuclear effects, which involves the neutrino actually interacting with a bound nucleon state. The impulse approximation in Equation 5.1.15 can be modified to take into account this multi-nucleon effect, changing the proton-hole pair to  $N$  proton-hole creations. This multi-nucleon interaction is therefore called np-nh effect, and has been developed in [74] and [78]. One expects these processes to occur at T2K and MiniBooNE energy ( $\sim 1 \text{ GeV}$ ) in QE process, but not at high energy ( $E \gtrsim 10 \text{ GeV}$ ) where DIS interactions dominate. When the  $Q^2$  transferred momentum is high enough, the quarks are resolved by the exchanged boson and a neutrino-quark interaction occurs, which corresponds to deep inelastic interactions. As nuclear effects are small, perturbative QCD can be used to deduce the cross section in this case. On the contrary, for low transferred momentum, nuclear effects prevent from using perturbative QCD and considerably complicate the process. Since most of the present experiments as T2K and Nova, but also possible future experiments (LBNO, LBNE, Hyper-Kamiokande) use a neutrino beam with  $\sim 1 \text{ GeV}$  energy, the understanding and measurements of these nuclear effects are crucial.

Figure 5.13 shows an example of 2 particles-2 holes (2p-2h). One notices that the production of two protons is possible through nucleon interactions. These interactions occur through charged mesons (mainly pions) at these energy, and are named Meson Exchange Current (MEC). This nuclear interaction clearly shows the possible differences between NOMAD and MiniBooNE for example: on the one side, NOMAD is defining as CCQE interactions in which a  $\mu^-$  and only one proton are detected. In such a case, the signal is not composed of interactions 2p-2h. On the opposite, MiniBooNE defines CCQE as  $\mu^- + N \cdot p + 0\pi$ , which implies that the np-nh interactions should be taken into account. This

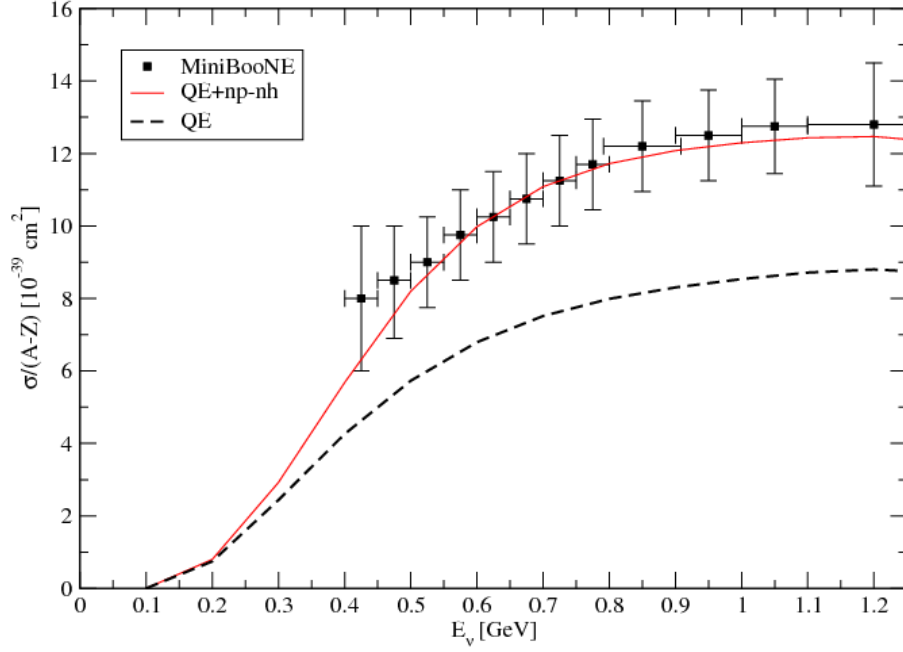


Figure 5.12: Quasi-elastic  $\nu_\mu$   $^{12}\text{C}$  cross section per neutron as a function of the neutrino energy. Taken from [74].

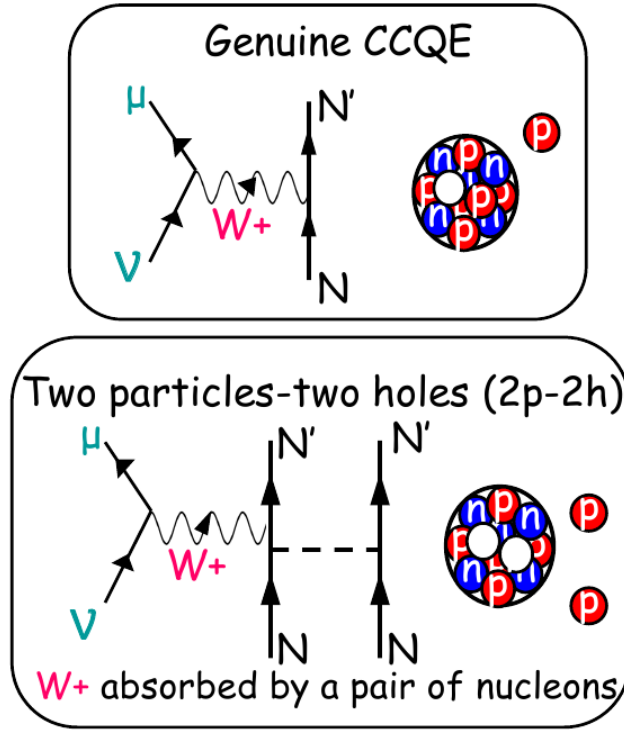


Figure 5.13: Comparison between a genuine CCQE interaction on a nucleus and a two particles-two holes interaction. Taken from [79].

may explain why models without nuclear effects reproduce NOMAD results well, but not MinibooNE ones.

The cross section is enhanced by the addition of  $\mu + N \cdot p$  signal with  $N > 1$  to the  $\mu + p$  signal, which explains the increase of the cross section observed in Figure 5.12 and the MiniBooNE large cross section in Figure 5.3. One also remarks that the classification of an interaction as “CCQE” is not unique, and is meaningless in case of nuclear effects. This classification is based on free nucleon principles, and becomes irrelevant when MEC interactions occur. In particular, interaction of the Z or

W boson directly with the strong field (interacting mesons) is possible. The different nuclear effects can be seen in Figure 5.15, and in particular, we can notice the possibility of a direct interaction of the massive bosons with pions in second MEC diagram. These diagrams can be read using the equivalent description shown in Figure 5.14. Various definitions of MEC are used: MEC can indicate either all the nuclear processes, or a sub-class of them as shown in Figure 5.14. In the latter case, the nucleon-nucleon (N-N) correlations can be described by a massive boson interacting with a nucleon which communicates with another nucleon through pion exchange. On the contrary, the MEC would be defined as massive boson interaction with the meson strong field. In this document, we will refer to MEC as including all nuclear effects.

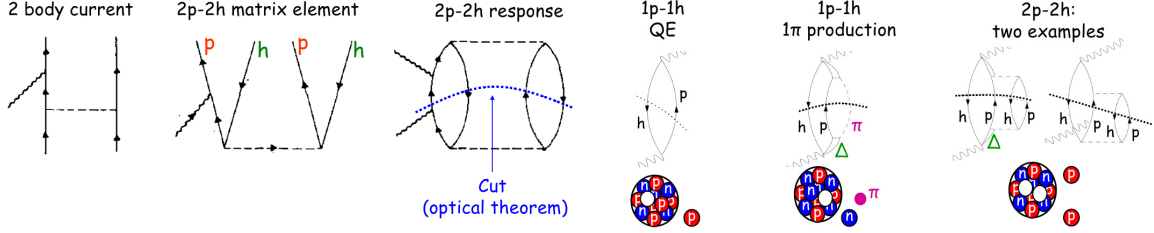


Figure 5.14: On the left, three different presentations of the same process are shown. This is compulsory to understand the right diagrams, which present a CCQE (left of the right plot), CC1 $\pi$  (center) and 2p-2h (right). Both plots are taken from [79].

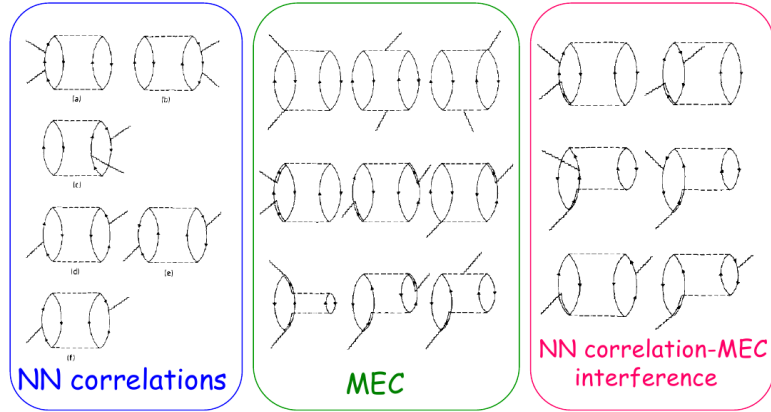


Figure 5.15: The two sub-classes of the MEC. The “standard” MEC interaction of the neutrino with the nucleus is shown in the center, while the interaction of the massive exchange W boson with another nucleon through  $\pi$  exchange is shown on the left. On the right, the interferences between the two processes are presented. Taken from [79].

## 5.2 $CC0\pi$ signal definition for a model independent study

We present the first  $\nu_\mu$   $CC0\pi$  double differential cross section measurement on hydrocarbon (CH) target in T2K. We used the PM detector presented in Chapter 2 and applied the calibration developed in Chapter 4. The term “double differential” refers here to the muon momentum  $p_\mu$  and angle  $\theta_\mu$ . This measurement maximises the information provided in comparison with the absolute cross section. Moreover, since the lepton variables can be measured, this measurement will not depend on the neutrino cross section model (a priori), whereas the neutrino energy does. The  $CC0\pi$  signal definition we chose is based on the final states of the interaction:

$$1 \mu + 0 \pi^{+/-/0} + N p \quad (5.2.1)$$

This definition is similar to the one MiniBooNE used in [67]. The core of this final state definition is to rely on observables, as the pion production and the proton observations. The  $CC0\pi$  is exactly as

its name indicates: a state where we can observe a muon (CC) without any pion production. We have seen that an important issue in neutrino cross section is the pion production/exchange/absorption models. Thus, the interactions classification according to the pion observation allows to accurately test various pion production models. Note that a further refinement could be done along the number of outgoing protons.

This measurement requires therefore in this analysis:

1. A dedicated CC0 $\pi$  selection in the PM.
2. To identify the muon.
3. To measure the muon angle, but also momentum in the PM without any magnetic field.

In the spirit of what has been shown for CC0 $\pi$  cross section, we define the following final state classification:

- CC or NC is related to the observation of one or no lepton (mainly muon in our case).
- The number of pions is related to the observations of charged or neutral pions. In this study, we will not isolate any interactions containing pion, and do not have any pion specific identifier. For this reason, we have not differentiated neutral and charged pions.
- The observation of protons is of minor importance.

For example, we will classify an interaction with the final state:  $A \mu + B \pi^{+/-/0} + C p$  as CC-B $\pi$  if  $A = 1$  and NC-B $\pi$  if  $A=0$ . To not overload the plots, we will classify the interactions containing more than one pion as (CC/NC)-N $\pi$  ( $N > 1$ ). We have shown in Figure 5.16 event displays for CC0 $\pi$ , CC1 $\pi$ , CC-N $\pi$  and NC-N $\pi$ .

In the Section 5.3, we will show how to isolate the CC0 $\pi$  signal from the other interactions. Moreover, we will also introduce how the muon momentum is measured in this analysis. We will see that it unfortunately involves a high event loss due to detector inappropriate acceptance.

### 5.3 The CC0 $\pi$ selection

The interacting neutrino spectrum is shown in Figure 5.17 for neutrino interacting in the PM fiducial volume. In this figure and for the next ones, we assume a neutrino statistics corresponding to  $10^{21}$  POT, unless something different is specified. It corresponds to the same order of magnitude as T2K run 2 to 4 data that we have used in this thesis. The spectrum is peaked at 1.5 GeV in the PM. The  $\nu_\mu$  interacts through charged and neutral current interactions respectively with a 72.7% and 27.6% ratios. The  $\bar{\nu}_\mu$  and  $\nu_e$  background to the  $\nu_\mu$  beam represents 2.3% of the interacting neutrinos. The most dominant interactions in the T2K oscillation analyses, the CC0 $\pi$  interactions, represent 40.6% of the interacting neutrinos.

**PM standard CC selection** The PM design has been optimised mainly for the detection of leptons arising from CC interactions, but also to detect the associated protons. The selection has been then originally adjusted to detect neutrino CC interactions. This standard CC selection is described in [80] and summarised in Chapter 4. This standard selection is applied both for INGRID and PM independently. On top of it, before the 3D matching, a 2D track matching is also performed between INGRID and PM tracks to gather the whole detector information for a given track. We will see that the INGRID information is crucial in this analysis. Figure 5.16 shows events interacting in the PM and for which some tracks propagate also through the downstream INGRID module.

The PM and INGRID 2D tracks are matched if they meet both these four conditions:

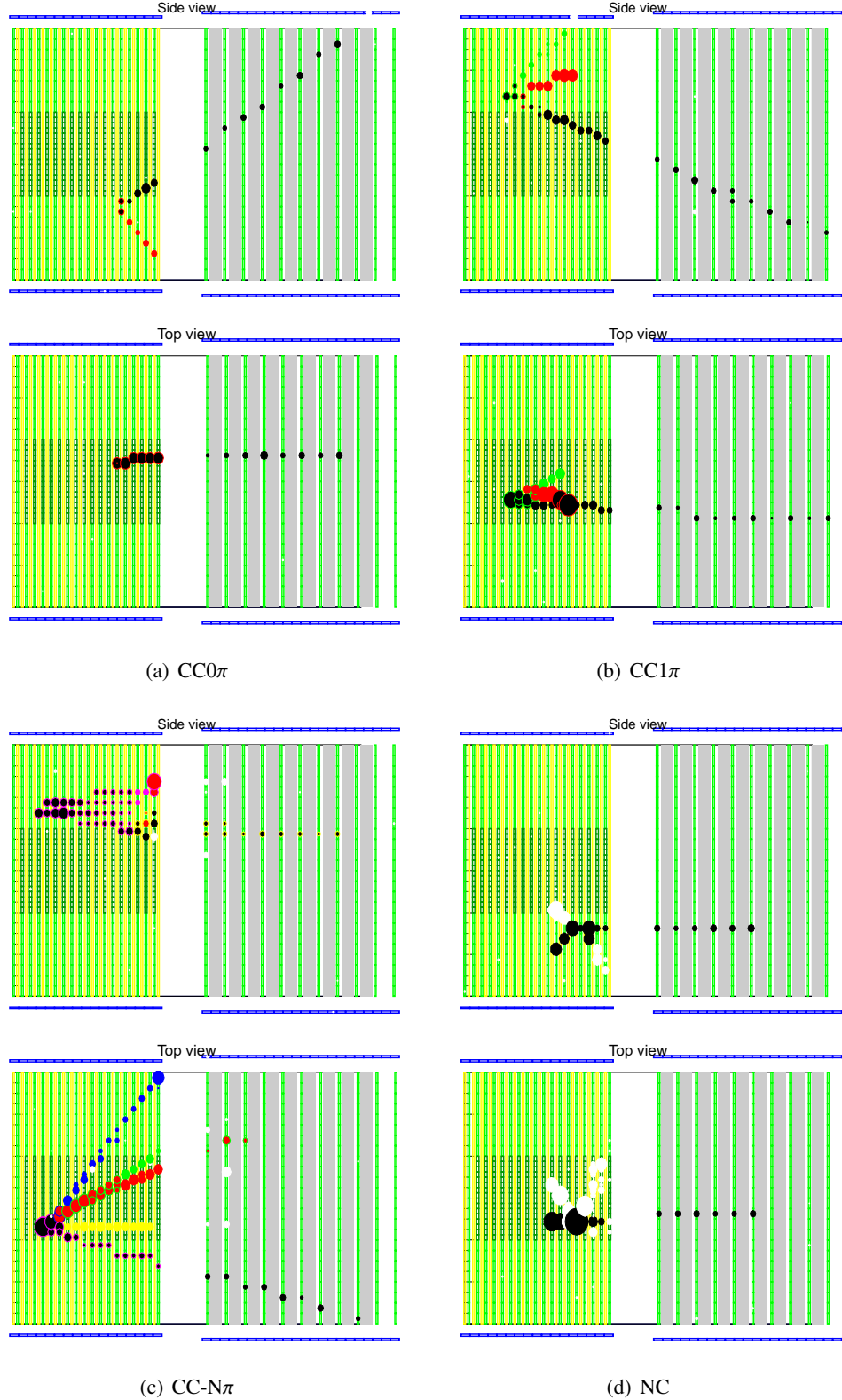


Figure 5.16: Event displays of different simulated neutrino interacting through  $CC0\pi$  (upper left),  $CC1\pi$  (upper right),  $CC-N\pi$  (bottom left) and NC (bottom right). The interactions occur in the PM and propagate to the INGRID central horizontal module. The dots size represents the amount of charge deposition. We indicated the true particle associated to the track with different colours: black for the muons, red for the protons, and the other colours represent the pions (green, blue, yellow). For the NC interaction, we have shown the pion in black and the other hadrons in white.

1. The PM track ends in the ultimate or penultimate PM tracking planes. This guarantees a

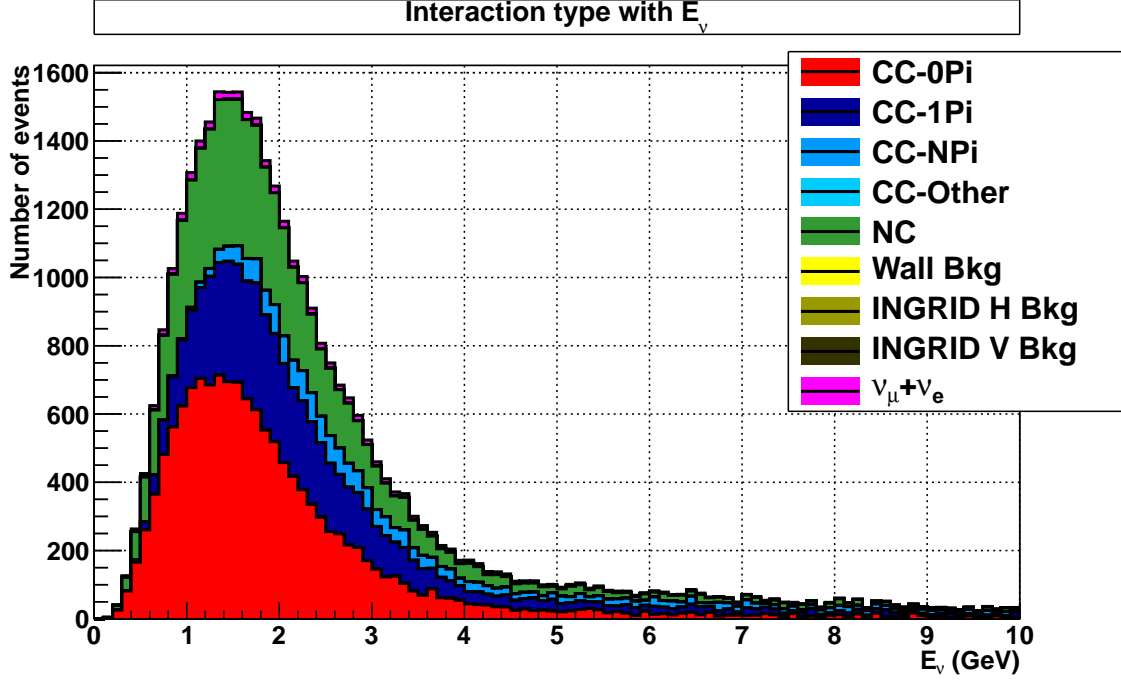


Figure 5.17: Simulated spectrum of neutrino interacting in the PM.

relatively high purity when the matching with INGRID track will be done, but prevents from studying possible high angle tracks that may leave the PM sideways and end in non-central INGRID modules.

2. The INGRID track starting plane is the first INGRID tracking plane. The pile-up possibilities between PM and INGRID hydrocarbon target only is very low, and most of the incoming background comes from external neutrino interactions which produce neutron background, photons or sand muons.
3. The angular difference between the INGRID and PM tracks is lower than  $35^\circ$ .
4. At the halfway point between INGRID and the PM (located 13.5 cm downstream the PM most downstream plane), the track transverse distance is lower than 8.5 mm.

Figure 5.18 shows both the reconstructed neutrino spectrum and the reconstruction efficiency of CC0 $\pi$  interaction as a function of the neutrino energy. The standard selection naturally removes the NC interactions, with a rejection efficiency of 53.4%, while slightly increasing the CC0 $\pi$  interaction purity to 44.8% with a mean efficiency of 75.1%. The standard INGRID reconstruction is not especially selecting the CC0 $\pi$  interactions, the slight increase in purity being directly related to NC interaction rejection. As a comparison, the CC1 $\pi$  interactions have a similar reconstruction efficiency (75.5%). It confirms that this reconstruction and selection are perfectly adapted for CC interaction but should be modified to select mostly CC0 $\pi$  interactions. In this section, we will present our study which consists in refining this existing selection to detect mainly neutrino interacting through CC0 $\pi$  interactions. We will define a selection as cross section model independent as possible to keep the systematics on model dependency small. In particular, cuts on the number of tracks or the energy deposition near the vertex will be avoided, since they considerably depend on Final State Interactions.

We will first describe the particle identification (PID) algorithm we developed to identify the muon in Section 5.3.1. Afterwards, we will describe the CC0 $\pi$  selection in Section 5.3.2 that relies on this PID and will show the final data and MC comparison in the very last part of this section.

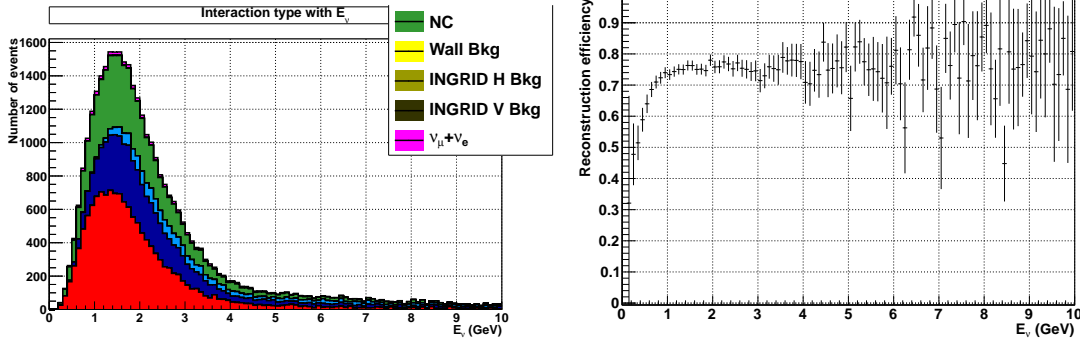


Figure 5.18: On the left is shown the spectrum of reconstructed neutrino, through the standard (CC) INGRID and PM reconstruction (defined in Chapter 4). On the right is shown the reconstruction efficiency of this selection as a function of the neutrino energy.

### 5.3.1 Muon particle identification

#### Particle topology definitions

We have classified each track (particle) based upon its topology to maximise the separation power of the PID, but also due to the necessity to measure muon momentum. The latter is developed in the next paragraphs. Considering these two different constraints, we have classified the tracks between 5 topologies summarised in Table 5.1 and shown in Figures 5.19 for the INGRID stopped, escaping and through-going tracks. Each sample distinction is mainly based on the difference in particle energy deposition information that we will use for our PID. We discuss here the main specificities of each of these 5 topologies:

1. Stopped in the PM: the last tracking plane of the PM is not active, nor the side channels of each planes (channels 0 and 31). Only the energy deposition in PM scintillators is used. The proton Bragg peak provides supplementary information (large energy deposition) to separate muons from protons.
2. Escaping the PM: the last tracking plane or side channels of PM are active. The particle does not deposit any energy in INGRID. This sample is similar to the previous one except for the Bragg peak that could not be used and thus, the muon and proton separation is not as accurate as in the previous sample.
3. INGRID prematurely stopped: the particle escapes from the PM and deposits energy in INGRID without being reconstructed as an INGRID track. These particles most likely stop within the first INGRID iron plane, and do not cross the 2 first INGRID iron planes that are necessary to be reconstructed as an INGRID track (3 active scintillator planes). The Bragg peak energy deposition is located in INGRID, and may be used in principle to increase the particle separation.
4. INGRID stopped: this topology is similar to the previous one, but with the particle reconstructed as an INGRID track. This sample possesses the same advantages than the prematurely stopped sample, but adding also a low background contamination. Together with the prematurely stopped one, this is the only topology that can be used to measure muon momentum above 100 MeV.
5. INGRID escaping (side-escaping or through-going): the particle reaches INGRID and is reconstructed as a track where the 2 downstream (through-going) or side INGRID channels (side-escaping) are active. The side INGRID channels are defined as the channels located on the edge of each INGRID tracking planes (channel 0 and 23). This topology should have an important muon discrimination power due to the important track length (and so, high number of hits), though it does not contain any Bragg peak as in the stopped track sample.

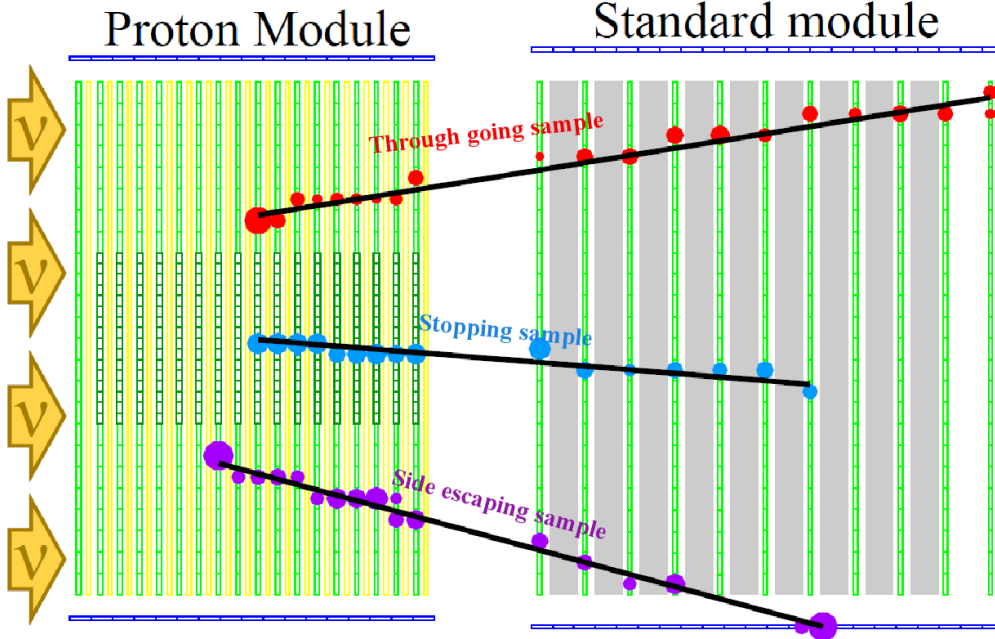


Figure 5.19: Event display showing the INGRID stopped and INGRID escaping samples. The escaping sample is constituted of side escaping and through going samples.

### Momentum determination

The PM has no magnetic field to determine the momentum of detected particles. Therefore, we use the INGRID modules located behind the PM (see Chapter 4) to determine the momentum based on the distance crossed in iron. To determine accurately the momentum, muons produced in the PM need to be stopped into the downstream INGRID module (Stopped topology in Figure 5.19).

This is compulsory to extrapolate the muon momentum from the accurate measurement of the iron distance crossed by the muon. We illustrate this expected correlation between momentum and distance crossed in matter in Figure 5.20, based on pure MC information. The use of INGRID iron is mandatory because the small density of PM plastic is too low to measure momentum above 100 MeV. Given the maximum effective iron distance a muon could cross longitudinally (58.5 cm) one expects to measure muon momentum up to  $\sim 1$  GeV using the downstream INGRID module. To determine the feasibility of this measurement, we study the impact of detector resolution on momentum determination. Assuming 1 GeV muons (close to minimum ionizing particles whose energy loss is  $1.5 \text{ MeV} \cdot \text{g}^{-1} \cdot \text{cm}^2$ ) their  $dE/dx$  in iron is around  $2.1 \text{ MeV} \cdot \text{g}^{-1} \cdot \text{cm}^2$  ([13]), which represents roughly 16.6 MeV/cm in iron (density  $7.9 \text{ g/cm}^3$ ). The 6.5 cm iron plates therefore allow a 108 MeV resolution for 1 GeV muons in iron. For 1 GeV muons, this represents a 11% detector resolution on muon momentum. This confirms the reasonable use of this observable (iron distance) to determine muon momentum from 100 MeV to 1 GeV with a 11% resolution (for a minimum ionizing particle).

In this study, we must not neglect the distance crossed by the muon in plastic scintillator. Given the plastic density ( $1.0 \text{ g/cm}^3$ ) and PM maximal plastic longitudinal distance (46.2 cm), this represents a

	PM stopped(1)	PM escaping(2)	INGRID prematurely stopped(3)	INGRID stopped(4)	INGRID escaping (5)
Stopped in PM	○	×	×	×	×
Reaching INGRID	×	×	○	○	○
Has a track in INGRID	×	×	×	○	○
Track stopped in INGRID	×	×	×	○	×
Track escaping INGRID	×	×	×	×	○

Table 5.1: Definition of the five track possible topologies. The INGRID escaping track is both constituted of through-going and side-escaping tracks.

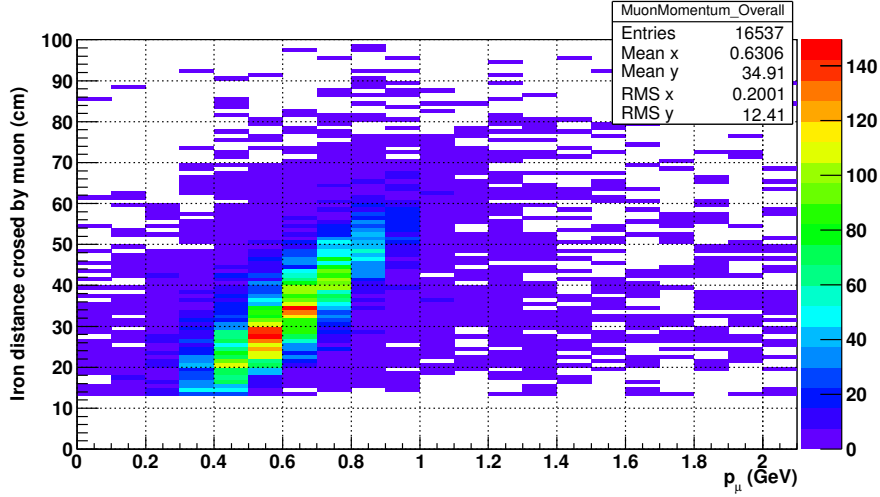


Figure 5.20: Simulated distance crossed in INGRID iron by muon of momentum  $p_\mu$  produced in a neutrino interaction in the PM Hydrocarbon.

$\sim 97$  MeV energy loss for a 1 GeV muon. This indicates that a neutrino interacting in the upstream detector part produces a muon that will lose nearly 100 MeV before reaching INGRID. It will not be the case for a muon coming from a neutrino interacting in the downstream part of the PM, and may introduce another smearing of the momentum distribution since it is absolutely not negligible towards INGRID detector resolution. For this reason, we have also used the plastic distance crossed by the muon to determine its momentum. To simplify the problem, we have set for each muon an equivalent iron distance crossed ( $d_\mu$ ) defined by:

$$d_\mu = \text{Iron distance crossed in INGRID} + \frac{\text{Plastic distance crossed in PM and INGRID}}{\text{Density ratio}} \quad (5.3.1)$$

with  $\text{Density ratio} = \frac{7.87}{1.03}$ . We have shown the relation between muon momentum and equivalent iron distance in Figure 5.20 taking into account detector resolution and reconstruction for true muons. The 100 MeV detector resolution is visible. The lack of events before 13 cm of iron crossed comes from the selection that we will describe in Section 5.3.2.

We will therefore only use samples where the muon is reconstructed in the INGRID stopped topology in order to be able to accurately measure its momentum. Up to here in this thesis, only the true muons from MC have been used. In order to be able to apply this study on data, we need a muon identifying algorithm to select the reconstructed muons.

### Muon particle identification

The muon particle identification is based on the particle energy loss in the detector,  $\frac{dE}{dx}$ . Experimentally,  $\frac{dE}{dx}$  is measured using the charge deposition in a scintillator corrected by the path length in the scintillator. As described in [13], the  $\frac{dE}{dx}$  of a particle is directly related to its velocity. The muons and pions are then often close to minimum ionizing particles (due to their small masses compared to protons), while heavy hadrons as protons are often too slow to be minimum ionizing at T2K energies. On the same argument, protons are more often stopped in the detector than muons. Before stopping, these proton tracks will deposit a large amount of energy, corresponding to the Bragg peak, enhancing the discrepancy between muons and protons. Figure 5.16 shows an event display of a  $CC-N\pi$ , that illustrates these differences between muon and proton energy depositions.

For comparison, Figure 5.21 shows the charge per hit distributions of the reconstructed muons, pions and protons. The  $\frac{dE}{dx}$  is represented by the number of photo-electrons (p.e) detected in a scintillator. The charge has been corrected from possible angle dependency and also from fiber attenuation. These corrections are developed in Appendix E. The distributions clearly confirm our hypotheses. A

minimum ionizing particle letting 1.5 MeV/g/cm<sup>2</sup>, the 1 cm PM INGRID type scintillator (density =1.03) should have a minimum ionizing particle peak around 1.5 MeV, represented here by a peak at 17 and 32 p.e respectively in the INGRID and SciBar type scintillators. One observes that we have not corrected attenuation in the scintillator, which could explain the different MeV to p.e conversion in the SciBar type scintillator plot.

As explained before, most of the differences between muons and protons are due to proton low velocity, which is especially true in the last hits of the tracks. One has the idea to focus mainly on these hits to distinguish between muons and protons. Though this was attempted, we decided to use all track hits information in order to be less sensitive to systematics on p.e detected in a scintillator for small tracks. Therefore, we developed a muon confidence level based on all the hit informations of each track. In order to maximise the separation between tracks, we only used the hits that are exclusive to each track, meaning not shared between different tracks.

The confidence level is based on the Bayes' theorem to identify the muon using the collection of the particle energy deposition ( $[\frac{dE}{dx}]_{nhits}$ ):

$$\mu_{CL} = P(\mu | [\frac{dE}{dx}]_{nhits}) = \frac{P([\frac{dE}{dx}]_{nhits} | \mu) \cdot P(\mu)}{P([\frac{dE}{dx}]_{nhits})} \quad (5.3.2)$$

with  $P(\mu | [\frac{dE}{dx}]_{nhits})$  the probability of the track to be associated to a muon considering its collection of energy deposition in the scintillators ( $[\frac{dE}{dx}]_{nhits}$ ).  $P([\frac{dE}{dx}]_{nhits} | \mu)$ ,  $P([\frac{dE}{dx}]_{nhits})$  and  $P(\mu)$  are respectively the probability that a muon deposits the collection of energy losses  $[\frac{dE}{dx}]_{nhits}$ , the probability of any particle to have the same energy loss, and the proportion of muons in the sample (among all the particles).

A complete partition of the particle space phase is represented by muon and its complement (to be anything except a muon), which implies:

$$P([\frac{dE}{dx}]_{nhits}) = P([\frac{dE}{dx}]_{nhits} | \mu) \cdot P(\mu) + P([\frac{dE}{dx}]_{nhits} | \mu_{bar}) \cdot P(\mu_{bar}) \quad (5.3.3)$$

Though the use of correlations between the energy losses may introduce a supplementary information, this procedure may be more adapted to a detector where the energy deposition is clearly constant for a minimum ionizing particle. In the PM, the scintillator dead areas, the scintillator attenuations and other effects are not corrected track by track and provide a relatively large dispersion in the energy loss of a minimum ionizing particle. For this reason, we assumed in this study that all hits of a given track are independent. This leads to:

$$P([\frac{dE}{dx}]_{nhits} | \mu) = \prod_{i=0}^{nhits} P([\frac{dE}{dx}]_i | \mu) \quad (5.3.4)$$

which is also correct for the non-muon ( $\mu_{bar}$ ) case. Injecting Equations 5.3.3 and 5.3.4 in Equation 5.3.2, this leads to the muon confidence level definition in the case of independent energy losses:

$$\mu_{CL} = \frac{(\prod_{i=0}^{nhits} P([\frac{dE}{dx}]_i | \mu)) \cdot P(\mu)}{(\prod_{i=0}^{nhits} P([\frac{dE}{dx}]_i | \mu)) \cdot P(\mu) + (\prod_{i=0}^{nhits} P([\frac{dE}{dx}]_i | \mu_{bar})) \cdot P(\mu_{bar})} \quad (5.3.5)$$

This muon confidence level is the base of our PID. As it exclusively uses the energy deposition information, the charge response of the detector needs to be accurately calibrated to pertinently provide the highest information without introducing large systematics. The calibration we introduced in Chapter 4 has been explicitly developed in order to use this PID. This is illustrated by observing the similarities between data and MC charge distribution both for “sand muons” and events in the fiducial volume defined in Chapter 4. The latter distribution has been shown in Chapter 4, though will not be used to select any cut considering the blind analysis we perform.

A different muon confidence level is built for each track topology. The classification summarised in Section 5.3.1 defines the motivation of such a separate treatment. For each topology, the confidence level is built as follow using the MC:

1. We collected all tracks reconstructed with a given topology, whatever the interaction type in the fiducial volume.

2. For each reconstructed track, the true particle closest from the track is associated.
3. If the track is associated to a true muon, each of its charge deposition is added in the muon charge distribution. A different distribution is filled depending on each channel hit in the track, namely whether INGRID type in PM, SciBar type in PM or INGRID type in INGRID. This separation is necessary to take into account the discrepancies between channel geometries (for INGRID or SciBar type) but also to differentiate between PM and INGRID hits. This latter caution is especially taken to deal with possible high energy hits in the PM due to vertex activity in the PM (low energy protons or pions...) that does not affect INGRID, being only interested in interactions in the PM. The number of muon in the topology is increased by one. The same goes for the “not-muon” distribution if the track is associated with a particle different from a muon
4. When all the tracks have been investigated, each of the 6 charge distributions are normalised to generate discrete probabilities to have a muon (or “not-a-muon”) having such charge deposition in such a channel (INGRID type in PM or INGRID, or SciBar type). The probability to have a muon or “not-a-muon” is naturally given by normalising the particle counter mentioned above.

Figures 5.22 shows the probability for a muon and “not-a-muon” ( $\bar{\mu}$ ) to let a hit of a given charge in the various topologies. Note that we observed an anomaly for low charge depositions in the MC in INGRID detector part in Chapter 4. Therefore, we decided not to use the hits that left a charge (corrected) lower than 8 p.e, in order not to be sensitive to this anomaly. Instead, we choose to study this effect as a systematics, instead of keeping it in the standard muon confidence level. For this reason, such a cut will not bias our study in the end.

One observes in Figures 5.22 that the charge corrected is generally higher in the  $\bar{\mu}$  sample than in the  $\mu$  one. We explained earlier that this was expected due to protons higher mass that generate a higher energy loss for a given momentum. We confirmed this energy loss dependency on particle velocity showing the charge deposition for  $\mu$ ,  $\pi$  and protons in Figures 5.21. Since the  $\mu$  and  $\pi$  have similar masses (105.7 MeV and 139.6 MeV), they have a similar energy loss through electromagnetic processes that dominate the hadronic ones in the 1 GeV energy region. The high proton mass (938.3 MeV) reduces the particle velocity as compared to a muon with similar momentum, which increases the energy loss (and so, the charge deposition) as can be shown in Figure 5.21. The particle composition shown in Figure 5.21 has to be read to understand Figure 5.22: the more the muon background ( $\bar{\mu}$ ) is populated by protons, the better is the charge deposit separation in Figure 5.22. This can be seen for example comparing the PM stopped and INGRID stopped topology, where the protons proportions in the  $\bar{\mu}$  sample are higher in the former. One sees in Figure 5.22 that the separation is clearly better in the PM stopped sample.

The muon confidence levels ( $\mu_{CL}$ ) of each sample are built using the Equation 5.3.5 and the distributions shown in Figures 5.22 and 5.23. These distributions have been normalised beforehand to obtain  $P(\mu)$  and  $P(\bar{\mu})$ . The  $\mu_{CL}$  for the 5 topologies is shown in Figure 5.24 for all particles in MC, and separated for each true particle type:  $\mu$ ,  $\pi$  and protons. The  $\mu_{CL}$  global shape is peaked near  $\mu_{CL} = 0$  and  $\mu_{CL} = 1$ , which confirms the separation abilities of this variable. Moreover, the separation between muons that populate high  $\mu_{CL}$  and protons for  $\mu_{CL}$  values confirms the discrepancies observed in the charge deposition distributions. Pion separation is also observed in much smaller proportions, due to some higher charge deposition in some hits. This may be due to some hadronic interactions, but is more likely due to pion production that happens in multi-tracks events where the tracks may generally be contaminated by 2 particles, in one of the 2 tracking planes.

Finally, we have summarised in Table 5.2 the proportions of tracks in each topology after the standard INGRID and PM reconstruction are applied. The muon purity for each topology is also shown. The cross section measurement will be performed only with muons stopping in the INGRID sample. We highlight here that this corresponds to only 3.7% of the total amount of tracks, though having a relatively important muon purity (43.9%) prior to applying the PID. Prior to applying the PID on signal data, we have shown the comparison between MC and data confidence level for the sand muon sample in Figure 5.25. This confirms the PID ability to select true muons as “muon-like” particle for

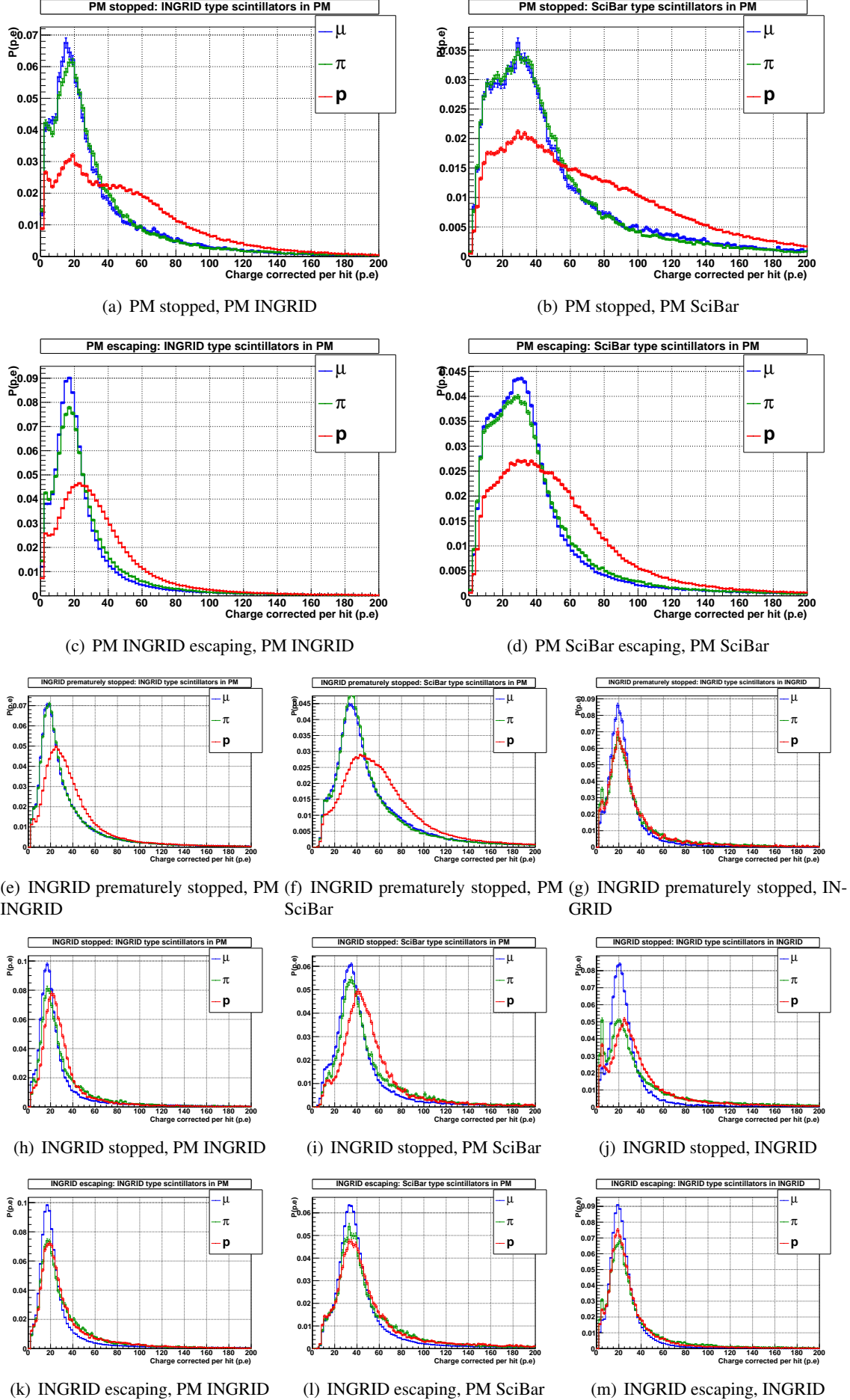


Figure 5.21: Charge distributions of simulated  $\mu$  (blue),  $\pi$  (green) and protons (red) for the five topologies defined in Table 5.1.

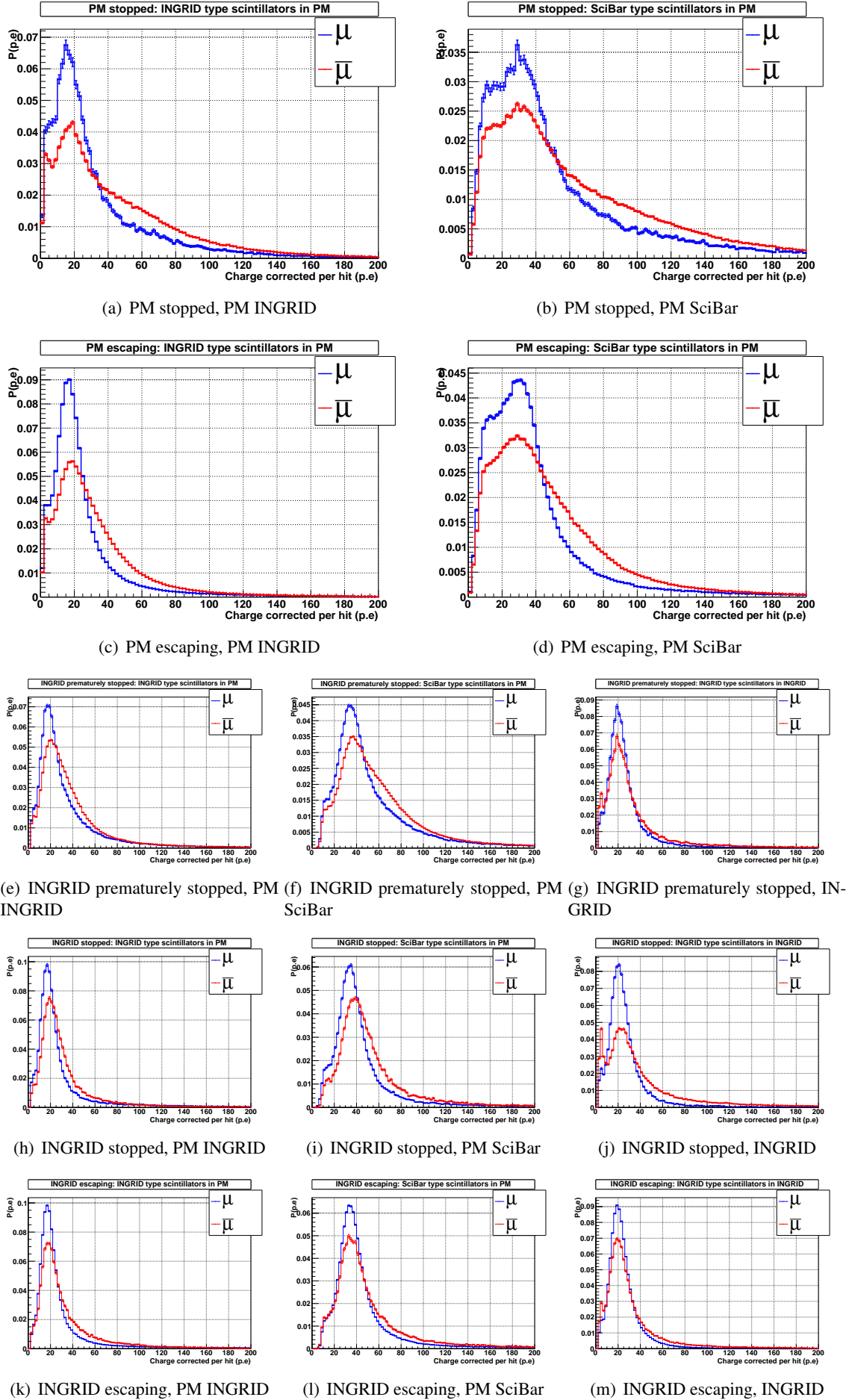
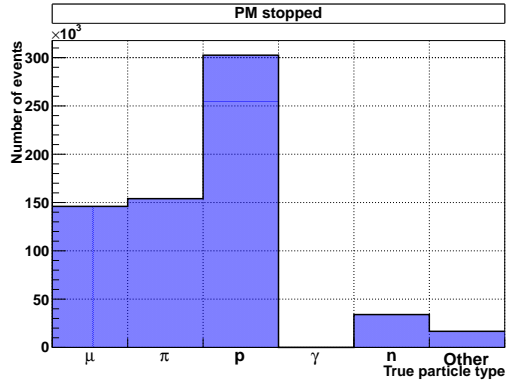
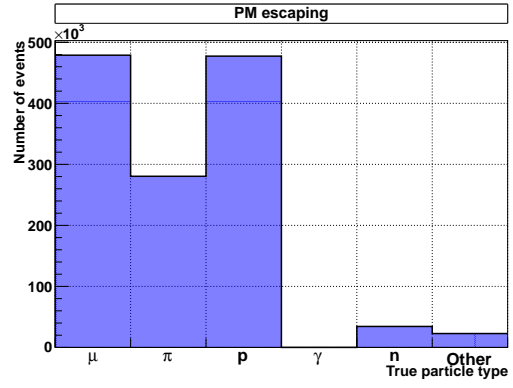


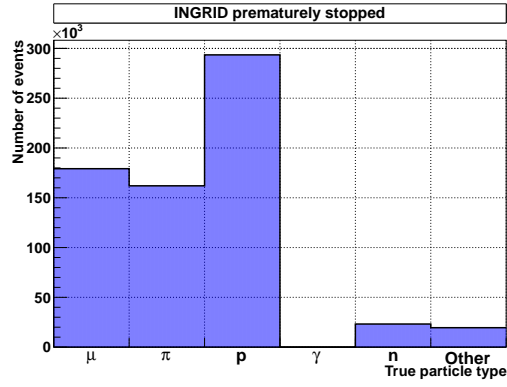
Figure 5.22: Charge distributions of simulated  $\mu$  (blue) and all the non muon particles  $\bar{\mu}$  (red) for the five topologies defined in Table 5.1.



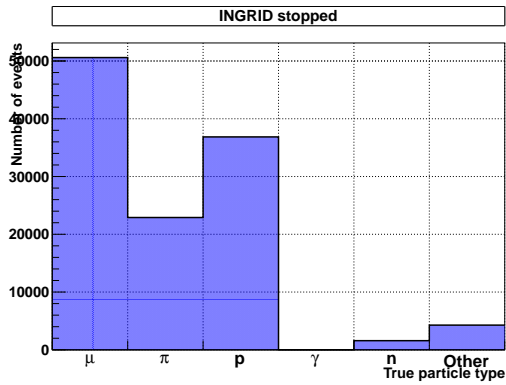
(a) PM stopped



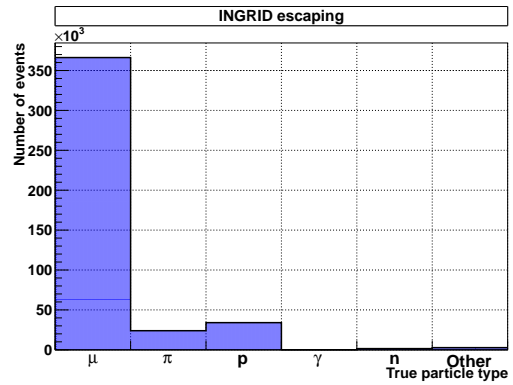
(b) PM escaping



(c) INGRID prematurely stopped



(d) INGRID stopped



(e) INGRID escaping

Figure 5.23: Particle content associated to tracks in each topology.

data, and opens the possibility to use it in the cross section study in more complicated events. The PID final optimisation for the  $CC0\pi$  study will be presented in Section 5.3.2.

	PM stopped	PM escaping	INGRID prematurely stopped	INGRID stopped	INGRID escaping
Number of events (proportions)	20.6%	41.1%	21.2%	3.7%	13.4%
Muon purity	22.5%	37.3%	27.1%	43.9%	86.9%

Table 5.2: Track proportions and muon purities in the different topologies.

### 5.3.2 $CC0\pi$ selection

In this section, we present the selection we used to enhance  $CC0\pi$  purity and measure the muon momentum (and angle). The selection is based on the following cuts, which has been applied in the following order:

1. **Only one  $\mu$ -like particle and several proton-like particles. The  $\mu$ -like particle should stop in INGRID.** A different cut value is used to define  $\mu$ -like and proton-like particles. The requirement of  $\mu$ -like particles to stop in INGRID is essential to maintain the possibility to measure their momentum. Note we will also use a part of the INGRID escaping sample, to populate the high momentum region. However, we will see in Section 5.5 that the statistics in these momentum bin should not be significantly larger compared to the other momentum bins since it can prevent the unfolding method from converging. Therefore, we only used one tenth of the INGRID escaping data in the current version of this analysis. An improvement of the unfolding method should lead to use the full sample.
2. **PM and INGRID track matching for the  $\mu$ -like track.** The INGRID MC does not perfectly describe the whole neutrino hall geometry, and module environments. We know that the external background is not well simulated in INGRID. For example, we have to tune the MC predicted sand muon background using data, since the MC predicts 1.4 less background than measured in data. Moreover, the dark noise simulation is not perfect either. This was the main reason we required three active planes also in INGRID to reconstruct a track. This contamination would typically affect mainly the short distance crossed in iron, and is unpredicted using MC. We tightened the cut on the matching between INGRID and PM 2D tracks to take this into account, and increase data and MC agreement. The cut value tuning is shown in the second part of this section.
3.  **$\mu$ -like track transverse width.** The interaction of the neutrino with electrons is not simulated in this analysis, and can represent a considerable systematic error source. The outgoing electron signature is an electromagnetic shower whose properties will be studied in Chapter 6 in INGRID. We will apply a cut on the transverse track width based on this analysis to remove the  $\mu$ -like tracks that have a large track transverse width, which is the signature of the shower of an electron.

In the coming three paragraphs, we describe the tuning of each cut value, before showing the final result at the end of this section. We used T2K data taken from run 2 to run 4, which have been taken between November 2010 and July 2013. The PM has been installed between run 1 and run 2, which explains we have not used the run 1. Moreover, we have not used data taken during T2K runs 3a (respectively 3b), since in this run, the horn current has been switched off (respectively, the current has been changed from 250 kA to 200 kA). The total amount of data used correspond to  $5.86 \times 10^{20}$  POT out of the  $6.04 \times 10^{20}$  available during the same period. In the following sections, we will therefore use MC simulations corresponding to  $5.86 \times 10^{20}$  POT.

#### Particle identification tuning

The  $CC0\pi$  signal is defined by observing the final state  $1\mu + Np + 0\pi$ . As shown previously, the PID has a capability to discriminate between muons and protons. This is particularly adapted to  $CC0\pi$

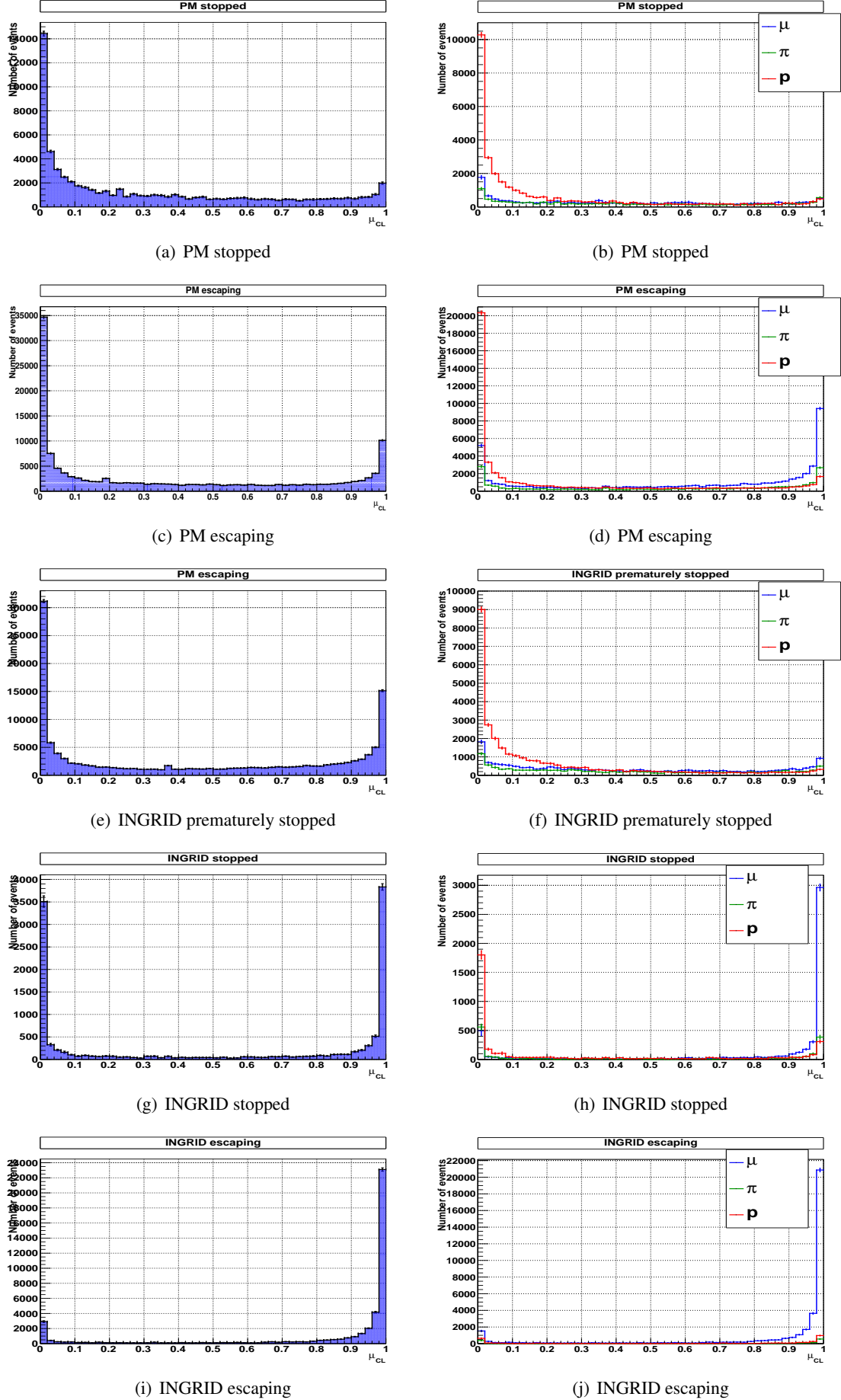


Figure 5.24:  $\mu_{CL}$  distributions comparison for the whole track samples reconstructed as a PM neutrino event (left). On the right, the distinction is shown between true  $\mu$  (blue),  $\pi$  (green) and proton (red) tracks.

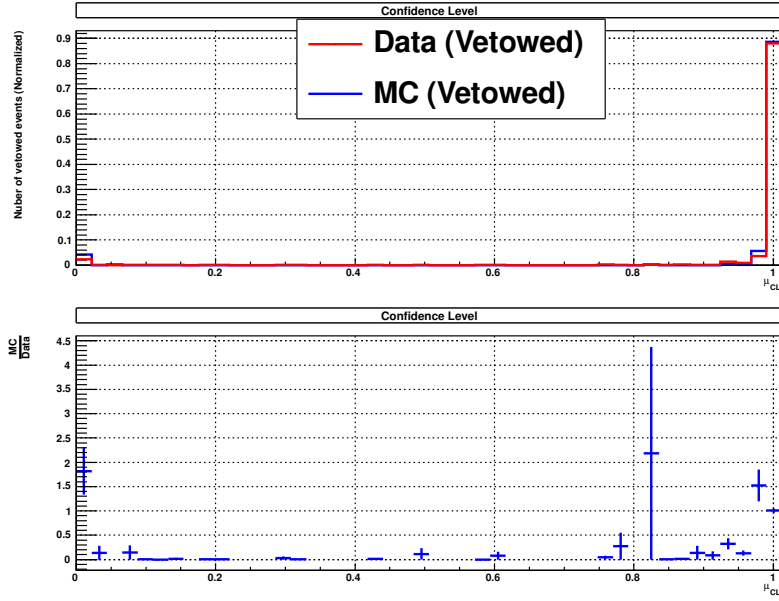


Figure 5.25: Confidence level comparison for data and MC sand muon events.

interactions, where we expect one and only one  $\mu$ -like particle in the neutrino decay product (no charged  $\pi$  that are essentially  $\mu$ -like).

To determine the cut value on  $\mu_{CL}$  for a particle to be  $\mu$ -like, we used all the available muons provided by the standard CC reconstruction described in the beginning of Section 5.3.

The PID cut values are tuned comparing  $\mu$  purity and relative efficiency with the original muon proportions. The relative efficiency is defined as:

$$\epsilon = \frac{N_{\mu}^{\text{selected}}}{N_{\mu}^{\text{reconstructed}}} \quad (5.3.6)$$

with  $N_{\mu}^{\text{selected/reconstructed}}$  the number of muons selected after the  $\mu_{CL}$  and reconstructed by the original INGRID selection respectively. The results are presented in Figure 5.26. Muons naturally populate high  $\mu_{CL}$  regions. Therefore, we applied a cut at the value  $m_{\text{cut}}$  defined by  $\mu_{CL} \geq m_{\text{cut}}$  to select the muons. The cut value has been chosen to maximise both purity and efficiency, but also to minimise sensitivity to systematic errors. This last condition requires a cut in a region with relatively small number of events in the  $\mu_{CL}$  to minimise impact of bin by bin migration in systematic error evaluation. Figure 5.26 shows that the muons are mainly spread from  $\mu_{CL} = 1.0$  to  $\mu_{CL} = 0.8$ . A relatively good compromise is obtained requiring  $m_{\text{cut}} = 0.7$ , which increases the muon purity from  $\mu_{\text{purity}} = 48\%$  to  $\mu_{\text{purity after cut}} = 75\%$  after this cut with a relative efficiency of  $\epsilon_{\mu} = 84\%$ .

The same procedure is applied to select protons. Protons naturally populate low muon confidence levels and we applied a cut  $p_{\text{cut}}$  defined by  $\mu_{CL} \leq p_{\text{cut}}$  to select them. Figure 5.27 shows the results for proton purity and selection efficiency. Using a similar argument as for muons, we defined the optimum cut value as  $p_{\text{cut}} = 0.3$ .

On one hand, we highlight that the selection optimisation is not referring to CC0 $\pi$  in particular: all muons and protons available in our sample were used. Though this could reduce in principle the purity and efficiency of the selection, this ensures that the PID is independent from a particular cross section model. Possible variations with the CC0 $\pi$  sample muons or protons are expected to only come from mis-reconstruction, *e.g.* coming from a different background in CC0 $\pi$  interactions. This background may vary with the cross section model, implying that we must not select explicitly CC0 $\pi$  interactions to tune the PID. On the other hand, one remarks that the proton and muon cut values  $\mu_{\text{cut}}$  and  $p_{\text{cut}}$  are different: a proton is not only a particle “which is not a muon”. Though an explanation based on optimisation of purity and efficiency in the PID was given, another correlated motivation lies in

the systematic error effects. Distorsion of the  $\mu_{CL}$  may happen, particularly with the error on the charge left by each particle in a scintillator. A “dead zone” in the  $\mu_{CL}$  has the advantage to prevent a large migration of muons/protons from one side to another of a single cut value. It leads to a lower dependency of the selection on the systematic error of charge deposition.

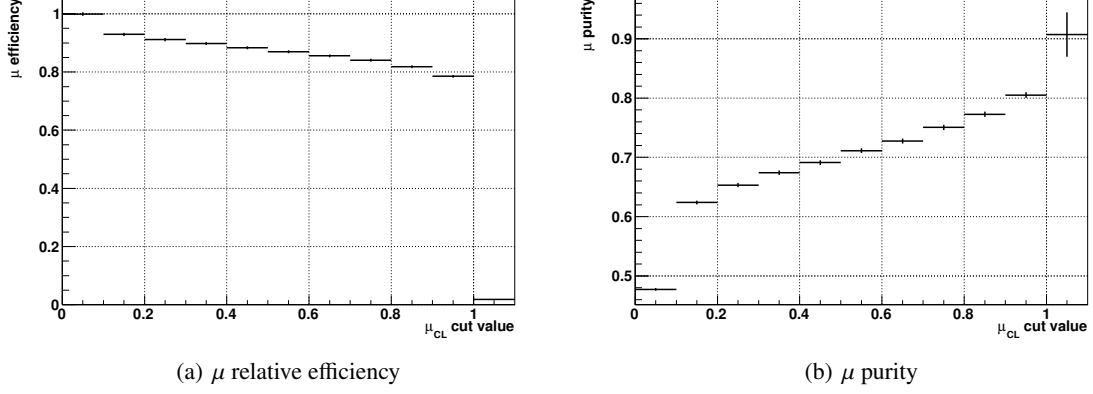


Figure 5.26: Relative efficiency and muon purity with the variation of  $\mu_{CL}$  cut value. The cut applied for muon selection in each bin is  $\mu_{CL} \geq \text{Bin Value}$ .

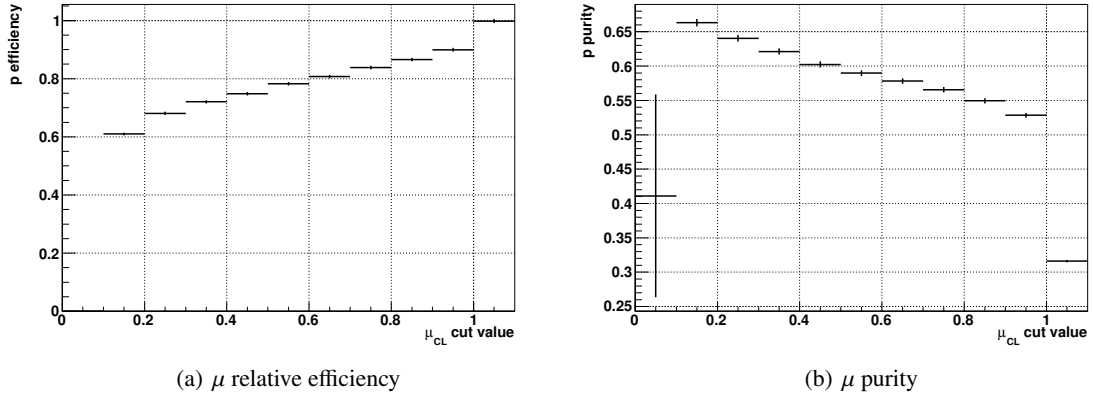


Figure 5.27: Relative efficiency and proton purity with the variation of  $\mu_{CL}$  cut value. The cut applied for proton selection in each bin is  $\mu_{CL} \leq \text{Bin Value}$ .

We apply the PID cuts and only consider interactions in which a  $\mu$ -like track stops in INGRID. Considering only interactions containing at least one track stopping in INGRID, the original CC0 $\pi$  purity is 39.4%. The PID cut requiring only one  $\mu$ -like track and other proton-like tracks increases the purity to 63.8% with an efficiency of 58.6% in CC0 $\pi$  interactions. The precise informations on this cut are summarised in Table 5.3. The MC and data comparisons after this cut is applied are shown in Figure 5.28 both in muon distance in iron  $d_\mu$  and angle  $\theta_\mu$ . The number of events selected is globally 9% higher in data than the MC. The relative discrepancy is especially higher for interactions whose muons produce short tracks in INGRID. This discrepancy is 58% in the first filled iron distance bin ( $d_\mu \in [15^\circ, 20^\circ]$ ). Though it may come from a cross section issue, this increasing discrepancy with the smaller depth in iron indicates a possible background contamination on the edge of INGRID. To separate the signal and a possible external background, the matching between 2D INGRID and PM tracks has been refined in the next section.

#### $\mu$ -like PM and INGRID track matching

The original matching conditions between PM and INGRID 2D tracks have been introduced in the beginning of Section 5.3. We consider possible sources of background such as sand muons, but also

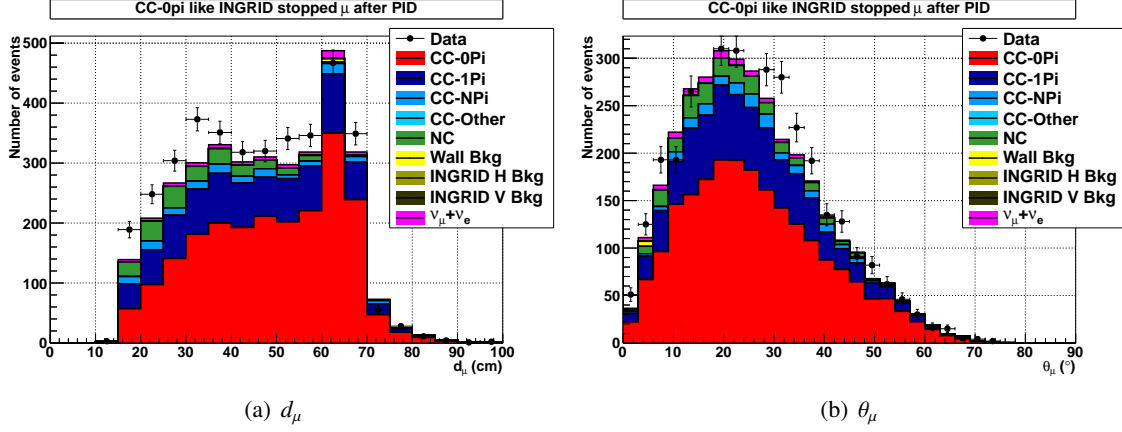


Figure 5.28: Event distribution of the data and MC as a function of distance in iron (left) and angle (right) after the PID is applied.

neutrons or gammas coming from interacting neutrinos in the hall. We know that the external background simulation is highly under-estimated in the MC, since we had to increase the external background predicted by MC by a factor 1.4 so that the number of sand muons matches the data one. This tuning does obviously not imply that the simulation of other background sources will be tuned enough. Moreover, the matching conditions shown in the beginning of Section 5.3 are clearly permissive, and might be reduced without losing as significant amount of signal (for a reasonably good tracking). Therefore, we change the matching conditions between PM and INGRID from:

$$|\theta_{PM}^X - \theta_{INGRID}^X| < 35^\circ \text{ and } |\theta_{PM}^Y - \theta_{INGRID}^Y| < 35^\circ \quad (5.3.7)$$

$$|h_{PM}^X - h_{INGRID}^X| < 8.5 \text{ cm and } |h_{PM}^Y - h_{INGRID}^Y| < 8.5 \text{ cm} \quad (5.3.8)$$

to

$$|\theta_{PM}^X - \theta_{INGRID}^X| < 25^\circ \text{ and } |\theta_{PM}^Y - \theta_{INGRID}^Y| < 25^\circ \quad (5.3.9)$$

$$|h_{PM}^X - h_{INGRID}^X| < 7 \text{ cm and } |h_{PM}^Y - h_{INGRID}^Y| < 7 \text{ cm} \quad (5.3.10)$$

with  $\theta_{PM/INGRID}^X$ ,  $\theta_{PM/INGRID}^Y$  the PM/INGRID 2D angle in the XZ, YZ planes respectively, and  $h_{PM/INGRID}^X$ ,  $h_{PM/INGRID}^Y$  the PM/INGRID transverse position at the halfway point between PM and INGRID in the XZ and YZ planes respectively.

These criteria have been only changed for the muon particles, since they may heavily affect the muon momentum and angle determination. The matching conditions are only based on geometrical considerations in order to not overtune this cut. Assuming the worst possible case, we may try to match a track crossing the 3 last tracking planes of PM and the 3 first ones in INGRID. Assuming a  $\pm 2.5 \text{ cm}$  resolution on the transverse position due to INGRID scintillator width ( $5 \text{ cm}$ ), we obtain the following resolution for low angle tracks:

$$\tan(\theta_{PM}) = \frac{2.5}{4.6 \cdot 2} \rightarrow \theta_{PM} = \arctan\left(\frac{2.5}{4.6 \cdot 2}\right) = \pm 10.3^\circ \quad (5.3.11)$$

$$\tan(\theta_{INGRID}) = \frac{2.5}{10.7 \cdot 2} \rightarrow \theta_{INGRID} = \arctan\left(\frac{2.5}{10.7 \cdot 2}\right) = \pm 6.7^\circ. \quad (5.3.12)$$

Considering the most pathological case, one expects for example the PM track angle to be positively over-estimated by  $10.3^\circ$  and the INGRID track to be negatively over-estimated by  $-6.7^\circ$ . This implies an angle discrepancy of  $17^\circ$  between the INGRID and PM tracks. Assuming a perfect reconstruction, this latter criterion is likely over-estimated since the angle difference between true and reconstructed values is likely to be correlated between INGRID and PM. In the case of 100% correlation, one would expect a maximal difference of  $10.3 - 6.7 = 3.6 \text{ cm}$  which is the most optimistic case. Because of the INGRID non perfect reconstruction, or possible dark noise hits along the track, we required the PM and INGRID track angle difference to be less than  $25^\circ$ .

The transverse track position at the half distance between the end of PM and starting of INGRID is also used. This halfway point is located 13.5 cm after the end of PM and before INGRID. Considering the most pessimistic case we defined for the angle, the resolution on the transverse track position at the halfway point is:

$$\frac{2.5}{h_{\text{PM}}} = \frac{4.6 \cdot 2}{4.6 \cdot 2 + 13.5} \rightarrow h_{\text{PM}} = \pm 6.1 \text{ cm if INGRID type} \quad (5.3.13)$$

$$\frac{2.5}{h_{\text{INGRID}}} = \frac{10.7 \cdot 2}{10.7 \cdot 2 + 13.5} \rightarrow h_{\text{INGRID}} = \pm 4.0 \text{ cm} \quad (5.3.14)$$

using Thales theorem. The same argument as for angle criteria can be used: assuming the worst possible case, one would expect a transverse position difference of 10.1 cm between INGRID and PM tracks. However, in the case of 100% correlated variations between transverse position in INGRID and PM, one would expect only 2.1 cm variation. We finally required the difference between the PM and INGRID transverse position to be less than 7 cm in order to tighten the existing cut, without losing too many events a priori due to resolution issues. This value has not been tuned neither on data nor MC, and maybe refined in the future.

This criterion only slightly increases the CC0 $\pi$  purity from 63.8% to 64.6% with a 71.2% efficiency. The event breakdown associated to the cut efficiency and remaining purities is summarised in Table 5.3. One clearly remarks that this cut has relatively low performances on MC. This is expected since it should mainly remove a background existing in data that is not simulated by MC. Figure 5.29 shows the data and MC distributions with the muon angle and its distance crossed in INGRID iron. One clearly observes on the latter that the better agreement between data and MC than compared to Figure 5.28. In fact, the discrepancy between MC and data has globally decreased from 9% to 6%. Moreover, one observes relative shape variations from Figure 5.28, coming from the decrease of events at small iron distances because of their lower angular and transverse position resolutions. Finally, a large event discrepancy remains for the tracks having a muon crossing only  $d_\mu \in [15 \text{ cm}, 20 \text{ cm}]$  in INGRID. Though the cut has highly increased data and MC agreement from 58% to 39%, the discrepancy is still high and seems un-related to cross section issues considering that this variation is absolutely not seen in the neighbour bins. We will investigate the source of such a discrepancy in the next section.

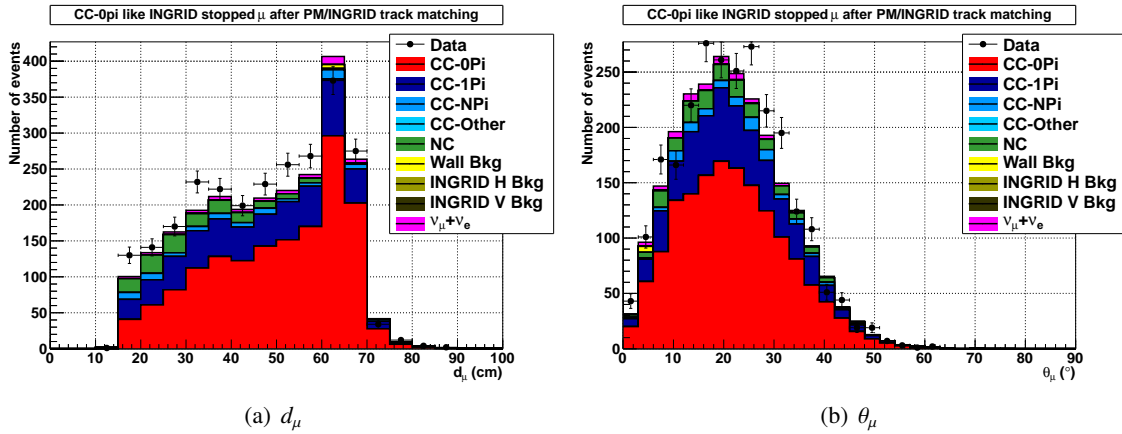


Figure 5.29: Event distribution of the data and MC as a function of distance in iron (left) and angle (right) after the PID and matching cuts are applied.

#### $\mu$ -like track transverse width

We observed in the previous section that a discrepancy between data and MC remains, especially in the first  $d_\mu \in [15 \text{ cm}, 20 \text{ cm}]$  bin. Among other possibilities, we figure out this background may be due to  $\nu_\mu$  interacting with the electrons of the PM. This interaction is not simulated in the MC. Those neutrinos would interact in a neutral current interaction:

$$\nu_\mu + e^- \rightarrow \nu_\mu + e^- \quad (5.3.15)$$

This would lead to a momentum transfer from the neutrino to the electron that may escape from the atom and produce a reconstructed track in PM and INGRID. We have performed a complete electron study in INGRID in Chapter 6 to remove the possible  $\nu_e$  background. The main results of this electron rejection may be adapted to the current study in order to remove what may be an electron background. In particular, we will see in Chapter 6 that the main feature of the electron tracks in INGRID are their smaller length, but also larger width (due to an electromagnetic shower production) compared to the muon track. But, though the muon track length can be equal to the high energy electrons one, the track width should be clearly higher for electrons independently from the particle energy. The track transverse width of an electromagnetic shower is a material property, and is around  $6.8\text{ cm}$  in INGRID iron (see Chapter 6). Since the scintillators have a  $5\text{ cm}$  resolution, this electromagnetic shower development can be clearly identified in INGRID. In this analysis, we only consider the electromagnetic shower development in INGRID. The conversion length in carbon is higher ( $\sim 40\text{ cm}$  [13]) and so, the electromagnetic shower may not develop in the PM. This study may be refined using the PM in the future. Using the MC, we generate electrons in PM and study their track transverse width in INGRID averaged over all INGRID planes. Figure 5.30 exhibits an important discrepancy between muons and electrons both produced in PM but propagating through INGRID. We have shown the average track width with the latest scintillator plane crossed in INGRID. The average track width is clearly higher for electrons ( $\sim 1.9$  channels) as compared to muons ( $\sim 1.3$  channels) due to the electromagnetic shower development. The further the electron track penetrates iron, the larger is the transverse width because of the electromagnetic shower development (See Chapter 6).

We set a cut on the average track width to reduce electron contamination coming from possible  $\nu_\mu$  interactions with electrons. The variation in track transverse width with iron distance penetrated in INGRID naturally implies a different cut for different iron distances. Figure 5.30 shows the muon and electron average track width distributions for various distances in iron. As predicted earlier, the average transverse track width difference between muons and electrons is smaller for tracks stopping in the first INGRID iron layers. Based on muon and electron track width distribution, we require a  $\mu$ -like track crossing less than  $30\text{ cm}$  in iron to have an average transverse track width lower than 1.3 channels. For the longer tracks ( $d_\mu > 30\text{ cm}$ ), we require the  $\mu$ -like track to have an average transverse width smaller than 1.5 channels.

We apply this cut both on the  $\mu$ -like track in MC and data. The transverse track width cut barely changes the MC  $CC0\pi$  purity from 64.6% to 65.1% with an efficiency of 99.6%, which confirms most of the  $\mu$ -like tracks in MC  $CC0\pi$  interactions are effectively muons. On the other hand, the total number of events in data is reduced by 2.2% while MC is reduced by 1.1%. Figure 5.31 shows the distribution of the iron depth of the muon and shows that this change mainly affects track crossing the iron distance  $d_\mu < 20\text{ cm}$ . The data and MC discrepancy is reduced from 36% to 16% in this bin. Figure 5.32 shows the data average track width distribution and confirms the data higher track width observation.

### Results on $CC0\pi$ selection

The  $CC0\pi$  selection described above is summarised in Table 5.3. Table 5.4 shows the data and MC relative comparison with the statistical error bars. The binning has been changed from previous plot to increase clarity, and is now the same as the one we will use for the unfolding (Section 5.5). The general agreement is reasonable though showing an overall higher rate in data. The data exhibit a  $3\sigma$  higher fluctuation in the bin ( $d_\mu \in [15\text{ cm}, 20\text{ cm}], \theta_\mu \in [0^\circ, 20^\circ]$ ).

## 5.4 Cross section analysis method

The double differential cross section will be measured as:

$$\frac{d^2\sigma}{dp_\mu d\theta_\mu} = \frac{N_{CC0\pi}^{\text{Selected}}(p_\mu \cap \theta_\mu)}{\phi \cdot N_T \cdot \epsilon(p_\mu \cap \theta_\mu) \cdot \delta p_\mu \cap \delta \theta_\mu} \quad (5.4.1)$$

with:

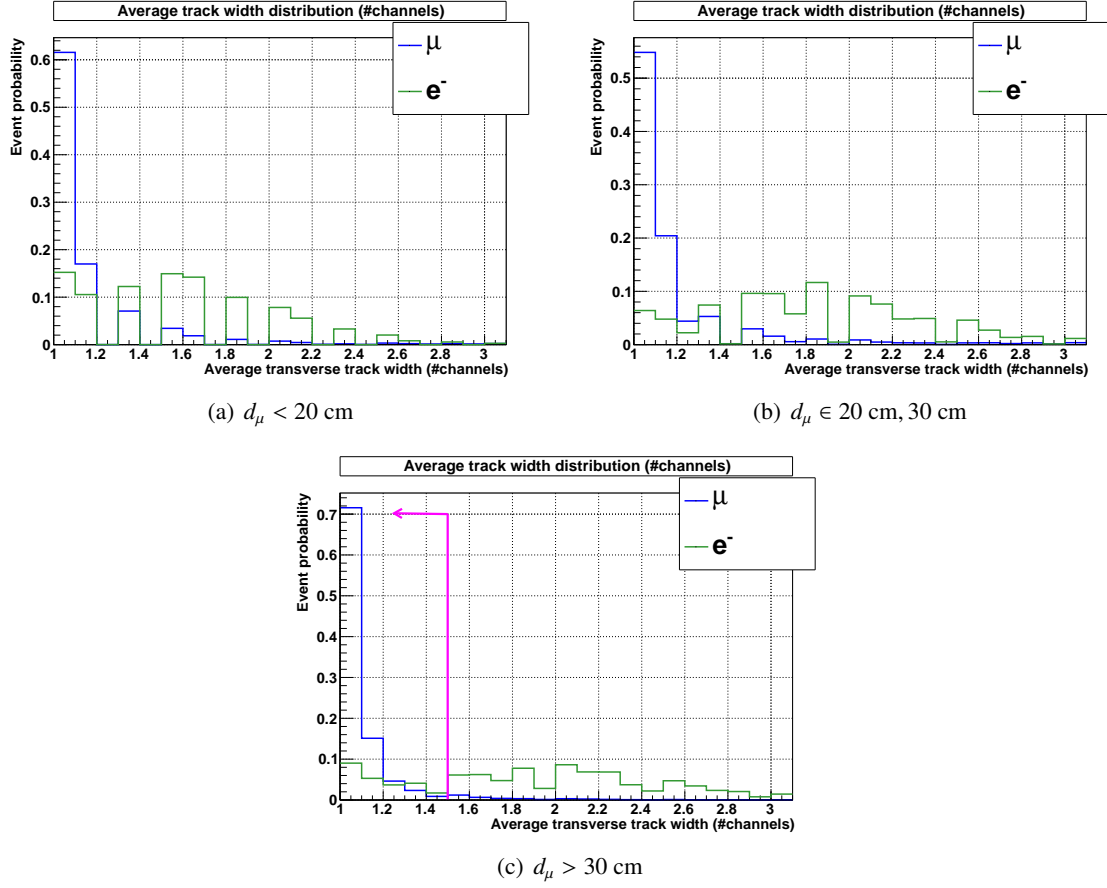


Figure 5.30: Distribution of the track width in INGRID for simulated muons (blue) and electrons (green) coming from respectively  $\nu_\mu$  and  $\nu_e$  interacting in the PM. The tracks are separated considering their penetration in INGRID iron.

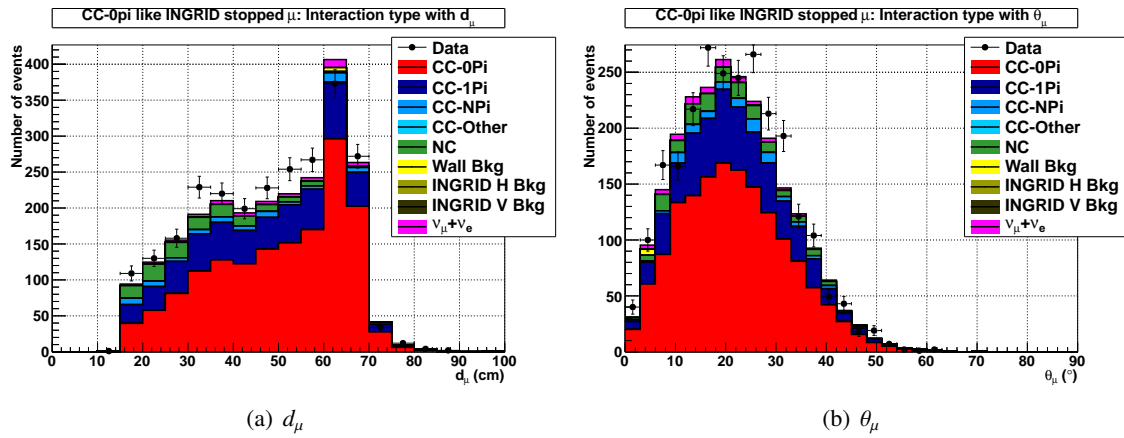


Figure 5.31: Event distribution of the data and MC as a function of distance in iron (left) and angle (right) of the muon after the PID; the matching and track width cuts are applied.

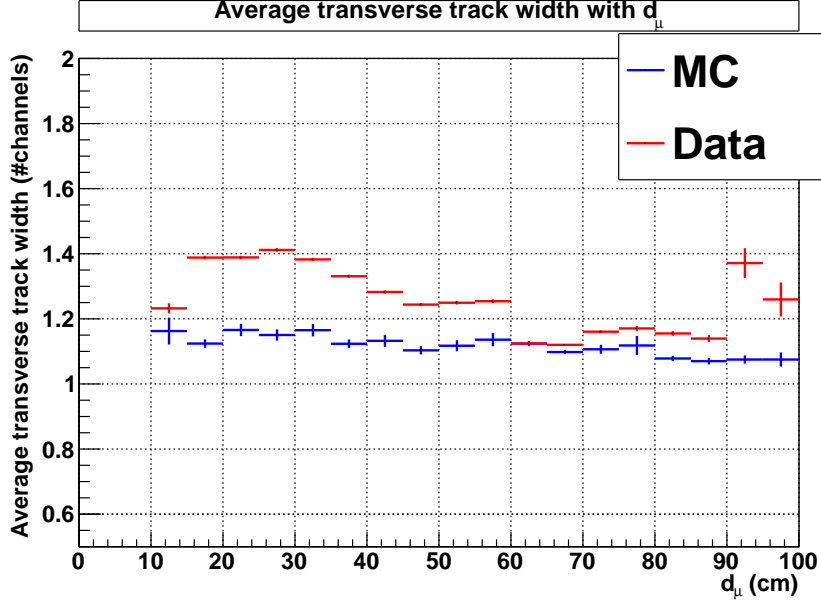


Figure 5.32: Distribution of the  $CC0\pi$  candidates  $\mu$ -like track (stopping in INGRID) for MC (blue) and data (red).

- $N_{CC0\pi}^{\text{Selected}}(p_\mu \cap \theta_\mu)$  the number of  $CC0\pi$  events passing the  $CC0\pi$  selection with a muon having a momentum and angle  $p \in [p_\mu, p_\mu \pm \delta p_\mu]$ ,  $\theta \in [\theta_\mu, \theta_\mu \pm \delta \theta_\mu]$ .
- $\epsilon(p_\mu \cap \theta_\mu)$  is the reconstruction and selection efficiency for such  $CC0\pi$  events with  $\mu$  falling in the same momentum and angle intervals. This efficiency correction is necessary to obtain the number of interacting neutrino from the number of reconstructed and selected ones.
- The cross section per neutrino, and per nucleon is obtained respectively dividing by  $\phi$ , the total neutrino flux going through the PM during the data taking, and  $N_T$  is the number of target nucleons in the same module.
- $\delta p_\mu$  and  $\delta \theta_\mu$  are the interval widths, respectively in GeV and degrees. The ideal double differential cross section measurement will be given by imposing  $\delta p_\mu \rightarrow 0$  and  $\delta \theta_\mu \rightarrow 0$ .

To apply the Equation 5.4.1 to the  $CC0\pi$  cross section, we will take into account the binning in  $p_\mu$  and  $\theta_\mu$  that naturally changes the equation to:

$$\frac{d^2\sigma}{dp_\mu^i d\theta_\mu^j} = \frac{N_{CC0\pi}^{\text{Selected}}(p_\mu^i \cap \theta_\mu^j)}{\phi \cdot N_T \cdot \epsilon(p_\mu^i \cap \theta_\mu^j) \cdot w^i \cdot w^j} \quad (5.4.2)$$

with  $i$  and  $j$  the bin indicators respectively in  $p_\mu$  and  $\theta_\mu$ , and  $w$  the bin width that replaces the interval width to achieve a cross section measurement per GeV per degrees. We will detail in this Section how the different variables are obtained.

Table 5.3: Event breakdown considering the different cuts to enhance  $CC0\pi$  purity.

	CC0 $\pi$	CC-Others	NC	Other bkg	CC0 $\pi$ Purity	CC0 $\pi$ Efficiency	Selected MC	Selected Data
One track INGRID stopped	3703.72	4059.16	1204.26	440.899	0.3936		9408.03	9263
One $\mu$ -like track only	2170.18	949.759	203.754	76.5119	0.6382	0.5859	3400.21	3710
$\mu$ -like track matching	1546.31	637.099	148.71	61.8697	0.6459	0.4175	2393.99	2548
$\mu$ -like track width	1540.43	627.891	139.121	59.2869	0.6509	0.4159	2366.73	2492

### 5.4.1 Number of CC0 $\pi$ selected events

Applying the CC0 $\pi$  selection on the data, we obtain the number of events in each reconstructed  $d_\mu$  and  $\theta_\mu$  bins (Data Selected $^{i,j}$ ). In order to deduce the number of CC0 $\pi$  events in each  $d_\mu$  and  $\theta_\mu$  bins, we will subtract the background using the MC production (MC Bkg Selected $^{i,j}$ ). Using Table 5.4, we deduce the number of CC0 $\pi$  selected events whose muon falls in the  $d_\mu^i$  and  $\theta_\mu^j$  bin as  $s^{i,j}$  (signal =  $N_{CC0\pi}^{\text{Selected}}(p_\mu \cap \theta_\mu)$ ):

$$s^{i,j} = \text{Data Selected}^{i,j} - \text{MC Bkg Selected}^{i,j} \quad (5.4.3)$$

We will retrieve the signal event in true  $p_\mu^a$ ,  $\theta_\mu^b$  bins from  $d_\mu^i$ ,  $\theta_\mu^j$  bins using a Bayesian unfolding method shown in Section 5.5. The background prediction will be purely MC based, and by this, is expected to change with the cross section model. We developed a CC0 $\pi$  selection whose cuts are as much model independent as possible to minimise this effect. However, the background prediction will be the main source of cross section model dependency (so systematics) in our result compared to the other MC based factor (efficiency). Therefore, to minimise the impact of the remaining cross section systematics, the CC0 $\pi$  selection needs not only to be relatively model independent but also to minimise the background contamination. The high CC0 $\pi$  purity of 65% is a prerequisite to minimise the background cross section model dependency on the final result. It also minimises the impact of detector and flux systematics. We expect the latter to mainly affect the neutrino flux prediction  $\phi$  for the rate, but to also affect the background estimation due to systematics coming from the flux shape.

Table 5.4: Data and MC CC0 $\pi$ -like selected events, for in each  $p_\mu, \theta_\mu$  bin.

	$\theta_\mu \in [0^\circ - 20^\circ]$	$\theta_\mu \in [20^\circ - 30^\circ]$	$\theta_\mu \in [30^\circ - 60^\circ]$	$\theta_\mu \in [60^\circ - 180^\circ]$
$d_\mu \in [0 \text{ cm}, 10 \text{ cm}]$	Data : 0.00 $\pm$ 0.00 MC: 0.00 $\frac{\text{Data-MC}}{\text{MC}}$ : 0.00 $\pm$ 0.00 %	Data : 0.00 $\pm$ 0.00 MC: 0.00 $\frac{\text{Data-MC}}{\text{MC}}$ : 0.00 $\pm$ 0.00 %	Data : 0.00 $\pm$ 0.00 MC: 0.00 $\frac{\text{Data-MC}}{\text{MC}}$ : 0.00 $\pm$ 0.00 %	Data : 0.00 $\pm$ 0.00 MC: 0.00 $\frac{\text{Data-MC}}{\text{MC}}$ : 0.00 $\pm$ 0.00 %
$d_\mu \in [10 \text{ cm}, 15 \text{ cm}]$	Data : 1.00 $\pm$ 1.00 MC: 1.19 $\frac{\text{Data-MC}}{\text{MC}}$ : -16.30 $\pm$ 83.70 %	Data : 0.00 $\pm$ 0.00 MC: 0.00 $\frac{\text{Data-MC}}{\text{MC}}$ : 0.00 $\pm$ 0.00 %	Data : 0.00 $\pm$ 0.00 MC: 0.00 $\frac{\text{Data-MC}}{\text{MC}}$ : 0.00 $\pm$ 0.00 %	Data : 0.00 $\pm$ 0.00 MC: 0.00 $\frac{\text{Data-MC}}{\text{MC}}$ : 0.00 $\pm$ 0.00 %
$d_\mu \in [15 \text{ cm}, 20 \text{ cm}]$	Data : 44.00 $\pm$ 6.63 MC: 23.55 $\frac{\text{Data-MC}}{\text{MC}}$ : 86.81 $\pm$ 28.16 %	Data : 37.00 $\pm$ 6.08 MC: 39.17 $\frac{\text{Data-MC}}{\text{MC}}$ : -5.55 $\pm$ 15.53 %	Data : 28.00 $\pm$ 5.29 MC: 31.50 $\frac{\text{Data-MC}}{\text{MC}}$ : -11.12 $\pm$ 16.80 %	Data : 0.00 $\pm$ 0.00 MC: 0.00 $\frac{\text{Data-MC}}{\text{MC}}$ : 0.00 $\pm$ 0.00 %
$d_\mu \in [20 \text{ cm}, 25 \text{ cm}]$	Data : 44.00 $\pm$ 6.63 MC: 47.34 $\frac{\text{Data-MC}}{\text{MC}}$ : -7.05 $\pm$ 14.01 %	Data : 41.00 $\pm$ 6.40 MC: 32.57 $\frac{\text{Data-MC}}{\text{MC}}$ : 25.89 $\pm$ 19.66 %	Data : 45.00 $\pm$ 6.71 MC: 44.79 $\frac{\text{Data-MC}}{\text{MC}}$ : 0.47 $\pm$ 14.98 %	Data : 0.00 $\pm$ 0.00 MC: 0.00 $\frac{\text{Data-MC}}{\text{MC}}$ : 0.00 $\pm$ 0.00 %
$d_\mu \in [25 \text{ cm}, 30 \text{ cm}]$	Data : 42.00 $\pm$ 6.48 MC: 37.58 $\frac{\text{Data-MC}}{\text{MC}}$ : 11.77 $\pm$ 17.25 %	Data : 43.00 $\pm$ 6.56 MC: 47.16 $\frac{\text{Data-MC}}{\text{MC}}$ : -8.81 $\pm$ 13.91 %	Data : 72.00 $\pm$ 8.49 MC: 70.08 $\frac{\text{Data-MC}}{\text{MC}}$ : 2.73 $\pm$ 12.11 %	Data : 1.00 $\pm$ 1.00 MC: 0.56 $\frac{\text{Data-MC}}{\text{MC}}$ : 78.64 $\pm$ 178.64 %
$d_\mu \in [30 \text{ cm}, 35 \text{ cm}]$	Data : 70.00 $\pm$ 8.37 MC: 58.95 $\frac{\text{Data-MC}}{\text{MC}}$ : 18.75 $\pm$ 14.19 %	Data : 102.00 $\pm$ 10.10 MC: 79.35 $\frac{\text{Data-MC}}{\text{MC}}$ : 28.54 $\pm$ 12.73 %	Data : 57.00 $\pm$ 7.55 MC: 52.93 $\frac{\text{Data-MC}}{\text{MC}}$ : 7.68 $\pm$ 14.26 %	Data : 0.00 $\pm$ 0.00 MC: 0.04 $\frac{\text{Data-MC}}{\text{MC}}$ : -100.00 $\pm$ 0.00 %
$d_\mu \in [35 \text{ cm}, 40 \text{ cm}]$	Data : 92.00 $\pm$ 9.59 MC: 91.08 $\frac{\text{Data-MC}}{\text{MC}}$ : 1.01 $\pm$ 10.53 %	Data : 71.00 $\pm$ 8.43 MC: 63.38 $\frac{\text{Data-MC}}{\text{MC}}$ : 12.03 $\pm$ 13.29 %	Data : 57.00 $\pm$ 7.55 MC: 55.47 $\frac{\text{Data-MC}}{\text{MC}}$ : 2.76 $\pm$ 13.61 %	Data : 0.00 $\pm$ 0.00 MC: 0.32 $\frac{\text{Data-MC}}{\text{MC}}$ : -100.00 $\pm$ 0.00 %
$d_\mu \in [40 \text{ cm}, 45 \text{ cm}]$	Data : 73.00 $\pm$ 8.54 MC: 75.56 $\frac{\text{Data-MC}}{\text{MC}}$ : -3.39 $\pm$ 11.31 %	Data : 58.00 $\pm$ 7.62 MC: 61.67 $\frac{\text{Data-MC}}{\text{MC}}$ : -5.94 $\pm$ 12.35 %	Data : 68.00 $\pm$ 8.25 MC: 56.02 $\frac{\text{Data-MC}}{\text{MC}}$ : 21.38 $\pm$ 14.72 %	Data : 0.00 $\pm$ 0.00 MC: 0.00 $\frac{\text{Data-MC}}{\text{MC}}$ : 0.00 $\pm$ 0.00 %
$d_\mu \in [45 \text{ cm}, 50 \text{ cm}]$	Data : 77.00 $\pm$ 8.77 MC: 71.13 $\frac{\text{Data-MC}}{\text{MC}}$ : 8.25 $\pm$ 12.34 %	Data : 101.00 $\pm$ 10.05 MC: 93.52 $\frac{\text{Data-MC}}{\text{MC}}$ : 8.00 $\pm$ 10.75 %	Data : 50.00 $\pm$ 7.07 MC: 44.53 $\frac{\text{Data-MC}}{\text{MC}}$ : 12.27 $\pm$ 15.88 %	Data : 0.00 $\pm$ 0.00 MC: 0.00 $\frac{\text{Data-MC}}{\text{MC}}$ : 0.00 $\pm$ 0.00 %
$d_\mu \in [50 \text{ cm}, 55 \text{ cm}]$	Data : 125.00 $\pm$ 11.18 MC: 103.05 $\frac{\text{Data-MC}}{\text{MC}}$ : 21.30 $\pm$ 10.85 %	Data : 79.00 $\pm$ 8.89 MC: 75.57 $\frac{\text{Data-MC}}{\text{MC}}$ : 4.54 $\pm$ 11.76 %	Data : 49.00 $\pm$ 7.00 MC: 41.00 $\frac{\text{Data-MC}}{\text{MC}}$ : 19.51 $\pm$ 17.07 %	Data : 1.00 $\pm$ 1.00 MC: 0.17 $\frac{\text{Data-MC}}{\text{MC}}$ : 490.11 $\pm$ 590.11 %
$d_\mu \in [55 \text{ cm}, 60 \text{ cm}]$	Data : 142.00 $\pm$ 11.92 MC: 132.41 $\frac{\text{Data-MC}}{\text{MC}}$ : 7.24 $\pm$ 9.00 %	Data : 74.00 $\pm$ 8.60 MC: 69.15 $\frac{\text{Data-MC}}{\text{MC}}$ : 7.02 $\pm$ 12.44 %	Data : 51.00 $\pm$ 7.14 MC: 40.64 $\frac{\text{Data-MC}}{\text{MC}}$ : 25.49 $\pm$ 17.57 %	Data : 0.00 $\pm$ 0.00 MC: 0.00 $\frac{\text{Data-MC}}{\text{MC}}$ : 0.00 $\pm$ 0.00 %
$d_\mu \in [60 \text{ cm}, 65 \text{ cm}]$	Data : 244.00 $\pm$ 15.62 MC: 291.11 $\frac{\text{Data-MC}}{\text{MC}}$ : -16.18 $\pm$ 5.37 %	Data : 104.00 $\pm$ 10.20 MC: 85.63 $\frac{\text{Data-MC}}{\text{MC}}$ : 21.45 $\pm$ 11.91 %	Data : 25.00 $\pm$ 5.00 MC: 29.76 $\frac{\text{Data-MC}}{\text{MC}}$ : -16.00 $\pm$ 16.80 %	Data : 0.00 $\pm$ 0.00 MC: 0.01 $\frac{\text{Data-MC}}{\text{MC}}$ : -100.00 $\pm$ 0.00 %
$d_\mu \in [65 \text{ cm}, 70 \text{ cm}]$	Data : 177.00 $\pm$ 13.30 MC: 164.42 $\frac{\text{Data-MC}}{\text{MC}}$ : 7.65 $\pm$ 8.09 %	Data : 68.00 $\pm$ 8.25 MC: 77.60 $\frac{\text{Data-MC}}{\text{MC}}$ : -12.37 $\pm$ 10.63 %	Data : 27.00 $\pm$ 5.20 MC: 21.31 $\frac{\text{Data-MC}}{\text{MC}}$ : 26.70 $\pm$ 24.38 %	Data : 0.00 $\pm$ 0.00 MC: 0.00 $\frac{\text{Data-MC}}{\text{MC}}$ : -100.00 $\pm$ 0.00 %
$d_\mu \in [70 \text{ cm}, 75 \text{ cm}]$	Data : 3.00 $\pm$ 1.73 MC: 2.07 $\frac{\text{Data-MC}}{\text{MC}}$ : 44.78 $\pm$ 83.59 %	Data : 19.00 $\pm$ 4.36 MC: 25.85 $\frac{\text{Data-MC}}{\text{MC}}$ : -26.50 $\pm$ 16.86 %	Data : 12.00 $\pm$ 3.46 MC: 13.84 $\frac{\text{Data-MC}}{\text{MC}}$ : -13.31 $\pm$ 25.02 %	Data : 0.00 $\pm$ 0.00 MC: 0.01 $\frac{\text{Data-MC}}{\text{MC}}$ : -100.00 $\pm$ 0.00 %
$d_\mu \in [75 \text{ cm}, 80 \text{ cm}]$	Data : 0.00 $\pm$ 0.00 MC: 0.47 $\frac{\text{Data-MC}}{\text{MC}}$ : -100.00 $\pm$ 0.00 %	Data : 4.00 $\pm$ 2.00 MC: 2.24 $\frac{\text{Data-MC}}{\text{MC}}$ : 78.42 $\pm$ 89.21 %	Data : 8.00 $\pm$ 2.83 MC: 6.55 $\frac{\text{Data-MC}}{\text{MC}}$ : 22.06 $\pm$ 43.15 %	Data : 0.00 $\pm$ 0.00 MC: 0.00 $\frac{\text{Data-MC}}{\text{MC}}$ : 0.00 $\pm$ 0.00 %
$d_\mu \in [80 \text{ cm}, 85 \text{ cm}]$	Data : 0.00 $\pm$ 0.00 MC: 0.00 $\frac{\text{Data-MC}}{\text{MC}}$ : 0.00 $\pm$ 0.00 %	Data : 0.00 $\pm$ 0.00 MC: 0.50 $\frac{\text{Data-MC}}{\text{MC}}$ : -100.00 $\pm$ 0.00 %	Data : 4.00 $\pm$ 2.00 MC: 2.57 $\frac{\text{Data-MC}}{\text{MC}}$ : 55.67 $\pm$ 77.84 %	Data : 0.00 $\pm$ 0.00 MC: 0.00 $\frac{\text{Data-MC}}{\text{MC}}$ : -100.00 $\pm$ 0.00 %
$d_\mu \in [85 \text{ cm}, 150 \text{ cm}]$	Data : 0.00 $\pm$ 0.00 MC: 0.00 $\frac{\text{Data-MC}}{\text{MC}}$ : 0.00 $\pm$ 0.00 %	Data : 0.00 $\pm$ 0.00 MC: 0.00 $\frac{\text{Data-MC}}{\text{MC}}$ : 0.00 $\pm$ 0.00 %	Data : 4.00 $\pm$ 2.00 MC: 1.29 $\frac{\text{Data-MC}}{\text{MC}}$ : 210.89 $\pm$ 155.44 %	Data : 0.00 $\pm$ 0.00 MC: 0.48 $\frac{\text{Data-MC}}{\text{MC}}$ : -100.00 $\pm$ 0.00 %

### 5.4.2 Efficiency

The reconstruction and selection efficiency is evaluated using the MC production. The efficiency is estimated in each true bin  $a, b$  as:

$$\epsilon(p_\mu^a, \theta_\mu^b) = \frac{N_{CC0\pi}^{\text{Selected}}(p_\mu^a \cap \theta_\mu^b)}{N_{CC0\pi}^{\text{FV interacting}}(p_\mu^a \cap \theta_\mu^b)} \quad (5.4.4)$$

with  $N_{CC0\pi}^{\text{FV interacting}}(p_\mu^a \cap \theta_\mu^b)$  the number of CC0 $\pi$  interactions in the MC fiducial volume (defined in Chapter 4). Table 5.5 summarises the efficiency of the true bins. The efficiency low values come mainly from imposing muons to stop in INGRID. The refinement of the selection will barely affect this primordial cut, which is the consequence of detector design which is not perfectly adapted to a differential muon momentum cross section study. The efficiency is purely MC based but is expected to

Table 5.5: Summary of the CC0 $\pi$  efficiency in the true  $(p_\mu, \theta_\mu)$  bins.

	[0 GeV, 0.5 GeV]	[0.5 GeV, 0.7 GeV]	[0.7 GeV, 1.0 GeV]	[1.0 GeV, 5 GeV]	[5 GeV, 30 GeV]
$\theta_\mu \in [0^\circ - 20^\circ]$	0.53%	1.64%	1.39%	0.13%	0.10%
$\theta_\mu \in [20^\circ - 30^\circ]$	0.42%	1.10%	0.82%	0.08%	0.00%
$\theta_\mu \in [30^\circ - 60^\circ]$	0.10%	0.22%	0.13%	0.06%	0.00%
$\theta_\mu \in [60^\circ - 180^\circ]$	0.01%	0.02%	0.05%	0.29%	0.00%

barely change under the neutrino flux or cross section model systematics. The fact that the detector efficiency is barely cross section model dependent is guaranteed by the model independent CC0 $\pi$  selection we developed. The efficiency is likely to be affected mostly by detector systematics, and we will show these errors are sub-dominant in this analysis.

### 5.4.3 Neutrino flux prediction

The flux prediction is done using the T2K flux simulation, JNUBEAM, which has been developed by the T2K beam group. Figure 5.33 shows the neutrino flux that intersects the PM fiducial volume for an intensity of  $10^{21}$  POT. The normalisation flux we will use is represented by the  $\nu_\mu$  component which corresponds to a total of  $5.09 \times 10^{13} \nu_\mu$ . The number of POT in data is monitored with CT5 at the end of the primary beam line, and corresponds to  $5.86 \times 10^{20}$  POT. We only selected data satisfying the “good spill” beam criteria which indicates that the beam is correctly delivered. The corresponding neutrino  $\nu_\mu$  flux is therefore equal to  $2.9959 \times 10^{13}$  neutrinos per  $\text{cm}^2$  in the PM. This flux prediction will obviously not be affected by any neutrino cross section model. However, the main systematics coming from the flux intensity and shape will mainly impact the flux predictions.

### 5.4.4 Number of target nucleons

We estimated the number of target nucleons in the PM fiducial volume for each target chemical element. The total mass of the scintillators contained in the longitudinal FV (namely from scintillator planes 4 to 31) has been measured as:

$$M^{\text{Sci}} = 364.19 \text{ kg} \quad (5.4.5)$$

which implies that the actual mass in the transverse and longitudinal PM FV is:

$$M^{\text{Sci}} = 364.19 \text{ kg} \times \frac{100}{120.3} = 302.73 \text{ kg}. \quad (5.4.6)$$

The scintillator has been weighted without any fiber inserted. Although fibers are a target for the neutrinos, only interactions on the hydrocarbon part of the scintillator (CH) are simulated in the MC. The scintillator fibers are cylinders of radius  $r^{\text{fib}} = 0.05 \text{ cm}$  and  $120.3 \text{ cm}$  length, but only  $100 \text{ cm}$  are contained in the fiducial volume. We have seen that their density is  $1.03 \text{ g.cm}^3$ . The number of

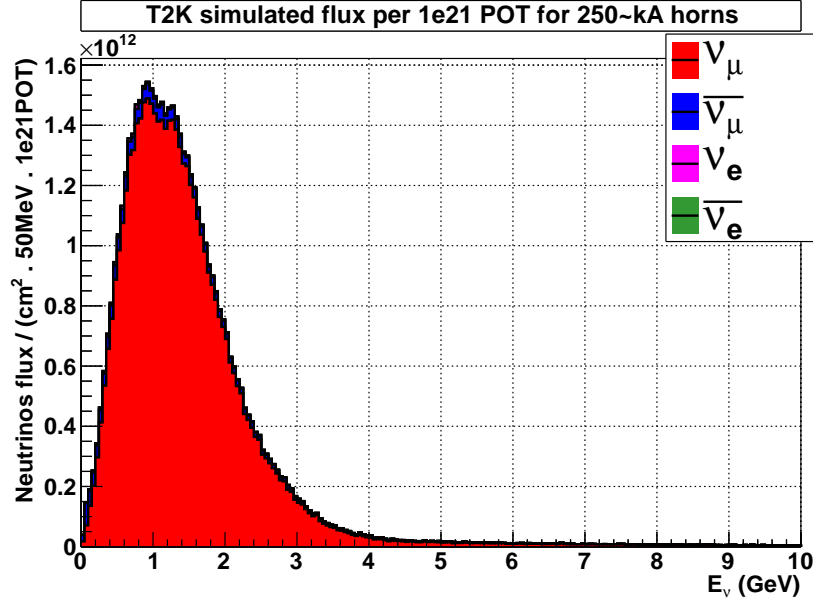


Figure 5.33: PM fiducial volume intersecting neutrino flux as a function of the neutrino energy  $E_\nu$  for different neutrino species. The flux is given per  $\text{cm}^2$ . The MC prediction is established for a beam intensity of  $10^{21}$  POT with 250kA horns, in the neutrino mode.

scintillators in one tracking plane and in the FV is 28, which implies  $28 \times (32 - 4 + 1 \text{ planes}) = 784$  scintillators. The actual mass of the scintillator fibers contained in the PM FV is therefore:

$$M^{Fib} = \pi \cdot 0.05^2 \times 100 \times 0.00103(\text{kg} \cdot \text{cm}^3) \times 784 = 0.63 \text{ kg}. \quad (5.4.7)$$

Finally, we can deduce the number of hydrocarbon target nucleons only if we know the hydrocarbon mass over the total scintillator and fiber mass. As we explained in Chapter 4, the scintillator is composed mainly of polystyrene ( $\text{C}_8\text{H}_8$ ) but also of 1% PPO ( $\text{C}_{15}\text{H}_{11}\text{NO}$ ) and 0.03% POPOP ( $\text{C}_{24}\text{H}_{16}\text{N}_2\text{O}_2$ ) by weight. The fiber is only made of polystyrene. Finally, the scintillator coating is composed of polystyrene with 15% infused  $\text{TiO}_2$  by mass. Finally, it is required to estimate the coating and active volume in a scintillator to obtain the mass composition of a scintillator and its fiber of each element. The estimation of these 2 volumes is done in the T2K internal note [80], and its results will be directly used here. It leads to the elemental composition summarised in Table 5.6:

We deduce that 98.57% of the total target in PM FV is made of hydrocarbon, in terms of mass. Ideally, one should have taken the remaining 1.43% other elements into account by generating the MC production, systematically considering any interaction in T, O or N as background and subtracting it from the data. In the study presented here, we have estimated the background considering only hydrocarbon. We will show that this global effect is negligible as compared to the flux systematics (Section 5.6). We will assume in this measurement that this effect is a 100% correlated systematic error equal to 1.4%. This assumes the neutrino cross section is similar for the same hydrocarbon and T, O, N mass, which is not exactly true, though being a good approximation. Finally, the only target nucleons are neutrons in the case of  $\text{CC}0\pi$ , and we will therefore not count the protons upon which the neutrino cannot interact through charged current interaction. Assuming only hydrocarbon, we deduce the number of target neutrons out of the total scintillator and fiber mass as:

Element	H	C	N	O	Ti
Mass ratio	7.61%	90.96%	0.07%	0.59%	0.76%

Table 5.6: Elemental composition of a coated scintillator with its fiber.

$$N_T = \frac{\text{CH mass in scintillators and fibers}}{\text{mass of 1 mole CH}} \cdot N_A \times N_{\text{Nucleons}}^{\text{CH}} \quad (5.4.8)$$

$$= \frac{0.9857 \cdot (M^{\text{Sci}} + M^{\text{Fib}})}{M^{\text{C}} + M^{\text{H}}} \cdot N_A \times ((A-Z)^{\text{C}} + (A-Z)^{\text{H}}) \quad (5.4.9)$$

$$= 8.299 \times 10^{28} \quad (5.4.10)$$

with  $N_A = 6.02214 \times 10^{23}$  the Avogadro constant,  $M^{\text{H}} = 1.008 \text{ g.mol}^{-1}$  and  $M^{\text{C}} = 12.011 \text{ g.mol}^{-1}$  the atomic masses of hydrogen and carbon and  $(A-Z)^{\text{H}} = 0$ ,  $(A-Z)^{\text{C}} = 6$  their amount of neutrons.

### 5.4.5 $p_\mu$ and $\theta_\mu$ binning

The binning used for the reconstructed  $d_\mu$  and  $\theta_\mu$  variables has been introduced in Section 5.3. The binning is chosen based on the detector resolution. In this section, we will define the binning we use in true  $p_\mu$  and  $\theta_\mu$  variables. The motivations for such a choice will be introduced in Section 5.5. Briefly, since the true variables are recovered from the reconstructed ones, they cannot convey more informations than the detectors allow to (except if we over use the MC). Therefore, the true binning should also represent the detector resolution and we introduced earlier that the INGRID plane thickness represents  $\sim 100 \text{ MeV}$  resolution in the most favoured case. The binning in true muon kinematic variables is summarised in Table 5.7 along with the MC true information on the number of CC0 $\pi$  event selected in each bin.

In this study, we will not use the bins  $\theta_\mu \in [60^\circ - 180^\circ]$  and  $[5 \text{ GeV}, 30 \text{ GeV}]$  for any measurement. These bins are only kept in order to cover the neutrino whole phase space which is mandatory not to lose any events in the other bins when we apply the Bayesian unfolding method. Additionnal comments on this bin choice will be given in Section 5.5.

## 5.5 The Bayesian unfolding method

### 5.5.1 Introduction to unfolding and motivations

We aim to use the data to deduce a direct cross section measurement with muon momentum and angle. This could be done either by a direct fit of the data from the simulation, or by an unfolding method. In a fitting procedure, one inputs a model in the MC and determines the parameter values that maximise the agreement between MC and data. By doing so, we are testing the parameter values that reproduce the best our data assuming a given model. For measurements whose models have been clearly established, this method would be preferred.

On the opposite, the unfolding method aims to retrieve the original data distribution by “unsmearing” the detector finite resolution effects. By doing so, our data sample would be modified to give directly the original distribution, and this will be our measurement. This is the exact opposite of a fitting method. In this undolfing procedure, only the distorsion due to detector effects is used. Therefore, rather than finding optimum parameters for a given model, the unfolding procedure allows to test different models and directly compare them to the unsmearred data distribution. As explained before, neutrino cross section models suffer from high uncertainties and there is no major indication towards one of them. For this reason, we develop a bayesian unfolding procedure to measure the double differential CC0 $\pi$  cross section. It aims to provide measurements that will ultimately be compared

	[0 GeV, 0.5 GeV]	[0.5 GeV, 0.7 GeV]	[0.7 GeV, 1.0 GeV]	[1.0 GeV, 5 GeV]	[5 GeV, 30 GeV]
$\theta_\mu \in [0^\circ - 20^\circ]$	24.37	98.98	261.94	281.46	28.69
$\theta_\mu \in [20^\circ - 30^\circ]$	28.42	116.20	241.53	83.70	0.00
$\theta_\mu \in [30^\circ - 60^\circ]$	45.23	118.46	110.05	49.75	0.00
$\theta_\mu \in [60^\circ - 180^\circ]$	15.26	8.36	5.95	3.28	0.00
Total	113.26	342.0	619.47	418.19	28.69

Table 5.7: True number of CC0 $\pi$  events selected by CC0 $\pi$  selection in the MC.

with existing and future models.

The Bayesian unfolding method [64] has the advantage of being robust on a large part of the cross section phase space since it ideally does not depend on the prior, although this is only reached for an infinite number of iterations. In practice, the number of iterations is limited which introduces a small dependency on the initial prior. We will see that the number of iterations should even be limited to relatively low values to prevent from possible fluctuations due to over-tuning on the data sample. We have chosen the iterative Bayesian unfolding over other possible alternatives, as:

1. bin-by-bin corrections since they do not take into account possible correlations between different observed and true distribution bins. Moreover, this requires to have similar binning for the true and observed distributions.
2. Matrix inversion with regularisation. We may build the transfer matrix from the true distribution (for example, momenta distribution) to generate the observed event distribution (iron distance distribution for example) after passing through the detector. After having inverted this matrix, one may expect to retrieve the true distribution from the observed distribution. However, this method has two important flaws: first, the transfer matrix may be non invertible. It is mostly the case when the matrix is degenerate, *e.g* for a highly non-diagonal matrix (broad detector compared to binning) or for cases where the MC sample used to estimate the matrix is limited. This may be solved using a higher statistics in MC and choosing larger bins to reduce the bin by bin migration. But even in the case of an invertible matrix, the results after inversion (“unfolding”) may be highly different from the true distribution. The transfer matrix is based on the MC sample which will involve an over-tuning of the “unfolding matrix” on this particular sample. When applied to the data, the statistical fluctuations in the data sample will be also unfolded as the real physical effect. Since the unfolding matrix has been built only to unsmear the physical detector effects, the unfolded statistical fluctuations may lead to a result that is very different from the possible data true distribution. This effect may be cured partly using a regularisation method to remove the high frequency fluctuations and “smooth” the corrections of the unfolding on data. However, this introduces a possible bias in choosing the regularisation factors and will highly depend on the MC ability to reproduce the data. Various methods are shown in [81].

In this section, we will introduce the unfolding method that we use to unsmear the detector effects. We will first introduce the unfolding method technique that we developed, based on [64]. Then we will insist on the unfolding method limitations or crucial aspects that we found in order to measure accurately the  $CC0\pi$  cross section. Finally, we will present the application of this method to the double differential cross section measurement.

### 5.5.2 Unfolding method construction

#### General unfolding method

The unfolding algorithm is based on the Bayes’ theorem:

$$P(A|B) \cdot P(B) = P(B|A) \cdot P(A), \text{ with A and B random variables.} \quad (5.5.1)$$

In our particular case, we aim to un-smear the detector smearing effects on the measured data distribution. The unfolding method consists in looking for the original causes  $C_i$  that has generated the measured effects  $E_j$  after propagation through the detector and distortion by finite resolution. The binning in  $E_j$  is established on the variable used in the measurement, while  $C_i$  is binned with the original variable. These 2 variables can be different, and so can be their binning. We wish to estimate  $P(C_i|E_j)$  to deduce the original causes from the data measured. A contrario, a MC simulation allows to estimate for a given cause  $C_i$ , the subsequent effects after passage through detector and reconstruction:  $P(E_j|C_i)$ . This represents the “likelihood” of a cause to produce an effect. But, one may retrieve  $P(C_i|E_j)$  directly by testing various causes  $C_i$  in the MC simulation, measuring the consequent effects  $E_j$  and deduce the probability for a given effect  $E_j$  to come from a cause  $C_i$  by simply dividing by the

probability of this event to induce all possible causes. In fact, one sees that this procedure is exactly analogous to apply the Bayes' theorem. Applying the Bayes' theorem, we obtain:

$$P(C_i|E_j) = \frac{P(E_j|C_i) \cdot P(C_i)}{P(E_j)} \quad (5.5.2)$$

which allows to deduce  $P(C_i|E_j)$  from  $L_i^j = P(E_j|C_i)$  directly obtained using the MC.  $L$  is named likelihood or smearing matrix. The probability density  $P(C_i)$  is also directly deduced from the MC, but can also be changed to other distributions in the case of unfolding as we will see. If the  $[C_k]$  are independent random variables from each other, one deduces that:  $P(E_j) = \sum_k P(E_j|C_k) \cdot P(C_k)$  which leads to:

$$P(C_i|E_j) = \frac{P(E_j|C_i) \cdot P(C_i)}{\sum_k P(E_j|C_k) \cdot P(C_k)}. \quad (5.5.3)$$

### Application to CC0 $\pi$ cross section measurement

We aim to measure the cross section defined in Equation 5.4.2. To do so, we need the number of selected events interacting through CC0 $\pi$  interaction in the PM fiducial volume,  $N_{CC0\pi}^{\text{Selected}} = \text{Data Selected}^{i,j} - \text{MC Bkg Selected}^{i,j}$ . The  $i$ -th and  $j$ -th exponents refer to the true  $\theta_\mu$  and  $p_\mu$  bins. The Bayesian unfolding method will be developed in order to retrieve these quantities based on the reconstructed corresponding variables, namely the muon angle ( $\theta_\mu^{\text{Rec}}$ ) and its distance crossed in IN-GRID iron ( $d_\mu$ ). As we discussed, this unsmearing matrix is constructed using the Bayes' theorem from the likelihood matrix. The latter is obtained by simulating various neutrino events in each  $\theta_\mu$  and  $p_\mu$  bins and measuring the associated  $\theta_\mu^{\text{Rec}}$  and  $d_\mu$  quantities after passage through the detector. Let  $U$  the unfolding matrix, that is defined in two dimensions as:

$$U_{k,l}^{i,j} = P((p_\mu^i \cap \theta_\mu^j) | (d_\mu^k \cap \theta_\mu^{\text{Rec } l})) = \frac{P((d_\mu^k \cap \theta_\mu^{\text{Rec } l}) | (p_\mu^i \cap \theta_\mu^j)) \cdot P(p_\mu^i \cap \theta_\mu^j)}{\sum_{n,m} P((d_\mu^k \cap \theta_\mu^{\text{Rec } l}) | (p_\mu^n \cap \theta_\mu^m)) \cdot P(p_\mu^n \cap \theta_\mu^m)} \quad (5.5.4)$$

the corresponding neutrino cross section is then given by:

$$\frac{d^2\sigma}{dp_\mu^i dd_\mu^j} = \frac{s^{i,j}(p_\mu^i \cap \theta_\mu^j)}{\phi \cdot N_T \cdot \epsilon(p_\mu^i \cap \theta_\mu^j) \cdot w^i \cdot w^j} = \frac{U_{kl}^{i,j} s^{k,l}(d_\mu^k \cap \theta_\mu^l)}{\phi \cdot N_T \cdot \epsilon(p_\mu^i \cap \theta_\mu^j) \cdot w^i \cdot w^j} \quad (5.5.5)$$

where the signal  $s^{k,l}$  is now expressed in the reconstructed quantities  $d_\mu^k$   $k$ -th and  $\theta_\mu^{\text{Rec } l}$   $l$ -th bins:

$$s^{k,l} = d^{k,l} - b^{k,l} \text{ where } d \text{ are the selected data and } b \text{ the selected non CC0}\pi \text{ background.} \quad (5.5.6)$$

We have indicated in blue the variables that rely on the cross section and detector simulation. One observes that the signal is the selected data with the MC evaluated background subtracted. the MC is also used to estimate the likelihood matrix  $L_{i,j}^{k,l} = P((d_\mu^k \cap \theta_\mu^{\text{Rec } l}) | (p_\mu^i \cap \theta_\mu^j))$ , the reconstruction efficiency  $\epsilon^i$  and in some cases, the prior  $P(p_\mu^i \cap \theta_\mu^j)$ . A cross section model dependency then exists in these quantities.

In Section 5.3, we have defined a selection we tried to keep as model independent as possible to minimise the model dependency of the efficiency  $\epsilon^{i,j}$ . The unfolding matrix connects the event distributions after detector smearing in muon depth in iron and angle to the original event distribution in muon true momentum and angle. We observe that this matrix should depend on the simulation of the detector, the particle propagation... However the cross section model dependency should be small, since the relation between final and original variables does not depend on it (in principle). This is the reason for choosing to study differential cross sections as a function of muon kinematic observables. Note that this would not have been the case studying the neutrino cross section with energy. In the latter case, the unfolding matrix should have connected muon observables and neutrino energy which implies the use of a cross section model. Therefore, one concludes that the background estimation  $b^{k,l}$  will be the main source of cross section model dependency in our result.

Instead of a complete two dimensional unfolding algorithm, we developed several sequential one-dimensional unfoldings in momentum and angle described in this section. For clarity, we will only

present the 1D momentum unfolding, and directly provide the results for the combined momentum and angular unfoldings at the end of this section. Equation 5.5.5 then becomes for the momentum unfolding:

$$\frac{d\sigma}{dp_\mu^i} = \frac{s^{i,j}(p_\mu^i)}{\phi \cdot N_T \cdot \epsilon(p_\mu^i) \cdot w^i} \quad (5.5.7)$$

### Unfolding matrix determination

In the example of muon momentum differential cross section, the cause bins  $C_i$  are naturally the number of events in a muon momentum bin, while the effect bins  $E_j$  are the number of events as a function of the iron distance penetrated by the muon. The two variables are not bijective due to the detector resolution, which is represented by the “non-diagonality” of the likelihood matrix, and by extension, of the unfolding matrix.

**Likelihood matrix:** The likelihood matrix is estimated using the CC0 $\pi$  selection defined in Section 5.3.2. We applied the PM reconstruction and CC0 $\pi$  selection on 1000 MC files containing neutrino interactions corresponding to  $10^{24}$  POT. For each true muon momentum  $p_\mu$ , the corresponding number of events in each  $d_\mu^{\text{Iron}}$  is counted and stored in the likelihood matrix. On top of this, for a given cause momentum  $p_\mu$ , we assumed that the events are dispersed over all the iron distance bins, which is equivalent to no trash bin in our analysis. The normalisation is chosen so that:

$$\sum_j P(E_j|C_i) \cdot P(C_i) = 1. \quad (5.5.8)$$

Figure 5.34 shows the likelihood distribution. One observes that the likelihood matrix is almost diagonal, which confirms that the binning choice is adapted to the detector resolution (see Figure 5.20). This aspect is further discussed in Appendix F.

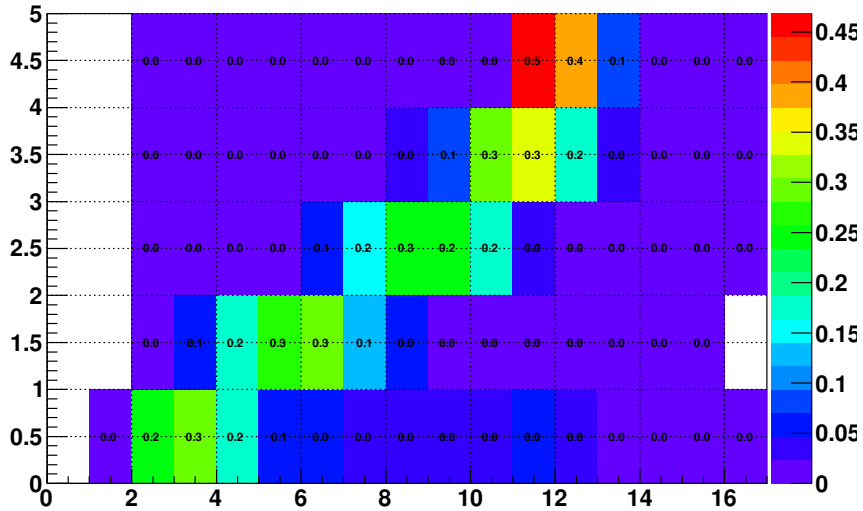


Figure 5.34: The likelihood matrix for the five momentum bin choice (nominal). The Y axis represents these momentum bins, and the X axis represents the bins in distance crossed in iron by the muon.

**Prior and iterations:** The distribution  $P(C_i)$  represents the density function for a muon in a CC0 $\pi$  interaction to have a momentum  $p_i$ . One might then use the MC momentum distribution as a prior. However, it implies that the data unfolded distribution will be affected by the MC prior  $P(C_i)$  we chose, i.e the result would depend on the MC ability to reproduce data and induces cross section

model dependency. To avoid this situation, we need to let the data constrain the result by themselves as much as possible. Ideally, we would use a prior that represents a total uncertainty state. As pointed out in [82], a flat prior does not match this condition since it imposes instead a high constraint on  $P(C_i)$  by imposing strict equiprobability in each bins. To solve this problem, we use an iterative procedure.

1. An original prior  $P(C_i)^0$  is chosen.
2. The data  $d_j$  and background  $b_j$  are used (Equation 5.5.7) to estimate the posterior distribution  $\text{Post}(C_j)^0 = U_i^j(d_j - b_j)$ . This distribution is then normalised to obtain the posterior distribution from the prior  $P(C_i)^0$  constrained by the likelihood  $L_i^j = P(E_j|C_i)$  and data  $d_j$ .
3. The prior  $P(C_i)^1$  is set equal to  $\text{Post}(C_j)^0$ . The procedure restarts at step 2 with  $P(C_i)^1$  as the prior, and is iteratively applied until  $|P(C_i)^{n+1} - P(C_i)^n| < \epsilon$  with  $\epsilon$  a convergence criterion defined by the user.

This procedure aims to reduce as much as possible the result dependency on the original prior (see Appendix F). For this reason, we have chosen in this analysis a flat original prior  $P(C_i)^0 = \frac{1}{N_{p_\mu}^{\text{bins}}}$ .

### Unfolding convergence and statistical error estimation

The algorithm convergence will be reached not only if the unfolded MC agrees with the true MC  $p_\mu$  distribution, but also if the statistical error estimation is correctly given by the unfolding method. In order to do so, we will use a pull variable in muon momentum which is defined as (for the  $i$ -th bin):

$$\text{Pull}^i = \frac{N^i - \langle N^i \rangle}{\sigma^i} \quad (5.5.9)$$

with  $N^i$  the number of events in the  $i$ -th bin in momentum,  $\langle N^i \rangle$  the average number of events for the various statistical fluctuations and  $\sigma^i$  the estimated error on the number of events in each bin. We expect a pull distribution to be gaussian in each momentum bin. A pull distribution mean value compatible with 0 indicates the result has converged and is not biased. On the other hand, the pull gaussian width should be compatible with 1 to guarantee a correct error estimation. To study these distributions, we need to estimate both the average number of events and the associated error contained in each momentum bin.

The statistical error for the true  $p_\mu$  bin can not be estimated as the square root of the number of events since each bin is populated using various reconstructed  $d_\mu$  bins with different statistics. It cannot be evaluated either as:

$$\delta p_\mu^i = \sqrt{\sum_{j=1}^N U_j^i d_\mu^j} \quad (5.5.10)$$

since this applies only if the statistical error does not impact the unfolding matrix. We will see that the unfolding matrix changes with the statistical error of the reconstructed bin. It implies that the estimation of the statistical error is not trivial, and we will therefore estimate the statistical error in each  $p_\mu$  bin numerically. In order to estimate the statistical error, we will:

1. generate random variations on the number of CC0 $\pi$ -like events in each MC  $d_\mu$  bin. We assume that the number of events in each bin follows an independent Poisson distribution.
2. subtract non-variated background in each  $d_\mu$  bin. The background has been estimated using the MC information (as in Table 5.3).
3. apply the unfolding method using the non-variated likelihood matrix and a flat prior to deduce the number of events in each  $p_\mu$  bin.

This method will be applied on the genuine 2D unfolding to finally estimate the statistical error in Section 5.6. Here, we will first show that the statistical error also impacts the unfolding matrix. In order to show this, we construct the pull distributions assuming the statistical error estimated in

Equation 5.5.10. One expects the pull distribution to behave as gaussian variables with  $\sigma = 1$  if the statistical error does not affect the unfolding matrix. In the opposite case, correlations appear between the  $p_\mu$  bins of the unfolding matrix that will change the statistical error in each bin. Figure 5.35 shows the pull distributions corresponding to the five momentum bins. One observes that the statistical error is reduced compared to the estimation in Equation 5.5.10, which indicates the momentum bins are mainly anti-correlated. Figure 5.36 shows the corresponding correlation matrix which confirms this result. **The unfolding method therefore introduces correlated statistical errors between the unfolded bins.**

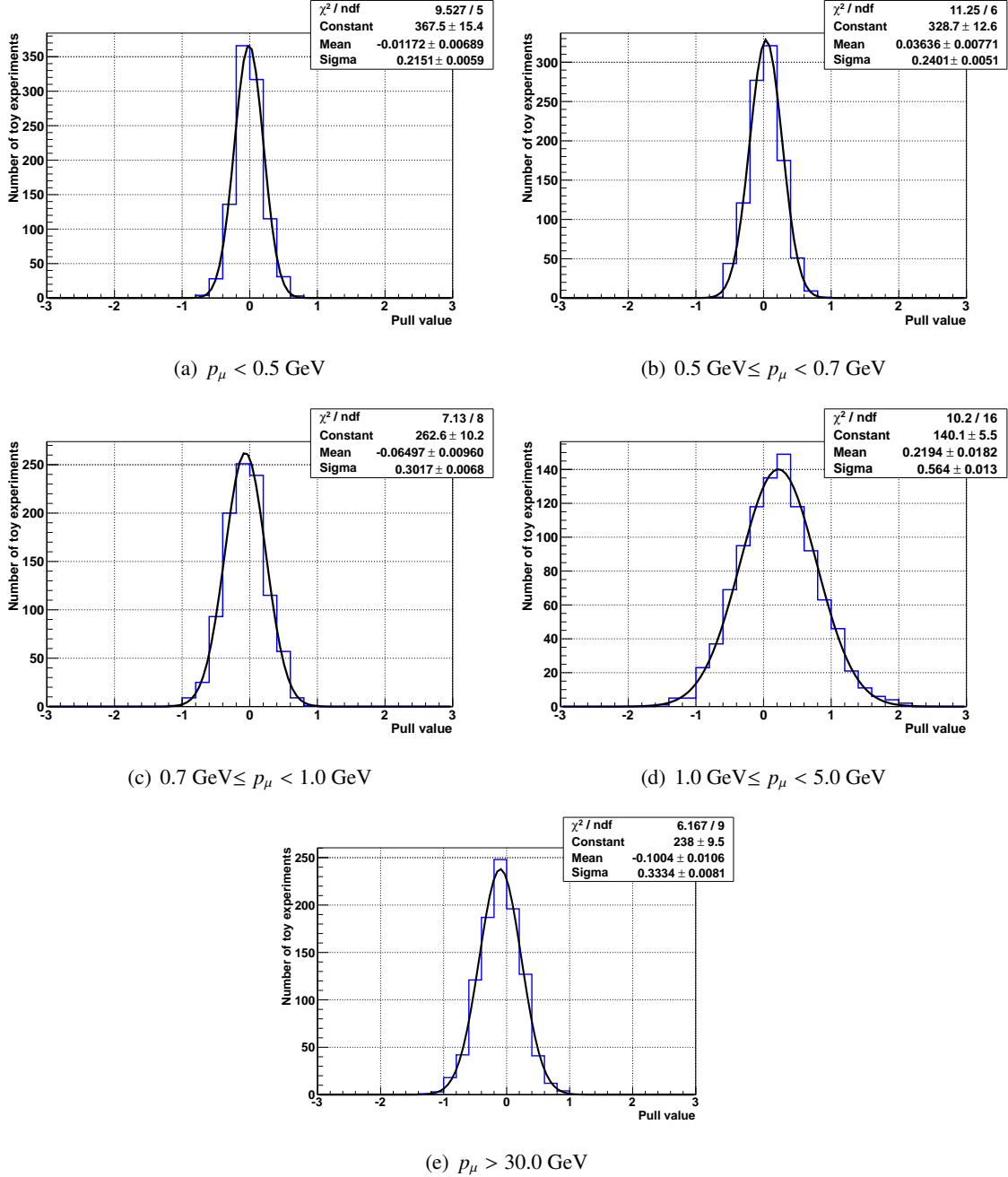


Figure 5.35: The pull distributions of the statistical error in each momentum bins assuming an error  $\sigma_i$  as defined in Equation 5.5.10.

For comparison, we will assume in the remaining of this section that the statistical error is given by Equation 5.5.10. This will allow to compare the variation of the unfolding matrix under statistical fluctuations through pull distribution. The correct numerical treatment of the statistical error we introduced will be only used for the genuine study in Section 5.6.

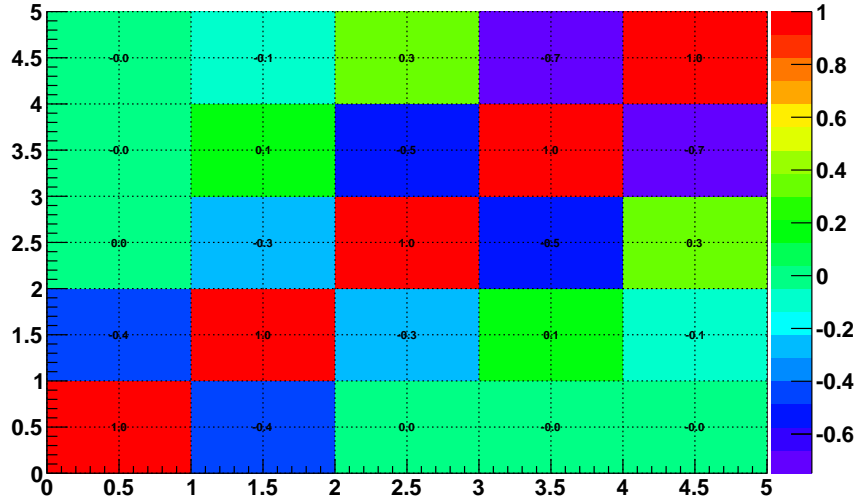


Figure 5.36: The correlation matrix of the statistical error in  $p_\mu$  bins

### Summary of the unfolding procedure

We present the validation and optimisation of our unfolding method in Appendix F. We will just summarise here the results and present the features of the unfolding method we will ultimately use. In the case of a two-dimensional unfolding, one has to take care of the higher number of bins which induces larger fluctuations through higher correlations. In order to control these fluctuations using a one-dimensional unfolding method, we have developed several one-dimensional unfoldings to mimic a two-dimensional unfolding. More explicitly, for a given signal distribution in the muon iron depth distance and angle:

- We select the corresponding binning in the reconstructed variables, namely  $d_\mu^k$  and  $\theta_\mu^{\text{Rec } l}$ . The binning in the reconstructed variables we used is defined in Section 5.3. The reconstructed binning does not require a specific tuning, but should only be kept thin enough to avoid to loose information.
- We select the binning in the true variables,  $p_\mu^i$  and  $\theta_\mu^j$ . This binning requires a specific care. Appendix F shows that the unfolding rapidly diverges after several iterations, if the true bins have a very different statistics and high correlations. For this reason, we have optimised the binning based on:
  - the expected number of events in each true bin.
  - the detector resolution that introduces correlations between the bins.

Due to the PM limited resolution in the muon momentum (6.5 cm thickness planes in INGRID) and in the angle (scintillator width), we choose an asymmetric binning in the true variables in order to minimise the correlations. Table 5.7 summarises this binning in true variables and the expected statistics in each bins.

- For each reconstructed angle bin, the momentum unfolding is applied. Ten iteration steps are required before the unfolding stops.
- For each momentum bin, the reconstructed angle bin is deduced from the previous unfoldings. The reconstructed angle distribution is unfolded for each momentum bin. Only five iteration steps are required for the unfolding along the angle variable.

- Finally, we chose original priors that are not totally flat. The reason is the high probability of a large angle or backward going muon ( $\theta_\mu > 60^\circ$ ) to be reconstructed having with  $\theta_\mu \in [0^\circ, 20^\circ]$ . This introduces some long range correlations between the true bins  $\theta_\mu \in [0^\circ, 20^\circ]$  and  $\theta_\mu > 90^\circ$  that prevents the convergence of the unfolding. Figure 5.37 shows the number of interacting true CC0 $\pi$  events with muon angle and momentum. It shows that only the low momentum region  $p_\mu < 0.5$  GeV has a significant amount of large angle muons. Therefore, we impose a flat angular prior for the  $p_\mu < 0.5$  GeV bin, while we assume the bin  $\theta_\mu > 60^\circ$  to have one tenth of the other bin content. The prior is assumed flat for the other angular bins. As for the momentum bins, we assume that the largest momentum bin  $p_\mu > 10.0$  GeV is empty in the initial prior, while the prior is flat for the other bins. Figure 5.38 shows these two initial priors. Considering the distribution of the number of events shown in Figure 5.37, we assume that the prior we chose is relatively independent from the cross section model and not fine-tuned on any specific MC distribution.

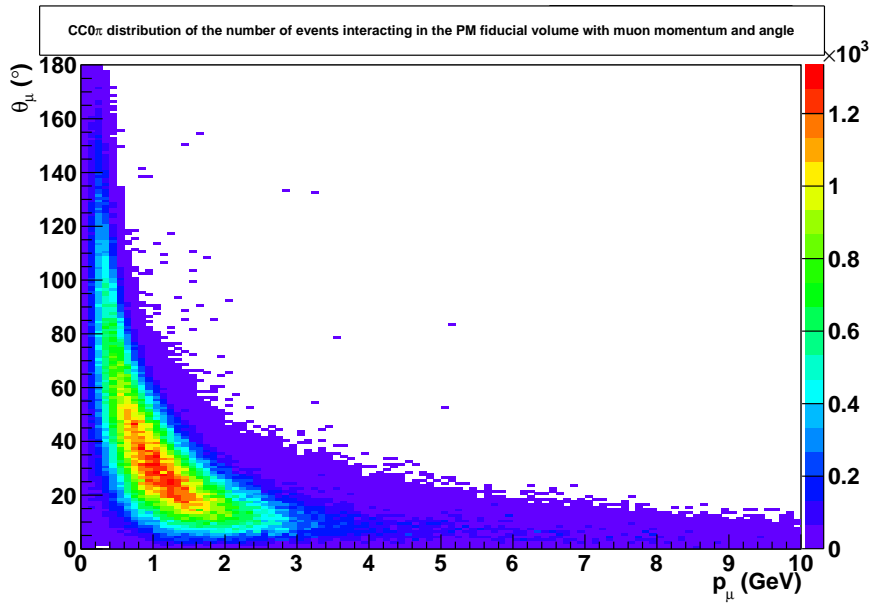


Figure 5.37: Distribution of the CC0 $\pi$  interactions in the PM as a function of the muon momentum and angle.

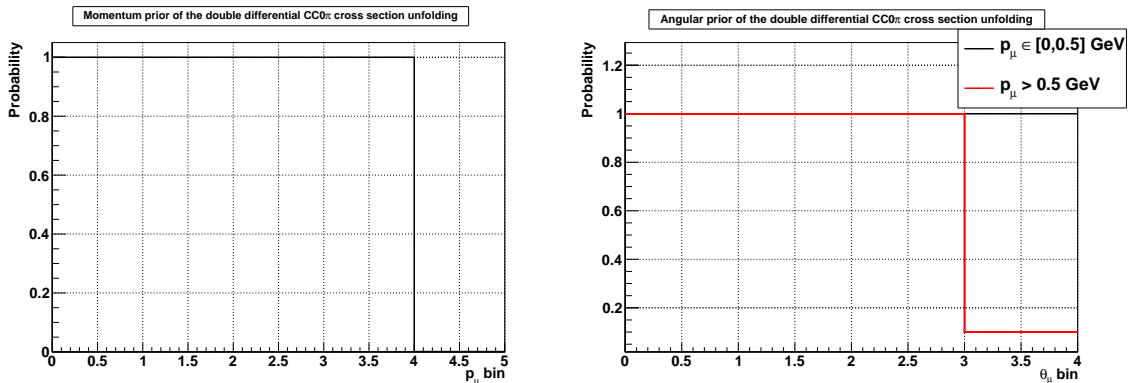


Figure 5.38: The different momentum (left) and angular (right) priors used in the final unfolding version. These distributions are shown without normalisation.

## 5.6 Systematic and statistical errors

We identify three main sources of systematic errors:

- The flux systematic errors (Section 5.6.2).
- The cross section model systematic errors (Section 5.6.4).
- The PM and INGRID detectors systematic errors (Section 5.6.3).

We assume that the correlations between the different main detector sources are negligible. The correlations between several systematic error sources within each main category will be discussed in each dedicated section.

### 5.6.1 Statistical error estimation

We have seen that the detector acceptance limits the double differential cross section statistics, since the stopping muon subsample has a very small statistics (Table 5.4). To evaluate the statistical error, we generated 5,000 toy experiments. Each of these toy experiments corresponds to a different collection of fake data set of selected  $CC0\pi$ -like in each  $(d_\mu^{\text{Rec}}, \theta_\mu^{\text{Rec}})$ . Each toy experiment set is obtained by simultaneously generating random numbers in each  $(d_\mu^{\text{Rec}}, \theta_\mu^{\text{Rec}})$  bin. We assume the number of fake data events follow the Poisson distributions, and the chosen mean in each bin is shown in Table 5.4. Figure 5.39 shows the variations of the unfolded cross section errors for each  $(p_\mu^{\text{True}}, \theta_\mu^{\text{True}})$  bin. It is important to recall that this statistical error is originally only driven by the number of events in each  $(d_\mu^{\text{Rec}}, \theta_\mu^{\text{Rec}})$ , but that these data distributions will also affect the unfolding matrix. As we explained, the statistical error is not only given by unfolding the fluctuations with the unfluctuated matrix, but cumulates both the effects of fluctuated unfolding matrix and fluctuations in data. This is clearly shown in the case of the bin  $(p_\mu^{\text{True}}, \theta_\mu^{\text{True}}) = (1, 2) \in ([0, 500 \text{ GeV}], [20^\circ, 30^\circ])$  for example, where the statistics is not small but which is highly correlated to their neighbour high statistics  $([0, 500 \text{ GeV}], [30^\circ, 60^\circ])$  bin. It shows that the current unfolding method gives limited predictions for the bins which have both a small statistics and high correlation to neighbouring bins having a high statistics. For this reason, the statistical error may be reduced by the improvement of the selection, binning choice and unfolding, and not only by data taking. We will discuss the possible improvements in the conclusion of this chapter. The error in each bin with significant data is between 10% and 35% and are assumed to be uncorrelated within each  $(p_\mu^{\text{True}}, \theta_\mu^{\text{True}})$  bin in this thesis. Since we explained most of the bins are anti-correlated to their neighbour bins (see Section 5.5.2), it is conservative.

### 5.6.2 Flux related systematics

The uncertainties in the neutrino beam production are dominated by the uncertainty on the hadron interaction models. This includes the proton-Carbon (target) cross section, the pion multiplicities and the secondary nucleon production. The uncertainties come from the NA61/SHINE measurements of pion and kaon production (see Chapter 2), that are adapted to T2K using the FLUKA2008 MC. The total proton-nucleus interaction uncertainties are also set to contain the discrepancy between the NA61/SHINE data and the other external data sets that we use in the NA61 uncovered space phase regions. As for uncertainties on the secondary nucleon production, they are set by comparing the FLUKA2008 predictions with other external data sets [83], [84]. Finally, uncertainties on the T2K beamline are also taken into account. These uncertainties include the proton beam incident position, profile and intensity on the target (measured by the devices presented in Chapter 2), the neutrino off-axis angle measured by INGRID and the horn magnetic field intensity and shape. Figure 5.40 summarises the contributions of each systematic error to the neutrino flux predictions at the PM and INGRID (using FLUKA2008). The result is shown using 43 neutrino energy bins that are defined as:

- one bin  $E_\nu \in [0 \text{ MeV}, 500 \text{ MeV}]$
- 35 bins of 100 MeV width from  $E_\nu = 500 \text{ MeV}$  to 4.0 GeV
- 6 bins of 1 GeV width from  $E_\nu = 4.0 \text{ GeV}$  to 10.0 GeV
- A final bin covering  $E_\nu \in [10.0 \text{ GeV}, 30.0 \text{ GeV}]$

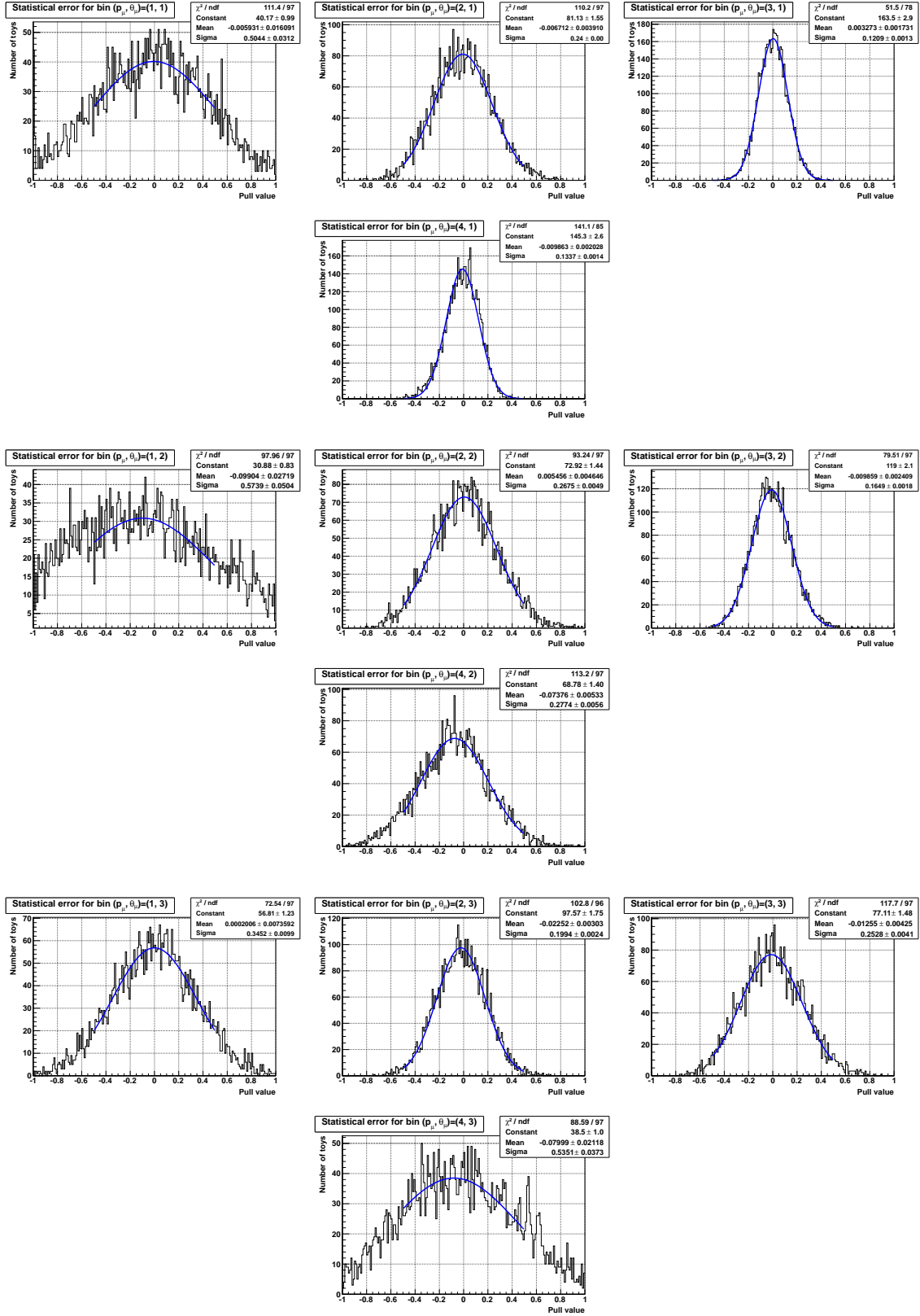


Figure 5.39: Relative statistical error in each  $(p_\mu^{\text{True}}, \theta_\mu^{\text{True}})$  bin using 5,000 generated toy fluctuated experiments.

One observes that the secondary nucleon, proton-nucleus and pion productions dominate for neutrino low energy  $E_\nu < 5$  GeV. As we explained in Chapter 2, the neutrino flux in this region has mostly pion parents. In the neutrino high energy region, the systematic error is instead driven by the uncertainty on kaon production as expected. Figure 5.41 shows the flux predictions in each bin combined using the FLUKA generated correlation matrix. The correlations in the neutrino energy region of interest for our measurement ( $0 - 5$  GeV) are high and positive ( $> 0.6$ ) for most of the energy bins. This comes from the cross section uncertainties on proton-nucleus and secondary nucleon production which are the dominant error sources at neutrino energy  $E_\nu < 5$  GeV and suffers from a global measurement uncertainty (normalisation factor of the whole spectra). In average, one observes an expected 10% – 20% (almost normalisation effect only) systematic error coming from the neutrino flux on any absolute measurement. As we have explained, this is highly reduced in the case of neutrino oscillation due to relative measurements. As for the cross section study, we are unfortunately driven by this error, though it could be removed in the case of relative measurements on two materials intercepting the same flux (*e.g* PM carbon and INGRID module 3 iron).

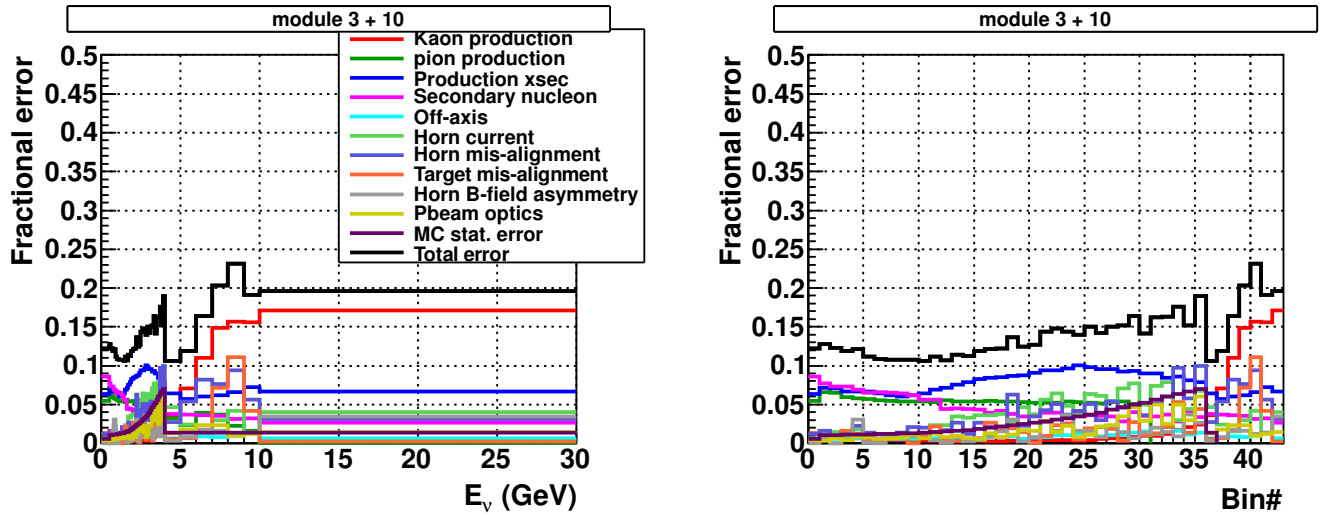


Figure 5.40: Relative error on the neutrino flux prediction for each energy bin at PM and INGRID coming from the T2K beam prediction MC.

We assume that the central horizontal INGRID module (module number 3) and PM intercept the same neutrino flux. The contribution of the flux systematic errors on the cross section study will mainly impact the neutrino flux absolute rate  $\phi$  at first order, and background prediction at second order. The selection efficiency should remain almost stable under flux uncertainties. To estimate the systematic error on the cross section measurement, we generate 2,000 toy experiments with different flux predictions. Each toy experiment is constructed as follow:

- A set of 43 correlated random numbers (one for each bin in neutrino energy) is generated using the correlation matrix. To do so, we generate 43 gaussian random numbers and apply the correlations using a Cholesky procedure. It provides a relative variation in each energy bin, “a reweighting factor” compared to the original flux prediction.
- The background, efficiency, and flux predictions are estimated applying the reweighting factor for each neutrino event considering its energy.
- The unfolding method is applied to recover the cross section value of the toy experiment.

Figure 5.42 shows the relative variations of the toy experiment cross section compared to the default one for each  $(p_\mu^{\text{True}}, \theta_\mu^{\text{True}})$  bin. As expected, we observe a  $\sim 20\%$  effect in most of the bins, which mainly comes from the neutrino flux variations. Unlike the statistical error, the unfolding matrix will be only negligibly changed in the case of neutrino flux systematic error. The first reason is that this

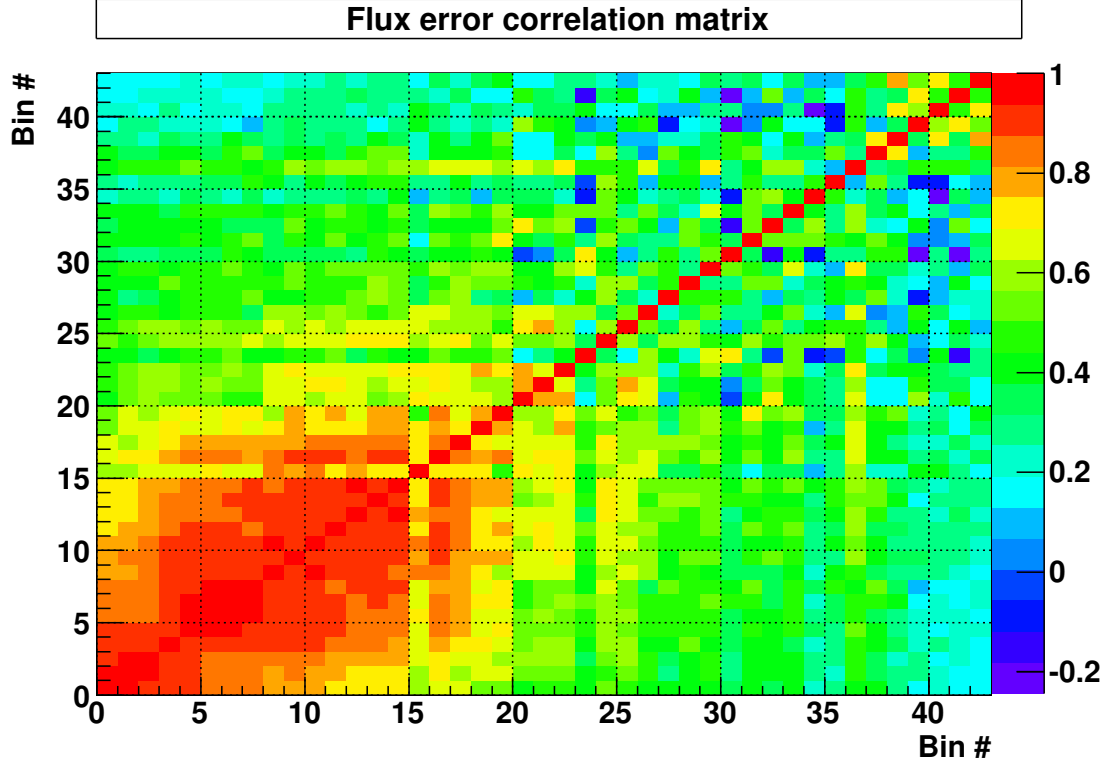


Figure 5.41: Correlation matrix of the flux uncertainties at the PM and INGRID, for the different neutrino energy bins.

error affects neither the detector resolution in momentum and angle, and therefore, nor the likelihood prediction. As for the prior, since the flux systematics are highly correlated between the reconstructed ( $d_{\mu}^{\text{Rec}}, \theta_{\mu}^{\text{Rec}}$ ) bin, the background should almost vary by the same normalisation factor in all bins, which lead  $\text{Data Selected}^{i,j} - \text{MC Bkg Selected}^{i,j}$  to change. But in the case the background is relatively small, it follows that the constraints on the iterative procedure from  $\text{Data Selected}^{i,j} - \text{MC Bkg Selected}^{i,j}$  are not changed. For this reason, the unfolding matrix is expected to be almost stable in the different toy experiments, and this is the reason why the original 10–20% flux error is reproduced in the CC0 $\pi$  cross section measurements in each bin. The latter errors are slightly higher due to the variation of the shape of neutrino spectra that affect the background predictions. The correlations between the ( $p_{\mu}^{\text{True}}, \theta_{\mu}^{\text{True}}$ ) is evaluated, and Figure 5.43 summarises this through the “root mean square matrix” in order to show both the exact errors and their correlations. We define the root mean square matrix as the square root of the covariance matrix for positive coefficients and minus the square root of the module of the coefficient for negative correlations. One observes the high correlations between the cross section bins due to the flux original correlations between the neutrino energy bins.

### 5.6.3 Detector systematics

The PM and INGRID detector systematics affect the cross section result mainly through the selection (see Section 5.3.2). The detector uncertainties we study and take into account are:

- the charge deposition of INGRID and PM hits.
- the scintillator inefficiency due to the imperfect simulation of the dead areas.
- the electronic noise that can affect the number of hits (dark noise).

Since this selection is based on the particle charge deposition that allows PID, we expect the charge deposition uncertainty to have the highest impact on the cross section results. In this study, we assumed that each detector systematic error are uncorrelated to each others. It seems a reasonable assumption in this case given the sources of these systematics.

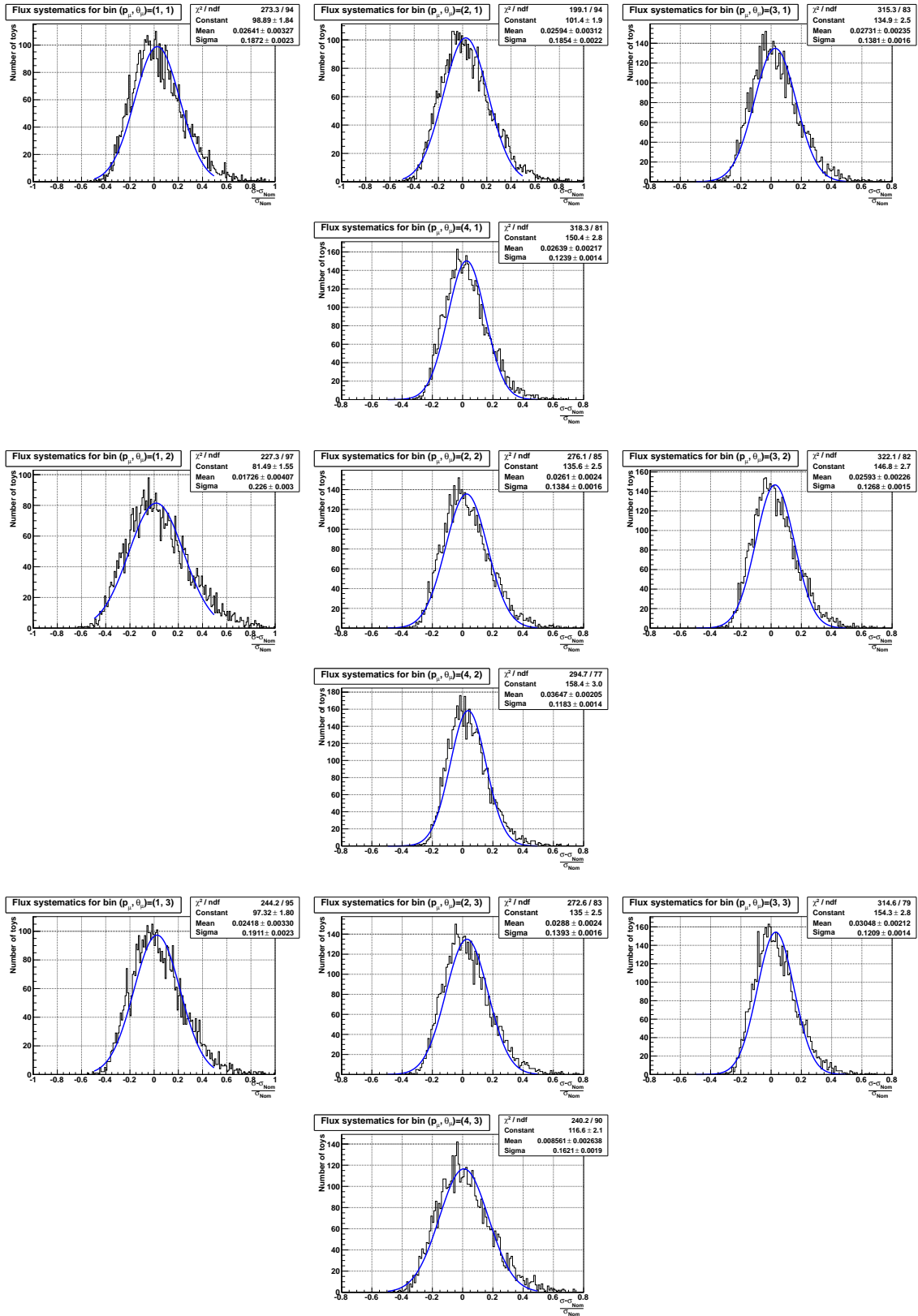


Figure 5.42: Relative systematic errors coming from the neutrino flux predictions in each  $(p_\mu^{\text{True}}, \theta_\mu^{\text{True}})$  bin using 2,000 generated toy fluctuated experiments.

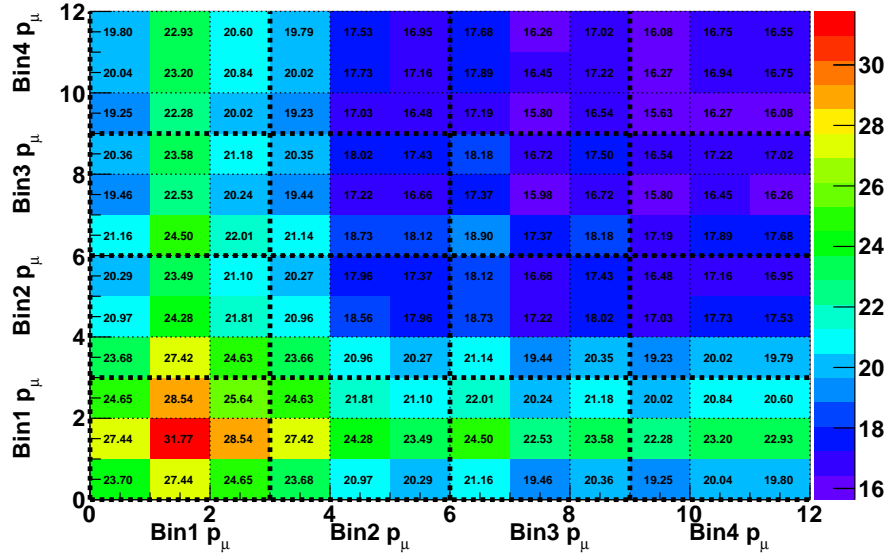


Figure 5.43: Root mean square matrix between  $(p_\mu^{\text{True}}, \theta_\mu^{\text{True}})$  bins of the relative systematic errors coming from the neutrino flux predictions. **These errors are given in percent for clarity.**

### Charge deposition

We identify three origins of difference between the data sample and the MC production:

- The charge deposition due to the imperfect tuning of the scintillator shape in the MC.
- The remaining charge deposition discrepancy between MC and data for particles (identified as hadrons) of very low charge deposition in INGRID scintillators that we observed in Chapter 4.
- The variation in the averaged number of photo-electrons measured with time. Though the corrections shown in Chapter 4, we observed an average charge deposition variation with the period of the data taking.

**Scintillator shape** In order to estimate the MC and data charge deposition discrepancies with the track angle, we have used the independent sand muon sample we presented in Chapter 4. We will refer to the “mean charge deposition” as the center of the gaussian we used to fit the minimum ionisation peak value (MIP). Note this is not the arithmetic mean of the hit charge distribution, in order to remove possible effects from very high energy hits. This mean charge deposition is evaluated separately for each angle. Figure 5.44 shows the distributions for the PM INGRID and SciBar scintillators. One observes the lack of MC sample at very large angles ( $\theta_\mu > 40$ ), preventing from any reasonable assumption. We assumed that the difference between data and MC in this high angle region is the same that for  $\theta_\mu \in [36^\circ, 39^\circ]$ .

The relative MIP positions  $(\frac{\text{MIP}_{\text{Data}} - \text{MIP}_{\text{MC}}}{\text{MIP}_{\text{MC}}})_\theta$  provide the differences of the charge deposition between MC and data for a given track angle. The impact of this systematic error on the cross section results is evaluated by reprocessing the MC sample, and applying to each hit the charge correction  $(\frac{\text{MIP}_{\text{Data}} - \text{MIP}_{\text{MC}}}{\text{MIP}_{\text{MC}}})_\theta$  depending on the track angle  $\theta$  the hit belongs to:

$$\text{Hit charge}_{\text{sys}} = \text{Hit charge} \times \left( \frac{\text{MIP}_{\text{Data}} - \text{MIP}_{\text{MC}}}{\text{MIP}_{\text{MC}}} \right)_\theta. \quad (5.6.1)$$

We expect such a variation to mainly impact the PID and therefore, the estimation of background and efficiency. Figure 5.45 summarises the error in each cross section bin and their correlations. One observes that the systematic error in most of the bins varies within  $\sim 1 - 10\%$ , with a higher impact on the region of low muon momentum, as it was expected.

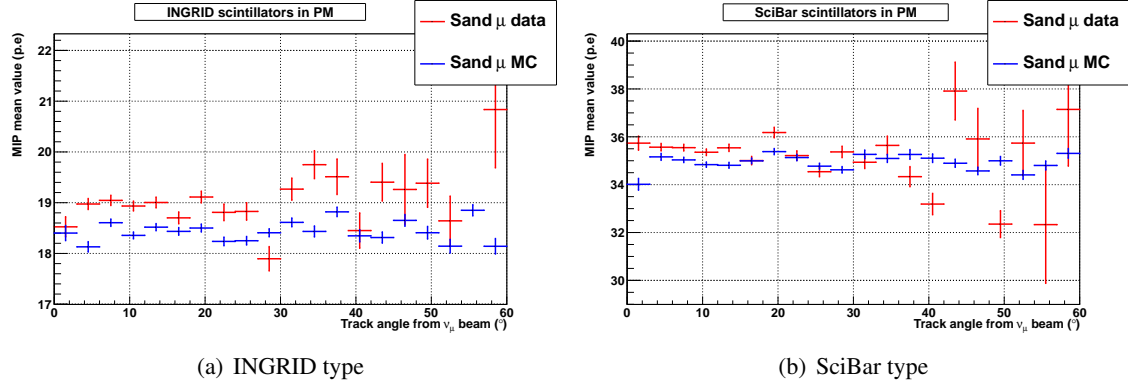


Figure 5.44: Sand muon average MIP charge (corrected by fiber attenuation and track angle) as a function of the track angle. A  $3^\circ$  binning resolution was chosen to adapt to detector resolution. One observes the relatively constant distribution due to the angle correction (path length in a scintillator). The INGRID and SciBar type scintillators are separated considering their different shape and so, inefficiency region.

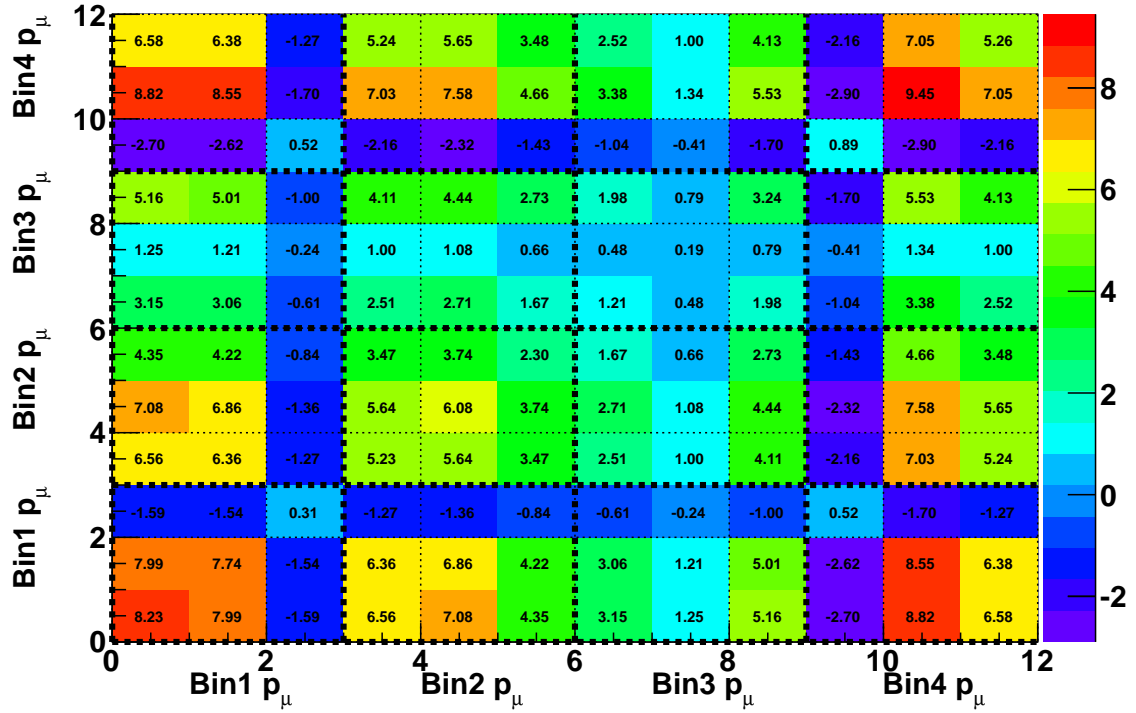


Figure 5.45: Root mean square matrix of the relative systematic error coming from charge deposition variations with angle on each  $(p_\mu^{\text{True}}, \theta_\mu^{\text{True}})$  bin. These errors are given in percent for clarity.

**Low energy hadron effect** This effect is only observed in INGRID (see Chapter 4). To estimate it, we release the imposed condition that a INGRID hit should have a higher charge than 8 p.e to be used in the PID (see Section 5.3.2). Figure 5.46 summarises the impact on the cross section measurement in each bins. This impact is lower than 5% in most of the bins, except for low statistics bins where the impact is enhanced by the unfolding matrix uncertainty to  $\sim 10\%$ .

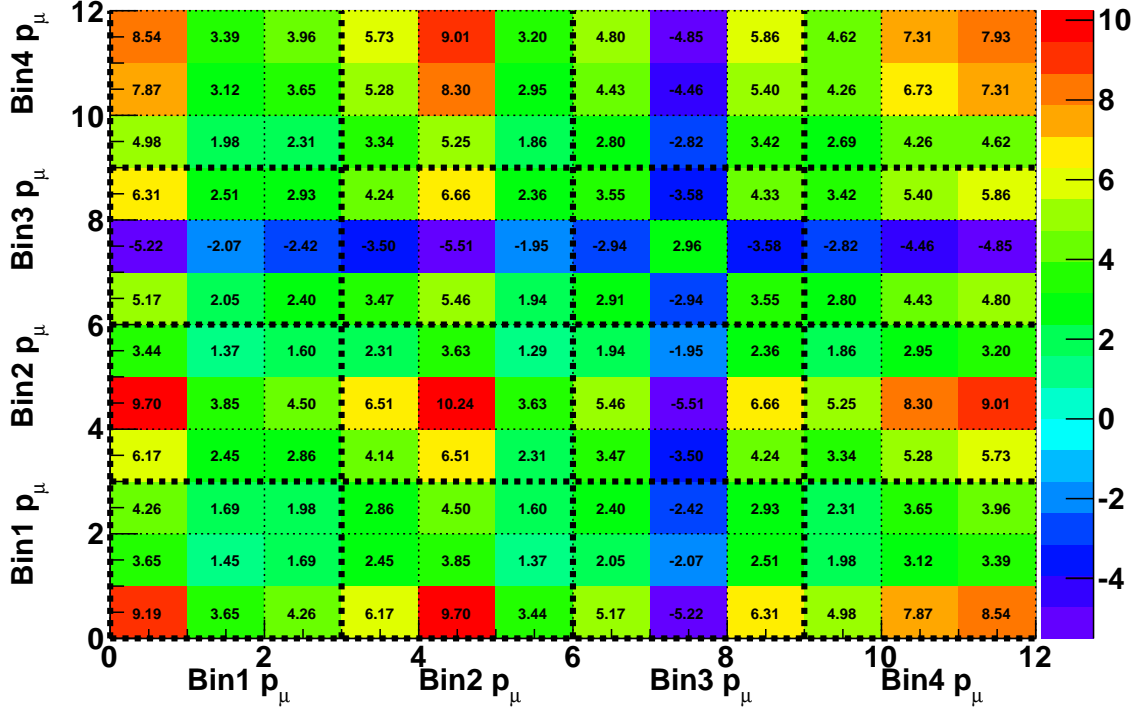


Figure 5.46: Root mean square matrix of the relative systematic error coming from low charge deposition in INGRID on each  $(p_\mu^{\text{True}}, \theta_\mu^{\text{True}})$  bin. **These errors are given in percent for clarity.**

**Charge deposition stability with time** We have observed in Chapter 4 that the MIP mean charge varies with the data taking period. This effect should impact the PID since we assumed a constant charge deposition in the MC to tune the muon confidence level. In order to evaluate the systematic error associated to this effect, we have separated the data taking time in 200 constant time intervals, and have estimated the MIP average value by fitting the sand muon charge distribution with a gaussian (see Chapter 4). Figure 5.47 shows the results for the INGRID type scintillators in PM, where a 7.3% relative error is observed. We assume that these time variations are distributed in a gaussian distribution. Based on Chapter 4, we assume that the MIP variations come from a remaining time dependency of the game. Therefore, we assume a 100% correlation between INGRID and SciBar type scintillators.

The impact of this MIP change on our cross section result has been estimated by generating 2 toy experiments changing the mean MIP value by  $-10\%$  and  $-5\%$  and reproducing the whole cross section analysis study. We proceed similarly to the estimation of the error coming from charge deposition variations with track angle. We scale the charge deposit in each hit by a different factor depending on the toy experiment. The only difference is that we re-applied the whole track reconstruction, considering that a lower or higher mean MIP can importantly affect the number of hits crossing the 2.5 p.e threshold, and thus, the track reconstruction. The relative variation in the example of  $(p_\mu^{\text{True}}, \theta_\mu^{\text{True}}) = ([0.7 \text{ GeV}, 1.0 \text{ GeV}], [0^\circ, 20^\circ])$  is displayed in Figure 5.48. The variation in each  $(p_\mu^{\text{True}}, \theta_\mu^{\text{True}})$  is fitted by a degree-one polynomial.

Finally, we use the polynomial fit of each bin to estimate the systematic error. The relative variation of the cross section corresponding to a  $\pm 7.3\%$  change in MIP mean value is calculated

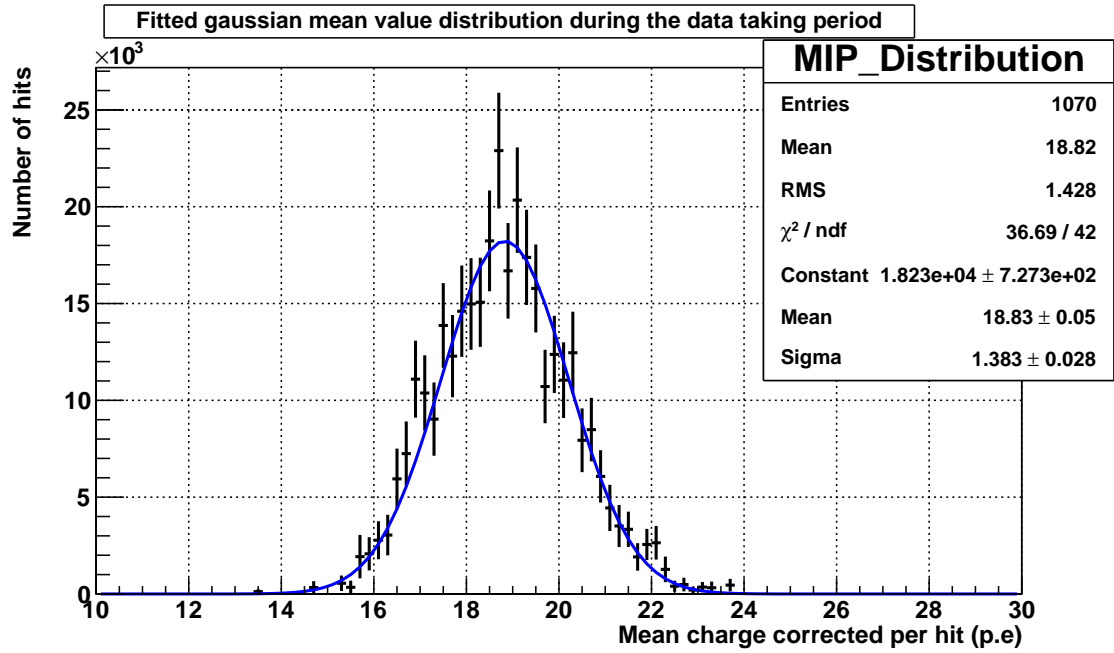


Figure 5.47: MIP mean variations in INGRID-type scintillator for different constant time intervals over the whole data taking period. Each entry for a given time interval has been weighted by the number of events to take into account the non-uniform intensity during the T2K data taking.

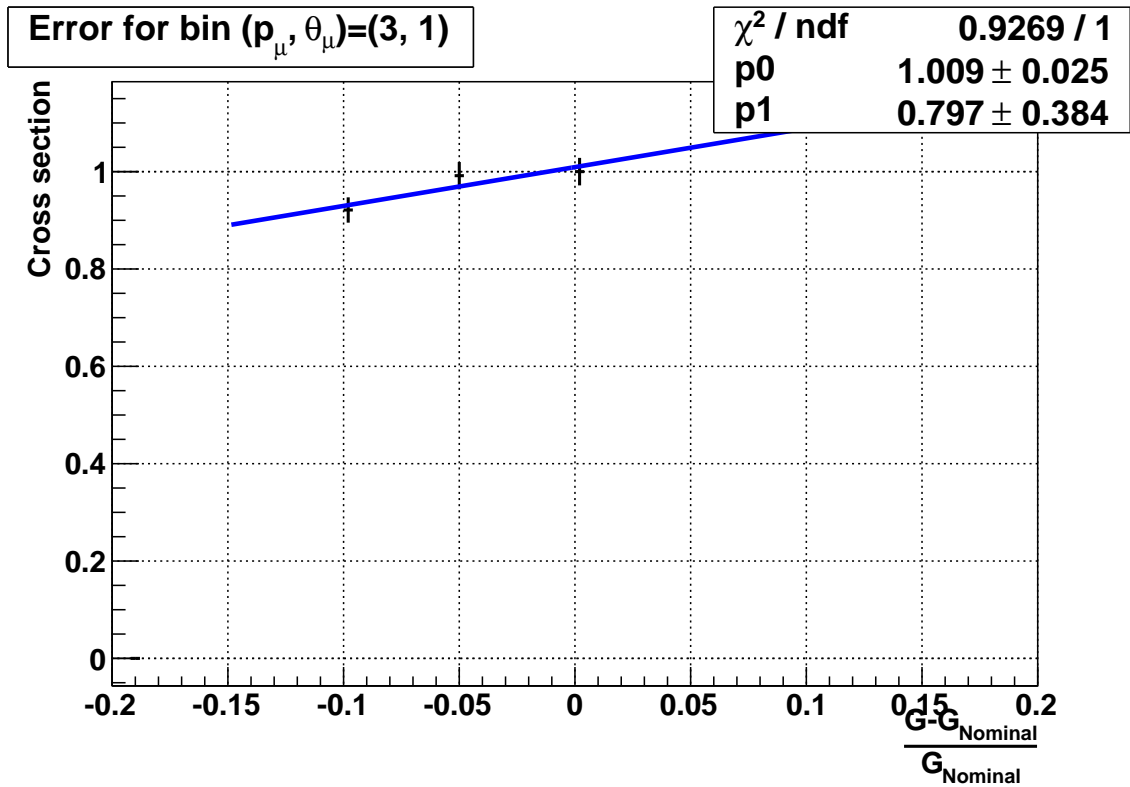


Figure 5.48: Cross section relative variation for the different toy experiments in which we changed the mean MIP value, shown in the special case of the  $(p_\mu^{\text{True}}, \theta_\mu^{\text{True}}) = ([0.7 \text{ GeV}, 1.0 \text{ GeV}], [0^\circ, 20^\circ])$  bin.

as  $\text{Error} = a_{p_\mu, \theta_\mu} \cdot 0.073 + b_{p_\mu, \theta_\mu}$ . Figure 5.49 summarises the systematic error in all the bins and their correlations. One observes that the systematic errors due to the MIP variations are relatively important ( $\sim 5 - 18\%$ ) and correlated.

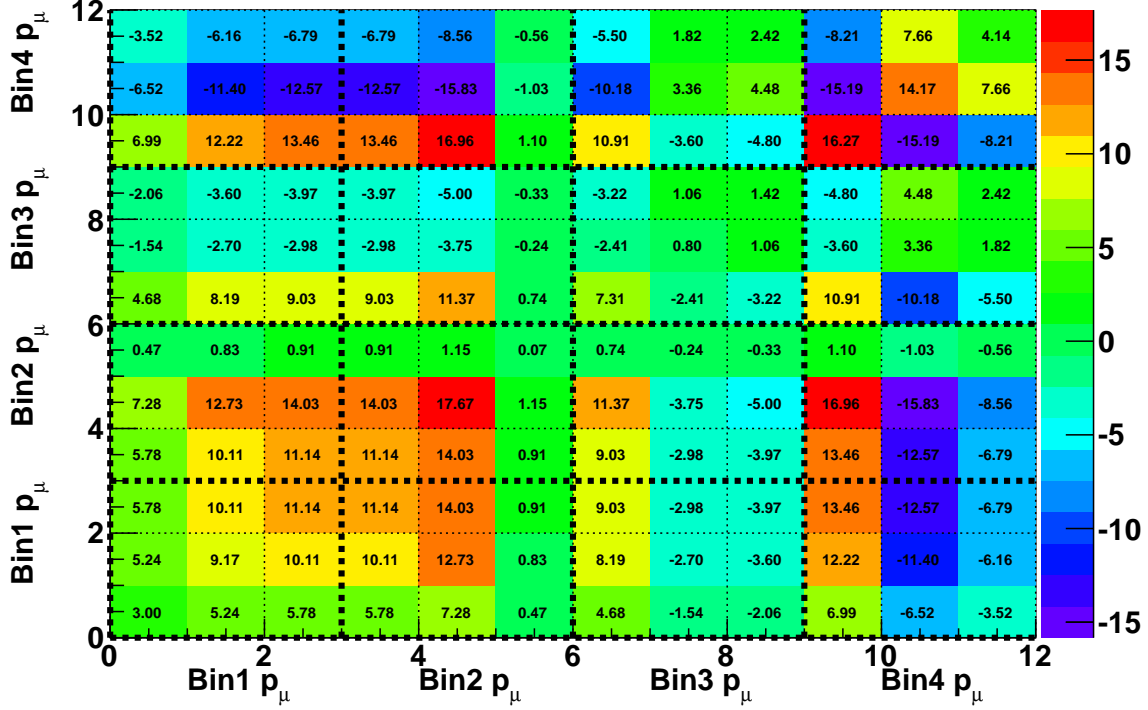


Figure 5.49: Root mean square matrix of the relative systematic error coming from the variation of charge average deposit on each  $(p_\mu^{\text{True}}, \theta_\mu^{\text{True}})$  bin. **These errors are given in percent for clarity.**

### Hit inefficiency

The extruded scintillators active material is an error source in the measurement. The  $\text{TiO}_2$  coating introduces a dead zone (non-interactive) between the scintillators. However, the variation of this coating with the different scintillator is not reproduced in the simulation. We use instead the same values for the  $\text{TiO}_2$  and active regions for all INGRID and SciBar type scintillators in the MC. The effect of the active material variations on charge collection has already been estimated in Section 5.6.3. This section is dedicated to evaluate the impact on the inefficiency of a potential hit. This can lead to a mis-reconstructed or non-reconstructed track. The effect is expected to vary with angle: a high angle track should nearly always hit an active region in a scintillator layer and therefore, have a low hit inefficiency. The inefficiency has been estimated using the sand muon sample according to the method developed in [48]. For each sand muon track, the hit inefficiency is estimated using the following method shown in Figure 5.50:

1. The starting and ending planes of the tracks are estimated as the most upstream and downstream scintillators hit in the reconstructed track (separately for XZ and YZ views).
2. For each 2D view, we turn off the first tracking plane and fit the remaining hits by an order one polynomial. The intersection of this polynomial with the turned-off tracking plane is then estimated. The scintillator located at this intersection is expected to be hit in reality. Therefore, we return to the tracking plane and check if this scintillator or one of its two closest neighbour is actually turned on.
3. We pursue the same analysis until the ending plane is reached.

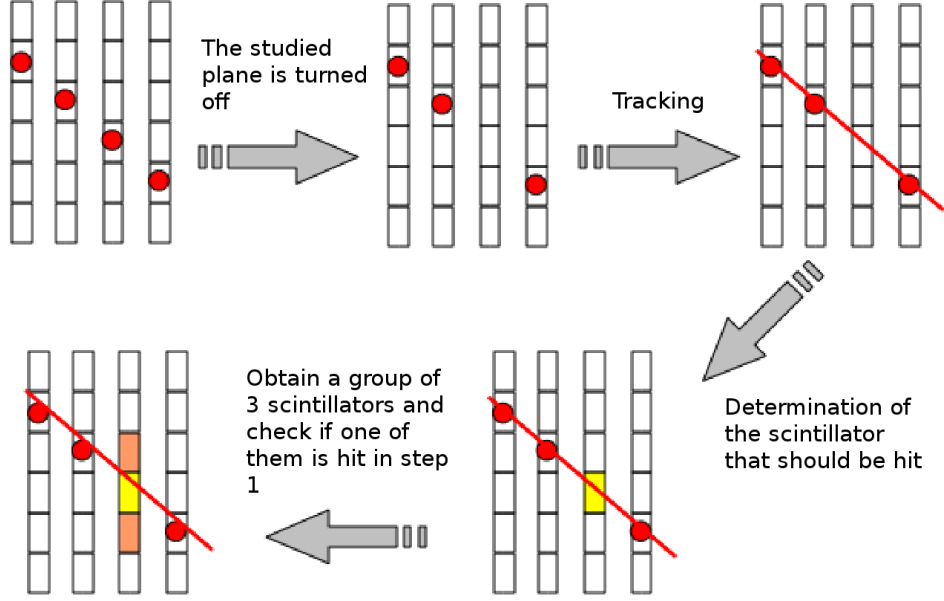


Figure 5.50: Scheme of the hit inefficiency determination. Extracted from [48].

Figure 5.51 shows the result of the hit efficiency comparison between the MC and data. As expected, the hit inefficiency decreases with the track angle. We estimated the inefficiency distribution without separating the SciBar and INGRID-type scintillators. In principle, this approximation should highly impact if the relative proportion of SciBar and INGRID scintillator types crossed is significantly different between the  $\text{CC}0\pi$  and sand  $\mu$  tracks, both for INGRID and SciBar type scintillators. This is expected not to be the case. One observes the lack of statistics in MC sand  $\mu$  for angles  $> 40^\circ$ . Therefore, we will assume that the discrepancy between MC and data for angles above  $40^\circ$  is the same than for the angle bin  $[36^\circ, 39^\circ]$ , which seems to overestimate the discrepancy. Fortunately, it corresponds to a region with a small number of events in our analysis, and so, this assumption will have a minor impact on the result. One observes the MC and data discrepancy to have a peak for track angles  $\sim 30^\circ$ .

The impact of the hit inefficiency on the  $\text{CC}0\pi$  cross section is evaluated in a very similar procedure than for the charge deposition error. The relative data and MC variations shown on Figure 5.51 have an average 0.3% root mean square, which represents the  $1\sigma$  inefficiency difference between MC and data. We simulate 6 different toy experiments, in which the inefficiency is increased compared to the default MC. The hit inefficiency is increased from 0 (which corresponds to the original MC) to 2.5% (larger inefficiency toy experiment) with a step of .5% between the different toy experiments. Then, we mask the hits given the corresponding inefficiency, and apply the reconstruction and selection on the MC in order to take into account both the original reconstruction and  $\text{CC}0\pi$  selection effects. The background, efficiency and likelihood matrix are re-evaluated for each toy experiment, and the cross section is deduced. The cross section variation with the toy experiment inefficiency is fitted with a linear function for each  $(p_\mu^{\text{True}}, \theta_\mu^{\text{True}})$  bin independently, since we expect the inefficiency to differently impact small (high impact) and long tracks (small impact). Figure 5.52 shows the result for the bin  $(p_\mu^{\text{True}}, \theta_\mu^{\text{True}}) = ([0.7 \text{ GeV}, 1.0 \text{ GeV}], [0^\circ, 20^\circ])$ , and one observes that the linear fit is a reasonable hypothesis to model the cross section increase with hit inefficiency. For each bin, the  $1\sigma$  error corresponds to the variation for a hit inefficiency of 0.3%, which represents a  $\sim 1\%$  variation of the cross section (see Figure 5.52). The variation of the cross section and inefficiency is not direct: the hit larger inefficiency results in a lower background and higher efficiency. Since the data remain the same, the overall effect is an increase in the predicted cross section.

Figure 5.53 summarises the  $1\sigma$  error value in the RMS matrix and confirm a 1% average effect. One observes a 7% effect in the bin  $([0.0 \text{ GeV}, 0.5 \text{ GeV}], [20^\circ, 30^\circ])$ , due to the unfolding procedure and the fact that the neighbour have a large statistics  $([0.0 \text{ GeV}, 0.5 \text{ GeV}], [30^\circ, 60^\circ])$ . Such an effect

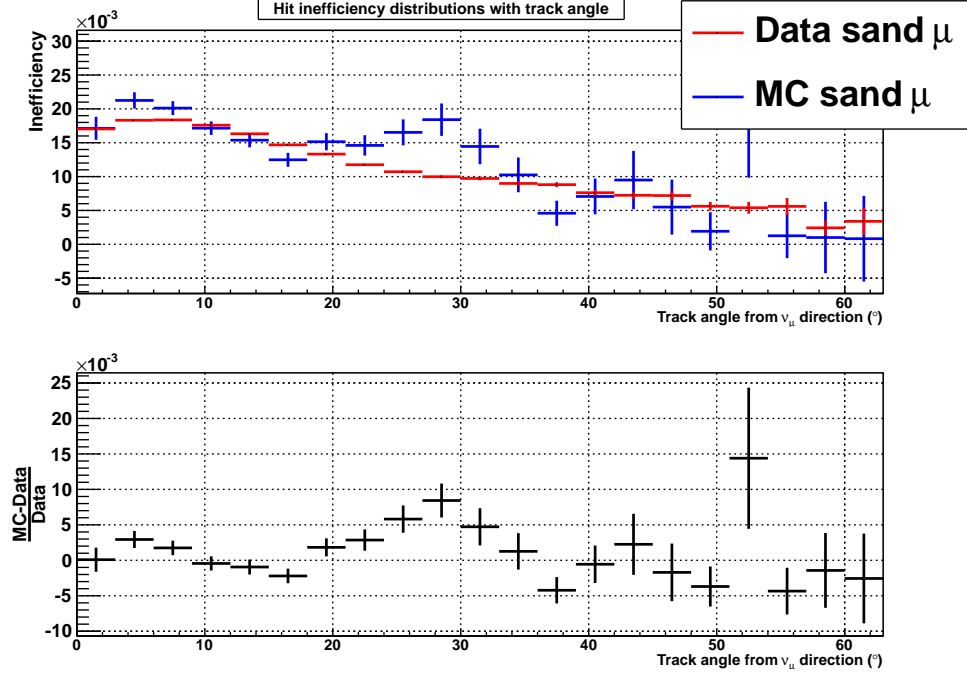


Figure 5.51: Hit inefficiency with the track angle for MC (blue) and data (red) sand  $\mu$  (top). The difference between MC and data is shown on the bottom figure.

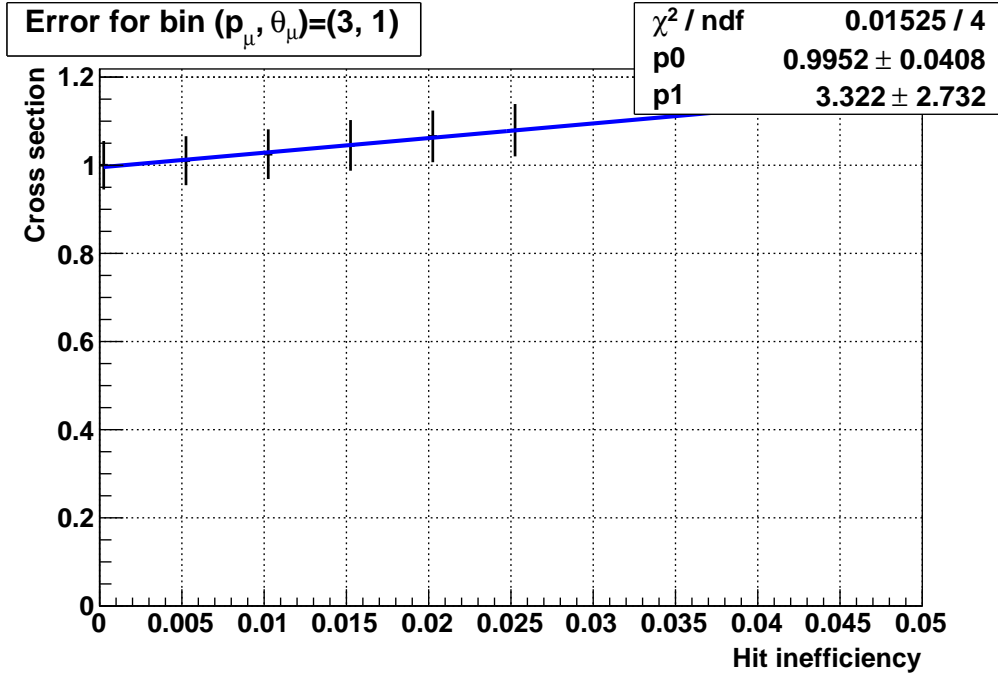


Figure 5.52: Relative variations of the cross section estimation in the  $(p_\mu^{\text{True}}, \theta_\mu^{\text{True}})$  bin for different hit inefficiencies.

can be decreased with an improvement of the current unfolding algorithm.

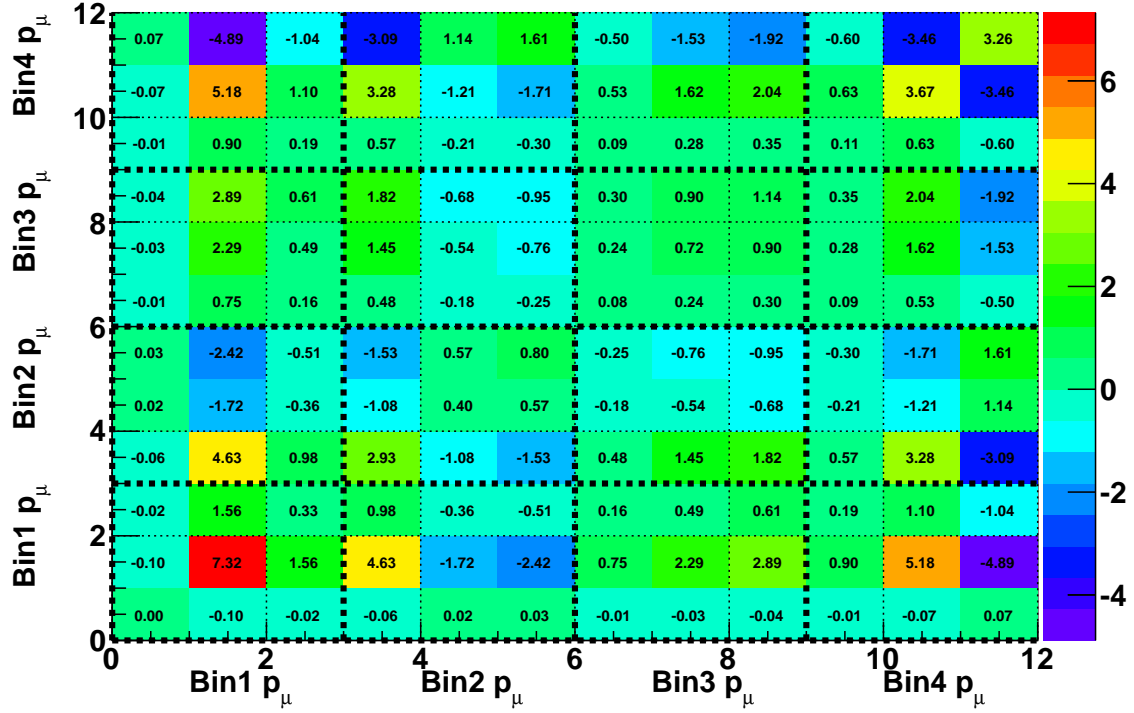


Figure 5.53: Root mean square matrix of the relative systematic error coming from the variation of hit inefficiency on each  $(p_\mu^{\text{True}}, \theta_\mu^{\text{True}})$  bin. **These errors are given in percent for clarity.**

### Electronic dark noise

We observed in Chapter 4 that the dark noise varies within the T2K data taking. The reasons are multiple, but should probably come from MPPC and electronic gain variations with temperature, humidity or beam intensity conditions. In the MC, such a variation is not reproduced and we assumed that the dark noise hit distribution follows a constant Poisson distribution with an average of 5.05 hits per electronic integration cycle (584 ns) per module. The increase in dark noise hit rate generally results in a possible track mis-reconstruction or no reconstruction, reducing the number of events. To study the impact of this time variation on the cross section, we first evaluate the dark noise variation with time for the data set we have used in this analysis. The method is exactly similar to what has been done for the MIP time variation previously: we divided the T2K data taking in the same constant time intervals. For each time interval, we measured the number of hits in off-time cycles for each cycle and separately for the PM and INGRID modules. Each of these distributions is fitted by a Poisson law, and the Poisson mean is taken as the average dark noise hit number during this time interval for the corresponding module. Figure 5.54 shows the time variation of the Poisson mean. Figure 5.55 shows the distribution of the dark noise in the INGRID horizontal module for the different time intervals. We assume a gaussian model to fit the time variation of the dark noise. Such a shape is not expected since data are not taken continuously during the year, which implies variable conditions between the different T2K runs and discontinuous dark noise average values. Nevertheless, we use the gaussian  $\pm 1\sigma$  variation as an estimator of the 68% confidence interval for dark noise value. Though the dark noise mean distribution seems broader than a gaussian, the very thin peak around 5.5 hits observed in Figure 5.55 should partly counter-balance this effect. Therefore, the gaussian approximation seems reasonable. We observe that the  $1\sigma$  variation corresponds to a change of 1.1 hit in the average dark noise hit per cycle per module. Note that this value is different for the PM and INGRID due to the higher number of channels in the former. We assume that the correlations between the PM and INGRID dark noise values are 100% correlated in time, since the modules are located so close that

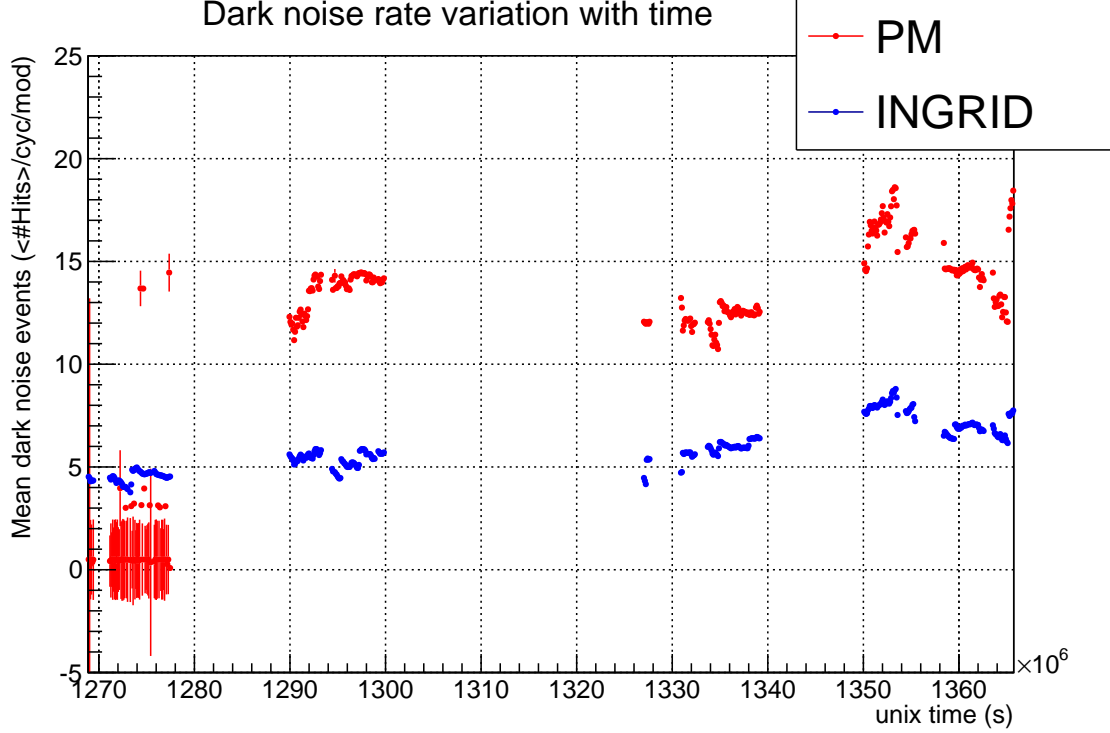


Figure 5.54: Time variation of the mean dark noise rate per cycle and per module during T2K running. The mean is obtained by fitting the dark noise (using off-time integration cycles) rate by a Poisson law. The INGRID horizontal central module is shown in blue, and the PM in red. One observes that the PM was not installed during the first time period (Run 1).

they should be subject to the very same external conditions. The variations of the PM dark noise rate will be therefore deduced from the INGRID module variations, scaling the number of dark noise hits by the nominal ratio of PM and INGRID dark noise hits  $R_{DN} = \frac{12.46}{5.05}$ .

In order to evaluate the impact on the cross section, four toy experiments have been constructed by changing the dark noise average number of dark noise hits (*i.e* the Poisson mean) in the MC, from the nominal 5.05 to 2, 4, 6 and 8 hits per cycle per module in INGRID modules (scaled by  $R_{DN}$  for the PM). The reconstruction, selection and unfolding procedures are applied, and the impact over the  $CC0\pi$  cross section is evaluated.

Figure 5.56 shows the relative variation of the  $CC0\pi$  cross section with the toy experiments, for the example of  $(p_\mu^{\text{True}}, \theta_\mu^{\text{True}}) = ([0.7 \text{ GeV}, 1.0 \text{ GeV}], [0^\circ, 20^\circ])$ . For each bin, we fit the variations with a different degree-one polynomial. The relative  $1\sigma$  error is finally estimated using the  $1\sigma$  variation of the dark noise, *i.e* the fit values for a dark noise rate of  $5.0 \pm 1.1$ . Figure 5.57 summarises the  $1\sigma$  errors for each bin and their correlations.

#### 5.6.4 Cross section model systematics

In Section 5.1, we introduced how to modify the neutrino interaction with a single quark to an interaction with a nucleus. To do so, we emphasized that a nuclear model (a generator) should be used. In this thesis, we use the T2K neutrino event generator, NEUTv5.1.4.2. This event generator is based on 25 parameters, whose central values are shown in Table 5.8. In particular, the CCQE interactions are based on the Smith-Moniz [70] relativistic Fermi gas repartition of the nucleon with a Fermi momentum set at  $p_F = 250 \text{ MeV}$  and a binding energy at  $E_B = 25 \text{ MeV}$ . The interaction with a single nucleon is based on the Llewellyn-Smith [85] formalism for which the axial mass has been set to  $M_A^{QE} = 1.21 \text{ GeV}$ . This relatively high value compared to bubble chamber experiment constraints ( $M_A^{QE} \in [1.0, 1.05] \text{ GeV}$ ) is set to take into account the MiniBooNE constraints with no MEC. In the nominal NEUT parametrisation, no meson exchange current is simulated. The use of a

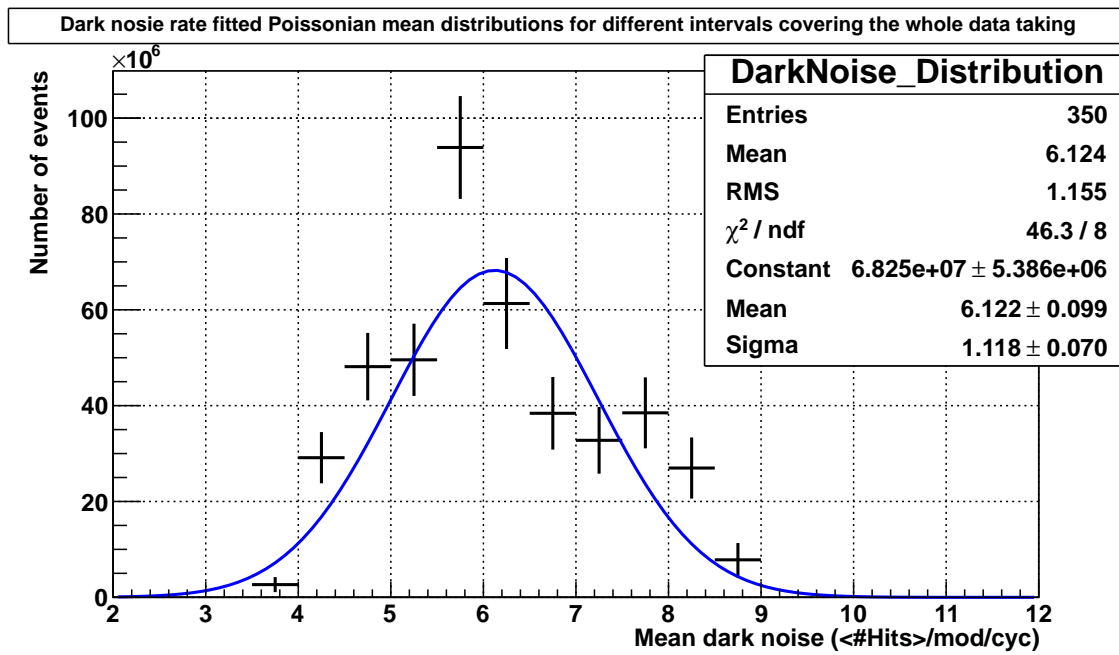


Figure 5.55: Dark noise hits Poisson mean variations in the INGRID horizontal module for different constant time intervals over the whole data taking period.

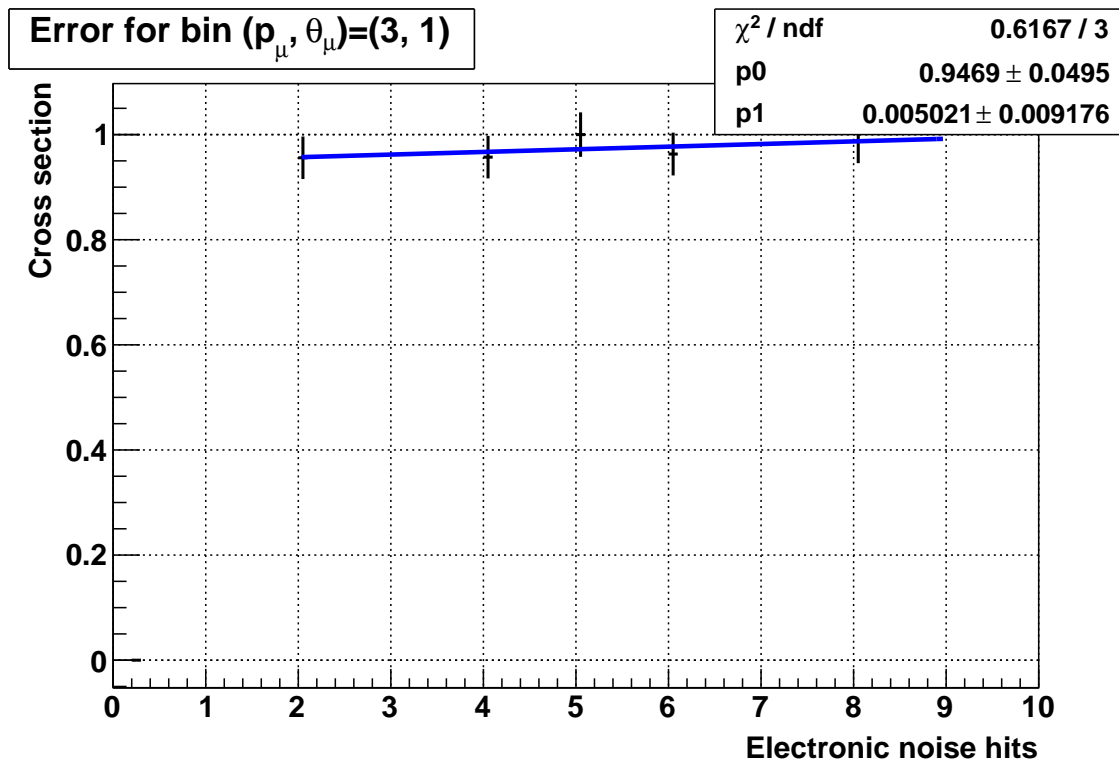


Figure 5.56: Relative variations of the cross section estimation in the  $(p_\mu^{\text{True}}, \theta_\mu^{\text{True}}) = ([0.7 \text{ GeV}, 1.0 \text{ GeV}], [0^\circ, 20^\circ])$  bin for different average dark noise rate toy experiments.

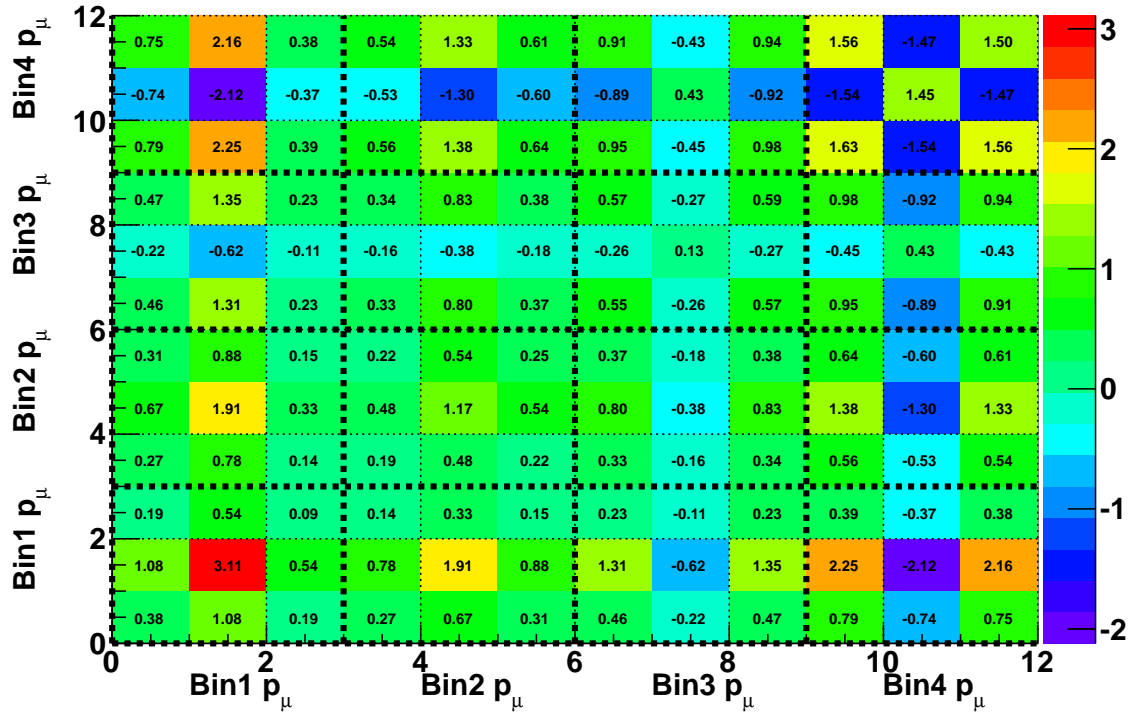


Figure 5.57: Root mean square matrix of the relative systematic error coming from the variation of dark noise rate on each  $(p_\mu^{\text{True}}, \theta_\mu^{\text{True}})$  bin. **These errors are given in percent for clarity.**

higher  $M_A$  value implies a larger cross section since it varies with the axial mass as  $G_A(Q^2) = \frac{g_A}{(1 + \frac{Q^2}{M_A^2})^2}$  (see Section 5.1), with a higher increase for large  $E_\nu$  since it implies larger W boson momentum  $Q^2$  in average. The pion production is based on the Rein and Seghal model [86], for which the axial mass is also set to  $M_A^{\text{RES}} = 1.21$  GeV in NEUT. The impact of this parameter on the axial coupling is similar to the CCQE case.

In order to illustrate what has been shown in Section 5.1, we vary the axial masses within the  $1\sigma$  errors defined in Table 5.8. Figure 5.58 shows the CC0 $\pi$  cross sections for these two different parameters. The increasing impact of  $M_A$  with  $E_\nu$  (in fact with the exchanged boson momentum  $Q^2$ ) is illustrated, along with the contribution of  $M_A^{\text{RES}}$  for high energy CC0 $\pi$ . We have already presented the effect of the spectral function model in Figure 5.9 and final state interactions as  $\pi$  absorption in Figure 5.11.

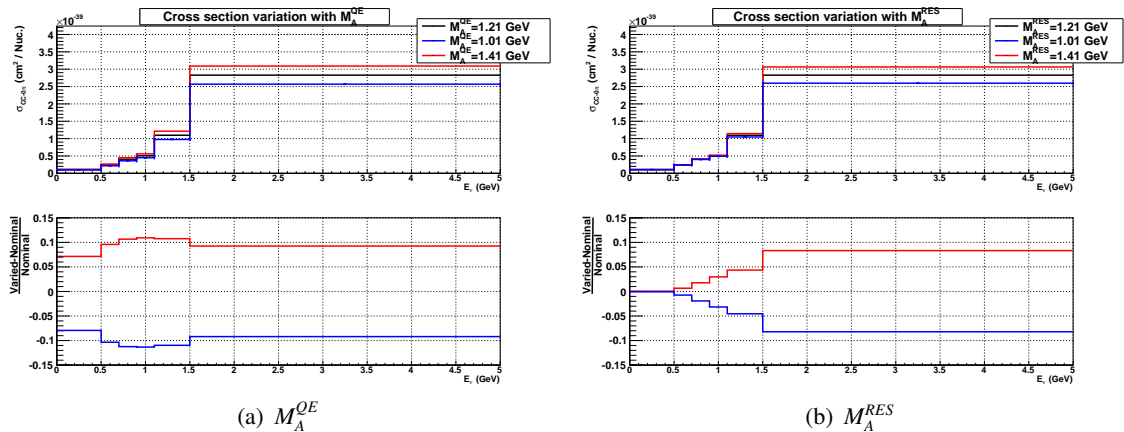


Figure 5.58: Comparison of the  $\nu_\mu$  CC0 $\pi$  cross section as a function of the neutrino energy, for different axial QE and resonant masses (left and right respectively).

The 25 parameters (Table 5.8) of the cross section model are varied. In this study, the  $1\pi E_\nu$  shape, the neutrino binding energy errors are neglected for now, due to incompatibility with the current MC version. The uncertainty of the models is expected to mainly contaminate the background prediction, and through it, the unfolding matrix. The efficiency is expected to be affected in small proportions since it mainly depends on the detector simulation. The likelihood matrix is also almost only detector-dependent, and we do not expect any important variation of it from cross section model uncertainties. We assumed that the 23 parameters we used are uncorrelated to each other. Figure 5.59 shows the root mean squared matrix combining the effect of the 23 systematic errors as a sum of the square. One observes that the cross section model uncertainty is  $\sim 10\% - 20\%$  in most of the bins, apart from the bin corresponding to  $p_\mu \in [1.0, 5.0]$  GeV. In fact, it appears that the cross section model highly impacts the unfolding of the angle and generates a large systematic error in this bin. An improvement of the unfolding method, alternating the momentum and angular unfolding one after another for each iteration step should therefore solve this issue in the future. As for the other bins, the residual cross section model dependency comes from the remaining important background ( $\sim 35\%$ ). The decrease of this systematic error will require to improve the particle identification algorithm to enhance the  $CC0\pi$  purity.

### 5.6.5 Summary

Figure 5.60 combines the statistical and systematic errors. One observes that the flux correlations are removed, mostly due to the statistical error small and negative correlations. Figure 5.61 shows the correlation matrix.

Cross section model parameter	Nominal	Uncertainty
$M_A^{QE}$	1.21 GeV	16.5%
$M_A^{RES}$	1.21 GeV	16.5%
$\pi$ less resonant $\Delta$ decay	1	16.5%
Spectral function	0	100%
Fermi momentum	250 MeV/c	12%
Binding energy	25 MeV/c	27.3%
CCQE normalisation low energy ( $E_\nu < 1.5$ GeV)	1	11%
CCQE normalisation medium energy ( $1.5 < E_\nu < 3.5$ GeV)	1	30%
CCQE normalisation high energy ( $E_\nu > 3.5$ GeV)	1	30%
$CC1\pi$ normalisation low energy ( $E_\nu < 2.5$ GeV)	1	21%
$CC\pi$ normalisation high energy ( $E_\nu > 2.5$ GeV)	1	21%
$CC$ coherent $\pi$ normalisation	1	100%
$CC$ other shape	0	40%
$NC\pi^0$ normalisation	1	31%
$NC$ coherent $\pi$ normalisation	1	30%
$NC\pi^\pm$ normalisation	1	30%
$NC$ other shape	1	30%
W shape	87.7 MeV	52%
$1\pi E_\nu$ shape	0	50%
Pion absorption	1	50%
Pion charge exchange (low energy)	1	50%
Pion charge exchange (high energy)	1	30%
Pion QE scattering (low energy)	1	50%
Pion QE scattering (high energy)	1	30%
Pion inelastic scattering	1	50%

Table 5.8: Nominal NEUT generator values for the 25 cross section model parameters and the associated  $1\sigma$  errors.

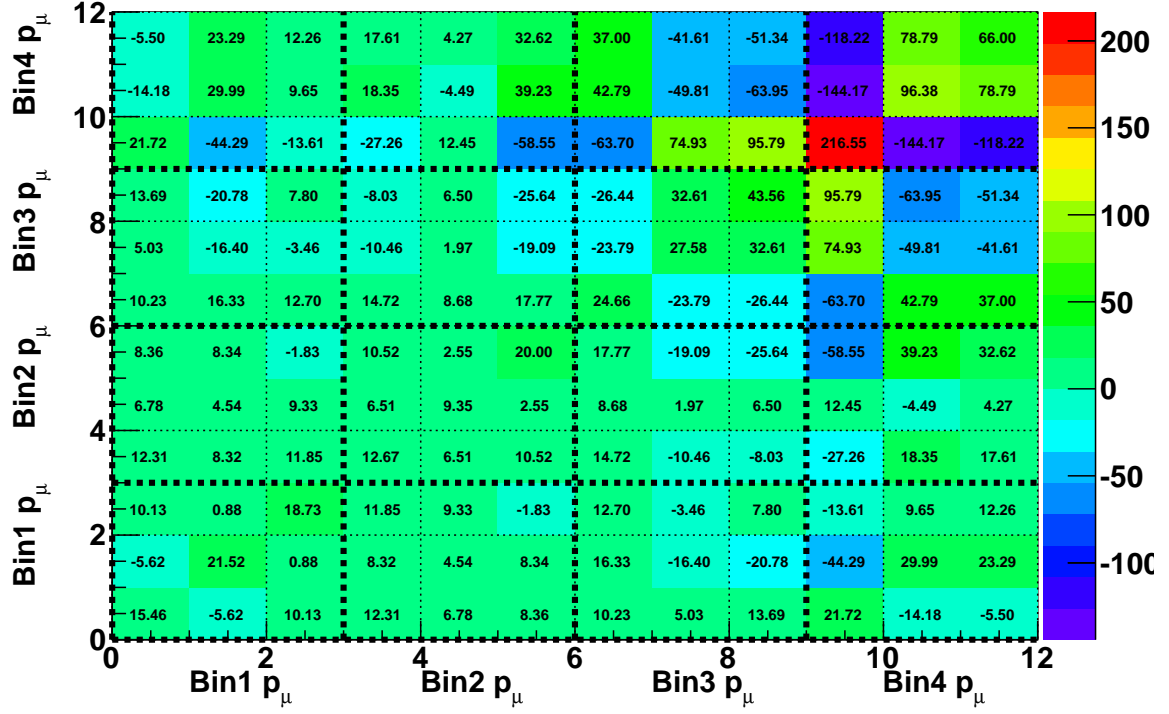


Figure 5.59: Root mean square matrix of the total cross section model systematic error on each  $(p_\mu^{\text{True}}, \theta_\mu^{\text{True}})$  bin. These errors are given in percent for clarity.

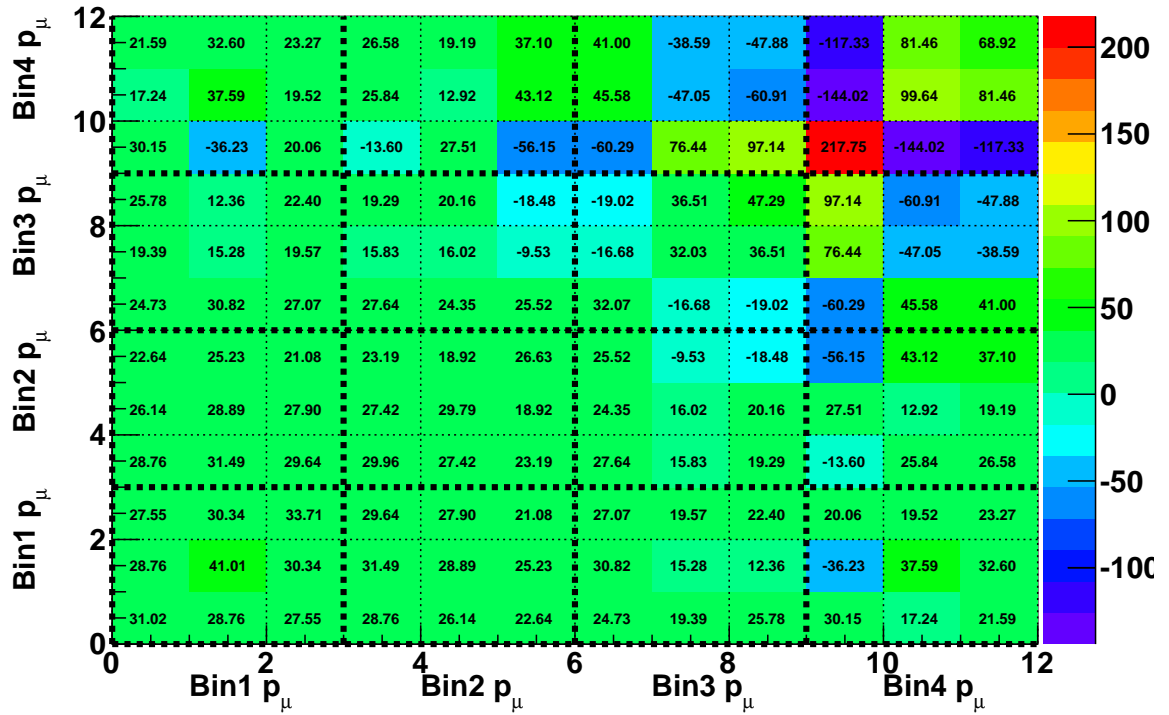


Figure 5.60: Root mean square matrix of the total error on each  $(p_\mu^{\text{True}}, \theta_\mu^{\text{True}})$  bin. These errors are given in percent for clarity.

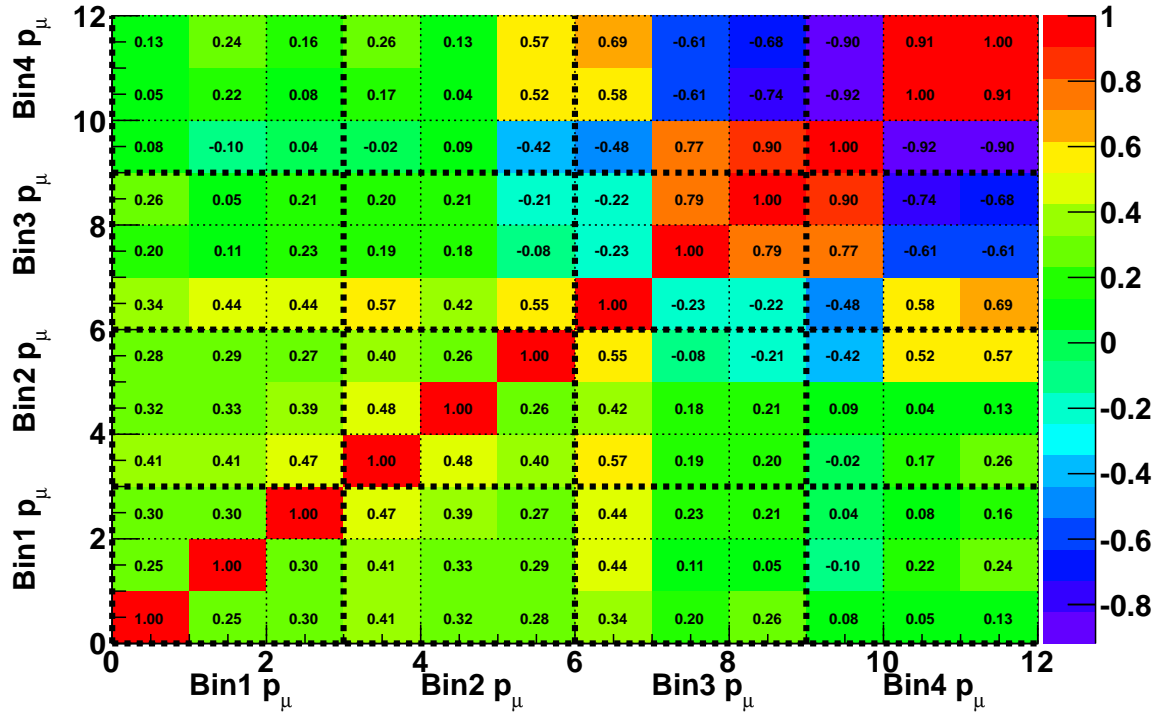


Figure 5.61: Correlation matrix of the systematic and statistical error added quadratically, for each  $(p_\mu^{\text{True}}, \theta_\mu^{\text{True}})$  bin. One observes that the original high correlations from neutrino flux are washed out for low statistics bins (small  $p_\mu$ ) where the statistical error dominates.

## 5.7 Cross section measurement results

### 5.7.1 The double differential cross section result

Figure 5.62 shows the final result of the CC0 $\pi$  double differential cross section. One observes that the cross section increases with the muon momentum, with a peak around 1 GeV, as was shown in Figure 5.1 (as a function of  $E_\nu$ ). In Figure 5.3, one observes that the neutrino CCQE cross section is nearly constant for  $E_\nu > 1$  GeV, which implies that the cross section per neutrino energy decreases after  $E_\nu \sim 1$  GeV. Since we observe a similar effect in Figure 5.62 and 5.3 (considering  $p_\mu \sim E_\nu$ ), it also confirms that the final state interaction CC0 $\pi$  is mostly composed of CCQE vertex interaction. The content of each  $p_\mu, \theta_\mu$  bin is shown in Table 5.9.

We have shown the  $\frac{d^2\sigma}{dp_\mu d\theta_\mu}$  double differential cross section with the statistical and systematic error

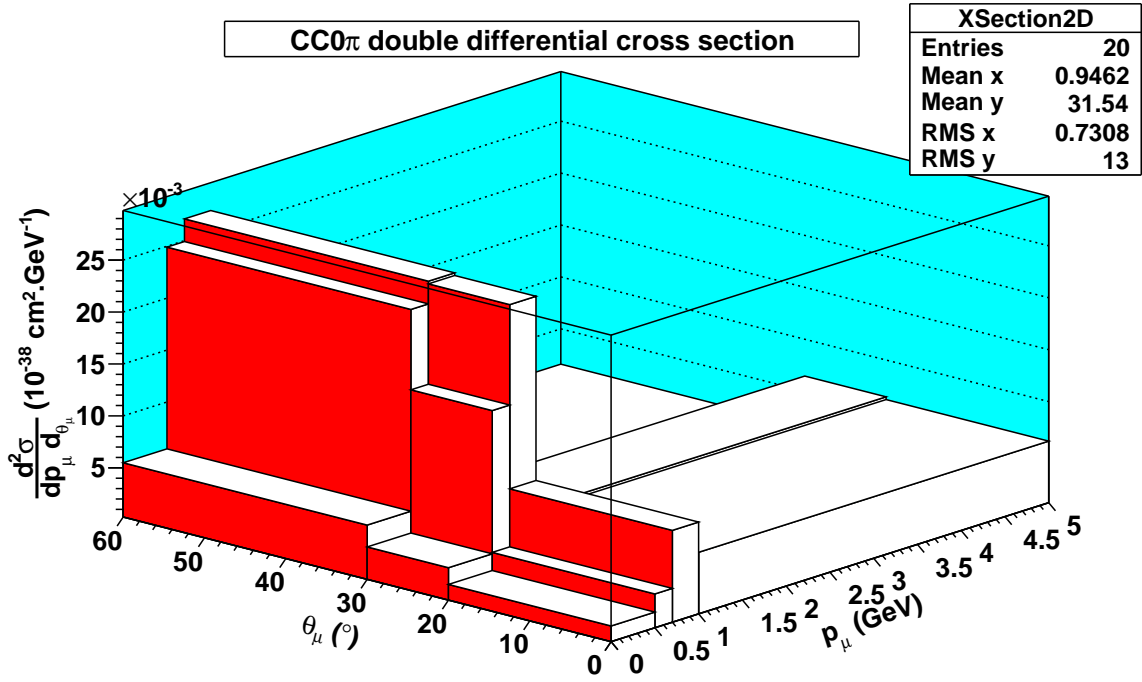


Figure 5.62: The CC0 $\pi$  double differential cross section on PM hydrocarbon with muon momentum and angle.

$p_\mu$	$\theta_\mu$	Data	MC	Stat.	Syst	Flux	XSec.	Det.
	[0.0°, 20.0°]	1.77	0.88	0.71	0.55	0.42	0.27	0.23
[0.0, 0.5] GeV	[20.0°, 30.0°]	3.38	3.35	1.35	1.39	1.07	0.73	0.49
	[30.0°, 60.0°]	5.49	6.85	1.67	1.85	1.41	1.03	0.62
	[0.0°, 20.0°]	3.52	3.56	0.72	1.05	0.83	0.45	0.47
[0.5, 0.7] GeV	[20.0°, 30.0°]	17.17	12.19	3.42	5.12	3.19	1.61	3.67
	[30.0°, 60.0°]	24.91	22.16	4.42	6.63	4.33	4.98	0.69
	[0.0°, 20.0°]	9.11	7.62	1.03	2.92	1.72	2.25	0.73
[0.7, 1.0] GeV	[20.0°, 30.0°]	26.84	22.70	3.12	8.60	4.29	7.40	0.85
	[30.0°, 60.0°]	27.10	22.40	2.71	12.81	4.74	11.80	1.55
	[0.0°, 20.0°]	6.19	6.90	0.51	13.48	0.97	13.41	1.03
[1.0, 5.0] GeV	[20.0°, 30.0°]	6.46	8.09	1.26	6.43	1.09	6.22	1.21
	[30.0°, 60.0°]	1.60	1.64	0.21	1.10	0.27	1.06	0.18

Table 5.9: CC0 $\pi$  cross section in each  $(p_\mu^{\text{True}}, \theta_\mu^{\text{True}})$  bin. The data are shown in the third column, the true MC in the fourth. The statistical and systematic errors are respectively shown in the fifth and sixth columns. the flux, cross section model and detector contributions in the systematic error are respectively shown in the seventh, eighth and ninth columns.

in Figure 5.63 and 5.64 which represent respectively the double differential cross section distribution with momentum in each angle bin and the same distribution with muon angle in each momentum bin. One observes in Figure 5.63 that the momentum bin corresponding to  $p_\mu > 1$  GeV is heavily affected by statistical and cross section model uncertainties (red) as we observed in the error Table 5.9. This important effect comes from the original statistic and cross section model uncertainties, and this effect is largely enhanced through the unfolding procedure. The reason is that our unfolding algorithm primarily operates a momentum unfolding for each bin angle, and then, an angular unfolding for each momentum bin. Since all the events in the bin  $p_\mu > 1$  GeV are almost contained in the sole reconstructed angular bin  $\theta_\mu \in [0^\circ, 20^\circ]$  (see Table 5.4 for large  $d_\mu \sim$  large  $p_\mu$ ), the unfolding in the last momentum bin is submitted to large fluctuations. As we explained, a reconstructed bin with a very large statistics compared to the bins it is correlated to (through the likelihood matrix) implies a divergence since a statistical variation in the high statistic bin leads to a very high change in small statistics bins to compensate the effect. A similar enhancement by the unfolding is also observed in Figure 5.64 for the same sample of high momentum outgoing muons  $p_\mu > 1$  GeV. This unfolding enhancement can be solved in the future, by unfolding alternatively in momentum and angle bins for each iteration step, or developing a full 2D unfolding.

Figures 5.63 and 5.64 show the MC prediction assuming the cross section model parameters defined in Table 5.8, *i.e* a RFG with a large axial mass  $M_A^{QE} = 1.21$  GeV compared to the bubble chamber best fit (Figure 5.6). One observes no significant discrepancy of the model as compared to our measurement, except from a general larger cross section in the data set than in the simulation. In order to improve clarity, we have shown the simple differential cross sections  $\frac{d\sigma}{dp_\mu}$  and  $\frac{d\sigma}{d\theta_\mu}$  in Figure 5.65 and 5.66 respectively. The systematic errors and their correlations are deduced from the errors shown in Table 5.9 and the correlation matrix shown in Figure 5.61. This result shown in Figure 5.65 and 5.66 confirms that the cross section predicted by the MC is lower than the measured one in the  $p_\mu \in [500 \text{ MeV}, 1 \text{ GeV}]$  region. The high correlations between the flux uncertainties do not totally explain this discrepancy, since the low and high momenta data bins are in relatively good agreement with the model. As the  $\text{CC}0\pi$  measurement presented here is aimed to be model-independent to provide direct input to test various models, we will dedicate the remaining part of this chapter to investigate the impact of the model on the agreement between the data and MC cross sections. In this analysis, the statistical error is dominant (Table 5.42) and is only slightly correlated between the bins. Therefore, we will assume here a simple model where there are no correlations between the bins. It leads to slightly over-estimate our sensitivity in the present case (considering the remaining correlations are mainly positive due to flux normalisation effect). In order to compare the different models, we adopt the following strategy:

- the cross section model uncertainties are removed, so that the comparison does not depend on external data set (which were used to tune these systematics).
- the model is fixed in the data (constant background) and only the simulation is varied according to the cross section model. The data are taken as pivot. We therefore neglect the impact of model variation on data.

### 5.7.2 The spectral function model

We introduced the spectral function (SF) in Section 5.1, and have shown that its effect corresponds to an equivalent binding energy that reduces the cross section at low energy. Figure 5.67 and 5.68 show the comparison between the RFG and SF models and the data as a function of the muon momentum and angle. Both figures show no improvement of the agreement between the MC and the data when changing the RFG into SF. This is understood since most of the spectral function effects occur in the low energy region, where our detector is less sensitive because of the requirement for tracks to cross three INGRID tracking planes. Since no preference is shown for the SF model, we will use the RFG one in the remaining part of this chapter. Note that Figures 5.67 and 5.68 also show the enhancement of the cross section for a larger axial mass  $M_A^{QE} = 1.41$  GeV.

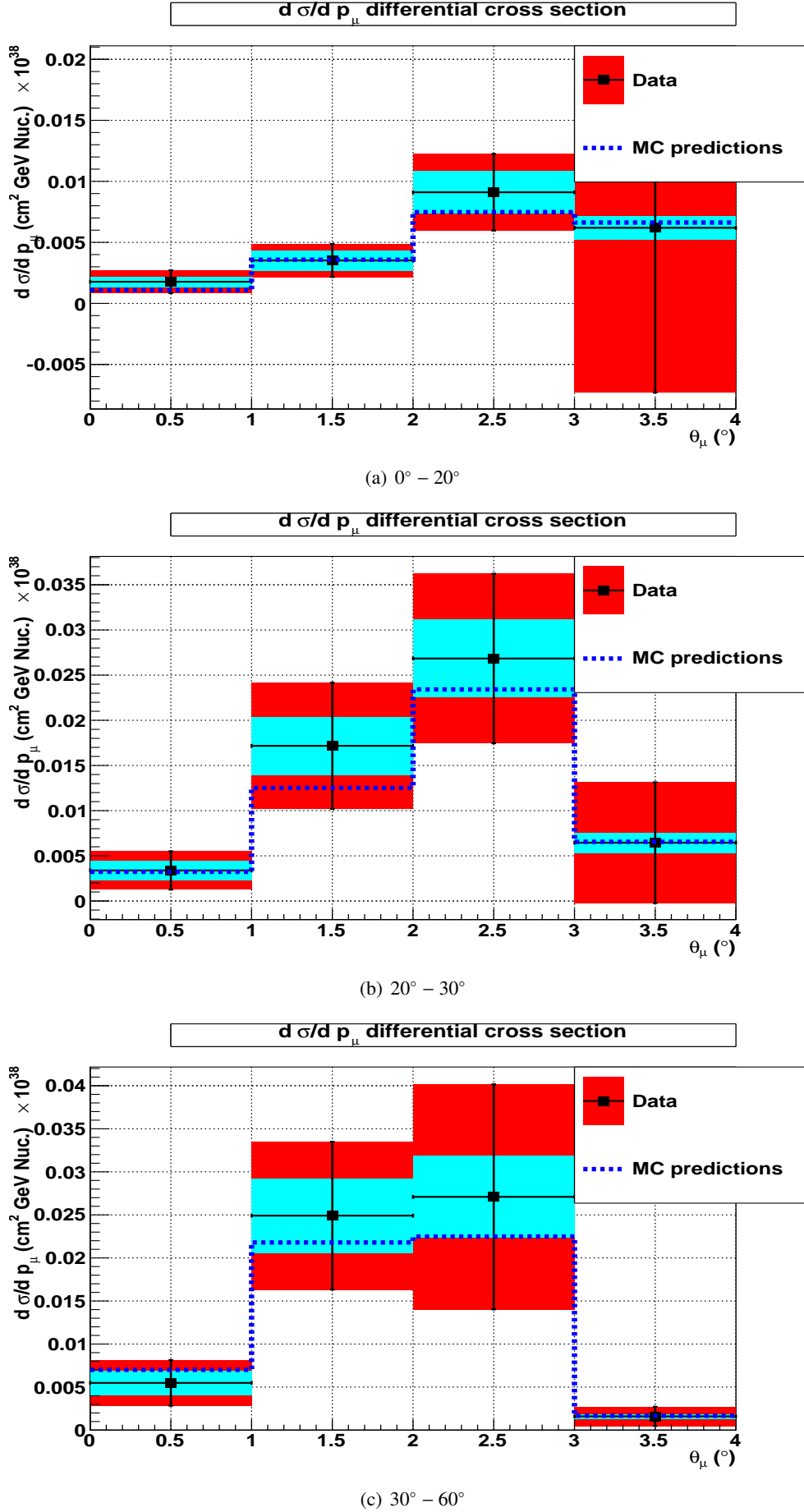


Figure 5.63:  $\text{CC0}\pi \frac{d\sigma}{dp_\mu d\theta_\mu}$  double differential cross section as a function of the muon momentum, in the low (top), medium (center) and high (bottom) angle muon regions. The total error is shown in red, and the flux errors (highly positively correlated) in light blue.

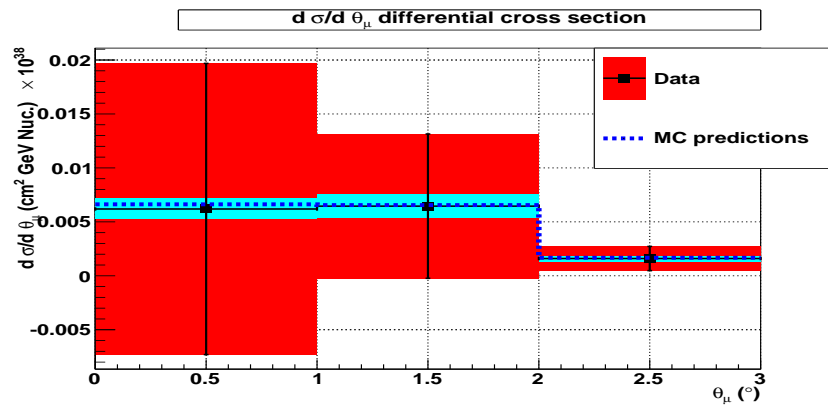
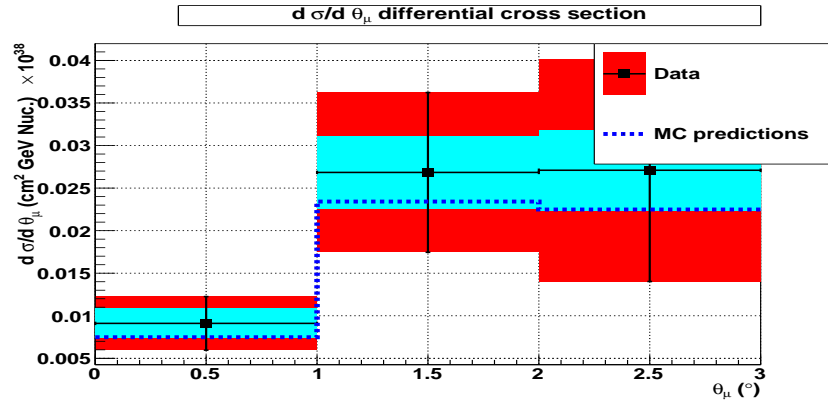
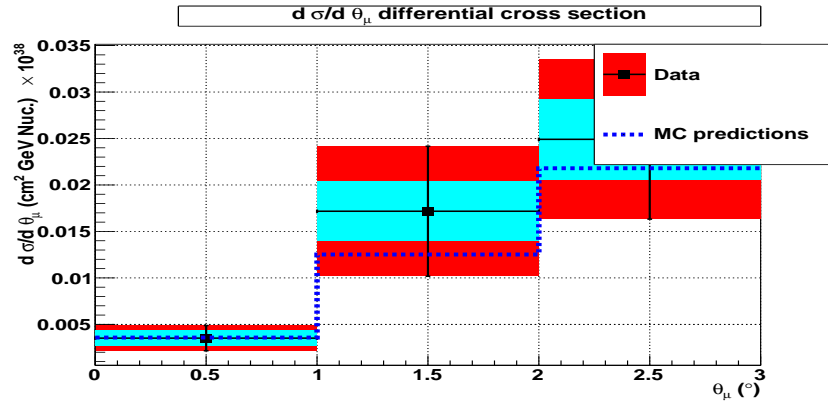
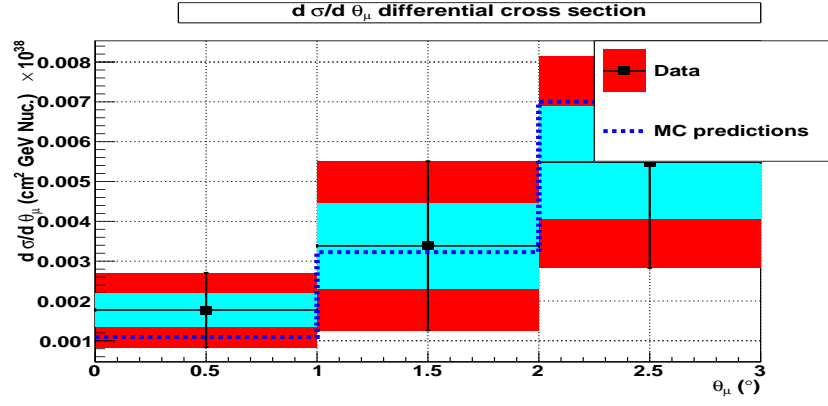


Figure 5.64:  $\text{CC}0\pi \frac{d\sigma}{dp_\mu d\theta_\mu}$  double differential cross section as a function of the muon angle, in the four momentum bins. The total error is shown in red, and the flux errors (highly positively correlated) in light blue.

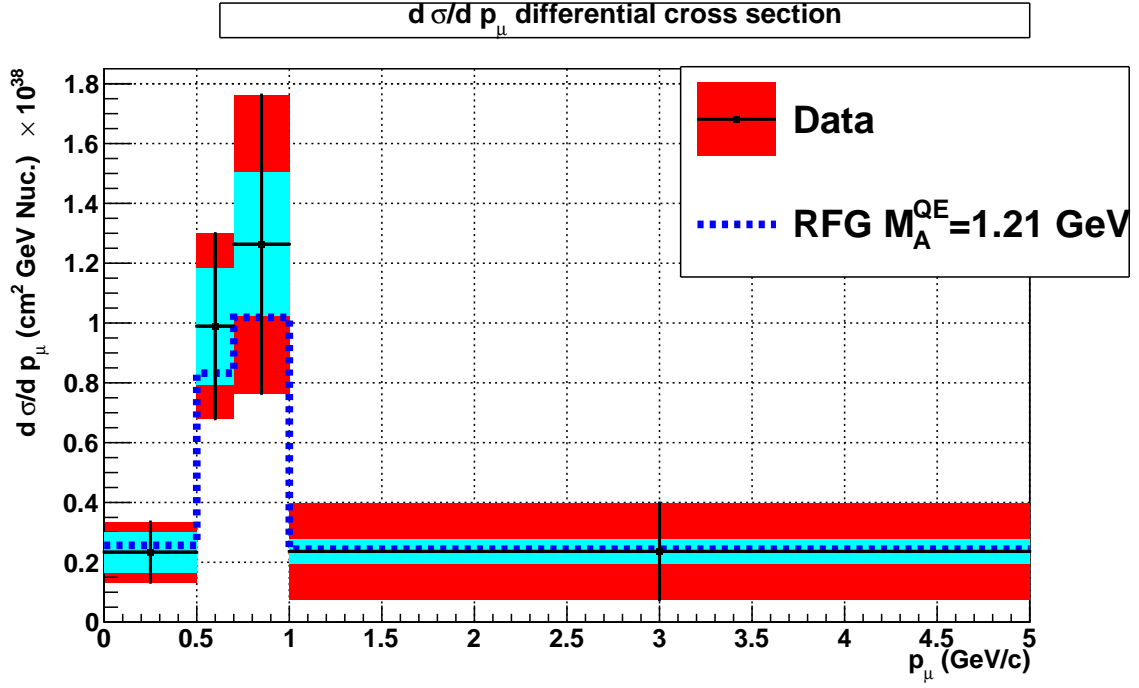


Figure 5.65: CC0 $\pi$   $\frac{d\sigma}{dp_\mu}$  differential cross section as a function of the muon momentum. The total error is shown in red, and the flux errors (highly positively correlated) in light blue. The model used for the comparison is a relativistic Fermi gas (RFG) with  $M_A^{QE} = 1.21$  GeV.

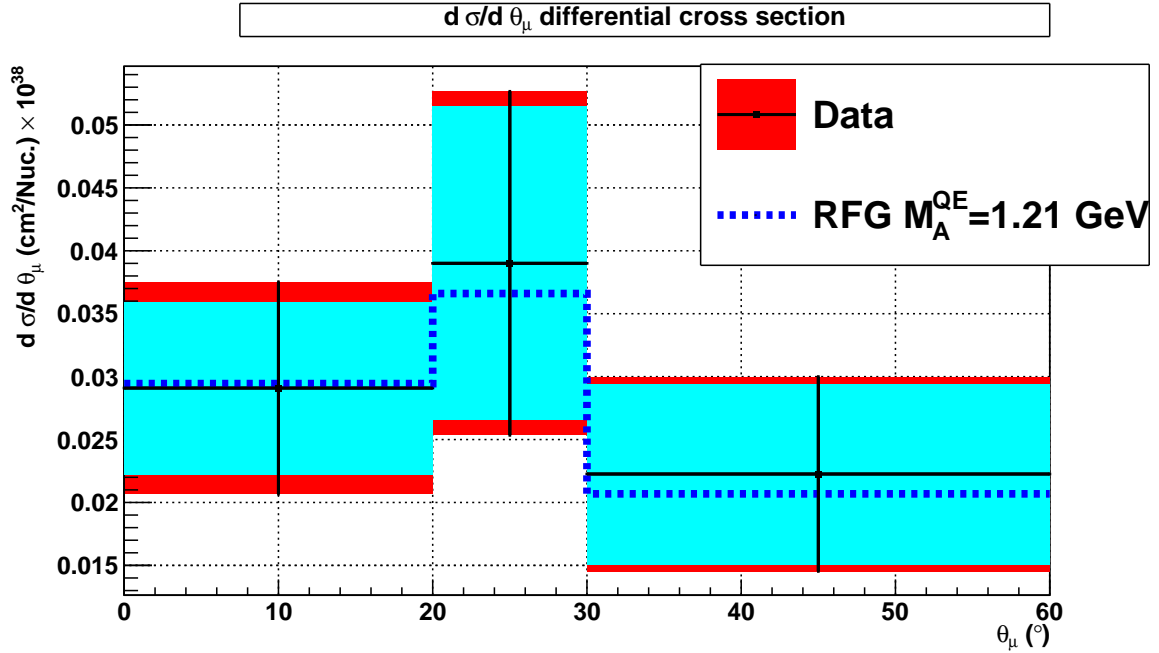


Figure 5.66: CC0 $\pi$   $\frac{d\sigma}{d\theta_\mu}$  differential cross section as a function of the muon angle. The total error is shown in red, and the flux errors (highly positively correlated) in light blue. The model used for the comparison is a relativistic Fermi gas (RFG) with  $M_A^{QE} = 1.21$  GeV.

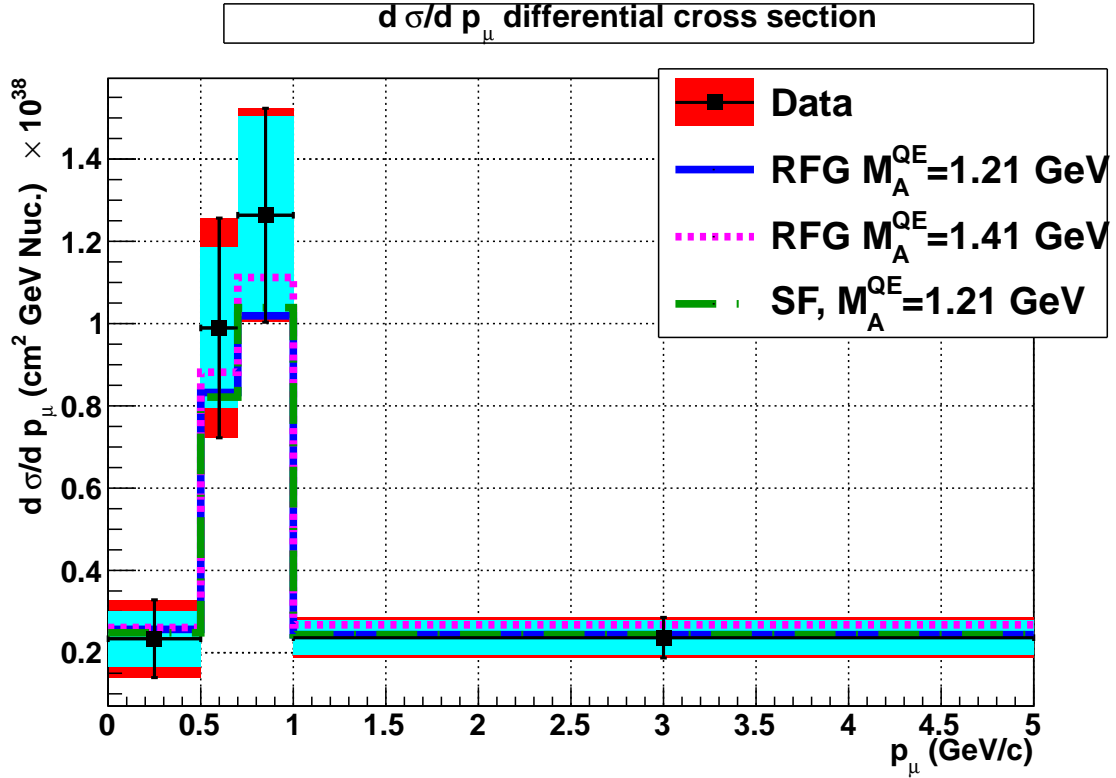


Figure 5.67: Comparison of different models with the data  $CC0\pi \frac{d\sigma}{dp_{\mu}}$  differential cross section as a function of the muon momentum. The total error is shown in red, and the flux errors (highly positively correlated) in light blue.

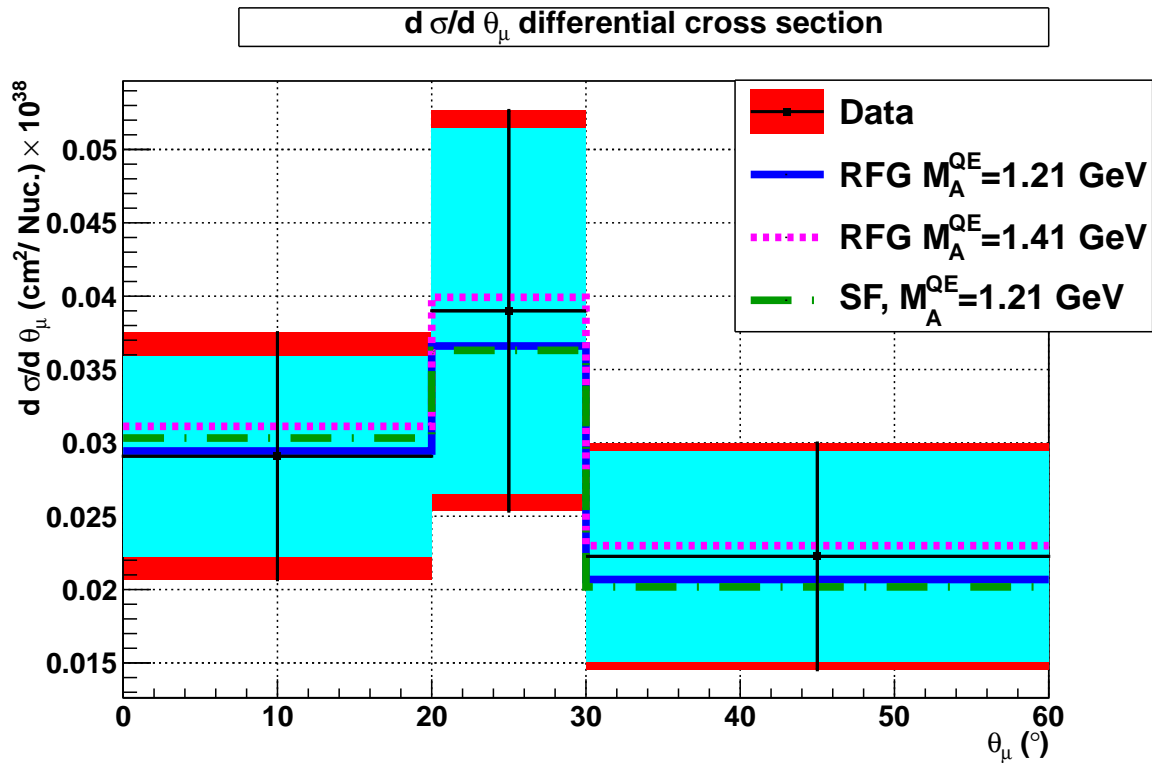


Figure 5.68: Comparison of different models with the data  $CC0\pi \frac{d\sigma}{d\theta_{\mu}}$  differential cross section as a function of the muon momentum. The total error is shown in red, and the flux errors (highly positively correlated) in light blue.

### 5.7.3 The axial mass fit

Since the RFG model is not excluded by the PM CC0 $\pi$  data, we performed a fit of the axial mass, considering no uncertainty on the neutrino model apart from the axial mass. It assumes that the entire difference between data and MC is due to an  $M_A^{QE}$  effect. We have generated 1,000,000 toy experiments, in which we varied the  $M_A^{QE}$  parameter uniformly in  $M_A^{QE} \in [0.0 \text{ GeV}, 3 \text{ GeV}]$  and estimated the MC cross section. We built the negative log-likelihood quantity to estimate the agreement between the model and data, under a bin uncorrelated hypothesis:

$$\ln L = -\left[ \sum_{i=1}^{\text{Nbins}_{p_\mu}} \frac{D_i - \text{MC}_i}{2\sigma_{i p_\mu}^2} + \sum_{j=1}^{\text{Nbins}_{\theta_\mu}} \frac{D_j - \text{MC}_j}{2\sigma_{j \theta_\mu}^2} \right] \quad (5.7.1)$$

where  $D_i$  and  $\text{MC}_i$  ( $D_j$  and  $\text{MC}_j$ ) are the content of data and MC  $i$ -th momentum bin (respectively  $j$ -th angle bin).  $\text{MC}_i$  is the quantity that varies among the toy experiments. The values  $\sigma_{i p_\mu}^2$  and  $\sigma_{j \theta_\mu}$  are respectively the  $1\sigma$  errors in the  $i$ -th momentum bin and  $j$ -th angle bin. They are extracted from Table 5.9 and from the correlation matrix (Figure 5.61) by summing the different angle contributions in each momentum bin (respectively the momentum contributions in each angular bin). Here, we use the information on both muon angle and momentum, and assumed they are independent. In fact, under the uncorrelated bin hypothesis we used from the beginning, the projections along the muon momentum and angle are independent. Figure 5.69 shows the result of the 1,000,000 toy experiments. The best fit value corresponds to the negative log-likelihood minimum and the  $1\sigma$  errors are defined for  $-\ln(L) = (-\ln(L))_{\min} + \frac{1}{2}$ . The corresponding  $M_A^{QE}$  value is:

$$M_A^{QE} = 1.33 \pm 0.17 \text{ GeV} \quad (5.7.2)$$

One first observes that we obtain a larger  $M_A^{QE}$  value as compared to the “bubble chamber experiments best fit”  $1.026 \pm 0.021 \text{ GeV}$ . There is a disagreement of nearly  $2\sigma$ . Our CC0 $\pi$  measurement favours a higher  $M_A^{QE}$  value in agreement with the MiniBooNE [67], MINOS [72] and K2K [71] results summarised in Equations 5.1.23 and 5.1.27. The small uncertainty on the PM  $M_A^{QE}$  best fit value (comparable to MiniBooNE result) is partly due to the fact we neglected bin correlations. In case of positive correlations, a higher  $M_A^{QE}$  value can be induced with a lower sensitivity, since the effect of  $M_A^{QE}$  is similar to a flux normalisation effect, with small differences on the  $p_\mu$  shape. Nevertheless, in this uncorrelated approximation, we confirm the discrepancy of the current measurements with the former bubble chamber constraints. In Section 5.1, we introduced the nuclear effects as a possible explanation of this discrepancy. Indeed, these effects are expected to be negligible in the case of deuterium or protons that constitutes most of the targets that contribute to the “bubble chamber experiments best fit”. On the opposite, these nuclear effects should be taken into account in more complex nuclei as  $^{12}\text{C}$  which constitute most of the PM target (90.96%).

### 5.7.4 Effect of meson exchange currents

We have therefore replaced the RFG model by including the meson exchange current (MEC) in the NEUT neutrino generator. The particular MEC model used in this study is the model from Bodek *et al.* [87]. As before, only the MC is varied. Figure 5.70 and Figure 5.71 show the comparison between data and MC CC0 $\pi$  cross sections as a function of muon momentum and angle respectively. One observes that the MEC effects are similar to an increase of the axial mass, and enhance the neutrino cross section. As we explained in Section 5.1, this enhancement is mainly due to np-nh effects. One observes in this case a better agreement between PM data and the simulation taking into account these nuclear effects.

We finally fit the axial mass value in the case of MEC. We used the same procedure as defined in the previous section, and generated 1,000,000 toys to construct a negative log-likelihood distribution. As before, we consider that bins are uncorrelated. Figure 5.72 shows the  $M_A^{QE}$  fit and indicates an axial mass:

$$M_A^{QE} = 1.11_{-0.17}^{+0.18} \text{ GeV} \quad (5.7.3)$$

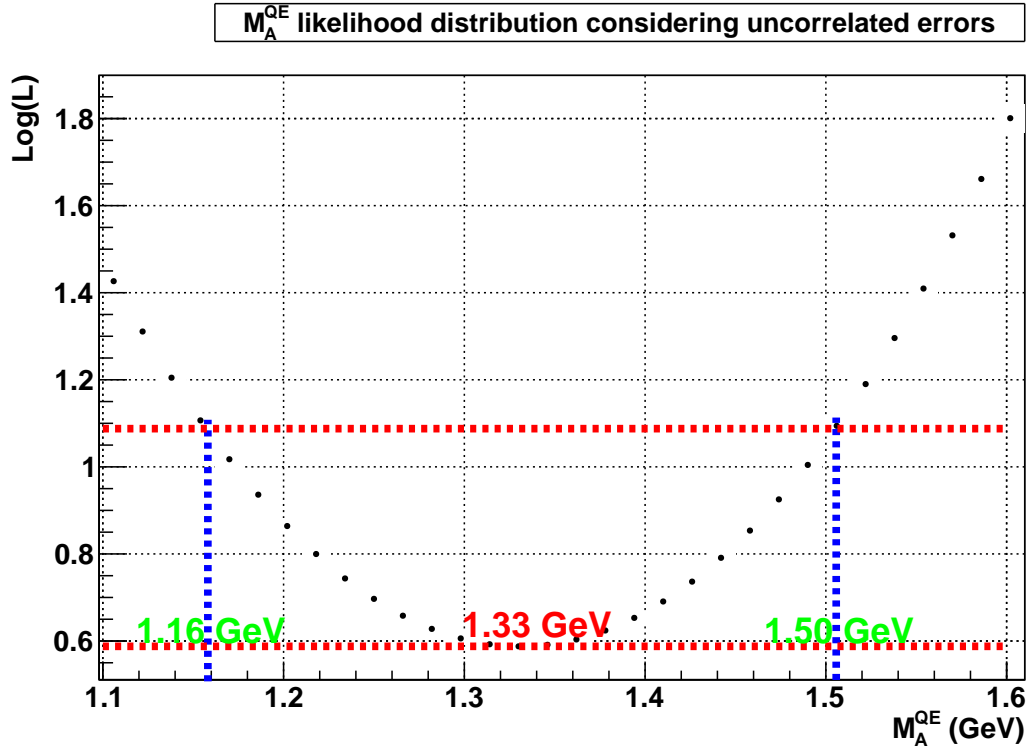


Figure 5.69: Negative log-likelihood distribution for  $10^6$  toy experiments varying uniformly  $M_A^{QE}$  between 0 and 3 GeV. The bin correlation and cross section model uncertainties are not considered.

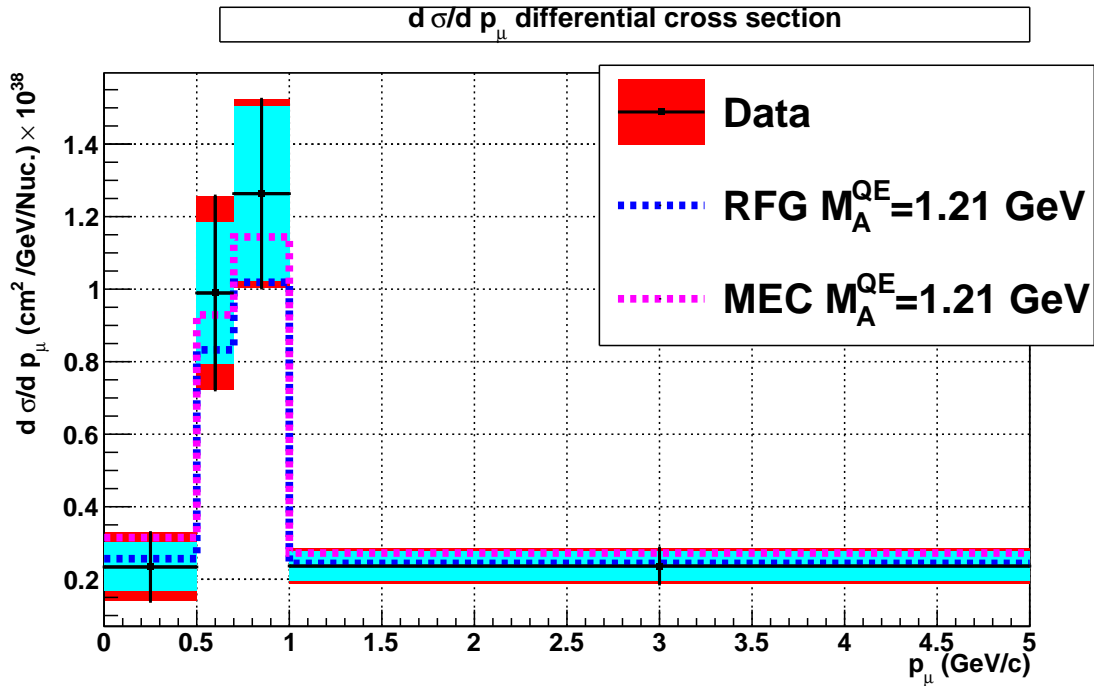


Figure 5.70: Impact of the meson exchange currents on the MC agreement with the  $CC0\pi \frac{d\sigma}{dp_\mu}$  differential cross section data with the muon momentum. The total error is shown in red, and the flux errors (highly positively correlated) in light blue.

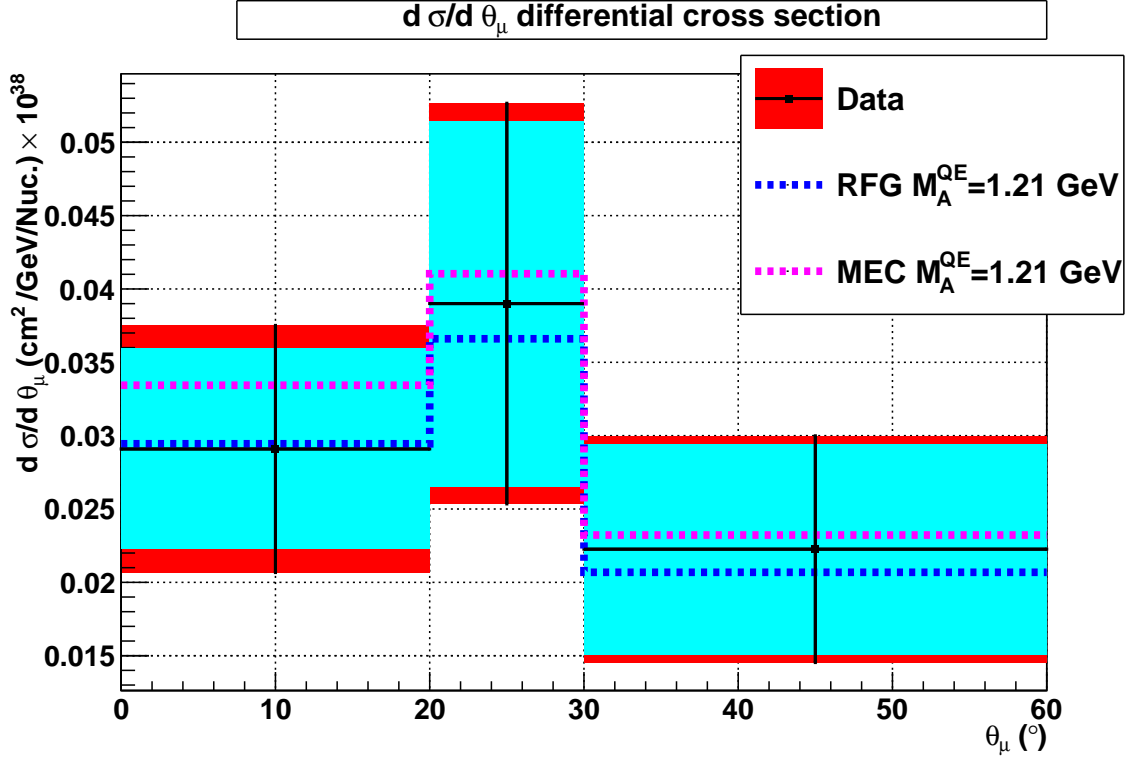


Figure 5.71: Impact of the meson exchange currents on the MC agreement with the CC0 $\pi$   $\frac{d\sigma}{d\theta_\mu}$  differential cross section data with the muon angle. The total error is shown in red, and the flux errors (highly positively correlated) in light blue.

This final result confirms that the RFG model fails to describe the neutrino interaction in the case of complex nuclei. One observes that we retrieve a relatively low  $M_A^{QE}$  value in agreement with the  $M_A$  fit shown in Figure 5.6 when one takes into account the nuclear effects. In this scenario, the enhancement is therefore interpreted as a n-particle-n-holes effect, and not due to a large  $M_A^{QE}$ . It confirms the behaviour observed in [67] and interpreted in [74]. As we explained, this constraint is limited, since we assumed uncorrelated bins and negligible background variations in the selected events compared to pure MC variations.

## 5.8 Conclusions

In Chapter 2, we have shown that the cross section model systematics are dominant in the T2K analyses. These analyses encompass precise measurements of the atmospheric parameters and search of CP violation through the  $\nu_e$  appearance channel. We studied the CC0 $\pi$  channel since this is the dominant interaction channel at T2K neutrino energy. We have developed the first double differential CC0 $\pi$  analysis in the PM, using the INGRID downstream module to measure the muon momentum. We also built a PID both to isolate a CC0 $\pi$  enhanced sample and to identify the muon. We have implemented an iterative Bayesian unfolding method, and have shown the advantages and limitation of this method and optimised it in the case of the PM. Finally, we provided the CC0 $\pi$  cross section measurement. We observed it agrees with the NEUT generator we used. The result mainly favours a large axial mass value, as it has been observed in recent neutrino experiments as MiniBooNE [67], MINOS [72] or K2K [71]. As for our measurement, we have shown that this large  $M_A$  value can be also interpreted as large nuclear effects with an axial mass compatible with the former bubble chamber measurements.

Though we have seen that the detector is not perfectly adapted to this measurement, this CC0 $\pi$  study can still be improved. We explained that an improved unfolding, as a full 2D or an alternative unfolding with the iteration step along muon momentum and angle, will increase the unfolding matrix stability,

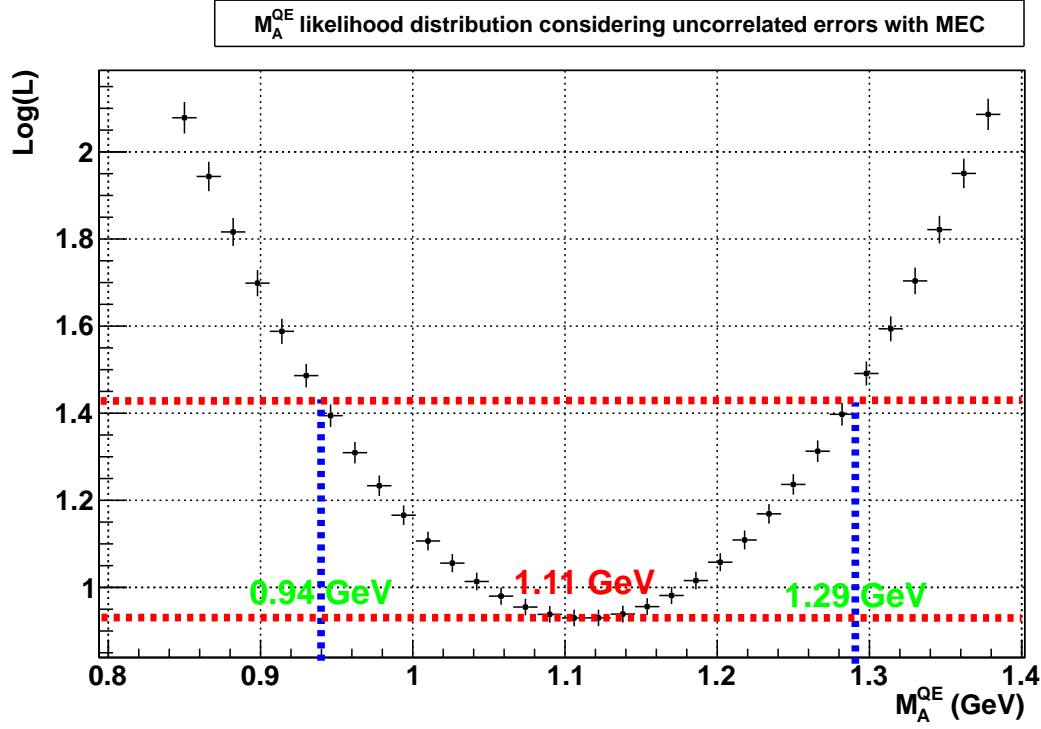


Figure 5.72: Negative log-likelihood distribution for  $10^6$  toy experiments varying uniformly  $M_A^{QE}$  between 0 and 3 GeV in the case meson exchanged current are added. The bin correlation and cross section model uncertainties are not considered.

and so should reduce the impact of the errors on the result. In particular, we observed a remaining important cross section model dependency, though having tried to minimise it. We observed that this dependency can be decreased either by improving the unfolding method (which is currently applied sequentially on momentum and angle), or improving the  $\text{CC}0\pi$  selection to reduce the background contamination.


The selection based on the PID and the unfolding method aimed to be as general as possible in order to be applied to a detector more adapted to cross section measurements. In particular, we plan to use the same method for the incoming WAGASCI detector that will be installed in the ND280 pit. This detector will be constituted of water and carbon targets, with 3D-grid scintillators that allow both to reconstruct large angle tracks and increase the detector granularity. The use of a downstream magnet and thinner iron planes should considerably increase the momentum measurement capability of this detector compared to the PM. Moreover, it will be possible to determine the antineutrino cross section using the charge separation in the downstream magnet. The ultimate goal of this WAGASCI detector and of this  $\text{CC}0\pi$  study is to drastically reduce the cross section uncertainty in the T2K appearance result, through the measurement of the relative cross section on WAGASCI hydrocarbon and water targets that should encompass the differences between the ND280 and SK targets.

## Chapter 6

# Search for Lorentz invariance violation at the T2K near detector

*There are two possible outcomes : if the result confirms the hypothesis, then you've made a measurement. If the result is contrary to the hypothesis, then you've made a discovery.*

Enrico Fermi

 In the Standard Model, the Lorentz transformation invariance is a fundamental symmetry that constrains the interactions between particles. It is also a symmetry of the Standard Model added with massive neutrino, that we introduced in Chapter 1. Nevertheless, the Lorentz symmetry violation is predicted in most of the theories beyond the Standard Model that attempt to describe the gravitation and the other interactions within a common framework. This violation occurs in super string [88], quantum gravity [89] or non commutative geometry [90] theories. In this chapter, we will first introduce the Lorentz invariance violation (or Lorentz violation) and its impact on the neutrino sector. Then, we will present the dedicated selection we built in order to search for a Lorentz violation effect in the INGRID detector. We will then present the fast Fourier transform and likelihood methods that we used in this search. Finally, we will present the results of the first search for Lorentz violation effects in T2K.

### 6.1 Introduction

Since the Lorentz violation effects appear when including the gravitation, one expects that the Lorentz violation effects becomes significant at the Planck mass scale, *i.e* at  $M_P \sim 10^{19}$  GeV. These effects are therefore suppressed by a factor  $\frac{E_{\nu}^{\text{T2K}}}{M_P} \sim 10^{-19}$  at the T2K energy scale. On one hand, a measurement of an absolute and direct Lorentz violation is therefore practically impossible at the current experiment energy ranges. It is therefore unlikely to observe such a violation in direct neutrino time of flight measurement for example. For example, considering the T2K 295 km baseline, it takes nearly 1 ms for a neutrino to fly from J-PARC to Super Kamiokande. One therefore expects the Lorentz violation effect to generate a possible effect of  $\Delta t \sim 10^{-22}$  s which would require a clock system with a  $10^{-10}$  ps accuracy to be observed.

On the other hand, relative measurements are expected to probe the Lorentz violation effect with a higher sensitivity. By analogy with the measurement of the speed of light in “ether” by Michelson and Morley, one expects that inteferometry provides a sensitivity that exceeds other methods, and especially, direct time of flight measurements. Neutrino oscillations occur indeed from an interference of different neutrino mass states at the detection point. Therefore, the neutrino oscillations are expected to be one of the most sensitive probes to search for Planck scale effects [91].

### 6.1.1 The Standard Model Extension and Lorentz invariance spontaneous symmetry breaking

We will define the low energy region in opposition with the Planck scale, that defines the high energy region. In the low energy region, it is for now practically impossible to extract any constraint directly from unification theories as the super strings or quantum gravitation. Therefore, the Lorentz violation effects at low energy are encompassed in an effective theory. This theory, called the “Standard Model Extension” [92] (SME), is based on the Standard Model to which are added arbitrary Lorentz violation terms that are coordinate independent. For this reason, the SME encompasses all effects of the Standard Model in the limit of no Lorentz violation. In particular, the causality, coordinate invariance, energy momentum conservation, spin statistics, CPT theorem and gauge structure  $SU(3)_c \times SU(2)_L \times U(1)_Y$  are retrieved in this limit. As for the Lorentz violating terms, they do not transform under an active Lorentz transformation since they are fixed in space-time (coordinate independent). It implies that physics is modified with active rotational and boost transformations.

In fact, one expects Lorentz violation to break also the fundamental properties of the Universe at the Planck scale, such as causality, or positivity of free energy states. This problematic situation can be avoided in the case of spontaneous Lorentz symmetry breaking (SLSB). For this reason, the SME describes the Lorentz invariance as a fundamental symmetry of the Lagrangian, whose only solutions break Lorentz transformation invariance. It leads to preserve causality and positive energy states even at high energy [93], given some special hypothesis.

In this description, the Lorentz symmetry breaking is described in analogy with the electroweak symmetry breaking. The Lorentz tensor fields are added to the Lagrangian to preserve covariance. The vacuum is filled with Lorentz violating tensor and Higgs fields, which have all a null value. When the Universe cools below the Planck scale, the Lorentz violating fields may acquire a non zero value in vacuum as shown in Figure 6.1. In this case, the fundamental solution of the Lagrangian (or vacuum expected “value”: VEV) at high energy is no more null, but becomes a tensor (as in the Higgs case, it becomes a scalar). The vacuum is now filled with a non zero tensor field, which therefore breaks the Lorentz invariance. Figure 6.1 shows this symmetry breaking in an example where the tensor is a vector. When the Universe continues to cool down, its temperature reaches the electroweak scale  $E_w$  at some point. At this energy, the Higgs field also acquires a VEV, which impacts on the vacuum fundamental state adding a scalar contribution (see Figure 6.1 and Chapter 1).

In conclusion, the Lagrangian preserves the Lorentz invariance, and therefore, physics is independent from the referential frame in the SLSB by Noether theorem. Note that neither this independence, nor the causality are preserved at the Planck scale in the case of explicit violation of the Lorentz symmetry. Since we believe Lorentz invariance and causality are fundamental properties of Nature, we will therefore use a spontaneous symmetry breaking and use the SME in this thesis.

As we explained, the spontaneous symmetry breaking restores the invariance of physics with the observer (referential frame). **However, we will show that physics does not depend on the observer, but on the direction observed in space-time.** For this purpose, we will define here what “active” and “passive transformations” mean. Figure 6.2 shows the difference between these two concepts. The active particle transformation corresponds to apply the transformation directly on the fields, as shown in Figure 6.2 (left) in the example of an active rotation on the particle field. On the opposite, the passive transformations correspond to transforming the observer referential frame instead, as shown on the right of Figure 6.2. The field (particle) is therefore transformed passively. This distinction is particularly important since these transformations are not equivalent anymore in the SME. As we have seen, there are some preferential directions since some Lorentz tensor fields generate the spontaneous symmetry breaking energy and have therefore a fixed and non zero VEV. One therefore expects these fields to be left invariant when Lorentz transformations are applied on them (active transformations). On the opposite, the other fields do transform following their spin and momentum, and therefore, physics is no more equivalent under active transformations as shown in Figure 6.2 in the case of a rotation. This is not the case for observer coordinate transformations, since the Lagrangian is Lorentz invariant. It explains that the physics is expected not to change with the referential frame, but to depend on space-time directions that one observes. As we explained, these effects are expected to be highly suppressed at the GeV scale though.

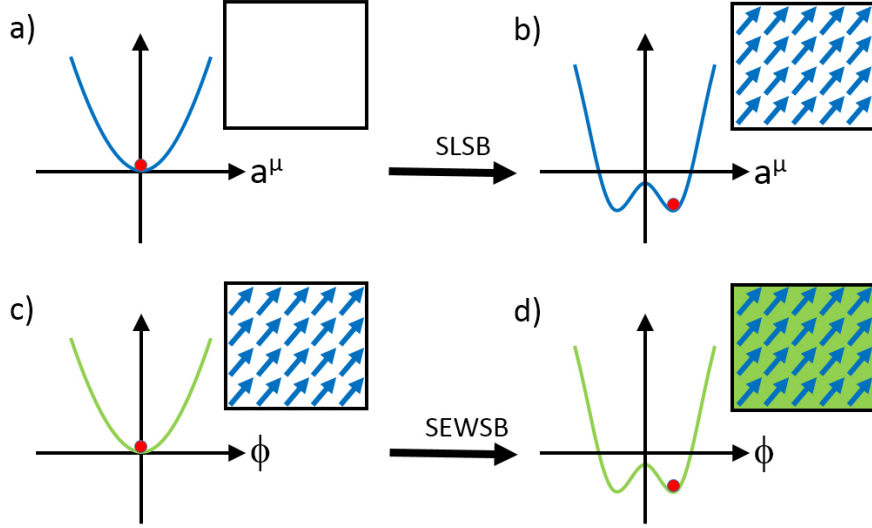


Figure 6.1: The spontaneous symmetry breaking in the case of a  $O(1)$  symmetry. Note that in this case, no Goldstone boson can appear since the solution has no additional degrees of freedom. In the case of electroweak or Lorentz symmetry spontaneous violation, the higher group dimensions involve the Goldstone bosons. In the cooling process of the Universe, the spontaneous Lorentz symmetry breaking (shown on the top figure) is followed by the electroweak symmetry breaking (bottom figure), as  $M_P \gg E_W$ ,  $E_W \sim 100$  GeV the scale of electroweak symmetry breaking. Adapted from [94].

### 6.1.2 Lorentz violation in neutrino oscillations

As for the neutrino sector, the addition of the Lorentz violating fields to the Standard Model Lagrangian (Chapter 1) provides the neutrino Lagrangian [95]:

$$L_{\text{SME}} = \frac{1}{2} i \bar{\psi}_A \Gamma_{AB}^\mu D_\mu \psi_B - \bar{\psi}_A M_{AB} \psi_B + h.c \quad (6.1.1)$$

where  $\psi_A$  is the neutrino flavour state  $\nu_A$ . Note that here, A ranges over  $2N$  values to describe both neutrinos and antineutrinos:  $A \in e, \mu, \tau, \dots, e^C, \mu^C, \tau^C, \dots$ , and  $\Gamma_{AB}^\mu$  and  $M_{AB}$  are defined as:

$$\Gamma_{AB}^\mu \equiv \gamma^\mu \delta_{AB} + c_{AB}^{\mu\nu} \gamma_\nu + d_{AB}^{\mu\nu} \gamma_5 \gamma_\nu + e_{AB}^\mu + i f_{AB}^\mu \gamma_5 + \frac{1}{2} g_{AB}^{\alpha\mu\nu} \sigma_{\alpha\nu} \quad (6.1.2)$$

$$M_{AB} \equiv m_{AB} + i m_{5AB} \gamma_5 + a_{AB}^\mu \gamma_\mu + b_{AB}^\mu + \frac{1}{2} H_{AB}^{\mu\nu} \sigma_{\mu\nu} \quad (6.1.3)$$

where  $\sigma$  are the Pauli matrices,  $a, b, e, f$  are Lorentz violating vector fields and  $c, d, g, H$  the order two Lorentz violating tensors. These tensor fields should depend on the neutrino flavour in the most general case (implying the need of A and B flavour indices). This description using eight additional fields is valid at low energy, and in particular, at the T2K  $E \sim 1$  GeV scale. At higher energy, since the background Lorentz fields are an infinite series in energy, additional terms should be added. The fields  $c_{AB}^{\mu\nu}, d_{AB}^{\mu\nu}, H_{AB}^{\mu\nu}$  are CPT conserving (even) while  $a_{AB}^\mu, b_{AB}^\mu, e_{AB}^\mu, f_{AB}^\mu, g_{AB}^{\mu\nu}$  are CPT violating terms (CPT-odd). One observes that the coefficients  $a, b, H$  have the dimension of a mass, while the others are dimensionless. The Lagrangian leads to the Dirac equation of the SME for a free neutrino (obtained if  $D_\mu \rightarrow \partial_\mu$ ):

$$(i \Gamma_{AB}^\mu \partial_\mu - M_{AB}) \psi_B = 0 \quad (6.1.4)$$

As we have shown in Chapter 1, the neutrino oscillations occur because of the energy difference between the eigenvalues of the Hamiltonian. In the case of SME, the Hamiltonian  $\mathcal{H}_{ab}$  can be constructed from Equation 6.1.4 (equivalent to the Schrodinger case shown in Chapter 1) and leads to:

$$\begin{aligned} \mathcal{H}_{ab} = & |\vec{p}| \delta_{ab} \begin{pmatrix} 1 & 0 \\ 0 & 1 \end{pmatrix} + \frac{1}{2|\vec{p}|} \begin{pmatrix} (m'^2)_{ab} & 0 \\ 0 & (m'^2)_{ab}^* \end{pmatrix} \\ & + \frac{1}{|\vec{p}|} \begin{pmatrix} [(a_L)^\mu p_\mu - (c_L)^{\mu\nu} p_\mu p_\nu]_{ab} & -i \sqrt{2} p_\mu (\epsilon_+)_{\nu} [(g^{\mu\nu\sigma} p_\sigma - H^{\mu\nu}) C]_{ab} \\ i \sqrt{2} p_\mu (\epsilon_+)^*_{\nu} [(g^{\mu\nu\sigma} p_\sigma + H^{\mu\nu}) C]_{ab}^* & [-(a_L)^\mu p_\mu - (c_L)^{\mu\nu} p_\mu p_\nu]_{ab}^* \end{pmatrix} \end{aligned} \quad (6.1.5)$$

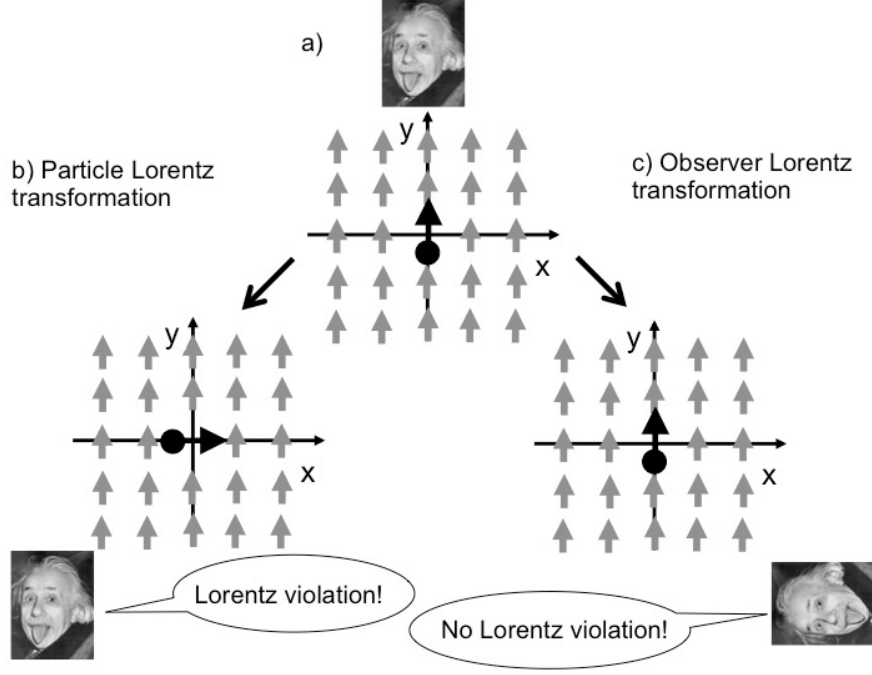


Figure 6.2: The active particle (left) and passive particle (right) transformations of an original particle moving along the y axis in a Lorentz violating field along the y axis. Einstein represents the observer, and the transformation operated here is a 2D rotation. Taken from [94].

where  $C$  is the charge conjugation matrix and  $\epsilon_+$  a complex vector [95] analogous to the neutrino helicity basis.  $\mathcal{H}_{ab}$  is expressed in the neutrino/antineutrino flavour basis, with  $a$  representing the standard flavour basis  $e, \mu, \tau$ , and  $b$  the antineutrino flavour states. Therefore, the top left and bottom right blocks respectively represent the  $\nu \rightarrow \nu$  and the  $\bar{\nu} \rightarrow \bar{\nu}$  oscillations. The first term can be removed through a phase rotation. In the second term,  $m'^2 \equiv m_i m_i^\dagger$  is the neutrino light mass matrix that derives from the usual seesaw mechanism (see Chapter 1), and which can be written in the flavour basis:

$$m' = M_L - m_D M_R^{-1} m_D^T = \begin{pmatrix} m_{ee} & m_{e\mu} & m_{e\tau} \\ m_{\mu e} & m_{\mu\mu} & m_{\mu\tau} \\ m_{\tau e} & m_{\tau\mu} & m_{\tau\tau} \end{pmatrix} \quad (6.1.6)$$

where the left ( $M_L$ ), right ( $M_R$ ) and Dirac ( $m_D$ ) mass matrices were defined in Chapter 1. Finally, the third term encompasses the Lorentz violation effects on neutrino oscillations. Following [95], we define  $(a_L)_{ab}^\mu \equiv (a + b)_{ab}^\mu$  and  $(c_L)_{ab}^\mu \equiv (c + d)_{ab}^\mu$  which are respectively CPT odd and even by construction. One observes that the Lorentz fields  $e, f$  do not contribute to neutrino oscillations, and should be probed for example through time of flight experiments. One also observes that:

- in the diagonal terms, the  $(c_L)_{ab}^\mu$  appears in a product with  $p_\mu$ , while the  $(a_L)_{ab}^\mu$  coefficients do not. This was expected through the dimensional analysis and will imply that the impact of  $(c_L)_{ab}^\mu$  on neutrino oscillation will increase with the neutrino energy. Note that both the coefficients come in factor of a general  $\frac{p_\mu}{|\vec{p}|}$  factor. It shows that  $\nu \rightarrow \nu$  and  $\bar{\nu} \rightarrow \bar{\nu}$  oscillations will depend on the neutrino direction.
- the Lorentz violation predicts non standard  $\nu \rightarrow \bar{\nu}$  oscillation also. The contribution of the  $g$  fields will vary with the neutrino energy, while it will not be the case for the  $H$  field

This lead to obtain the neutrino oscillation formula in the case of the SME. Before that, one shows that the  $\nu \rightarrow \bar{\nu}$  are negligible compared to diagonal terms that modify  $\nu \rightarrow \nu$  and  $\bar{\nu} \rightarrow \bar{\nu}$  oscillations [96]. For this reason, we will not take into account the  $\nu \rightarrow \bar{\nu}$  effects here.

### 6.1.3 Application to short baseline compared to standard oscillation

As we have shown, the Lorentz violation modifies the neutrino oscillation by adding effects that both depend on neutrino direction and energy. These effects should therefore be seen at the Super-Kamiokande detector as a modification of the standard three flavour oscillations. Moreover, one shows that these terms also impact on smaller baselines. Therefore, this effect can be also probed in the near detectors of the T2K experiment. In this chapter, we present the study we have performed using the INGRID near detector. This detector has been chosen because its data statistics is significantly larger than the one of the ND280 off-axis detector. In this study, we will measure the variation of the neutrino oscillation with the beam direction in an absolute reference frame in space. For this purpose, we select a frame centered on the INGRID detector, based on the Sun-centered frame considering the Sun is motionless during the T2K data taking period we use. Figure 6.3 shows this coordinate system, except for the time origin  $T = 0$ , which is chosen as the UNIX time origin. The oscillation dependency with the absolute direction in space can therefore be probed using the Earth revolution and rotation around the Sun, that will induce variations in the Target-INGRID neutrino directions. Therefore, neutrino oscillations should vary with the sidereal time  $T_\oplus$ , since the absolute direction in space varies with the latter.

In the case of a small baseline compared to the standard neutrino oscillation  $L \ll L_{osc}$ , the standard

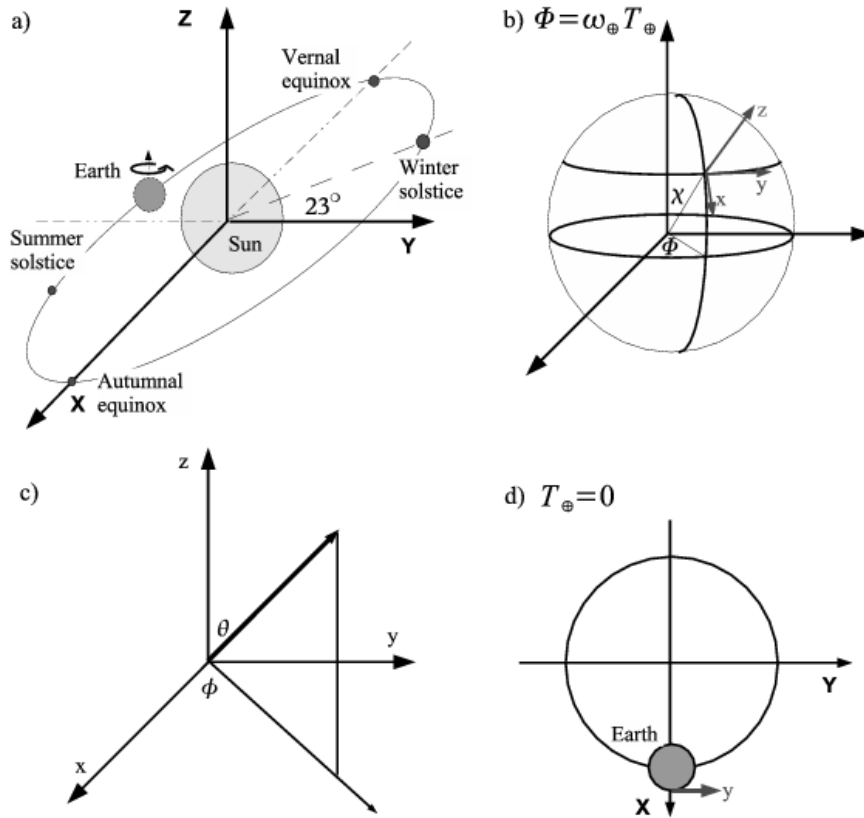


Figure 6.3: The Sun-centered coordinate system used in this thesis. The motion of the Earth in the Sun-centered frame (X,Y,Z) is shown on a). Then, the same axis are shown in the Earth centered referential frame, and the Earth coordinates (x,y,z) of the detector are introduced in Figure b). Finally, the neutrino beam direction is given in the referential frame we have shown in Figure c), and is centered at the INGRID detector with the polar axis. Taken from [94].

neutrino oscillations are suppressed. Therefore, the effective Hamiltonian (Equation 6.1.5) is reduced to:

$$\mathcal{H}_{ab} = \frac{1}{|\vec{p}|} [(a_L)^\mu p_\mu - (c_L)^{\mu\nu} p_\mu p_\nu]_{ab} \quad (6.1.7)$$

The oscillation probability from a flavour state  $\nu_\mu$  to another state  $\nu_x$  can then be estimated as:

$$P_{\nu_\mu \rightarrow \nu_x} = \left(\frac{L}{hc}\right)^2 |(C)_{\mu x} + (A_s)_{\mu x} \sin(\omega_\oplus T_\oplus) + (A_c)_{\mu x} \cos(\omega_\oplus T_\oplus) + (B_s)_{\mu x} \sin(2\omega_\oplus T_\oplus) + (B_c)_{\mu x} \cos(2\omega_\oplus T_\oplus)|^2 \quad (6.1.8)$$

where  $L$  is the neutrino baseline,  $\omega_\oplus$  is the sidereal time angular frequency defined as  $\omega_\oplus = \frac{2\pi}{23^h 56^m 04.0982^s}$  and  $T_\oplus$  the local sidereal time we defined earlier. The  $A, B, C$  coefficients are the amplitude of the different  $\omega_\oplus$  variations, and are expressed with the  $(a_L)^\mu$  and  $(c_L)^{\mu\nu}$  coefficients. They can be separated into constant and energy dependent terms:

$$(C)_{ab} = (C)_{ab}^{(0)} + E(C)_{ab}^{(1)} \quad (6.1.9)$$

$$(\mathcal{A}_s)_{ab} = (\mathcal{A}_s)_{ab}^{(0)} + E(\mathcal{A}_s)_{ab}^{(1)} \quad (6.1.10)$$

$$(\mathcal{A}_c)_{ab} = (\mathcal{A}_c)_{ab}^{(0)} + E(\mathcal{A}_c)_{ab}^{(1)} \quad (6.1.11)$$

$$(\mathcal{B}_s)_{ab} = E(\mathcal{B}_s)_{ab}^{(1)} \quad (6.1.12)$$

$$(\mathcal{B}_c)_{ab} = E(\mathcal{B}_c)_{ab}^{(1)} \quad (6.1.13)$$

$$(6.1.14)$$

where each term is given by:

$$(C)_{ab}^{(0)} = (a_L)_{ab}^T - \hat{N}^Z (a_L)_{ab}^Z \quad (6.1.15)$$

$$(C)_{ab}^{(1)} = -\frac{1}{2}(3 - \hat{N}^Z \hat{N}^Z)(c_L)_{ab}^{TT} + 2\hat{N}^Z (c_L)_{ab}^{TZ} + \frac{1}{2}(1 - 3\hat{N}^Z \hat{N}^Z)(c_L)_{ab}^{ZZ} \quad (6.1.16)$$

$$(\mathcal{A}_s)_{ab}^{(0)} = \hat{N}^Y (a_L)_{ab}^X - \hat{N}^X (a_L)_{ab}^Y \quad (6.1.17)$$

$$(\mathcal{A}_s)_{ab}^{(1)} = -2\hat{N}^Y (c_L)_{ab}^{TX} + 2\hat{N}^X (c_L)_{ab}^{TY} + 2\hat{N}^Y \hat{N}^Z (c_L)_{ab}^{XZ} - 2\hat{N}^X \hat{N}^Z (c_L)_{ab}^{YZ} \quad (6.1.18)$$

$$(\mathcal{A}_c)_{ab}^{(0)} = -\hat{N}^X (a_L)_{ab}^X - \hat{N}^Y (a_L)_{ab}^Y \quad (6.1.19)$$

$$(\mathcal{A}_c)_{ab}^{(1)} = 2\hat{N}^X (c_L)_{ab}^{TX} + 2\hat{N}^Y (c_L)_{ab}^{TY} - 2\hat{N}^X \hat{N}^Z (c_L)_{ab}^{XZ} - 2\hat{N}^Y \hat{N}^Z (c_L)_{ab}^{YZ} \quad (6.1.20)$$

$$(\mathcal{B}_s)_{ab}^{(1)} = \hat{N}^X \hat{N}^Y [(c_L)_{ab}^{XX} - (c_L)_{ab}^{YY}] - [\hat{N}^X \hat{N}^X - \hat{N}^Y \hat{N}^Y](c_L)_{ab}^{XY} \quad (6.1.21)$$

$$(\mathcal{B}_c)_{ab}^{(1)} = -\frac{1}{2}(\hat{N}^X \hat{N}^X - \hat{N}^Y \hat{N}^Y)[(c_L)_{ab}^{XX} - (c_L)_{ab}^{YY}] - 2\hat{N}^X \hat{N}^Y (c_L)_{ab}^{XY} \quad (6.1.22)$$

where  $N^i$  is the vector of the neutrino beam direction, in the Sun centered coordinates. This vector can be expressed as a function of the co-latitude  $\chi$  of the detector location in the Earth centered system, and  $\theta, \phi$  the zenith and azimuthal angles shown in Figure 6.3:

$$\begin{pmatrix} \hat{N}^X \\ \hat{N}^Y \\ \hat{N}^Z \end{pmatrix} = \begin{pmatrix} \cos \chi \sin \theta \cos \phi + \sin \chi \cos \theta \\ \sin \theta \sin \phi \\ -\sin \chi \sin \theta \cos \phi + \cos \chi \cos \theta \end{pmatrix} \quad (6.1.23)$$

In conclusion, we expect to observe neutrino oscillations that change with the sidereal time. Moreover, these oscillations are enhanced with the square of the baseline length. Note that this particular trend is slightly modified for long distance oscillations ( $L \simeq L_{osc}$ ) as for Super-Kamiokande Lorentz violation search. One also observes a linear and square energy dependency of the neutrino oscillation. As expected, the energy dependency comes in factor of the  $(c_L)^{\mu\nu}$  coefficients only. We remind the  $(c_L)^{\mu\nu}$  only probes the Lorentz violation, while the  $(a_L)^{\mu\nu}$  coefficients offer the possibility to also test the CPT violation. One observes that a constant term  $(C)_{ab}$  does not introduce any sidereal time dependency in the amplitude. Expanding the Equation 6.1.8, one shows that the time averaged oscillation can be written:

$$\langle P_{\nu_\mu \rightarrow \nu_x} \rangle_{\text{Sidereal Time}} = |(C)_{\mu x}|^2 + \frac{1}{2}(|(A_s)_{\mu x}|^2 + |(A_c)_{\mu x}|^2 + |(B_s)_{\mu x}|^2 + |(B_c)_{\mu x}|^2) \quad (6.1.24)$$

One observes the Lorentz violation does not only predict a sidereal time effect, but also a time averaged oscillation. Such an effect can therefore be probed to explain the time independent effects, as the LSND [97] or MiniBooNE low energy anomalies [94]. It is an alternative explanation to the sterile neutrino hypothesis.

### 6.1.4 The Lorentz violation search in INGRID

In neutrino mode, more than 95% of the flux is composed of  $\nu_\mu$ . Moreover, INGRID has little capacity of identifying electron neutrinos due to the relatively poor longitudinal and transverse granularity. Therefore, LV effects are studied in INGRID using the oscillation mode with the highest statistics, namely the  $\nu_\mu$  disappearance mode. We expect the survival probability to vary with time as:

$$P_{\nu_\mu \rightarrow \nu_\mu} = \left(\frac{L}{hc}\right)^2 |(C)_{\mu\mu} + (A_s)_{\mu\mu} \sin(\omega_\oplus T_\oplus) + (A_c)_{\mu\mu} \cos(\omega_\oplus T_\oplus) + (B_s)_{\mu\mu} \sin(2\omega_\oplus T_\oplus) + (B_c)_{\mu\mu} \cos(2\omega_\oplus T_\oplus)|^2 \quad (6.1.25)$$

The neutrino beam direction from the target to INGRID is given by the vector  $N^i$  which is shown in Equation 6.1.23 with the geographical coordinates:

$$\chi = 55.551^\circ, \theta = 93.637^\circ, \phi = 270.319^\circ \quad (6.1.26)$$

On Figure 6.4, we show that Lorentz violation is expected to impact on the neutrino oscillation as a function of the sidereal time, at the mean INGRID neutrino energy  $E_\nu = 2.7$  GeV. The set of coefficients used is summarised in Table 6.1. It corresponds to the current limits on the SME parameters [91]. Note we used all best limits, except the MINOS ones. One observes both the time independent effects and the sidereal time oscillation. One observes that the time dependent effect is  $\lesssim 1\%$  which highlights the accuracy required in this search. Since the errors on the neutrino flux predictions are  $\gtrsim 10\%$ , the INGRID sensitivity to the time independent effects is small. For this reason, we only search for Lorentz violation for an average neutrino energy. This shape only analysis simplifies the treatment of the systematic errors, without almost changing the sensitivity.

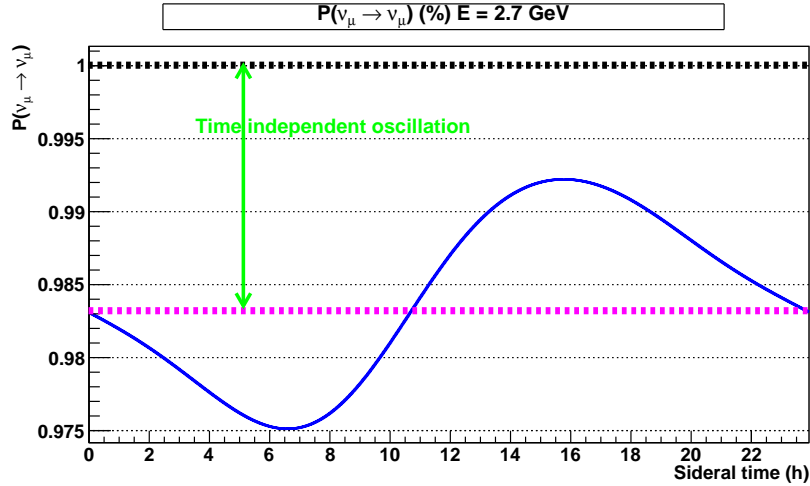


Figure 6.4: The  $\nu_\mu$  survival probability as a function of the sidereal time in the INGRID detector, for a neutrino energy  $E_\nu = 2.7$  GeV which corresponds to the average neutrino energy of reconstructed neutrino in INGRID. Generated using [98].

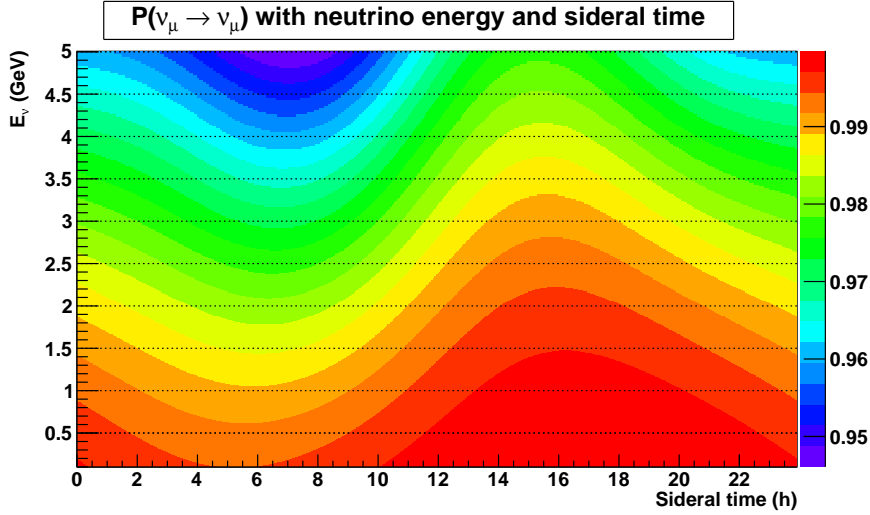
Moreover, we explained, the oscillation amplitude and average values depend on the neutrino energy. Figure 6.5 shows this enhancement of the oscillation with the neutrino energy, and its impact can be seen on both time independent and dependent oscillations. In the study presented in this thesis, we will only search for Lorentz violation for an average neutrino energy. We will show in Section 6.6 that the neutrino energy dependent study cannot improve this result at the present time.

Since the beam intensity varies during T2K data taking, we cannot simply consider the  $\nu_\mu$  rate as an indicator of Lorentz violation. For this reason, we will use the number of  $\nu_\mu$  detected per POT as the observable equivalent to the  $\nu_\mu$  survival probability in Figures 6.4 and 6.5. Moreover, we will also use the local sidereal phase (LSP) defined as:

$$\text{LSP} = \frac{T_\oplus}{23^h 56^m 04.0982^s} \quad (6.1.27)$$

Table 6.1:  $3\sigma$  sensitivity to SME coefficients related to  $\nu_\mu \rightarrow \nu_e$  oscillation, for various experiments (all values given in  $\times 10^{-20}$ ). Extracted from [91].

Coefficient	MiniBooNE	Double Chooz	MINOS
$a_L^T$	4.2 GeV	-	-
$a_L^X$	6.0 GeV	1.6 GeV	2.2 GeV
$a_L^Y$	5.0 GeV	6.1 GeV	2.2 GeV
$a_L^Z$	5.6 GeV	-	-
$c_L^{TT}$	9.6	-	-
$c_L^{TX}$	8.4	-	0.009
$c_L^{TY}$	6.9	-	0.009
$c_L^{TZ}$	7.8	-	-
$c_L^{XX}$	-	-	0.46
$c_L^{XY}$	-	-	0.22
$c_L^{XZ}$	11	-	0.11
$c_L^{YY}$	-	-	0.45
$c_L^{YZ}$	9.2	-	0.11
$c_L^{ZZ}$	34	-	-


 Figure 6.5: The  $\nu_\mu$  survival probability as a function of the sidereal time and neutrino energy in the INGRID detector. One observes both the time independent and sidereal time variations increased with the neutrino energy. Generated using [98].

The variation of  $P_{\nu_\mu \rightarrow \nu_\mu}$  with the sidereal time ( $\in [0, 23^h56^m04.0982^s]$ ) is therefore replaced by the variation of the number of  $\nu_\mu$  per POT with the local sidereal phase ( $\in [0, 1]$ ).

## 6.2 The INGRID selection

To construct a  $\nu_\mu$  sample only, one needs to remove the possible contamination from oscillated other neutrino flavours that can wash out the oscillations. LV effects allow  $\nu_\mu$  to oscillate to  $\nu_\tau$  and  $\nu_e$  flavor states. Figure 6.6 shows the charged current cross sections for  $\nu_\tau$  and  $\nu_\mu$  interactions, as a function of the neutrino energy, along with their ratio.  $\nu_\tau$  interactions start to be significant only above 4 GeV, well into the tail of the INGRID energy spectrum distribution (see Figure 6.56). For these kinematic reasons, the charge current interactions from  $\nu_\tau$  are neglected. The effect on the  $\nu_\mu$  rate versus LSP, in the case of the size predicted as shown in Figure 6.4, when including  $\nu_\tau$  can be seen in Figure 6.7. There is a very small global enhancement in the total rate, that cannot be detected by this analysis, and the distortion of the rate versus LSP is estimated to be below 0.05%, and therefore negligible. In

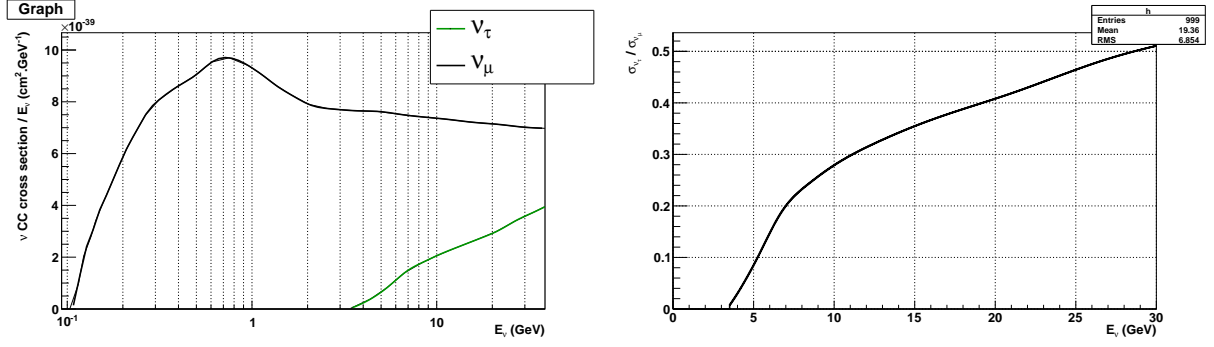


Figure 6.6: Left:  $\nu_\mu$  and  $\nu_\tau$  cross sections as function of the neutrino energy; right: ratio of the two cross section distributions.

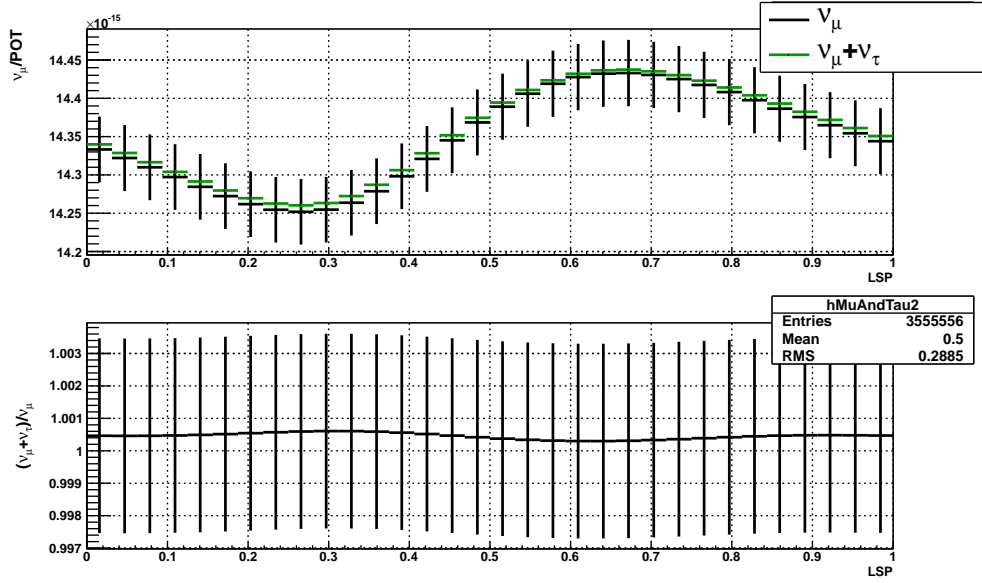


Figure 6.7: Top:  $\nu_\mu$  rate versus LSP, when  $\nu_\tau$  contribution is ignored (black) or not (green). Bottom: ratio of the distributions shown in the top.

addition, although the SME coefficients pertaining to  $\bar{\nu}_\mu$  may be, in principle, different than the ones governing  $\nu_\mu$  oscillations, it is assumed that such a difference would not be detectable in INGRID, given the small number of intrinsic  $\bar{\nu}_\mu$  in the T2K beam. As we explained, the possibility of  $\nu_\mu \rightarrow \bar{\nu}_\mu$  oscillation is also assumed to be negligible. Since there can not be any contamination from sterile neutrino, we will only consider the  $\nu_e$  as a possible contamination source in our  $\nu_\mu$  sample.

The original INGRID reconstruction we introduced in Chapter 4 focuses on reconstructed charged current interactions. No specific treatment of the electron neutrino contamination has been studied since they represent a very low ( $\sim 1\%$ ) proportion of the T2K interacting flux. However, in the case of Lorentz violation study, such a small effect will be an issue. In fact, we aim to study the time dependent oscillations in order to remove most of the systematic errors that can affect our sensitivity. Therefore, a 1% effect is no longer negligible. Moreover, in the case all the oscillated  $\nu_\mu$  are changed into  $\nu_e$ , the oscillation effect will be totally washed out if they are not separated and if their reconstruction efficiency is the same. Therefore, we will develop a proper  $\nu_\mu$  selection in this section. We will not focus on the neutrino interacting through NC in this selection, since they only contribute to change the rate, but not the shape of the event rate distribution with sidereal time. Indeed, since the sum of the three flavour  $\nu_e + \nu_\mu + \nu_\tau$  is constant with sidereal phase (whether or not there is LV) and the NC cross section is the same for each flavours, one deduces that the number of neutrino interacting through NC is time-independent.

### 6.2.1 The neutrino baseline

It was shown, in Equation 6.1.25, that the  $\nu_\mu$  oscillation probability in the case of Lorentz Violation depends on the square of the baseline, that is the distance between the  $\nu_\mu$  production point and the detector. In the case of INGRID, neutrinos are produced in the 100 m long decay volume downstream of the T2K target; given that this distance is sizeable with respect to the 280 m distance between the detector and the target, it will have to be taken into account in this analysis. Figure 6.8 shows the  $\nu_\mu$  production  $z$  coordinate distribution in the T2K decay volume; it is possible to define an effective baseline, to be used in the calculation of the oscillation probability, by determining the mean of this distribution. As such mean is 37.8 m, the effective INGRID baseline from the T2K target is 242.2 m.

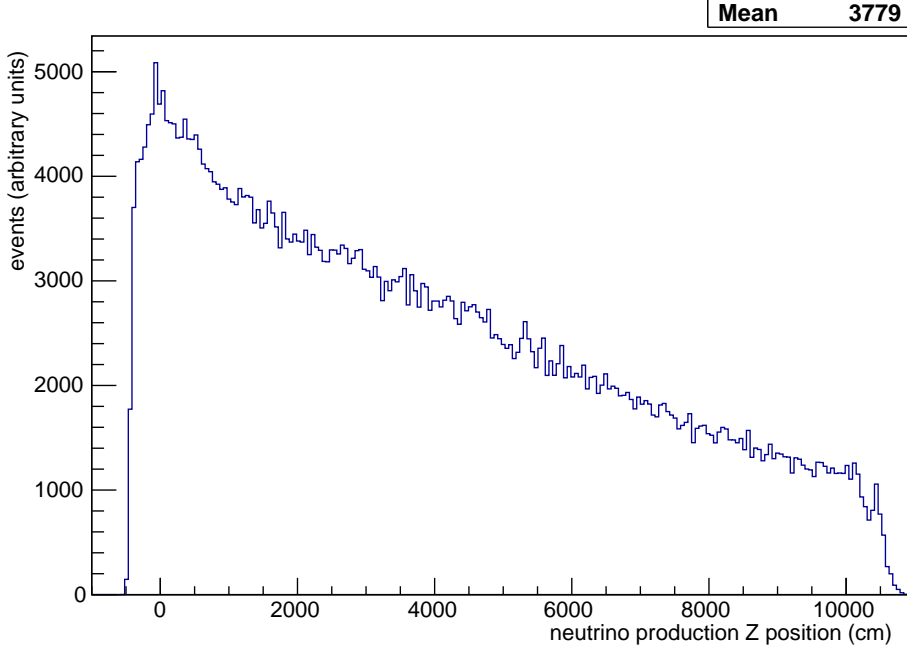


Figure 6.8:  $\nu_\mu$  production  $z$  coordinate distribution in the T2K decay volume.

### 6.2.2 The muon neutrino selection

Although LV effects have been studied through several different oscillation channels [91], the method and extraction of the SME parameters in this analysis is widely different from previous experiments. For this reason, a model independent study is implemented assuming no prior on the possible LV effects in T2K. In particular, the number of oscillated  $\nu_\mu$  events in INGRID is left as a free parameter in the analysis. All  $\nu_\mu$  are conservatively assumed to oscillate into  $\nu_e$ . From this assumption, criteria to exclude  $\nu_e$  events in INGRID can be developed. The reconstruction efficiency for both  $\nu_\mu$  and  $\nu_e$  using the standard INGRID selection was evaluated. The definition of efficiency used in this analysis is:

$$\epsilon \equiv \frac{\# \text{ of } \nu \text{ events passing all analysis cuts}}{\text{Total } \# \text{ of } \nu \text{ events in fiducial volume}} \quad (6.2.1)$$

As shown in Table 6.2, the  $\nu_e$  reconstruction efficiency (48.4%) is comparable to the  $\nu_\mu$  reconstruction efficiency (52.7%).

The high efficiency obtained for  $\nu_e$  lies in the fact that although a 1 GeV electron only crosses 7.2 cm in iron before stopping [99], it creates an electromagnetic shower, a small fraction of which propagates through a much longer distance. As can be observed in Figure 6.9(left), for 30 GeV electrons, about half of the shower energy is deposited at a depth greater than  $8X_0$ , corresponding to  $\approx 13$  cm in iron. A study of longitudinal profiles of electron induced showers in iron [100] shows that for 10 GeV electrons,

Table 6.2: Reconstruction efficiency for INGRID standard selection. The efficiency is shown for both  $\nu_\mu$  and  $\nu_e$ .

	$\nu_\mu$	$\nu_e$
Reconstruction efficiency	52.7%	48.4%

25% of the shower energy is deposited downstream 12.5 cm. Although lower energies have not been investigated in this paper, it can be seen by extrapolating the trend observed in Figure 6.9 (right) that around 3 GeV, still a few percents of the shower energy can be deposited at even larger depths. This can allow electron showers to be reconstructed as tracks, since it is only required for a particle to be detected in INGRID that it crosses at least 13 cm. As a consequence, the reconstruction efficiency for  $\nu_e$  events cannot be neglected with respect to the reconstruction efficiency of  $\nu_\mu$  events in INGRID. Furthermore, these efficiencies even become equivalent at high energies, as can be seen in Figure 6.10. An example of  $\nu_\mu$  and  $\nu_e$  induced tracks in INGRID can be seen in Figure 6.11.

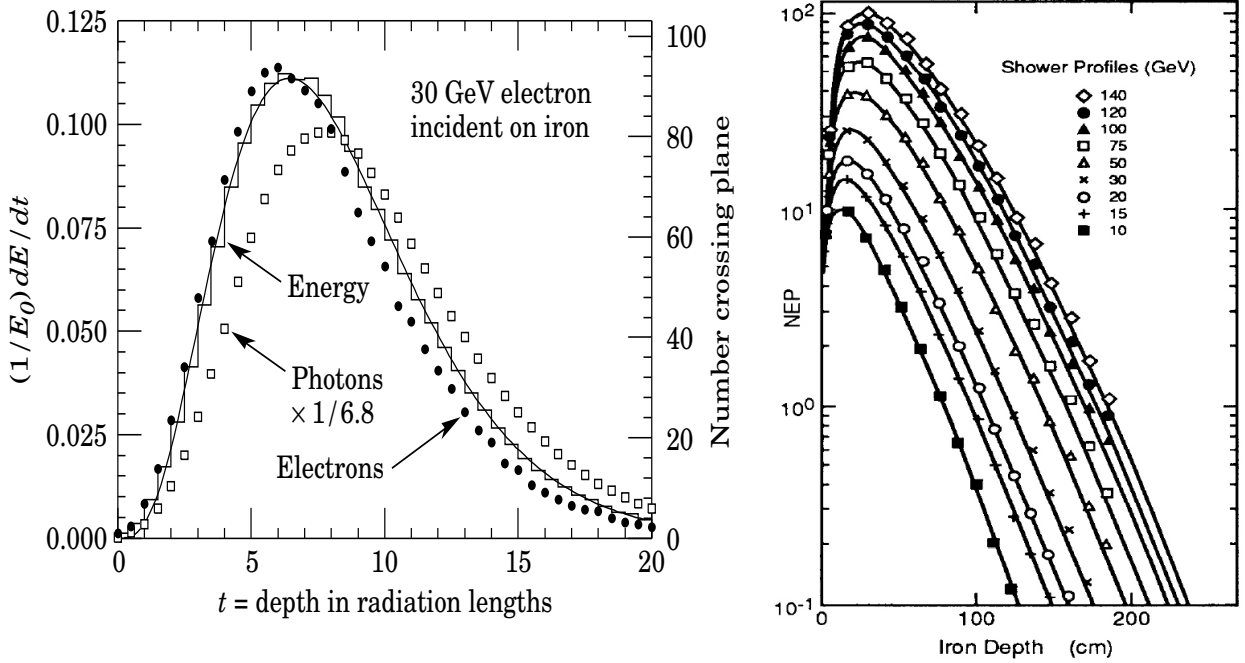


Figure 6.9: Left: Energy loss of a 30 GeV electron induced shower, plotted here as the fraction of initial shower energy deposited as a function of depth (expressed radiation lengths) ([13]). In iron, the radiation length is  $X_0 = 1.76 \text{ cm}$  ([13]). Right: Shower profile in iron for various incident energies. The unit used (NEP) is proportional to the amount of energy deposited, and the depth is here expressed in cm ([100]).

- $\nu_e$  intrinsic contamination in the beam. This one represents a very small fraction ( $< 1\%$ ) of the interacting neutrinos and does not vary with sidereal time in the disappearance mode. Therefore, possible LV oscillations to  $\nu_\mu$  from beam intrinsic  $\nu_e$  are neglected.
- $\nu_e$  coming from  $\nu_\mu$  oscillations due to LV. In this case, if the detection efficiency is similar for  $\nu_\mu$  and  $\nu_e$ , the  $\nu_\mu$  disappearance would be partially washed out (partially only because of  $\nu_\tau$ ). This contamination source should be removed.

#### $\nu_e$ rejection requirement

The systematic error introduced by the  $\nu_e$  rejection requirement can be evaluated using simulation, but cannot be checked by directly comparing to data, since no  $\nu_e$  control sample exists. To overcome

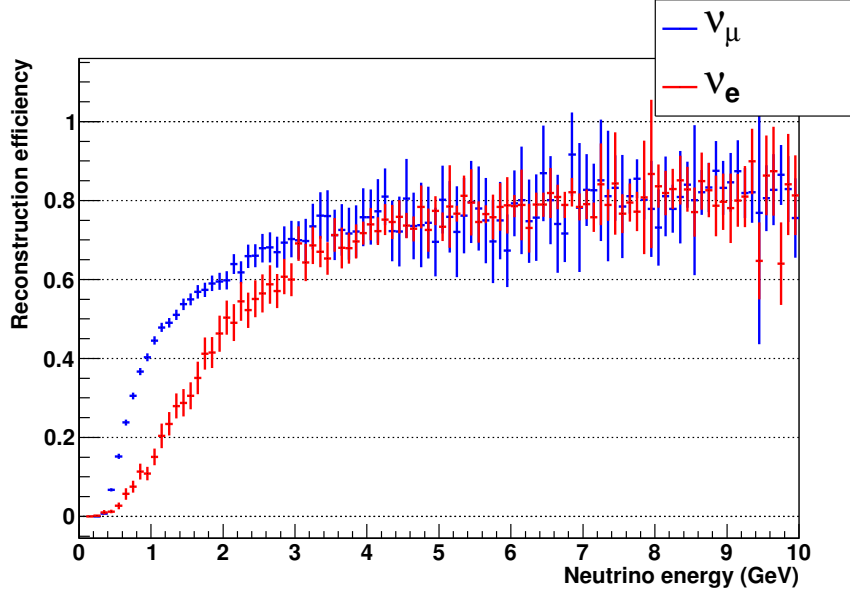


Figure 6.10: Reconstruction efficiencies for  $\nu_\mu$  and  $\nu_e$  induced tracks, as a function of the neutrino energy. No distinction is made between charged-current and neutral-current interactions.

this difficulty, the selection criteria will be tuned in order to minimise its impact on the  $\nu_\mu$  systematic error. For this, the selection criterion will be set such that the  $\nu_e$  contamination is lower than the  $\nu_\mu$  statistical error. Therefore, the statistical error on the  $\nu_\mu$  sample will still be the dominant source of error even with a 100% systematic uncertainty on the  $\nu_e$  selection. The optimisation of the  $\nu_e$  rejection requirement consists of adjusting the balance between the efficiency of the optimised cuts and purity of the  $\nu_\mu$  sample defined under this requirement. On one hand, a large  $\nu_e$  selection efficiency corresponds to a low  $\nu_\mu$  purity and, therefore, to a high  $\nu_e$  contamination that can wash out the LV effect. On the other hand, a stricter requirement diminishes the  $\nu_e$  contamination but reduces the statistics of the  $\nu_\mu$  sample at the same time, leading to a loss of sensitivity.

The optimisation of the  $\nu_e$  rejection requirement is driven only by the INGRID potential of Lorentz Violation discovery. In particular, by:

- the need to be able to detect a  $3\sigma$  deviation from a no-LV signal. In order to be conservative, a  $5\sigma$  deviation from a no-LV signal will be assumed, which induces a larger Lorentz violation effect and, therefore, a larger contamination from electron neutrinos.
- the requirement that the number of reconstructed electron neutrinos be smaller than the muon neutrino statistical error.

In the following,  $\sigma_\mu$  ( $\sigma_e$ ) is the interaction cross section for  $\nu_\mu$  ( $\nu_e$ ) in INGRID;  $\epsilon_\mu$  ( $\epsilon_e$ ) is the reconstruction efficiency, that is the probability for a  $\nu_\mu$  induced ( $\nu_e$  induced) event to be reconstructed and kept as a  $\nu_\mu$  event in the analysis, as defined in 6.2.1. Letting  $\nu_a^{\text{LV}}$  and  $\nu_a^{\text{Rec}}$  be the number of incident neutrinos after LV oscillation and reconstructed neutrino events of flavor  $a$  respectively, one has:

$$\nu_\mu^{\text{Rec}} = \nu_\mu^{\text{LV}} \sigma_\mu \epsilon_\mu \quad (6.2.2)$$

and

$$\nu_e^{\text{Rec}} = \nu_e^{\text{LV}} \sigma_e \epsilon_e. \quad (6.2.3)$$

Assuming the conservative approach that all oscillating muon neutrinos oscillate into electron neutrinos, and the  $\nu_\mu$  selection efficiency is 100%, a  $5\sigma$  signal corresponds to the detection of a number of oscillated muon neutrinos,  $\nu_\mu^{\text{Rec,osc}}$ , corresponding to:

$$\nu_\mu^{\text{Rec,osc}} \simeq 5\text{Error}(\nu_\mu^{\text{Rec}}) = 5\sqrt{\nu_\mu^{\text{Rec}}}, \quad (6.2.4)$$

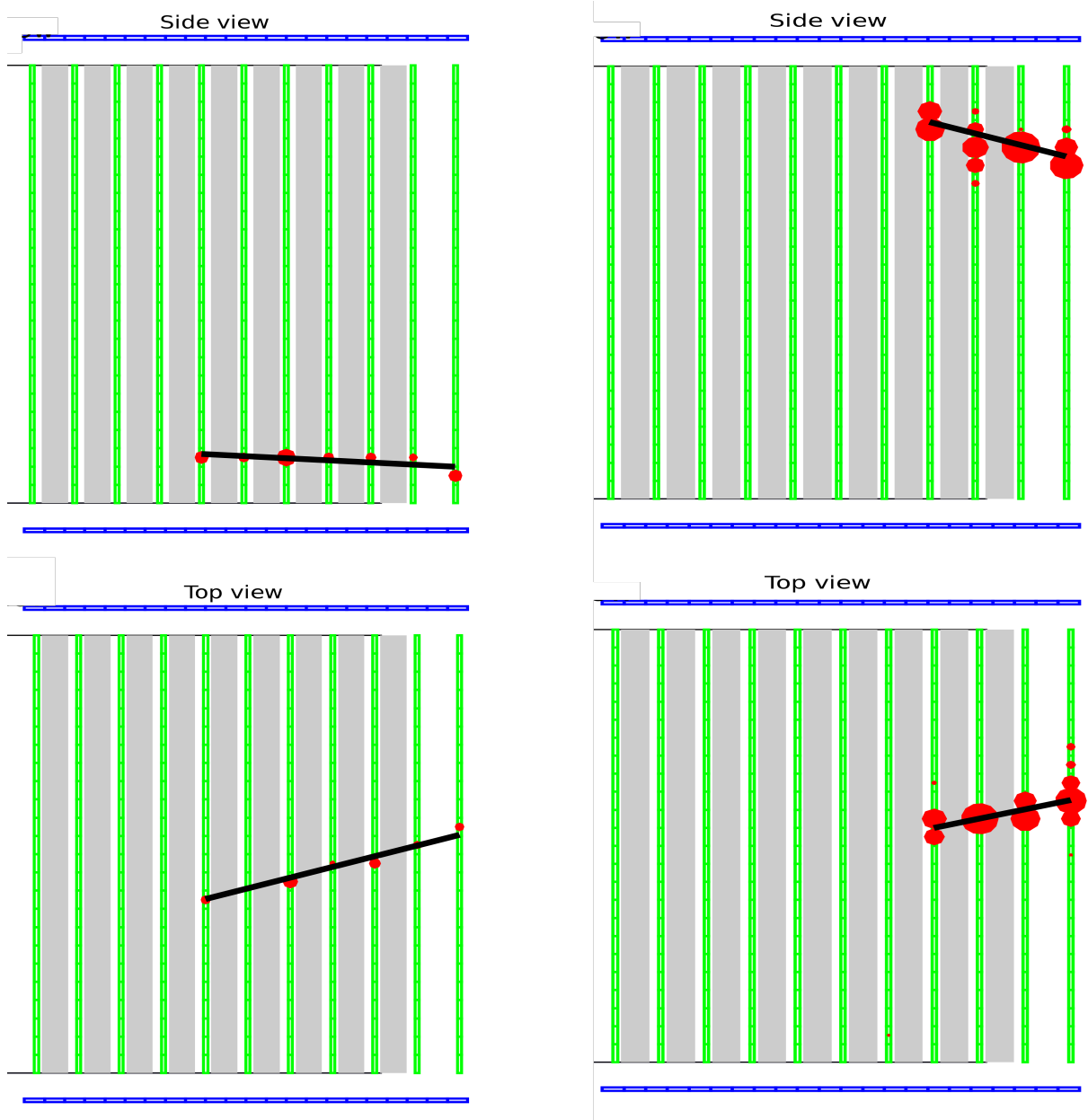


Figure 6.11: Event display showing a  $\nu_\mu$  (left) and  $\nu_e$  (right) CCQE interaction in the INGRID central horizontal module. The track is associated to the charged lepton, respectively the  $\mu$  and  $e$ . One observes the electromagnetic shower in the case of the electron propagation through the detector.

which, in case of 100%  $\nu_\mu$  reconstruction efficiency, is equivalent to:

$$\nu_\mu^{\text{Int,osc}} = 5 \sqrt{\nu_\mu^{\text{Int}}}, \quad (6.2.5)$$

where  $\nu_\mu^{\text{Int}}$  and  $\nu_\mu^{\text{Int,osc}}$  are, respectively, the number of interacting events in the INGRID fiducial volume, and the number of interacting events in the INGRID fiducial volume that have undergone oscillation. In a conservative approach, all  $\nu_\mu$  oscillate into  $\nu_e$ , *i.e.*:

$$\nu_e^{\text{LV}} = \nu_\mu^{\text{LV,osc}}, \quad (6.2.6)$$

with  $\nu_i^{\text{Int}} = \sigma_i \nu_i^{\text{LV}}$ ,  $i = e, \mu$  and  $\sigma_i$  the cross section. Assuming that the neutrino cross section of the two species are almost the same in the INGRID energy range [101], it implies that:

$$\nu_e^{\text{Int}} = \nu_\mu^{\text{Int,osc}}, \quad (6.2.7)$$

Using Equation 6.2.7, Equation 6.2.5 can be therefore written as:

$$\nu_e^{\text{Int}} = 5 \sqrt{\nu_\mu^{\text{Int}}}. \quad (6.2.8)$$

The second requirement, that the number of reconstructed  $\nu_e$  be small compared to the uncertainty on  $\nu_\mu$ , can be expressed as:

$$\nu_e^{\text{Rec}} \leq \sqrt{\nu_\mu^{\text{Rec}}}. \quad (6.2.9)$$

Since  $\nu_i^{\text{Rec}} = \epsilon_i^{\text{Rec}} \nu_i^{\text{Int}}$ ,  $i = e, \mu$ , with  $\epsilon_i^{\text{Rec}}$  the reconstruction efficiency of the  $i$ -th neutrino species, Equation 6.2.9 can be written as:

$$\epsilon_e^{\text{Rec}} \nu_e^{\text{Int}} \leq \sqrt{\epsilon_\mu^{\text{Rec}} \nu_\mu^{\text{Int}}}. \quad (6.2.10)$$

The requirement expressed in Equation 6.2.8 can therefore be written as:

$$5 \epsilon_e^{\text{Rec}} \leq \sqrt{\epsilon_\mu^{\text{Rec}}}, \quad (6.2.11)$$

giving the requirement:

$$\frac{\epsilon_e^{\text{Rec}}}{\sqrt{\epsilon_\mu^{\text{Rec}}}} \leq 0.2. \quad (6.2.12)$$

As the standard INGRID selection does not match this criterion (see Table 6.3), a new  $\nu_\mu$  selection method was developed, based on 4 variables that aim to distinguish tracks produced by an electromagnetic showers from muon tracks:

1. Average track transverse width,
2. Track length,
3. Root mean square of the track  $\frac{dE}{dx}$ ,
4. Number of hits close to the interaction vertex.

Since the criterion defined in Equation 6.2.12 is checked after all the cuts are applied (and not cut by cut), the interplay between cuts to match the criterion will not be trivial to optimize. To simplify this optimisation, these variables will be used to define a likelihood (see Section 6.2.2).

### Reweighting

In this analysis, the detected  $\nu_e$  we want to reject come from  $\nu_\mu$  oscillations. Since the  $\nu_\mu$  survival probability introduces a dependence on the SME  $c_L$  coefficient values (equation 6.1.22), the probability in turn depends on  $E^2$ . Without any prior on this energy dependence, it is impossible to know the oscillated  $\nu_e$  energy spectrum. Therefore, it is assumed that the  $\nu_e$  spectrum shape is the same as the  $\nu_\mu$  spectrum one.

As no oscillated  $\nu_e$  is introduced in our simulations, the only  $\nu_e$  we can use correspond to the beam intrinsic  $\nu_e$ , whose energy spectrum is different. A reweighting factor is therefore necessary to reproduce the oscillated  $\nu_e$ , *i.e.* the  $\nu_\mu$  beam spectrum. For each intrinsic  $\nu_e$  event in the beam, the reweighting factor is taken as:

$$C_{reweight}(E) = \frac{\nu_\mu \text{ probability}(E)}{\text{beam intrinsic } \nu_e \text{ probability}(E)} \quad (6.2.13)$$

where  $\nu_a \text{ probability}(E)$  is the weight of a type “a” neutrino of energy  $E$ . This  $C_{reweight}$  factor is then applied to the intrinsic beam  $\nu_e$  spectrum to modify its shape according to the  $\nu_\mu$  spectrum.

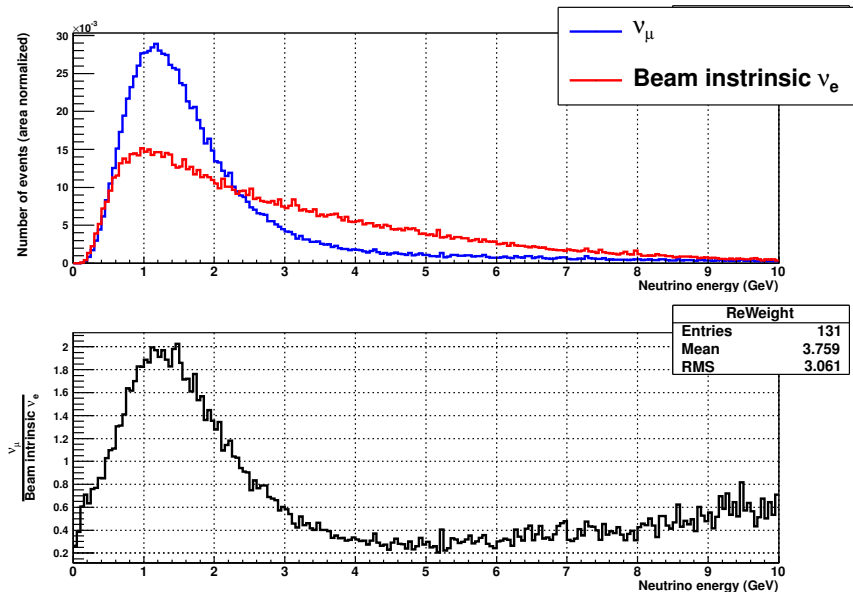


Figure 6.12: Estimation of the re-weighting factor to be applied to intrinsic  $\nu_e$  beam to match the  $\nu_\mu$  spectrum.

### Average track width

Because of bremsstrahlung and pair production, electromagnetic showers have a transverse width that is generally larger than muon tracks. The scattering of electrons on different materials makes the average transverse width increase with the material density. Properties of an electromagnetic shower in a material are defined by the Molière Radius,  $R_M$ . This radius corresponds to the radius of a cylinder containing 90% of the shower energy and is independent of the initial particle energy. Moreover, 99% of shower energy is contained in the transverse width,  $2R_M$ . The Molière radius of iron is  $R_M = 1.719$  cm which corresponds to a transverse width of  $2R_M = 3.4$  cm. Therefore, 99% of the shower energy is contained in a transverse width of  $4R_M = 6.8$  cm. Because the INGRID scintillator granularity is 5 cm, the average electromagnetic shower transverse width is expected to be incident on more than one scintillator bar. Figure 6.13 shows the profile of an electromagnetic shower in INGRID and confirms this trend, as in average, electron induced showers intercept more than 2 scintillator bars.

The track width in each plane might be biased due to the uncertainty on the electromagnetic shower development. This uncertainty arises mainly from the simulation of the energy deposition in INGRID scintillators. Because of electromagnetic shower processes, a lot of small hits deposit energy in the

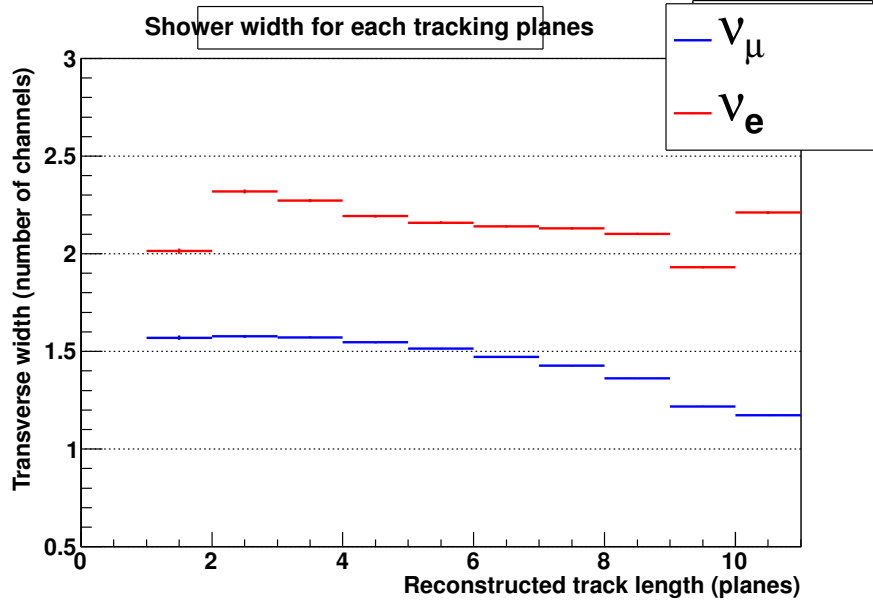


Figure 6.13: Average width of muon tracks and electron induced electromagnetic showers in the transverse direction (given in number of 5 cm scintillators), as a function of the distance from the vertex (number of tracking planes crossed).

scintillators, and an error on each deposition may cause the hit not to pass the 2.5 p.e threshold. Therefore, the track transverse width, averaged over all the tracking planes, is used instead of the information on individual planes. Figure 6.14 shows the corresponding average width distributions for muon tracks and electron showers.

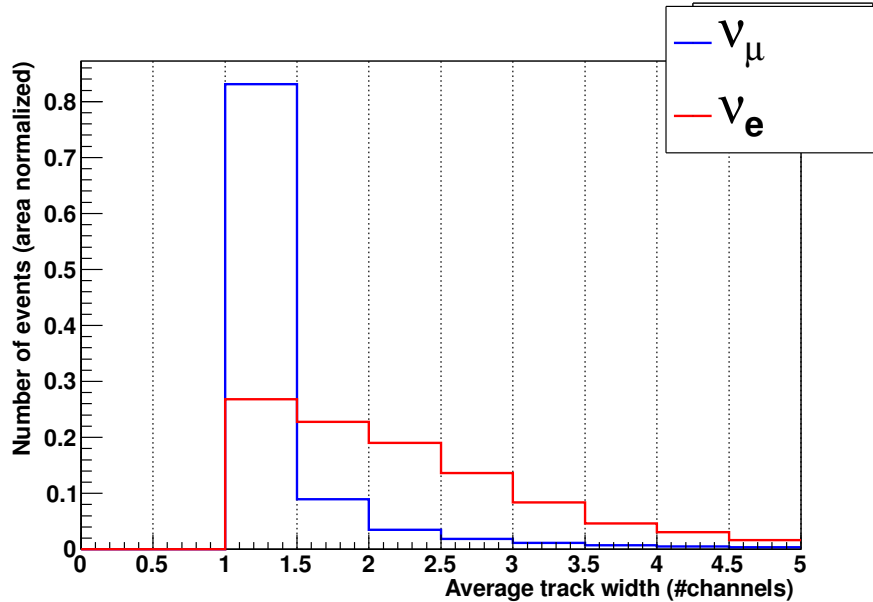


Figure 6.14: Transverse width of the track averaged over all tracking planes. Muon tracks (blue) are generally not spread over more than one scintillator, whereas electromagnetic showers are spread over several ones.

### Track length

The average track length of an electromagnetic shower is generally smaller than muon tracks because of electron scattering and transverse energy loss. The distribution of track length shown in Figure 6.15 shows an average 20 cm difference between the two.

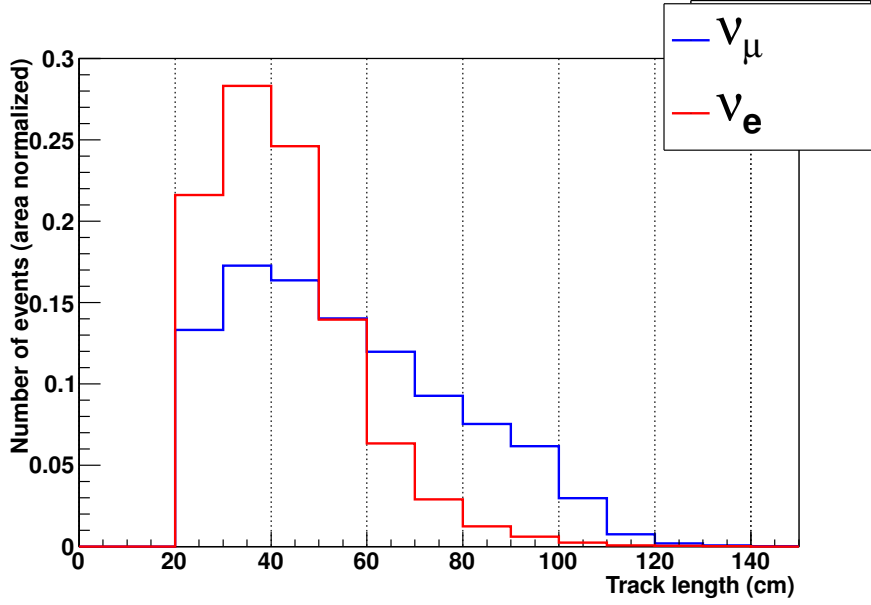


Figure 6.15: Track length comparison between electromagnetic showers (red) and muon tracks (blue).

#### Dispersion of the charge deposition: root mean square of $\frac{dE}{dx}$ distribution

In the electromagnetic shower process, various particles ( $e^-$ ,  $e^+$  and  $\gamma$ ) of various energies are produced. The  $\frac{dE}{dx}$  is expected to change greatly among hits from the same electromagnetic shower. On the contrary, most of the muons behave as minimum ionizing particles (except for the last hits of stopping muon tracks, which are very rare), and so have a uniform  $\frac{dE}{dx}$ . The RMS of the  $\frac{dE}{dx}$  distribution was selected for all hits in each track to exploit these differences. Distributions of the  $\frac{dE}{dx}$  RMS for muon and electron tracks shown in Figure 6.16 confirm these expectations and exhibit a clear higher RMS for electromagnetic showers. Because of cross-section model uncertainties, the error associated with energy deposition near the vertex is high. For this reason, only hits separated from the vertex by 2 or more planes are considered.

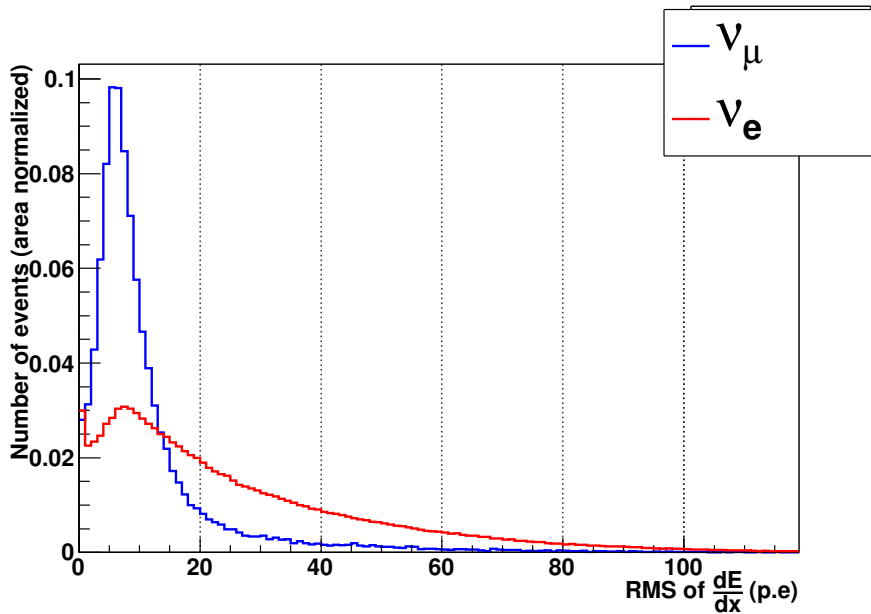


Figure 6.16: Root mean square distributions for electromagnetic showers (red) and muon tracks (blue). The region around the vertex, defined by  $\pm 2$  planes around the reconstructed vertex, and a transverse distance of  $\pm 3$  scintillators ( $\pm 15$  cm), is excluded from this RMS calculation.

### Hits near the vertex

The large amount of particles created during an electromagnetic shower is used to discriminate it from the muon tracks. However, the number of hits might be highly correlated to the RMS of the  $\frac{dE}{dx}$ , which is already used. Only hits located around the vertex, which have been left out of the RMS estimation, are selected. This should provide a more independent variable than using the total number of hits of the track. Unlike the  $\frac{dE}{dx}$ , the number of hits is far more robust to cross-section model variations. The comparison between electromagnetic showers and muon tracks is shown in Figure 6.17, and confirms the higher number of hits for EM showers.

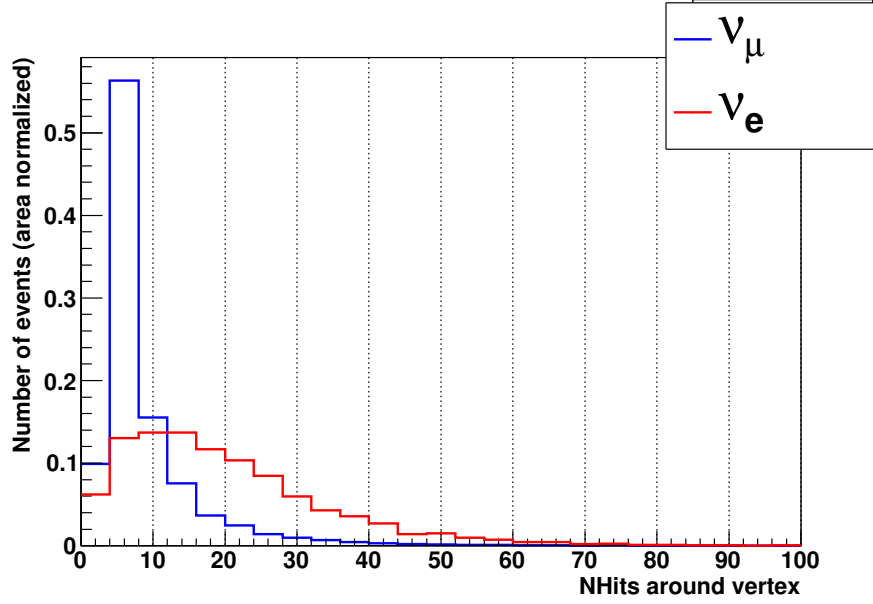


Figure 6.17: Distribution of the number of hits around the vertex for both electromagnetic showers (red) and muon tracks (blue). The region around the vertex is defined as  $\pm 2$  planes around the reconstructed vertex, and a transverse distance of  $\pm 3$  scintillators ( $\pm 15$  cm).

### Optimisation of the $\nu_e$ rejection requirement

The muon likelihood is defined by converting muon distributions for track width (Figure 6.14), track length (Figure 6.15), hit charge dispersion (Figure 6.16) and number of hits near the vertex (Figure 6.17) into probability distributions. The  $\nu_\mu$  likelihood is built by multiplying the conditional probability to be a muon considering the neutrino candidate different values for these four variables. For a candidate having track width  $w$ , track length  $l$ , hit charge dispersion  $q_{RMS}$  and number of hits around the vertex  $n_V$ , the  $\nu_\mu$  likelihood is defined as:

$$\begin{aligned} \mathcal{L}_{\nu_\mu} &= P(\nu_\mu | [w, l, q_{RMS}, n_V]) \\ &= \frac{P(w|\nu_\mu) \cdot P(l|\nu_\mu) \cdot P(q_{RMS}|\nu_\mu) \cdot P(n_V|\nu_\mu)}{P(w|\nu_\mu) \cdot P(l|\nu_\mu) \cdot P(q_{RMS}|\nu_\mu) \cdot P(n_V|\nu_\mu) + P(w|\nu_e) \cdot P(l|\nu_e) \cdot P(q_{RMS}|\nu_e) \cdot P(n_V|\nu_e)} \end{aligned} \quad (6.2.14)$$

where  $P(\nu_\mu|w)$ ,  $P(\nu_\mu|l)$ ,  $P(\nu_\mu|q_{RMS})$ ,  $P(\nu_\mu|n_V)$  are the probability of a  $\nu_\mu$  event to have respectively, a track width  $w$  (Figure 6.13), a track length  $l$  (Figure 6.15), a dispersion of charge disposition (Figure 6.16), and a number of hit near the vertex  $n_V$  (Figure 6.17). Figure 6.18 shows the distribution of this likelihood, where the separation between muon and electron neutrinos is evident. The  $\nu_\mu$  confidence level, defined as the  $\nu_\mu$  likelihood value that matches the criterion defined in Equation 6.2.12 and maximizes the  $\nu_\mu$  reconstruction efficiency, is  $\mu_{CL} = 0.54$ . The corresponding  $\nu_\mu$  reconstruction efficiency is 44.0% as shown in Table 6.3. The  $\nu_e$  reconstruction efficiency is therefore 13%. Figure 6.19 also show that the the criterion defined in 6.2.12 is fulfilled, for the new  $\nu_\mu$  selection, for the whole neutrino energy spectrum.

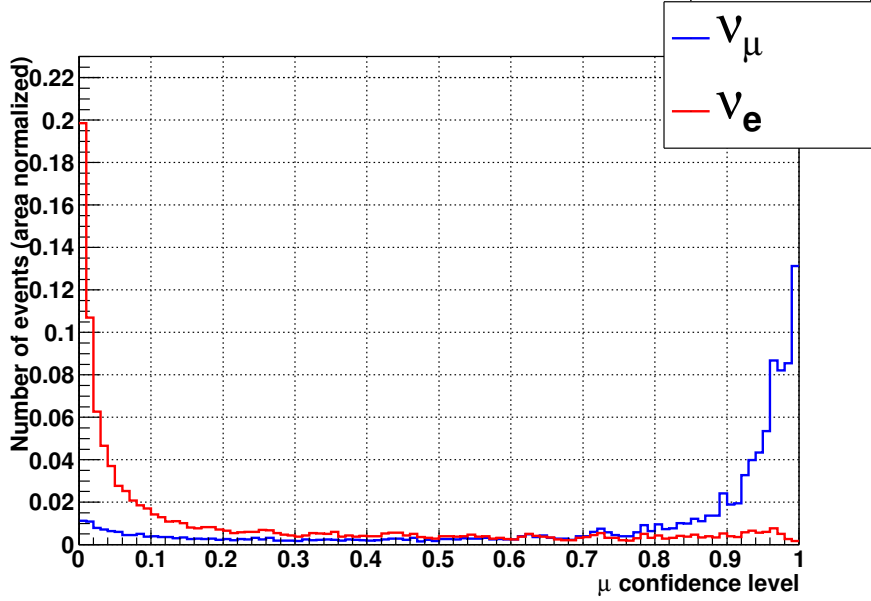


Figure 6.18:  $\nu_\mu$  likelihood distributions for both  $\nu_\mu$  (blue) and  $\nu_e$  (red). The confidence level ( $\mu_{CL}$ ) is based on a likelihood ratio obtained from the 4 variables presented before: track length, average transverse width, RMS of the  $\frac{dE}{dx}$  and number of hits near the vertex.

Table 6.3: Reconstruction efficiencies and their ratio for 2 different selections.

	Standard INGRID selection	$\nu_\mu$ selection
$\frac{\epsilon_e}{\sqrt{\epsilon_\mu}}$	0.91	0.20
$\epsilon_\mu$	53.6%	44.0%

### 6.2.3 Signal sample

The  $\nu_\mu$  sample is defined as the set of neutrino candidates reconstructed with the INGRID original selection, and for which the  $\nu_\mu$  confidence level criterion  $\mu_{CL} \geq 0.54$  is verified. Neutrino candidates interacting in the fourteen standard INGRID modules are considered. The whole INGRID data taken during the T2K runs 1 (March 2010-June 2010), 2 (November 2010-March 2011), 3c (April 2012 - May 2012) and 4 (October 2012 - May 2013) were analysed. Table 6.4 shows the total number of events passing the different selections, with the total number of  $\nu_\mu$  event candidates using the new selection being  $6.75 \times 10^6$ . The number of events after the standard INGRID selection, normalised to the number of POT, for data and MC simulation agree within 2%, which is compatible with the 1.94% systematic error estimated in [62]. It can be seen that the difference between MC and data is relatively larger in the  $\nu_\mu$  sample used in this analysis. The systematic error for this new selection was evaluated for this analysis, and it was found to increase to 5.3% for the  $\nu_\mu$  sample; therefore, the number of  $\nu_\mu$  candidates in data and MC shown in Table 6.4 is in agreement within the systematic error( [62]). Though it provides a cross check of the  $\nu_\mu$  selection, the systematic error study shown in [62] does not depend on LSP, and therefore does not affect the present Lorentz violation study. The number of  $\nu_\mu$  candidates in INGRID data corresponding to each LSP bin and T2K run period can be seen in Table 6.5 and so does the number of POT. T2K Run 4 was split into two separate periods, to account for differences in  $\nu_\mu$  event rate, that will be discussed in Section 6.3.3.

## 6.3 Corrections and systematic uncertainties

LV effects that are independent of sidereal time would change the overall normalisation of the  $\nu_\mu$  rate versus LSP distributions. As shown in Chapter 2 and 5 (for absolute measurements), there are important errors on the absolute number of neutrino arising from the flux ( $> 10\%$ ), the cross section

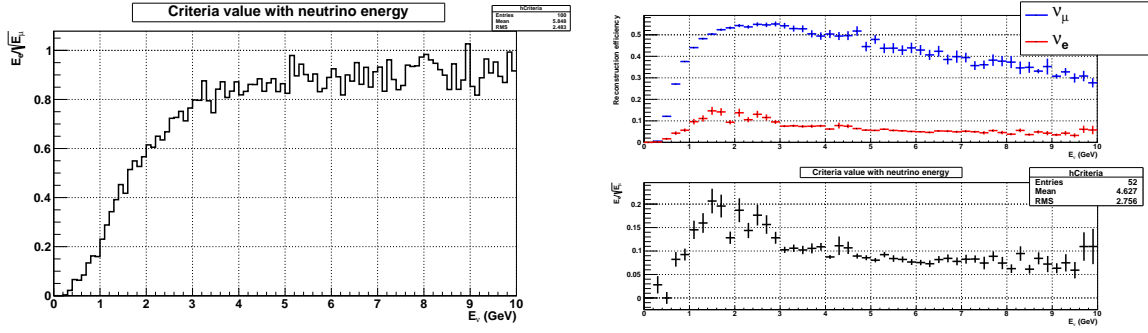


Figure 6.19: On the left,  $\epsilon_e / \sqrt{\epsilon_\mu}$  for the standard INGRID selection. The requirement expressed in Equation 6.2.12 is fulfilled only for  $E_\nu \lesssim 1$  GeV. On the right top: reconstruction efficiencies for  $\nu_\mu$  (blue) and  $\nu_e$  (red) for the new INGRID selection. Bottom:  $\epsilon_e / \sqrt{\epsilon_\mu}$  for the new INGRID selection. The requirement expressed in Equation 6.2.12 is fulfilled for the whole neutrino energy spectrum.

Table 6.4: Number of reconstructed events in the data and MC with the INGRID standard selection and the  $\nu_\mu$  selection.

	Data	MC	$\frac{Data-MC}{MC}$
Standard INGRID selection	$8.07 \times 10^6$ events	$7.92 \times 10^6$ events	1.9%
$\nu_\mu$ selection	$6.75 \times 10^6$ events	$6.57 \times 10^6$ events	2.7%

models ( $> 5\%$ ) or the detector uncertainties ( $> 1\%$ ). Therefore, time independent  $\nu_\mu$  disappearance is not studied in this analysis and, only time-dependent LV effects that introduce a distortion of the  $\nu_\mu$  rate versus LSP distribution are. As a consequence, a careful evaluation of possible time dependent variations that may mimic a Lorentz violation effect is necessary. We separate these effects in two possible sources. Some of these variations affect the detector, such as gain and dark noise variations with time, or changing temperatures between night and day (summer/winter). Other affect the beamline, like the variation of the delivery of POT per spill, shown in Figure 6.21, the shift of the beam center due to changes in accelerator tuning or tidal forces (Figure 6.34-6.36), or the variations in the neutrino flux between T2K runs. The LSP dependence of these effects will generally exhibit variations (see, for example, Figure 6.23). One notes that the impact of time-dependent effects depends on the variation of their source with the sidereal time. For example, the dark noise rate varies with temperature. One expects for example a higher dark noise during the day as compared to night. If the T2K data taking is continuous over the whole year, one expects this effect to be almost washed out since local sidereal phase corresponding to day in summer will correspond to the night in summer. However, the T2K datasets we use only cover partially the LSP, due to the fact that a typical T2K run only covers a small fraction of a year (see Section 6.2.3). Therefore, we will observe some remaining effects of the dark noise due to this partial coverage. One notes that it is also due to an average difference of temperature between winter and summer, which prevents from a total compensation of this effect even with uniform LSP coverage.

In this section, we will study the time dependent effects possibly coming from the INGRID detector and from the neutrino beam. We will deduce a correction factor to apply to the  $\nu_\mu$  rate per POT with the local sidereal phase. We will also study the systematics on this correction factor.

### 6.3.1 INGRID detector effects

The following time-dependent detector effects will be considered in the following sections: Neutrino event pile-up, MPPC dark noise, and MPPC gain variation.

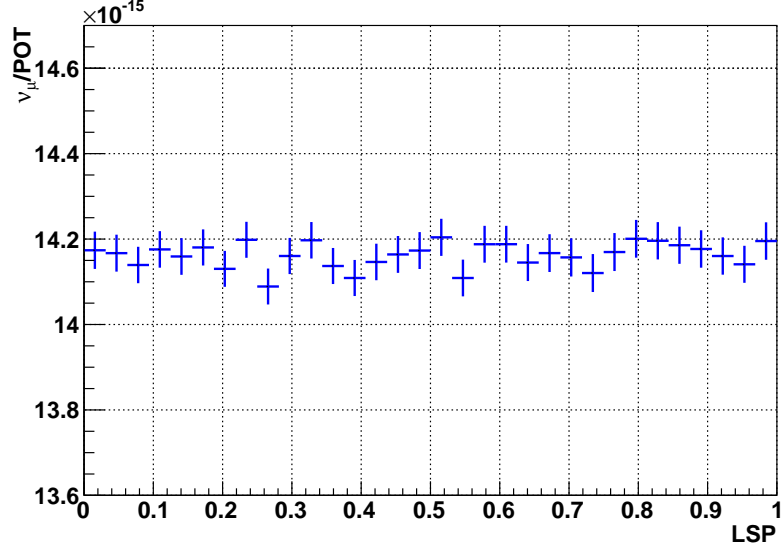


Figure 6.20:  $\nu_\mu$  rate versus LSP distribution using Run 1 to Run 4 data before corrections are applied.

### Neutrino event pile-up

The standard INGRID reconstruction is tuned to reconstruct only one vertex in each INGRID electronic cycle (581 ns). In case of several events happening during one integration cycle, one event is therefore often missed. One expects this effect to increase with the neutrino beam intensity and cause distortions in the neutrino rate distribution which can mimic an LV signal. For this reason, the intensity variation of the beam with the local sidereal phase has been studied. Figure 6.21 shows this variation, using the beam spills used in this analysis. One observes a significant variation with respect to the statistical error, which implies that the pile-up effect must be taken into account to deduce a correction in the study. A maximal 5% variation of the intensity is observed. The pile-up correction

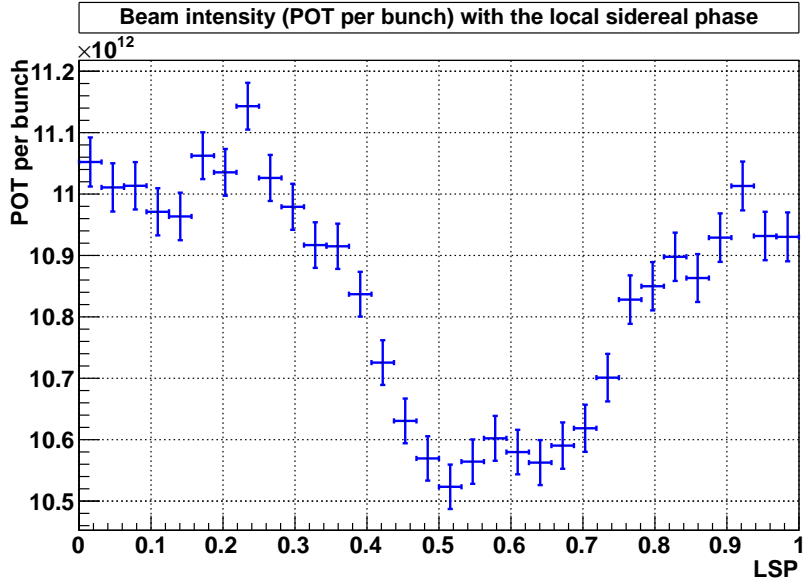


Figure 6.21: POT per spill variation with LSP using T2K run 1 to run 4 data.

has been studied using the standard INGRID selection [62]. The event loss follows a linear decrease with the beam intensity, as expected if the pile-up effect of three or more events is negligible. In this

approximation, the event loss is given by:

$$\text{Nevents}_{\text{Pile-up corrected}} = \frac{\text{Nevents}}{1 - C_{\text{loss}} n_{\text{ppb}}} \quad (6.3.1)$$

where  $C_{\text{loss}}$  is the event loss constant and  $n_{\text{ppb}}$  the number of POT per bunch (i.e. the beam intensity) that is shown in Figure 6.21. In the case of 250 kA horn current, the event loss constant has been determined for each INGRID module [62]. Figure 6.22 shows the INGRID module numbering. Their value is summarised in Table 6.6.

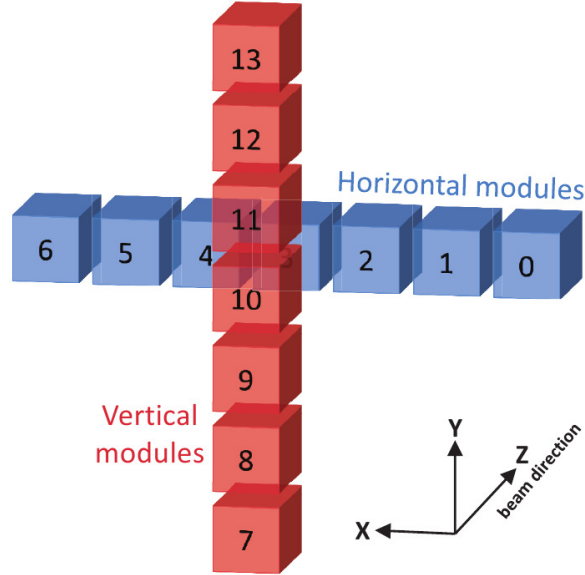


Figure 6.22: INGRID modules numbering.

The correction is applied for each event depending on the associated number of pot per bunch. The systematic error on this correction is obtained considering the statistical error associated to the event loss constant estimation, namely  $0.05 \times 10^{-15}$ . It represents an event loss variation of 3% to 7% depending on the module (see Table 6.6). Figure 6.23 shows the correction that should be applied to the  $\nu_\mu$  event rate versus LSP distributions along with the  $\pm 1\sigma$  variations in the case of the INGRID central horizontal module. There is an overall correction of  $\sim 1.3\%$ , which has no impact in this study since it only affects the total rate of  $\nu_\mu$  candidates versus LSP. As for any effect on the shape of the distribution, it can be seen (black histogram) that the maximum difference between the  $\pm 1\sigma$  variations is less than 0.1%. It is assumed here that the event loss constant does not change with the  $\nu_\mu$  selection as compared to the standard INGRID selection, which is motivated by fact that the vertex reconstruction efficiency is little affected by the  $\nu_\mu$  confidence level cut (efficiency is changed from 53.6% to 44.0%).

Given the smallness of the event loss correction ( $\lesssim 0.1\%$ ), it seems that this error is negligible (this is 0.1% of a 1% effect, which is  $< 0.01\%$ ) as compared to the statistical error of about 0.3%. Figure 6.23 shows its effect in the example of module 3. One observes that it affects the average correction factor by  $\pm 0.05\%$  which is small but does not affect the shape. As for the shape, one observes almost no variations between the varied event loss constant within  $\pm 0.01\%$ , which indeed leads to a negligible systematic error as compared to the statistical uncertainty. Therefore, the systematic error associated with the neutrino event pile-up in INGRID is neglected. Figure 6.24 shows a plot of the  $\nu_\mu$  rate versus LSP after we applied the pile-up correction.

### MPPC dark noise

The dark noise rate in the INGRID electronics varies with the external conditions, and therefore with the T2K data taking time. This variation with time also affects the detection of neutrino candidates

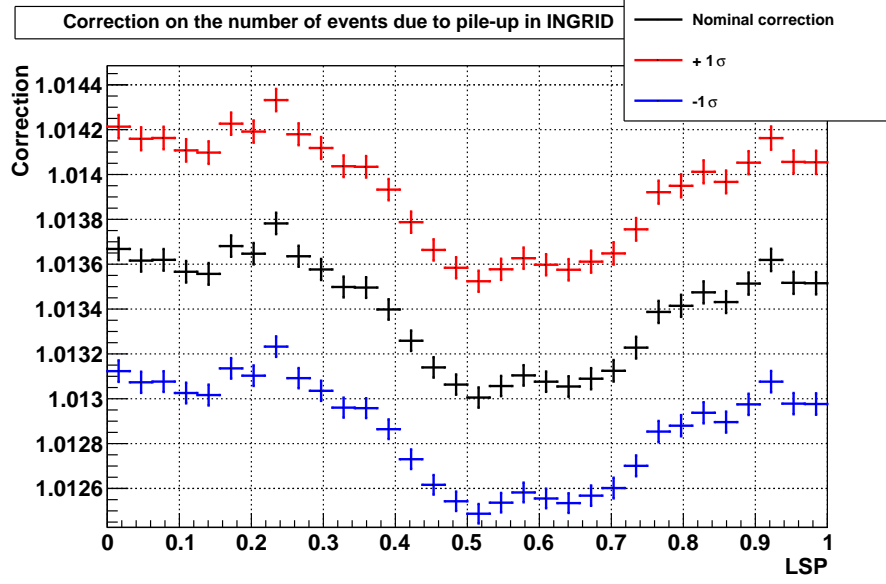


Figure 6.23: Correction of the number of events per POT as a function of the local sidereal phase in the INGRID horizontal central module (module 3). The associated event loss constant is  $C_{\text{loss}} = 1.22 \times 10^{-15}$ . The  $\pm 1\sigma$  variations correspond to variations of the event loss constant within its statistical error of  $0.05 \times 10^{-15}$ .

at INGRID, and may induce distortions in the distribution of the neutrino rate versus local sidereal phase. The dark noise rate variation with the local sidereal phase is estimated in the data analysed in this study. The rate is estimated using the off-beam INGRID Trip-T integration cycles and collecting the number of hits, and is obtained as the mean of the fitted Poisson distribution (Figure 6.25). Its variation with the local sidereal phase is shown in Figure 6.26 (top). Note that the dark noise hit rate in the MC (before opening the data) was chosen to be 5.05 hits per cycle per module, whereas for data, the dark noise rate is between 6.02 and 6.15 hits per cycle per module. However, this difference only leads to a time independent correction factor. The impact on the  $\nu_\mu$  per POT shape variations is estimated generating 21 MC toy experiments where the dark noise rate was varied from 0 to 10 hits per cycle per module, by steps of 0.5. Figure 6.27 shows the impact on the  $\nu_\mu$  efficiency (and so, on  $\nu_\mu$  per POT). The variation of the efficiency with the dark noise rate is estimated by fitting this distribution with a linear function, which is found as:

$$\epsilon_{\nu_\mu} = a \times \text{DN rate} + b \quad (6.3.2)$$

with:

$$a = -(5.59 \pm 0.06) \times 10^{-4} \text{ and } b = 0.44290 \pm 0.00003 \quad (6.3.3)$$

The correction on the the number of  $\nu_\mu$  per POT versus LSP is deduced combining the top Figure 6.26 and Figure 6.27, and the bottom Figure 6.26 shows the result, together with variations corresponding to  $\pm 1\sigma$  errors taken as the MC statistical errors on the fitted coefficients (shown in Equation 6.3.3). One observes that the shape correction varies between 1.00138 and 1.00124, which represents a relative variation of  $\sim 0.01\%$ . Therefore, the MC correction is expected to have a negligible impact on the shape of the  $\nu_\mu$  per POT distribution versus the local sidereal phase. No systematic error is associated to this correction, given the negligible effect of the  $\pm 1\sigma$  variations of the fitted coefficients shown in Figure 6.26. Considering that the correction is small, a module by module correction has not been studied.

A plot of the  $\nu_\mu$  rate versus LSP after pile-up and MPPC dark noise corrections are applied is shown in Figure 6.28.

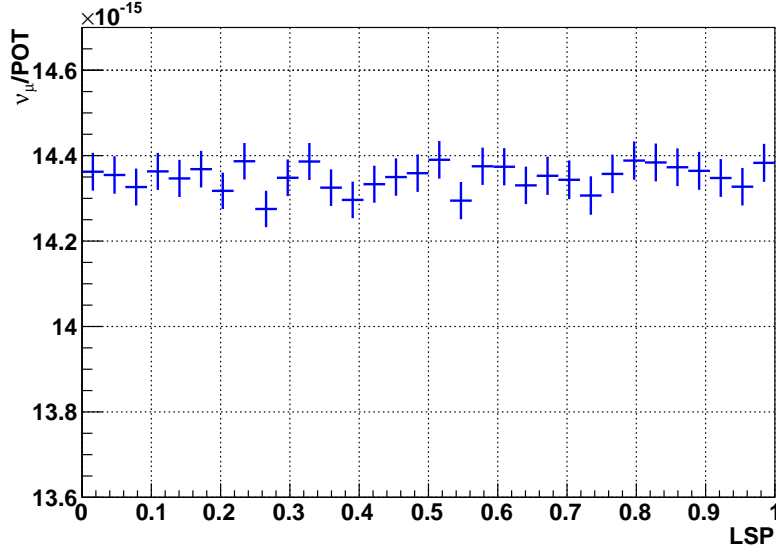


Figure 6.24:  $\nu_\mu$  rate versus LSP distribution after pile-up corrections have been taken into account.

### MPPC gain variation

The average minimum ionizing peak (MIP) charge value changes with the T2K data taking time; this will both impact the reconstruction, where only hits giving more than 2.5 p.e in a scintillator are used, and the  $\nu_\mu$  selection since the root mean square of  $dE/dx$  is used. Considering that the temperature conditions are not uniform between all the modules (some are closer to the climate control system), a module by module study is performed. As an example, Figure 6.29 shows the MIP variation with the T2K data taking period for the horizontal modules number zero (edge) to number three (central). A similar trend between the modules is observed, with a larger MIP in the T2K run 2, and lower in the end of run 4 and in run 1. It can also be seen that the edge module zero has a more stable MIP than others. This systematic time-dependent variation can cause distortions in the distribution of the number of neutrino candidates in INGRID and has therefore been investigated. Figure 6.30 shows the MIP variation with the local sidereal phase in the specific case of the central horizontal module three. A significant effect above the statistical error of the sand muon sample used to determine the MIP variation is observed, with a magnitude of about 1%. In order to take into account correctly these time variations, data are used to study this correction. From Figure 6.29, a correction factor is defined for each module and each time period. The reference used for each module is the lowest MIP value over the whole T2K running period. More precisely, the charge of each hit is scaled by a factor that depends on the module and time period  $F(\text{mod.}, t)$ :

$$Q_{Hit}^{cor} = Q_{Hit}/F(\text{mod.}, t), \quad (6.3.4)$$

where  $F(\text{mod.}, t)$  is evaluated by dividing the MIP value for the module “mod” at time “t” by the MIP lowest value for module “mod” (both shown in Figure 6.29). This naturally implies that  $F \geq 1$ , and one deduces from Equation 6.3.4 that  $Q_{Hit}^{cor} \leq Q_{Hit}$ . We use the MIP lowest value as a reference since it requires more than 2.5 p.e deposit to register a hit. It is therefore straitfoward to decrease the charge of existing hits with a software cut, while this is not possible the other way since it may miss some hits.

The data are then reconstructed and the  $\nu_\mu$  selection is applied. Figure 6.31 shows the comparison with the nominal (no MIP/gain correction) data sample. We observe a higher  $\nu_\mu$  rate after the gain correction, since a larger gain implies a larger noise and larger  $dE/dx$  dispersion that decreases both the reconstruction and the  $\nu_\mu$  selection efficiencies. The bottom part of Figure 6.31 shows that the impact on the shape is within the data sample statistical errors. No systematic uncertainty is therefore associated, considering that the sand muon statistics used to generate Figure 6.30 is enough to show

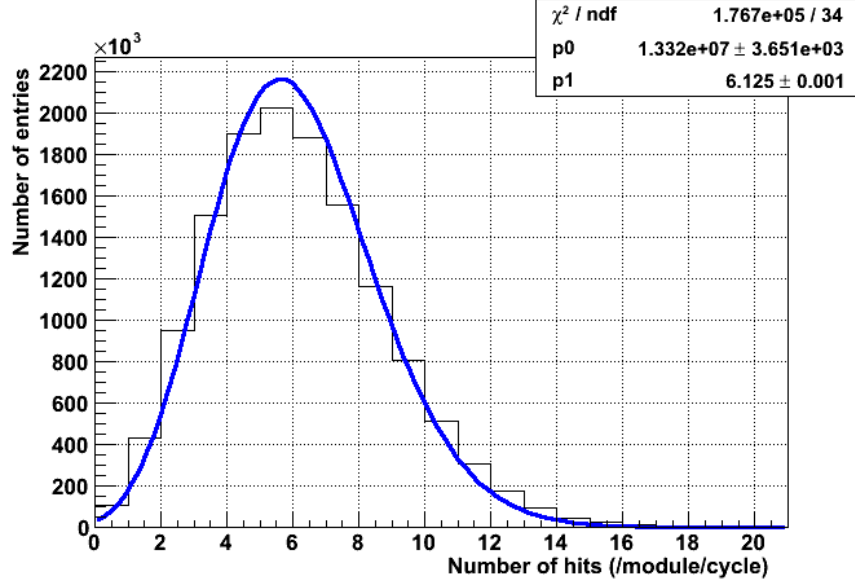


Figure 6.25: Distribution of the dark noise rate per INGRID module and per cycle for a given time interval. It is fitted by a Poisson distribution.

that the MIP variation with LSP has no impact on the time variation of the number of events.

Figure 6.32 shows a plot of the  $\nu_\mu$  rate versus LSP after pile-up, MPPC dark noise and MPPC gain corrections are applied.

### 6.3.2 Neutrino beam effects

Though the number of POT is an indicator of the neutrino beam intensity, possible differences between the number of POT and the neutrino flux can arise, and induce variations in the neutrino event rate that mimic a LV signal. In particular, the proton beam alignment with the target can vary with time and impact the neutrino flux for a given number of POT. For this reason, the number of  $\nu_\mu$  per POT should be corrected in order to take into account the real neutrino flux impinging upon INGRID without LV effect. Therefore, the change in beam alignment with INGRID is studied, assuming the global shape distortion is a second order effect. In order to study the beam position variations with time, we analysed data in different ways according to data taking periods and time scales:

- For each T2K run 1 to 4, the beam position is determined using INGRID. This allows direct determination of the beam position in the detector where Lorentz violation is studied, reducing possible systematic errors.
- Within a given run, the statistics in INGRID is too low to determine the beam position with a significant accuracy. Therefore, we use the MuMon instead to calculate rate variations. A correction based on MuMon data will mitigate, among others, the tidal effect that can shift the beam position and may mimic a Lorentz violation effect.

#### Run by run beam position

The  $\nu_\mu$  selection is applied in each of the fourteen INGRID modules, run by run. The beam position is determined independently for the vertical and horizontal modules using a gaussian fit of the number of neutrino interactions in the modules. Figure 6.33 shows the results of this procedure.

The beam position changes from -6.4 cm to 8.4 cm horizontally, and from 1.4 cm to 3.7 cm vertically.

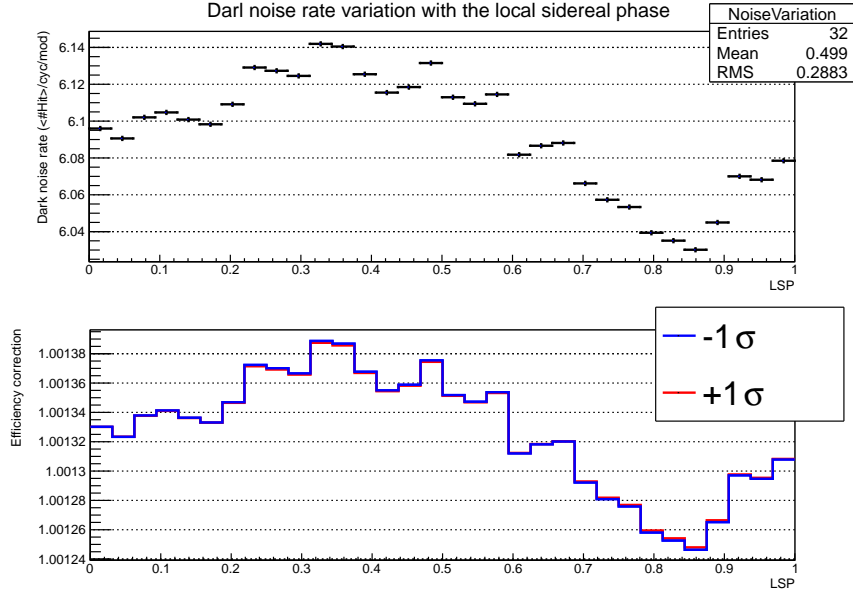


Figure 6.26: Variation of the dark noise rate with the local sidereal phase (top). The associated correction on the number of events is shown in the bottom figure. The rate average correction is not equal to 1, since a dark noise rate of 5.05 hits per cycle per module is assumed in the MC used to determine the efficiency listed in Table 6.3. In order to retrieve the correct time independent number of interacting events, an average correction is therefore to be applied to the number of events (or efficiency) which is the correction averaged over LSP. Note  $+1\sigma$  represents the largest dark noise effect, in which  $b$  is overestimated by  $1\sigma$  and  $a$  underestimated by  $1\sigma$ . On the opposite,  $-1\sigma$  represents the flattest variations of the efficiency with dark noise, *e.g*  $b$  is underestimated by  $1\sigma$  and  $a$  overestimated by  $1\sigma$

### Beam position variation within one run and tidal effect

Due to lack of statistics in INGRID, the Silicon Pixel detector part of the MuMon is used to correct the beam position within one T2K run. It provides the highest accuracy on the beam position [102]. For each neutrino spill used in the Lorentz violation study, the muon beam position is measured in the MuMon as a function of the local sidereal phase. For kinematic reasons, the muon beam center is aligned with the neutrino beam center. The corresponding position of the neutrino beam center at INGRID is extrapolated using the MuMon measurement by applying a geometrical scaling factor:

$$\text{Pos}_{X/Y}^{\text{INGRID}} = \text{Pos}_{X/Y}^{\text{MuMon}} \times \frac{280}{115}, \quad (6.3.5)$$

which is the ratio of the INGRID and MuMon distance in meters from the target. Figure 6.34 and 6.35 show the extrapolated beam position variation in INGRID for the horizontal and vertical centers respectively. We observe a pattern that depends on different effects, such as tidal variations coupled with incomplete LSP coverage run by run, and changes in beam orbit after beam stops. A relatively small variation ( $\sim 0.2$  cm) within the run 4 compared to other runs is observed. Since this run provides almost half of the statistics, important variations in other low statistic runs will be almost washed out (for example, for run 1 the variation is  $\sim 1$  cm). This correction takes into account the tidal effect which distorts the beam and deviates its direction. Figure 6.36 shows the beam position variation in the MuMon with time which shows that the MuMon is sensitive enough to observe the tidal effects, and therefore, to correct them.

### Beam position correction

To study the impact of a variation of the beam center position on the number of  $\nu_\mu$  candidates at INGRID, MC simulation was used. Several different toy experiments were generated changing the beam horizontal position from 0 (nominal) to 0.2 cm, 0.8 cm, 1.5 cm, 1.9 cm, 3.0 cm, 6.0 cm, 6.4 cm, 9.0 cm. In this study, we assumed that:

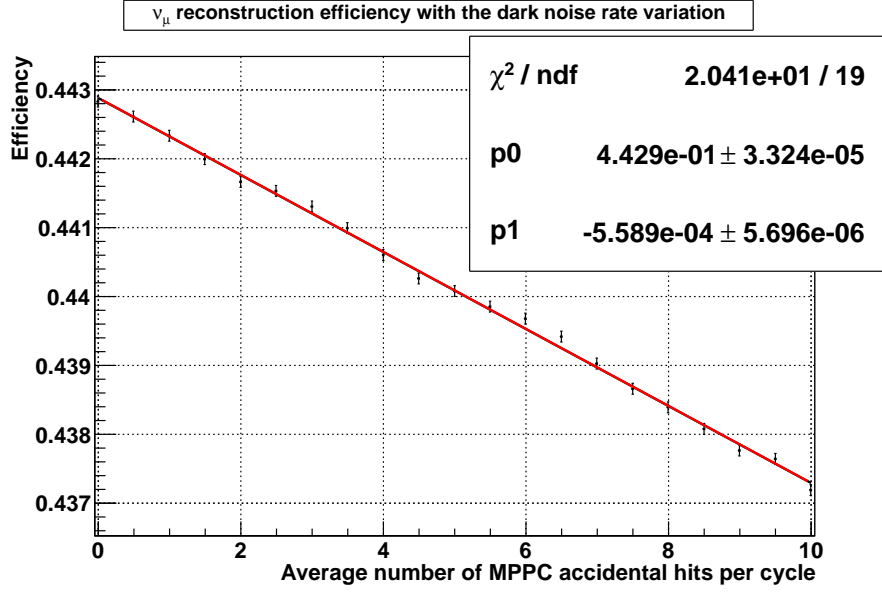


Figure 6.27: Variation of  $\nu_\mu$  selection efficiency with the dark noise rate. Because of mis-reconstruction, the efficiency naturally decreases with the dark noise rate. This variation is fitted with a 1st degree polynomial and the associated equation found is  $-5.6 \times 10^{-4} \times \text{DN rate} + 0.4429$ .

- The variation of the event rate in the vertical modules as a function of the vertical beam direction is the same as for the horizontal component in horizontal modules, scaled by a factor  $S = \frac{\text{Horizontal beam width}}{\text{Vertical beam width}}$ . One expects the relative variations to be higher in a narrower beam. Using the high statistics Run 4 data, a constant factor  $S = \frac{452}{434}$  was taken.
- The event rate correction on the horizontal and vertical beam positions are independent and only affect the horizontal and vertical modules respectively. Considering that the beam is almost gaussian and have a width larger than 4 m, it is reasonable to assume that the flux is almost uniform in the central module (1.2 m).
- The beam has a left/right symmetry around its center, as well as a top/bottom one.

Figure 6.37 shows the variation of the number of events in the INGRID horizontal modules. The decrease in the number of events can be represented by a linear curve. The correction is applied event by event using the following method:

- For each event, its T2K run, the module type (horizontal or vertical) and local sidereal phase are determined.
- Within a T2K run, the relative variation in the event rate is deduced by reporting the beam center position shown in Figures 6.33 on Figure 6.37, and the event variations  $E_{Run}$  is calculated. If the event is within a vertical module, the variation is multiplied by  $S$ . The correction is taken as the inverse of  $E_{Run}$ . These correction are summarised for each run in Table 6.7, separating the horizontal and vertical modules.
- The correction due to the variation within a single run is estimated in the same way: the local sidereal phase of the event is taken, and the corresponding variation around the run position is taken from Figure 6.34 (if the horizontal module is hit) or Figure 6.35 (vertical). The correction is then estimated as for the run by run correction.

Figure 6.37 (right) shows the systematics variation with the beam center. Figure 6.34 and 6.35 shows that the maximal variation within one run is 1.5 cm (run 1). Figure 6.37 shows the systematics associated to the correction and is  $\sim 0.02\%$  for the horizontal module. If the systematic on the correction in the vertical modules is summed in quadrature (maximal shift of 0.6 cm), the resulting

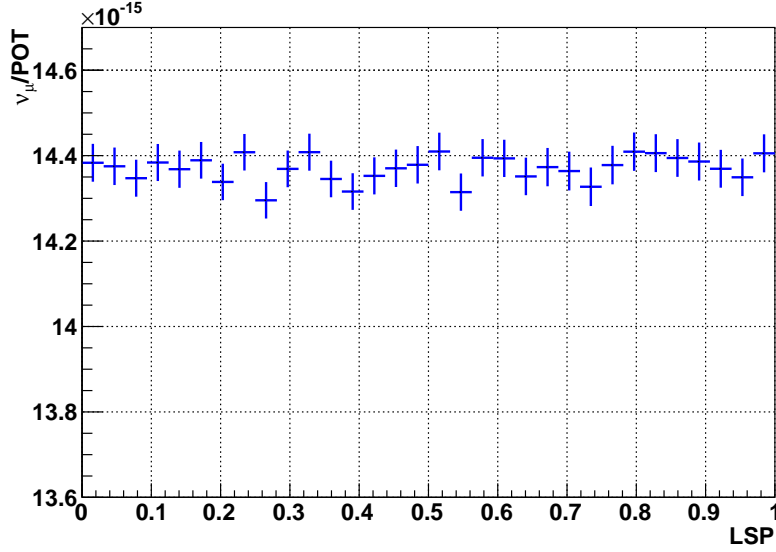


Figure 6.28:  $\nu_\mu$  rate versus LSP distribution after pile-up and MPPC dark noise corrections have been taken into account.

systematic uncertainty on the beam position variation within one run is  $\lesssim 0.03\%$ , and therefore negligible in comparison to the statistical error.

As for the correction between the different runs, the maximal difference on the correction applied is for run 2 (minimal correction) and run 3 (maximal) given their beam center shown on Figure 6.33. The total number of events in run 3 is corrected by a total factor which is approximatively the mean of the vertical and horizontal corrections, since the number of events is almost the same in horizontal and vertical modules (Figure 6.33). The approximate total correction factor is therefore 1.0055 for run 3 and 1.0005 for run 2. The difference between the corrections is therefore 0.005 which corresponds to an effective beam center variation of 5.5 cm (using the left part of Figure 6.37). The systematics uncertainty is therefore given by Figure 6.37 (right), and is equal to 0.08%. Considering the current statistical uncertainty is  $\sim 0.3\%$ , this systematic error is neglected.

Figure 6.38 shows a plot of the  $\nu_\mu$  rate versus LSP after all corrections described so far have been applied.

### 6.3.3 Residual rate correction

As a final correction, we study the possible remaining variations of the event rate with time. The detector and beam sources are no more separated, and a global correction is applied. To evaluate the possible corrections, the data taking period is divided into the four different runs used in this analysis. On top of this, the T2K run 4 is divided into two periods: end of 2012 (October 2012 - 31 December 2012) and beginning of 2013 (January 2013 - May 2013). The T2K run 4 lasted long and was stopped for the new year, therefore, possible variations in the event rate (due, among other things, to different beam tuning) are expected during this run. It is known that the total event rate can change significantly between T2K runs, and even between Main Ring runs [103] mainly because of the changes in the beam position between runs. Therefore, we decided to calculate a correction, extracted from the average event rate of each of the five periods. However, one should not correct possible differences due to the Lorentz violation effect. Ideally, it would be possible if the data taking for each run covered the same sidereal phase space, but this is not the case. In order to remove any correction with a potential Lorentz violation effect, the following method is applied:

1. For each of the five periods (that for simplicity will be called runs), the POT coverage in LSP is estimated and shown in Figure 6.39.
2. The POT distributions for each run are fitted by a constant  $\langle \text{POT} \rangle_{\text{Run}}$ . For each LSP bin  $i$

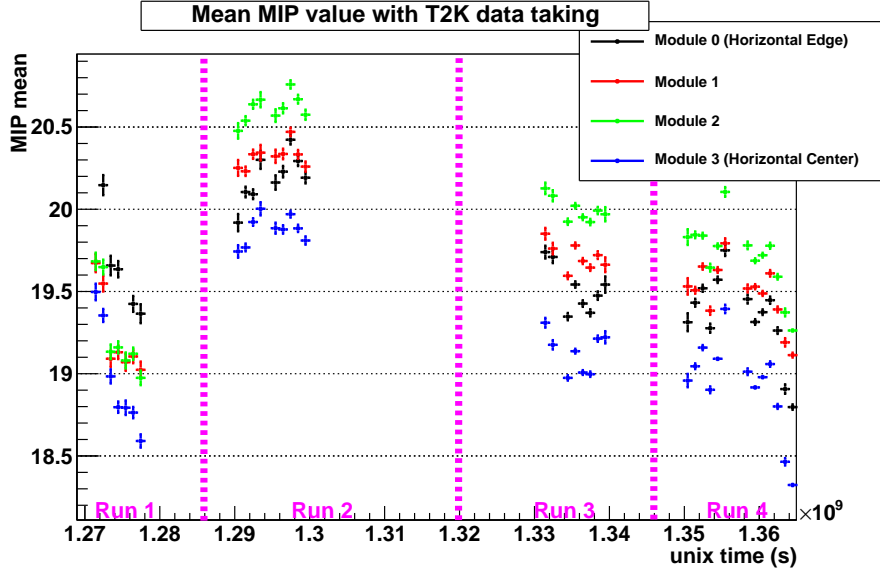


Figure 6.29: MIP distribution as a function of time. Different INGRID horizontal modules from number zero to three are shown, along with the different T2K run periods. The MIP is evaluated by fitting the sand muon charge distribution with a gaussian function around the muon mean charge deposition value [].

and run  $r$ , the ratio with the average run POT (averaged over LSP) is therefore  $d_r^i = \text{POT}_r^i / \langle \text{POT} \rangle_r$ .

3. A flat POT coverage in LSP is simulated by producing the event rate distributions  $\frac{\nu_\mu}{\text{POT}}$  but reweighting each  $\nu_\mu$  and POT events by a factor  $w_r^i = 1/d_r^i$ . The correction is applied event by event, depending on the run and the sidereal phase of the event.

This method produces new event rates distributions for each run, but with a flat POT coverage. This should wash out any event rate variation between runs due to different LSP coverage of the data taking (if there is Lorentz violation). Figure 6.40 shows the five event rate distributions. Finally, the correction is evaluated run by run as follow:

1. Each event rate distribution with sidereal time is fitted by a constant, which represents the average rate of the run  $\langle \frac{\nu_\mu}{\text{POT}} \rangle_{\text{Run}}$ .
2. For each run, a correction factor is estimated as the ratio between a reference event rate and the run average event rate:

$$c_{\text{Run}} = \frac{\langle \frac{\nu_\mu}{\text{POT}} \rangle_{\text{Run4,2013}}}{\langle \frac{\nu_\mu}{\text{POT}} \rangle_{\text{Run}}} \quad (6.3.6)$$

where the second part of run 4 was taken as reference. Corrections are summarised in Table 6.8. One observes the difference between run 4 2012 and 2013, which is due to changes in running conditions after the end of year shutdown.

3. Data are reprocessed, and the correction factor  $c_{\text{Run}}$  is applied event by event on the number of  $\nu_\mu$  depending on the run of the detected  $\nu_\mu$ .

Figure 6.41 (left) shows the relative correction with the LSP. One observes a 0.3% increase of the event rate, since the run 4 2013 has a higher event rate compared to most of the other runs (except run 4 2012). This correction has no impact on the Lorentz violation shape study. In addition, a 0.2% correction that affects the shape is observed. This is because most of the spills populating the LSP between 0.2 and 0.8 comes from the run 4 2013, while the remaining LSP (between 0 and 0.2, and 0.8 and 1) are more populated by other runs which have mostly a lower event rate. The systematic error

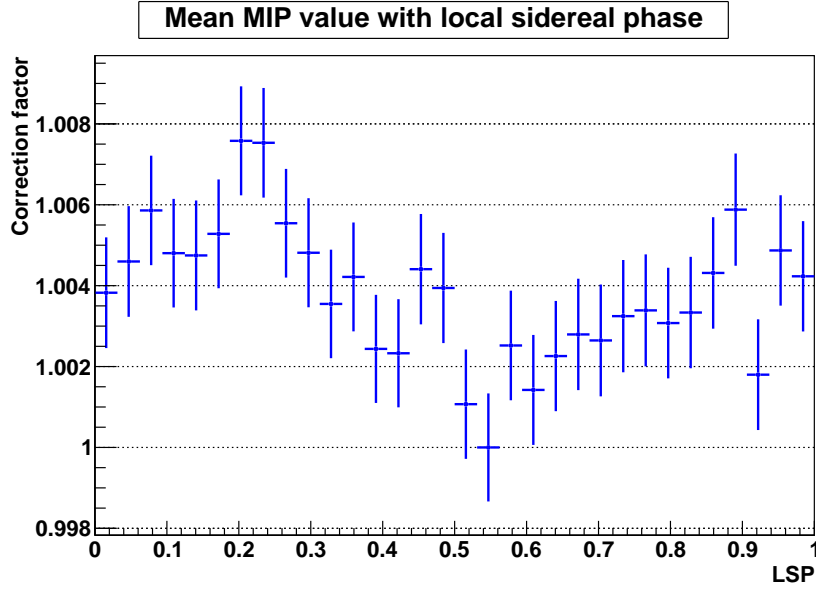


Figure 6.30: MIP distribution as a function of the local sidereal phase for the horizontal central module. The MIP value was normalised to the lowest MIP of the horizontal central module. One observes that the latter is located at the end of run 4 (see Figure 6.29).

on this correction is evaluated as the statistical uncertainty coming from the correction  $c_{\text{Run}}$ . The  $+1\sigma$  error estimation is defined as the highest possible correction factor. It is obtained by maximising each corrections shown on Table 6.8 except the correction on run 4 2012, which should be minimised to increase difference with run 4 2013 (run 4 2012 has a larger event rate than run 4 2013). Figure 6.41 (right) shows the  $\pm 1\sigma$  corrections. One observes the relative error on the shape correction varies from 1.0002 to 1.0007 for the  $+1\sigma$  error. Therefore, a 0.05% systematic error is expected. Thus, the systematic error is neglected.

### 6.3.4 Summary

Figure 6.42 shows the distribution of the  $\nu_\mu$  rate versus the local sidereal phase after having applied the corrections. Only the statistical error is relevant, as the systematic error coming from all the sources was found to be negligible, as we summarised in Table 6.9.

We will search for Lorentz invariance violation quantitatively using two different methods, the Fourier transform shown in Section 6.4 and the likelihood method shown in Section 6.5.

## 6.4 The discrete Fourier transform

We perform the Lorentz violation search using two different methods to increase the discovery potential of this study. First, we use a Fourier transform to deduce the  $C, A_s, A_c, B_s, B_c$  coefficients from Equation 6.1.25. In the case of a LV effect, the  $\nu_\mu$  disappearance probability should vary with fixed frequencies. Namely, the expansion of Equation 6.1.25 shows that the expected variations occur for fixed angular frequencies which are multiples of the sidereal (angular) frequency:  $\omega_\oplus$ ,  $2\omega_\oplus$ ,  $3\omega_\oplus$  and  $4\omega_\oplus$ . Since the angular frequencies are fixed, only the associated amplitudes should be fitted. A discrete Fourier transform is therefore completely adapted, and the amplitudes are directly given in the angular frequency space. Since we are searching for the multiples of the sidereal angular frequency, the sampling size in the angular frequency space should be one sidereal angular frequency  $\omega_\oplus$ . As for the extension, the angular frequency phase space should at least spread from 0 to  $4\omega_\oplus$  in the present case. Note the case  $0 \cdot \omega_\oplus$  represents the constant (non oscillating) term. Therefore, the sampling should be done to contain at least five bins of width  $\omega_\oplus$  in the phase space of the angular frequency. The discretisation is therefore done denoting the angular frequency bin with  $n \in [0, N]$  with  $N = 5$  in this example. It implies each bin corresponds to  $n \cdot \omega_\oplus$ . The probability of  $\nu_\mu$  disappearance at a

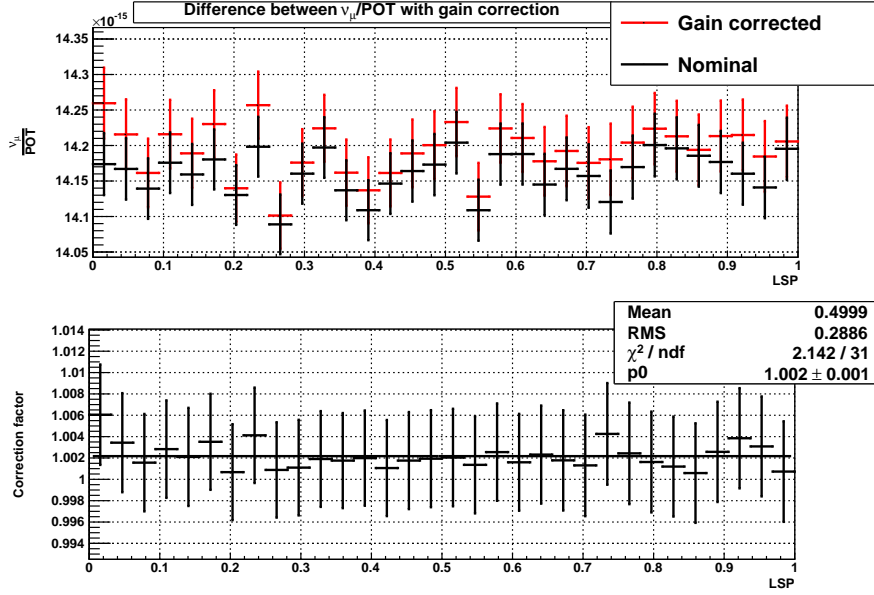


Figure 6.31: (Top) Comparison between the nominal distribution of the  $\nu_\mu$  per POT with LSP and the same distribution after applying the gain correction. A constant function is fitted to the (corrected/uncorrected) ratio which is shown on the bottom. The small  $\chi^2/\text{NDF} = 0.07 \ll 1$  value indicates that this ratio is time independent.

given angular frequency bin  $n$  is denoted as  $\mathcal{P}[n]$ . The probability of  $\nu_\mu$  disappearance in the local sidereal phase space can therefore be deduced as a superposition of the five plane waves having the angular frequencies  $n \cdot \omega_\oplus$  ( $n \leq 4$ ) and different amplitudes. In the most general case, the sidereal phase (time) space is continuous, and one should use a Fourier transform that is continuous for sidereal phase and discrete for the angular frequency. In our case, we will also sample the local sidereal phase space for computational reasons, and use a pure discrete Fourier transform. The same binning  $N = 5$  should therefore be used, and  $k \in [0, N]$  represents each bin in local sidereal phase ( $\text{LSP} = k/N$ ). The probability of  $\nu_\mu$  disappearance in the local sidereal phase can therefore be written as:

$$P[k] = P_{\text{Re}}[k] + iP_{\text{Im}}[k] = \frac{1}{N} \sum_{n=0}^{N-1} \mathcal{P}[n] e^{\frac{ikn}{N}} \quad (6.4.1)$$

The inverse transformation is used to determine the spectral amplitudes associated to each angular frequency  $\mathcal{P}[n]$  (with  $\omega = n \cdot \omega_\oplus$ ):

$$\mathcal{P}[n] = \mathcal{P}_{\text{Re}}[n] + i\mathcal{P}_{\text{Im}}[n] = \sum_{k=0}^{N-1} P[k] e^{-\frac{ikn}{N}} \quad (6.4.2)$$

One observes that the sampling used  $N \geq 5$  is determined by the prior knowledge on the sidereal angular frequencies that are searched. It shows that the discrete Fourier transform method is only adapted to signals which angular frequency is known. In the opposite case, a continuous spectrum should be searched through a continuous Fourier transform. For computational reason, we avoided this method in our case.

A fast Fourier transform method (FFT) is used to perform the discrete Fourier transform [104]. Such a method allows to reduce the number of needed operations to Fourier transform the signal, from roughly  $N^2$  to  $N \times \log_2 N$ . In the case of  $N = 5$  bins, this method does not have any significant interest. However,  $N$  also corresponds to the sampling we use in the sidereal phase space. Therefore, one needs to choose a larger binning than  $N = 5$  in order not to reduce the sensitivity to the signal. Since the fast Fourier transform method requires a binning choice of the form  $N = 2^L$ , we have used  $L = 5$  i.e.  $N = 32$  bins in this analysis. This is a compromise between the sample statistics in each bin and the goal not to wash out the oscillations with too small a binning. Since the input signal data shown in Figure 6.42

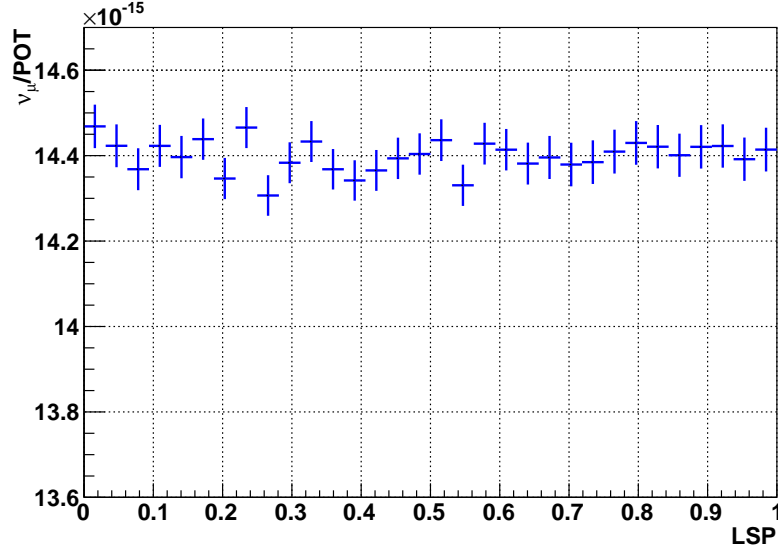


Figure 6.32:  $\nu_\mu$  rate versus LSP distribution after pile-up, MPPC dark noise, and MPPC gain corrections have been taken into account.

is real, one shows that the FFT method provides the symmetric result in spectral amplitudes [104]:

$$\mathcal{P}[N - n] = \mathcal{P}[n]^* \quad (6.4.3)$$

The fast Fourier transform method provides both the real part, imaginary part and module of the amplitude corresponding to each of the 32 Fourier modes. For the latter, since it is a real quantity, we derive from Equation 6.4.3 that the module of the amplitude is symmetric for bins  $N \in [1, N/2]$  and  $N \in [N/2 + 1, N]$ .

In this analysis, we will only study the module of the amplitude corresponding to each Fourier mode. Though these amplitudes are complex, it is not the purpose of this Fourier analysis to provide a fit of the phase for each parameters. We will only probe the potential sidereal time variations, whose impact is directly a function of the module of the amplitude. Since the Fourier transform separate the impact of each mode on the distribution, the relative phase between the amplitudes has no impact on the discovery potential since no destructive interferences occur. This is an advantage of the Fourier transform, and one of the main reason we have used it. We will therefore only study the module of each amplitudes of the fifth first Fourier modes, that we will denote as “magnitude”, naturally defined as:

$$\text{MAG} = |F[n]| = \sqrt{(F_{Re}[n])^2 + (F_{Im}[n])^2} \quad (6.4.4)$$

Figure 6.43(left) shows an example of a Fourier transform on a flat distribution with the sidereal phase. One observes that the first (flat) mode is enhanced, while the other modes are negligibly small. Since we do not expect any impact of Lorentz invariance violation on the Fourier modes from the sixth to the fifteenth one, their value can be used as an evaluation of the pure statistical fluctuations. Therefore, one expects a Lorentz violation signal to appear if one of the second to the fifth Fourier mode is enhanced comparatively to the higher Fourier modes.

### 6.4.1 Sidereal time variation thresholds

We will search for an evidence of Lorentz violation *i.e* a  $3\sigma$  deviation with the Standard Model, which is defined as a  $3\sigma$  deviation of the  $\nu_\mu$  survival probability with local sidereal phase as compared to a flat ( $P=1$ ) survival probability. It provides a model independent constraint on sidereal variations, since only the compatibility with no sidereal variation is tested (in the modes of  $\omega_\oplus$ ,  $2\omega_\oplus$ ,  $3\omega_\oplus$  and  $4\omega_\oplus$  angular frequencies only). Figure 6.42 shows the signal analysed is the number of selected  $\nu_\mu$  per POT. We will determine the  $3\sigma$  detection threshold as follow:

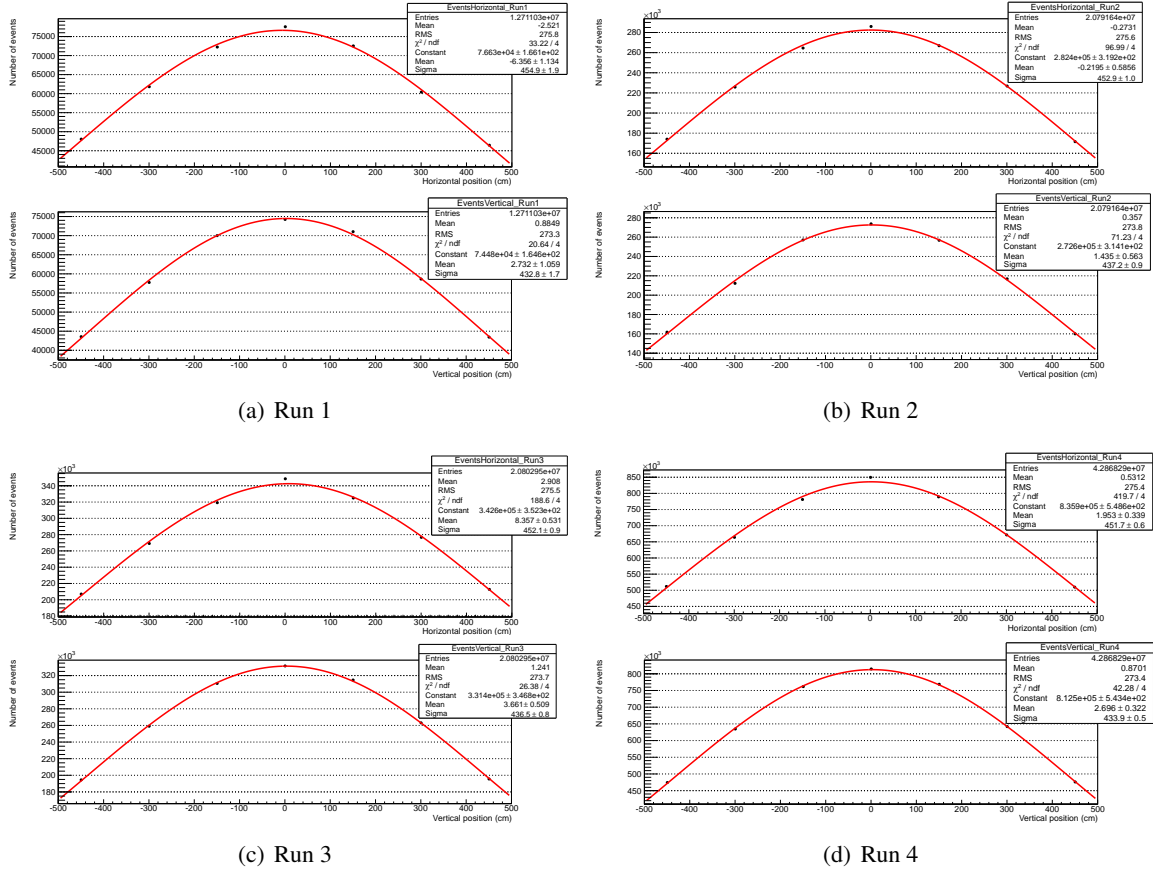


Figure 6.33: The  $\nu_\mu$  horizontal and vertical beam profiles for the different T2K runs.

1. Using the data signal shown in Figure 6.42, 10,000 toy experiments are generated by randomly shuffling the time of each event. We expect therefore the potential sidereal variations to be removed, which provides a set of 10,000 flat toy experiments. Figure 6.44 shows an example of these flat toy experiment.
2. We apply the FFT method on each toy experiment and determine the magnitude of each of the relevant five Fourier modes : constant,  $\omega_\oplus$ ,  $2\omega_\oplus$ ,  $3\omega_\oplus$  and  $4\omega_\oplus$ .
3. We therefore construct the distribution of each Fourier mode for the 10,000 flat toy experiments.
4. A  $3\sigma$  threshold  $p_n$  ( $n \leq 4$ ) is then determined for each Fourier mode. This threshold is defined at the FFT magnitude value for which only 0.27% of the toy experiments provide higher Fourier mode magnitude. In other terms, it corresponds to the upper value for which 99.73% of the flat toy magnitude are located at lower values, which corresponds to a  $3\sigma$  threshold. In the present case, it represents the value for which only 27 events are located above:

$$\int_{Mag=0}^{Mag=p_n} (\text{MAG FFT})_n = 0.9973 \quad (6.4.5)$$

where  $n$  denotes the Fourier mode.

5. We will claim we observe a  $3\sigma$  deviation from no sidereal variation if data crosses at least one of the four non flat thresholds.

Figure 6.45 shows the distribution of the different Fourier mode magnitudes. One observes that the distributions are very similar between the different modes, which is expected since the pure statistical variations should impact the different mode in the same proportions. Consequently, the  $3\sigma$  threshold is the same for all the Fourier mode, and has been found equal to  $p_n = 0.026$ ,  $0 < n < 5$ . The data will therefore present a  $3\sigma$  deviation from the no sidereal variation hypothesis if one of its Fourier mode amplitude is higher than 0.026. We will show the result on data in Section 6.4.4.

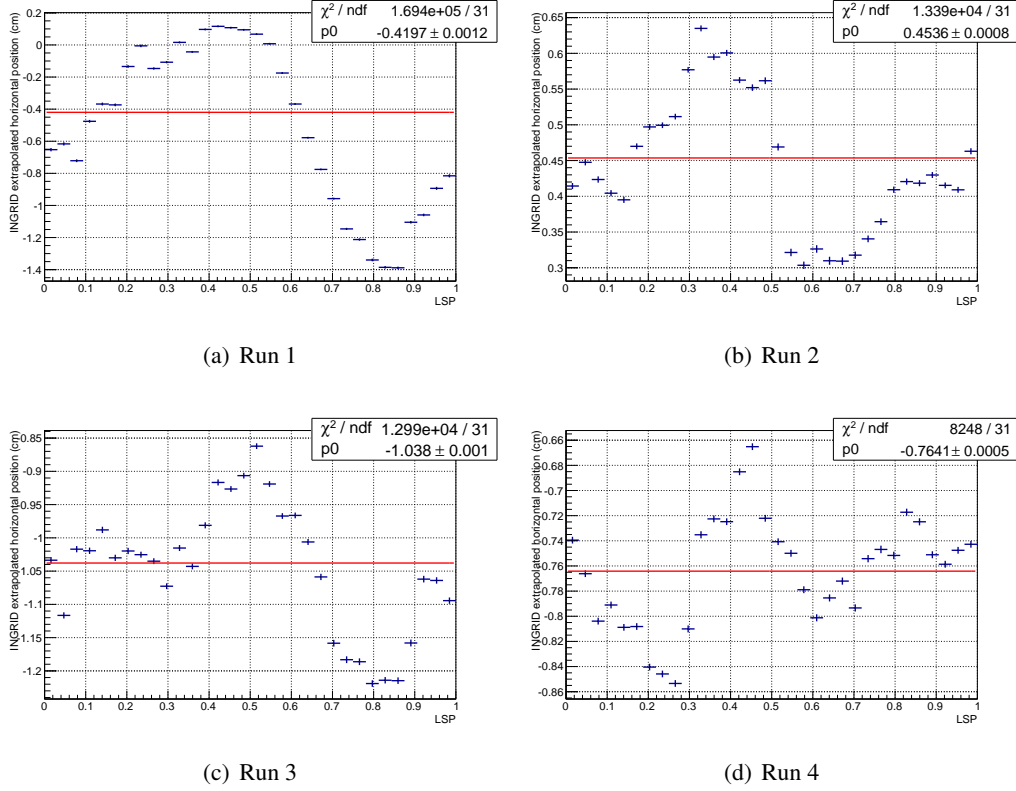


Figure 6.34:  $\nu_\mu$  beam horizontal beam positions in the Silicon pixel part of the MuMon for the different T2K runs.

### 6.4.2 Sensitivity on the SME parameters

We have shown in Section 6.1.3 that the Lorentz violation impacts on short baseline oscillations through twenty parameters, namely  $a_{\mu\mu}^\alpha$  4-vector and  $c_{\mu\mu}^{\alpha\beta}$   $4 \times 4$  matrix. One shows [105] that the  $c_{\mu\mu}^{\alpha\beta}$  matrix is symmetric, which involves the reduction from twenty to fourteen parameters. These coefficients are complex, which implies that there are twenty eight real degrees of freedom. Considering the Lorentz violation only impacts on the five Fourier modes  $n \cdot \omega_\oplus$  ( $n \leq 4$ ), the constraints that will be extracted on the twenty eight parameters will be very highly correlated. We will develop in Section 6.5 a likelihood method to reduce these correlations by increasing the number of fitted parameters.

In this situation, we have adopted the same strategy used in the Lorentz violation search of the MINOS experiment [106]. In this approach, the correlations between the SME parameters are neglected. Though we do not expect this method to give the appropriate constraints, we have used it in this study in order to present this T2K result in the same way as MINOS. Moreover, it provides first hints of the sensitivity of this analysis. This approach follows the following strategy for each of the  $a_{\mu\mu}^\alpha$  and  $c_{\mu\mu}^{\alpha\beta}$  coefficients. For clarity, let's take the example of the  $a_{\mu\mu}^X$  coefficient:

1.  $a_{\mu\mu}^\alpha$  and  $c_{\mu\mu}^{\alpha\beta}$  coefficients are set to zero.
2.  $a_{\mu\mu}^X$  is increased by a given small step compared to the expected sensitivity (namely,  $10^{-23}$  GeV step). The corresponding  $\nu_\mu$  variation with local sidereal phase distribution is generated.
3. The FFT is applied on the distribution and the magnitude of the modes  $n=1$  to 5 is tested. If one of the  $3\sigma$  thresholds is crossed in these bins, one stops and the current  $a_{\mu\mu}^X$  value represents the sensitivity we have on this parameter. If none of the thresholds is crossed (which should be the case for the first iteration, if not, change the step),  $a_{\mu\mu}^X$  is increased again by the  $10^{-23}$  and the same procedure is applied.
4. This procedure ends when one of the  $3\sigma$  threshold is crossed, and the current  $a_{\mu\mu}^X$  value is therefore the  $3\sigma$  sensitivity of this analysis to the  $a_{\mu\mu}^X$  coefficient. Figure 6.46 shows the  $\nu_\mu$  variation with

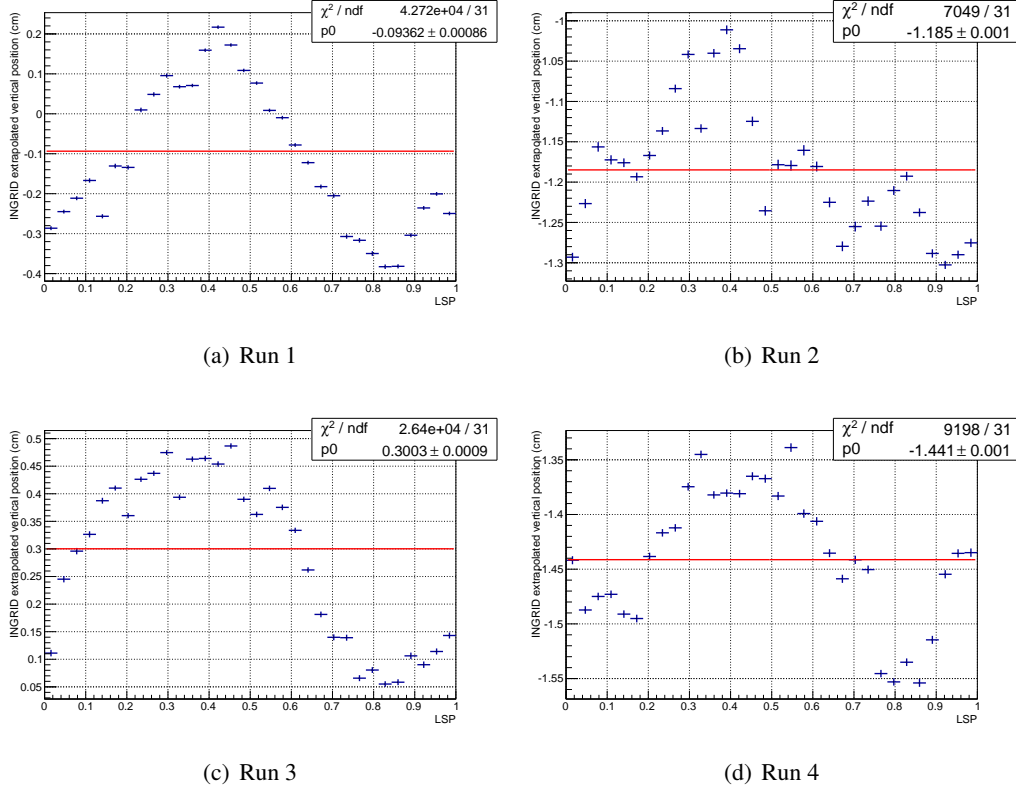


Figure 6.35:  $\nu_\mu$  beam vertical beam positions in the Silicon pixel part of the MuMon for the different T2K runs.

local sidereal phase and the associated FFT in the example of the  $a_{\mu\mu}^X$  value introducing a  $3\sigma$  deviation from the flat hypothesis (namely  $a_{\mu\mu}^X = 4.0$  GeV). One observes the threshold crossing in the Fourier mode  $n=2$ .

As we explained, this totally neglects the correlations between the coefficients since all others coefficients are set to zero except the one which is studied. Moreover, it removes possible sensitivity to some coefficients. Namely, in the example of the  $a_{\mu\mu}^T$  coefficient, one observes in Equation 6.1.22 that this coefficient only impacts the shape of the sidereal time variation by coupling to other coefficients. If all the others are set to zero, this term only contributes to the rate, and therefore, we have no sensitivity on it in this analysis. It shows the limit of this approach that neglects the correlations. In a similar way, we show that the coefficients  $a_{\mu\mu}^T$ ,  $a_{\mu\mu}^Z$ ,  $c_{\mu\mu}^{TT}$ ,  $c_{\mu\mu}^{TZ}$  and  $c_{\mu\mu}^{ZZ}$  only impact the rate if all other coefficients are set to zero. It therefore reduces the number of parameters from twenty eight to eighteen real degrees of freedom. Finally, this assumption that all other parameters are null except the one tested implies that the phase of the coefficient has absolutely no impact on the  $\nu_\mu$  survival probability, as one observes in Equation 6.1.25 which becomes for example for  $a_{\mu\mu}^X$ :

$$P_{\nu_\mu \rightarrow \nu_\mu} = \left(\frac{L}{hc}\right)^2 |\hat{N}^Y (a_L)_{ab}^X \sin(\omega_\oplus T_\oplus) - \hat{N}^X (a_L)_{ab}^X \cos(\omega_\oplus T_\oplus)|^2 = \left(\frac{L}{hc}\right)^2 |(a_L)_{ab}^X|^2 |\hat{N}^Y \sin(\omega_\oplus T_\oplus) - \hat{N}^X \cos(\omega_\oplus T_\oplus)|^2 \quad (6.4.6)$$

Therefore, the real degrees of freedom corresponding to the phase have no impact in this approach. This reduces the number of constraints on real coefficients from eighteen to nine. We will therefore summarise the  $3\sigma$  sensitivity for these nine parameters. Using the method we described above, we provide the  $3\sigma$  sensitivity Table 6.10. It first confirms that the short baseline oscillation in INGRID are sensitive to a  $\sim 10^{-20}$  GeV effect, which shows the sensitivity of this study to Planck scale effects. Second, the sensitivity is higher for the  $c_{\mu\mu}^{\alpha\beta}$  coefficients since their effect is enhanced by the neutrino energy as we explained in Section 6.1.

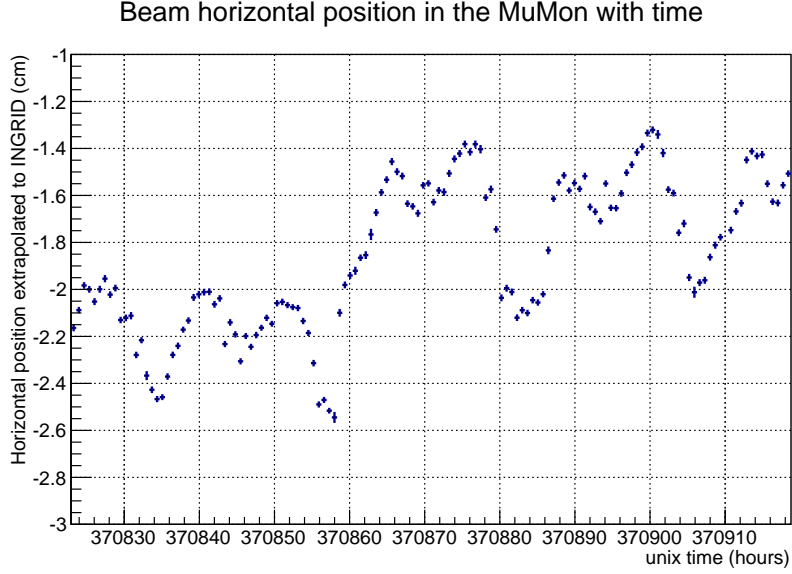


Figure 6.36:  $\nu_\mu$  beam horizontal beam position variation in the MuMon with time during a given time period of the T2K data taking. The tidal effect every  $\sim 6$  hours can be seen.

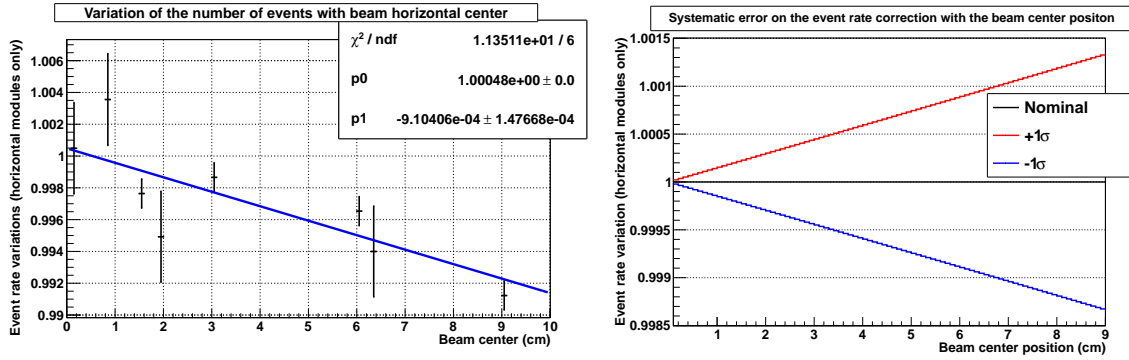


Figure 6.37: Left: number of  $\nu_\mu$  events with different beam horizontal center positions. A linear decrease with the beam center position difference with the INGRID center is assumed. The fitting result shows the relative variation on the number of events in the horizontal module to be  $9.1 \times 10^{-4} \cdot \text{Beam center (cm)} + 1$ . Right: the associated systematic error on the correction with the center beam position (comes from the fitting error).

### 6.4.3 Day and night LSP distributions

Whether a Lorentz violation effect exists or not, one does not expect any difference between the day and night distributions of events with local sidereal phase. However, one expects different beam and detector conditions between the two samples, since, for example, beam tuning mainly occurs in the morning, or temperature is lower at night. Therefore, the comparison between day and night provides a control sample that tests if the corrections that are applied (Section 6.3) are effective and provide a signal sample where LSP variations from detector and beam effects are washed out. The day and night samples are constructed using the very same data sample used for the analysis, separating the day as events occurring from 6 a.m. to 6 p.m. JST, and night as the complement. Figure 6.47 shows the day and night event rate distribution with the sidereal phase. The straight line fit shows that the day and night event rate distributions are the same within the statistical error. This agreement is further checked by applying the FFT method to both the day and night distributions. To be conservative, the detector and beam effects correction will be considered effective if both the day and night magnitude of each Fourier mode are below the  $3\sigma$  detection threshold determined in Section 6.4.1. This is conservative because the thresholds were determined analyzing the full data sample, but the statistics pertaining to day and night samples are about one half of the full data sample. The magnitude of

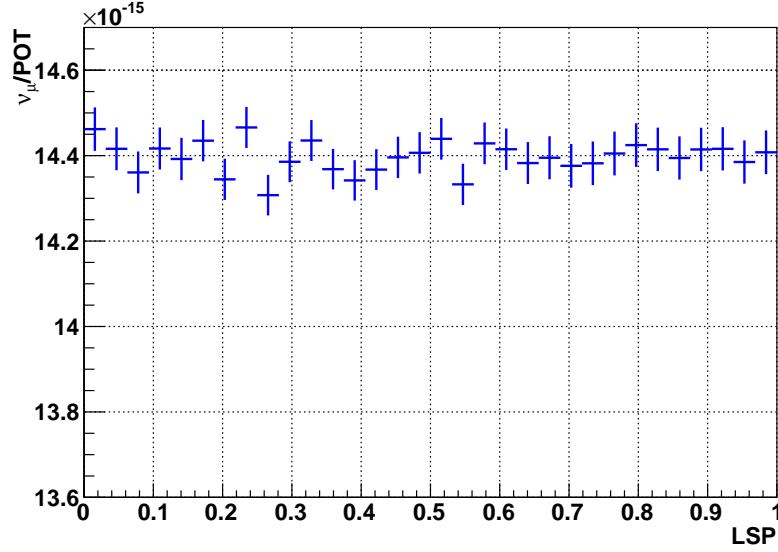


Figure 6.38:  $\nu_\mu$  rate versus LSP distribution after pile-up, MPPC dark noise, MPPC gain, and beam position corrections have been taken into account.

each Fourier mode are shown in Figure 6.48 for both day and night. It confirms the quality of the corrections that were applied, and the readiness of the sample for data unblinding. It is important to point out that a variation was originally seen before the corrections were applied, as shown in Figure 6.49. This variation was mostly washed out by the corrections presented in Section 6.3.3. By confirming the efficiency of the corrections we applied, this control sample leads us to apply the FFT on the data in Section 6.4.4.

#### 6.4.4 Results

We first measure the data compatibility with the no sidereal variation hypothesis. For this purpose, we apply the FFT on the data distribution shown in Figure 6.42 and we display the result in Figure 6.50. One observes that none of the magnitude for the Fourier modes  $\omega_\oplus$ ,  $2\omega_\oplus$ ,  $3\omega_\oplus$  and  $4\omega_\oplus$  overcomes the  $3\sigma$  threshold. It implies the INGRID number of  $\nu_\mu$  per POT is compatible with no sidereal time variation hypothesis. We summarise the value of each Fourier mode of data in Table 6.11, along with the associated p-value to be a statistical fluctuation of a flat LSP distribution. One observes no effect even above  $1\sigma$ .

Therefore, this measurement provides the  $3\sigma$  constraints on the SME parameters listed in Table 6.10. For comparison purpose, we have shown the latest constraints from the MINOS, MiniBooNE and Double Chooz studies in Table 6.1 using both their neutrino and antineutrino modes. It shows the MINOS experiment is more sensitive to the Lorentz violation effect at the near detector **under the assumption of uncorrelated effects on the sidereal time variation of the different SME parameters**. This can be understood since the MINOS near detector has a longer baseline  $L \sim 1$  km (which impacts on all the coefficients), and a flux average larger energy which impacts on the  $c_{\mu\mu}^{\alpha\beta}$  coefficients. However, the MINOS study assumes no correlations between the coefficients. We will show in the next paragraph that these correlations are crucial to take into account.

**Correlations** Here, we have studied only two parameter correlations for clarity purpose. We will show the impact of the correlations on the detection threshold. To do so, we apply the same procedure as we defined in Section 6.4.2, but keeping two coefficients different from 0 instead of only the varied coefficient. In the example of the correlations between the  $a_{\mu\mu}^X$  and  $a_{\mu\mu}^Y$  coefficients, we select a value of  $a_{\mu\mu}^Y$  and determine the  $a_{\mu\mu}^X$  value for which the  $3\sigma$  detection threshold is overcome. Changing  $a_{\mu\mu}^Y$  to other values, one studies the impact of the correlations on the sensitivity to the  $a_{\mu\mu}^X$  parameter. Figure 6.51 shows the variation of the sensitivity on the  $a_{\mu\mu}^X$  parameter for different values of  $a_{\mu\mu}^Y$  and

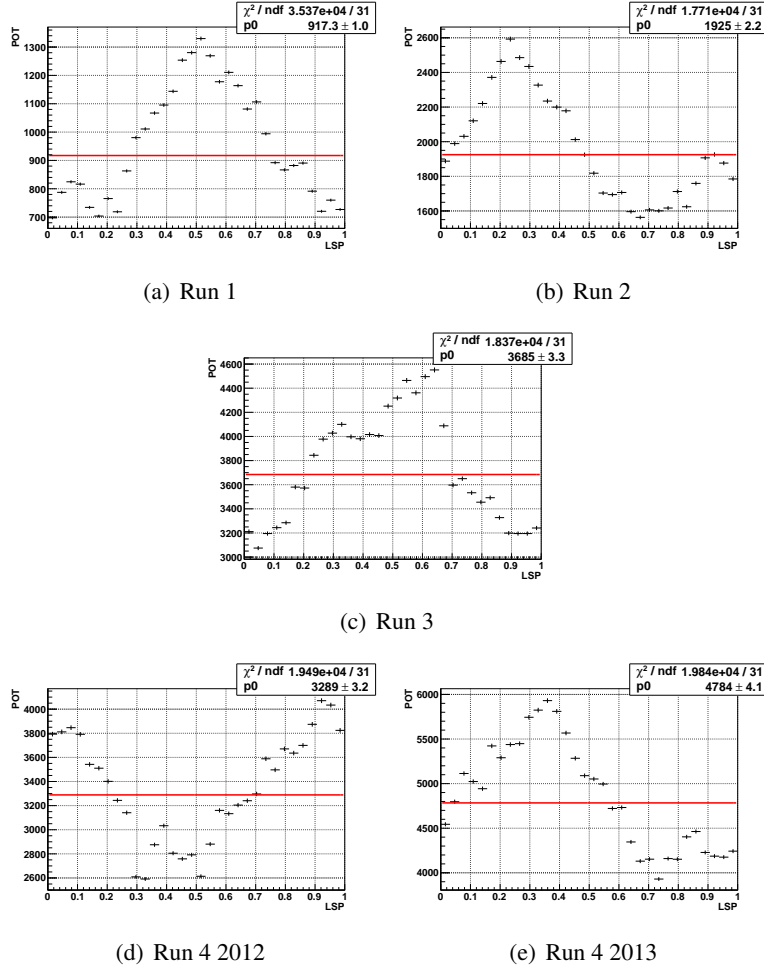
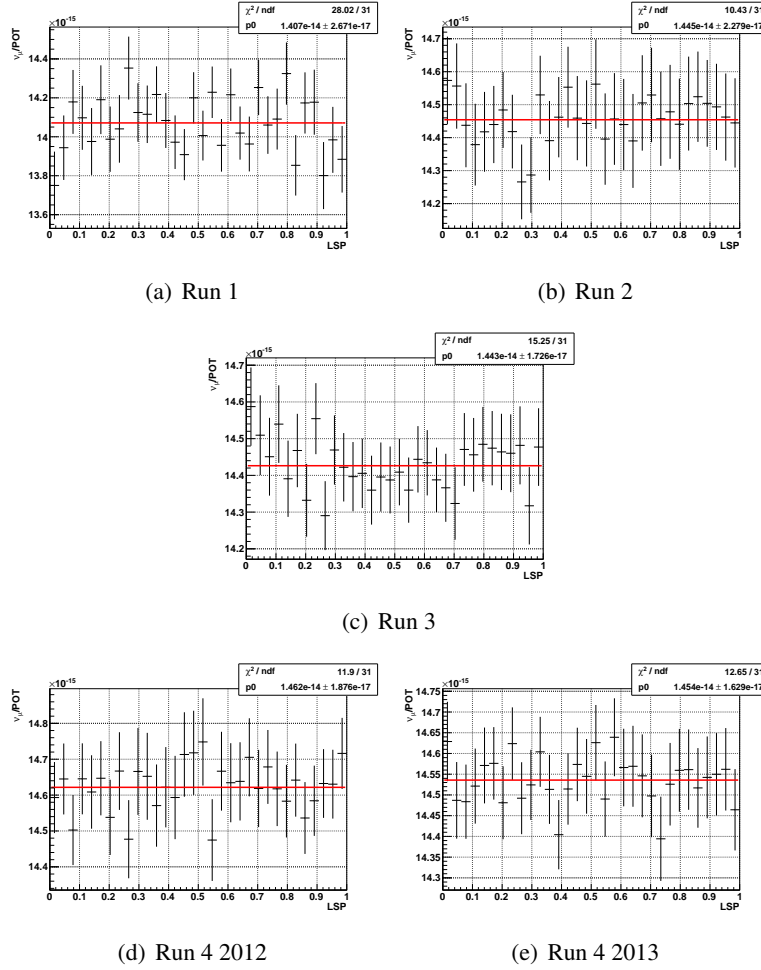


Figure 6.39: POT distributions versus LSP for the different runs.

$c_{\mu\mu}^{TX}$ . One observes an anticorrelation with the  $a_{\mu\mu}^Y$  parameter, which reflects that lower  $a^X$  value are needed to explain a  $3\sigma$  deviation from the flat hypothesis for larger  $a^Y$ . Therefore, the sensitivity on  $a^X$  increases with larger  $a_{\mu\mu}^Y$  value. This trend is a function of the neutrino beam direction as shown in Equation 6.1.22, and can be inverted in the case of MINOS for example. We conclude that the study assuming no correlations underestimates the sensitivity on the  $a^X$  parameter since we assumed  $a^Y = 0$ . One observes that the impact is large, and a  $2 \times 10^{-20}$  GeV  $a^Y$  (which is not rejected by MINOS) can change the sensitivity of this study to  $a^X$  from  $4.0 \times 10^{-20}$  GeV to  $3.5 \times 10^{-20}$  GeV in the simple case of only two parameter correlations. One notes that the two point correlations does not represent the complexity of the whole correlations, and that higher effects can be even expected. Since this effect is different in MINOS, the sensitivity shown in Table 6.10 does not represent the real sensitivity of this analysis, and does not show that the sensitivity is better in MINOS (Table 6.1). Finally, a more problematic issue is observed studying the impact of  $c_{\mu\mu}^{TX}$  on the sensitivity to the  $a_{\mu\mu}^X$  parameter. One observes in Figure 6.51 that a higher  $c_{\mu\mu}^{TX}$  value implies a lower sensitivity to  $a_{\mu\mu}^X$  (larger value to cross the threshold). It shows our sensitivity provided in Table 6.10 can potentially be overestimated. Therefore, neglecting the correlations can lead to reject the Lorentz violation for energies at which the violation occurs, and miss the effect.

In a nutshell, the FFT provides the most sensitive method to sidereal variations, but is not adapted to extract the associated limits on the SME parameters. In order to solve this issue, we developed a likelihood method we will show in the next Section 6.5.

Figure 6.40: Number of  $\nu_\mu$  per POT distributions versus LSP for the different runs.

## 6.5 The likelihood method

### 6.5.1 Motivations

As we have seen, there is a large number of SME coefficients and we only use one data set in this analysis. It implies that important correlations exist between the coefficients. For this reason, the parameters should not be treated as independent. To extract the best limits on the SME coefficients, we develop a 5 parameter fit to fit the  $C$ ,  $A_s$ ,  $A_c$ ,  $B_s$  and  $B_c$  amplitudes (Equation 6.1.25) which are linear combinations of the SME coefficients. A full 20 SME coefficient fit was initially desired, but because of the high degeneracy of the fitter in the SME coefficients, this method was discarded.

The fit is based on a binned likelihood method. Though using bins may slightly underestimate our sensitivity due to loss of information from binning, the high statistics of the INGRID sample tends to reduce differences between unbinned and binned likelihood methods. Moreover, a binned likelihood method easily allows determination of the goodness of fit, that we will test in 6.5.2.

The binning used in the FFT method is used for the likelihood method, namely 32 bins in LSP. As shown in Section 6.3, only statistical errors are meaningful in this analysis. The statistical errors are Poisson distributions in each local sidereal phase bin. Considering the very high statistics of each bins, we will work in the gaussian approximation for simplicity. In each data LSP bin, the probability that a given MC simulation corresponds to data in the  $i$ -th local sidereal phase bin is:

$$P_i = e^{-\frac{(d_i - m_i)^2}{2\sigma_i^2}} \quad (6.5.1)$$

where  $d_i$  and  $m_i$  are the  $\frac{\nu_\mu}{\text{POT}}$  respectively in data and MC, and

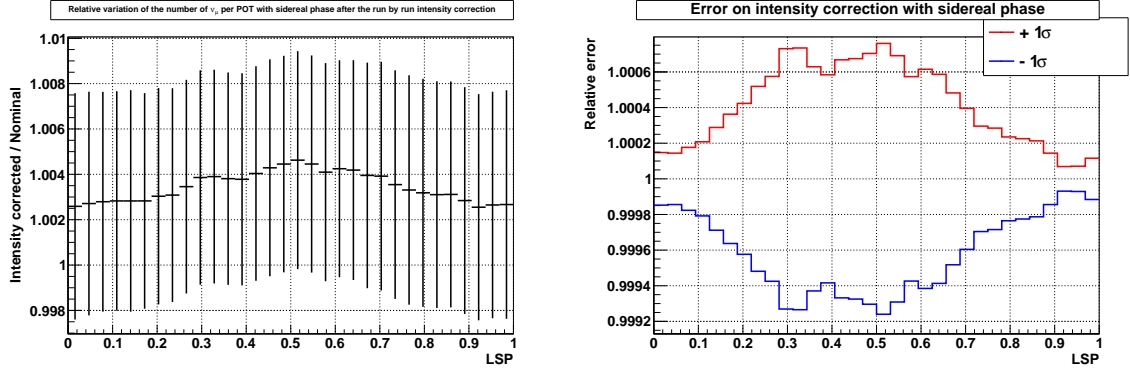


Figure 6.41: The relative correction coming from run per run event rate correction (left) and the associated relative variation of this correction from the  $\pm 1\sigma$  systematic error.

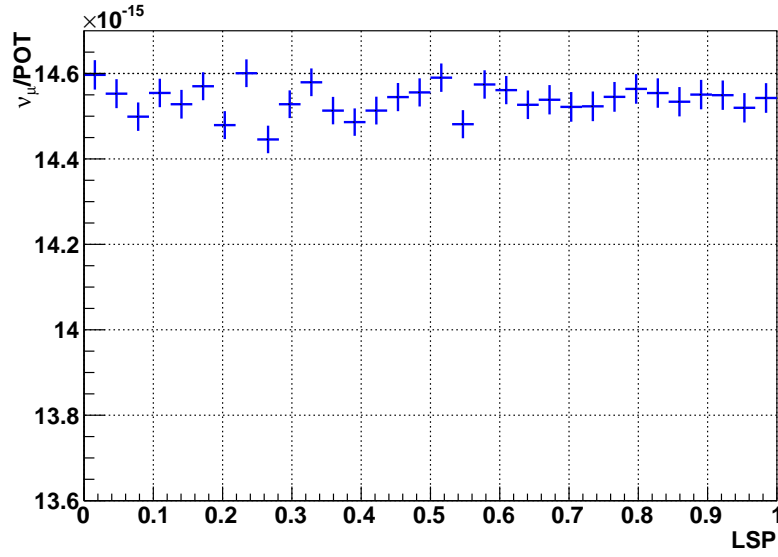


Figure 6.42: Corrected  $\nu_\mu$  event rate versus LSP.

$$\sigma_i = \frac{\nu_\mu}{\text{POT}} \sqrt{\frac{\delta \nu_\mu^2}{\nu_\mu^2} + \frac{\delta \text{POT}^2}{\text{POT}^2}} \quad (6.5.2)$$

Based on this probability, the binned likelihood fit is constructed as:

$$L = \prod_{i=1}^{32} P_i = \prod_{i=1}^{32} e^{-\frac{(d_i - m_i)^2}{2\sigma_i^2}} \quad (6.5.3)$$

**Real coefficients:** As we explained, we will only fit the five coefficients  $C$ ,  $A_s$ ,  $A_c$ ,  $B_s$  and  $B_c$ . Moreover, we will only fit the shape of the distribution. Finally, we will assume in this fit that these five coefficients are real, and therefore, that no relative phase effect impacts the result (apart from phase shift  $0 \rightarrow \pi$  for negative coefficients). Though a complex coefficient fit was attempted, we have shown it does not provide any constraint on the phase of each coefficient due to the limited amount of information of the  $\nu_\mu$  distribution. Using an energy dependent study as shown in Section 6.6, this complex coefficient fit may be used in the future with a larger statistics.

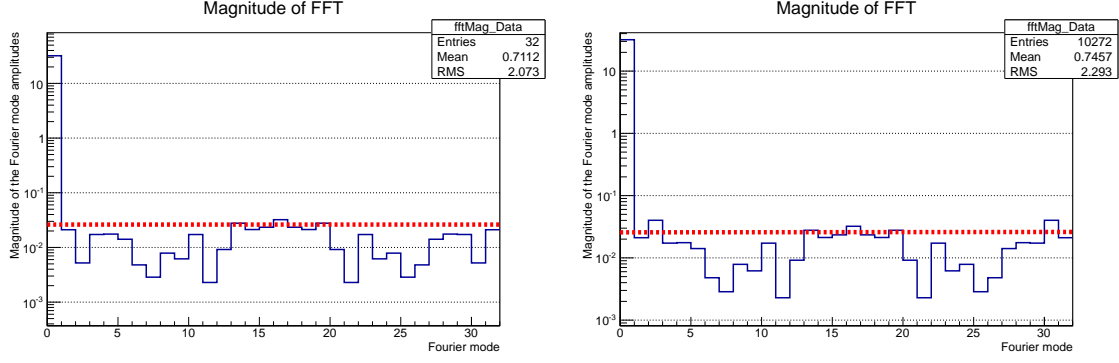


Figure 6.43: Magnitude of each Fourier modes in the case of no sidereal variation of the  $\nu_\mu$  per POT rate (left) and in the case of an example where the variation is significant (right). In red, we have shown the magnitude value above which a  $3\sigma$  deviation with the flat hypothesis is observed. This threshold is detailed in Section 6.4.1. One observes this enhancement of the Fourier mode  $n=2$  ( $2\omega_\oplus$ ) in the case of significant sidereal variation. Note that the highest Fourier modes (13 and 16) do cross this threshold by pure statistical fluctuations. The coincidence of this effect on the two Figures and in Figure 6.46 is only due to the fact we generated exactly the same fluctuations in these examples.

**Minimisation method** We have used the MINUIT [107] package as the minimisation method to provide the likelihood best fit values. One understands the errors associated will be asymmetric in this analysis, since the values are close to zero which is not favoured by the fitter. For this reason, we have used the “MIGRAD” MINUIT minimisation method, and then, the “MINOS” method to provide the correct asymmetric errors for each parameter and the correlations between them. The fitter performances are first checked. They are described in Appendix G. We verify that the fitter converges and is unbiased, and that the errors are correctly estimated in Appendix G.1 and G.2. We will test the performance of the algorithm on the fit of only one parameter to study whether the fitter is unbiased. It is necessary since it removes the possible correlations between parameters that can affect the fitter central value, and mimic a bias where there is actually none. We will then apply the fitter on the data in Section 6.5.2 and provide the latest constraints on the Lorentz violation search in INGRID.

## 6.5.2 Results

We finally apply the fitting method to the data. We have summarised the best fit value for each parameter in Table 6.12. The large correlations between the coefficients are shown in Figure 6.55. Figures 6.52 to 6.54 show three projections of the five-dimensional coefficient space, with the best fit,  $1\sigma$  and  $2\sigma$  contours.

One observes that the sensitivity of this analysis reaches  $\sim 10^{-20}$  GeV, which shows we are able to measure possible suppressed Lorentz invariance violation effects occurring at the Planck scale. It confirms the result obtained with the FFT, but taking into account the correlations. Moreover, we confirm that none of the parameter shows a deviation from the Standard Model above  $1\sigma$  in this energy range of parameters. Therefore, we conclude that we do not measure any hint of Lorentz invariance violation using the INGRID near detector in the energy phase space region corresponding to  $\gtrsim 10^{-20}$  GeV.

## 6.6 Energy dependent study

### 6.6.1 INGRID module energy

As described in Equation 6.1.22, the 5 SME parameters  $C$ ,  $A_s$ ,  $A_c$ ,  $B_s$  and  $B_c$  depend on the neutrino energy,  $E$ . Particularly, the  $C$ ,  $A_s$ , and  $A_c$  coefficients are composed of an energy-independent part and an energy-dependent part which is linear in  $E$ . Using different neutrino energies, it may be possible to decorrelate the effect of the energy-independent and energy-dependent part of these coefficients. The

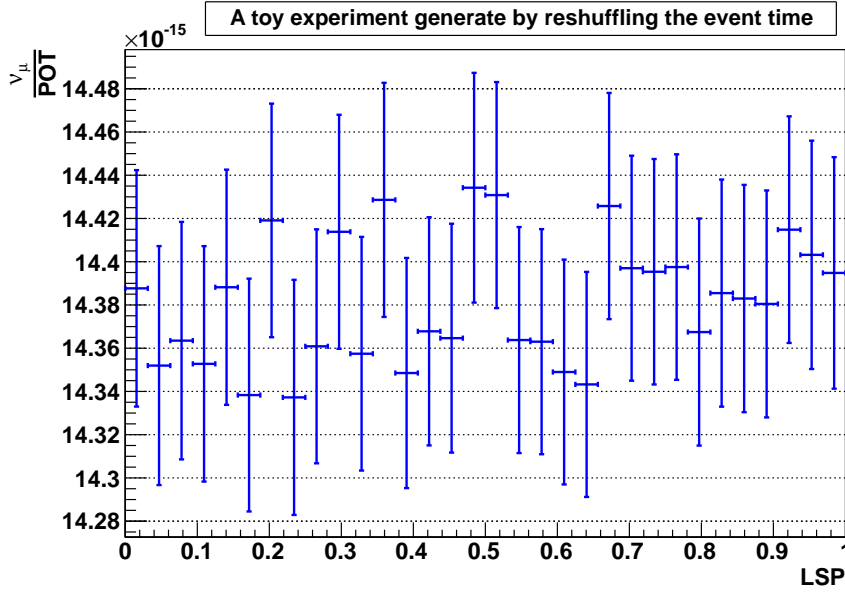


Figure 6.44: An example of a flat toy experiment, randomly chosen among the 10,000 experiments.

energy dependence is studied within INGRID itself because of its high statistics and high neutrino energy that enhance LV effects. The INGRID cross geometry covers off-axis angles from  $0^\circ$  to  $1.0^\circ$  and so, different neutrino energies. Figure 6.56 shows the neutrino energy spectrum variations for these different off-axis angles, whose mean energies are summarised in Table 6.13. Figure 6.22 summarises the module numbers.

As shown in Equation 6.1.25 and 6.1.22, the oscillation probability does not depend linearly on the neutrino energy, but rather on  $E^2$ . Therefore, the mean neutrino energy in a module cannot be substituted to the actual neutrino flux. While the main energy peak position differs greatly between modules (covering from 1.2 GeV to 1.6 GeV), the mean neutrino energy is roughly the same. This is the consequence of high energy neutrino for which the parent mesons are not focused by the magnetic horns which are tuned for lower energies. Therefore, these events are isotropic in space and affect the mean neutrino energy in the same proportion for all the modules. For these two reasons, we study the LV energy dependency by implementing the true neutrino flux for each module instead of a mean neutrino energy.

### 6.6.2 LV energy dependent study

Various LV signals are implemented in toy MC experiments. Differences between the most extreme modules (namely, central module 3 and edge module 0) are checked. An example of the LSP distribution for these 2 modules can be seen in Figure 6.57 in the particular case of relatively large LV effect. The coefficient values are listed in Figure 6.57. We chose their value according to the order of magnitude of current sensitivity of other experiments. The differences between modules is still negligible with the current INGRID statistics. The statistical error has been added to the histogram for comparison purpose. One concludes that for a measurable given LV effect, current statistics is too low to detect a possible difference between INGRID modules at the present time.

## 6.7 Future sensitivity at T2K near detectors

We study the future sensitivity to the Lorentz violation in the INGRID and future near detectors in the context of the Tokai-to-HyperKamiokande experiment. It assumes a 7.5 MW beam which provides  $1.56 \times 10^{22}$  POT [108]. The T2HK experiment will use these POT with a proportion of 1:3 for the neutrino and antineutrino modes. It leads to  $3.9 \times 10^{21}$  POT in the neutrino mode and  $11.7 \times 10^{21}$  POT

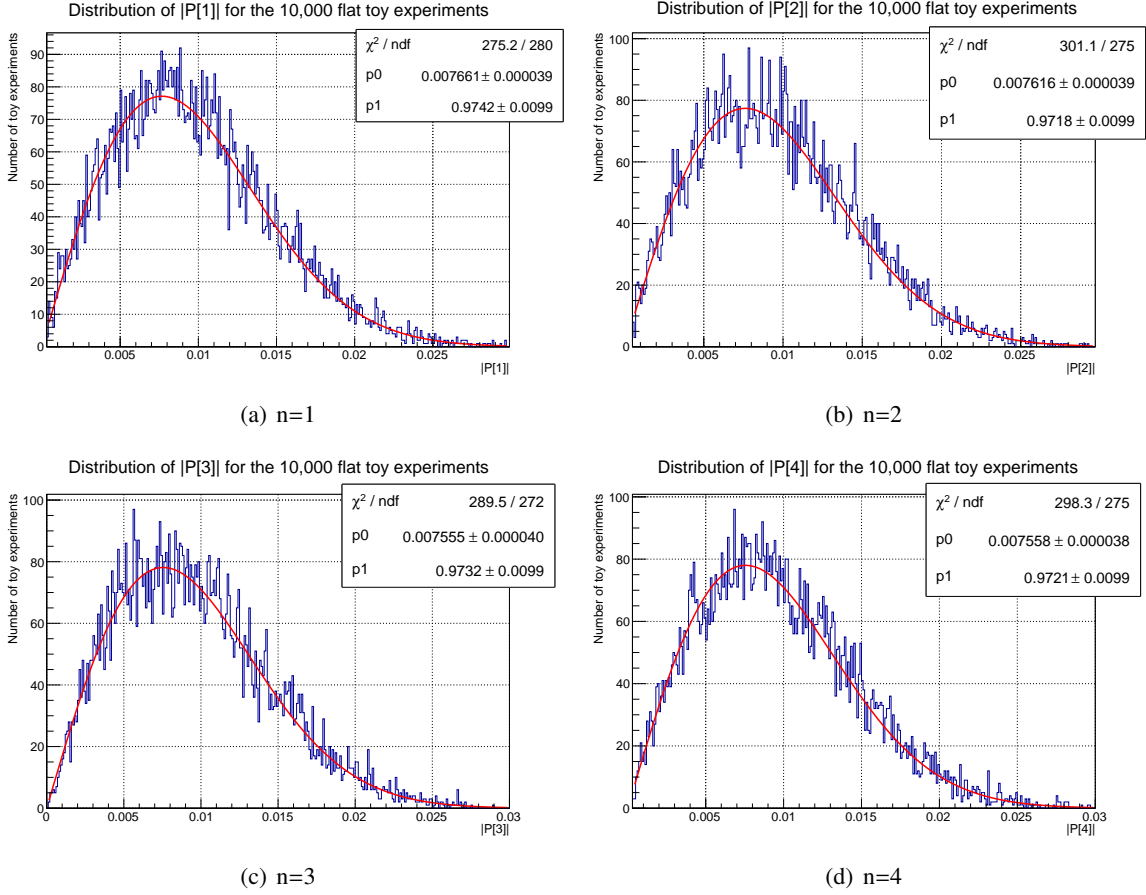


Figure 6.45: Distribution of the magnitudes of the different Fourier modes for the 10,000 flat toy experiments. The  $3\sigma$  threshold are the equal to 0.026 for the different Fourier modes. The distributions are fitted with Rayleigh functions.

for the antineutrino mode. The corresponding neutrino and antineutrino rate depends on the detector target and reconstruction. Considering the high neutrino contamination in the antineutrino mode, we only focus on the neutrino mode. Therefore, we do not use the full statistics in this study, nor the possible combination between neutrino and antineutrino results. Considering the  $\nu_\mu$  selection we developed in Section 6.2, we expect to detect a number of neutrino candidates equal to  $5.57 \times 10^7$ . This estimate neglects the pile-up effect. As we have seen, the advantage of INGRID compared to off-axis detector is its very high statistics and energy. As for the latter, it provides a higher sensitivity to the  $c_{\mu\mu}^{\alpha\beta}$  coefficients. This result can be combined with other near detectors. In particular, a water Cherenkov detector located off-axis at 1 km from the neutrino target is under study. This aims to reduce both the beam and the cross section uncertainty. Two different designs are studied, and called TITUS and  $\nu$ PRISM. Considering the Lorentz violation effect increases as the baseline squared, we consider that these future detector sensitivity may highly improve the sensitivity to the Lorentz violation effect. Therefore, we have studied them on top of INGRID. Using only the neutrino mode component, the total number of expected candidate events is  $3.9 \times 10^6$  in the  $\nu$ PRISM detector [108]. We have applied the fast Fourier transform method shown in Section 6.4 to determine the sensitivity of INGRID and  $\nu$ PRISM to the Lorentz violation. It assumes no correlation between the SME parameters, in order to show the raw sensitivity of the future T2HK experiment. We have summarised the parameter values in Table 6.14 for both the detectors. It corresponds to the parameter value at which the no sidereal variation hypothesis is rejected with  $3\sigma$  confidence level. One observes first the highest sensitivity on the  $c_{\mu\mu}^{\alpha\beta}$  parameters is clearly deduced from INGRID, as we forecast. As for the  $a_{\mu\mu}^\alpha$  parameters, one observes that the highest sensitivity is given by  $\nu$ PRISM. It is expected since these coefficients are not enhanced by the energy, and therefore, only statistics and baseline increase the sensitivity. In particular, one observes that the sensitivity on the  $a_{\mu\mu}^\alpha$  parameters overcomes MINOS one (see

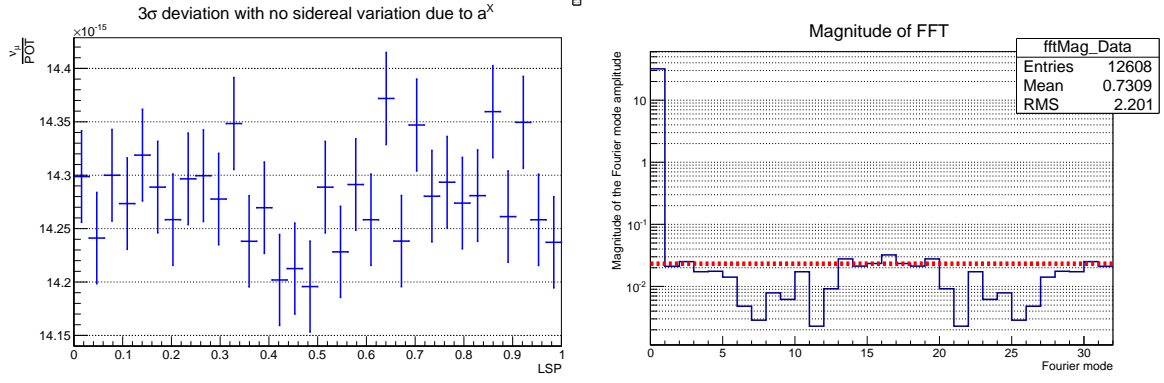


Figure 6.46: The  $\nu_\mu$  variation with local sidereal phase in the example of the  $a_{\mu\mu}^X = 4.0$  GeV (left), which correspond to this analysis  $3\sigma$  sensitivity to this parameter. On the right, the associated FFT is shown. The red line correspond to the threshold =0.026 studied in the previous Section.

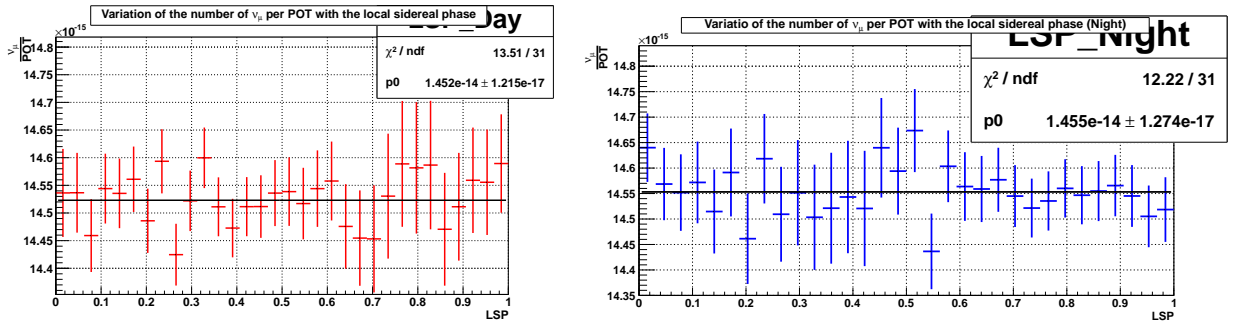


Figure 6.47:  $\nu_\mu$  event rate versus LSP for day (left) and night (right) data samples.

Table 6.1), and will correspond to the world leading constraints. The constraint on  $c_{\mu\mu}^{\alpha\beta}$  may be finally increased in the future using an energy dependent study as we presented in previous section.

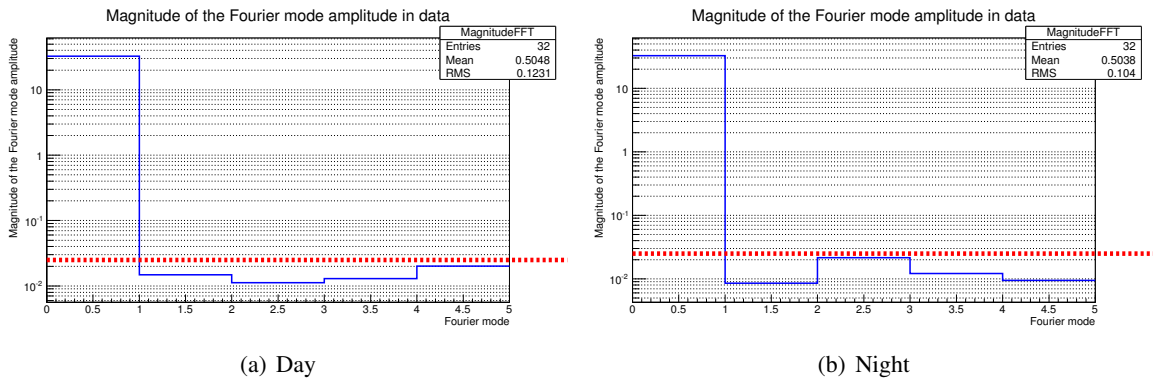


Figure 6.48: Fourier magnitudes for the data corresponding to day (left) and night (right) time period. The red line indicates the value corresponding to the  $3\sigma$  detection threshold.

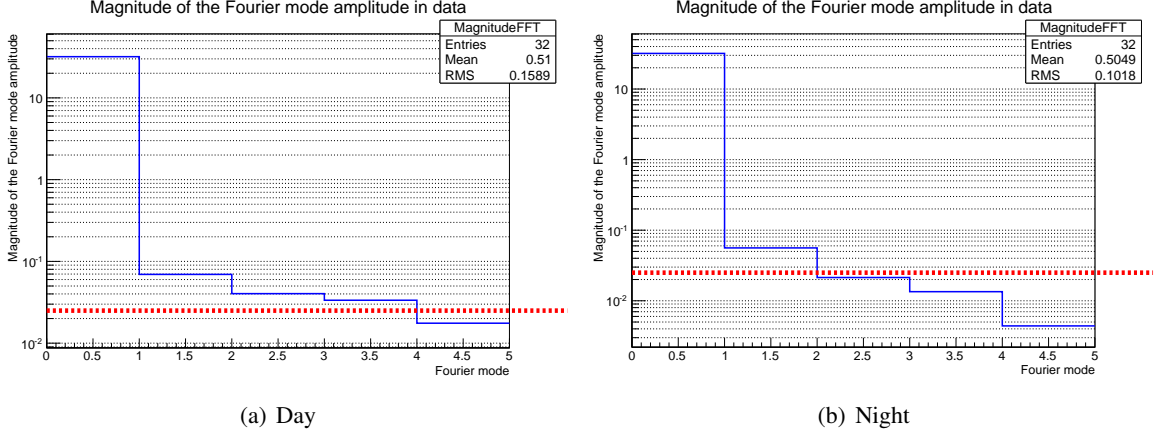


Figure 6.49: Fourier magnitudes for the data corresponding to day (left) and night (right) time period before any corrections were applied to INGRID data. The red line indicates the value corresponding to the  $3\sigma$  detection threshold.

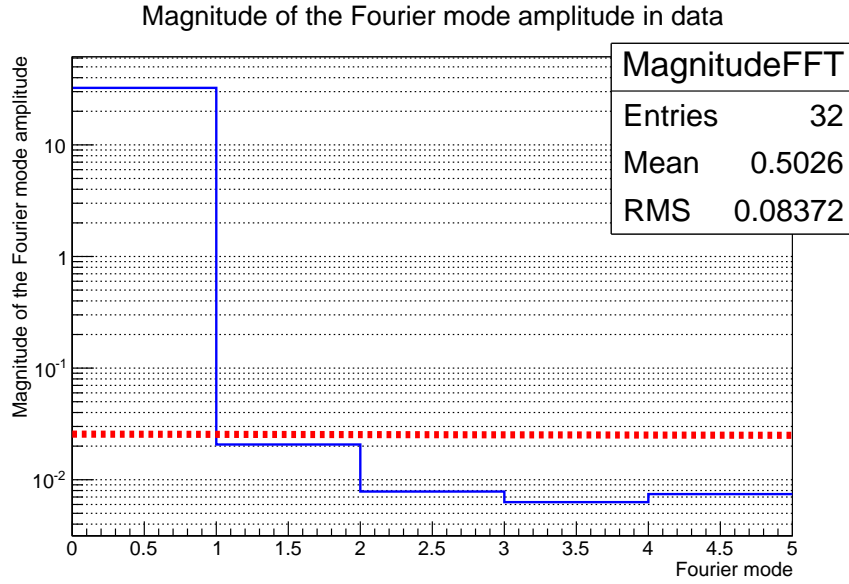


Figure 6.50: The magnitude of the first five Fourier modes of the data representing the  $\nu_\mu$  variation with the local sidereal phase. We have shown in red the  $3\sigma$  detection threshold (0.026).

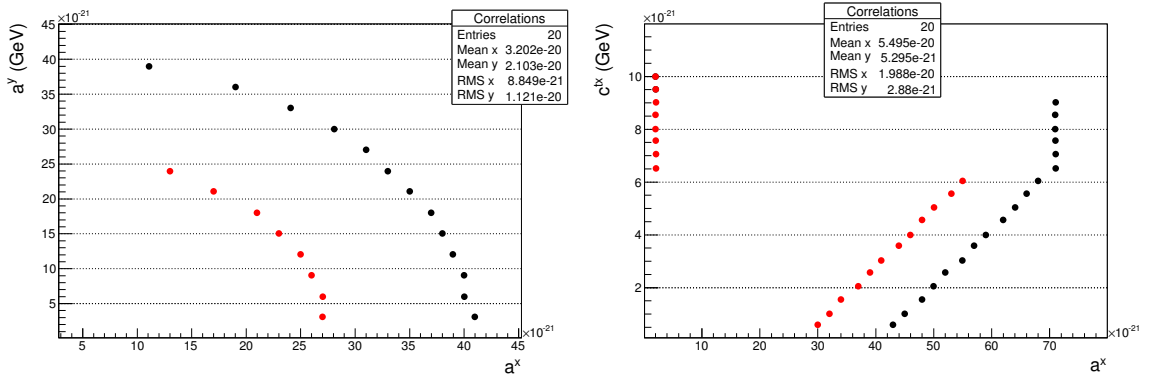


Figure 6.51: Variation of the sensitivity to  $a_{\mu\mu}^X$  parameter with the variation of the  $a_{\mu\mu}^Y$  (left) and  $c_{\mu\mu}^{TX}$  (right) coefficients. The red dots represent the value of  $a^X$  at which the  $1\sigma$  threshold is overcome, and the black ones correspond to the  $3\sigma$  threshold.

Table 6.5: Number of  $\nu_\mu$  candidates in INGRID data (top) and number of POT corresponding (bottom) per LSP bin and T2K run period.

Bin number	1	2	3	4	5	6	7	8	9	10	11	12	13	14	15	16
Run 1	9587	10979	11692	11509	10263	9986	10707	10092	12386	13848	14270	15172	15426	15982	17438	18182
Run 2	27510	28953	29322	30493	32017	34242	35681	37380	35457	34782	33807	32158	31812	31702	29097	27803
Run 3	46844	44614	46172	47165	47270	51796	51201	55947	56842	58276	59134	57542	57347	57665	57689	61166
Run 4, 2012	55348	55820	55782	55524	51745	51415	49445	47572	45472	38265	37969	41898	44353	40938	40586	41089
Run 4, 2013	66473	69496	74062	72947	72024	79044	76609	79526	78955	83425	85054	86075	83691	80807	77009	74023
Bin number	17	18	19	20	21	22	23	24	25	26	27	28	29	30	31	32
Run 1	18627	18060	16435	17211	16316	15099	15770	13977	12569	12413	12220	12624	11221	9944	10626	10092
Run 2	26474	24521	24496	24644	22965	22671	23335	23141	23410	24725	23557	25550	27655	27917	27138	25781
Run 3	62227	64106	62998	64895	65485	58731	51515	52819	51077	50045	50546	48124	46256	46270	45744	46922
Run 4, 2012	38550	41696	46352	45853	46905	47654	48194	52673	51111	53526	53229	53776	56502	59557	59016	56276
Run 4, 2013	73891	72382	69119	68927	63316	60084	60206	56569	60422	60451	64114	64789	61487	60917	60805	61369
Bin number	1	2	3	4	5	6	7	8	9	10	11	12	13	14	15	16
Run 1	$9.2 \cdot 10^{17}$	$1.0 \cdot 10^{18}$	$1.1 \cdot 10^{18}$	$1.1 \cdot 10^{18}$	$9.7 \cdot 10^{17}$	$9.3 \cdot 10^{17}$	$1.0 \cdot 10^{18}$	$9.5 \cdot 10^{17}$	$1.1 \cdot 10^{18}$	$1.3 \cdot 10^{18}$	$1.3 \cdot 10^{18}$	$1.4 \cdot 10^{18}$	$1.4 \cdot 10^{18}$	$1.5 \cdot 10^{18}$	$1.6 \cdot 10^{18}$	$1.7 \cdot 10^{18}$
Run 2	$3.4 \cdot 10^{18}$	$3.6 \cdot 10^{18}$	$3.6 \cdot 10^{18}$	$3.6 \cdot 10^{18}$	$3.7 \cdot 10^{18}$	$3.8 \cdot 10^{18}$	$3.9 \cdot 10^{18}$	$3.9 \cdot 10^{18}$	$3.7 \cdot 10^{18}$	$3.7 \cdot 10^{18}$	$3.3 \cdot 10^{18}$	$3.3 \cdot 10^{18}$	$3.2 \cdot 10^{18}$	$3.2 \cdot 10^{18}$	$3.1 \cdot 10^{18}$	$3.0 \cdot 10^{18}$
Run 3	$3.9 \cdot 10^{18}$	$3.8 \cdot 10^{18}$	$3.9 \cdot 10^{18}$	$4.0 \cdot 10^{18}$	$4.0 \cdot 10^{18}$	$4.4 \cdot 10^{18}$	$4.4 \cdot 10^{18}$	$4.7 \cdot 10^{18}$	$4.9 \cdot 10^{18}$	$5.0 \cdot 10^{18}$	$5.1 \cdot 10^{18}$	$5.0 \cdot 10^{18}$	$4.9 \cdot 10^{18}$	$5.0 \cdot 10^{18}$	$5.0 \cdot 10^{18}$	$5.2 \cdot 10^{18}$
Run 4, 2012	$3.3 \cdot 10^{18}$	$3.3 \cdot 10^{18}$	$3.3 \cdot 10^{18}$	$3.3 \cdot 10^{18}$	$3.1 \cdot 10^{18}$	$3.0 \cdot 10^{18}$	$3.0 \cdot 10^{18}$	$2.8 \cdot 10^{18}$	$2.7 \cdot 10^{18}$	$2.3 \cdot 10^{18}$	$2.2 \cdot 10^{18}$	$2.5 \cdot 10^{18}$	$2.6 \cdot 10^{18}$	$2.4 \cdot 10^{18}$	$2.4 \cdot 10^{18}$	$2.4 \cdot 10^{18}$
Run 4, 2013	$7.1 \cdot 10^{18}$	$7.2 \cdot 10^{18}$	$7.5 \cdot 10^{18}$	$7.4 \cdot 10^{18}$	$7.4 \cdot 10^{18}$	$7.7 \cdot 10^{18}$	$7.7 \cdot 10^{18}$	$7.8 \cdot 10^{18}$	$7.5 \cdot 10^{18}$	$7.9 \cdot 10^{18}$	$8.0 \cdot 10^{18}$	$8.1 \cdot 10^{18}$	$7.9 \cdot 10^{18}$	$7.5 \cdot 10^{18}$	$7.2 \cdot 10^{18}$	$7.0 \cdot 10^{18}$
Bin number	17	18	19	20	21	22	23	24	25	26	27	28	29	30	31	32
Run 1	$1.7 \cdot 10^{18}$	$1.7 \cdot 10^{18}$	$1.5 \cdot 10^{18}$	$1.6 \cdot 10^{18}$	$1.5 \cdot 10^{18}$	$1.4 \cdot 10^{18}$	$1.5 \cdot 10^{18}$	$1.3 \cdot 10^{18}$	$1.2 \cdot 10^{18}$	$1.1 \cdot 10^{18}$	$1.2 \cdot 10^{18}$	$1.2 \cdot 10^{18}$	$1.0 \cdot 10^{18}$	$9.5 \cdot 10^{17}$	$1.0 \cdot 10^{18}$	$9.6 \cdot 10^{17}$
Run 2	$2.8 \cdot 10^{18}$	$2.6 \cdot 10^{18}$	$2.7 \cdot 10^{18}$	$2.8 \cdot 10^{18}$	$2.7 \cdot 10^{18}$	$2.8 \cdot 10^{18}$	$2.7 \cdot 10^{18}$	$2.7 \cdot 10^{18}$	$2.8 \cdot 10^{18}$	$3.0 \cdot 10^{18}$	$3.1 \cdot 10^{18}$	$3.2 \cdot 10^{18}$	$3.3 \cdot 10^{18}$	$3.4 \cdot 10^{18}$	$3.4 \cdot 10^{18}$	$3.3 \cdot 10^{18}$
Run 3	$5.3 \cdot 10^{18}$	$5.5 \cdot 10^{18}$	$5.3 \cdot 10^{18}$	$5.5 \cdot 10^{18}$	$5.6 \cdot 10^{18}$	$5.0 \cdot 10^{18}$	$4.4 \cdot 10^{18}$	$4.5 \cdot 10^{18}$	$4.4 \cdot 10^{18}$	$4.3 \cdot 10^{18}$	$4.3 \cdot 10^{18}$	$4.2 \cdot 10^{18}$	$3.9 \cdot 10^{18}$	$3.8 \cdot 10^{18}$	$3.9 \cdot 10^{18}$	$4.0 \cdot 10^{18}$
Run 4, 2012	$2.3 \cdot 10^{18}$	$2.5 \cdot 10^{18}$	$2.7 \cdot 10^{18}$	$2.7 \cdot 10^{18}$	$2.8 \cdot 10^{18}$	$2.8 \cdot 10^{18}$	$2.9 \cdot 10^{18}$	$3.1 \cdot 10^{18}$	$3.0 \cdot 10^{18}$	$3.2 \cdot 10^{18}$	$3.2 \cdot 10^{18}$	$3.2 \cdot 10^{18}$	$3.4 \cdot 10^{18}$	$3.5 \cdot 10^{18}$	$3.5 \cdot 10^{18}$	$3.3 \cdot 10^{18}$
Run 4, 2013	$7.1 \cdot 10^{18}$	$7.2 \cdot 10^{18}$	$7.1 \cdot 10^{18}$	$6.9 \cdot 10^{18}$	$6.6 \cdot 10^{18}$	$6.3 \cdot 10^{18}$	$6.5 \cdot 10^{18}$	$6.3 \cdot 10^{18}$	$6.7 \cdot 10^{18}$	$6.6 \cdot 10^{18}$	$7.0 \cdot 10^{18}$	$7.0 \cdot 10^{18}$	$6.9 \cdot 10^{18}$	$6.8 \cdot 10^{18}$	$6.8 \cdot 10^{18}$	$6.8 \cdot 10^{18}$

Horizontal modules	0	1	2	3	4	5	6
$C_{\text{loss}} \times 10^{15}$	0.87	1.06	1.13	1.22	1.32	1.22	0.92
Vertical modules	7	8	9	10	11	12	13
$C_{\text{loss}} \times 10^{15}$	0.81	1.00	1.05	1.22	1.19	1.09	0.71

Table 6.6: Event loss constant estimated in [62] for a 250 kA horn current, using the standard INGRID selection for Run 1 to 3. The statistical error on each constant is  $0.05 \times 10^{-15}$ .

T2K run	Run 1	Run 2	Run 3	Run 4
Correction (horizontal)	1.006	1.000	1.008	1.002
Correction (vertical)	1.002	1.001	1.003	1.002

Table 6.7: Correction factor to apply to each event according to its run number and module (vertical or horizontal).

T2K run	Run 1	Run 2	Run 3	Run 4 2012	Run 4 2013
Correction	$1.033 \pm 0.003$	$1.006 \pm 0.003$	$1.007 \pm 0.003$	$0.995 \pm 0.004$	1.

Table 6.8: Correction factor to apply to each event according to its run number, due to event rate variations between runs. The  $\pm 1\sigma$  error is shown, taking into account error on Run 4 2013 event rate.

Source	Systematic uncertainty (%)
Pile-up	0.01
MPPC dark noise	0.01
MPPC gain variation	0.06
Beam position	0.03
Rate correction	0.05
Total systematic	0.08

Table 6.9: Summary of systematic uncertainties coming from time-dependent effects, to be compared with a statistical uncertainty of 0.3%.

Table 6.10: SME  $3\sigma$  sensitivity to each coefficients using the FFT method.

	$\times 10^{-20}$		$\times 10^{-20}$
$a_L^X$	4.8 GeV	$a_L^Y$	4.8 GeV
$c_L^{TX}$	0.9	$c_L^{TY}$	0.9
$c_L^{LX}$	3.8	$c_L^{LY}$	1.6
$c_L^{XZ}$	3.1	$c_L^{YY}$	3.8
$c_L^{YZ}$	3.1		

Table 6.11: FFT results.

Fourier Mode	Threshold	Magnitude	p-value
1	0.026	0.01076	0.35
2	0.026	0.00930	0.48
3	0.026	0.00620	0.69
4	0.026	0.00893	0.51

Table 6.12: Best fit values and  $1\sigma$  errors on the different SME parameters using the likelihood method.

	$C$	$A_c$	$A_s$	$B_c$	$B_s$
Best fit (GeV)	$(2.4 \pm 3.8) \times 10^{-20}$	$(1.4^{+1.8}_{-2.4}) \times 10^{-20}$	$(-0.4^{+1.1}_{-3.2}) \times 10^{-20}$	$(2.7^{+5.1}_{-9.8}) \times 10^{-21}$	$(0.7^{+5.3}_{-4.8}) \times 10^{-21}$

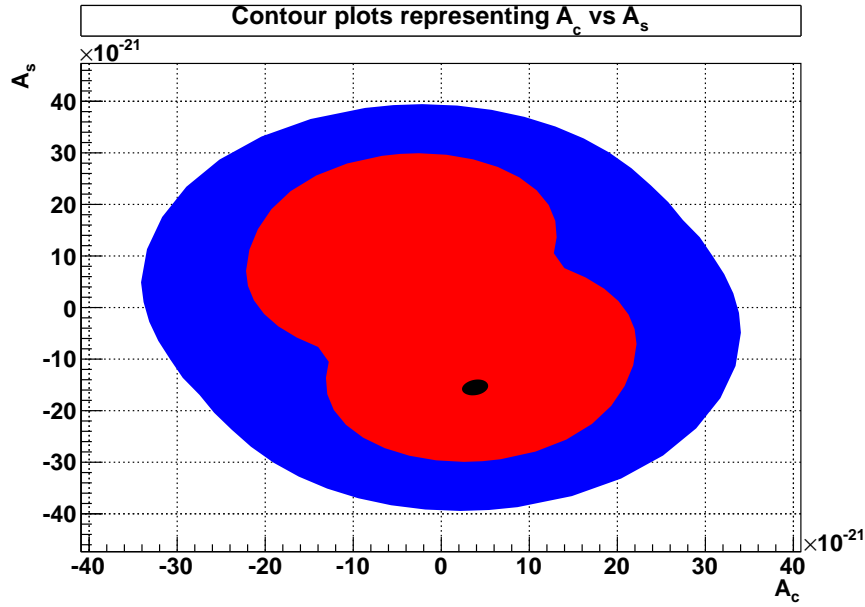


Figure 6.52: Projection of the 5-coefficient fit results in the  $A_c, A_s$  coefficient space. The best fit point is marked in black, with  $1\sigma$  and  $2\sigma$  contours shown in red and blue.

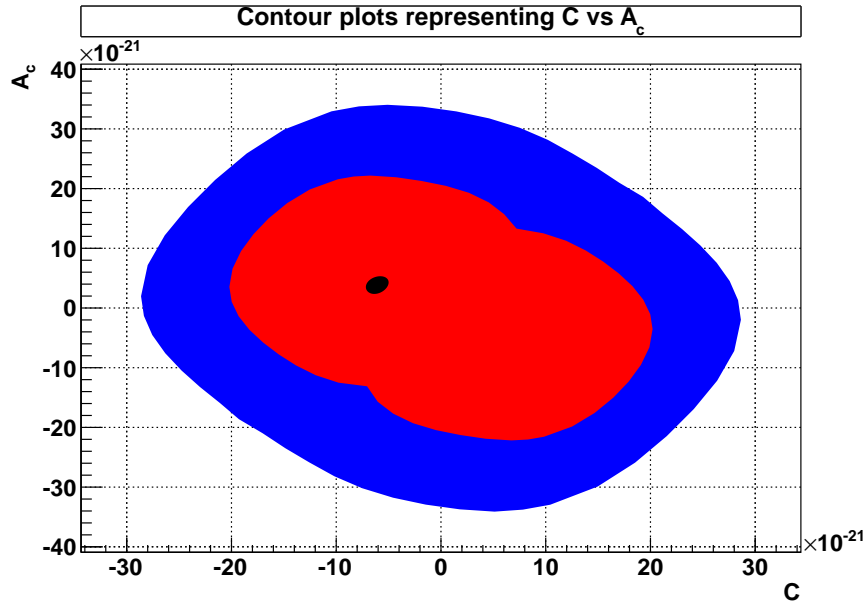


Figure 6.53: Projection of the 5-coefficient fit results in the  $C, A_c$  coefficient space. The best fit point is marked in black, with  $1\sigma$  and  $2\sigma$  contours shown in red and blue.

Table 6.13: Energy spectrum properties for INGRID different modules. Module's number is shown in Figure 6.22.

	Modules 0/6/7/13	Modules 1/5/8/12	Modules 2/4/9/11	Modules 3/10
Mean (GeV)	2.7 GeV	2.6 GeV	2.6 GeV	2.6 GeV
Main peak position (GeV)	1.2 GeV	1.3 GeV	1.5 GeV	1.6 GeV

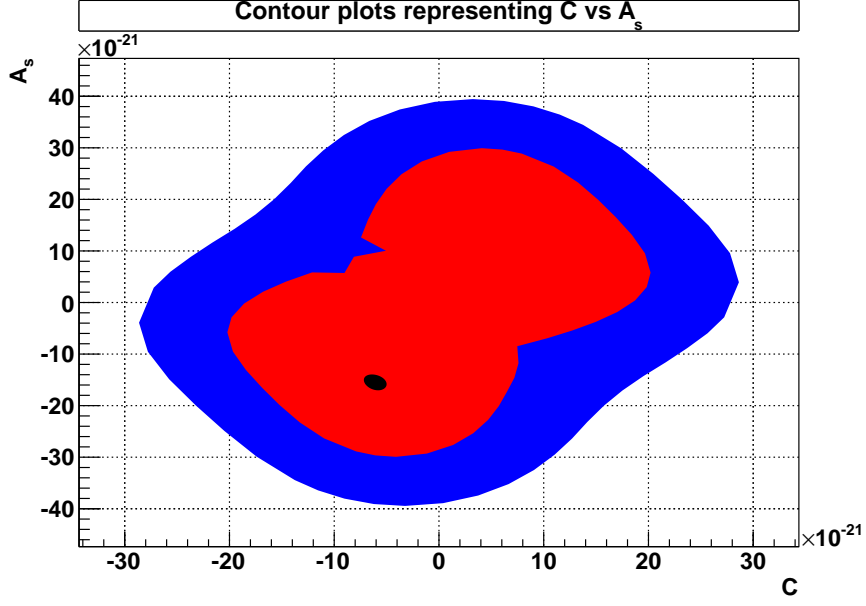


Figure 6.54: Projection of the 5-coefficient fit results in the  $C, A_s$  coefficient space. The best fit point is marked in black, with  $1\sigma$  and  $2\sigma$  contours shown in red and blue.

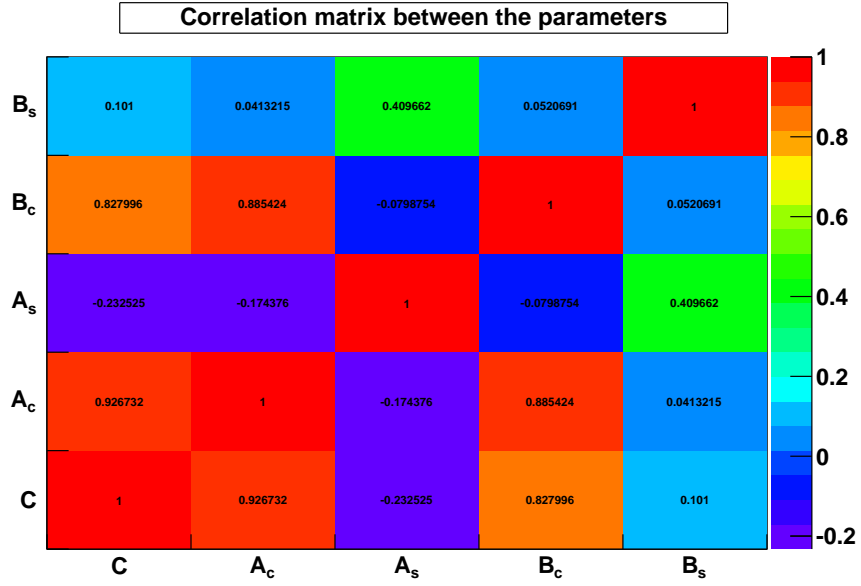


Figure 6.55: Correlations matrix between the fitted coefficients.

Table 6.14: SME  $3\sigma$  sensitivity to each coefficients using the FFT method for the T2HK near detectors. **IN-GRID** is shown in red (along to the current value) and **vPRISM** in blue.

	$\times 10^{-20}$			$\times 10^{-20}$	
$a_L^X$	4.0 GeV $\rightarrow$ 2.1 GeV	1.0 GeV	$a_L^Y$	4.0 GeV $\rightarrow$ 2.1 GeV	1.0 GeV
$c_L^{TX}$	0.8 $\rightarrow$ 0.5	0.8	$c_L^{TY}$	0.8 $\rightarrow$ 0.5	0.8
$c_L^{XX}$	3.1 $\rightarrow$ 2.0	3.5	$c_L^{XY}$	1.6 $\rightarrow$ 1.0	1.7
$c_L^{XZ}$	2.3 $\rightarrow$ 1.6	2.8	$c_L^{YY}$	3.1 $\rightarrow$ 2.0	3.5
$c_L^{YZ}$	2.6 $\rightarrow$ 1.6	2.8			

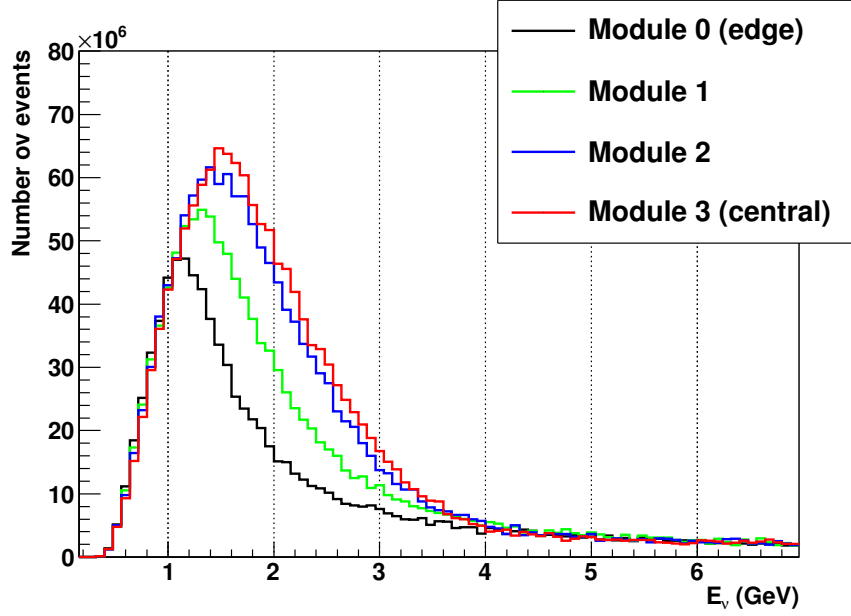
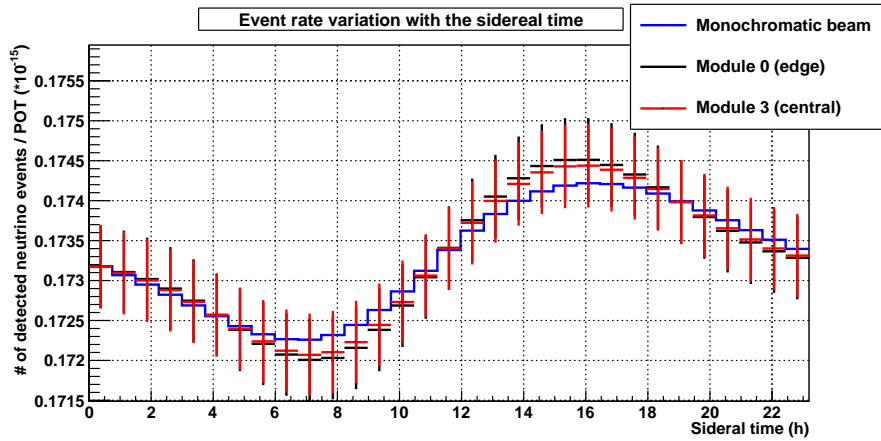


 Figure 6.56:  $\nu_\mu$  spectrum for different INGRID modules.


Figure 6.57: LSP distributions for a given LV effect. The coefficient were chosen to match the order of magnitude of current limits set by other experiments, listed in [91]. The statistical error bars are added for comparison purposes. The coefficient values are the one listed in Table 6.1, without the MINOS constraints (as in Figures 6.4 and 6.5).

# Conclusion

URING the first half of the twentieth century, the model of particle physics has been highly improved until the Standard Model was born in the sixties. The second half of this century has seen a multitude of experimental confirmations of this model, though it is known to be incomplete. In particular, this model cannot describe the gravitational interaction. At the end of the twentieth century, it was experimentally proved that neutrino oscillates, which contradicts the Standard Model predictions. The singular neutrino particle has been therefore intensively studied as a potential entrance to physics beyond the Standard Model. In the last fifteen years, the mixing angles and squared mass differences that rule the neutrino oscillations have therefore been measured in various sectors as solar, atmospheric, reactor and accelerator neutrino experiments. The T2K experiment was built in order to measure the very last mixing angle,  $\theta_{13}$ . The CHOOZ experiment having shown this angle is very small as compared to others, it was investigated if  $\theta_{13}$  has a non zero value which is necessary for any CP violation to occur in the lepton sector. In 2012, the Daya Bay and Reno experiments have provided the first observation of a non zero value of this angle. This result was confirmed by the T2K measurement in 2013. Moreover, the tension between these results has open the possibility of a large CP violation effect. Since the CP violation effect only arises through neutrino appearance channel, it cannot be observed in the high precision reactor experiments. In the current generation of experiments, only T2K and Nova have therefore the sensitivity to significantly constrain the CP violation effect. Though next generation experiments are under preparation, none of them will be installed in a short term period.

In this context, the reduction of the uncertainties on the existing experiment is absolutely crucial. As for T2K, the cross section uncertainties dominate and limit the sensitivity not only to CP violation, but also to the accurate measurements of the atmospheric parameters  $\theta_{23}$  and  $\Delta m_{32}^2$ . This thesis work is therefore focused on the measurement of muon neutrino cross section to reduce the model uncertainties. This measurement has been performed with the on-axis proton module of the T2K INGRID detector, whose target is the same as the off-axis ND280 detector.

As a first step, we calibrated the on-axis detector. In particular, our studies and the future ones require particle identification based on the charge deposition. In this thesis, we have provided a full charge deposition calibration in the INGRID and proton module detectors. Moreover, we have measured an optical cross-talk between the scintillators which has been removed in these analyses.

In addition, we have finalised the study of a setup, called the “cone generator”, that was initially constructed prior to this thesis to study the  $\pi^0$  background in  $\nu_e$  appearance in Super-Kamiokande. We have corrected and evaluated the main limitations of this setup. It allowed to perform a calibration study of the Super-Kamiokande detector, and to identify the simulation deficit of the light reflection on Super-Kamiokande wall. It has also shown an imperfect tuning of the dark noise charge, as a check of Super-Kamiokande uniformity with direction and height. However, the remaining uncertainties prevent this device from being used in the  $\pi^0$  background study, and a simpler device should be designed if one want to perform this study in Super-Kamiokande or future Hyper-Kamiokande detectors.

Using the INGRID and proton module calibration, we have measured the first double differential cross section in the on-axis detector, according to the outgoing muon variables. It leads both to reduce the cross section model uncertainties, and to maximise the constraints on models compared to non differential studies. We confirmed the latest results on neutrino cross section measurements, as in MiniBooNE or MINOS experiments. In particular, we have shown that this result is in tension with the former measurements on light targets, and predicts a higher axial mass value  $M_A = 1.33 \pm 0.17 \text{ GeV} \cdot c^{-2}$ . We

have shown the tension is removed when nuclear collective effects are taken into account, which leads to an axial mass  $M_A = 1.11 \pm 0.17 \text{ GeV} \cdot c^{-2}$  in agreement with the former experiments. It confirms the MiniBooNE predictions and indicates the nuclear effects should be taken into account from now on. In the medium term, these results can be used directly as an additional constraint to ND280 neutrino cross section to reduce the systematic error on the neutrino flux prediction in the Super-Kamiokande experiment. Moreover, this study can be used for the incoming WAGASCI detector, to drastically reduce these systematic errors.

Finally, in this thesis we propose the first Lorentz invariance violation search in T2K. We focus on the impact of Planck scale Lorentz violation effects on the near detector INGRID, which was chosen for its very high statistics. The neutrino oscillation is used as a very sensitive probe for beyond Standard Model effects that are predicted in most of the theories. We have developed the first selection to discriminate between  $\nu_\mu$  and oscillated  $\nu_e$  in the on-axis detector. Using two different methods, we observed no discrepancy between the INGRID data and the standard neutrino oscillation scenario. We have finally shown the sensitivity improvement in the near detectors of the Tokai-to-Hyper-Kamiokande project, which will allow to probe potential Lorentz invariance violation that has occurred earlier in the cooling process of the Universe ( $\gtrsim 10^{20} \text{ GeV}$ ).

# Appendix A

## Cone generator systematic errors and tables

### A.1 Systematic error estimation

**I**N this appendix, we give an overview of systematic errors coming both from SK data and MC. Since the MC is based on Photon Flux (PF) data, errors associated to PF data taking should be taken into account. Errors from SK data set and coming from PF measurement are detailed in the followings subsections. They are evaluated for a typical run (vertex at  $z=0$  m,  $+y$  direction) in this section, but errors for additionnal runs are summarized in Tables A.1 and A.2.

#### A.1.1 Evaluation of systematic errors for SK data set

##### Reconstructed position and direction of the CG

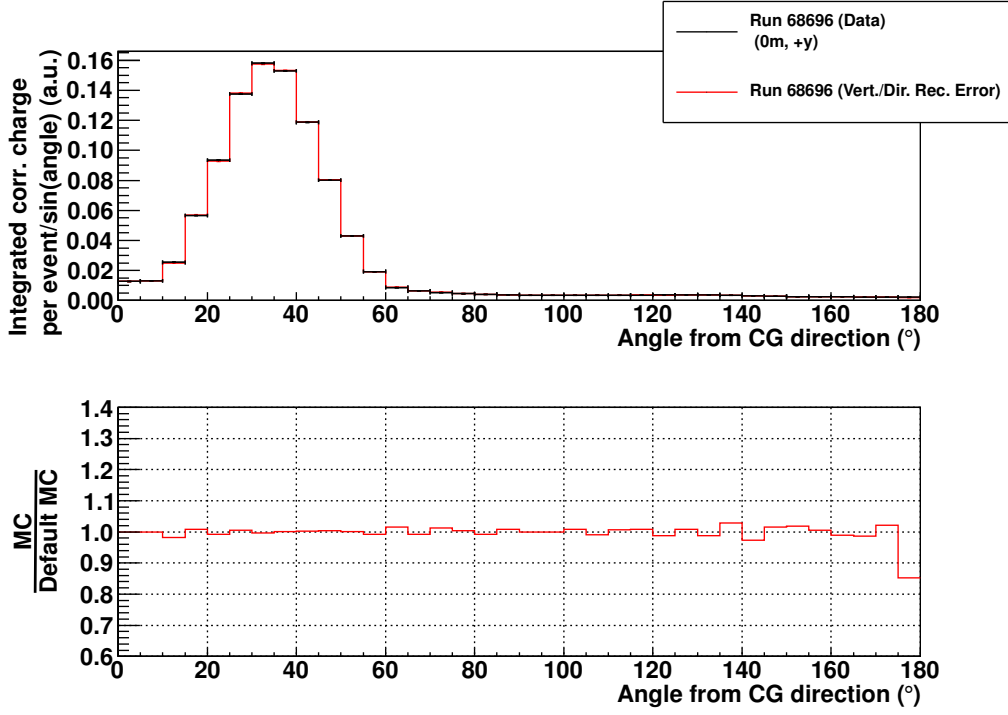
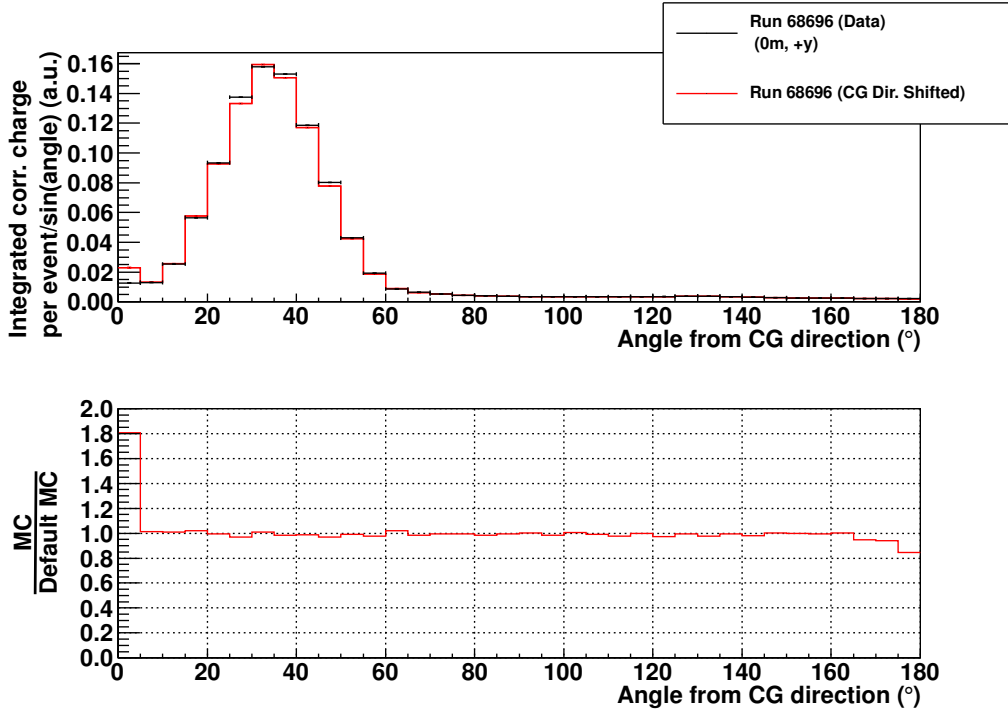
As previously explained, this error is evaluated from the locator data. Moreover, since errors on position and direction are deduced from the locator vertex reconstruction, there are 100% correlated. To take this effect into account, we changed the vertex position within the  $1\sigma$  error and the reconstructed position is deduced as the direction between this vertex and the locator spot (in CG direction). The impact on charge profile is shown in Figure A.1 and is within 3% in most of the bins, confirming that vertex resolution of locator is sufficient. This error has a large impact only on directions far from the CG main direction (at  $180^\circ$ ). The reason is the impact of a PMT migration from one bin to another is high at  $180^\circ$ , since these bins contain very few PMTs due to the small solid angle. In first order, this error shows the geometrical impact of the SK detector on the charge profile, particularly its discrete PMTs distribution.

##### Shift between Locator and CG direction

As shown in the Chapter 3, there is probably a mechanical shift between Locator and CG vessel of around  $0.7^\circ$ , together with a foward cone shift which creates a small direction shift. We decided that the best way to estimate this error was as a constant shift between Locator and CG directions. Though it doesn't represent the complexity of a foward cone shift (charge asymmetry, width differences, direction shift), it remains a good estimator to evaluate the impact on the direction shift it creates. Moreover, this error is uncorrelated to the previous one and so, can be added quadratically. The impact on charge profile is shown in Figure A.2 and is within 3% in most of the bins. For the same reason as errors on vertex and direction, the impact of the shift between locator and CG direction is high at small and high angles because of important impact on PMTs migration from one bin to another.

##### Stability of the data

We will use data sets measured in similar nominal conditions (altitude and direction) to check the evaluation of systematic errors, and the goodness of our systematic error list. However, these data do not allow to check a possible bending of the optical fiber between runs at different directions, since we didn't rotate the CG vessel differently in these different runs. Moreover, we haven't taken into


 Figure A.1:  $1\sigma$  error on Vertex position and Locator direction on charge profile

 Figure A.2: Effect of a  $0.7^\circ$  shift between CG and Locator direction on charge profile

account the laser intensity stability, which we associated to the MC. As can be seen on Figure A.3, the two data sets agree within the systematic error bars, despite  $2\sigma$  fluctuations around the peak (at  $25^\circ$  for example). This confirms the laser intensity stability, and also, the reliability of the estimated errors.

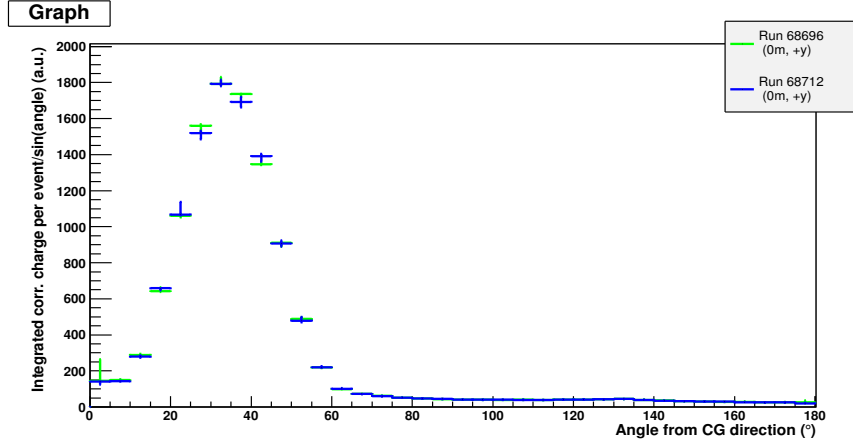


Figure A.3: Charge profiles comparison between 2 runs at the same nominal conditions (height, direction) but at different time. Both statistic and systematic errors are shown.

Since the laser is always shutdown before the data taking at different heights, and realigned after, the use of the 8 meters data should give relevant information. At this altitude, we took another data set (run 68739) before finishing the data taking at SK, after runs at +16 m and 0 m. A comparison between these 3 runs could provide also a good check of the laser stability after a shutdown. The comparison between these 3 runs displayed on Figure A.4, shows a very good agreement between these different directions, and confirms both the stability of our laser diode and the reproducibility of our measurement.

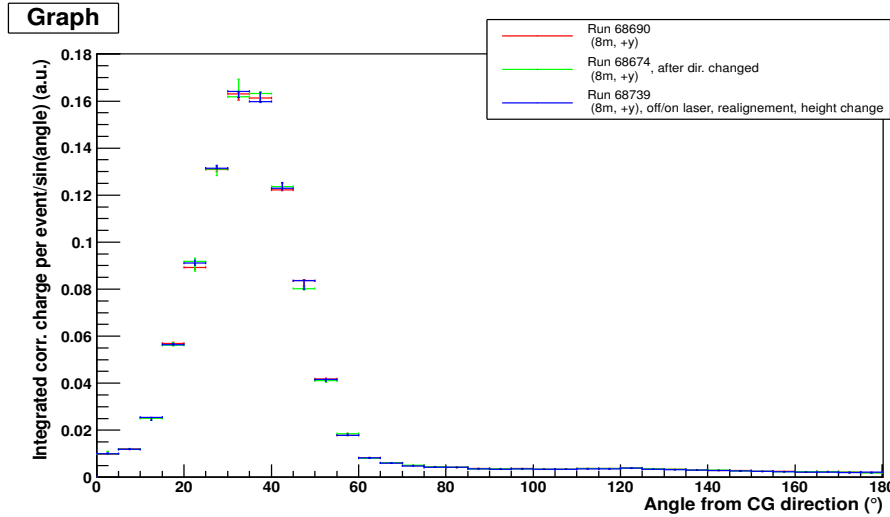


Figure A.4: Data stability check: Charge Profile Comparison of two data sets at the same nominal conditions (height, direction) but after having shutdown the laser in between.

### A.1.2 Evaluation of systematic errors coming from photon flux measurement

All the detailed effects of each error estimation are summarized in Table A.2.

### Statistical Error from the pedestal measurement

As described in Chapter 3, the pedestal measured without photon in sequential data is in good agreement with the special “pedestal data”. Moreover, no time variation were observed during the data taking, as shown on Figure 3.12. We decided to use the sequential data (high statistics) to estimate the pedestal value and its error (statistical error). The effects on the charge profile can be seen on Figure A.5 and is within 1% in almost all the angular region.

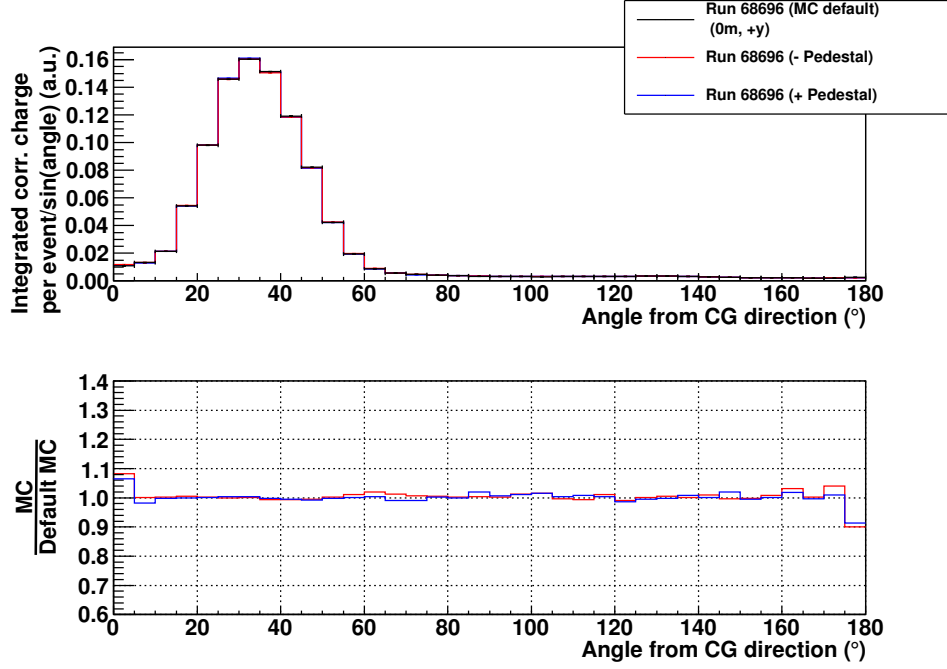


Figure A.5: Pedestal error effect on charge profile for a  $1\sigma$  change in the pedestal value. The effect on the peak region is less than 1%

### Laser intensity stability

The laser intensity has been found to be stable in time (see Chapter 3). To estimate the error associated to this stability, we decided to use the total charge emitted with time. We remind that a special data set, “stability data”, is used for this purpose. Using this data set, we fit the charge time dependence with a degree one polynomial and implement this variation in the photon flux generation. This is a maximization of the laser intensity error (which can be alternatively evaluated with errors on the order 0 polynomial fit). The impact on charge profile of this light intensity variation (Figure A.6) is very small, which reflects the laser intensity stability (below 1% in the peak region).

### CG Vessel shift

The error on the CG vessel horizontal shift is estimated as the fitting error on the “CGV offset data”, as described on Figure 3.15. Given the poor  $\chi^2$  value, we decided to take it into account by multiplying the fitting error by  $\sqrt{\chi^2}$ , which is correct for a linear fit and remains a good estimation for a gaussian fit. The impact on charge profile is shown on Figure A.7. The effect is small in the main peak and the backward region ( $< 2\%$ ) but high on the peak edge (angle from CG direction  $\sim 15^\circ$  or  $\sim 60^\circ$ ) due to peak shift.

### PMTV motor offset

The systematic error on the PMTV motor offset was estimated using January 2011 photon flux data by applying the same procedure shown here for CGV=22° (Figure 3.14) for other different CGV angle

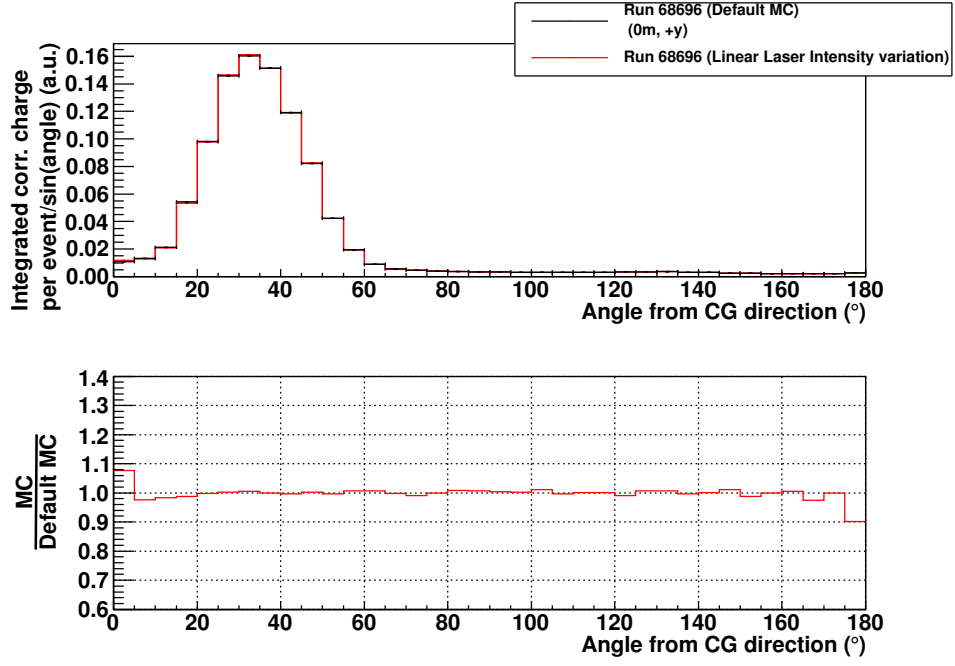


Figure A.6: Linear variation of laser intensity effect on charge profile for a degree one polynomial

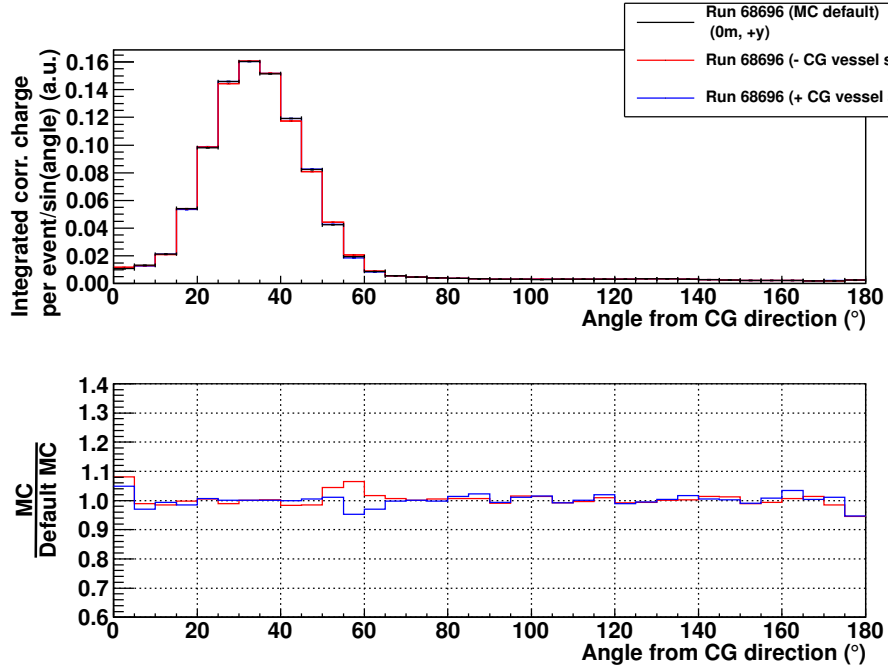


Figure A.7: CG vessel shift error effect on charge profile. We changed the CG Vessel shift value by  $\pm 1\sigma$  in the error. The impact on the charge profile is under 1% in the main peak region, though about 4% and 6% in the inner and outer peak regions respectively

values and evaluating the standard deviation of these measurements from the average PMTV offset measured, shown in Figure A.9. It is not possible to reproduce this systematic error study done with January 2011 photon flux data using the May 2011 photon flux data because there is not enough ADC counts at other values of CGV to reasonably fit (3.3.1). Indeed, the probability that light reflects at the wall of the cone shaped channel of the CG vessel is smaller when the CG vessel is under water than in the air, because refraction index of Delrin plastic is closer to water than air one<sup>1</sup>. This estimation method is probably conservative, given we used reflected light which statistical error is higher than for direct light. However, we have still not tried to further reduce this uncertainty given the need to improve the fitting function which is put in evidence by the poor reduced  $\chi^2$  value. The impact on charge profile is shown on Figure A.8. We can clearly distinguish a shift in direction, which represents a 3% impact on the peak region, and a smaller one on the backward region.

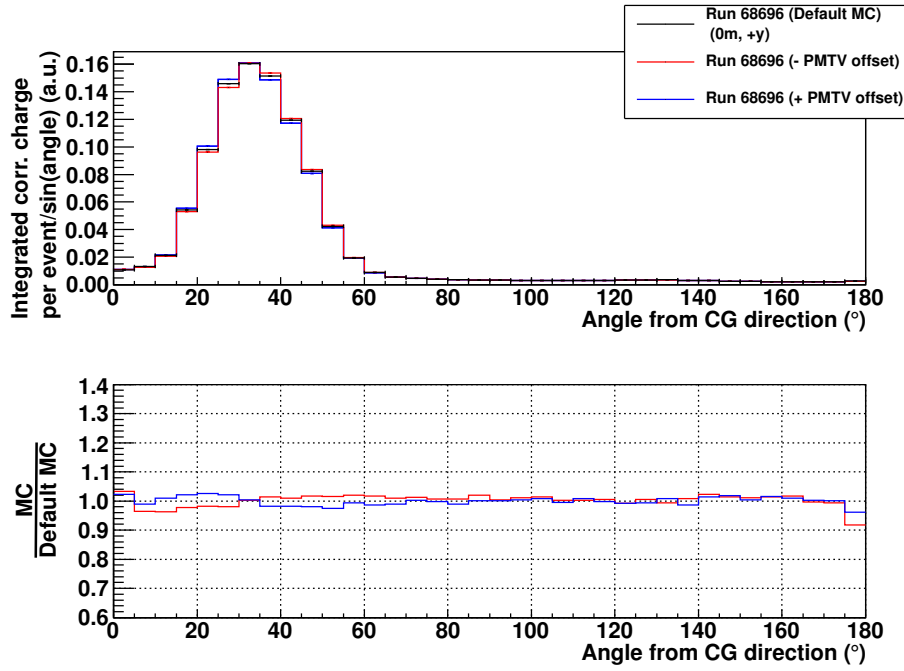


Figure A.8: Effect of the PMTV motor offset error on charge profile. We changed the PMTV offset value for  $\pm 1\sigma$ . The impact on the charge profile is around 3% in the peak region

### Statistical fluctuation of the PMT light collection

The PMT light collection has statistical fluctuations for each angle set (CGV, PMTV, PMTH). Since the number of ADC counts is low in the backward and front regions, we expect the associated statistical error to be larger in those regions. To estimate the impact of such an uncertainty, we decided to generate a random number with a gaussian distribution with  $(\mu, \sigma) = (\langle ADC \rangle, \frac{\langle ADC \rangle}{\sqrt{ADC}})$  for each angle set, and to generate several MC. To estimate number of MC needed, we estimated how likely it is that for all angles, there is never a random number deviated more than  $1\sigma$  from the mean. We decided to generate enough MC so that this probability is lower than 1 %. The required number of MCs needed should be higher than 22. We decided to generate 22 MC and to use the wrapping of the differences with the default MC as an estimation of this error. The impact of one of this MC is shown on Figure A.10, while the effect of all MCs is described in Tables A.1 and A.2. The quantitative impact can rise to  $\sim 7\%$  for some bins in the edge of the light peak, showing that statistical fluctuations of the PMT light collection is one of the main systematic error.

<sup>1</sup>This is explained by the Fresnel equations.

Table A.1: Systematic Error estimated for each bin for the Run 68718 (16 m, +Y direction). We represented the lower and upper values of  $1\sigma$  error (lower error bound, upper error bound) in percent.

Angle	Pedestal	Laser Intensity	CG Vessel shift	PMTV offset	PMT light col.	Total MC	Shift of direction	Rec. CG vertex/direction	Total Data Error
2.5	(0, 3)	(0, 4)	(0, 5)	(0, 3)	(3, 6)	(3, 9)	(0, 0)	(1, 1)	(1, 1)
7.5	(0, 0)	(2, 0)	(3, 0)	(3, 0)	(6, 0)	(8, 0)	(0, 0)	(1, 0)	(1, 0)
12.5	(0, 0)	(1, 0)	(0, 0)	(3, 2)	(7, 1)	(8, 3)	(0, 0)	(1, 3)	(1, 3)
17.5	(0, 0)	(1, 0)	(0, 1)	(2, 2)	(3, 2)	(3, 3)	(1, 0)	(1, 3)	(2, 3)
22.5	(0, 0)	(0, 0)	(0, 1)	(2, 2)	(1, 1)	(2, 3)	(4, 0)	(2, 1)	(4, 1)
27.5	(0, 0)	(0, 1)	(0, 0)	(1, 2)	(0, 1)	(1, 3)	(0, 3)	(1, 2)	(1, 3)
32.5	(0, 0)	(0, 0)	(0, 0)	(1, 0)	(1, 1)	(1, 1)	(3, 0)	(3, 7)	(5, 7)
37.5	(0, 0)	(0, 0)	(0, 1)	(1, 2)	(0, 2)	(1, 3)	(0, 15)	(8, 7)	(8, 17)
42.5	(1, 0)	(0, 0)	(1, 0)	(2, 2)	(1, 1)	(3, 2)	(6, 0)	(14, 3)	(15, 3)
47.5	(0, 0)	(0, 0)	(2, 1)	(2, 1)	(2, 1)	(3, 2)	(8, 0)	(5, 0)	(9, 0)
52.5	(0, 0)	(0, 0)	(0, 4)	(2, 2)	(3, 3)	(4, 5)	(1, 0)	(10, 15)	(10, 15)
57.5	(0, 1)	(0, 0)	(5, 6)	(2, 2)	(4, 2)	(7, 7)	(0, 1)	(1, 2)	(1, 2)
62.5	(0, 2)	(1, 0)	(3, 2)	(2, 2)	(5, 5)	(6, 6)	(2, 0)	(1, 0)	(2, 0)
67.5	(0, 1)	(0, 1)	(2, 0)	(1, 2)	(0, 4)	(2, 5)	(1, 0)	(3, 0)	(3, 0)
72.5	(0, 0)	(1, 0)	(3, 0)	(0, 0)	(1, 3)	(3, 3)	(0, 2)	(2, 4)	(2, 4)
77.5	(0, 1)	(0, 0)	(3, 0)	(0, 1)	(0, 2)	(3, 3)	(1, 0)	(0, 2)	(1, 2)
82.5	(0, 1)	(0, 0)	(3, 0)	(0, 1)	(0, 2)	(3, 2)	(0, 1)	(1, 1)	(1, 1)
87.5	(0, 0)	(0, 0)	(5, 0)	(0, 1)	(1, 1)	(5, 2)	(0, 1)	(4, 2)	(4, 2)
92.5	(0, 1)	(1, 0)	(6, 0)	(0, 2)	(1, 1)	(6, 3)	(2, 0)	(2, 4)	(3, 4)
97.5	(0, 0)	(0, 0)	(7, 0)	(0, 2)	(1, 1)	(7, 2)	(0, 1)	(0, 2)	(0, 2)
102.5	(0, 0)	(0, 0)	(9, 0)	(1, 1)	(1, 1)	(9, 2)	(1, 0)	(2, 2)	(2, 2)
107.5	(0, 0)	(1, 0)	(14, 0)	(1, 0)	(1, 1)	(14, 1)	(0, 0)	(1, 1)	(1, 1)
112.5	(0, 0)	(0, 1)	(14, 0)	(0, 2)	(0, 2)	(14, 2)	(0, 2)	(1, 1)	(1, 2)
117.5	(1, 0)	(0, 0)	(18, 0)	(3, 0)	(2, 1)	(19, 1)	(0, 0)	(2, 1)	(2, 1)
122.5	(0, 0)	(1, 0)	(12, 0)	(1, 1)	(1, 0)	(12, 1)	(0, 0)	(3, 1)	(3, 1)
127.5	(0, 0)	(0, 0)	(6, 0)	(1, 1)	(1, 1)	(7, 1)	(2, 0)	(2, 3)	(3, 3)
132.5	(0, 1)	(0, 1)	(4, 0)	(0, 1)	(0, 3)	(4, 3)	(5, 0)	(3, 0)	(5, 0)
137.5	(1, 0)	(0, 0)	(6, 0)	(0, 0)	(3, 0)	(7, 0)	(0, 2)	(1, 3)	(1, 4)
142.5	(0, 0)	(0, 1)	(3, 0)	(0, 1)	(1, 2)	(3, 3)	(0, 1)	(4, 1)	(4, 2)
147.5	(3, 0)	(0, 0)	(5, 0)	(1, 0)	(3, 1)	(7, 1)	(0, 3)	(0, 4)	(0, 5)
152.5	(0, 1)	(0, 0)	(3, 0)	(0, 2)	(3, 5)	(4, 5)	(5, 0)	(5, 2)	(7, 2)
157.5	(3, 0)	(0, 0)	(3, 0)	(0, 0)	(1, 4)	(5, 4)	(0, 5)	(2, 2)	(2, 6)
162.5	(4, 0)	(0, 1)	(7, 0)	(3, 0)	(2, 3)	(9, 3)	(1, 0)	(0, 4)	(1, 4)
167.5	(1, 0)	(0, 2)	(5, 0)	(0, 4)	(2, 6)	(6, 7)	(0, 1)	(2, 1)	(2, 1)
172.5	(0, 0)	(0, 0)	(6, 0)	(0, 4)	(1, 5)	(6, 6)	(0, 0)	(4, 2)	(4, 2)
177.5	(11, 0)	(8, 0)	(8, 0)	(5, 0)	(11, 0)	(20, 0)	(1, 0)	(6, 6)	(6, 6)

Table A.2: Systematic Error estimated for each bin for the Run 68696 (0 m, +Y direction). We represented the lower and upper values of  $1\sigma$  error (lower error bound, upper error bound) in percent.

Angle	Pedestal	Laser Intensity	CG Vessel shift	PMTV offset	PMT light col.	Total MC	Shift of direction	Rec. CG vertex/direction	Total Data Error
2.5	(0, 8)	(0, 8)	(0, 8)	(0, 3)	(13, 52)	(13, 54)	(0, 81)	(0, 0)	(0, 81)
7.5	(2, 0)	(2, 0)	(3, 0)	(4, 0)	(7, 1)	(9, 1)	(0, 1)	(0, 2)	(0, 2)
12.5	(0, 0)	(2, 0)	(1, 0)	(4, 1)	(9, 5)	(10, 5)	(0, 1)	(2, 0)	(2, 1)
17.5	(0, 1)	(1, 0)	(1, 0)	(2, 2)	(3, 4)	(4, 5)	(0, 2)	(1, 1)	(1, 2)
22.5	(0, 0)	(0, 0)	(0, 1)	(2, 3)	(1, 1)	(2, 3)	(1, 0)	(1, 1)	(1, 1)
27.5	(0, 0)	(0, 0)	(1, 0)	(2, 2)	(2, 1)	(3, 3)	(3, 0)	(0, 1)	(3, 1)
32.5	(0, 0)	(0, 1)	(0, 0)	(0, 0)	(0, 1)	(0, 2)	(0, 1)	(0, 1)	(0, 1)
37.5	(1, 0)	(0, 0)	(0, 0)	(2, 1)	(1, 1)	(2, 2)	(2, 0)	(1, 0)	(2, 0)
42.5	(1, 0)	(0, 0)	(2, 0)	(2, 1)	(1, 0)	(3, 1)	(1, 0)	(0, 1)	(1, 1)
47.5	(1, 0)	(0, 0)	(2, 0)	(2, 2)	(3, 1)	(4, 2)	(3, 0)	(1, 0)	(3, 0)
52.5	(0, 0)	(0, 0)	(0, 4)	(3, 2)	(3, 4)	(4, 6)	(1, 0)	(0, 2)	(1, 2)
57.5	(0, 1)	(0, 1)	(5, 7)	(1, 2)	(4, 4)	(6, 8)	(2, 0)	(1, 0)	(3, 0)
62.5	(0, 2)	(0, 1)	(3, 2)	(1, 2)	(4, 7)	(5, 8)	(0, 2)	(0, 2)	(0, 3)
67.5	(1, 1)	(0, 0)	(0, 1)	(1, 1)	(1, 3)	(2, 4)	(2, 0)	(1, 0)	(2, 0)
72.5	(1, 1)	(1, 0)	(0, 0)	(0, 1)	(0, 2)	(1, 3)	(0, 0)	(0, 1)	(0, 1)
77.5	(0, 0)	(0, 0)	(0, 1)	(0, 1)	(1, 1)	(1, 2)	(1, 0)	(0, 1)	(1, 1)
82.5	(0, 0)	(0, 1)	(0, 1)	(1, 1)	(1, 1)	(2, 2)	(2, 0)	(1, 1)	(2, 1)
87.5	(0, 2)	(0, 1)	(0, 2)	(0, 2)	(0, 2)	(0, 4)	(0, 0)	(1, 1)	(1, 1)
92.5	(0, 1)	(0, 0)	(1, 0)	(0, 0)	(1, 1)	(1, 1)	(0, 0)	(0, 1)	(0, 1)
97.5	(0, 1)	(0, 0)	(0, 2)	(0, 1)	(0, 2)	(0, 3)	(2, 0)	(1, 0)	(2, 0)
102.5	(0, 2)	(0, 1)	(0, 2)	(0, 1)	(0, 3)	(0, 4)	(0, 0)	(0, 1)	(0, 1)
107.5	(0, 0)	(0, 0)	(1, 0)	(0, 0)	(2, 1)	(2, 1)	(1, 0)	(1, 0)	(1, 0)
112.5	(1, 1)	(0, 0)	(0, 0)	(0, 1)	(2, 2)	(2, 2)	(3, 0)	(1, 1)	(3, 1)
117.5	(0, 1)	(0, 0)	(0, 2)	(0, 1)	(0, 2)	(0, 3)	(0, 0)	(1, 1)	(1, 1)
122.5	(1, 0)	(1, 0)	(1, 0)	(1, 0)	(3, 1)	(4, 1)	(3, 0)	(1, 1)	(3, 1)
127.5	(0, 0)	(0, 1)	(1, 0)	(1, 0)	(2, 1)	(2, 1)	(1, 0)	(1, 1)	(1, 1)
132.5	(0, 0)	(0, 1)	(0, 0)	(1, 1)	(1, 2)	(2, 2)	(2, 0)	(2, 0)	(3, 0)
137.5	(0, 1)	(0, 0)	(0, 2)	(1, 1)	(0, 1)	(1, 2)	(1, 0)	(0, 3)	(1, 3)
142.5	(0, 1)	(0, 0)	(0, 1)	(0, 2)	(2, 2)	(2, 4)	(2, 0)	(3, 1)	(3, 1)
147.5	(0, 2)	(0, 1)	(0, 1)	(0, 2)	(0, 3)	(0, 4)	(0, 0)	(1, 2)	(1, 2)
152.5	(0, 0)	(1, 0)	(1, 0)	(0, 1)	(2, 1)	(3, 2)	(0, 0)	(2, 3)	(2, 3)
157.5	(0, 1)	(0, 0)	(1, 1)	(0, 2)	(2, 3)	(2, 3)	(0, 0)	(1, 1)	(1, 1)
162.5	(0, 3)	(0, 1)	(0, 3)	(0, 2)	(0, 4)	(0, 6)	(0, 0)	(3, 1)	(3, 1)
167.5	(0, 0)	(3, 0)	(0, 1)	(0, 0)	(6, 2)	(7, 2)	(5, 0)	(1, 2)	(6, 2)
172.5	(0, 4)	(0, 0)	(2, 1)	(1, 0)	(6, 4)	(6, 5)	(6, 0)	(2, 6)	(6, 6)
177.5	(10, 0)	(10, 0)	(5, 0)	(8, 0)	(25, 0)	(30, 0)	(15, 0)	(15, 40)	(21, 40)

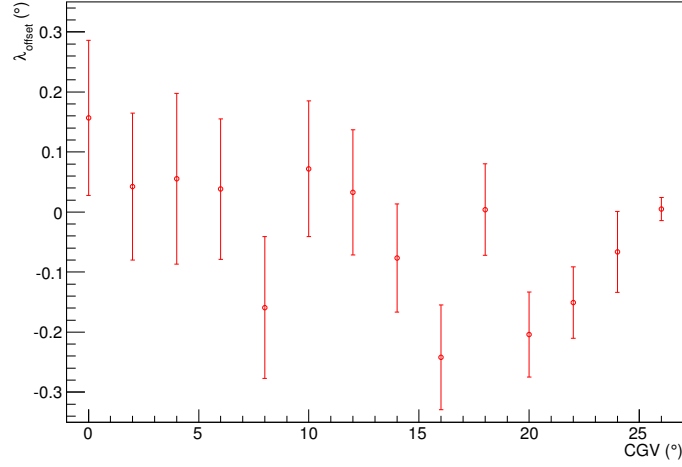


Figure A.9: Value of  $\lambda_{\text{offset}}$  (see equation (3.3.1)) fitted using the PMTV distribution of ADC with pedestal subtracted for different values of CGV, with PMTH=0° always. Error bars show the fit uncertainty calculated by ROOT. These fits used photon flux data taken at January 2011, therefore the measured value of  $\lambda_{\text{offset}}$  is not exactly the same as the one measured with the usual (May 2011) data set. The standard deviation of the fitted value of  $\lambda_{\text{offset}}$  of the above fits is of  $0.113^\circ \pm 0.021^\circ$ .

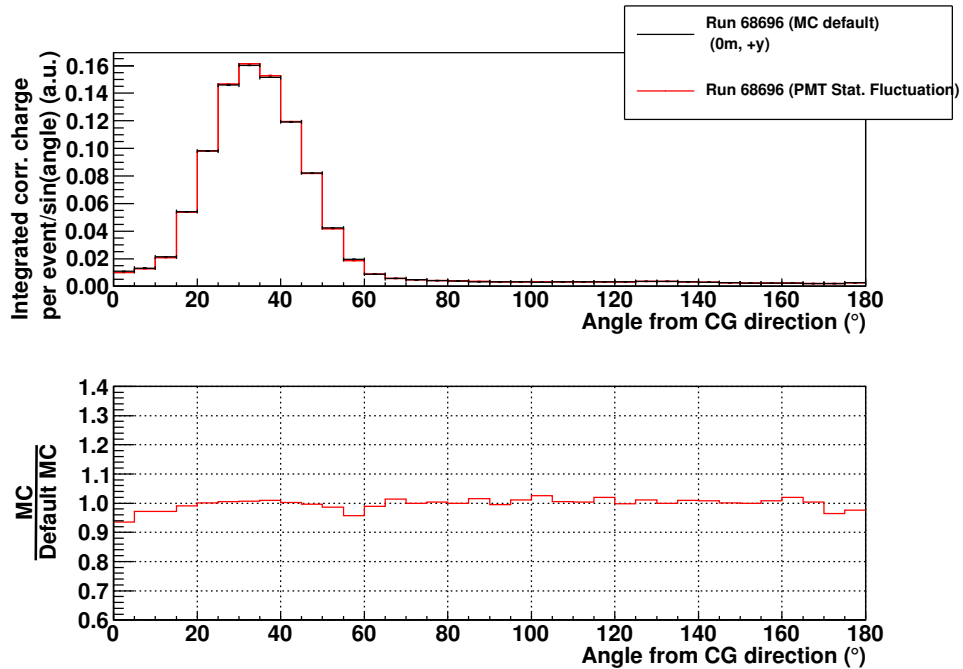



Figure A.10: Effect of a fluctuation of the PMT light collection. For each angle configuration, we randomly choose the ADC value according to a gaussian distribution whose mean is the mean ADC value and  $\sigma$  is the statistical uncertainty of the mean value. We decided to draw here the comparison with only one of these configurations. The effect of all the 22 configurations we used is around  $-2\%$  in the peak region



## Appendix B

# Timing calibration of the INGRID detector

 In order to discriminate between the various hypotheses, we have checked if the anomaly in the low charge region was correlated with signal. To do so, we have performed a time calibration of the INGRID detector. Three different effects have been considered:

1. Mean tdc difference between the different TFB electronics boards: all the channels in one tracking plane are connected to the same TFB.
2. Time walk correction. The timing of the hit registered by the detector is the tdc at which the integrated charge in a channel overcomes a given threshold. In the case of a high charge deposition, this threshold is overcome more quickly than for low charge deposition hit. The latter may require additional noise to effectively cross the threshold. The tdc value for low charge hits is therefore expected to be lower in average than for high charge hits.
3. Propagation of light in fiber.

We haven't taken into account the fiber attenuation in this calibration. Considering the speed of light in polystyrene ( $\sim \frac{c}{1.55}$ ), the time difference that occurs for the propagation in  $\pm 0.6$  m is  $\Delta t = \pm 3$  ns. Considering the TFB (up to 12 ns) and time walk (can reach 20 ns) leading corrections shown on Figure B.1, we have neglected the time propagation in the optical fiber.

### B.1 TFB mean time difference:

We have first evaluated the time difference between the TFB. In order to measure these differences, we used a sand muon sub-sample which is only composed of sand muons passing through the front plane of the PM and escaping from the last PM plane. This sample is then named as “through-going sand muon” sample. This allows to correct both the different calibration between TFB but also to correct the time difference due to particle propagation from the front to the most downstream plane of the PM. For each track, we chose the average tdc value of the front plane as the reference time to compare different tracks. The result is shown on Figure B.1 for the 18 TFB (gathering two tracking planes) of the PM. At first order, one can observe a nearly 12 ns shift between all tracking planes and the third and the eighteenth planes. This shift corresponds to a difference in TFB relative tdc calibration. This effect can be also observed in the first plane compared to the others showing a 2 ns shift. On top of this, one notices a global 1 ns shift from the second to the seventeenth plane which is due to the particle propagation. In the time calibration we used, we correct each average hit measured in each plane by the average TFB tdc value shown on Figure B.1.

### B.2 Time walk:

The time walk effect has been evaluated using the hits belonging to the tracks of through going sand muon sub-sample defined above. TFB relative mean tdc difference has been first corrected. The time reference used was the average time over all hits of the front plane of the PM. The tdc value as a

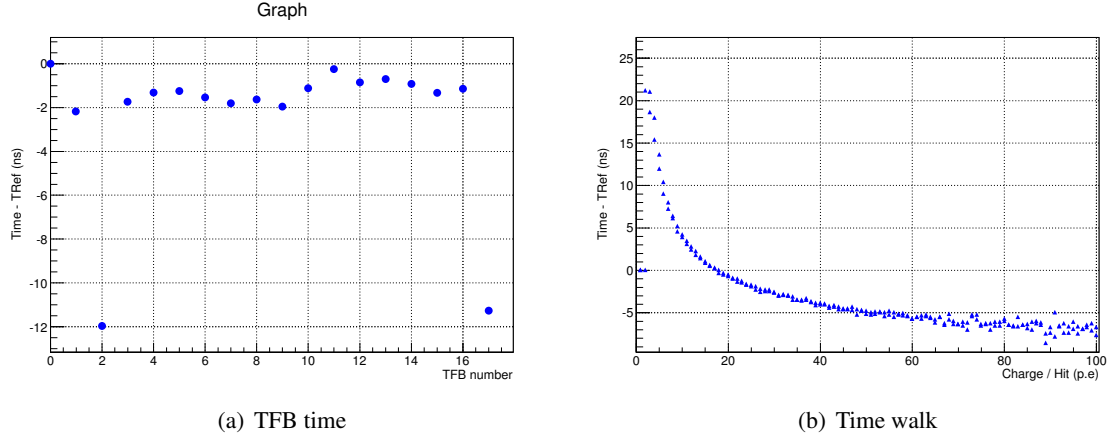


Figure B.1: TFB timing and time walk corrections in the PM. The time walk effect shown here has been studied using SciBar scintillator types.

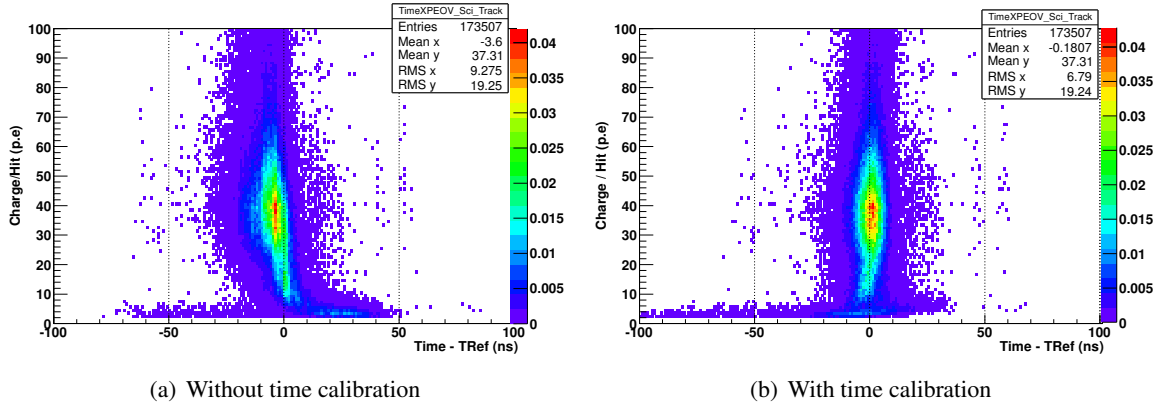


Figure B.2: Comparison between the hits charge and time distributions after having applied the time calibration.


function of the charge deposition in a hit is shown on Figure B.1. This effect is clearly the dominant source that should be calibrated, since one can observe a nearly  $27\text{ ns}$  difference between timing of low charge ( $\sim 5\text{ p.e}$ ) and high charge ( $> 80\text{ p.e}$ ) hits. We added to the TFB time correction this time walk correction by subtracting the time shift shown on Figure B.1 depending on the charge of the hit.

We show the time calibration effect on hit timing on Figure B.2 for the sand muon sample only. Most of the bias is corrected using the time calibration since the mean tdc value is changed from  $-3.6\text{ ns}$  before the calibration is applied to  $0.2\text{ ns}$  after. Moreover, one observes that the time shift for the different hit charges seems to have a similar average which validates the time walk correction. Finally, the relative calibration between the different hits is improved by observing that the timing spread (root mean square value) is changed from  $9.3\text{ ns}$  to  $6.8\text{ ns}$  applying the time calibration. This validates the effectiveness of the calibration and we will then use it for the neutrino event sample.

## Appendix C

# Calculation of the neutrino cross section on a free quark

### C.1 Basics of the cross section

 THE cross section of an interaction has the dimension of a surface. This is analogous to the image of an incoming particle (1) having a radius  $r_1$  impacting a surface  $S$  of a target made of particles (2) of radius  $r_2$  and containing  $n_2$  particles per unit of volume. One can see that 2 particles may interact only if the distance between their centres is lower than  $r_1 + r_2$ . The interaction between these two particles can be treated equivalently using an incoming point particle (1) and an equivalent target made of particles (2) of radius  $r_1 + r_2$ , whose area is called  $\sigma = \pi(r_1 + r_2)^2$ . The interaction of an incoming particle (1) with the whole target can be described with the probability of an interaction to occur. The probability of interaction is given by the number of particles (2) seen by (1) times the fraction of the total surface  $S$  represented by a particle (2), namely  $\frac{\sigma}{S}$ . If the particle (1) travels at speed  $|\vec{v}_1|$ , it will go through a region with  $n_2 S |\vec{v}_1| dt$  particles (2) of the target. The probability of interaction  $dP$  is then:

$$dP = n_2 S |\vec{v}_1| dt \frac{\sigma}{S} = n_2 |\vec{v}_1| dt \sigma. \quad (\text{C.1.1})$$

Therefore, the interaction rate is:

$$\Sigma = \frac{dP}{dt} = n_2 |\vec{v}_1| \sigma. \quad (\text{C.1.2})$$

In particle physics, one may like to study not only the case of a single incoming particle (1) but a beam hitting a target. Let  $n_1$  be the particle density of the incoming beam. The rate estimated in Eq C.1.2 is therefore multiplied by the number of possible interacting particles of the beam in the volume  $V$  intersecting the target. One obtains:

$$\sigma = \frac{\Sigma}{N_2 \phi} = \frac{\text{number of interactions per unit time per nucleon}}{\text{flux of incident particles}} \quad (\text{C.1.3})$$

where  $\phi = n_1 |\vec{v}_1|$  is the flux of the incoming particles and  $N_2 = n_2 V$  the number of particles in the effective target. Note that this calculation has been done assuming a fixed target. The flux may be re-defined as  $\phi = \frac{1}{V} |\vec{v}_1|$  using  $n_1 = \frac{1}{V}$ . In the most general case of a non-fixed target, one only has to replace  $\phi = \frac{1}{V} |\vec{v}_1|$  by  $\phi = \frac{1}{V} |\vec{v}_1 - \vec{v}_2|$ . The cross section is then defined as:

$$\Sigma = n_2 |\vec{v}_1 - \vec{v}_2| \sigma n_1 V = \sigma N_2 \phi. \quad (\text{C.1.4})$$

The interaction rate per unit time from an initial state  $|i\rangle$  made of  $n_i$  particles to a final state  $|f\rangle$

made of  $n_f$  particles may be defined using the transition rate as shown in [109] as:

$$d\Sigma_{i \rightarrow f} = V^{1-n_i} (2\pi)^4 \delta^{(4)} \left( \sum_{j=1}^{n_f} p'_j - \sum_{i=1}^{n_i} p_i \right) |M_{fi}|^2 \prod_{i=1}^{n_i} \frac{1}{2E_i} \prod_{j=1}^{n_f} \frac{d^3 \vec{p}'_j}{(2\pi)^3 2E'_j} \quad (\text{C.1.5})$$

$$d\Sigma_{2 \rightarrow 2} = V^{-1} (2\pi)^4 \delta^{(4)}(p'_1 + p'_2 - p_1 - p_2) |M_{fi}|^2 \frac{1}{4E_1 E_2} \frac{d^3 \vec{p}'_1 d^3 \vec{p}'_2}{(2\pi)^6 4E'_1 E'_2} \text{ in case of } n_i = 2 = n_f \quad (\text{C.1.6})$$

with  $V$  the volume of 3-space and  $M_{fi}$  the Lorentz invariant scattering amplitude that we will compute using Feynman diagram and rules. With our notation,  $p', E'$  correspond to the momentum and energy of outgoing particles, while  $p, E$  correspond to the momentum and energy of incoming particles. In the case of a CCQE interaction defined in Figure C.1 where  $n_f = 2 = n_i$ , one can use in Eq C.1.6 the interaction rate  $\Sigma$  estimated in Eq C.1.3 :

$$d\sigma = \frac{d\Sigma_{2 \rightarrow 2}}{N_2 \phi} = \frac{1}{4E_1 E_2 |\vec{v}_1 - \vec{v}_2|} (2\pi)^4 \delta^{(4)}(p'_1 + p'_2 - p_1 - p_2) |M_{fi}|^2 \frac{d^3 \vec{p}'_1 d^3 \vec{p}'_2}{(2\pi)^6 4E'_1 E'_2}. \quad (\text{C.1.7})$$

One observes that neither the flux factor  $F = E_1 E_2 |\vec{v}_1 - \vec{v}_2|$  and therefore, nor the differential cross section are Lorentz invariants. Nevertheless, one shows by expressing  $\frac{\vec{v}_1}{c^2}$  as  $\frac{\vec{p}_1}{E_1}$  that this factor is Lorentz invariant in the case of 2 collinear beams (1) and target(2). In the particular case of a fixed target, the cross section is therefore Lorentz invariant. In fact:

$$F = E_1 E_2 \left| \frac{\vec{p}_1}{E_1} - \frac{\vec{p}_2}{E_2} \right| \stackrel{\text{colin\&opposed}}{=} E_1 E_2 \left( \frac{|\vec{p}_1|}{E_1} + \frac{|\vec{p}_2|}{E_2} \right) = |\vec{p}_1| E_2 + |\vec{p}_2| E_1 \quad (\text{C.1.8})$$

in the case  $\vec{p}_1$  and  $\vec{p}_2$  are colinear and in opposite directions. It follows that:

$$F^2 = |\vec{p}_1|^2 E_2^2 + |\vec{p}_2|^2 E_1^2 + 2|\vec{p}_1| E_2 |\vec{p}_2| E_1. \quad (\text{C.1.9})$$

Moreover:

$$p_1 p_2 \stackrel{\text{colin}}{=} E_1 E_2 + |\vec{p}_1| |\vec{p}_2| \Rightarrow (p_1 p_2)^2 = E_1^2 E_2^2 + |\vec{p}_1|^2 |\vec{p}_2|^2 + 2E_1 E_2 |\vec{p}_1| |\vec{p}_2| \quad (\text{C.1.10})$$

We deduce:  $F^2 - (p_1 p_2)^2 = |\vec{p}_1|^2 (E_2^2 - |\vec{p}_2|^2) + E_1^2 (|\vec{p}_2|^2 - E_2^2) = |\vec{p}_1|^2 m_2^2 - E_1^2 m_2^2 = -m_1^2 m_2^2$ .

Therefore, one obtains:

$$F = \sqrt{(p_1 p_2)^2 - (m_1 m_2)^2} \quad (\text{C.1.11})$$

and deduce the cross section formula in case of colinear particles (1) and (2):

$$d\sigma = \frac{d\Sigma_{2 \rightarrow 2}}{N_2 \phi} = \frac{1}{4 \sqrt{(p_1 p_2)^2 - (m_1 m_2)^2}} (2\pi)^4 \delta^{(4)}(p'_1 + p'_2 - p_1 - p_2) |M_{fi}|^2 \frac{d^3 \vec{p}'_1 d^3 \vec{p}'_2}{(2\pi)^6 4E'_1 E'_2} \quad (\text{C.1.12})$$

The Center of mass frame is defined by  $\sum_{i=1}^{n_i} \vec{p}_i^* = 0 = \sum_{i=1}^{n_f} \vec{p}_i^*$ , which leads in the case of 2 incoming particles to  $\vec{p}_1^* = -\vec{p}_2^* \Rightarrow |\vec{p}_1^*| = |\vec{p}_2^*| = |\vec{p}^*|$  and for 2 outgoing particles  $|\vec{p}_1^*| = |\vec{p}_2^*| = |\vec{p}^*|$ . Therefore, in the Center of mass frame, we have  $p_i = (E_i^* = \sqrt{|\vec{p}^*|^2 + m_i^2}, |\vec{p}^*|)$  for each incoming particle. It follows from Eq C.1.11 that  $F = (E_1^* + E_2^*) |\vec{p}^*| = \sqrt{s} |\vec{p}^*|$ . In the center of mass frame, one also deduces  $\delta^{(4)}(p'_1 + p'_2 - p_1 - p_2) = \delta(E_1'^* + E_2'^* - \sqrt{s}) \delta^3(\vec{p}_1'^* + \vec{p}_2'^*)$  which turns Eq C.1.12 into:

$$d\sigma = \frac{d\Sigma_{2 \rightarrow 2}}{N_2 \phi} = \frac{1}{4 \sqrt{s} |\vec{p}^*| (2\pi)^2} \delta(E_1'^* + E_2'^* - \sqrt{s}) \delta^3(\vec{p}_1'^* + \vec{p}_2'^*) |M_{fi}|^2 \frac{d^3 \vec{p}_1'^* d^3 \vec{p}_2'^*}{4E_1'^* E_2'^*}. \quad (\text{C.1.13})$$

This Eq C.1.13 describes the cross section for a given initial state  $(p_1, p_2)$  to find outgoing particles in a final state  $d^3 \vec{p}_1', d^3 \vec{p}_2'$ . In this chapter, we are interested in the cross section to find the outgoing lepton in a given state, and don't use information of the proton final state. Therefore, we decided to integrate Eq C.1.13 over the kinematical space of the proton, and to express the final cross section according to the lepton solid angle  $d\Omega^* = \sin \theta^* d\theta^* d\phi^*$ :

$$d\sigma = \frac{d\Sigma_{2 \rightarrow 2}}{N_2 \phi} = \frac{1}{4\sqrt{s}|\vec{p}^*|(2\pi)^2} \delta(E_1'^* + E_2'^* - \sqrt{s}) |M_{fi}|^2 \frac{d^3 p_1^{\vec{*}}}{2E_1'^*} \int \int \int \delta^3(\vec{p}_1^{\vec{*}} + \vec{p}_2^{\vec{*}}) \frac{d^3 p_2^{\vec{*}}}{2E_2'^*} \quad (\text{C.1.14})$$

$$= \frac{d\Sigma_{2 \rightarrow 2}}{N_2 \phi} = \frac{1}{4\sqrt{s}|\vec{p}^*|(2\pi)^2} \delta(E_1'^* + E_2'^* - \sqrt{s}) |M_{fi}|^2 \frac{d^3 p_1^{\vec{*}}}{2E_1'^*} \frac{1}{2E_2'^*} \quad (\text{C.1.15})$$

$$= \frac{d\Sigma_{2 \rightarrow 2}}{N_2 \phi} = \frac{1}{4\sqrt{s}|\vec{p}^*|(2\pi)^2} \delta(E_1'^* + E_2'^* - \sqrt{s}) |M_{fi}|^2 \frac{|\vec{p}^*|^2 d|\vec{p}^*| d\Omega^*}{2E_1'^*} \frac{1}{2E_2'^*} \text{ in spherical coordinates.} \quad (\text{C.1.16})$$

One needs to integrate over the radius  $|\vec{p}^*|$  to obtain the cross section for a given solid angle:

$$d\sigma \frac{d\Sigma_{2 \rightarrow 2}}{N_2 \phi} = \frac{1}{4\sqrt{s}|\vec{p}^*|(2\pi)^2} \int_{|\vec{p}^*|^2=0}^{+\infty} \delta(\sqrt{|\vec{p}^*|^2 + m_1^2} + \sqrt{|\vec{p}^*|^2 + m_2^2} - \sqrt{s}) |M_{fi}|^2 \frac{|\vec{p}^*|^2 d|\vec{p}^*| d\Omega^*}{4\sqrt{|\vec{p}^*|^2 + m_1^2} \sqrt{|\vec{p}^*|^2 + m_2^2}}. \quad (\text{C.1.17})$$

We have integrated over the proton three-momentum, and would like not to integrate over the solid angle, namely contained in  $\vec{e}_1^{\vec{*}} = \frac{\vec{p}^{\vec{*}}}{|\vec{p}^{\vec{*}}|}$ . One can see that the total energy  $E'^* = E_1'^* + E_2'^*$  is then independent from the muon solid angle and we decided to change variables as:

$$E'^* = E_1'^* + E_2'^* = \sqrt{|\vec{p}^{\vec{*}}|^2 + m_1^2} + \sqrt{|\vec{p}^{\vec{*}}|^2 + m_2^2} \quad (\text{C.1.18})$$

$$dE'^* = |\vec{p}^{\vec{*}}|^2 d|\vec{p}^{\vec{*}}| \frac{\sqrt{|\vec{p}^{\vec{*}}|^2 + m_1^2} + \sqrt{|\vec{p}^{\vec{*}}|^2 + m_2^2}}{\sqrt{|\vec{p}^{\vec{*}}|^2 + m_1^2} \sqrt{|\vec{p}^{\vec{*}}|^2 + m_2^2}} \quad (\text{C.1.19})$$

which turns Equation C.1.17 into:

$$\frac{d\sigma}{d\Omega^*} = \frac{d\Sigma_{2 \rightarrow 2}}{N_2 \phi} = \frac{1}{16\sqrt{s}|\vec{p}^{\vec{*}}|(2\pi)^2} \int_{E'^*=m_1'+m_2'}^{+\infty} \delta(E'^* - \sqrt{s}) |M_{fi}|^2 \frac{dE'^*}{E'^*} |\vec{p}^{\vec{*}}| \quad (\text{C.1.20})$$

which finally gives:

$$\frac{d\sigma}{d\Omega^*} = \frac{d\Sigma_{2 \rightarrow 2}}{N_2 \phi} = \frac{1}{64(\pi)^2 s} |M_{fi}|^2 \frac{|\vec{p}^{\vec{*}}|}{|\vec{p}^{\vec{*}}|} \quad (\text{C.1.21})$$

On the amplitude part, we just need to calculate  $\overline{|M|^2}$ .

## C.2 Calculation of the amplitude

Using the Feynman rules (see [109] for example), the scattering amplitude M is simply:

$$M = \frac{4}{\sqrt{2}} G_F (\overline{u}_u \gamma^\mu \frac{I - \gamma^5}{2} u_d) (\overline{u}_l \gamma_\mu \frac{I - \gamma^5}{2} u_{\nu_l}) \quad (\text{C.2.1})$$

$$\overline{|M|^2} = \frac{1}{2} \sum_{s_1} \frac{1}{2} \sum_{s_2} \sum_{s'_1} \sum_{s'_2} |M|^2 \quad (\text{C.2.2})$$

$$\overline{|M|^2} = \frac{1}{2} \sum_{s_1} \frac{1}{2} \sum_{s_2} \sum_{s'_1} \sum_{s'_2} \frac{16}{2} G_F^2 (\overline{u}_u \gamma^\mu \frac{I - \gamma^5}{2} u_d) (\overline{u}_l \gamma_\mu \frac{I - \gamma^5}{2} u_{\nu_l}) (\overline{u}_u \gamma^\nu \frac{I - \gamma^5}{2} u_d)^* (\overline{u}_l \gamma_\nu \frac{I - \gamma^5}{2} u_{\nu_l})^* \quad (\text{C.2.3})$$

We can re-write the previous equation adding their component in spin state and noting  $G^\mu = \gamma^\mu \frac{(I - \gamma^5)}{2}$ :

$$\overline{|M|^2} = \frac{1}{2} \sum_{s_1} \frac{1}{2} \sum_{s_2} \sum_{s'_1} \sum_{s'_2} \frac{16}{2} G_F^2 ((\overline{u}_u)_a (G^\mu)_b^a (u_d)^b) ((\overline{u}_l)_c (G_\mu)_d^c (u_{\nu_l})^d) ((\overline{u}_u)_e (G^\nu)_f^e (u_d)^f)^* ((\overline{u}_l)_g (G_\nu)_h^g (u_{\nu_l})^h)^* \quad (\text{C.2.4})$$

We used this notation because  $(u_\alpha)^a$  and  $(G^\alpha)_b^a$  are scalar in both spinor space and spacetime. For this reason, we can re-arrange the previous equation as:

$$\overline{|M|^2} = \frac{16}{2} G_F^2 \frac{1}{2} \sum_{s_2} \sum_{s'_2} ((\overline{u}_u)_a (G^\mu)_b^a (u_d)^b) ((\overline{u}_u)_e (G^\nu)_f^e (u_d)^f)^* \frac{1}{2} \sum_{s_1} \sum_{s'_1} ((\overline{u}_l)_c (G_\mu)_d^c (u_{\nu_l})^d) ((\overline{u}_l)_g (G_\nu)_h^g (u_{\nu_l})^h)^* \quad (C.2.5)$$

$$\overline{|M|^2} = \frac{16}{2} G_F^2 L^{\mu\nu}(\text{quark}) L_{\mu\nu}(\text{lepton}) \quad (C.2.6)$$

with:

$$L_{\mu\nu}(\text{lepton}) = \frac{1}{2} \sum_{s_1} \sum_{s'_1} ((\overline{u}_l)_c (G_\mu)_d^c (u_{\nu_l})^d) ((\overline{u}_l)_g (G_\nu)_h^g (u_{\nu_l})^h)^* \quad (C.2.7)$$

$$L^{\mu\nu}(\text{quark}) = \frac{1}{2} \sum_{s_2} \sum_{s'_2} ((\overline{u}_u)_a (G^\mu)_b^a (u_d)^b) ((\overline{u}_u)_e (G^\nu)_f^e (u_d)^f)^* \quad (C.2.8)$$

Using these notation, we may like to contract spinors using the completeness relation:

$$\sum_s u_s \overline{u}_s = p + m, \quad \sum_{s'} v_{s'} \overline{v}_{s'} = p - m \quad (C.2.9)$$

For doing so, we will transform  $((\overline{u}_l)_g (G_\nu)_h^g (u_{\nu_l})^h)^* \stackrel{scal.}{=} ((\overline{u}_l)_g (G_\nu)_h^g (u_{\nu_l})^h)^\dagger = (((u_{\nu_l})^h)^\dagger ((G_\nu)_h^g)^\dagger (\gamma^0)_g^i (u_l)_i)$  since it is a scalar in spinor space. Using the gamma matrices commutation properties ([109] for example), we deduce  $((G_\nu)_h^g)^\dagger (\gamma^0)_g^i = (G_{\nu\nu}^\dagger \gamma^0)_h^i \stackrel{commut.}{=} (\gamma^0 G_{\nu\nu}^\dagger)_h^i \stackrel{Ghermit.}{=} (\gamma^0 G_{\nu\nu})_h^i = (\gamma^0)_h^g (G_{\nu\nu})_g^i$ .

We therefore obtain:  $((\overline{u}_l)_g (G_\nu)_h^g (u_{\nu_l})^h)^* = (((u_{\nu_l})^h)^\dagger (\gamma^0)_h^g (G_{\nu\nu})_g^i (u_l)_i) = ((u_{\nu_l}^\dagger \gamma^0)_g^i (G_{\nu\nu})_g^i (u_l)_i) = (\overline{u}_{\nu_l}^g (G_{\nu\nu})_g^i (u_l)_i)$ . Using this relation, the leptonic part defined in Eq C.2.8 becomes:

$$L_{\mu\nu}(\text{lepton}) = \frac{1}{2} \sum_{s_1} \sum_{s'_1} ((\overline{u}_l)_c (G_\mu)_d^c (u_{\nu_l})^d) (\overline{u}_{\nu_l}^g (G_{\nu\nu})_g^i (u_l)_i) \quad (C.2.10)$$

$$= \left( \sum_{s'_1} ((u_l)_i \overline{u}_l)_c \right) (G_\mu)_d^c \frac{1}{2} \sum_{s_1} (\overline{u}_{\nu_l}^g (u_{\nu_l})^d) (G_{\nu\nu})_g^i \quad (C.2.11)$$

since  $s'_1$  only affects  $u_l$  and  $s_1$   $u_{\nu_l}$ . Note we could not decompose the sum if it weren't the case. The leptonic component therefore can be transformed as:

$$L_{\mu\nu}(\text{lepton}) = \left( \sum_{c,i} ((u_l)_i \overline{u}_l)_c \right) (G_\mu)_d^c \frac{1}{2} \sum_{g,d} (\overline{u}_{\nu_l}^g (u_{\nu_l})^d) (G_{\nu\nu})_g^i \text{ since } s'_1 \text{ only affects } u_l \text{ and } s_1 \text{ } u_{\nu_l} \quad (C.2.12)$$

$$= (p' + m_l)_{ic} (G_\mu)_d^c \frac{1}{2} (p + m_{\nu_l})^{dg} (G_\nu)_g^i \quad (C.2.13)$$

Using the contraction over spinor index, it leads to:

$$L_{\mu\nu}(\text{lepton}) = \frac{1}{2} \text{Tr}((p' + m_l) G_\mu (p + m_{\nu_l}) G_\nu). \quad (C.2.14)$$

The trace of a matrix being linear, it follows that:

$$L_{\mu\nu}(\text{lepton}) = \frac{1}{2} [\text{Tr}(p' G_\mu p G_\nu) + m_{\nu_l} \text{Tr}(p' G_\mu G_\nu) + m_l \text{Tr}(G_\mu p G_\nu) + m_l m_{\nu_l} \text{Tr}(G_\mu G_\nu)] \quad (C.2.15)$$

At this point, we will not neglect the neutrino mass  $m_{\nu_l}$  since we will use the same calculation for the

quark sector. Using the Clifford algebra properties (summarised in [109] for example), we deduce:

$$m_l m_{\nu_l} \text{Tr}(G_\mu G_\nu) = m_l m_{\nu_l} \text{Tr}(\gamma_\mu(I - \gamma^5)\gamma_\nu(I - \gamma^5)) \quad (\text{C.2.16})$$

$$= m_l m_{\nu_l} \text{Tr}(\gamma_\mu(I - \gamma^5)(I + \gamma^5)\gamma_\nu) = 0 \text{ since } P_L P_R = 0 \text{ (projectors defined in Chapter 1)} \quad (\text{C.2.17})$$

$$m_{\nu_l} \text{Tr}(p' G_\mu G_\nu) = m_l \text{Tr}(G_\mu p G_\nu) = 0 \text{ since it is an odd product of gamma matrices} \quad (\text{C.2.18})$$

$$\text{Tr}(p' G_\mu p G_\nu) = p'^\alpha p^\beta \text{Tr}(\gamma_\alpha G_\mu \gamma_\beta G_\nu) \quad (\text{C.2.19})$$

$$= \frac{1}{2} p'^\alpha p^\beta [\text{Tr}(\gamma_\alpha \gamma_\mu \gamma_\beta \gamma_\nu) - \text{Tr}(\gamma_\alpha \gamma_\mu \gamma^5 \gamma_\beta \gamma_\nu) - \text{Tr}(\gamma_\alpha \gamma_\mu \gamma_\beta \gamma_\nu \gamma^5) + \text{Tr}(\gamma_\alpha \gamma_\mu \gamma^5 \gamma_\beta \gamma_\nu \gamma^5)]. \quad (\text{C.2.20})$$

$$(\text{C.2.21})$$

Using the  $\gamma^5$  anti-commutation with other gamma matrices:

$$\text{Tr}(\gamma_\alpha \gamma_\mu \gamma^5 \gamma_\beta \gamma_\nu \gamma^5) = \text{Tr}(\gamma_\alpha \gamma_\mu \gamma_\beta \gamma_\nu (\gamma^5)^2) = \text{Tr}(\gamma_\alpha \gamma_\mu \gamma_\beta \gamma_\nu) \quad (\text{C.2.22})$$

On top of this, we use cyclicity trace property to change:

$$\text{Tr}(\gamma_\alpha \gamma_\mu \gamma^5 \gamma_\beta \gamma_\nu) = \text{Tr}(\gamma^5 \gamma_\beta \gamma_\nu \gamma_\alpha \gamma_\mu) \quad (\text{C.2.23})$$

and to change:

$$\text{Tr}(\gamma_\alpha \gamma_\mu \gamma_\beta \gamma_\nu \gamma^5) = \text{Tr}(\gamma^5 \gamma_\alpha \gamma_\mu \gamma_\beta \gamma_\nu) \quad (\text{C.2.24})$$

which leads to express  $\text{Tr}(p' G_\mu p G_\nu)$  as:

$$\text{Tr}(p' G_\mu p G_\nu) = \frac{1}{2} p'^\alpha p^\beta [2\text{Tr}(\gamma_\alpha \gamma_\mu \gamma_\beta \gamma_\nu) - \text{Tr}(\gamma_\alpha \gamma_\mu \gamma^5 \gamma_\beta \gamma_\nu) - \text{Tr}(\gamma_\alpha \gamma_\mu \gamma_\beta \gamma_\nu \gamma^5)] \quad (\text{C.2.25})$$

$$= \frac{1}{2} p'^\alpha p^\beta [2\text{Tr}(\gamma_\alpha \gamma_\mu \gamma_\beta \gamma_\nu) - \text{Tr}(\gamma_\alpha \gamma_\mu \gamma^5 \gamma_\beta \gamma_\nu) - \text{Tr}(\gamma_\alpha \gamma_\mu \gamma_\beta \gamma_\nu \gamma^5)] \quad (\text{C.2.26})$$

$$= \frac{1}{2} p'^\alpha p^\beta [2.4(g_{\alpha\mu}g_{\beta\nu} - g_{\alpha\beta}g_{\mu\nu} + g_{\alpha\nu}g_{\mu\beta}) + 4i\epsilon_{\beta\nu\alpha\mu} + 4i\epsilon_{\alpha\mu\beta\nu}] \quad (\text{C.2.27})$$

$$\text{using the gamma matrices relations on the trace (see [109] for example)} \quad (\text{C.2.28})$$

$$= \frac{1}{2} p'^\alpha p^\beta [2.4(g_{\alpha\mu}g_{\beta\nu} - g_{\alpha\beta}g_{\mu\nu} + g_{\alpha\nu}g_{\mu\beta}) + 2 \cdot 4i\epsilon_{\alpha\mu\beta\nu}] \quad (\text{C.2.29})$$

$$\text{using anti-symmetric properties of the } \epsilon \text{ tensor} \quad (\text{C.2.30})$$

$$= 4p'^\alpha p^\beta [g_{\alpha\mu}g_{\beta\nu} - g_{\alpha\beta}g_{\mu\nu} + g_{\alpha\nu}g_{\mu\beta} + i\epsilon_{\alpha\mu\beta\nu}] \quad (\text{C.2.31})$$

$$= 4[p'_\mu p_\nu - p'^\alpha p_\alpha g_{\mu\nu} + p'_\nu p_\mu + ip'^\alpha p^\beta \epsilon_{\alpha\mu\beta\nu}] \quad (\text{C.2.32})$$

We therefore deduce:

$$L_{\mu\nu}(\text{lepton}) = \frac{1}{2} 4[p'_\mu p_\nu - p'^\alpha p_\alpha g_{\mu\nu} + p'_\nu p_\mu + ip'^\alpha p^\beta \epsilon_{\alpha\mu\beta\nu}] \quad (\text{C.2.33})$$

and:

$$L^{\mu\nu}(\text{quark}) = \frac{1}{2} 4[p_2'^\mu p_2^\nu - p_2'^\gamma p_{2\gamma} g^{\mu\nu} + p_1'^\nu p_2^\mu + ip_{2\alpha}' p_{2\beta} \epsilon^{\gamma\mu\delta\nu}] \quad (\text{C.2.34})$$

using the very same calculation on the quark term. We therefore obtain:

$$L_{\mu\nu}(\text{lepton}) L^{\mu\nu}(\text{quark}) = 4[p'_{1\mu} p_{1\nu} - p_1'^\alpha p_{1\alpha} g_{\mu\nu} + p'_{1\nu} p_{1\mu} + ip_1'^\alpha p_1^\beta \epsilon_{\alpha\mu\beta\nu}] \quad (\text{C.2.35})$$

$$\times [p_2'^\mu p_2^\nu - p_2'^\gamma p_{2\gamma} g^{\mu\nu} + p_1'^\nu p_2^\mu + ip_{2\alpha}' p_{2\beta} \epsilon^{\gamma\mu\delta\nu}]$$

$$L_{\mu\nu}(\text{lepton}) L^{\mu\nu}(\text{quark}) = 4[2p_1 \cdot p_2 p_1' \cdot p_2' + 2p_1 \cdot p_2' p_1' \cdot p_2 + ip_{1\alpha} p_{1\beta}' p_{2\mu} p_{2\nu}' \epsilon^{\alpha\mu\beta\nu} + ip_{1\alpha} p_{1\beta}' p_{2\nu} p_{2\mu}' \epsilon^{\alpha\mu\beta\nu} + ip_{1\mu} p_{1\nu}' p_{2\alpha} p_{2\beta}' \epsilon_{\alpha\mu\beta\nu} + ip_{1\nu} p_{1\mu}' p_{2\alpha} p_{2\beta}' \epsilon_{\alpha\mu\beta\nu} - ip_{1\alpha} p_{1\beta}' p_{2\gamma} p_{2\delta}' \epsilon_{\alpha\mu\beta\nu} \epsilon^{\gamma\mu\delta\nu}] \quad (\text{C.2.36})$$

using  $\epsilon_{\alpha\mu\beta\nu}g^{\mu\nu} = 0$  since  $g^{\mu\nu} \neq 0$  when  $\mu = \nu$ , for which  $\epsilon_{\alpha\mu\beta\nu} = 0$ . In Equation C.2.36, the third and fourth terms will cancel using  $\epsilon^{\alpha\mu\beta\nu} = -\epsilon_{\alpha\nu\beta\mu}$  antisymmetry in the third term. By doing the same for the fifth and sixth terms, they cancel each other. Finally, using furthermore the antisymmetric property of  $\epsilon$ , one shows:  $\epsilon_{\alpha\mu\beta\nu}\epsilon^{\gamma\mu\delta\nu} = \epsilon_{\mu\nu\alpha\beta}\epsilon^{\mu\nu\gamma\delta} = -2(\delta_\gamma^\alpha\delta_\delta^\beta - \delta_\delta^\alpha\delta_\gamma^\beta)$ . Using this final property in Equation C.2.36, we deduce:

$$L_{\mu\nu}(\text{lepton})L^{\mu\nu}(\text{quark}) = 4(2p_1 \cdot p_2 p'_1 \cdot p'_2 + 2p_1 \cdot p'_2 p'_1 \cdot p_2 + 2p_{1\alpha}p'_{2\beta}p'_2{}^\gamma p'_2{}^\delta (\delta_\gamma^\alpha\delta_\delta^\beta - \delta_\delta^\alpha\delta_\gamma^\beta)) \quad (\text{C.2.37})$$

$$= 16p_1 \cdot p_2 p'_1 \cdot p'_2 \quad (\text{C.2.38})$$

Because of four-momentum conservation, we deduce the form of  $p_1 \cdot p_2 p'_1 \cdot p'_2$ :

$$p_1 + p_2 = p'_1 + p'_2 \implies (p_1 + p_2)^2 = (p'_1 + p'_2)^2 \quad (\text{C.2.39})$$

$$\implies m_1^2 + m_2^2 + 2p_1 p_2 = m_1'^2 + m_2'^2 + 2p'_1 p'_2 \quad (\text{C.2.40})$$

$$\implies p_1 p_2 = p'_1 p'_2 \text{ in the case where all masses are neglected.} \quad (\text{C.2.41})$$

$$(\text{C.2.42})$$

The square of the center of mass energy available is  $s = (p_1 + p_2)^2 \cong 2p_1 \cdot p_2$  in the small mass hypothesis. We finally deduce the module squared amplitude inserting the quark and leptonic current effects (Equation C.2.38) in Equation C.2.6 which leads to:

$$\overline{|M|^2} = \frac{16}{2}G_F^2 16p_1 \cdot p_2 p'_1 \cdot p'_2 \quad (\text{C.2.43})$$

$$= \frac{1}{2}G_F^2 \frac{s^2}{4} = \frac{1}{8}G_F^2 s^2. \quad (\text{C.2.44})$$

$$(\text{C.2.45})$$

In the hypothesis of small masses, Eq C.2.42 becomes in the center of mass frame:  $p^* = p'^*$  and implies that  $|\vec{p}^*| = |\vec{p}'^*|$ . We deduce the final cross section:

$$\frac{d\sigma}{d\Omega^*} = \frac{1}{64\pi^2 s} \overline{|M|^2} \frac{|\vec{p}'^*|}{|\vec{p}^*|} = \frac{1}{64\pi^2 s} \frac{1}{2}G_F^2 \frac{s^2}{4} = \frac{1}{512\pi^2}G_F^2 s, \quad (\text{C.2.46})$$

$$\implies \sigma = \frac{G_F^2 s}{\pi}. \quad (\text{C.2.47})$$

### C.3 $|M|^2$ energy dependency

One naturally expect that the kinematical term of the cross section depends on the neutrino energy: the higher the energy is, the more likely it is to produce the outgoing lepton.

As for the squared module amplitude part  $|M|^2$ , one observes that  $|M|^2 \propto s^2 \propto E_\nu^2$  in the lab frame, and so not only the kinematical part of the cross section depends on neutrino energy. We have investigated the source of this  $E^2$  dependency in the amplitude part. A priori, we observed that the  $q^2$  value increases with neutrino energy, which would be the source of an increasing amplitude with neutrino energy, since the virtual W boson will be closer to on-shell value. Figure C.1 shows that the W boson exchanged has a four-momentum  $q^2 = (p_1 - p'_1)^2$  (t-channel diagram). Since  $M \propto \Delta_W$  with  $\Delta_W$  the electroweak propagator, it implies  $M \propto \Delta_W \propto \frac{1}{q^2 - M_W^2}$ . Therefore, the higher  $q^2$ , the higher the amplitude: this represents the fact that the W boson is more and more on-shell since  $q^2 = E_W^2 - |\vec{p}_W|^2 = M_W^{virtual^2}$  represents the squared mass of the virtual W boson. However, this naive explanation is wrong, since the calculation assumes no  $q^2$ -dependency since we use the point-like Fermi approximation ( $q^2 \ll M_W^2$ ) to describe the interaction. It is interesting to note that introducing the propagator, does not increase necessarily with neutrino energy. This naive assumption is based on s-channel diagrams whose propagator four-momentum is directly function of the incoming total particle energy in the center of mass frame. In a t-channel, we will show that this needs to be refined. The four-momentum of the exchanged boson can be written:

$$q^2 = (p_1 - p'_1)^2 = p_1^2 + p_1'^2 - 2p_1 \cdot p'_1 \text{ (in the lab frame)} \quad (\text{C.3.1})$$

$$= m_1'^2 - 2(E_1 E'_1 - \vec{p}_1 \cdot \vec{p}'_1) = m_1'^2 - 2(|\vec{p}_1| |\vec{p}'_1| \cos(\theta_{11'})) \quad (\text{C.3.2})$$

if the neutrino mass is neglected and with  $\theta_{11'}$  the angle of the outgoing lepton with the neutrino in the lab frame. This finally leads to the  $q^2$ -value:

$$q^2 = m_1'^2 - 2|\vec{p}_1|E_1'(1 - \frac{|\vec{p}_1'|}{E_1'})\cos(\theta_{11'}) \quad (\text{C.3.3})$$

Since  $|\vec{p}_1'| < E_1'$ , it follows that  $\frac{|\vec{p}_1'|}{E_1'}\cos(\theta_{11'}) < 1$  which implies that  $(1 - \frac{|\vec{p}_1'|}{E_1'}\cos(\theta_{11'}))$  is always positive. Adding this constraint in Equation C.3.3, we observe that an increasing neutrino energy  $E_1 = |\vec{p}_1|$  necessarily decreases the  $q^2$  value for a given outgoing lepton energy  $|E_1'|$ . Moreover, one shows analytically that  $q^2 < 0$  whatever the value of the four-momenta of the neutrino and of the lepton, and whatever their angle  $\theta_{11'}$ . The same calculation shows that lower and upper bound differences on  $q^2$  increase with neutrino energy, which can be expressed by “neutrino energy increasing implies that  $q^2$  has more capacity to be negative, while remaining always bound to 0 upper limit”. We have shown the behaviour of  $q^2$  with the neutrino and muon momentum in Figure C.2.

This shows that the naive assumption “W boson vector should be closer to on-shell particle with increasing neutrino energy” is wrong for a t-channel diagram since  $M \propto \frac{1}{q^2 - M_W^2}$  with average increase of the negative  $q^2$  with neutrino energy.

To understand the  $|M|^2$  quadratic dependency with s, we observe that s-dependency comes from the completeness relations shown earlier where we have shown that  $[u]^2 \propto m \Rightarrow [u] \propto \sqrt{E}$ . This implies that the spinors u and v have the dimension of the square of an energy. This dimension study can be improved using Dirac equation solutions, from which are derived the completeness relations ([109] for details). It leads to  $u^\dagger u = 2E$  with E the energy of the fermion. We will use an analogy with Dirac sea of fermionic states to finally explain the  $|M|^2$  quadratic dependency with s:

1. Since fermions obey the Pauli exclusion principle, each state can be maximally populated by 2 fermionic state of the same energy but opposite spin.
2. The fundamental dynamic principle involves that each system tends to minimise its total energy: the lower energy Fermionic states will be populated in priority.
3. To create one particle and antiparticle of energy E, an available 2E energy is required.

It follows that the available energy s (in the center of mass frame) to create final state particles (lepton and up quark here) increases with neutrino energy. This is the analogous to the 2E energy available in the Dirac sea representation. With this energy, we can create a lepton having an energy from  $m_\mu$  (case where most of the energy is transferred to the quark) to  $E - (m_u - m_d)$  (in the opposite case). For the lepton, it means that the possible different energy states available are higher than for a low energy neutrino. For a given neutrino energy, we can imagine different cases of outgoing particle momentum which can be represented by different diagrams. The number of these diagrams then increases with the neutrino energy for the reason we just discussed. Since the total amplitude is obtained by summing all possible diagrams amplitudes, the total amplitude will increase with neutrino energy as we have shown earlier. This naturally explains the  $|M|^2$  dependency in neutrino energy by the outgoing particle phase space expansion. Finally, one observes that this information was contained in Figure C.2 in a different way: for a higher neutrino energy, the phase space for  $q^2$  values increases with the neutrino energy.

## C.4 Cross section dependency on $q^2$

Though  $|M|^2$  is always Lorentz invariant, we have seen earlier that the differential  $d\sigma$  is also in the case of colinear incident particles, as in the present case. Therefore, we can directly deduce the cross section in the lab frame from C.1.16. On top of this, we'd like to express the cross section with the four-momentum exchange q since it is easier to link with the variables we will use to discuss the

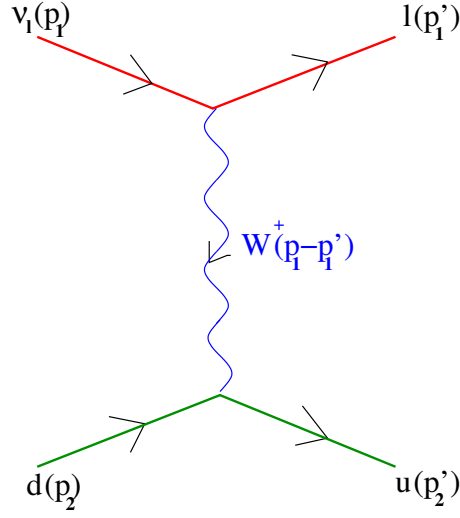


Figure C.1: Definition of the four momenta for the quarks and leptons interacting through the exchange of a  $W$  boson.

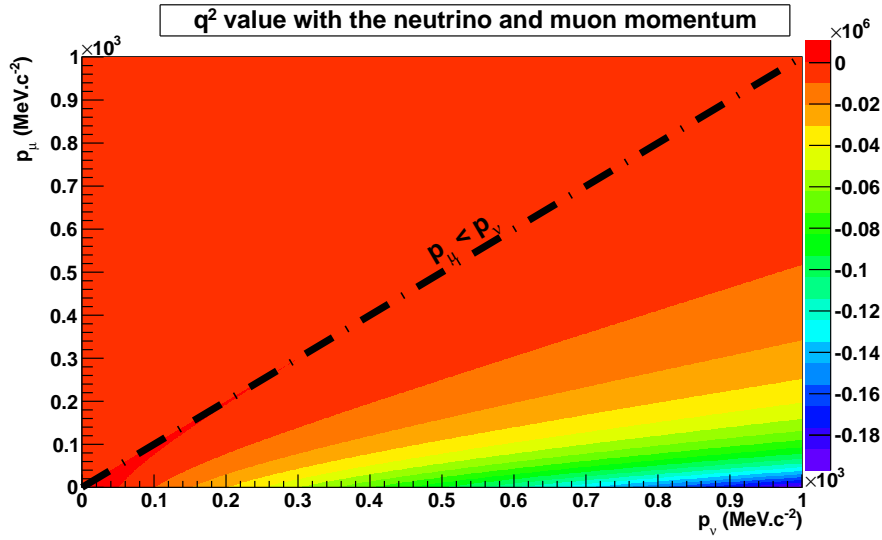


Figure C.2: Value of the  $q^2$  four-momentum exchanged (Z axis) with the neutrino and muon momenta. One observes that the space phase increases at large  $p_\nu$ .

results, namely  $E_\nu$ ,  $\mu$  and  $\cos \theta_\mu$ . Equation C.1.16 then becomes (in the limit of small neutrino masses compared to the lepton):

$$\frac{d\sigma}{dq^2} = \frac{1}{16\pi} \frac{\overline{|M|^2}}{(s - m_\mu^2)^2}. \quad (\text{C.4.1})$$

Using the amplitude estimated in Eq C.2.45, the cross section can be re-written as:

$$\frac{d\sigma}{dq^2} = \frac{1}{8 \cdot 16\pi} \frac{G_F^2 s^2}{(s - m_\mu^2)^2}. \quad (\text{C.4.2})$$

In the case the energy available in the center of mass frame is large compared to the outgoing lepton mass ( $s \gg m_\mu^2$ ), we finally obtain:

$$\frac{d\sigma}{dq^2} = \frac{1}{128\pi} G_F^2 \quad (\text{C.4.3})$$

which implies that the cross section varies linearly with the exchange momentum squared  $q^2$ :

$$\sigma = \frac{1}{128\pi} G_F^2 q^2. \quad (\text{C.4.4})$$



## Appendix D

# Calculation of the neutrino cross section on a nucleon

THE cross section of a neutrino on a nucleon can be estimated similarly to the case of a free quark. The hadronic “quark” sector current will be only replaced by a “nucleon” current to take into account quark interactions, valence and sea quarks. In the case of a free quark, the amplitude of the process is given in Appendix C. In the case of a nucleon, let’s note  $\langle n(p_p) |$  and  $| n(p_n) \rangle$  the final outgoing proton and initial incoming neutron states. To keep the V-A nature of the weak interactions as observed in data, we should replace  $\bar{u}_u \gamma^\mu \frac{1-\gamma^5}{2} u_d$  by  $\langle p(p_p) | h_W^\mu | n(p_n) \rangle$  with  $h_W^\mu$  the hadronic transition matrix that should satisfy the V-A structure of weak interactions [22]. The hadronic transition matrix can be therefore re-written:

$$\begin{aligned} h_W^\mu &= v_W^\mu - a_W^\mu \text{ with:} \\ v_W^\mu &\text{the vector part so } \propto \gamma^\mu \\ a_W^\mu &\text{the axial part so } \propto \gamma^\mu \gamma^5 \end{aligned} \quad (\text{D.0.1})$$

The vector and axial terms should be constructed with the available kinematic quantities. The only two independent quantities are the four-momenta of the proton and neutron  $p_p$  and  $p_n$ . Note that  $q = (p_p - p_n)$  is not independent from the two kinematical quantities mentioned above. Therefore, the most general vector we can construct is of the type:

$$\langle p(p_p) | v_W^\mu | n(p_n) \rangle = \bar{u}_p(p_p) [\alpha(q^2) \gamma^\mu + \beta(q^2) p_p^\mu + \gamma(q^2) p_n^\mu] u_n(p_n) \quad (\text{D.0.2})$$

where the  $q^2$ -dependency is proven below. By construction, the above coefficients  $\alpha$ ,  $\beta$  and  $\gamma$  depend on all possible Lorentz scalars. However, the only available independent scalars we can construct from  $p_p$  and  $p_n$  are:

1.  $p_p^2 = m_p^2$  and  $p_n^2 = m_n^2$
2.  $p_p \cdot p_n = \frac{1}{2}(m_p^2 + m_n^2 - (p_p - p_n)^2) = \frac{1}{2}(m_p^2 + m_n^2 - q^2)$

Since the nucleon masses are constant, the coefficients in equation only vary with  $q^2$ .

We can re-organize the terms in Eq D.0.2 as:

$$\langle p(p_p) | v_W^\mu | n(p_n) \rangle = \bar{u}_p(p_p) [f_1(q^2) \gamma^\mu + f_2(q^2) (p_p^\mu + p_n^\mu) + f_3(q^2) (p_p^\mu - p_n^\mu)] u_n(p_n) \quad (\text{D.0.3})$$

with  $f_1 = \alpha$ ,  $f_2 = \beta + \gamma$  and  $f_3 = \beta - \gamma$ . The proton and neutron  $u$  fermionic spinors obey the Dirac equation which implies:

$$\bar{u}_p i \sigma^{\mu\nu} q_\nu u_n(p_n) = \bar{u}_p [p_p^\mu + p_n^\mu - (m_p + m_n) \gamma^\mu] u_n(p_n) \quad (\text{D.0.4})$$

with  $\sigma$  the Pauli matrices. We use this previous equation to remove the  $[p_p^\mu + p_n^\mu]$  part in Eq D.0.3. Assuming finally that:  $m_n \simeq m_p \simeq m_N$ , we can transform Eq D.0.3 in:

$$\langle p(p_p) | v_W^\mu | n(p_n) \rangle = \bar{u}_p(p_p) [F_1(q^2) \gamma^\mu + \frac{i \sigma^{\mu\nu} q_\nu}{2m_N} F_2(q^2) + \frac{q^\mu}{m_N} F_3(q^2)] u_n(p_n) \quad (\text{D.0.5})$$

The axial part of the hadronic matrix may also be written as Eq D.0.5 with an additional  $\gamma^5$  factor. Simply using  $q^2$  definition, one deduces the most general form of the axial part:

$$\langle p(p_p) | a_W^\mu | n(p_n) \rangle = \overline{u}_p(p_p) [G_A(q^2) \gamma^\mu \gamma^5 + \frac{q^\mu}{m_N} \gamma^5 G_P(q^2) + \frac{p_p^\mu + p_n^\mu}{m_N} \gamma^5 G_3(q^2)] u_n(p_n) \quad (\text{D.0.6})$$

We can re-write Eq D.0.5 and Eq D.0.6 in a more standard way defining  $Q^2 \equiv -q^2$  that is a positive quantity for CC inclusive cross section calculation.

The next calculation has been skipped in this work in order not to lose clarity. Unlike the whole cross section calculation on free quark, the following simplifications will not bring much in the understanding and are quite lengthy. One may find a very detailed explanation of this calculation in Ref [22]. We will directly extract the main results:

- QCD is invariant under CPT and CP in the standard model. The subsequent T invariance may be used to show that the form factors in Eq D.0.5 and D.0.6 are real (Ref [110]).
- Assuming the strong isospin symmetry (neglecting quark u and d masses differences), one shows (Ref [22]) that  $u \rightarrow d$  and  $d \rightarrow -u$ , which implies:  $|n(p_n)\rangle \rightarrow |p(p_n)\rangle$  and  $|p(p_p)\rangle \rightarrow -|n(p_p)\rangle$ . Vector and axial currents may be naturally expressed with the strong isospin creation operator since they turn a d quark into a u quark (In particular, we can write  $v_W^\mu = v_+^\mu$ , the strong isospin creation operator). It follows that:  $\langle p(p_p) | v_W^\mu | n(p_n) \rangle = \langle p(p_p) | a_W^\mu | n(p_n) \rangle^*$  and  $\langle p(p_p) | v_W^\mu | n(p_n) \rangle = \langle p(p_p) | a_W^\mu | n(p_n) \rangle^*$ , which leads respectively to  $F_3(q^2) = 0$  and  $G_3(q^2) = 0$ . These 2 form factors are called second class currents.
- The strong isospin symmetry implies that the vector current defined in Eq D.0.1 is conserved ( $\partial_\mu v_a^\mu, \forall a$ ). This hypothesis is often referred to as “conserved vector current hypothesis (CVC)”, that is a direct consequence of the strong isospin symmetry hypothesis. The  $v_a^0$  are then the strong isospin charges along the 3 isospin directions, while  $v_a^{1,2,3}$  are the strong isospin vectors using Noether theorem in analogy with  $U(1)_{QED}$ . This implies that  $\langle p(p_p) | v_W^\mu | n(p_n) \rangle = \langle p(p_p) | v_3^\mu | p(p_n) \rangle - \langle n(p_p) | v_3^\mu | n(p_n) \rangle$ , with  $v_3^\mu$  the vector current of the third isospin component. One notices in the last expression that “ $v_3^\mu$  does not change the nucleon type, unlike  $v_W^\mu$ ”, and can therefore be expressed as an electromagnetic current (having the same  $\gamma^\mu$  structure). It finally implies that the  $F_1$  and  $F_2$  form factors in Eq D.0.5 can be expressed with the electromagnetic form factors of the nucleons  $F_1^{Nucleon}$  (Dirac form factor) and  $F_2^{Nucleon}$  (Pauli form factor):

$$F_1(Q^2) = F_1^p(Q^2) - F_1^n(Q^2) \quad (\text{D.0.7})$$

$$F_2(Q^2) = F_2^p(Q^2) - F_2^n(Q^2) \quad (\text{D.0.8})$$

The advantage of such a change is that we can express [22] these Pauli and Dirac form factors at  $Q^2 = 0$  using respectively the electric charges of the nucleon and their anomalous magnetic moments:

$$F_1^p(0) = 1 \quad (\text{D.0.9})$$

$$F_1^n(0) = 0 \quad (\text{D.0.10})$$

$$F_2^p(0) = \frac{\mu_p}{\mu_n} - 1 \text{ with } \mu_{p/n} \text{ the proton/neutron magnetic moments.} \quad (\text{D.0.11})$$

$$F_2^n(0) = \frac{\mu_n}{\mu_N} \text{ with } \mu_N \text{ the nuclear magneton.} \quad (\text{D.0.12})$$

It implies that the  $F_1(Q^2)$  and  $F_2(Q^2)$  form factors can be measured directly in electron scattering experiments, as long as the strong isospin hypothesis holds. This has been widely used to simplify measurements in neutrino experiments.

- Unlike the vector part, the axial current is not conserved because quark mass terms are not invariant under chiral strong isospin transformations. It can be shown (Ref [22]) that charged pions would not decay if the axial current were conserved. This hypothesis is often referred to as “partially conserved axial charged current” hypothesis (PCAC). This led Gell-Mann and Levy (Ref [111]) to express the axial current derivative according to the pion decay constant  $f_\pi$ :

$$\partial a_W^\mu = f_\pi m_\pi^2 \pi^- \quad (\text{D.0.13})$$

with  $\pi^-$  the negative pion field which satisfies the Klein-Gordon equation of a spin-0 particle:

$$(\square + m_\pi^2)\pi^- = j_{\pi^-} \quad (\text{D.0.14})$$

with  $j_{\pi^-}$  the source of the pion field that would decay in  $\mu^-$  and  $\bar{\nu}_\mu$ . It becomes:

$$(-q^2 + m_\pi^2) \langle p(p_p) | \pi^- | n(p_n) \rangle = \langle p(p_p) | j_{\pi^-} | n(p_n) \rangle \quad (\text{D.0.15})$$

We selected the pion four-momentum as  $q^2$  (decay in s-channel) which is the four-momentum exchanged in our charged current interaction (t-channel). The four-momentum conservation at pion decay vertex implies that the  $W$  boson exchanged in the pion decay has a four-momentum  $q^2$ . This is natural since we'd like to describe the axial current involving a  $W$  boson with the  $q^2$  four-momentum.

Finally,  $\langle p(p_p) | j_{\pi^-} | n(p_n) \rangle$  may be expressed in the most general case as (since  $j_{\pi^-}$  is the pion source that decays only through an axial current):

$$\langle p(p_p) | j_{\pi^-} | n(p_n) \rangle = i \sqrt{2} g_{\pi N}(Q^2) \bar{u}_p(p_p) \gamma^5 u_n(p_n) e^{ix \cdot q} \quad (\text{D.0.16})$$

with  $g_{\pi N}(Q^2)$  the so-called “pion-nucleon” form factor that can be measured through pion-nucleon experiments (Ref [68]). Deriving Eq D.0.6 and using Eq D.0.13 with Eq D.0.15 and Eq D.0.16 as inputs, one deduces

$$(-q^2 + m_\pi^2)[2m_N G_A(Q^2) + \frac{q^2}{m_N} G_P(Q^2)] = \sqrt{2} g_{\pi N}(Q^2) f_\pi m_\pi^2 \quad (\text{D.0.17})$$

This allows ultimately to express the pseudoscalar weak charged-current form factor  $G_P(Q^2)$  with the axial one  $G_A(Q^2)$ .

In a nutshell, we observed that the second class current form factors disappear ( $F_3$  and  $G_3$ ) under strong isospin symmetry hypothesis. Moreover, we have shown that the  $F_1$  and  $F_2$  form factors can be expressed with electromagnetic nucleon form factors under CVC hypothesis. Therefore, these factors are the same as those directly measured in electron scattering experiments. Finally, we have expressed the pseudoscalar form factor  $G_P$  as a function of  $g_{\pi N}(Q^2)$  that can be measured in pion-nucleon experiments and  $G_A$  the axial form factor. As a consequence of CVC and PCAC, neutrino experiments have then historically only focused on measuring the axial form factor  $G_A$ .

Under these hypotheses, we finally obtain for a quasi-elastic charged current cross section:

$$\begin{aligned} M = & -i \frac{G_F}{\sqrt{2}} V_{ud} \bar{u}_l(p'_1) \gamma_\mu (1 - \gamma^5) u_{\nu_l}(p_1) \\ & \times \bar{u}_p(p_p) [F_1(q^2) \gamma^\mu + \frac{i \sigma^{\mu\nu} q_\nu}{2m_N} F_2(q^2) - G_A(q^2) \gamma^\mu \gamma^5 - \frac{q^\mu}{m_N} \gamma^5 G_P(q^2)] u_n(p_n) \end{aligned} \quad (\text{D.0.18})$$

The differential cross section with  $Q^2$  in the laboratory frame can then be calculated using Eq D.0.18 instead of the free quark  $M$  amplitude in the previous section. This calculation has been derived in Ref [85]:

$$\frac{d\sigma}{dQ^2} = \frac{G_F^2 |V_{ud}|^2 M_N^2}{8\pi(p_\nu \cdot p_{N_i})} [A(Q^2) \pm \frac{s-u}{M_N^2} B(Q^2) + \frac{(s-u)^2}{M_N^4} C(Q^2)] \quad (\text{D.0.19})$$

with

$$A = \frac{(m^2 + Q^2)}{M_N^2} [(1 + \eta)G_A^2 - (1 - \eta)F_1^2 + \eta(1 - \eta)F_2^2 + 4\eta F_1 F_2 - \frac{m^2}{4M_N^2} ((F_1 + F_2)^2 + (G_A + 2G_P)^2 - (\frac{Q^2}{M_N^2} + 4)G_P^2)] \quad (\text{D.0.20})$$


$$B = \frac{Q^2}{M_N^2} G_A (F_1 + F_2) \quad (\text{D.0.21})$$

$$C = \frac{1}{4} (G_A^2 + F_1^2 + \eta F_2^2) \quad (\text{D.0.22})$$

$\eta = \frac{Q^2}{4M_N^2}$  The form factors  $F_1(Q^2)$ ,  $F_2(Q^2)$ ,  $G_A(Q^2)$  and  $G_P(Q^2)$  are respectively called Dirac, Pauli, axial and pseudo-scalar weak charged current form factors of the nucleon[22].

## Appendix E

# Charge corrections and hit matching

 THE measurement of the energy deposition distribution of a particle in a scintillator is smeared by different effects: the Landau fluctuations, attenuation in the scintillator, reflection on the scintillator painting, attenuation in the fiber, distance crossed in a scintillator, etc... Therefore, we have applied several corrections to the measured charge in the scintillator to “un-smear” these effects. 2 effects were corrected:

1. Particle angle which changes the energy deposition in a scintillator due to variable path length (dx).
2. Light attenuation in the fiber.

### E.1 dx correction

The charge measured is corrected with the angle of the track from the longitudinal z direction. As shown in Figure E.1, for a particle with an angle  $\theta$  from the z direction, the correction applied to a charge Q is  $Q' = \frac{Q}{\cos(\theta)}$  with:

$$\cos(\theta) = \frac{\text{Scintillator Thickness}}{dx} \implies dx = \frac{\text{Scintillator Thickness}}{\cos(\theta)} \quad (\text{E.1.1})$$

The scintillator thickness is 1 cm for the INGRID type scintillator, and 1.3 cm for the SciBar type scintillators. Note that this correction is only exact in the case of through-going particles (Figure E.1), while it is not correct in the case of scintillator side escaping particles. We can evaluate roughly the effect expected in SciBar and INGRID type scintillators. In this cross section measurement, we will only observe muons with a maximal angle of  $60^\circ$  but most of the reconstructed events have  $\theta_\mu < 40^\circ$ . As shown in Figure E.1, the larger the angle is, the higher is the probability of a particle side escaping the scintillator. For a given angle, we have estimated the proportion of cases where the dx correction would not be exact. As shown in Figure E.1, this area corresponds to  $\frac{x}{\text{Scintillator Width}}$ , which represents in fact  $\frac{\tan(\theta) \cdot \text{Scintillator Thickness}}{\text{Scintillator Width}}$ . Assuming a maximal angle of  $40^\circ$ , this proportion of scintillator side escaping track is 44% for a SciBar type and 17% for an INGRID type. For an angle of  $60^\circ$ , these proportions increase to 90% and 34% respectively. This indicates that a dedicated correction, using the charge deposition between neighbour hits can help to improve the PID in the case of large track angles. In this study, we have not considered this correction since  $\theta_\mu < 40^\circ$  in most of the tracks, even for the bin corresponding to the larger angle  $\in [30^\circ, 60^\circ]$  we use in this analysis.

### E.2 Correction of the attenuation in the optical fiber

The light attenuation in the optical fiber follows an exponential decreasing law:

$$I_{\text{Meas}} = I_{\text{Col}} \cdot e^{-\frac{x}{l_0}} \quad (\text{E.2.1})$$

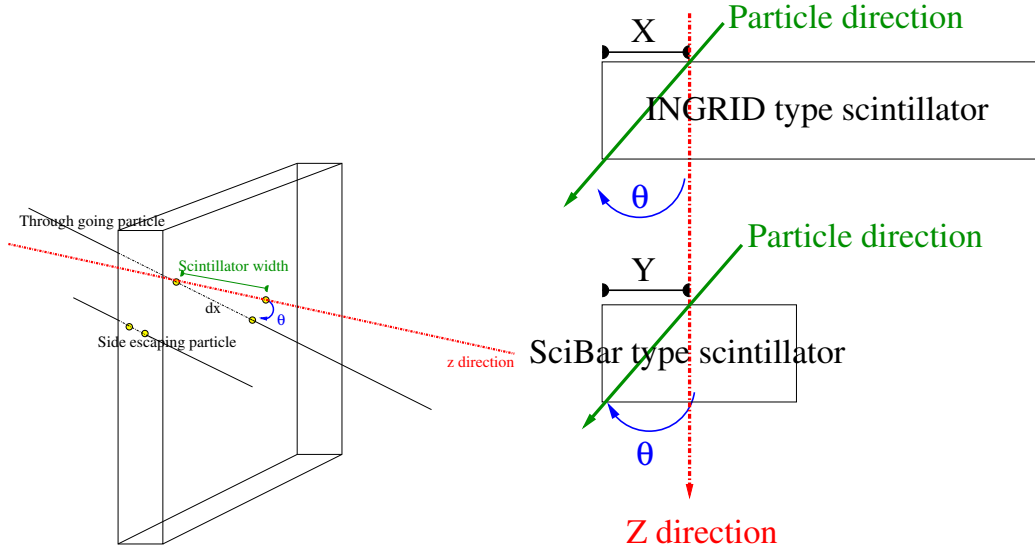


Figure E.1: Scintillator 3D (left) and 2D (right) views. The X and Y regions correspond to the area where, if a track for a given angle  $\theta$  goes through, it will leave the scintillator by its side (repectively for INGRID and SciBar type scintillators).

with  $I_{\text{Meas}}$  and  $I_{\text{Col}}$  the light measured and collected by the fiber respectively, and  $L_0$  the attenuation length. The attenuation length in the scintillator is measured using 3 GeV electron beam data for different distances to the MPPC. The attenuation length was found to be equal to  $L_0 = 238$  cm as shown in Figure E.2. To apply the correction, one needs to know the position of the particle in the

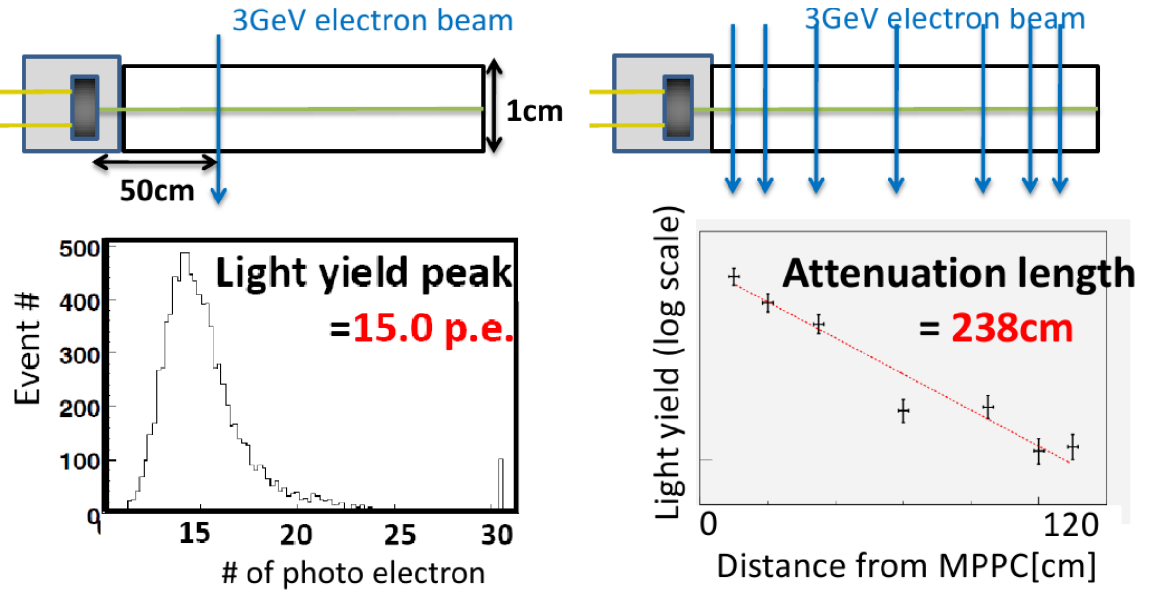


Figure E.2: Measure of the INGRID and PM fiber attenuation using a 3 GeV electron beam for different distances from the MPPC.

scintillator. For horizontal scintillators (X), one needs the information of the X position to measure the attenuation length. This position could only be given by vertical scintillators. For each tracking plane, we have then matched hits in horizontal and vertical planes to create “3D hits” and correct the attenuation length. Two hits in the same tracking planes are matched if the hits are in the same track and same tracking plane.

When the position P in the scintillator is determined with the hit matching, the collected charge is deduced from the measured charge and the distance to the MPPC:

$$I_{\text{Col}} = I_{\text{Meas}} \cdot e^{\frac{P}{L_0}} \quad (\text{E.2.2})$$

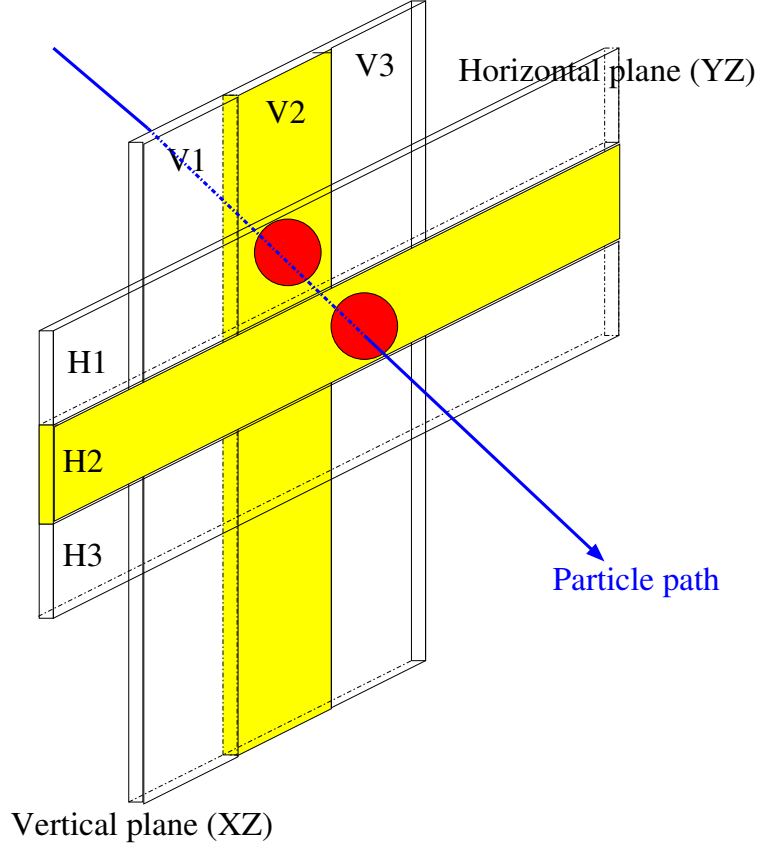


Figure E.3: 3D matching of hits using the X and Y scintillator consecutive planes.

Note that the 3D hit matching algorithm we developed may be refined in the case of several hits of the same track in one plane, we have not considered this issue yet. This is likely to happen in the case of large angle tracks, but also for highly energetic neutrino events where the tracks are almost colinear with the neutrino direction. This can be improved in the future using the particle charge deposition regularity along the track, starting from the downstream hit of a track where superimposition is unlikely.



## Appendix F

# PM unfolding method validation

IN this appendix, we have studied the convergence, but also the limitations of the Bayesian unfolding method. The convergence tests will be done with the momentum unfolding and using the  $p_\mu$  binning defined in Table 5.7. We will test the Bayesian unfolding method robustness with different tests:

1. Convergence as a function of the number of iteration steps.
2. Convergence dependency on the prior.

In parallel, we will show that the crucial part of the unfolding method is the correct choice of the binning in the unfolded variables, namely  $p_\mu$  here. Therefore, the same convergence tests will be performed with a higher number of momentum bins (10). This binning is summarised in Table F.1. We will keep the same binning in the reconstructed variable  $d_\mu$ . The associated likelihood matrix is shown in Figure F.1 and shows higher correlations between the momentum bins, as expected considering the detector resolution.

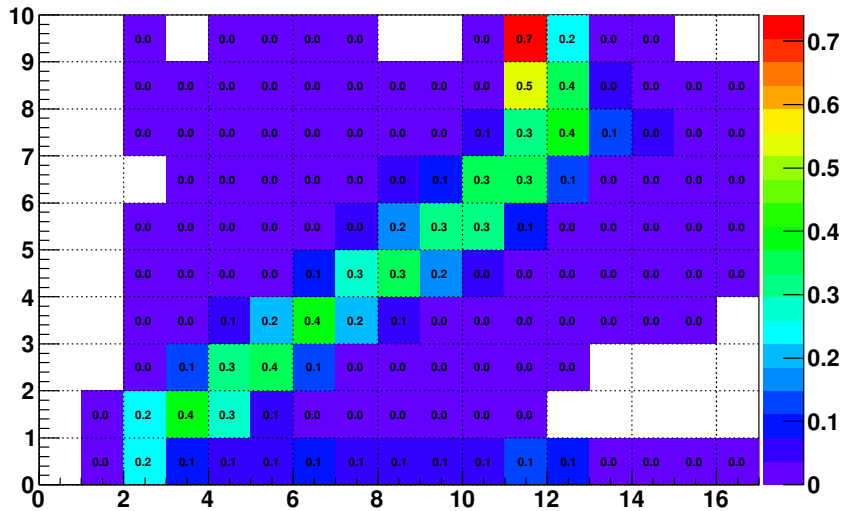


Figure F.1: The likelihood matrix for ten momentum bins. The Y axis represents these momentum bins, and the X axis represents the bins in distance crossed in iron by the muon.

$p_\mu$ (GeV)	[0, 0.4]	[0.4, 0.5]	[0.5, 0.6]	[0.6, 0.7]	[0.7, 0.8]	[0.8, 0.9]	[0.9, 1.0]	[1.0, 1.5]	[1.5, 5.0]	[5.0, 30.0]
---------------	----------	------------	------------	------------	------------	------------	------------	------------	------------	-------------

Table F.1: An example of a ten-momentum binning for  $CC0\pi$  events selected by  $CC0\pi$  selection in the MC.

The convergence will be studied showing the reduced  $\chi^2$  value of the difference between the unfolded simulation and the true content of each bin. We have used a MC production in order to perform the following test. Unless the opposite is specified, we will choose a flat prior to avoid any bias. Note that we will use the statistical error definition:

$$\delta p_\mu^i = \sqrt{\sum_{j=1}^N U_j^i d_\mu^j}. \quad (\text{F.0.1})$$

We insisted in Chapter 5 that this definition is true only if the unfolding matrix is independent of the statistical error. We chose this convention in order to study this dependency, that should affect the pull distribution width.

### Convergence with iteration steps

**General convergence:** The convergence of the iterative unfolding method will be first checked. For this purpose, we have generated a toy MC signal with the CC0 $\pi$  selection and statistics defined in Section 5.3. We have selected two different indicators based on the agreement between the unfolded distribution, the true distribution, and the previous iteration distribution. We have estimated the  $\chi^2$  per degrees of freedom combining all the bins in these two cases as a function of the number of iterations. In the first convergence criterion, we only estimate:

$$\chi^2/NDF = \frac{1}{N=5} \sum_{i=0}^N \left( \frac{p^i - t^i}{\sigma^i} \right)^2 \quad (\text{F.0.2})$$

with N the number of bins, and p, t respectively the posterior distribution (in momenta or angle) and the true event distribution. Here,  $\sigma^i$  is the statistical error in each bin i defined in Equation 5.5.10. As for the criterion based on the difference with the previous iterations, the criterion at the n<sup>th</sup> step of iterations is given by:

$$\chi_{Relative}^2/NDF = \frac{1}{N=5} \sum_{i=0}^N \left( \frac{p_n^i - p_{n-1}^i}{\sigma^i} \right)^2 \quad (\text{F.0.3})$$

We will say the algorithm converges under the condition:

$$\chi^2/NDF \leq 1 \quad (\text{F.0.4})$$

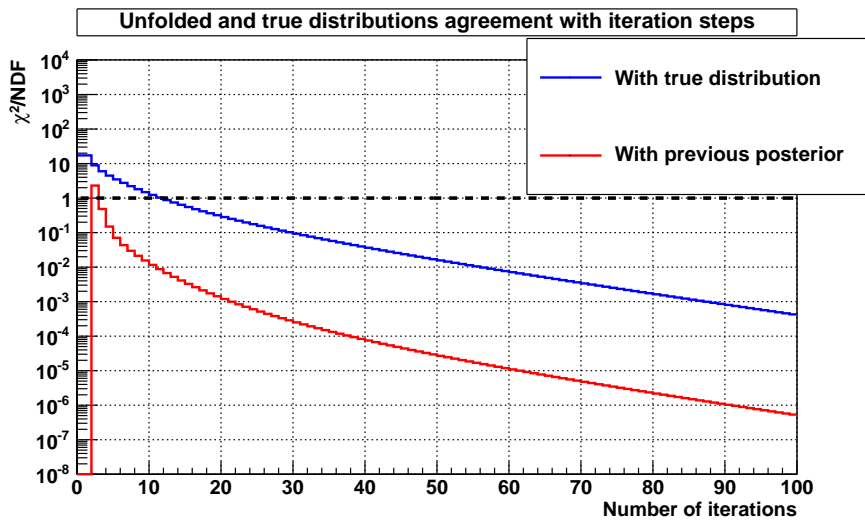


Figure F.2: General convergence of the unfolded distribution to the true distribution. Both the reduced  $\chi^2$  (blue) and  $\chi_{Relative}^2$  (red) are shown and have the same convergence speed with the iteration step.

The results are shown in Figure F.2 for the two convergence criteria applied on the MC CC0 $\pi$  sample without any statistical fluctuation. It indicates first that the algorithm converges after 10 iterations assuming a flat prior. This relatively small amount of iterations required is due to the appropriate choice of the binning given the detector resolution, as we will see. It confirms the algorithm ability to retrieve the true distribution shape given the observed one and assuming the flat prior. Note that there is nothing surprising that the convergence criteria keeps decreasing after  $\chi^2/NDF = 1$  since we assumed a signal without any statistical fluctuations. Moreover, one observes that the  $\chi^2_{Relative}/NDF$  value based on the difference between iteration steps is lower but varies similarly to the absolute  $\chi^2/NDF$  value. It indicates that the  $\chi^2_{Relative}/NDF$  is an indicator that determines the algorithm convergence. Though such a criterion could be the only one that may directly be applied on data, one must be careful using it. Figure F.3 shows a similar convergence with the iteration steps, but for an MC containing a statistical fluctuation in the  $d_\mu$  signal. We observe that the convergence criterion is reached for the relative  $\chi^2_{Relative}/NDF$  value after only 3 iterations steps, though the absolute  $\chi^2/NDF = 9.3$ . This latter value indicates that the compatibility between the unfolded and true distributions is only 0.98% likely to due to statistical fluctuations, and that the algorithm has not converged after only 3 iteration steps. In fact, the statistical distortions in the signal affect the algorithm convergence, and

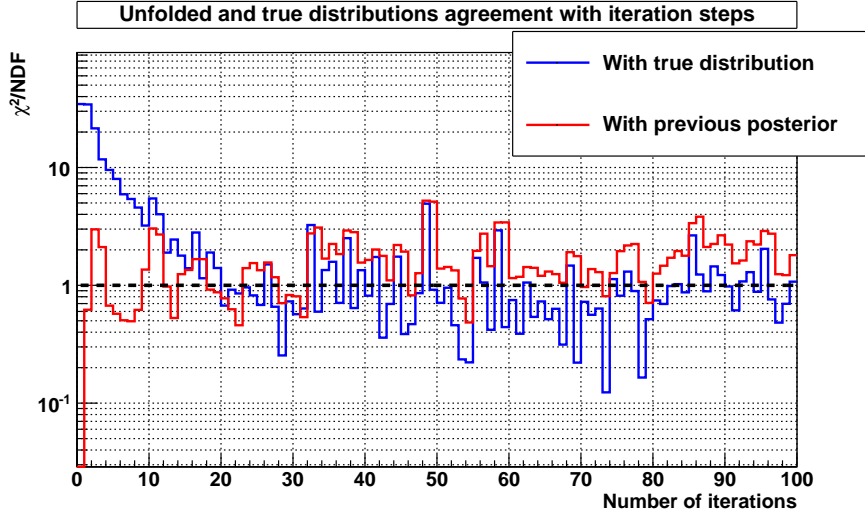


Figure F.3: General convergence of the unfolded distribution to the true distribution, for an MC  $d_\mu$  distribution with statistical fluctuations.

may cause the unfolding value to oscillate around the true value as shown in Figure F.3. For this reason, we will rather determine convergence using the pull average and error values on pure MC, and not attempt to use a similar relative criteria based on  $\chi^2_{Relative}/NDF$  to determine convergence of the data.

**Bin by bin convergence:** We have also studied the bin by bin convergence since it is absolutely not guaranteed by the general convergence. Moreover, the study of bin by bin allows a better understanding of the unfolding convergence in using the  $d_\mu$  signal to distort the momentum prior and find the posterior. The unfolding convergence is in fact ruled by the likelihood matrix diagonality. A bin converges quicker if:

1. The unfolded momentum bin is almost diagonal, *i.e.* is populated by events in  $d_\mu$  bins that are not shared with other momentum bins.
2. The unfolded bin has higher statistics than the bins it is correlated to. If the likelihood matrix is not diagonal,  $d_\mu$  bins impact different  $p_\mu$  bins. The bin migration will therefore induce relative correlated variations between the bins. As for bins with large statistics, they quickly converge since the modification of their neighbour momentum bins with low statistics has small impact on them. On the contrary, any momentum bin that shares  $d_\mu$  events in important proportion

with a larger statistics bin will be heavily affected by any modification of the large momentum bin distribution. Therefore, it will only converge after the large statistics bin has converged.

Therefore, the bins with large diagonal coefficients in the prior are drastically modified after each iteration, and the impact of this change in the other bins is important if their statistics is much higher. We have shown the convergence speed in Figure F.4 for the five momentum bins using the criterion based on the difference between posterior and true distribution. We will define the posterior convergence when the reduced  $\chi^2$  value reaches 1. The information on bin statistics is shown in Table 5.7 and the likelihood matrix is shown in Figure 5.34.

First, one observes that the fifth bin corresponding to  $p_\mu \in [5.0 \text{ GeV}, 30.0 \text{ GeV}]$  is the last bin that converges. As one observes in Table 5.7, the reason is that this bin has a very small statistics, and is highly correlated to the neighbouring fourth bin (Figure 5.34). This relatively slow convergence will impact its neighbour bin, corresponding to  $p_\mu \in [1.0 \text{ GeV}, 5.0 \text{ GeV}]$ , since these bins are highly correlated. Since the fourth bin has also high correlations with the third bin (which has the highest statistics of all bins), the fourth bin will also converge more slowly than the other bins. On the opposite, the second bin corresponding to  $p_\mu \in [0.5 \text{ GeV}, 0.7 \text{ GeV}]$  is the first bin that converges. This bin has not the highest statistics but is the most diagonal which implies the prior modifications in this bin are almost not driven by other bin constraints. It means that there is almost a bijectivity between this momentum bin and the  $d_\mu$  bins that populate it. Though having the highest statistics, the third bin converges more slowly due to its high correlation with the fourth bin which has high statistics too and converges slowly. When the second bin has converged, it will be used as a pivot for the bins which are correlated to it. One observes in Figure F.4 that the first bin corresponding to  $p_\mu \in [0.5 \text{ GeV}, 0.7 \text{ GeV}]$  therefore converges quickly after the second bin convergence, as the third bin corresponding to  $p_\mu \in [0.7 \text{ GeV}, 1.0 \text{ GeV}]$ . One observes that it is only after these bins have converged that the fourth and then the fifth bins can finally converge.

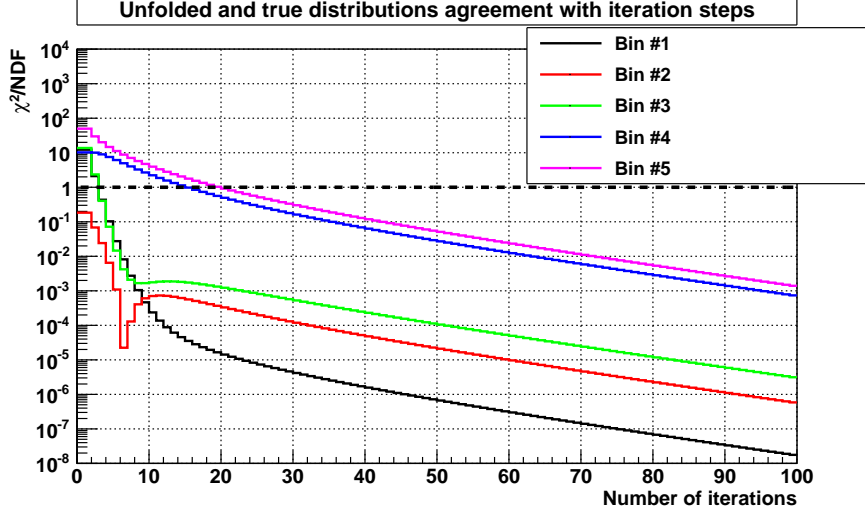


Figure F.4: Bin by bin reduced  $\chi^2$  distribution of the unfolded distribution to the true distribution, for an MC  $d_\mu$  distribution without statistical fluctuations.

**Binning of the unfolded variable** The binning of the unfolded variable has to be chosen carefully in agreement with the detector resolution. A larger number of bins than the detector resolution implies higher sharing in signal  $d_\mu$  events, *i.e.* larger bin migrations (correlations) as shown in Figure F.1 compared to Figure 5.34. As we have seen, this should impact the convergence speed which is not an important issue if the processing time is reasonable. However, we will show that an inappropriate binning can prevent the convergence of the bins that share lots of events with others. To study this effect, we have generated a toy MC with statistical fluctuations in the signal event distribution in  $d_\mu$ . We have shown the reduced  $\chi^2$  value for each of the bins in Figure F.5. One observes that

the momentum bins corresponding to  $p_\mu \in [1.5 \text{ GeV}, 5.0 \text{ GeV}]$  and  $p_\mu \in [5.0 \text{ GeV}, 30.0 \text{ GeV}]$  do not converge in the case of ten bins in momentum, while the bins  $p_\mu \in [1.0 \text{ GeV}, 5.0 \text{ GeV}]$  and  $p_\mu \in [5.0 \text{ GeV}, 30.0 \text{ GeV}]$  does converge in the case of five momentum bins. The reason is that the statistical fluctuations can be amplified by the unfolding. Due to the statistical fluctuations, even the high statistics momentum bins do not reach the true bin values since the signal in  $d_\mu$  does not constrain the prior into the true momentum distribution. The consequence is that these high statistics bins convergence towards inappropriate values will highly impact on the low statistics bin which are correlated with the high statistics bins. Therefore, these latter bins will not converge. The signal statistical fluctuations lead the unfolding to distort the prior after each iteration, which can even lead to non-physical solutions if the fluctuations are large. One understands that this effect increases with the number of iterations. In the case of five momentum bins, both lower correlations and more similar statistics in the momentum bins involve lower impact of the high statistics bin, which explains that the low statistics bin converges. We observe in Figure F.5 that the fluctuations appear after 4 to 5 iterations in the five momentum bin choice, which indicates that the unfolded distribution has unsmeared most of the detector effects and started to try to unfold some statistical fluctuations. One observes that in the case of ten bins in momentum, the large bins correlations and low statistics lead the unfolding algorithm to unfold the fluctuations even in the first iteration step, showing that the fluctuations are at least as large as the physics content (cross section constraint) of each bin. The choice in the binning of the unfolded variable is therefore crucial to maximise the information in the  $CC0\pi$  measurement. While the choice of a larger binning is more robust, it decreases the amount of information provided by the cross section measurement. In the case of two unfolding variables  $p_\mu$  and  $\theta_\mu$ , the choice is more complicated, since relative statistics in  $p_\mu$  bins can vary depending on the  $\theta_\mu$  bin. The binning summarised in Table 5.7 has been optimised and is the most appropriate for the double differential cross section study given the current PM accumulated statistics. An appropriate limit in the number of iterations should be also estimated for the binning, not to start to unfold the statistical fluctuations which artificially decrease the predictive power.

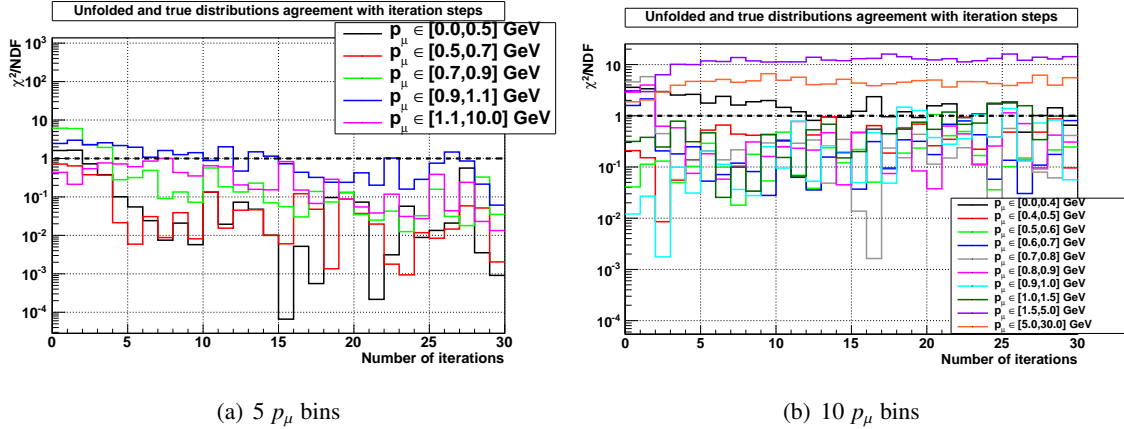


Figure F.5: Bin by bin reduced  $\chi^2$  distribution of the unfolded distribution to the true distribution, for an MC  $d_\mu$  distribution with statistical fluctuations in the case of five (left) and ten (right) momentum bins (Table F.1).

### Error on the unfolded distributions

We have seen that an inappropriate binning choice in unfolded quantities impacts the convergence in low statistics bins. We will show here that it also impacts the error in the other bins. To study this effect, we have generated 1,000 toy experiments with varied statistics for the ten momentum bin choice, using the same procedure we have done previously in the case of five momentum bins. We have shown the results of the pull distributions for three selected momentum bins in Figure F.6. The pull distributions allow to compare directly with the result in the case of five momentum bins in Figure 5.35, since the different statistics in reconstructed  $d_\mu$  bin are corrected. One observes that the convergence is lost also in the low statistics bin  $p_\mu \in [0 \text{ GeV}, 0.4 \text{ GeV}]$ . As for the relatively high

statistics bins  $p_\mu \in [0.5 \text{ GeV}, 0.6 \text{ GeV}]$  and  $p_\mu \in [0.6 \text{ GeV}, 0.7 \text{ GeV}]$ , one observes the statistical error to be higher than the error predicted by Equation 5.5.10. We recall that the actual statistical error is lower than the latter for the five momentum bin, and shows that the correlations are mainly positive in the case of ten bins. Therefore, the choice of a thinner binning does not necessarily provide a higher constraint than for larger binning. This effect appears as the result of a binning which is too thin compared to the detector resolution, and does not only impact on the momentum bins with low statistics. We have seen it both biases the result in low statistics bins and artificially increases the statistical error in high momentum bins through the unfolding matrix. A similar result is expected for the systematic error, and especially the detector systematics that affect the likelihood matrix.

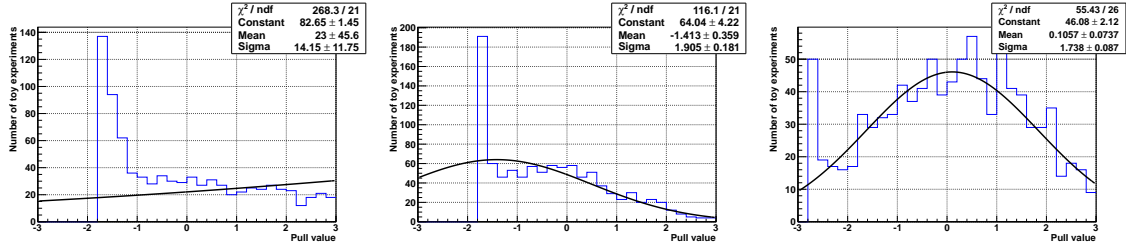


Figure F.6: The pull distributions of the statistical error for selected momentum bins assuming an error  $\sigma_i$  as defined in Equation 5.5.10 in the case of ten momentum bins defined in Table F.1. The left, center and right distributions correspond to  $p_\mu \in [0 \text{ GeV}, 0.4 \text{ GeV}]$ ,  $p_\mu \in [0.5 \text{ GeV}, 0.6 \text{ GeV}]$  and  $p_\mu \in [0.6 \text{ GeV}, 0.7 \text{ GeV}]$  respectively.

### Dependency on the prior

Finally, we will test the dependency of the result with the prior. The unfolding result should be ideally totally independent from the prior, and only driven by the data constraints. It is practically impossible since this situation only occurs for an infinite number of iterations. A residual prior dependency is then contained in this study. In the previous section, we have shown that the higher the number of iterations, the lower is the prior dependency due to the repeating constraints from the signal on the unfolding matrix. We have shown in Figure F.7 the general reduced  $\chi^2$  variations as a function of the number of iterations for different priors in the case of no statistical fluctuation in the signal. As expected, the convergence occurs for a smaller number of iteration steps for a prior closer to the true momentum distribution. In the case of statistical fluctuations, one understands that the closer the prior is from the true momentum distribution, the better will be the agreement between the true and unfolded distributions but the higher will be the dependency to the MC cross section model. As the number of iteration increases, the original dependency will be washed out by the signal constraints, and the statistical fluctuations will re-appear. For this reason, we chose an adequate prior choice that allows both to minimise the model dependency, and allows the quick convergence of the unfolding, even with a relatively small statistics (see Chapter 5).

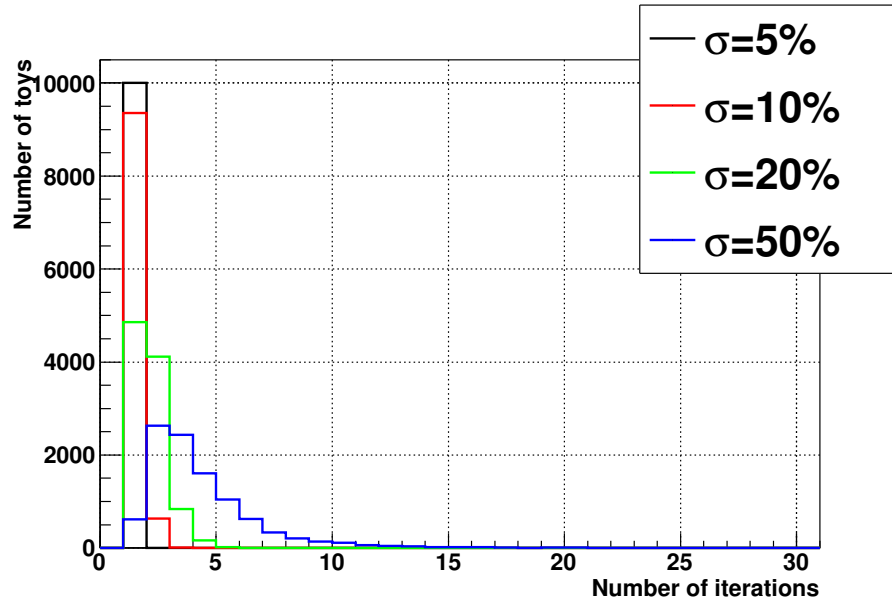


Figure F.7: Reduced  $\chi^2$  value as a function of the number of iteration step. The different priors correspond to distortion of the true momentum distribution, assuming a gaussian with  $\sigma = 0.05$  (black),  $\sigma = 0.1$  (red),  $\sigma = 0.2$  (green) and  $\sigma = 0.5$  (blue). We represented the case of 5 bins in momentum.



## Appendix G

# Likelihood tests for the search of Lorentz invariance violation

### G.1 The tests of the one parameter fit

**D**IFFERENT points in the parameter space were selected to test if the fit is un-biased and the error estimation was correct. The origin of the 5 parameter space (0,0,0,0,0) was chosen because the LV effect is likely to be around this value and there is no physical boundary at this origin. Finally, two other points described in Table G.1 were selected to check the fit results for a possible LV effect of a  $1\sigma$  current statistical error.

Toy MC were generated by setting the 5 SME coefficients to a fixed true value. The probability of  $\nu_\mu$  disappearance is then scaled by the average number of POT:  $\frac{\text{events}}{\text{POT}} = 1.43 \times 10^{-13}$ . Finally, from each toy MC, the pull distribution is estimated by:

1. For each LSP bin, the associated  $\frac{\text{events}}{\text{POT}}$  is varied within the gaussian statistical error (according to data).
2. Sequentially for each coefficient, the associated distribution is fitted, fixing all but one coefficient to their true value.

This procedure is performed 10,000 times to generate the pull distribution showing the  $\frac{\text{Fit-True}}{\text{Error}}$  distributions. Results for 3 coefficient configurations are shown in Figure G.1, G.2 and G.3. The results are also summarised in Table G.1 and confirm that the fitter is unbiased and the error is correctly estimated for a LV signal.

The case of no LV signal shown in Figure G.1 is special because it is peaked at 0. This is expected and the 1 parameter fit with no LV signal is only shown for example purposes. The reason the distributions are peaked at 0 only reveals the fitter inability to fit some sine or cosine distribution with opposite phase. In the case of only one parameter fit with all others equal to 0, the probability distribution is reduced to:

$$P_{\nu_\mu \rightarrow \nu_x} = 1 - \left(\frac{L}{hc}\right)^2 |A_c^{\mu x} \cos(\omega_\oplus T_\oplus)|^2 \quad (\text{G.1.1})$$

In the case of a statistical fluctuation that mimics a signal of the form  $1 + (\frac{L}{hc})^2 |A_c^{\mu x} \cos(\omega_\oplus T_\oplus)|^2$ , the fitter is unable to find a negative  $|A_c^{\mu x}|^2$  value. In this case, the fitter naturally converges to parameter values as close to 0 as possible, which explain the peak in the distributions. On top of this, though there are two possible solutions (positive or negative) for  $A_c^{\mu x}$ , these two solutions are totally symmetric in this case where all coefficient true values is 0 (Equation G.1.1). Since the fitter initial value is positive, the fitter will therefore always remain in the positive region, which explains the asymmetry between positive and negative values in Figure G.1. One notes that for parameter true values different from 0,

the signs of the coefficients take part in the interferences between the terms, and the fitter is therefore sensitive to it.

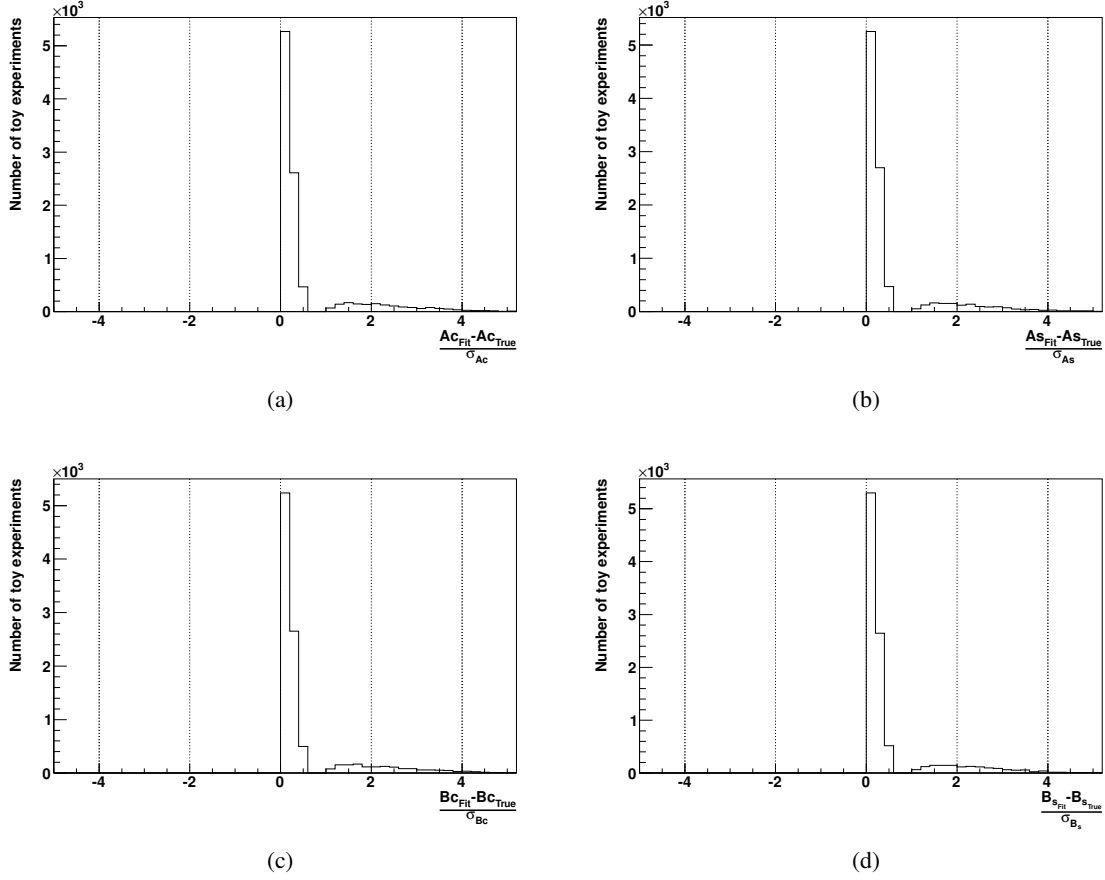


Figure G.1: Pull distributions for no LV signal ( $C = 0$ ,  $A_c = 0$ ,  $A_s = 0$ ,  $B_c = 0$ ,  $B_s = 0$ ).

Table G.1: Pull distributions bias of the mean and error estimations by the fitter.

$(C, A_c, A_s, B_c, B_s)$ value	Pull mean compatibility with 0 (in $\sigma$ )	Pull $1\sigma$ error compatibility with 1 (in $\sigma$ )
$(10, 1, 10, 10, 10) \times 10^{-20}$	(0.4, 0.9, 0.2, 0.1, 0.6)	(0.1, 2.0, 0.8, 0.1, 0.1)
$(5, 6, 7, 8, 9) \times 10^{-21}$	(0.5, 1.2, 0.2, 0.7, 0.7)	(1.4, 2.5, 0.8, 1.0, 0.4)

## G.2 The five parameter fit

The 5-coefficient fit was tested on toy experiments, to determine its robustness and error estimation. The toy experiments were built using 2 different methods:

1. 10,000 flat toy experiments based on data. The spill time of each event is reshuffled to erase any possible LV effect, as described in Section 6.4.
2. 10,000 signal toy experiments based on a LV signal.

### G.2.1 Flat toy experiments

The consistency of the mean values with no signal within the  $1\sigma$  error was tested first. The results are shown in the form of pull distributions in Figure G.5. Firstly, a shift in the mean value is observed due to coefficient correlations. However, the fitter converges correctly since each mean of the  $C$ ,  $A_s$ ,  $A_c$ ,  $B_s$  or  $B_c$  parameters is compatible with their true value within  $1\sigma$ .

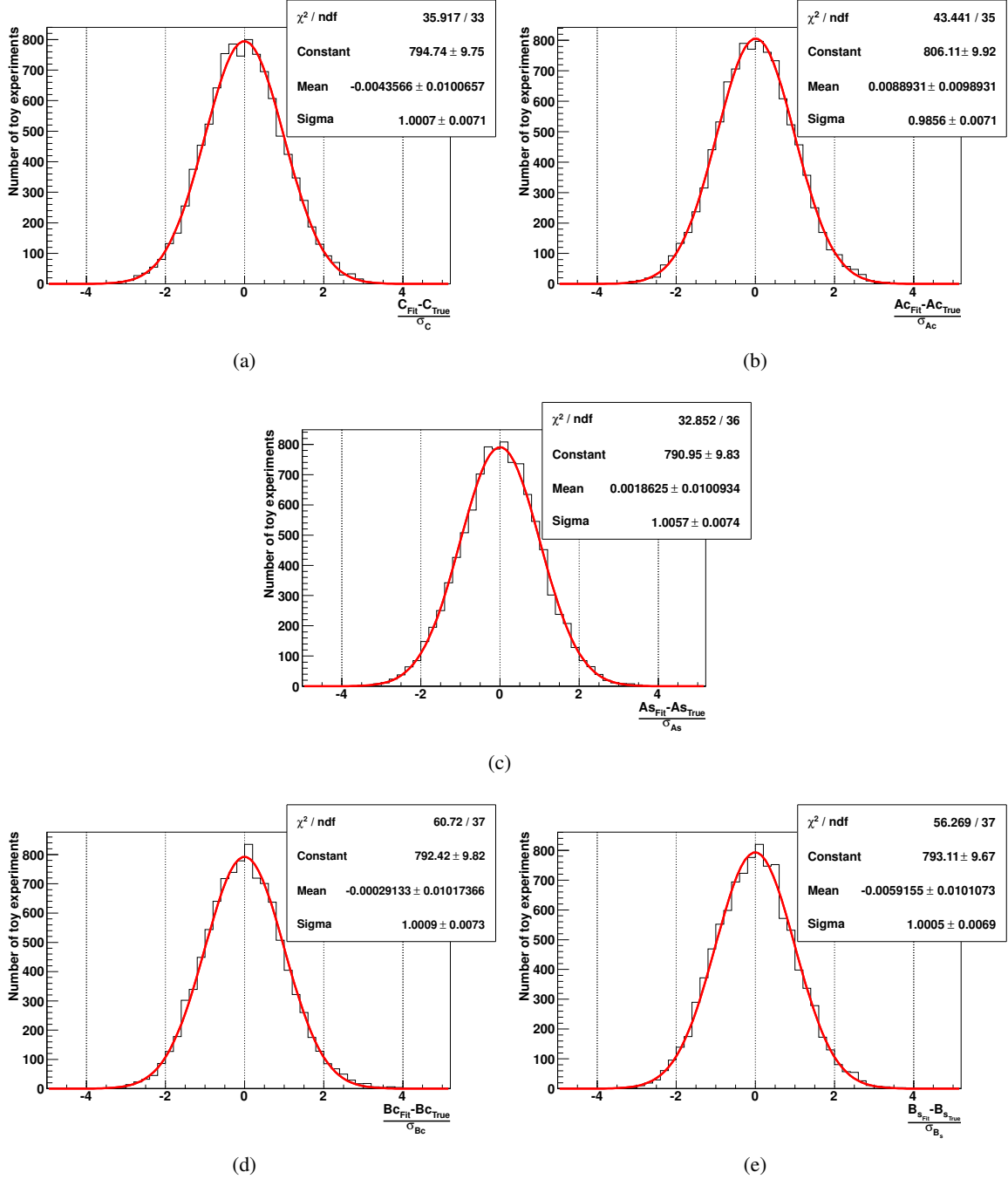
Secondly, the pull distributions  $1\sigma$  errors are systematically and significantly larger than 1. This might

indicate the fitting error is slightly underestimated. In the present case, this discrepancy between the pull distributions  $1\sigma$  errors and 1 seems to be due only to the non Gaussian shape of the pull distributions. Assuming 68% of the toy experiments are contained within a Gaussian  $1\sigma$  error tends to be wrong since the distributions are peaked at 0.

### **G.2.2 Signal toy experiments**

To test the robustness of the 5 parameter fit, various toy experiments with different LV signals are generated. On top of them, a statistical error fluctuation according to the data set is added. A particular case is shown in Figure G.6, confirming the convergence of the fitting method in this case.

As for the 10,000 equivalent toys, the results are shown in Figure G.7 directly comparing fitting results and true coefficients value. The general agreement between fitted and true value confirms the robustness of the fit. Moreover, this agreement is independent of the true value of the various coefficients. It confirms robustness of the fit and its ability to fit a random signal, which is absolutely mandatory before applying the fit to data.


 Figure G.2: Pull distributions for  $C = 10^{-20}$ ,  $A_c = 10^{-21}$ ,  $A_s = 10^{-20}$ ,  $B_c = 10^{-20}$ ,  $B_s = 10^{-20}$ .

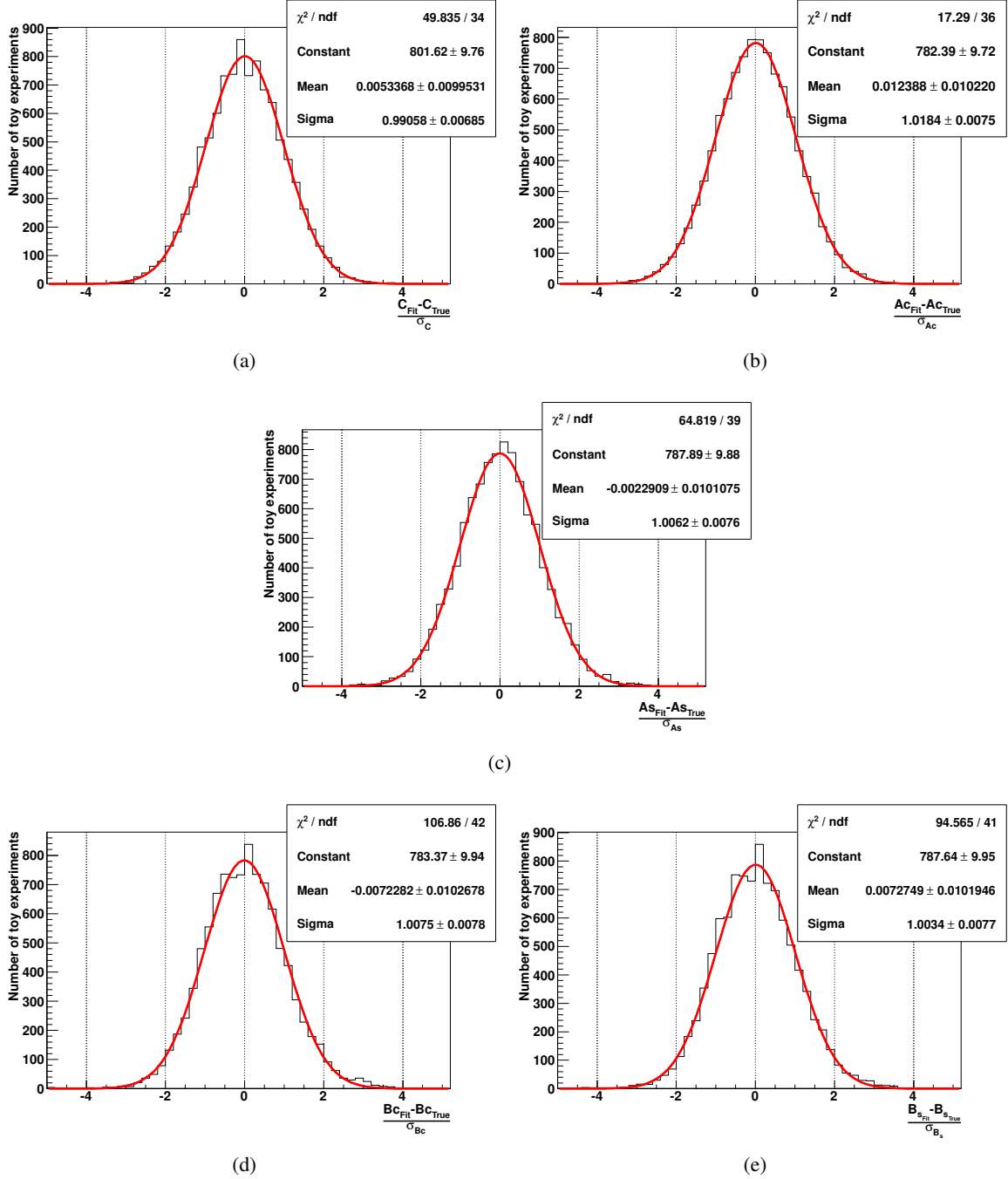


Figure G.3: Pull distributions for  $C = 5.10^{-21}$ ,  $A_c = 6.10^{-21}$ ,  $A_s = 7.10^{-21}$ ,  $B_c = 8.10^{-21}$ ,  $B_s = 9.10^{-21}$ .

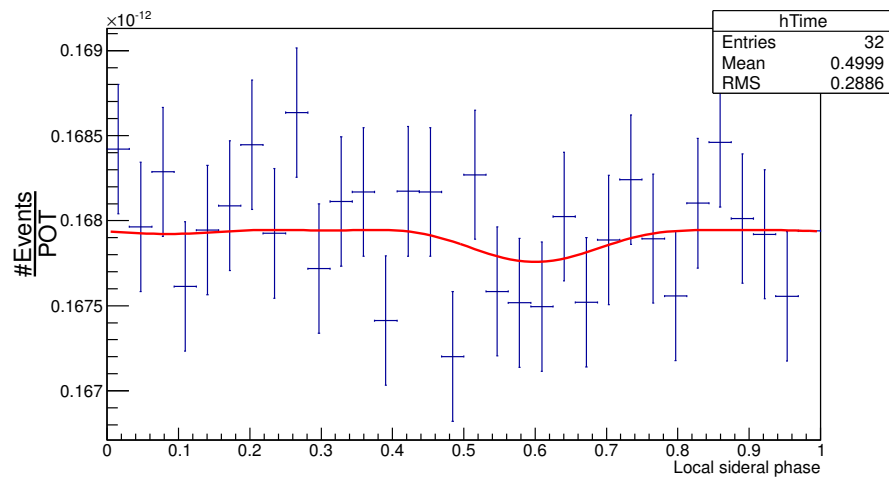


Figure G.4: Example of a flat toy MC fitted by the 5 parameter fit.

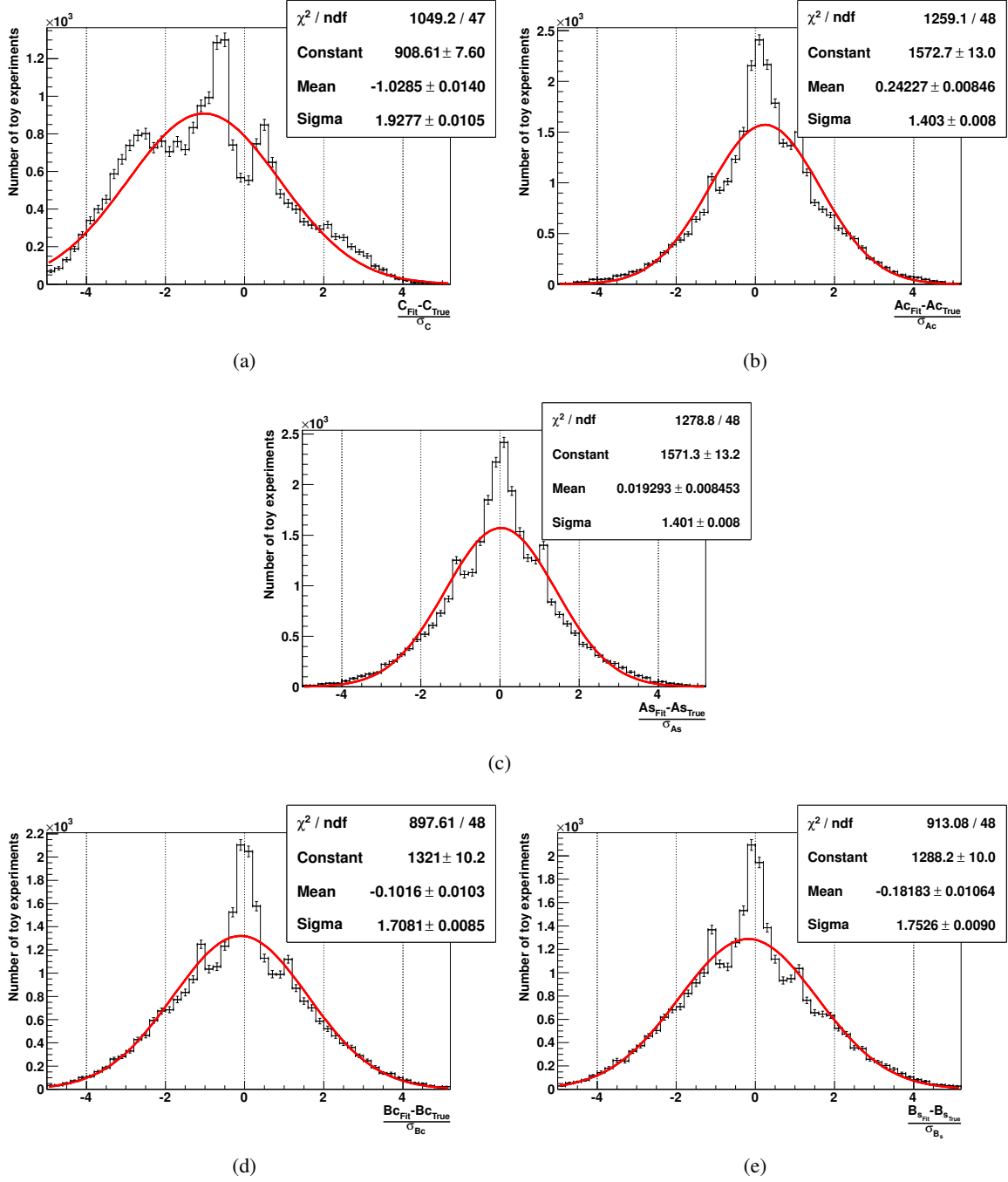


Figure G.5: Pull distributions for  $C$ ,  $A_c$ ,  $A_s$ ,  $B_c$ , and  $B_s$  coefficients, for the 5 parameter fit in case of a flat LV signal.

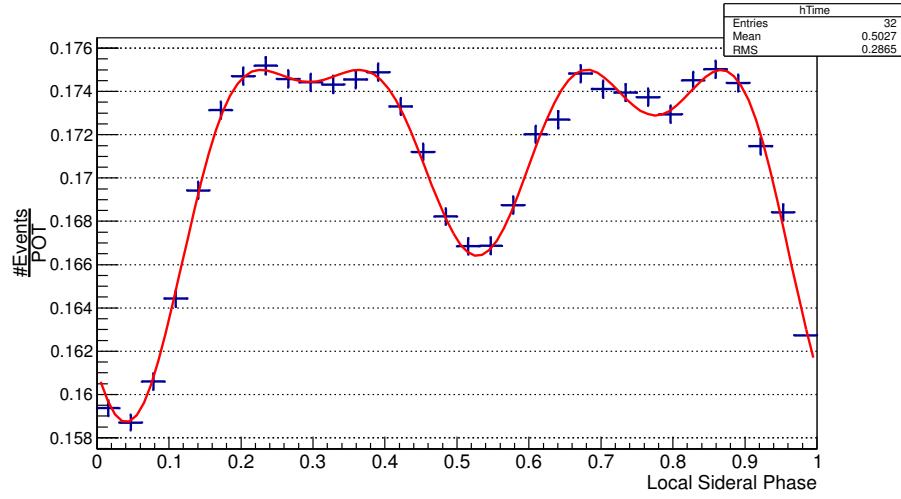


Figure G.6: Example of an LSP histogram for a toy experiment with an LV signal. The signal corresponds to coefficients  $C$ ,  $A_s$ ,  $A_c$ ,  $B_s$  and  $B_c$  all equals to  $5 \times 10^{-20}$ . The fit is shown as a red line.

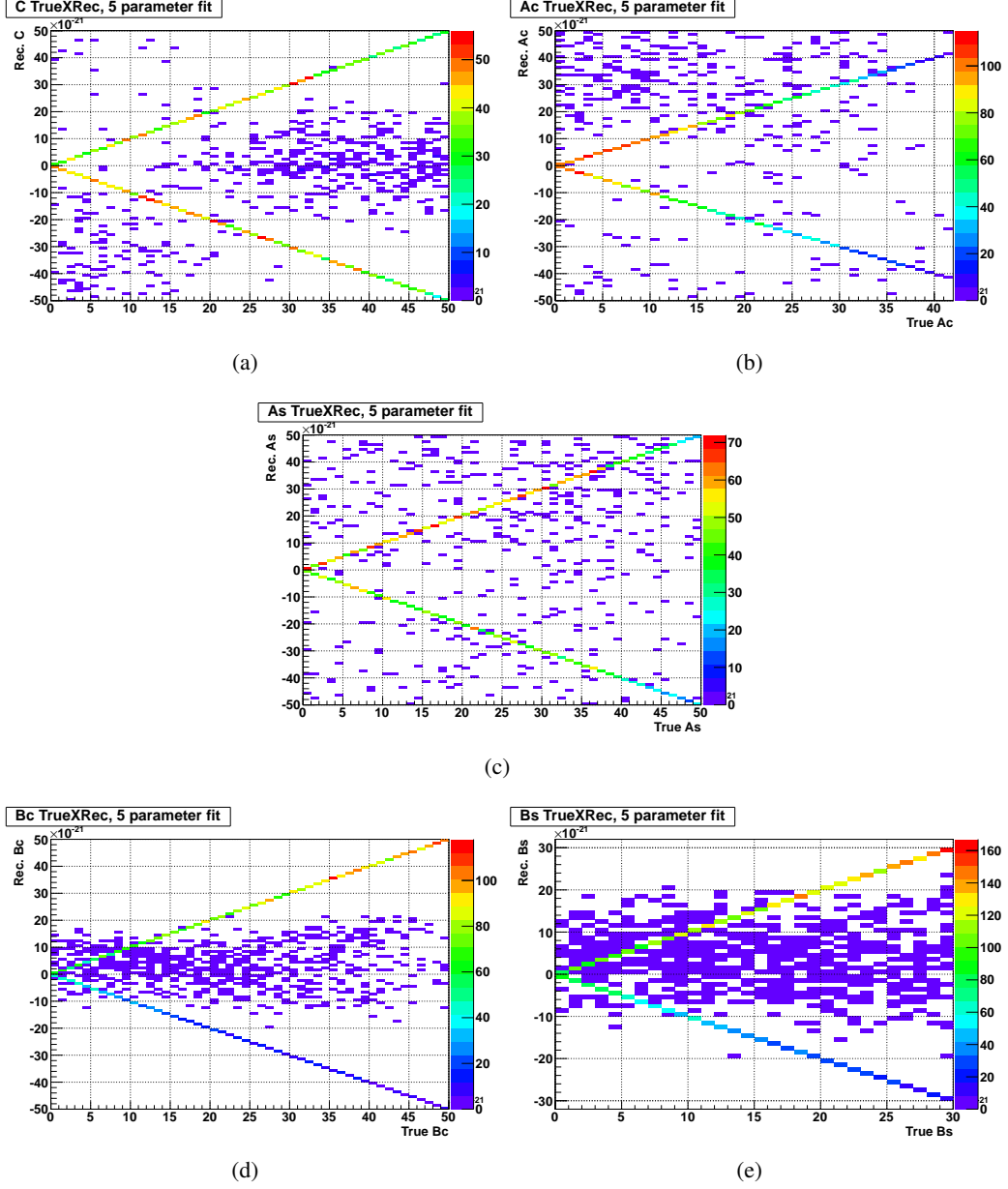


Figure G.7: Correlations between the true and fitted values obtained with the 5 parameter fit for various LV signals.



# Bibliography

- [1] A. H. Becquerel. On the rays emitted by phosphorescence. *Comptes Rendus*, 122:420–421, 1896.
- [2] J. Chadwick. The intensity distribution in the magnetic spectrum of  $\beta$  particles from radium (B + C). *Verh. Phys. Gesell.*, 16:383–391, 1914.
- [3] W. Pauli. Dear radioactive ladies and gentlemen. *Phys. Today*, 31N9:27, 1978.
- [4] Enrico Fermi. Tentativo di una teoria dei raggi  $\beta$ . *Il Nuovo Cimento*, 11(1):1–19, 1934.
- [5] C. L. Cowan et al. Detection of the free neutrino: A Confirmation. *Science*, 124:103–104, 1956.
- [6] G. Danby et al. Observation of High-Energy Neutrino Reactions and the Existence of Two Kinds of Neutrinos. *Phys. Rev. Lett.*, 9:36–44, 1962.
- [7] K. Kodama et al. Observation of tau-neutrino interactions. *Phys. Lett.*, B504:218–224, 2001.
- [8] S Schael, R Barate, R Bruneliere, D Buskulic, I De Bonis, D Décamp, P Ghez, C Goy, S Jézéquel, JP Lees, et al. Precision electroweak measurements on the z resonance. *Physics Reports A Review Section of Physics Letters*, 427(5-6):257–454, 2006.
- [9] Bruce T Cleveland, Timothy Daily, Raymond Davis Jr, James R Distel, Kenneth Lande, CK Lee, Paul S Wildenhain, and Jack Ullman. Measurement of the solar electron neutrino flux with the homestake chlorine detector. *The Astrophysical Journal*, 496(1):505, 1998.
- [10] Y. Fukuda et al. Evidence for oscillation of atmospheric neutrinos. *Phys. Rev. Lett.*, 81:1562–1567, 1998.
- [11] Q. R. Ahmad et al. Direct evidence for neutrino flavor transformation from neutral-current interactions in the Sudbury Neutrino Observatory. *Phys. Rev. Lett.*, 89, 2002.
- [12] Rajan Gupta. Introduction to lattice qcd. *arXiv preprint hep-lat/9807028*, 1998.
- [13] Juerg Beringer, JF Arguin, RM Barnett, K Copic, O Dahl, DE Groom, CJ Lin, J Lys, H Murayama, CG Wohl, et al. Review of particle physics. *Physical Review D*, 86(1), 2012.
- [14] Wolfgang Pauli. Dear radioactive ladies and gentlemen. *Phys. Today*, 31(9):27, 1978.
- [15] Tsung D Lee and Chen-Ning Yang. Parity nonconservation and a two-component theory of the neutrino. *Physical Review*, 105(5):1671, 1957.
- [16] CS Wtj, E Ambler, RW Hayward, DD Hoppes, and RP Hudson. Experimental test of parity conservation in beta decay. *Phys. Rev.*, 104:1315, 1956.
- [17] FJ Hasert, S Kabe, W Krenz, J Von Krogh, D Lanske, J Morfin, K Schultze, H Weerts, GH Bertrand-Coremans, J Sacton, et al. Observation of neutrino-like interactions without muon or electron in the gargamelle neutrino experiment. *Physics Letters B*, 46(1):138–140, 1973.
- [18] G Arnison, A Astbury, B Aubert, C Bacci, G Bauer, A Bezaguet, R Böck, TJV Bowcock, M Calvetti, T Carroll, et al. Experimental observation of isolated large transverse energy electrons with associated missing energy at  $s = 540$  gev. *Physics Letters B*, 122(1):103–116, 1983.

- [19] Tadao Nakano and Kazuhiko Nishijima. Charge independence for  $\nu$ -particles. *Progress of Theoretical Physics*, 10(5):581–582, 1953.
- [20] François Englert and Robert Brout. Broken symmetry and the mass of gauge vector mesons. *Physical Review Letters*, 13(9):321–323, 1964.
- [21] Peter W Higgs. Spontaneous symmetry breakdown without massless bosons. *Physical Review*, 145(4):1156, 1966.
- [22] Carlo Giunti and Chung W Kim. *Fundamentals of neutrino physics and astrophysics*. Oxford university press, 2007.
- [23] Hideki Yukawa. Interaction of elementary particles. part i. In *Proc. Phys. Math. Soc. Jpn.*, volume 17, pages 48–57, 1935.
- [24] Ettore Majorana. Teoria simmetrica dell’elettrone e del positrone. *Il Nuovo Cimento*, 14(4):171–184, 1937.
- [25] E Kh Akhmedov. Neutrino physics. *arXiv preprint hep-ph/0001264*, 2000.
- [26] Elena Giusarma, Roland de Putter, Shirley Ho, and Olga Mena. Constraints on neutrino masses from planck and galaxy clustering data. *Physical Review D*, 88(6):063515, 2013.
- [27] Anthony Zee. *Quantum field theory in a nutshell*. Princeton university press, 2010.
- [28] F Ardellier, I Barabanov, JC Barriere, F Beißel, S Berridge, L Bezrukov, A Bernstein, T Bolton, NS Bowden, Ch Buck, et al. Double chooz, a search for the neutrino mixing angle  $\theta_{13}$ . 2006.
- [29] FP An, JZ Bai, AB Balantekin, HR Band, D Beavis, W Beriguete, M Bishai, S Blyth, K Boddy, RL Brown, et al. Observation of electron-antineutrino disappearance at daya bay. *Physical Review Letters*, 108(17):171803, 2012.
- [30] JK Ahn, S Chebotaryov, JH Choi, S Choi, W Choi, Y Choi, HI Jang, JS Jang, EJ Jeon, IS Jeong, et al. Observation of reactor electron antineutrinos disappearance in the reno experiment. *Physical Review Letters*, 108(19):191802, 2012.
- [31] K Abe, J Adam, H Aihara, T Akiri, C Andreopoulos, S Aoki, A Ariga, T Ariga, S Assylbekov, D Autiero, et al. Observation of electron neutrino appearance in a muon neutrino beam. *Physical review letters*, 112(6):061802, 2014.
- [32] Thomas Schwetz, Mariam Tórtola, and Jose WF Valle. Three-flavour neutrino oscillation update. *New Journal of Physics*, 10(11):113011, 2008.
- [33] SP Mikheyev and A Yu Smirnov. Resonant amplification of  $\nu$  oscillations in matter and solar-neutrino spectroscopy. *Il Nuovo Cimento C*, 9(1):17–26, 1986.
- [34] The Super Kamiokande Collaboration. <http://www-sk.icrr.u-tokyo.ac.jp/sk/physics/solarnu-intro-e.html>.
- [35] J. N. Abdurashitov et al. Measurement of the solar neutrino capture rate with gallium metal. *Phys. Rev.*, C60, 1999.
- [36] Wolfgang Hampel, J Handt, G Heusser, J Kiko, T Kirsten, M Laubenstein, E Pernicka, W Rau, M Wojcik, Yu Zakharov, et al. Gallex solar neutrino observations: Results for gallex iv. *Physics Letters B*, 447(1):127–133, 1999.
- [37] M. Altmann et al. GNO solar neutrino observations: Results for GNO I. *Phys. Lett.*, B490:16–26, 2000.
- [38] Y. Fukuda et al. Solar neutrino data covering solar cycle 22. *Phys. Rev. Lett.*, 77:1683–1686, 1996.

- 
- [39] J. P. Cravens et al. Solar neutrino measurements in Super-Kamiokande-II. *Phys. Rev.*, D78, 2008.
  - [40] John N Bahcall, Aldo M Serenelli, and Sarbani Basu. New solar opacities, abundances, helioseismology, and neutrino fluxes. *The Astrophysical Journal Letters*, 621(1):L85, 2005.
  - [41] S. Abe et al. Precision Measurement of Neutrino Oscillation Parameters with KamLAND. *Phys. Rev. Lett.*, 100, 2008.
  - [42] Thomas Mueller. Exprience Double Chooz : simulation des spectres antineutrinos issus de racteurs.
  - [43] R. Becker-Szendy et al. The Electron-neutrino and muon-neutrino content of the atmospheric flux. *Phys. Rev.*, D46:3720–3724, 1992.
  - [44] W. W. M. Allison et al. Measurement of the atmospheric neutrino flavour composition in Soudan-2. *Phys. Lett.*, B391:491–500, 1997.
  - [45] Y. Ashie et al. A Measurement of Atmospheric Neutrino Oscillation Parameters by Super-Kamiokande I. *Phys. Rev.*, D71, 2005.
  - [46] M. Apollonio et al. Search for neutrino oscillations on a long base-line at the CHOOZ nuclear power station. *Eur. Phys. J.*, C27:331–374, 2003.
  - [47] K Eguchi, S Enomoto, K Furuno, J Goldman, H Hanada, H Ikeda, K Ikeda, K Inoue, K Ishihara, W Itoh, et al. First results from kamland: evidence for reactor antineutrino disappearance. *Physical Review Letters*, 90(2):021802, 2003.
  - [48] Christophe Bronner. Contribution la caractrisation du faisceau de neutrinos de lxprience T2K avec le dtecteur proche INGRID.
  - [49] Joo Pedro Athayde Marcondes de Andr. *Evaluation of the  $\pi^0$  background for the  $\nu_e$  appearance search in the T2K experiment. First study of the leptonic CP violation phase.* PhD thesis, 2012.
  - [50] K Abe, N Abgrall, H Aihara, Y Ajima, JB Albert, D Allan, P-A Amaudruz, C Andreopoulos, B Andrieu, MD Anerella, et al. The t2k experiment. *Nuclear Instruments and Methods in Physics Research Section A: Accelerators, Spectrometers, Detectors and Associated Equipment*, 659(1):106–135, 2011.
  - [51] K Hirata, Takaaki Kajita, Masatoshi Koshiba, M Nakahata, Y Oyama, N Sato, A Suzuki, M Takita, Y Totsuka, T Kifune, et al. Observation of a neutrino burst from the supernova sn1987a. *Physical Review Letters*, 58(14):1490, 1987.
  - [52] Nicolas Abgrall, A Aduszkiewicz, B Andrieu, T Anticic, N Antoniou, J Argyriades, AG Asryan, B Baatar, A Blondel, J Blumer, et al. Measurements of cross sections and charged pion spectra in proton-carbon interactions at 31 gev/c. *Physical Review C*, 84(3):034604, 2011.
  - [53] Nicolas Abgrall, A Aduszkiewicz, T Anticic, N Antoniou, J Argyriades, B Baatar, A Blondel, J Blumer, M Bogusz, L Boldizsar, et al. Measurement of production properties of positively charged kaons in proton-carbon interactions at 31 gev/c. *Physical Review C*, 85(3):035210, 2012.
  - [54] SP Denisov, SV Donskov, Yu P Gorin, RN Krasnokutsky, AI Petrukhin, Yu D Prokoshkin, and DA Stoyanova. Absorption cross sections for pions, kaons, protons and antiprotons on complex nuclei in the 6 to 60 gev/ $i\hbar$  c/ $i\hbar$  momentum range. *Nuclear Physics B*, 61:62–76, 1973.
  - [55] Giorgio Bellettini, G Cocconi, AN Diddens, E Lillethun, G Matthiae, JP Scanlon, and AM Wetherell. Proton-nuclei cross sections at 20 gev. *Nuclear Physics*, 79(3):609–624, 1966.
  - [56] AS Carroll et al. *Phys. Rev. Lett.*, B 80 319, 1979.

- [57] K Abe, J Adam, H Aihara, T Akiri, C Andreopoulos, S Aoki, A Ariga, T Ariga, S Assylbekov, D Autiero, et al. Measurement of neutrino oscillation parameters from muon neutrino disappearance with an off-axis beam. *Physical review letters*, 111(21):211803, 2013.
- [58] Mine Shun'ichi private communications.
- [59] K Abe, Y Hayato, T Iida, K Iyogi, J Kameda, Y Kishimoto, Y Koshio, Ll Marti, M Miura, S Moriyama, et al. Calibration of the super-kamiokande detector. *Nuclear Instruments and Methods in Physics Research Section A: Accelerators, Spectrometers, Detectors and Associated Equipment*, 737:253–272, 2014.
- [60] Wikipedia. <http://en.wikipedia.org/wiki/forsterresonanceenergytransfer>.
- [61] Wikipedia. <http://en.wikipedia.org/wiki/flashadc>.
- [62] The T2K collaboration. Ingrid new analysis technical note. *T2K internal note*, TN-132.
- [63] S Agostinelli, John Allison, K al Amako, J Apostolakis, H Araujo, P Arce, M Asai, D Axen, S Banerjee, G Barrand, et al. Geant4a simulation toolkit. *Nuclear instruments and methods in physics research section A: Accelerators, Spectrometers, Detectors and Associated Equipment*, 506(3):250–303, 2003.
- [64] Giulio D'Agostini. A multidimensional unfolding method based on bayes' theorem. *Nuclear Instruments and Methods in Physics Research Section A: Accelerators, Spectrometers, Detectors and Associated Equipment*, 362(2):487–498, 1995.
- [65] Joseph A Formaggio and GP Zeller. From ev to eev: Neutrino cross sections across energy scales. *Reviews of Modern Physics*, 84(3):1307, 2012.
- [66] Q Wu, SR Mishra, A Godley, R Petti, S Alekhin, P Astier, D Autiero, A Baldisseri, M Baldo-Ceolin, M Banner, et al. A precise measurement of the muon neutrino–nucleon inclusive charged current cross section off an isoscalar target in the energy range 2.5j 40 gev by nomad. *Physics Letters B*, 660(1):19–25, 2008.
- [67] AA Aguilar-Arevalo, CE Anderson, AO Bazarko, SJ Brice, BC Brown, L Bugel, J Cao, L Coney, JM Conrad, DC Cox, et al. First measurement of the muon neutrino charged current quasielastic double differential cross section. *Physical Review D*, 81(9):092005, 2010.
- [68] Veronique Bernard, Latifa Elouadrhiri, and Ulf-G Meißner. Axial structure of the nucleon. *arXiv preprint hep-ph/0107088*, 2001.
- [69] Hiroki Nakamura and Ryoichi Seki. Quasi-elastic neutrino-nucleus scattering and spectral function. *Nuclear Physics B-Proceedings Supplements*, 112(1):197–202, 2002.
- [70] RA Smith and EJ Moniz. Neutrino reactions on nuclear targets. *Nuclear Physics B*, 43:605–622, 1972.
- [71] R. Gran et al. Measurement of the quasi-elastic axial vector mass in neutrino-oxygen interactions. *Phys.Rev.*, D74:052002, 2006.
- [72] M. Dorman. Preliminary results for CCQE scattering with the MINOS near detector. *AIP Conf.Proc.*, 1189:133–138, 2009.
- [73] Vladimir Lyubushkin. A Study of Quasi-Elastic Muon (Anti)Neutrino Scattering in the NOMAD Experiment. *AIP Conf.Proc.*, 1189:157–162, 2009.
- [74] Marco Martini, Magda Ericson, Guy Chanfray, and Jacques Marteau. Unified approach for nucleon knock-out and coherent and incoherent pion production in neutrino interactions with nuclei. *Physical Review C*, 80(6):065501, 2009.
- [75] O Benhar, A Fabrocini, S Fantoni, and I Sick. Spectral function of finite nuclei and scattering of gev electrons. *Nuclear Physics A*, 579(3):493–517, 1994.

- 
- [76] Artur M Ankowski and Jan T Sobczyk. Argon spectral function and neutrino interactions. *Physical Review C*, 74(5):054316, 2006.
  - [77] Jakub Zmuda. Constructing efficient monte carlo generators. In *VANISH school*, 2014.
  - [78] Juan Nieves, M Valverde, and MJ Vicente Vacas. Inclusive nucleon emission induced by quasielastic neutrino-nucleus interactions. *Physical Review C*, 73(2):025504, 2006.
  - [79] Mar. Neutrino-nucleus interactions. In *NuInt 11*, 2011.
  - [80] The T2K colabration. Measurement of the flux averaged charge current inclusive muon neutrino cross section with ingrid and proton module. *T2K internal note*, TN-160.
  - [81] [http://www.epj-conferences.org/articles/epjconf/pdf/2013/16/epjconf\\_os2012\\_3002.pdf](http://www.epj-conferences.org/articles/epjconf/pdf/2013/16/epjconf_os2012_3002.pdf).
  - [82] Giulio D’Agostini. Improved iterative bayesian unfolding. *arXiv preprint arXiv:1010.0632*, 2010.
  - [83] Th Eichten, Dieter Haidt, JBM Pattison, W Venus, HW Wachsmuth, O Wörz, TW Jones, B Aubert, LM Chounet, P Heusse, et al. Particle production in proton interactions in nuclei at 24 gev. *Nuclear Physics B*, 44(2):333–343, 1972.
  - [84] James V Allaby, Alan M Thorndike, Pierre Duteil, Jean Pierre Peigneux, Jean-Pierre Stroot, Robert Meunier, Alan M Wetherell, EJ Sacharidis, Maurice Spighel, Freddy G Binon, et al. High-energy particle spectra from proton interactions at 19.2 gev/c. Technical report, Cern, 1970.
  - [85] CH Llewellyn Smith. Neutrino reactions at accelerator energies. *Physics Reports*, 3(5):261–379, 1972.
  - [86] Dieter Rein and Lalit M Sehgal. Neutrino-excitation of baryon resonances and single pion production. *Annals of Physics*, 133(1):79–153, 1981.
  - [87] Arie Bodek and Howard Budd. Neutrino quasielastic scattering on nuclear targets: Parametrizing meson exchange currents. Technical report, 2011.
  - [88] V Alan Kostelecký and Stuart Samuel. Spontaneous breaking of lorentz symmetry in string theory. *Physical Review D*, 39(2):683, 1989.
  - [89] Stephen W Hawking. Breakdown of predictability in gravitational collapse. *Physical Review D*, 14(10):2460, 1976.
  - [90] Ian Hinchliffe, N Kersting, and YL Ma. Review of the phenomenology of noncommutative geometry. *International Journal of Modern Physics A*, 19(02):179–204, 2004.
  - [91] V Alan Kostelecký and Neil Russell. Data tables for lorentz and c p t violation. *Reviews of Modern Physics*, 83(1):11, 2011.
  - [92] Don Colladay and V Alan Kostelecký. Lorentz-violating extension of the standard model. *Physical Review D*, 58(11):116002, 1998.
  - [93] V Alan Kostelecký and Ralf Lehnert. Stability, causality, and lorentz and cpt violation. *Physical Review D*, 63(6):065008, 2001.
  - [94] Teppei Katori. Tests of Lorentz and CPT violation with MiniBooNE neutrino oscillation excesses. *Mod.Phys.Lett.*, A27:1230024, 2012.
  - [95] V Alan Kostelecký and Matthew Mewes. Lorentz and cpt violation in neutrinos. *Physical Review D*, 69(1):016005, 2004.
  - [96] Jorge S Diaz, V Alan Kostelecký, and Matthew Mewes. Perturbative lorentz and c p t violation for neutrino and antineutrino oscillations. *Physical Review D*, 80(7):076007, 2009.

- [97] LB Auerbach, RL Burman, DO Caldwell, ED Church, AK Cochran, JB Donahue, AR Fazely, GT Garvey, R Gunasingha, RL Imlay, et al. Tests of lorentz violation in  $\nu^- \mu \nu^- e$  oscillations. *Physical Review D*, 72(7):076004, 2005.
- [98] Roger A. Wendell. Prob3++.
- [99] Stopping-power and range tables for electrons, protons, and helium ions, <http://www.nist.gov/pml/data/star/index.cfm>.
- [100] Emlyn Hughes. Study of hadronic and electromagnetic shower development between 10-GeV and 140-GeV by an iron scintillator calorimeter. 1990.
- [101] The T2K Collaboration. Measurement of the inclusive electron neutrino charged current cross section on carbon with the t2k near detector. *T2K internal note*, TN 187.
- [102] Private communication with takahiro hiraki.
- [103] T. T. The T2K collaboration. Internal study from event rate working group.
- [104] [http://en.wikipedia.org/wiki/fast\\_fourier\\_transform](http://en.wikipedia.org/wiki/fast_fourier_transform).
- [105] V Alan Kostelecký and Matthew Mewes. Lorentz violation and short-baseline neutrino experiments. *Physical Review D*, 70(7):076002, 2004.
- [106] P Adamson, C Andreopoulos, KE Arms, R Armstrong, DJ Auty, DS Ayres, B Baller, G Barr, WL Barrett, BR Becker, et al. Testing lorentz invariance and cpt conservation with numi neutrinos in the minos near detector. *Physical review letters*, 101(15):151601, 2008.
- [107] F James. Minuit, function minimization and error analysis, reference manual, version 94.1 cern program library long write-up d506. *CERN, Geneva*, 1994.
- [108] <http://j-parc.jp/researcher/hadron/en/pac1405/pdf/p5820142.pdf>.
- [109] P. Paganini. *Physique des particules avance: An introduction to the Standard Model of Particle Physics*. 2013.
- [110] S M Bilenky and Samoil M Bilen'kij. *Basics of introduction to Feynman diagrams and electroweak interactions physics*. Atlantica Séguier Frontières, 1994.
- [111] Murray Gell-Mann and Maurice Lévy. The axial vector current in beta decay. *Il Nuovo Cimento*, 16(4):705–726, 1960.

## Résumé

L'expérience T2K, située au Japon, est une expérience étudiant l'oscillation des neutrinos à longue distance. Elle vise à mesurer les paramètres décrivant ce phénomène d'oscillations quantiques, et plus particulièrement, l'angle de mélange  $\theta_{13}$ . Ce dernier est mesuré par la production de neutrinos muons à J-PARC et la détection de neutrinos électroniques 295 km plus loin, dans le détecteur Super-Kamiokande. Etant donné que T2K a mesuré un angle de mélange  $\theta_{13} \neq 0$  à plus de  $7\sigma$  de confiance, cela ouvre la possibilité de mesurer la phase de violation CP dans les expériences d'oscillation de neutrino. Par la mesure précise des paramètres d'oscillations, T2K a pour but d'apporter les premières contraintes sur l'existence possible d'une phase de violation CP dans le secteur leptonique.

Après avoir introduit la théorie d'oscillation des neutrinos ainsi que l'expérience, nous présentons le Générateur de Cone, un dispositif que nous avons développé afin de calibrer le détecteur lointain Super-Kamiokande. Nous étudions ensuite l'uniformité et l'isotropie de ce dernier, avant de mettre en évidence les différentes sources de désaccord entre les données et la simulation du détecteur. Nous montrons en particulier une imperfection dans la simulation de la réflexion de la lumière sur le mur du détecteur.

Par la suite, nous présentons la calibration du dépôt de charge que nous avons effectuée pour les détecteurs proches et sur axe, INGRID et le Module Proton. En particulier, nous observons un phénomène de diaphonie optique entre des scintillateurs d'un certain type, que nous avons corrigé. Cette calibration est ensuite utilisée pour effectuer la première mesure de section efficace double différentielle des interactions ( $CC0\pi$ ) des neutrinos avec le Module Proton. L'incertitude provenant des sections efficaces est l'une des sources principales d'erreurs sur la mesure des oscillations de neutrinos, et le canal  $CC0\pi$  est le canal principal d'interaction des neutrinos dans l'expérience T2K. Nous montrons que notre mesure est en accord avec les mesures récentes de l'expérience MiniBooNE.

Enfin, nous présentons la première recherche de signaux de violation de l'invariance de Lorentz dans l'expérience T2K. Nous montrons que les oscillations de neutrinos constituent l'une des sondes les plus sensibles pour ce phénomène. Nous dévoilerons d'abord les raisons de la recherche d'un tel effet, avant de présenter notre résultat de recherche de violation d'invariance de Lorentz qui utilise le détecteur INGRID nouvellement calibré. Nous montrons qu'aucun effet de cette violation n'est observé dans ce détecteur proche de T2K.

**Mots-clés :** T2K, oscillations de neutrino, angle de mélange  $\theta_{13}$ , Super-Kamiokande, Générateur de Cone, INGRID, section efficace, CCQE,  $CC0\pi$ , violation de l'invariance de Lorentz

## Abstract

The T2K experiment is a long baseline neutrino oscillation experiment located in Japan. It aims to measure the parameters describing this quantum phenomenon, and particularly, the mixing angle  $\theta_{13}$ . The latter is measured through the production of a muon neutrino at J-PARC and detection of an electron neutrino 295 km away, at Super-Kamiokande. Since T2K has measured that  $\theta_{13} \neq 0$  with more than  $7\sigma$  CL, it leads to the possibility to observe CP violation phase through neutrino oscillation. Through the accurate measurement of the oscillation parameters, T2K aims to determine the first constraints on the CP violation in the leptonic sector.

After presenting the theory of neutrino oscillations and the T2K experiment, this thesis first presents the calibration setup, the Cone Generator, that we developed for the Super-Kamiokande far detector. We study the detector uniformity and isotropy, and disentangle the different sources of discrepancies with the detector simulation. We particularly highlight a discrepancy in the simulation of the light reflection on the detector wall.

Second, we present the calibration of the charge deposit in the on-axis near detectors, INGRID and the Proton Module. We show that an optical cross-talk between the scintillators of one type is observed, and we correct it. This calibration is used for the first measurement of the  $CC0\pi$  double differential cross section in the Proton Module. The cross section uncertainty is one of the dominant error on neutrino oscillations, and the  $CC0\pi$  channel is dominant in T2K interactions. We show that this measurement is in agreement with the recent results of MiniBooNE.

Finally, we present the first Lorentz invariance violation search in the T2K experiment. We show that the neutrino oscillations are one of the most sensitive probes for this effect. We first review the motivations of this search and then present the result using the calibrated INGRID detector. We show that no Lorentz invariance violation is observed in the T2K near detector.

**Keywords :** T2K, neutrino oscillations,  $\theta_{13}$  mixing angle, Super-Kamiokande, Cone Generator, INGRID, cross section, CCQE,  $CC0\pi$ , Lorentz violation